

Understanding and Engineering Molecular Order in Organic Semiconductors

A DISSERTATION
SUBMITTED TO THE FACULTY OF
UNIVERSITY OF MINNESOTA
BY

Thomas Robert Fielitz

IN PARTIAL FULFILLMENT OF THE REQUIREMENTS
FOR THE DEGREE OF
DOCTOR OF PHILOSOPHY

Russell J. Holmes, Advisor

August 2017

© Thomas Robert Fielitz, 2017

ACKNOWLEDGEMENTS

It is my great pleasure to acknowledge the many people who have helped me with the work in this thesis. First, my advisor, Russ Holmes, has critically shaped my academic development in ways I could not have foreseen five years ago. His technical acumen, insatiable curiosity, and insightful questioning are far better than I could ask for and will influence the way I work for years to come. The Holmes Group has similarly provided a superb environment in which to work and play, and for that I am grateful to those I have been lucky enough to interact with – Richa, Kai, Nick, Matt, Yunlong, Tyler, Nathan, Yi, Whitney, Meng, Ian, Kyle, Abbey, Gang, Tao, Deepesh, Catherine, John, and Kaicheng.

I have had the privilege of helpful and stimulating conversation with many people in the department, but especially Alyssa McKenna, Jeff Peterson, Claire Morgan, Ed Cussler, and Mike Manno. I also thank my friends, whose jokes, personalities, and friendship helped the last five years pass with much laughter and happiness. My time here has been made much more productive by the excellent staff, especially Teresa Bredahl, Julie Prince, Gayle Gabrielski, and Courtney Billing in CEMS, Greg Haugstad, Javier Garcia Barriocanal, and Joel Overlander in Charfac, and Bill Voje in the Physics Student Machine Shop.

It has also been my good fortune to serve as a mentor for several high school students and undergraduates. Their fundamental questions and unique skill sets pushed me to become a better teacher and scientist, and for that I am grateful to Wolfie, Easton, Sung-Wan, and Jiaheng from Breck School, and Chris and Trevor from the U. I would like to especially acknowledge Chris, who put up with two years of my questionable research ideas and still managed to produce useful data, a paper, and an honors thesis along the way.

Some work in this thesis required skills and equipment which were much easier to borrow than acquire. I would like to particularly thank Dan Cremons for several rounds of beautiful TEM images and patterns critical to Chapter 10. I would also like to thank Mike Manno and Javier Garcia Barriocanal for providing insightful XRR data in Chapter 10. Mike Toney and Chris Tassone at the Stanford Synchrotron Radiation Lightsource were instrumental in helping me collect and interpret the patterns in Appendix H.2. Finally, I am grateful to the groups of Dan Frisbie and Paul Dauenhauer who allowed me use of their AFM and high-speed camera, respectively.

I am very grateful to have been funded by the Peter and Gene Pierce Family Fellowship, the Erling A. Dalaker Fellowship, the University of Minnesota Initiative for Renewable Energy and the Environment, and by NSF grants DMR-1307066. That I was fully supported to do this work is truly the icing on the cake, and is sincerely appreciated.

DEDICATION

I dedicate this thesis to all of my teachers and mentors, especially my parents Rob and Cathy, sister Laura, and partner in science and life Alyssa McKenna.

Without your constant support and guidance,
I would not be who I am or where I am today.

ABSTRACT

Organic semiconductors often exist in disordered material phases which have sub-optimal optical and electrical properties. Bringing some degree of order to these materials with crystals and even oriented amorphous phases has been shown to be fruitful for many applications, but is challenging to achieve. This is largely because of the variability between different materials and poorly understood dynamics in device-relevant thin films. This thesis describes progress towards understanding and tuning crystallization and ordering in organic thin films to realize enhancement in parameters relevant to organic optoelectronic devices.

In particular, this thesis demonstrates that in thin-film crystallization processes, the crystal structure, crystal shape, and growth type can be controlled most effectively with film thickness, temperature, and strategic incorporation of secondary additives within the film. These variables change the rate at which crystals grow as well as the crystal shape during growth by altering the ability of molecules to attach and conform to the growing crystal front. When films are heated to bring about these processes through increased molecular mobility, secondary processes may occur to transform the microscopic film morphology through the addition, subtraction, and long-range motion of material. This motion can be connected to substrate-film interactions and the material phase of the starting film. Material interactions within the film bulk can kinetically trap molecular conformations, with the extent of this trapping depending on interaction type and deposition conditions. These properties can be further exploited to produce useful and spontaneous structures within a thin film.

Ultimately, the desired result of ordering an organic semiconductor is to produce more efficient and stable structures for devices. This is demonstrated here through engineering the motion of excited states with crystallization, then applying such techniques to different organic solar cell geometries to study how different crystallization methods affect device properties. First, the mobility of excited states in boron subphthalocyanine chloride (SubPc), an archetypal organic solar cell molecule, is shown to increase upon crystallization with rigorous calculations explaining the origin. Such an increase provides motivation to study the effects of induced crystallization *via* homoepitaxial growth using the well-studied transistor material rubrene in a solar cell geometry. This serves as a platform by which to generalize the study to mixed epitaxial growth in a material which is not intrinsically crystalline, showing marked morphological and electronic changes with changes in mixture composition. This is ultimately applied to heteroepitaxial growth of SubPc, which does not crystallize when deposited onto a template at ambient temperature. These projects explore crystallization techniques as a solution to improve the performance of organic solar cells, resulting in an improved fundamental understanding of such processes and avenues for future progress.

TABLE OF CONTENTS

Acknowledgements	i
Dedication	ii
Abstract.....	iii
Table of Contents	iv
List of Tables	xi
List of Figures.....	xii
Variables, Symbols, Acronyms, and Chemicals	xxxi
1. Organic Electronic Devices	1
1.1. Uses of Organic Electronics	1
1.1.1. Light-Emitting Devices.....	2
1.1.2. Photovoltaic Cells	2
1.1.3. Field-Effect Transistors	3
1.2. Challenges for Organic Electronic Devices.....	4
1.2.1. Durability and Reliability	5
1.2.2. Efficiency	5
1.2.3. Scaling Device Size	6
1.2.4. Yield and Reproducibility.....	7
1.3. Scope and Relevance of This Thesis	7
2. Organic Semiconductors	8
2.1. Energetics and Optical Behavior	8
2.1.1. Intramolecular Bonding and Effects	8
2.1.2. Optical Absorption and Emission	12
2.1.3. Energy Level Determination Methods.....	13
2.2. Excitons	15
2.2.1. Wannier-Mott Excitons.....	15
2.2.2. Frenkel Excitons	15
2.2.3. Charge-Transfer or Exciplex.....	16
2.2.4. Exciton Recombination.....	17
2.3. Exciton Motion	17
2.3.1. Cascade Energy Transfer	18
2.3.2. Förster Energy Transfer	19
2.3.3. Dexter Energy Transfer.....	23
2.3.4. Comparison of Energy Transfer Methods.....	24

2.4. Polarons	27
2.5. Polaron Motion	27
2.6. Exciton and Polaron Transport Equations	29
2.6.1. Diffusion	30
2.6.2. Drift (Advection) and Drift-Like Transport.....	34
2.7. Function and Characterization in Devices	38
2.8. Conclusions.....	40
3. Phases and Crystallization of Organic Materials	41
3.1. Bonding and Solid Phases.....	41
3.1.1. Intermolecular Bonding	42
3.1.2. Amorphous.....	42
3.1.3. Glass.....	44
3.1.4. Crystal	47
3.2. Crystal Growth Mechanisms	50
3.2.1. Theory of Crystal Nucleation, Growth, and Shape.....	50
3.2.2. Types of Growth and Transitions	55
3.3. Crystal Growth Techniques	57
3.3.1. Vapor-Solid.....	58
3.3.2. Liquid-Solid	61
3.3.3. Solid-Solid	63
3.4. Material Deposition	64
3.4.1. Vapor-Phase	64
3.4.2. Liquid-Phase	66
3.5. Conclusions.....	67
4. Crystallization of Annealed Rubrene Films	68
4.1. Introduction.....	68
4.1.1. Rubrene	70
4.2. Polymorphs and Selection Methods	71
4.2.1. Rubrene Polymorphs.....	72
4.2.2. Heating Rate Effects	74
4.2.3. Annealing Temperature Effects	75
4.2.4. Film Thickness Effects.....	77
4.2.5. Effects of Light	78
4.2.6. Selection Mechanisms	79
4.3. Crystal Growth Mode and Shape	83
4.3.1. Crystal Growth Mode.....	83
4.3.2. Crystal Shape	86
4.3.3. Proposed Growth Mechanism.....	89

4.4. Crystal Growth Rate and Activation Energy	92
4.5. Conclusions.....	95
5. Manipulating Rubrene Crystal Shape and Growth	97
5.1. Introduction.....	97
5.2. Additive Concentration Effects	99
5.3. Additive Location Effects	100
5.4. Crystal Growth Rate and Aspect Ratio	102
5.5. Film Morphology Effects.....	104
5.6. Varying Additive Type	106
5.7. Directions of Interest	107
5.8. Conclusions.....	108
6. Highly Periodic Small-Molecular Weight Organic Films by Annealing	109
6.1. Introduction.....	109
6.2. Film Transformation	111
6.3. Surface Morphology	114
6.4. Proposed Mechanism.....	115
6.5. Optical Properties	119
6.6. Conclusions.....	121
7. Engineering Exciton Diffusion with Crystallization.....	122
7.1. Introduction.....	122
7.2. Exciton Diffusion Length Measurement.....	123
7.3. Enhancements in Excitonic Energy Transfer.....	126
7.4. Effects of Changes in Optical Properties	127
7.5. Molecular Aggregation	127
7.6. Effects of Changes in Molecular Configuration	130
7.7. Effects of Film Roughness.....	137
7.8. Effects of Site Energy Distribution.....	140
7.9. Theoretical Limitations.....	143
7.10. Conclusions.....	144
8. Describing Exciton Transport in Energy-Cascade Structures	146
8.1. Introduction.....	146
8.2. The Validity of Exciton Motion as Diffusive	147
8.3. Exciton Gates as Advective Transport.....	149
8.3.1. Derivation of an Exciton Velocity	150
8.3.1. Velocity Edge Effects	152
8.4. Posing the Problem	153
8.5. Equilibrium Conditions.....	154
8.6. Non-Equilibrium Conditions	158
8.7. Numerical Solution for the General Case	159

8.8. Model Validation	160
8.8.1. Boundary Layer Effects in Neat Film	160
8.8.2. Comparison to Monte Carlo Simulations	161
8.9. Model Results	162
8.10. Conclusions.....	164
9. Homoepitaxy and Mixture Epitaxy in OPVs	165
9.1. Introduction.....	165
9.2. Homoeptaxy.....	166
9.2.1. Film Growth and Characterization.....	167
9.2.2. Homoeptaxial Devices	170
9.3. Mixture Epitaxy	172
9.3.1. Mixture Epitaxy with an Inert Additive.....	173
9.3.2. Mixture Epitaxy with C ₆₀	176
9.4. Discussion of Mixture Epitaxial Growth.....	179
9.5. Conclusions.....	181
10. Molecular Templating in SubPc OPVs.....	182
10.1. Introduction.....	182
10.2. Template Optimization	183
10.3. Heterostructure Morphology Characterization	185
10.3.1. Surface Characterization	185
10.3.2. Structural Characterization	188
10.4. Optical Characterization	195
10.5. Planar Heterojunction Devices	197
10.5.1. Device Parameters	197
10.5.2. Charge-Transfer State Energy.....	200
10.5.3. Exciton Diffusion Length Measurement.....	202
10.5.4. Alternative Electron Acceptors	208
10.6. Alternate Device Architectures.....	210
10.6.1. Mixture and Gradient Heterojunction Devices	211
10.6.2. Dilute Donor Devices.....	213
10.6.3. Schottky Devices	215
10.7. Conclusions.....	217
11. Future Work.....	219
11.1. Shape Selection in Thin Films	219
11.1.1. Mechanism Determination and Generalization	220
11.1.2. As a Means to Detect Molecular Concentration and Diffusion	222
11.1.3. Optoelectronic Properties of Mixed Crystals.....	223
11.2. Role of Mechanical Strain on Ordering.....	224

11.3. Ordered Glasses in OLEDs	225
11.3.1. Film Thermodynamics, Kinetics, and OLED Performance	225
11.3.2. Crystallization	227
11.4. Imaging Ultrafast Organic Semiconductor Dynamics	228
11.4.1. Structural Dynamics.....	228
11.4.2. Exciton and Polaron Dynamics.....	230
12. Conclusions.....	235
12.1. Annealing-Induced Crystallization in Organic Films	235
12.2. Epitaxial Growth of Crystalline Organic Films.....	237
12.3. Optoelectronic Properties of Crystalline Organic Films.....	239
12.4. Outlook	240
13. Bibliography	242
14. Appendices.....	277
Appendix B. Publications	278
Appendix B. Presentations	279
B.1. Oral Presentations	279
B.2. Poster Presentations	279
B.3. Awards	280
Appendix C. Copyright Permissions	281
Appendix D. Characterization Techniques	283
D.1. Optical Spectroscopy	283
D.2. Microscopy	289
D.3. Structural and Energetic.....	297
D.4. Optoelectronic	299
Appendix E. AFM Scan Rate Limitations	303
E.1. Fundamental Limitations of Scan Rate	304
E.2. Alternating Contact (Tapping) Mode	306
E.3. Contact Mode	308
E.4. Conclusions	310
Appendix F. Photovoltage <i>LD</i> Measurement <i>Voc</i> Effects.....	311
Appendix G. Derivations and Discussion of Energy Transfer.....	314
G.1. Classical Derivation of Förster Energy Transfer	314
G.2. Quantum-Mechanical Derivation of Förster Energy Transfer	316
G.3. Derivation Consequences for Förster Theory	318
G.4. Förster Energy Transfer in Anisotropic Media.....	320

G.5. Quantum-Mechanical Derivation of Dexter Energy Transfer	323
Appendix H. Additional Images from Chapter 10.....	326
H.1. BP2T Template Optimization	326
H.2. SubPc, C ₆₀ , and C ₇₀ Synchrotron Characterization.....	331
H.3. BP2T, SubPc, and C ₆₀ TEM Characterization	335
H.4. Kelvin Probe Force Microscopy Measurements.....	337
H.5. External Quantum Efficiency Fitting Plots	338
Appendix I. Secondary Film Evolution Mechanisms	340
I.1. Introduction	340
I.2. Flow and Capillarity	341
I.3. Sublimation and Deposition	343
I.4. Diffusion: Surface and Bulk	344
I.5. Surface Reactions and Adsorbates	344
Appendix J. Selected Organic Molecule Crystal Lattice Parameters.....	346
J.1. OLED Materials	346
J.2. Acenes and Acene Cores.....	347
J.3. Phthalocyanines and SubPhthalocyanines	348
J.4. Fullerenes	349
J.5. Perylenes and Related	349
J.6. Miscellaneous Organics	350
J.7. Common Substrate Materials	350
Appendix K. Selected Organic Semiconductor Properties	351
Appendix L. Inventions	354
L.1. Heated Microscope Stage	354
L.2. Gradient Heater	358
L.3. Heated Ellipsometry Stage	360
Appendix M. High School Mentor Projects	364
M.1. Melt Crystallization of Anthracene	364
M.2. Growth and Characterization of Optically-Pumped Organic Lasers	369
Appendix N. Substrate Cleaning and Film Annealing Procedure	372
N.1. Substrate Cleaning	372
N.2. Film Annealing	374
Appendix O. Morphology of ITO, Glass, and Metals.....	375
O.1. Indium Tin Oxide Films on Glass.....	375
O.2. Metals: Evaporated Aluminum, Silver, and Gold.....	377
Appendix P. Chamber Chuck Rotation and Heating.....	378

Appendix Q. Finite Difference Methods	379
Appendix R. Relevant Computer Software	382
R.1. Transfer Matrix Model (Matlab)	382
R.2. Microscope Image Capture (Fiji/ImageJ)	388
R.3. Image Compilation and Sorting (Matlab)	390
R.4. Crystal Growth Image Analysis (Fiji/ImageJ)	392
R.5. Crystal Growth Fitting (Matlab)	428
R.6. TEM Diffraction Pattern Simulation (Matlab).....	436
R.7. Simulating Energetic Disorder in Exciton Diffusion with KMC (Matlab).....	441
R.8. AFM Tip Motion Simulation (Matlab)	446
R.9. Finite Element Exciton Gating Code (Matlab)	447

LIST OF TABLES

Table 2.1. Cascade energy transfer efficiency ($\eta C E T$, %) and apparent cascade exciton diffusion length ($L D$, nm) for films of different materials and thickness. $\eta P L$ values are given next to material names (%).	19
Table 4.1. Rubrene crystal structures, lattice parameters, and crystallization conditions. An asterisk next to a reference denotes the source of the listed lattice parameters for each crystal system. X = not observed.	73
Table 4.2. Comparison of calculated and measured facet angles corresponding to those measured in Figure 4.13a-b.....	87
Table 4.3. Planar densities, spacing, and growth rates for orthorhombic rubrene.....	89
Table 4.4. Measured activation energy E_a , Arrhenius prefactor r_0 , and interpolated growth rate at 160°C r 160°C for orthorhombic (O) and triclinic (T) rubrene on ITO.....	94
Table 7.1. Radiative and non-radiative exciton decay rates for the 710-nm (aggregate) peak	129
Table 7.2. Simulated and experimental $L D$ values (nm) for amorphous (A) and crystalline (X) films.....	140
Table 10.1. Fitted parameters for the XRR measurements shown in Figure 10.10, including film thickness, density (ρ), and roughness (σR) for the different layers and stacks.	194
Table 10.2. Fitted $\eta E Q E$ parameters for the devices in Figure 10.18.	204
Table 10.3. Calculated exciton diffusion lengths for the devices in Figure 10.21.	207

LIST OF FIGURES

Figure 1.1. OLED applications including (a) a foldable concept phone (Lenovo), ²⁰ (b) plate chandelier (OLEDworks/Carl Stahl Architektur), ²¹ and (c) rollable television (LG). ²²	2
Figure 1.2. OPVs in (a) simplified installation (Heliatek), ³⁵ (b) flexible panels (InfinityPV), ³⁶ and (c) rooftop solar at the African Union, Addis Ababa, Ethiopia (OPVius). ³⁷	3
Figure 1.3. OFETs in (a) flexible circuit roll (PolyIC) ⁴⁶ and (b) a transparent, flexible printed RFID tag (PolyIC). ⁴⁷	4
Figure 1.4. Examples of degradation of (a) normalized OLED luminance from Giebink <i>et al.</i> , ⁵⁶ (b) normalized OPV power conversion efficiency from Gevorgyan <i>et al.</i> , ⁷² and (c) OFET sensing response with and without analyte (red and blue arrow, resp.), from Yun <i>et al.</i> ¹⁵	5
Figure 1.5. Examples of (a) dark spot formation in OLED light emission, and (b) an SEM image showing OLED cathode delamination and active layer crystallization after use. Figure adapted with permission from Smith <i>et al.</i> ⁵⁹	7
Figure 2.1. Molecular orbital diagrams of (a) H ₂ and (b) N ₂ , with schematics of (c) s orbitals in a σ bond, (d) p orbitals in a σ bond, and (e) p orbitals forming π bonds	9
Figure 2.2. Molecular orbital energy manifold plotted over the molecular coordinate, or the molecular state in real space, including vibrational energy. The vibrational modes are drawn over each harmonic.	10
Figure 2.3. Schematic showing electron spin configurations in a (a) singlet and (b) triplet excited state	10
Figure 2.4. (a) Jablonski diagram showing excitonic processes in singlet (S ₀ , S ₁) and triplet (T ₁) manifolds with approximate timescales: 1. Excitation (~1 fs) 2. Relaxation (10 fs-10 ps) 3. Fluorescence 1-100 ns 4. Intersystem crossing (10-1000 ps) 5. Phosphorescence (1 μ s-100 s). (b) Fictional absorption (1) and emission (3) spectra for an organic molecule, with the vibrational transitions labeled for (1) S ₀ \rightarrow S ₁ and (3) S ₁ \rightarrow S ₀ . Spectral shape in real molecules would be determined by Franck-Condon factors	12
Figure 2.5. Methods of determining energy levels in organic semiconductors (a) ultraviolet photoelectron spectroscopy (UPS), (b) inverse photoelectron spectroscopy (IPES), (c) optical absorption, and (d) cyclic voltammetry. Other variables explained in the text.	14
Figure 2.6. Photoconversion process in OPVs, showing the processes and efficiencies of absorption (ηA), exciton diffusion (ηD), charge transfer (ηCT), charge separation (ηCS), and charge collection (ηCC)	16

Figure 2.7. Diagrams showing different definitions of the orientation factor, with (a) purely geometric and (b) based on the donor electric field. Variables defined in the text ...	21
Figure 2.8. Diagram of rotating exciton donor μD and acceptor μA transition dipoles ..	23
Figure 2.9. Schematics for (a) Förster and (b) Dexter energy transport, with the resulting distance dependence (c) for each style of motion. The calculations in (c) are for arbitrary molecules with $R0 = 1 \text{ nm}$ and $\tau = 1 \text{ ns}$ (Förster) and $KJ = 1011 \text{ s} - 1$, $L = 1 \text{ \AA}$, and $\tau = 1 \mu\text{s}$ (Dexter). ^{198,876}	25
Figure 2.10. Exciton diffusion lengths as a function of kR and kNR for (a) Förster energy transfer, with $R0/\eta PL = 1 \text{ nm}$ and a cubic lattice of $a = 1 \text{ nm}$, and (b) Dexter energy transfer, with $kD = 109 \text{ s} - 1$	26
Figure 2.11. Marcus electron transfer diagram, showing (a) normal activated transfer ($ \Delta Go < \lambda$), (b) transfer with the minimum energy barrier ($ \Delta Go = \lambda$), and (c) inverted regime, where increased driving force causes an increase in the activation energy between states ($ \Delta Go > \lambda$).....	28
Figure 2.12. Diagram showing (a) energy or electron transfer from molecule i to j with rate kij and (b) the first four molecular shells for an arbitrary two-dimensional lattice..	31
Figure 2.13. Electrical characterization of organic solar cells by sweeping the applied voltage (V) and measuring the resulting current (current density, J) passing through the device ..	38
Figure 2.14. External quantum efficiency of rubrene:C ₆₀ devices for different C ₆₀ concentrations ..	39
Figure 3.1. Example plots of transitions between liquid and solids, with (a) showing regions of (I) glass, (II) transition, (III) supercooled liquid (SCL), and (IV) equilibrium liquid. The glass transition, fictive, and onset temperatures (Tg , Tf , TO) are identified by extrapolation of the glassy region to the liquid line (green dots). (b) shows the effects of cooling rate on liquid-glass transitions (blue lines) and film stability on glass-liquid transitions (red). Intersection of the liquid line with crystal leads to the paradoxical Kauzmann temperature, TK	46
Figure 3.2. Interaction of molecules with a substrate in (a) very thin films, showing the conjugated molecular orbitals coordinating with a polar substrate in a face-on arrangement, (b) thick films where substrate interactions dominate, and (c) thick films where intermolecular interactions are dominant.....	47
Figure 3.3. Effects of the excitonic density of states width σ on exciton diffusion. Schematics of (a) exciton trapping in the limit $\sigma > kBT$ and (b) activated hopping when $\sigma \leq kBT$, and (c) statistics of LD as a function of σ , calculated using Kinetic Monte Carlo simulations for $5 \leq \sigma \leq 75 \text{ meV}$ and $T = 295\text{K}$. ²⁹⁷ In both (a) and (b), the total number of sites are the same, but the number of deep ($>kBT$) traps is lower in (b). The y-axis of (c) is the probability of each diffusion length occurring out of 10^4 trials,	

with each value of σ represented by a different color.	48
Figure 3.4. Crystal shape determination (a) polar plot of crystal surface energy as a function of crystal surface normal direction $\gamma(\mathbf{n})$, (b) a growing crystal with (I) invisible and (II) observed planes, and (c) growing crystal with growth rates g_i and distances l_i from the crystal center to plane normal.	51
Figure 3.5 Diagram of plane 2 “growing out” of a crystal. In this case, $g_2 \approx g_1 + g_3$	52
Figure 3.6 Attachment sites for material adding to a growing crystal with coordination number 1 (a), 2 (b), 3 (c), and 4 (d).	54
Figure 3.7. Thermal motion in an anthracene crystal, adapted from Sleigh <i>et al.</i> ⁴¹⁹	55
Figure 3.8. Examples of (a), (c) single crystal growth, (b), (d) spherulite growth, and dendritic growth in the inset of (a). Scale bars in (a)-(b) 100 μm , (c)-(d) 10 μm . For more information about these images, see (a)-(b) Figure 4.11, (c)-(d) Figure 4.12, and inset of (a) Figure 5.8.....	56
Figure 3.9. General classes of crystal growth, with those in red boxes applicable to organic semiconductors, and those in solid red boxes common in organic semiconductors. Based on a figure in Pamplin <i>et al.</i> ²⁷⁹	57
Figure 3.10. Example of a physical vapor deposition system. Within an evacuated high-vacuum chamber, sources containing the deposition material are heated resistively, subliming material into a vapor plume which condenses onto a substrate to form a film.	58
Figure 3.11. Schematic of a physical vapor transport system. A carrier gas enters on the left (laminar flow velocity profile shown) and blows over a source holding the deposition material. Heat from the surrounding furnace evaporates or sublimes the material into a plume which is conveyed to the right by the carrier gas, condensing onto a substrate to form a film. Excess gas exits the tube, typically to a low-vacuum pump to maintain a desired chamber pressure.	59
Figure 3.12. Examples of homoepitaxial growth, showing (a) regions of substrate, template, and epitaxial layer, (b) magnified view of the epitaxial region showing screw dislocation sites, and molecular terraces in the inset of (b). Inset scale bar is 300 nm. For additional information on these images, see Figure 9.2.....	60
Figure 3.13. Deposition chamber used for this thesis, with (a) source, (b) QCM, (c) shutter, (d) substrate holder, and (e) substrate heater.	66
Figure 3.14. Example spin coating process.	67
Figure 4.1. Rubrene molecule as (a) chemical structure, and in solid phase viewed (b) along and (c) perpendicular to the tetracene backbone, phenyl rings colorized to emphasize staggering. Images generated using Mercury 3.3 software. ⁷⁸⁹	70
Figure 4.2. The reversible oxidation and cycloreversion of rubrene (1) to an endoperoxide	

(2), followed by irreversible pyramidalization by loss of phenol to (3).....	71
Figure 4.3. Rubrene molecular and crystal structures: (a) solid phase rubrene molecule, (b) triclinic, (d) orthorhombic, and (e) monoclinic crystal structures. For clarity, only the tetracene backbone of rubrene is shown in the crystal structures. (c) shows the appearance of (I) amorphous, (II) orthorhombic, and (III) triclinic regions between crossed polarizers.....	72
Figure 4.4. (a) XRD spectra of annealed films containing orthorhombic and triclinic rubrene, with unit cell orientations of the orthorhombic ⁴⁸² (b) and triclinic ⁶⁰⁹ (c) unit cell inferred from 2D XRD with samples grown, annealed, and measured on silicon.	73
Figure 4.5. (a) DSC heating trace for amorphous rubrene, 80 °C/min adapted from Lee <i>et al.</i> ⁴⁵¹ (b) Comparison DSC traces for vapor-deposited rubrene at different heating rates. Both plots are exothermic heat flow upward.	74
Figure 4.6. Cu K α XRD on rubrene powders scraped from DSC pans heated at different rates, then scraped onto double-sided tape on a silicon wafer piece. Both polymorphs appear prominently, regardless of heating rate, implying that heating rate alone is insufficient to control polymorph composition.....	75
Figure 4.7. (a) Polymorph selection by choice of annealing temperature. Each temperature represents three 20-nm films on ITO annealed for three minutes.	76
Figure 4.8. (a) Polymorphic composition of completely annealed rubrene films as a function of annealing temperature. Each data point represents multiple films on ITO, with the error bars describing the standard deviation between films. (b) Appearance of (I) orthorhombic and (II) triclinic rubrene grown at 200 °C (inset at 160 °C, 100 μ m scale) in a 64 nm film.....	77
Figure 4.9. Polarized optical micrographs of 64 nm rubrene films annealed at 170 °C with (a) 300 and (b) 120 mW/cm ² of light during annealing. The area illuminated during annealing is the dotted hexagon. (c) Film composition as a function of illumination power, inset showing the incandescent tungsten microscope lamp spectrum with increasing power.	78
Figure 4.10. Unpolarized episcopic optical micrographs showing the process of rubrene cross-nucleation and grain ripening on ITO at 170°C as a function of time after annealing begins. (a) Amorphous film at t = 6.2 s; (b) triclinic and orthorhombic nuclei at t = 10.1 s; (c) cross-nucleation of orthorhombic grains on triclinic spherulites at t = 12.5 s, highlighted in white ovals; (d) continuing cross-nucleation and growth of orthorhombic rubrene at t = 16.9 s; (e) complete truncation of triclinic growth at t = 23.5 s; (f) grain ripening (t = 218.6 s), showing grain boundaries between different orthorhombic regions and cross-nucleation sites extracted from these boundaries depicted by white dots.	80
Figure 4.11. Polarized optical micrographs of orthorhombic rubrene growth on ITO viewed	

at (a), (b) 162°C and (c), (d) 179°C (scale bar 100 µm). The inset of (c) is the calculated intensity of an ideal, radially symmetric birefringent polycrystal.	84
Figure 4.12. Atomic force micrographs of orthorhombic rubrene films grown on silicon and annealed at (a) 160°C, (b) 170°C, and (c) 200°C. Scale bars 10 µm. Growth on silicon reduces the triclinic-orthorhombic transition temperature by approximately 10°C but does not change the observed morphology trend.	87
Figure 4.13. Determination of crystallographic axes and correspondence to grain location at high temperature. (a) and (b) AFM images of rubrene on ITO, annealed at (a) 170°C for 180 seconds and (b) 180°C for 600 seconds, scale bars 3 µm.	88
Figure 4.14. Planar density diagrams for orthorhombic rubrene planes: (a) (001), (b) (100), (c) (010), and (d) {110}. Diagrams to scale.	88
Figure 4.15. Diagram of the orthorhombic growth transitions during rubrene thin film annealing, showing (a) nucleation of the orthorhombic polymorph, with the red arrows denoting the local direction of the b axis, (b) growth front of the {110} devolving into individual rays of crystalline material, (c) continued disorientation of branching crystals, and (d) termination of the core single crystal growth.	90
Figure 4.16. Contrast between films on ITO annealed past complete crystallization at (a) 170°C, 180 seconds and (b) 210°C, 300 seconds. (a) is an atomic force micrograph, scale bar 3 µm; (b) is an optical micrograph, scale bar 50 µm. At low temperature, the holes which appear in the ripening crystal are faceted and aligned across the crystal, whereas the high temperature crystals show a more centrosymmetric deterioration.	91
Figure 4.17. (a) Plot of crystal dimensions as a function of time at 160°C, showing the average radius of triclinic spherulites and crystal radius along the [100] and [010] directions of orthorhombic grains. All crystals shown nucleated in the bulk. (b) Plot of the growth rates of the identified crystal planes for the orthorhombic polymorph and the average growth rate of triclinic spherulites, where the {110} growth is calculated from the measured growth along [010]. All films are 20-nm-thick on ITO-coated glass substrates.....	93
Figure 5.1. . Crystal shapes at different compositions (vol% TPBi) and annealing temperatures: (a) 0, 160 °C (b) 10, 170 °C (c) 15, 170 °C (d) 15, 190 °C (e) 20, 170 °C (f) 25, 170 °C (g) 80, 200 °C (h) 90, 190 °C and (i) 100, 190 °C. The inset molecular structures are (a) rubrene and (i) TPBi. Annealing times in seconds are inset in the upper-right corner of each image, and all images are polarized optical micrographs.	99
Figure 5.2. Effects of additive location on crystal shape in annealed rubrene films, including linearly graded films with the composition varied from (a) 20-0 vol% TPBi, (b) 0-20 vol% annealed at 180 °C, and uniformly mixed 35 vol% TPBi films at (c) 53, (d) 71, and (e) 75 sec and 210 °C. White arrows highlight the new growth of dark and light TPBi-rich phases. All images are polarized optical micrographs.	101

Figure 5.3. Thermogravimetric data for rubrene and TPBi showing (a) percent mass loss with temperature and (b) mass loss rate with temperature, plotted on an Arrhenius plot.	102
Figure 5.4. Properties of rubrene films with varying TPBi concentration: (a) maximum crystal aspect ratio, (b) nucleation time, t_{Nuc} , and (c) growth rate along the elongated crystal axis.	103
Figure 5.5. X-ray diffraction patterns for films of varying TPBi compositions (vol% TPBi) on ITO.	104
Figure 5.6. Topography and temperature dependence of 20 vol% TPBi films. (a) Atomic force micrograph of a crystal grown at 190 °C, (b) unpolarized optical micrograph of light-colored depleted regions around growing crystals in a film quenched after annealing at 180 °C, and polarized optical micrographs showing branching of crystals grown at (c) 185 and (d) 200 °C.	105
Figure 5.7. AFM profiles and corresponding micrographs for a 25 vol% TPBi film annealed for 30 seconds at 190 °C: (a) profile along the needle length shown in (c); (b) profiles perpendicular to the needle length as shown in (d). The profile in (a) is offset from (b) by +50 nm. Arrows denote the (a) needle tip and (b) needle center. Scale bars in (c)-(d) are 10 μm with a logarithmic height scale of 156 nm.	105
Figure 5.8. Polarized optical micrographs of crystal shapes of rubrene doped with (a) 30 vol% α-NPD at 190 °C, (b) 15 vol% 4p-NPD at 180 °C, (c) 10 vol% TCTA at 180 °C, and (d) 10 vol% TCTA and 10 vol% TPBi at 180 °C.	106
Figure 6.1. Unpolarized optical micrographs of TPBi films annealed at different temperatures: (a) 180 °C, (b) 175 °C, (c) 190 °C. Arrows depict the direction of crystal growth, and the insets of (a) and (c) are Fast Fourier Transforms (FFTs) of the images, showing periods centered at (a) 1.23, 0.73, 0.6, and 0.53 μm, and (c) 1.2-1.3 and 0.25-0.3 μm. Films are 30 nm with a 60 nm epitaxial TPBi layer deposited after annealing to improve visibility. All scale bars are 20 μm.	111
Figure 6.2. Unpolarized optical micrograph of a TPBi film annealed at 180 °C, showing growth from the nucleation site (arrows) and areas of periodic (I) and aperiodic (II) domains. Films are 30 nm with a 60 nm epitaxial TPBi layer deposited after annealing to improve visibility. Scale bar 50 μm.	112
Figure 6.3. Time series during annealing 30-nm-thick films at 180 °C, showing growth of aperiodic and periodic regions in the films. Arrows highlight the propagation of undulations along the growth interface. Time between frames is 200 ms, scale bar is 5 μm.	113
Figure 6.4. Morphology of TPBi films annealed at 180 °C of thickness (a) 40 nm and (b) 50 nm. Insets are FFTs showing periods centered at (a) 1.35 μm and (b) 1.02 μm. Scale bars are 30 μm.	114

Figure 6.5. Surface morphology of 30-nm TPBi films annealed at (a) 180 °C, (b)-(d) 190 °C. (a)-(c) are height images, with (d) the phase image of (c). Plotted in (e) are height profiles shown in (a). Scale bars are (a), (c), (d) 3 μ m, (b) 2 μ m.	115
Figure 6.6. Mechanism of pattern formation in annealed TPBi films showing motion of the crystal (X), liquid (L), and glass (G) phases. (a) 180 °C, where the top solid layer remains continuous and deforms into a sinusoid. The top layer at higher growth rates (b), causing the glassy solid to relax towards the substrate (black arrow) and producing motion in the supercooled liquid (blue arrow). This pushes the crystalline solid away from the substrate (c) and forces the glassy solid towards the substrate as it relaxes laterally. Image not to scale.	116
Figure 6.7. Diffraction from 30 nm annealed TPBi films on silicon showing (a) the whole sample and (b) just the illuminated region. Spot size is approximately 1 cm diameter, unpolarized light.	119
Figure 6.8. Diagram of the diffraction order sign convention.	119
Figure 6.9. Diffraction of p-polarized light ($\theta i = 30^\circ$) from a 30 nm TPBi grating coated with 50 nm aluminum (a) 300-450 nm, (b) 400-675 nm. Diffraction orders shown correspond to $d = 3.05 \mu$ m. The change in the background of (a) at 350 nm is due to the insertion of a long-pass filter in the monochromator. Color scale is logarithmic to bring out the weak diffraction features.	120
Figure 7.1. Optical properties of amorphous (A) and crystalline (X) SubPc: (a) refractive index n, extinction coefficient k, and photoluminescence PL, (b) PL spectra deconvoluted into two gaussian features. The high- and low-energy features yield 0.5% and 2.5% ηPL for amorphous, and 0.6% and 1.7% ηPL for crystalline, respectively, with the remainder in the low-energy tail.	124
Figure 7.2. . (a) Unquenched excitation spectra and (b) quenching ratios as measured at $\lambda = 640$ nm and $\lambda = 720$ nm for the amorphous and crystalline SubPc films used in this work. The solid lines and shaded regions in (b) represent the transfer matrix fits and fit uncertainty ranges.	125
Figure 7.3. Exciton lifetime histograms for ~400 nm crystalline SubPc films on glass grown on a 20-nm crystalline template by attaching the substrate to the deposition shield near the source. (a) Emission spectrum for very thick crystalline film with lines showing the location of the lifetime measurements in (b).	128
Figure 7.4. Exciton lifetime histograms for amorphous and crystalline SubPc films. ...	128
Figure 7.5. (a) Orientation of two molecular dipoles with angles used to calculate the orientation factor, $\kappa 2$. (b) Depiction of the plane which contains the transition dipole on a SubPc molecule (red).	131
Figure 7.6. (a) Diagram of an exciton donor μD and acceptor μA transition dipole, with other variables defined in the text. (b) Schematic of the coordinate system used to	

rotationally average degenerate transition dipoles.....	132
Figure 7.7. (a) SubPc density-based exciton diffusivity enhancement ellipsoid (crystalline over amorphous values). (b) Orientation of SubPc lattice on the substrate. (c) Corresponding diffusivity ellipses in planes along primary crystal planes (a-b, a-c, and b-c, where the first axis is at 0°, the second at 90°). The arrow is a projection along the direction orthogonal to the substrate for the b-c plane.	135
Figure 7.8. Variation in κ_2 along selected crystal directions compared to the amorphous orientation factor. Selected values of κ_2 are shown in (a), the SubPc unit cell in (b). ..	136
Figure 7.9. X-Ray diffraction of 70 nm crystalline SubPc films on Si: (a) 2D diffraction pattern with peaks labeled; (b) integrated pattern (red and blue) compared to simulated (black). ⁶⁹⁷	137
Figure 7.10. Determination of branching angles for SubPc spherulite growth: (a) lines tracing branches of SubPc crystals from Figure 7.11b and (b) lines of the same angles overlaid on SubPc crystal structure viewed orthogonal to the (022) plane, implying the primary growth direction is along [100].	138
Figure 7.11. Film morphology changes upon crystallization and with a quenching layer. Films are 40 nm SubPc (a), (d) amorphous, (b), (c), (d), (e) crystalline, with (a)-(c) bare SubPc and (d)-(f) SubPc with 13 nm HATCN deposited on top. Scale bars 1 μ m, except (c), (d) which are 200 nm; height scales in nm.	138
Figure 7.12. Effects of film roughness on exciton diffusion. Histograms of distance distributions from points in a plane xx nm from the substrate to the nearest interface in (a) the amorphous film of Figure 4a and (b) the crystalline film of Figure 4b. (c) Simulated PL quenching ratio for amorphous (A) and crystalline (X) films compared to the experimentally measured ratios excited at $\lambda = 575$ nm and measured at $\lambda = 640$ nm or 720 nm.	139
Figure 7.13. Exciton diffusion length (LD) and number of hops before decay as a function of the width of the excitonic density of states, σ . The gray region shows the narrowing of σ required to account for the additional diffusion length increase due to crystallization.....	142
Figure 8.1. Diagram of exciton convection, showing (a) the sphere of available energy acceptors at different locations and (b) the calculated advective velocity.....	152
Figure 8.2. Simple model for a 4-layer gated structure, showing rate anisotropy (top) and spatial positions (bottom).....	153
Figure 8.3. (a) Exciton concentration in a 10 nm, 4-layer stack for different rate imbalances, and exciton diffusion efficiency (a) in a 10 nm, 4-layer stack for different LD and (c) stacks of different thickness and numbers of layers for LD linearly interpolated between 1-10 nm and $K=5$. In all simulations, $F=1$ exciton/nm 2 ns and $\tau = 1$ ns.	156

Figure 8.4. Plot from Menke <i>et al.</i> ²³⁸ showing exciton concentration varying with anisotropic transport.....	157
Figure 8.5. Effects of boundary layer thickness on (a) exciton velocity and (b) density in a two-layer stack, each layer 5 nm with $R0 = 1$ nm. The data in (b) also include the results for an analytical calculation of the exciton density. $G = 1/\text{nm}^3 \text{ ns}$	160
Figure 8.6. The effects of energy transfer rate anisotropy in a two-layer gating stack on (a) exciton velocity and (b) exciton density. Each layer is 5 nm thick. In (b), solid lines are the equilibrium model, dots are the non-equilibrium advection model.	163
Figure 8.7. The effects of energy transfer rate anisotropy on the exciton diffusion efficiency, ηD in a two-layer gating stack. The legend shows the origin of the anisotropy, with x:1 arising from a larger forward transfer rate and 1:x from a smaller backward transfer rate.	164
Figure 9.1. Data published by Verreet <i>et al.</i> ¹⁷⁴ showing an increased device efficiency for crystalline rubrene OPVs with increasing rubrene thickness starkly contrasted to amorphous.....	166
Figure 9.2. Comparison of epitaxial films (I) and templates (II): (a) POM image of 100 nm epitaxial rubrene film on a template, (b) X-ray scattering intensity for epitaxial and template films, (c) atomic force micrograph of the border for a 100 nm epitaxial film, and (d) close-up of a 100 nm epitaxial rubrene film, with inset showing molecular terraces, scale bar 200 nm.	168
Figure 9.3. Homoepitaxial rubrene films on single crystals (a) single crystal surface, (b) homoepitaxy of 50 nm rubrene grown at 1 Å/s onto single crystal using a cleaved silicon edge as a mask, and (c) trimmed 3D rendering of (b), showing molecular steps and diffusing islands.	169
Figure 9.4. Homoepitaxial rubrene (RUB) devices, showing the architectures used for (b) 20 nm and (c) 120 nm devices and (c) resulting optoelectronic performance.....	171
Figure 9.5. (a) Extinction coefficient k for rubrene and C_{60} for comparison to the external quantum efficiencies of crystalline rubrene epitaxial devices varying with rubrene thickness (18.7 nm is an amorphous comparison) (b) as collected and (c) normalized to the C_{60} peak at 350 nm.....	172
Figure 9.6. Device parameters for rubrene planar devices as a function of epitaxial layer UGH2 concentration: (a) V_{oc} , (b) J_{sc} , (c) fill factor, and (d) power conversion efficiency. Device architectures: ITO // Rubrene 20 nm (1 Å/s, anneal 45 sec at 170 °) // Rubrene:UGH2 55 nm (2 Å/s) // C_{60} 15 nm (2 Å/s) // BCP 20 nm (2 Å/s) // Ag 75 nm (0.5 Å/s).	173
Figure 9.7. Dark currents of rubrene devices with increasing UGH2 content for (a) amorphous and (b) polycrystalline template films.....	174
Figure 9.8. ηEQE for rubrene devices with increasing UGH2 content. A = amorphous, PC	

= polycrystalline template.....	175
Figure 9.9. AFM images of the epitaxial rubrene:UGH2 active layer on crystalline template, with UGH2 content (a) 0, (b) 10, (c) 20, (d) 30 vol%. All scale bars 3 μ m.....	175
Figure 9.10. Performance of mixture epitaxy devices with C ₆₀ as the impurity and a crystalline template: (a) device parameters and (b) ηEQE with the rubrene:C ₆₀ ratio. Architecture: ITO // Rubrene 20 nm (1 $\text{\AA}/\text{s}$, anneal 45 sec at 170 $^{\circ}\text{C}$) // Rubrene:C ₆₀ 45 nm (2 $\text{\AA}/\text{s}$) // C ₆₀ 15 nm (2 $\text{\AA}/\text{s}$) // BCP 20 nm (2 $\text{\AA}/\text{s}$) // Ag 75 nm (0.5 $\text{\AA}/\text{s}$).....	176
Figure 9.11. Electroluminescence of mixed rubrene:C ₆₀ devices with an (a) amorphous and (b) crystalline template layer.	177
Figure 9.12. AFM images of the epitaxial rubrene:C ₆₀ active layer on crystalline template, with rubrene:C ₆₀ ratios (a), (d) 20:1; (b), (e) 8:1, (c), (f) 6:1. Scale bars (a)-(c) 1 μ m, (d)-(f) 200 nm.	178
Figure 9.13. Models for mixture epitaxy: concentration effects for (a) low and (b) high host fraction; diffusivity effects showing (c) low and (d) high diffusivity; and defect accumulation (e) dominant and (f) minor.	180
Figure 10.1. Effects of substrate type and growth rate of 10-nm BP2T films grown at 100 $^{\circ}\text{C}$ on (a)-(c) bare ITO, (d)-(f) quartz, and (g)-(i) ITO spin-coated with 50 nm PEDOT:PSS. The film deposition rate increases across columns left to right: 0.1 $\text{\AA}/\text{s}$, 0.3 $\text{\AA}/\text{s}$, and 1.0 $\text{\AA}/\text{s}$. AFM scale bars 1 μ m, height in nm.....	184
Figure 10.2. The morphology of SubPc planar device stacks grown on top of (a), (d) bare ITO, (b), (e) ITO with BP2T 8 nm, 0.3 $\text{\AA}/\text{s}$, 100 $^{\circ}\text{C}$, and (c), (f) ITO planarized with 50 nm PEDOT-PSS, then with BP2T 8 nm, 0.3 $\text{\AA}/\text{s}$, 100 $^{\circ}\text{C}$. (a)-(c) are the top-most organic surface, (d)-(f) are the aluminum cathode surface. AFM scale bars 1 μ m, height in nm. Device structure: ITO//SubPc 13 nm//C ₆₀ 35 nm//BCP 10 nm//Al.....	186
Figure 10.3. The morphology of 13 nm SubPc grown on (a)-(c) bare ITO, and (d)-(f) 8 nm BP2T, with BP2T grown at 0.3 $\text{\AA}/\text{s}$, 100 $^{\circ}\text{C}$. SubPc growth rates are (a), (d) 0.1 $\text{\AA}/\text{s}$, (b), (e) 1.0 $\text{\AA}/\text{s}$, and (c), (f) 10.0 $\text{\AA}/\text{s}$. All scale bars 1 μ m, height scales in nm.	187
Figure 10.4. X-ray diffraction patterns with a lab-based Cu K _{α} source for (a) SubPc/C ₆₀ , (b) C ₆₀ , and (c) SubPc grown on silicon with (dashed) and without (solid) an 8 nm BP2T layer on silicon grown at 0.3 $\text{\AA}/\text{s}$, 100 $^{\circ}\text{C}$. SubPc 13 nm, C ₆₀ 35 nm. (d) 75 nm and (e) ~700 nm SubPc films on silicon annealed at 150 $^{\circ}\text{C}$ for 30 min. Distances near peaks represent the interplanar spacing for that diffraction angle.	188
Figure 10.5. Brightfield TEM images of (a) 25 nm BP2T (0.3 $\text{\AA}/\text{s}$, 100 $^{\circ}\text{C}$) on Quantifoil and (b), (c) 25 nm SubPc (1 $\text{\AA}/\text{s}$, 25 $^{\circ}\text{C}$) on 25 nm BP2T (0.3 $\text{\AA}/\text{s}$, 100 $^{\circ}\text{C}$) deposited onto SiO ₂ window TEM grids. Scale bars (a) 0.5, (b) 5, and (c) 2 μ m. Images captured by Dan Cremons, processing by the author.	189
Figure 10.6. Electron diffraction on a ~32 μ m diameter area of a 25 nm SubPc (1 $\text{\AA}/\text{s}$, 25	

°C) on 25 nm BP2T (0.3 Å/s, 100 °C) deposited onto Quantifoil TEM grids. (a) 2D pattern and (b) integrated data compared to calculated peaks. Films with no BP2T show only amorphous rings. Pattern in (a) captured by Dan Cremons, analysis by the author.	190
Figure 10.7. Selected area electron diffraction of a ~1.6 μm diameter area of a on 25 nm SubPc (1 Å/s, 25 °C) on 25 nm BP2T (0.3 Å/s, 100 °C) deposited onto Quantifoil TEM grids. (a) example BP2T pattern showing similar grain orientation among neighboring grains compared to a simulated BP2T pattern along the [001] zone axis. A possible epitaxial relationship is shown in (b), with the BP2T pattern overlaid and the SubPc spots identified in (c). A similarity in the misorientation angle between the two BP2T and SubPc grains suggests a possible alignment between layers. Patterns captured by Dan Cremons, analysis by the author.	191
Figure 10.8. Selected area electron diffraction of a ~1.6 μm diameter area of a 25 nm SubPc (1 Å/s, 25 °C) on 25 nm BP2T (0.3 Å/s, 100 °C) deposited onto Quantifoil TEM grids. SubPc shows (a) and (b) [011] zone axes on BP2T [001]. Green arrows denote directions of the SubPc unit cell, white of BP2T. Red circles correspond to SubPc peaks, with additional images provided in Appendix H.3. Patterns captured by Dan Cremons, analysis by the author.	192
Figure 10.9. Comparison of organic film thicknesses by ellipsometry, including SubPc (1.0 Å/s, 25 °C) on silicon, BP2T on silicon (0.3 Å/s, 100 °C), and SubPc on BP2T on silicon (just SubPc component).	193
Figure 10.10. XRR on (a) 25 nm SubPc on Si (1.0 Å/s, 25 °C), and (b) 50 nm SubPc on 8 nm BP2T on silicon (0.3 Å/s, 100 °C). The first several interference features are shown in the inset plots. Data in (a) collected by Mike Manno and (b) by Javier Garcia-Barriocanal. Analysis by the author.	194
Figure 10.11. Photoluminescence emission spectra of SubPc films excited at 525 nm. (a) SubPc (13 nm, 1.0 Å/s, 25 °C) on glass previously deposited with different BP2T films (8 nm, 0.3 Å/s). (b) SubPc uniformly mixed with BP2T (net rate 1.0 Å/s, 25 °C) with thicknesses given in the legend. Films deposited on glass.	195
Figure 10.12. Time-correlated single photon counting measurement of SubPc (25 nm, 1.0 Å/s, 25 °C) exciton lifetime on bare glass and glass with BP2T (8 nm, 0.3 Å/s, 100 °C) as measured from the photoluminescence emission peaks at 620 nm and 710 nm from Figure 10.11.	196
Figure 10.13. Device parameters for SubPc planar heterojunctions, including (a) V_{oc} , (b) responsivity, (c) fill factor, (d) power conversion efficiency, and current-voltage characteristics at (e) 0 and (f) 1 sun AM1.5G illumination. Device architecture: ITO // [BP2T 8 nm (0.3 Å/s, 100 °C)] // SubPc 13 nm (1 Å/s) // C ₆₀ 35 nm (2 Å/s) // BCP 10 nm (2 Å/s) // Al 100 nm (3 Å/s). All layers other than BP2T deposited at 25 °C....	198
Figure 10.14. Current-voltage characteristics of planar SubPc devices over time.	

Architecture as described in Figure 10.13, except (a) has 50 nm PEDOT:PSS planarizing the ITO, (b) has 50 nm AQ1200 planarizing the ITO with no BP2T, and (c) has 50 nm AQ1200 planarizing the ITO with BP2T. Each scan spaced approximately 5 seconds, with devices first exposed to dark, then 0.03 suns AM1.5G illumination.	199
.....	
Figure 10.15. External quantum efficiencies of the planar SubPc devices described in Figure 10.13.	200
Figure 10.16. Electroluminescence of SubPc/C ₆₀ planar (a), (c) and mixture (b), (d) devices without (a)-(b) and with (c)-(d) BP2T. Applied voltage increases from black to red. Vertical lines show the positions of the 620 nm and 710 nm SubPc photoluminescence peaks and the anticipated 1.55 eV SubPc-C ₆₀ CT state peak. Planar architectures the same as Figure 10.13; mixture architecture ITO // [BP2T 8 nm (0.3 Å/s, 100 °C)] // SubPc 12 nm : C ₆₀ 48 nm (net 2 Å/s) // BCP 10 nm (2 Å/s) // Al 100 nm (3 Å/s). All layers other than BP2T deposited at 25 °C.	201
Figure 10.17. Temperature-dependent device performance for BP2T-SubPc planar devices, including current-voltage properties at (a) 0 and (b) 1 sun AM1.5G and (c) V _{oc} with temperature compared to Zou <i>et al.</i> ⁷³⁷ Planar device architecture is the same as that in Figure 10.13, with the curves in (a) and (b) corresponding to device #2 in (c). Maximum V _{oc} in (c) from top to bottom are 1.49 V, 1.01 V, and 0.86 V.	202
Figure 10.18. Fitted ηEQE for (a) bare and (b) BP2T SubPc planar devices, with experiment as a blue line and fit in green circles ($\eta CC = 0.99$). Device architectures are: Bare = ITO // SubPc 28 nm (1 Å/s) // C ₆₀ 10 nm (2 Å/s) // BCP 10 nm (2 Å/s) // Al 100 nm (3 Å/s); BP2T = same as bare, but with BP2T 16 nm (0.3 Å/s, 100 °C) between ITO and SubPc. All layers besides BP2T deposited at room temperature.	203
Figure 10.19. Measured ηEQE as a function of applied reverse bias and SubPc thickness (nm) at (a) 335, (b) 545 and (c) 595 nm, corresponding to (a) SubPc Soret band, (b) SubPc Q-band vibronic, and (c) SubPc Q-band main peak absorption. Device architectures are: Bare = ITO // SubPc XX nm (1 Å/s) // C ₆₀ 5 nm (2 Å/s) // BCP 10 nm (2 Å/s) // Al 100 nm (3 Å/s); BP2T = same as bare, but with BP2T 8 nm (0.3 Å/s, 100 °C) between ITO and SubPc. XX = 13 or 20 nm, as given in the legend. All layers besides BP2T deposited at room temperature.	205
Figure 10.20. Example (a) charge extraction and (b) transient photovoltage curves for the SubPc planar architecture in Figure 10.13.	206
Figure 10.21. SubPc exciton diffusion lengths in a planar heterojunction extracted using a photovoltage-based measurement. Diffusion lengths are fit with a variable exciton dissociation efficiency (θ) at the BP2T-SubPc interface, with C ₆₀ LD = 16 nm. Device architectures are: Bare = ITO // SubPc 25 nm (1 Å/s) // C ₆₀ 10 nm (2 Å/s) // BCP 10 nm (2 Å/s) // Al 100 nm (3 Å/s); BP2T = same as bare, but with BP2T 8 nm (0.3 Å/s, 100 °C) between ITO and SubPc. All layers besides BP2T deposited at room	

temperature.....	207
Figure 10.22. SubPc planar heterojunction device parameters without (left) and with (right) BP2T. (a)-(b) V_{oc} , (c)-(d) responsivity, (e)-(f) fill factor, (g)-(h) ηP . Device architectures: ITO // [BP2T 8 nm (0.3 Å/s, 100 °C)] // SubPc 25 nm (1.0 Å/s) // Acceptor 20 nm (1 Å/s) // BCP 10 nm (2.0 Å/s) // Al 100 nm (3.0 Å/s). Acceptor layer specified in legend; all layers besides BP2T deposited at room temperature.....	209
Figure 10.23. ηEQE and dark current for the devices with architectures given in Figure 10.22. (a), (c) are on bare ITO, (b), (d) have a BP2T interlayer.....	210
Figure 10.24. SubPc bulk heterojunction device parameters without (left) and with (right) BP2T. (a)-(b) V_{oc} , (c)-(d) responsivity, (e)-(f) fill factor, (g)-(h) ηP . Device architectures: ITO // [BP2T 8 nm (0.3 Å/s, 100 °C)] // [SubPc 5 nm (1.0 Å/s)] // BHJ XX nm (1 Å/s) // BCP 10 nm (2.0 Å/s) // Al 100 nm (3.0 Å/s). BHJs are: gradient 1:4 SubPc:C ₆₀ nonzero endpoint graded composition cells (66 nm); ⁹⁸ mixture 1:4 SubPc:C ₆₀ (60 nm). ⁷²⁸ Neat/BHJ devices include the 5 nm SubPc layer beneath the BHJ. All layers besides BP2T deposited at room temperature.....	212
Figure 10.25. ηEQE and dark current for the mixture and gradient devices, with architectures given in Figure 10.24. (a), (c) are on bare ITO, (b), (d) have a BP2T interlayer.....	213
Figure 10.26. Dilute-donor SubPc devices without (left) and with BP2T (right). Schottky device parameters. (a)-(b) V_{oc} , (c)-(d) responsivity, (e)-(f) fill factor, (g)-(h) ηP . Device architectures: ITO // [BP2T 8 nm (0.3 Å/s, 100 °C)] // [SubPc 5 nm (1.0 Å/s)] // SubPc:UGH2 XX% 12 nm (1.0 Å/s) // SubPc 5 nm (1.0 Å/s) // C ₆₀ 35 nm (2.0 Å/s) // BCP 10 nm (2.0 Å/s) // Al 100 nm (3.0 Å/s). Bracketed layers are only present when specified in legend; all layers besides BP2T deposited at room temperature.....	214
Figure 10.27. ηEQE for dilute donor devices, with architectures given in Figure 10.26. Devices are on (a) bare ITO, (b) BP2T interlayer.....	215
Figure 10.28. SubPc (left) and SubNc (right) Schottky device parameters. (a)-(b) V_{oc} , (c)-(d) responsivity, (e)-(f) fill factor, (g)-(h) ηP . Device architectures: ITO // [MoO _x 10 nm (0.5 Å/s)] // [BP2T 8 nm (0.3 Å/s, 100 °C)] // SubPc or SubNc 25 nm (1.0 Å/s) // BCP 10 nm (2.0 Å/s) // Al 100 nm (3.0 Å/s). Bracketed layers only present when specified in legend; all layers besides BP2T deposited at room temperature.....	216
Figure 11.1. Proposed architecture for determination of material diffusivities. (a) Bilayer stack of two materials, with the material on bottom (orange) of interest for determining molecular diffusivity within the top material (black). After ageing (b), the bottom material has diffused into the top, which can then be capped with a rubrene film (c) and annealed (d) to form crystals, the shape of which are correlated to the surface composition of the diffusing molecule.....	223
Figure 11.2. Method of etching a rubrene microwire (a) with possible vertical variations in	

composition or properties into a wedge (b), where the vertical variation is now spread laterally and resolvable by KPFM	224
Figure 11.3. 40-nm epitaxial layers (highly birefringent center circles) on 20-nm crystalline templates on ITO. (a) NPD, (b) TCTA. Template treatments were (a) 220 °C for 5 min, (b) 240 °C for 6 min.....	227
Figure 11.4. Proposed architecture for visualization of exciton and polaron dynamics in an organic heterostructure. A single crystal of rubrene has a quencher deposited on top of a facet, is thinly sliced vertically using a microtome, and is then viewed in transmission during laser excitation.....	231
Figure 14.1. Polarized light passing through a birefringent material. (a) polarization state from (i) unpolarized, (ii) after the polarizer, (iii) after the birefringent material, and (iv) after the analyzer. (b) shows the vector analysis of polarized light with variables defined in text. The result of (b) for perpendicular polarizer and analyzer is shown in (c), with the polar intensity plot on the left and a visual representation of the intensity on the right (white = more intense).....	290
Figure 14.2. (a) Raster pattern, showing the fast and slow scan axes with the data collected on trace and retrace. (b) Response of a tapping mode cantilever to changing sample topography. (i) Oscillations are at specified setpoint, until a sample edges is reached (ii), allowing the cantilever to oscillate more freely, increasing its amplitude. The system then corrects the tip height until the amplitude setpoint is again reached (iii).	294
Figure 14.3. Diagram of KPFM operation, showing the first topographic scan (c) and amplitude setpoint (e), followed by a second scan with electrical excitation (b) at that setpoint (d), and the resulting surface potential detected (a). All curves display the transitions in behavior described in Figure 14.2b for regions (i)-(iii).	296
Figure 14.4. Tip displacement for different values of Q , with steady-state amplitudes shown in dashed lines. Simulations conducted with $\omega_0 = \omega = 2\pi(250 \text{ kHz})$, $k_c = 40 \text{ N/m}$, $F_0 = 0.1 \text{ nN}$, $R = 10 \text{ nm}$, $H = 6.4 \times 10 - 20 \text{ J}$, $E = 1.51 \text{ GPa}$, $z_0 = 15 \text{ nm}$, and $a = 5 \text{ \AA}$. Parameters are taken from experiment or Garcia <i>et al.</i> ⁷⁹⁹ (except F_0 , to which the simulations are not very sensitive) and simulated with Eqns. 14.27-14.28. Code given in Sec. R.8.....	305
Figure 14.5. $5 \times 5 \mu\text{m}$ 512×512 pixel height (top row) and error (bottom row) images of an annealed rubrene film on ITO imaged at (a), (e) 1, (b), (f) 3.5, (c), (g) 5.4, and (d), (h) 7 Hz line rates, corresponding to 1.9-13.7 mHz frame rates. Height scale 110 nm for height images, images collected on tip retrace.....	306
Figure 14.6. $5 \times 5 \mu\text{m}$ 512×512 height images of an annealed rubrene film on ITO imaged at (a) 1, (b) 3, (c) 5.4, (d) 7.5, (e) 9.8, and (f) 1 (after) Hz line rates. All height scales approximately 130 nm.	307

Figure 14.7. 40 x 40 μm 512 x 512 height images of an annealed rubrene film on ITO imaged at (a) 1, (b) 2, (c) 3, (d) 4, (e) 5.4, (f) 7.5, (g) 9.8, and (h) 1 (after) Hz line rates. All height scales approximately 700 nm.....	307
Figure 14.8. 40 x 40 μm 512 x 512 height images of an annealed rubrene film on ITO imaged at (a) 3, (b) 4, (c) 5.4, (d) 7.5, (e) 9.8, and (f) 12.2 (g) 16.3, (h) 19.5, and (i) 3 (after) Hz line rates. All height scales approximately 190 nm.	308
Figure 14.9. 40 x 40 μm 512 x 512 height image of an annealed rubrene film on ITO imaged 19.5 Hz line rate. Image is a composite of retrace (left) and trace (right) scans to eliminate oscillations. Height scale 180 nm.	309
Figure 14.10. Optoelectronic performance for the devices used in this section, including (a) V_{oc} , (b) responsivity, (c) fill factor, (d) ηP , (e) dark current, and (f) ηEQE . Architectures are the same as Figure 10.13.	311
Figure 14.11. (a) Electrons extracted as a function of V_{oc} , (b) established V_{oc} as a function of incident photon flux, and (c) device dark voltage, plotted vs. current density and an estimated photon flux equivalent.	312
Figure 14.12. (a) Morphology of BP2T deposited onto bare ITO as a function of deposition rate and substrate temperature. Deposition rate increases across columns: (a), (d), (g) 0.1 \AA/s , (b), (e), (h) 0.3 \AA/s , and (c), (f), (i) 1 \AA/s , while temperature increases down rows: (a)-(c) 75 $^{\circ}\text{C}$, (d)-(f) 100 $^{\circ}\text{C}$, and (g)-(i) 115 $^{\circ}\text{C}$. All scale bars 1 μm , height scales in nm.	326
Figure 14.13. (a) Closer examination of the morphology of BP2T deposited onto bare ITO as a function of deposition rate and substrate temperature. Deposition rate increases across columns: (a), (d), (g) 0.1 \AA/s , (b), (e), (h) 0.3 \AA/s , and (c), (f), (i) 1 \AA/s , while temperature increases down rows: (a)-(c) 75 $^{\circ}\text{C}$, (d)-(f) 100 $^{\circ}\text{C}$, and (g)-(i) 115 $^{\circ}\text{C}$. All scale bars 200 nm, height scales in nm.	327
Figure 14.14. (a) Morphology of BP2T deposited onto bare quartz as a function of deposition rate and substrate temperature. Deposition rate increases across columns: (a), (d), (g) 0.1 \AA/s , (b), (e), (h) 0.3 \AA/s , and (c), (f), (i) 1 \AA/s , while temperature increases down rows: (a)-(c) 75 $^{\circ}\text{C}$, (d)-(f) 100 $^{\circ}\text{C}$, and (g)-(i) 115 $^{\circ}\text{C}$. All scale bars 1 μm , height scales in nm.	328
Figure 14.15. (a) Morphology of BP2T deposited onto ITO with 50 nm PEDOT:PSS as a function of deposition rate and substrate temperature. Deposition rate increases across columns: (a), (d), (g) 0.1 \AA/s , (b), (e), (h) 0.3 \AA/s , and (c), (f), (i) 1 \AA/s , while temperature increases down rows: (a)-(c) 75 $^{\circ}\text{C}$, (d)-(f) 100 $^{\circ}\text{C}$, and (g)-(i) 115 $^{\circ}\text{C}$. All scale bars 1 μm , height scales in nm.	329
Figure 14.16. (a) Morphology of BP2T deposited onto quartz with 50 nm PEDOT:PSS as a function of deposition rate and substrate temperature. Deposition rate increases across columns: (a), (d), (g) 0.1 \AA/s , (b), (e), (h) 0.3 \AA/s , and (c), (f), (i) 1 \AA/s , while	

- temperature increases down rows: (a)-(c) 75 °C, (d)-(f) 100 °C, and (g)-(i) 115 °C. All scale bars 1 μm, height scales in nm..... 330
- Figure 14.17. (a) 2D GIWAXS pattern of neat 13 nm SubPc film on silicon, with (b) the χ -integrated pattern. The inset in (b) shows the dominant orientation of the SubPc crystallites with the (022) plane parallel to the substrate. GIWAXS data collected at the Stanford Synchrotron Radiation Lightsource (SSRL) beamline 11-3..... 331
- Figure 14.18. (a) 2D GIWAXS pattern of neat 13 nm C₆₀ film on silicon, with (b) the χ -integrated pattern. (c) shows the textured orientation of the C₆₀ crystallites with the (111) plane parallel to the substrate. GIWAXS data collected at the Stanford Synchrotron Radiation Lightsource (SSRL) beamline 11-3..... 332
- Figure 14.19. (a) 2D GIWAXS pattern of mixed SubPc:C₆₀ films with a volume ratio of 1:4, with (b) the χ -integrated pattern for films of various composition. The peak widths give crystallite sizes of 9.1 nm (C₆₀), 3.7 nm (1:4), 2.5 nm (1:1), 1.5 nm (4:1), and 15.6 nm (SubPc). GIWAXS data collected at the Stanford Synchrotron Radiation Lightsource (SSRL) beamline 11-3..... 333
- Figure 14.20. (a) 2D GIWAXS pattern of a neat C₇₀ film on silicon, showing stronger orientation of the (111) parallel to the substrate than C₆₀. (b) is the χ -integrated pattern, showing a very similar pattern to C₆₀ but with slightly larger d-spacing shifting the peak to smaller q. GIWAXS data collected at the Stanford Synchrotron Radiation Lightsource (SSRL) beamline 11-3..... 334
- Figure 14.21. Selected area electron diffraction on a ~1.6 μm diameter area of 25 nm SubPc (1 Å/s, 25 °C) on 8 nm BP2T (0.3 Å/s, 100 °C) on a Quantifoil grid. Simulated BP2T pattern along the [001] zone is overlaid for (a) and (c), with simulated SubPc patters overlaid, with (b) [011] and (d) [101] zones. Red circles denote SubPc peaks. These orientations were used to deduce the epitaxial relationships shown in Figure 10.8. Patterns collected by Dan Cremons, analysis by the author..... 335
- Figure 14.22. (a) Selected area electron diffraction on a ~1.6 μm diameter area of 25 nm SubPc (1 Å/s, 25 °C) on 8 nm BP2T (0.3 Å/s, 100 °C) on a Quantifoil grid. Simulated BP2T pattern along the [001] zone is overlaid on the image. (b) Dark-field TEM image of BP2T grains (8 nm, 0.3 Å/s, 100 °C) underneath SubPc (13 nm, 1 Å/s, 25 °C) and 35 nm C₆₀ (35 nm, 2 Å/s, 25 °C), showing a grain sizes 500-1000 nm. Scale bar 1 μm. Data collected by Dan Cremons, analysis by the author..... 336
- Figure 14.23. KPFM measurements on 25 nm SubPc on 8 nm BP2T (0.3 Å/s, 100 °C) on ITO, with (a)-(c) topography images and (d)-(f) surface potential images. SubPc deposited at 25 °C and (a), (d) 0.1 Å/s, (b), (e) 1 Å/s, and (c), (f) 10 Å/s. Regions in each image are (clockwise from top) SubPc, ITO, BP2T, BP2T/SubPc. Scale bars 10 μm, height scales in (a)-(c) in nm, (d)-(f) in V below vacuum, calibrated to a clean gold film..... 337
- Figure 14.24. Plots showing the results of ηEQE fitting, with (a), (d) bare, (b), (e) BP2T

not dissociating, and (c), (f) BP2T dissociating. (a)-(c) are for $\eta CC = 0.99$, (d)-(f) ηCC optimized for goodness of fit. Device structures given in Figure 10.18, fit parameters in Table 10.2.	338
Figure 14.25. Reverse biased ηEQE plots for the devices described in Figure 10.19. (a) Bare, 13 nm SubPc, (b) Bare, 20 nm SubPc, (c) BP2T, 13 nm SubPc, (d) BP2T, 20 nm SubPc.	339
Figure 14.26. Heater element, with yellow nichrome wire inset into aluminum.....	355
Figure 14.27. Completed heater from (a) the front, showing (i) sample compartment, (ii) sliding door, (iii) thermocouple wire, and (b) from the back, with (i) ground wire, (ii) nitrogen purge source, (iii) 12 VDC power input, and (iv) spring-loaded actuating lever for the sliding door.....	356
Figure 14.28. Temperature over the sample viewing area when set at 200 °C. Colorbar in °C.	357
Figure 14.29. Gradient heater as viewed from the (a) top and (b) side.	359
Figure 14.30. Gradient heating element (a) as cement is applied and (b) with a glass slide piece clipped on to protect the cement.....	360
Figure 14.31. Heated ellipsometer stage (a) with cover off and (b) assembled.....	361
Figure 14.32. Raw ellipsometric data (a) Ψ and (b) Δ collected on a sample of TPD over time, with (c) temperature profile of 4 °C/min heating rate and average convective cooling rate of ~7 °C/min. Data collected without cover in ambient.	362
Figure 14.33. Fitted parameters for a TPD film on silicon: (a) thickness and (b) static index of refraction from the Cauchy model An parameter.....	363
Figure 14.34. Diagrams of (a) glass slides and (b) melt crystallization apparatus used in this work.....	365
Figure 14.35. Different melt-grown anthracene crystal morphologies (a) dendritic polycrystal, (b)-(c) single crystal, (d) dewetted. All polarized optical micrographs are 2.94 mm wide. (e) photograph of slides post-growth, showing regions that correspond to (I) dendritic polycrystal, (II) single crystal, and (III) dewetted.	366
Figure 14.36. (a)-(b) Crystal structure of anthracene, with (c) x-ray scattering with a Cu $K\alpha$ source and (d) inferred orientation of the unit cell between glass slides (blue). 367	
Figure 14.37. Suggested revised melt crystallization design, with clips and offset slides allowing for material placement at (a).	368
Figure 14.38. Molecular structures of (a) Alq ₃ and (b) DCM, and architectures of (c) slab and (d) cladded lasers.....	369
Figure 14.39. Photographs of (a) laser deposited onto a flexible plastic substrate and (b) lasing of the organic laser (orange) as pumped by a nitrogen arc laser (visible by blue	

paper fluorescence in background)	370
Figure 14.40. Schematic of the laser characterization setup, including the nitrogen laser (a) which produces 337 nm light (blue arrow) which goes through neutral density filter wheels (b), horizontal cylindrical lens (c), and beam stops (d) onto the organic laser (e) which is mounted on a goniometer translation stage (f). Extra laser light is blocked by a beamstop (i). The organic laser emits light in the substrate plane (red arrows), one side of which is focused using a microscope objective (g) into a detector or spectrometer (h).	371
Figure 14.41. Chemical structure of Tergitol NP-40	372
Figure 14.42. DI water on (a) solvent-cleaned silicon and (b) solvent-cleaned with 10 minutes UV-ozone.	373
Figure 14.43. Schematic of stainless steel plate used to break scored substrates in the glovebox. Diagram not to scale.	374
Figure 14.44. Images of ITO with and without film deposited on it. Bare Xin Yan ITO from 9/18/13 with RMS roughness (a) 2.31 and (b) 2.40 nm. (c) is Xin Yan ITO with 20 nm rubrene, RMS roughness 1.4 nm, and (d) is Xin Yan ITO with 50 nm PEDOT:PSS, RMS roughness 1.69 nm. ITO from Delta Technologies, with RMS roughness (e) 3.89, and (f) 2.2 nm with 20 nm rubrene. The film roughness in (c) and (f) give increased interface areas of 0.08 % and 0.22 %, respectively. All scale bars 1 μ m, height scales in nm.	375
Figure 14.45. Morphology and step characterization of patterned Xin Yan ITO as of 9/20/14. (a) View of patterned corner region with two images stitched together (height scales for the ITO in lower left, glass substrate in upper right). Scale bar 2 μ m. (b) Edge characterization of bare ITO, with two images stitched together as in (a), scale bar 1 μ m. (c) Edge characterization of ITO planarized with 50 nm PEDOT:PSS, scale bar 3 μ m. (d) Height profiles of the regions shown in (b)-(c). All height scales in nm. ...	376
Figure 14.46. Morphology of (a), (b) Xin Yan ITO and (c), (d) Delta Technologies ITO. Scale bar 250 nm, height scales in nm.	376
Figure 14.47. Morphology of vapor-deposited metals, including (a) 100 nm aluminum on C ₆₀ (scale bar 1 μ m), (b) silver on silicon (scale bar 2 μ m), (c) 150 nm gold on 3 nm chromium wetting layer (scale bar 1 μ m, height scale 7 nm), and (d) 50 nm gold on silicon (scale bar 10 μ m). All height scales in nm.	377
Figure 14.48. Chuck rotational speed in terms of the control dial setting on the control console.	378
Figure 14.49. Cooling characteristics of the Angstrom chamber chuck and lamp, according to thermocouples mounted onto the 9" copper chuck ("Chuck") and in the chamber shroud next to the lamp ("Lamp").	378
Figure 14.50. Simulated electric field in a SubPc planar OPV described in Zou &	

Holmes. ⁷³⁷ Intensity scale ranges from 0-150% of the incident field.....	382
Figure 14.51. Processing options for images.....	392
Figure 14.52. Nuclei measurement options.....	393
Figure 14.53. Examples of crystal analysis results and suitable crystals. (a),(e) +/-45 deg, (b),(f) 360 deg, (c),(g) crystal directions, and (d),(h) rod radius. Green dots in (a)-(d) denote areas that were tracked.....	394
Figure 14.54. Simulated transmission electron diffraction pattern for the [001] zone of BP2T in (a) single crystal, (b) CBED, (c) randomly oriented powder, and (d) textured polycrystalline film.....	436
Figure 14.55. Schematic for exciton diffusion as simulated by Kinetic Monte Carlo....	441

VARIABLES, SYMBOLS, ACRONYMS, AND CHEMICALS

Variable and Symbol Conventions

1. Tensor variables are bolded and underlined, with the number of underbars denoting the tensor order, *e.g.*, \underline{x} is a vector, $\underline{\underline{D}}$ is a second-order tensor diffusivity, etc.
2. Vectors of unit length are denoted with a hat, *e.g.*, $\hat{\underline{n}}$ is a surface normal of magnitude 1.
3. Variables which may be extensive are denoted a per molar basis by a tilde (*e.g.*, \tilde{S} is molar entropy) and a per mass basis by a hat (*e.g.*, \hat{S} is entropy per unit mass)
4. Multiplication explicitly and intentionally uses dot products (\cdot) for vector dot products and scalar products, double dots ($:$) for second-order tensor dot products, and crosses (\times) for vector cross products. The absence of a multiplier implies a simple scalar or dyadic product (for scalar and vector variables, respectively).
5. When convenient, equations are manipulated and expressed in Index or Einstein notation (*e.g.*, $\underline{x} \cdot \underline{y} \equiv x_i y_i$, where i represents the implicit sum over the components of \underline{x} and \underline{y}). Excellent introductions to such terminology are provided in *Incompressible Flow* by R. L. Panton and *Analysis of Transport Phenomena* by W. M. Deen.

Symbols

$\underline{\nabla}$	Del, the gradient differential operator equal to $\sum_{i=1}^3 e_i \partial_i$
∇^2	Laplacian, equal to $\underline{\nabla} \cdot (\underline{\nabla})$ or $\sum_{i=1}^3 \partial_i \partial_i$

Greek Letters

α	Absorption coefficient (1/nm), or angle between donor transition dipole and a connecting radius in energy transfer (°)
α_f	Film thermal expansion coefficient (1/K)
α_s	Substrate thermal expansion coefficient (1/K)
β	Angle between acceptor transition dipole and a connecting radius in energy transfer (°)
γ	Angle between donor and acceptor transition dipoles in energy transfer (°) or surface energy (dyn)
ϵ	Mechanical strain
ϵ_0	Vacuum electrical permittivity (dielectric constant), 8.854×10^{-12} F/m

ϵ_r	Relative electrical permittivity
ϵ_y	Mechanical yield strain
κ^2	Orientation factor for intermolecular electromagnetic coupling
λ	Wavelength (nm)
λ_e	Equilibrium wavelength of an elastic film on an elastic substrate (μm)
λ_i	Intrinsic wavelength of an elastic film on a viscoelastic substrate (μm)
λ_M	Molecular reorganization energy (eV)
λ_{MFP}	Molecular mean free path (without collisions) in a medium (nm)
μ	Viscosity (cP)
μ_A	Energy acceptor transition dipole (D)
μ_D	Energy donor transition dipole (D)
μ_q	Charge mobility for a hole μ_h or electron μ_e of charge q ($\text{cm}^2/\text{V s}$)
η_A	Photon absorption efficiency
η_{CC}	Charge collection efficiency
η_{CS}	Charge separation efficiency from a CT state into polarons
η_{CT}	CT state formation efficiency
η_D	Exciton diffusion efficiency
η_{EQE}	External quantum efficiency, the efficiency of light conversion into charge or <i>vice versa</i> as measured external to the device
η_{IQE}	Internal quantum efficiency, the efficiency of photoconversion inside the device. Calculated by dividing out η_A (OPV) or outcoupling efficiency (OLED).
η_{PL}	Photoluminescence efficiency
σ	Excitonic density of states width (eV)
σ_A	Absorption cross-section of an energy acceptor (1/molecule)
σ_T	Thermal strain (GPa)
σ_Y	Yield strain (GPa)
ϕ	Molecular diameter (\AA) or spin wavefunction
ψ	Angle between donor transition dipole and connecting radius in energy transfer ($^\circ$), or spatial wavefunction, or general wavefunction
ρ	Continuous exciton density on an energy donor (#/volume)
ρ_A	Acceptor density (#/area or #/volume)
ρ_D	Discrete exciton density on an energy donor (#)
ρ_{hkl}	Planar density of the (h, k, l) crystal plane (#/ nm^2)
ν_1, ν_2	Angle of rotation of donor-acceptor transition dipoles when considering degenerate transitions in highly symmetric molecules ($^\circ$)
ν_i	Poisson's ratio for a film ($i = f$), elastic substrate (s), elastic layer (e), or viscoelastic layer (v)
ω	Angular frequency (radians)
τ	Exciton natural lifetime (ns)
τ_q	Time between scattering events for a hole τ_h or electron τ_e of charge q (ns)
τ_{rad}	Radiative exciton lifetime, not counting non-radiative pathways (ns)

θ	Any number of angles, including that between an energy acceptor transition dipole and donor electric field, ($^{\circ}$)
θ_d	Angle of a diffracted beam relative to the sample normal ($^{\circ}$)
θ_i	Angle of incidence relative to the sample normal ($^{\circ}$)
ζ	Vapor sticking coefficient to a surface

Variables

a	Molecular lattice constant for a cubic lattice (nm)
A_i	Area of crystal facet i (mm^2)
A_{TP}	Area of testing hole plate for solar simulation testing (mm^2)
A_{Dev}	Illuminated device area for solar simulation testing (mm^2)
c	Speed of light in vacuum, 2.998×10^8 m/s
d	Distance between molecules considered for energy transfer (nm)
d_{hkl}	Interplanar spacing for crystal plane (h, k, l) (\AA)
D	Diffusivity (cm^2/s)
e	Charge of an electron, 1.602×10^{-19} C
e_i	Unit vector along the i th principle direction used in index notation
E_A	Activation energy, often in Arrhenius expressions (J/mol or eV)
E_B	Exciton binding energy (eV)
E	Electric field strength (esp. if vectorial), energy (V/cm or J), or elastic modulus (GPa)
E_i	Elastic modulus for a film ($i = f$), elastic substrate (s), elastic layer (e), or viscoelastic layer (v) (GPa)
FF	Fill factor, the ratio of the greatest power produced by an OPV to its theoretical maximum power based on J_{sc} and V_{oc}
F_D	Area-normalized emission spectrum of an energy donor
g_i	Growth rate of crystal plane i
ΔG°	Gibbs free energy change between initial and final states (J)
G_i	Exciton generation rate in layer i
G_c	Gibbs free energy of crystallization (J)
\hbar	Planck's constant, h (6.626×10^{-34} m 2 kg / s), divided by 2π
h_i	Layer thickness for a film ($i = f$), elastic layer (e), and viscoelastic layer (v), (nm)
\tilde{H}	Molar enthalpy (J)
I_{Det}	Current measured by a photodetector (A)
I_{Dev}	Current flowing from a device (A)
J	Spectral overlap integral in Dexter transport with emission and absorption area-normalized, or current density (A/cm 2)
J_{MP}	Current density at the maximum power point of a solar cell (A/cm 2)
J_{sc}	Short-circuit current density, the maximum current a solar cell can produce at a given illumination intensity (A/cm 2)
k	Extinction coefficient

K	Quantum-mechanical terms in the Dexter energy transfer equation (1/ns)
k_B	Boltzmann's constant, 1.380×10^{-23} J/K or 8.617×10^{-5} eV/K
k_D	Dexter energy transfer rate (1/ns)
$k_{ET}(\underline{x})$	Energy transfer rate in continuous space over a the vector \underline{x} (1/ns)
k_F	Förster energy transfer rate for dipole-dipole coupling (1/ns)
k_{F_p}	Förster energy transfer rate for dipole-acceptor plane coupling (1/ns)
k_{F_s}	Förster energy transfer rate for dipole-acceptor slab coupling (1/ns)
k_{ij}	Rate of energy or electron transfer between discrete molecules i and j (1/ns)
k_M	Marcus electron transfer rate (1/ps)
k_{NR}	Exciton non-radiative decay rate (1/ns)
k_R	Exciton radiative decay rate (1/ns)
l_i	Distance from Wulff point in crystal to the surface of facet i
L	Average Bohr radius or van der Waals radius of an excited donor and ground state acceptor in Dexter energy transport (\AA)
L_D	Exciton diffusion length (nm)
m	Mass (g) or diffraction order/harmonic
m^*	Effective mass of a charge carrier in a medium (kg)
M_s	Spin angular momentum
n	Index of refraction or surface normal vector
N_A	Avogadro's number, 6.02×10^{23} 1/mol
n_B	Energy harmonic or energy level
N_s	Number of adsorbed surface molecules required to form a monolayer (#/ m^2)
P	Pressure or power (N or W)
P_{opt}	Optical power density (W/cm^2)
q	Elementary charge, $\pm 1.602 \times 10^{-19}$ C
r	Radius of an object (m)
r_o	Arrhenius prefactor of crystal growth, the growth rate at infinite temperature ($\mu\text{m}/\text{s}$)
r_c	Critical radius of a heterogeneous nucleus in order to be stable
R_0	Förster radius, the intermolecular separation for equal probability of energy transfer and decay (nm)
R_{Det}	Detector responsivity, current produced per incident power (A/W)
S	Orbital spin quantum number
\tilde{S}	Molar entropy (J/K)
t	Time (sec)
t_{ML}	Time required for the adsorption of a gas monolayer to a surface
T	Temperature (K)
T_C	Crystallization temperature, the approximate temperature required for the onset of rapid growth of crystals from the solid (K)
T_D	Substrate temperature during film deposition
T_f	Fictive temperature, an imaginary temperature where a stabilized glassy solid has the same properties as a supercooled liquid at the same temperature (K)

T_F	Film temperature
T_g	Glass transition temperature, where a liquid transforms into a glassy solid (K)
T_K	Kauzman paradox temperature, where liquid and crystal phases have the same entropy (K)
T_O	Onset temperature, when a glassy solid transforms into a supercooled liquid (K)
v	Velocity (m/s)
V	Voltage (V)
\tilde{V}	Molar volume (m^3/mol)
V_{oc}	Open-circuit voltage, the maximum voltage a solar cell can produce at a given illumination intensity (V)
V_{MP}	Voltage at the maximum power point of a solar cell
V_{ij}	Coupling between initial and final states (transfer integral)
Z	Atomic number

Acronyms

AFM	Atomic force microscopy
CT	Charge transfer
CV	Cyclic voltammetry
DSC	Differential scanning calorimetry
EA	Electron affinity
FET	Field-effect transistor
GIXS	Grazing incidence x-ray scattering
HOMO	Highest occupied molecular orbital
IE	Ionization energy
IPES	Inverse photoemission spectroscopy
KPFM	Kelvin probe force microscopy
LED	Light-emitting device
LUMO	Lowest unoccupied molecular orbital
OFET	Organic field-effect transistor
OLED	Organic light-emitting device
OPV	Organic photovoltaic cell
ORP	Oxidation/reduction potential
PID	Proportional, integral, and differential control
POM	Polarized optical microscopy
PV	Photovoltaic device
PVD	Physical vapor deposition
PVT	Physical vapor transport
QCM	Quartz crystal monitor
STM	Scanning tunneling microscopy
TCSPC	Time-correlated single photon counting
TEM	Transmission electron microscopy

TGA	Thermogravimetric analysis
UPS	Ultraviolet photoelectron spectroscopy
UV-Vis	Ultraviolet-visible spectroscopy
WAXS	Wide angle x-ray scattering
XRD	X-ray diffraction
XRR	X-ray reflectivity

Full Names of Chemical Compounds

3TPYMB	Tris(2,4,6-triMethyl-3-(pyridin-3-yl)phenyl)borane
4CzIPN	2,4,5,6-Tetra(9H-carbazol-9-yl)isophthalonitrile;2,4,5,6-tetrakis(carbazol-9-yl)-1,3-dicyanobenzene;2,4,5,6-Tetra-9H-carbazol-9-yl-1,3-benzenedicarbonitrile;(4r,6r)-2,4,5,6-tetra(9H-carbazol-9-yl)isophthalonitrile
4p-NPB	N4,N4'''-di(naphthalen-1-yl)-N4,N4'''-diphenyl-[1,1':4',1":4",1'''-quaterphenyl]-4,4'''-diamine
α -6T, 6T	Sexithiophene,
Alq ₃	Tris-(8-hydroxyquinoline)aluminum
AQ-1200	Plexcore®, a product of Sigma Aldrich
BCP	Bathocuproine, 2,9-Dimethyl-4,7-diphenyl-1,10-phenanthroline
BP2T	2,5-bis(4-biphenyl)-bithiophene
BPhen	Bathophenanthroline, 4,7-Diphenyl-1,10-phenanthroline
C545T	2,3,6,7-tetrahydro-1,1,7,7-tetramethyl-1H, 5H,11H-10-(2-benzothiazolyl)quinolizino[9,9a,1gh]coumarin
C ₆₀	Fullerene C ₆₀
C ₇₀	Fullerene C ₇₀
CBP	4,4'-Bis(carbazol-9-yl)biphenyl
ClAlPc	Chloroaluminum phthalocyanine
CoPc	Cobalt phthalocyanine
CuPc	Copper phthalocyanine
DBP	5,10,15,20-Tetraphenylbisbenz[5,6]indeno[1,2,3-cd:1',2',3'-lm]perylene
DIP`	Diindeno[1,2,3-cd:1',2',3'-lm]perylene
DPDCPB	2-{{7-(4-N,N-diphenylaminophenyl-1-yl)-yl)methylene}malononitrile 2,1,3-benzothiadiazol-4-
DPDCTB	2-{{7-(5-N,N-diphenylaminothiophen-2-yl)-yl)methylene}malononitrile 2,1,3-benzothiadiazol-4-
DTDCPB	2-{{7-(4-N,N-ditarylaminophenyl-1-yl)-2,1,3-benzothiadiazol-4-yl)methylene}malononitrile
DTDCTB	2-{{7-(5-N,N-Ditarylaminothiophen-2-yl)-2,1,3-benzothiadiazol-4-yl)methylene}malononitrile
H ₂ Pc	Phthalocyanine
HATCN	Dipyrazino[2,3-f:2',3'-h]quinoxaline-2,3,6,7,10,11-hexacarbonitrile
ITO	Indium tin oxide
LiF	Lithium Fluoride

mCP	1,3-Bis(carbazol-9-yl)benzene
MoO _x	Molybdenum oxide
NiPc	Nickel phthalocyanine
NPD	N,N' -Bis(naphthalen-1-yl)-N,N' -bis(phenyl)-2,2'-dimethylbenzidine, purified
NTCDA	1,4,5,8-Naphthalenetetracarboxylic dianhydride
Perylene	Dibenz[<i>de,kl</i>]anthracene
PEDOT	Poly(3,4-ethylenedioxythiophene)
PSS	Polystyrene sulfonate
PTCBI	Bisbenzimidazo[2,1-a :1',2-b']anthra[2,1,9-def :6,5,10-d'e'f']diisoguineoline-10,21-dione
PTCDA	3,4,9,10-Perylenetetracarboxylic dianhydride
PTCDI	Perylene-3,4,9,10-tetracarboxylic-3,4,9,10-diimide
Pyrene	Benzo[<i>def</i>]phenanthrene
Rubrene	5,6,11,12-Tetraphenylnaphthacene
SubPc	Boron subphthalocyanine chloride
SubNc	Boron subnaphthalocyanine chloride
TCNQ	Tetracyanoquinodimethane
TCTA	Tris(4-carbazoyl-9-ylphenyl)amine
TPBi	2,2',2''-(1,3,5-Benzinetriyl)-tris(1-phenyl-1-H-benzimidazole)
TPD	N,N'-Bis(3-methylphenyl)-N,N'-diphenylbenzidine
TTF	Tetrathiafulvalene
UGH1	Bis(2-methylphenyl)diphenylsilane
UGH2	1,4-Bis(triphenylsilyl)benzene
ZnPc	Zinc phthalocyanine

1. ORGANIC ELECTRONIC DEVICES

Civilization continually seeks newer, better, less expensive products to enhance lives. Organic electronic devices, devices in which the operative material is predominantly carbon-based, increasingly satisfy these demands in both niche applications and broader markets. Their reasons for use vary, but have created significant impetus for further development. This chapter introduces some of the many uses and features of these devices, open challenges in the field, and the relevance of this thesis in exploring these challenges.

1.1. Uses of Organic Electronics

Organic materials exhibit a remarkable array of optical, mechanical, and electrical properties which allow for the construction of devices with a correspondingly diverse array of functionalities. Some attractive features of organic electronic devices include high mechanical flexibility and compatibility with flexible supports,^{1–3} tunable light absorption and emission,^{4–7} and high-throughput manufacturing.^{8–10} This has enabled organic equivalents for many inorganic devices, such as light-emitting devices (LEDs),^{11–13} field-effect transistors (FETs),^{14–16} and photovoltaic cells (PVs)^{17–19} with new features that are challenging to create using inorganic materials and their manufacturing techniques.

1.1.1. Light-Emitting Devices

The organic LED, or OLED, is a prominent example of a market-changing technology (Figure 1.1).^{13,20–22} OLEDs feature an emissive material which generates light from an applied current and are gradually displacing conventional liquid crystal displays,²³ largely due to the higher brightness, efficiency, contrast, and frame rates made possible by electrically switching the display pixels on and off rather than molecularly shuttering them with liquid crystals. Furthermore, OLEDs can be manufactured extremely thin (50-500 nm) and without high temperatures, allowing them to be constructed on inexpensive, flexible plastic films which can be used in conformal coatings, novel light designs, and lightweight or even rollable applications.^{12,24–26} All of these features enable more efficient, more unique, and more attractive devices for consumers willing to pay for the added performance.

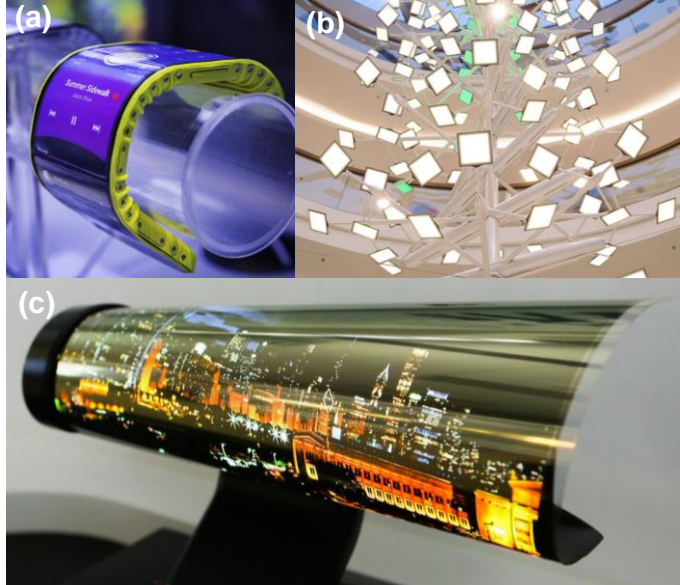


Figure 1.1. OLED applications including (a) a foldable concept phone (Lenovo),²⁰ (b) plate chandelier (OLEDworks/Carl Stahl Architektur),²¹ and (c) rollable television (LG).²²

1.1.2. Photovoltaic Cells

Organic photovoltaic cells (OPVs) have the ability to be disruptive in a different manner. Although solar power costs have fallen,^{27–29} it is still relatively expensive: without subsidies, the price per watt of installed power ranges from \$3.3-\$4.6 (2012 figures).^{28,30}

Organic Electronic Devices

Surprisingly, a large fraction of this cost originates not in the solar cell, but in the infrastructure and labor required to stabilize and install the delicate cells.^{30,31} Conventional inorganic PVs consist of brittle, toxic materials which are thick (100-1000 μm) to compensate for their poor light absorption, leading to PVs which are rigid, heavy, and require considerable support except in select thin-film products.³²⁻³⁴

Contrast this case with that of OPVs: cells comprised of highly absorptive, lightweight, and flexible materials which can be deposited on cheap, flexible substrates (Figure 1.2).³⁵⁻³⁸ In addition to greatly simplifying installation (Figure

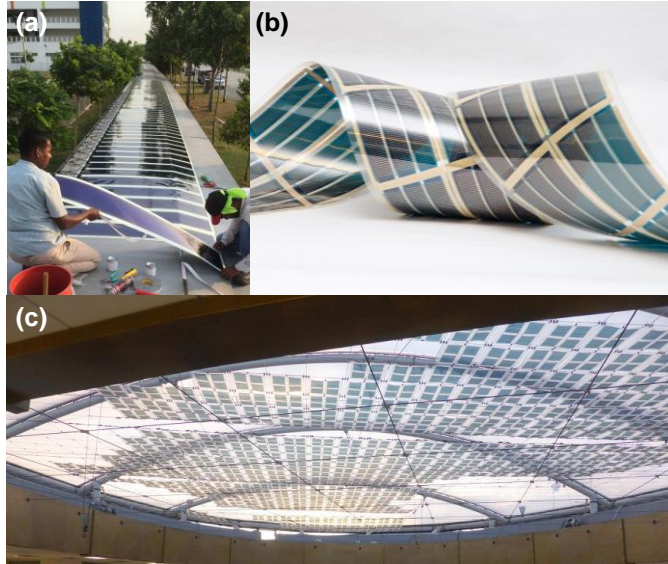


Figure 1.2. OPVs in (a) simplified installation (Heliatek),³⁵ (b) flexible panels (InfinityPV),³⁶ and (c) rooftop solar at the African Union, Addis Ababa, Ethiopia (OPVIus).³⁷

1.2a), these benefits also inspire portable, deployable technologies to bring solar electricity to remote or disaster areas.^{39,40} The tunable absorption of the active materials means power can be generated by solar cells on building walls and windows,^{41,42} where visibly transparent cells generate electricity while reducing optical heating.^{43,44}

1.1.3. Field-Effect Transistors

The final appreciable area of infiltration for organic electronics is the organic FET (OFET).¹⁴ Transistors are the ubiquitous data-processing, current-switching, and signal-amplifying components in modern circuits;⁴⁵ thus, flexible circuits with advanced

Organic Electronic Devices

capabilities demand truly flexible transistors (Figure 1.3).^{46,47} Furthermore, a driver of flexible circuitry is the extreme cost-effectiveness which enables even disposable applications such as radio frequency identification (RFID),⁴⁸ single-use medical diagnostic

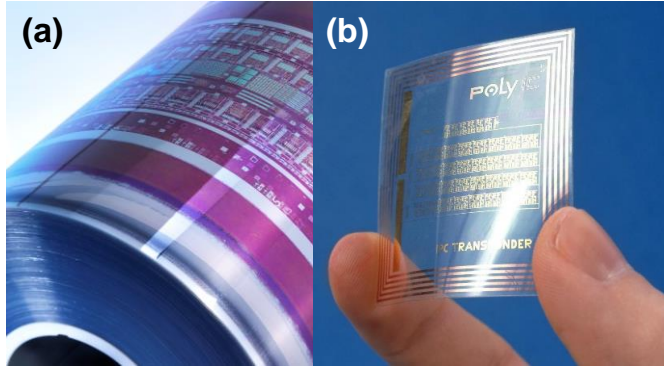


Figure 1.3. OFETs in (a) flexible circuit roll (PolyIC)⁴⁶ and (b) a transparent, flexible printed RFID tag (PolyIC).⁴⁷

equipment,^{49,50} and widely distributed counter-terrorism chemical sensors.^{16,48} For these reasons, flexibility and inexpensive manufacturing remain primary motivators of the technology. The

transparency of OFETs is also an advantage for some display applications, where transistors are used to switch pixels on and off. This enables novel consumer electronics and military gear with a wide array of capabilities.^{16,48,50–55}

1.2. Challenges for Organic Electronic Devices

Despite the many intriguing features of organic electronics, devices comprised of organic molecules are not commonplace in most applications (except OLEDs), primarily due to current restrictions in materials and ease of processing. The materials themselves vary in complexity and cost to synthesize, and generally suffer from inefficiencies in moving energy as charges or excited states. In OLEDs and OPVs, there is an additional efficiency loss in the conversion of this energy into light or *vice versa*. Furthermore, these finite efficiencies typically decrease over time as the material is exposed to light, heat, or electrical stress. These are all challenges that must be addressed by the field.

1.2.1. Durability and Reliability

The nature of the bonds within and among organic semiconductors generally makes them sensitive to long-term exposure to energy applied as electricity,^{56,57} heat,^{58–61} or light,^{62–65} and can result in undesired chemistry and material rearrangement within devices.^{54,59,66–68} In general, organic devices decay in performance with time, whether in light emission,^{56,69,70} power conversion,^{62,71,72} or signal amplification,^{15,54} with typical behaviors shown in Figure 1.4. In OLED displays, this means higher-energy blue pixels degrade (dim) more quickly than the greens and reds, causing an undesirable color and brightness shift over time.^{23,56,70,73} Some amount of decay is unavoidable, yielding an anticipated product lifetime even in inorganics.^{74–76} A particular challenge with organic materials is to increase lifetimes to be compatible with the designs and goals of a particular product, which requires an understanding of degradation and mitigation routes. Also, for single-use or disposable applications, lifetime is not the differentiating factor for organic electronics.

1.2.2. Efficiency

Even devices immune to degradation would be impractical to implement without an acceptable operating efficiency. Organic materials suffer from an array of electrical and

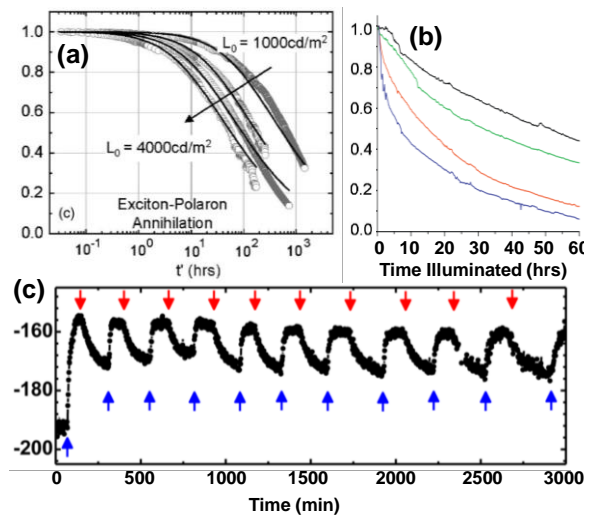


Figure 1.4. Examples of degradation of (a) normalized OLED luminance from Giebink *et al.*,⁵⁶ (b) normalized OPV power conversion efficiency from Gevorgyan *et al.*,⁷² and (c) OFET sensing response with and without analyte (red and blue arrow, resp.), from Yun *et al.*¹⁵

Organic Electronic Devices

optical loss mechanisms which siphon off useful forms of energy (often as heat) and can feed back into device degradation introduced in Section 1.2.1.^{18,29,56,77–88} Overcoming these limits is often phrased as a synthetic question –surely chemists can make “better” molecules – but in reality, targeted synthesis can be an extreme challenge in terms of reaction selectivity and yield,^{89–91} let alone theorizing what exactly creates “better” devices.^{92,93} A variety of device architectures and treatment options also exist,^{16,85,94–107} enabling specific bypassing of particularly poor material properties, but these treatments and architectures cannot always solve an arbitrary combination of performance problems and in some cases vary dramatically in effectiveness for different materials.^{103,108–111}

1.2.3. Scaling Device Size

As devices are scaled to production sizes, a variety of problems can occur in the materials processing steps. In OPVs, the jump from lab-scale devices (1 mm^2) to consumer cells (10^4 mm^2) changes the manner in which materials can be applied to a given substrate: one simply cannot spin a 1 m^2 glass sheet like a 1 cm^2 slide. In OFETs, devices are pushed to be smaller; challenging deposition and patterning techniques to become ever more precise while still remaining economical.^{112–115} Some methods of deposition also depend on the rate at which material is applied and treated,^{116–119} which is an issue for much faster industrial manufacturing. Size and speed changes also complicate distribution of materials in mixed or pure layers to yield consistent thicknesses and concentrations across large areas.¹²⁰ Improvements in these areas require further development of processing techniques in parallel with harnessing serendipitous material properties and physics.^{121–124}

1.2.4. Yield and Reproducibility

Industrial devices manufactured at scale should ideally have consistent properties in every product. However, there exist a number of ways in which anomalies are introduced to devices both through processing and materials,^{125–127} and this causes some statistical amount of defects and variation in manufactured devices. Within functional organic devices, slight variations in performance (*e.g.*, color, lifetime, efficiency) can occur from changes in the material purity or concentration,^{128–133} leading to further issues with device reproducibility.

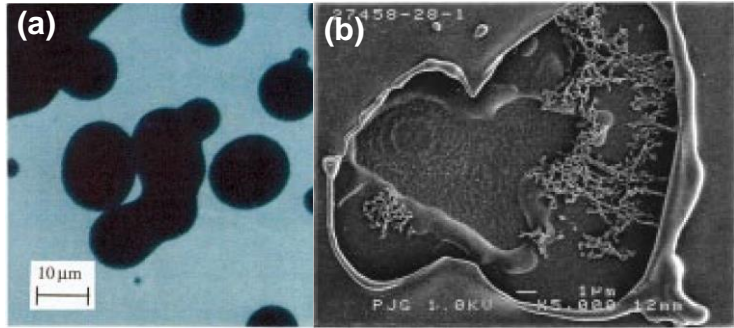


Figure 1.5. Examples of (a) dark spot formation in OLED light emission, and (b) an SEM image showing OLED cathode delamination and active layer crystallization after use. Figure adapted with permission from Smith *et al.*⁵⁹

1.3. Scope and Relevance of This Thesis

This thesis explores questions related to materials processing and device architectures, targeting parts of all of the challenges presented above. First, an understanding of materials crystallization by heating in device-relevant thin films is developed, including methods to tailor crystal growth by anneal conditions and inclusion of film additives. This leads directly into engineering of novel thin-film structures using intrinsic mechanical properties of the organic films, and finally into organic optoelectronic devices. This includes a study of parameters which improve excited state motion and thus OPV efficiency followed by methods to induce crystallization in layered architectures and effects on devices.

2. ORGANIC SEMICONDUCTORS

This chapter is designed to provide information and perspective on the fundamental characteristics, physics, and processes which define the materials of focus for the remainder of this thesis. As such, the chapter begins with defining features of organic semiconductors, including excitons, polarons, and their motion, transitions into common material phases in these materials, and ends by focusing on crystals, crystallization processes, deposition techniques, and their use in devices.

2.1. Energetics and Optical Behavior

2.1.1. Intramolecular Bonding and Effects

Molecules are comprised of atoms which interact within a given molecule through a bonding network involving *s*, *p*, and occasionally *d* orbitals. In H₂ (Figure 2.1a), each of the starting hydrogen atoms has one electron in isotropic *s* orbitals which energetically split into two hybrid orbitals as they are brought together, one attractive and one repulsive. The attractive orbital has in-phase electron density between the two nuclei and is lower in energy (more stable) than the two free atoms, tending to stabilize the bond when occupied by electrons as a “bonding” or “gerade” (German for “even” due to inversion symmetry)

Organic Semiconductors

orbital. These s orbitals form σ bonding orbitals (Figure 2.1c), more specifically denoted σ , σ_g , or the Mulliken label a_{1g} , which convolutes symmetry and energy. The second orbital is the opposite of the former: out-of-phase, destabilizing, with no internuclear density, and is an “antibonding” or “*ungerade*” (odd) orbital denoted σ^* , σ_u , or a_{1u} .

Atoms with greater numbers of electrons, like nitrogen, bond with anisotropic p or d orbitals (Figure 2.1b). p orbitals are capable of hybridizing with s orbitals to form intermediate σ bonds (Figure 2.1d) or forming p -only π bonds (Figure 2.1e). Nitrogen has two π bonds (π_g , b_{1g}) and one σ (σ_g , a_{3g}) bond, a triple bond ($N \equiv N$). For large molecules, the diagrams are complicated by differences in atomic electronegativity and proximity, requiring rigorous computation.^{134–138}

Note that for N_2 and H_2 , there is one orbital which contains electrons of the highest energy, the “highest occupied molecular orbital” (HOMO), akin to a valence band. The empty orbital just above it is the “lowest unoccupied molecular orbital” (LUMO), similar to a conduction band. If an electron in the HOMO is sufficiently excited, it may transition to the LUMO, as discussed in Section 2.1.2.

Bonds act as a restorative force if the atoms are perturbed away from the equilibrium spacing. In reality, these bonds are continuously vibrating around their equilibrium

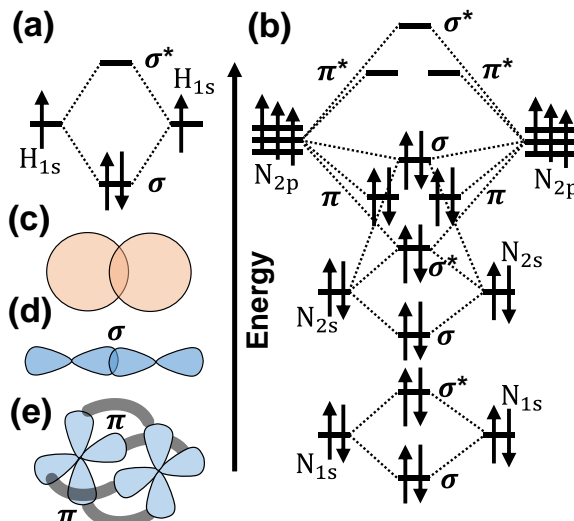


Figure 2.1. Molecular orbital diagrams of (a) H_2 and (b) N_2 , with schematics of (c) s orbitals in a σ bond, (d) p orbitals in a σ bond, and (e) p orbitals forming π bonds.

Organic Semiconductors

spacing, adding vibrational energy to the base energy level of the orbital proportional to the given harmonic of the fundamental bond frequency, shown in Figure 2.2. The bold

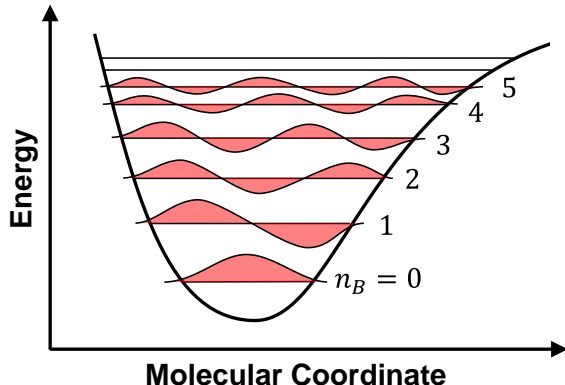


Figure 2.2. Molecular orbital energy manifold plotted over the molecular coordinate, or the molecular state in real space, including vibrational energy. The vibrational modes are drawn over each harmonic.

quadratic bond potential, where \hbar is Planck's constant h divided by 2π , ω is the fundamental bond oscillation angular frequency, and n_B is the harmonic or energy level. The non-parabolic potential shape and energy levels which approach one another with increasing harmonic number are a result of the finite limits of the bond potential. The alignment of the wavefunction density (the waves superimposed on each level in Figure 2.2) gives the probability of transitioning between vibronic states, the Franck-Condon factor.^{139,140}

The spin of the electrons also influences the type and energetics of the molecular orbital they occupy. To satisfy the Pauli exclusion rule, electrons in the same orbital have opposite spins which cancel, but electrons in different orbitals

outline shows the average difference in bond length between fully compressed (left) and fully extended (right) molecules during bond oscillation. Horizontal connecting lines represent discrete energies of the vibrational harmonic which is excited, equal to $\hbar\omega\left(\frac{1}{2} + n_B\right)$ for a

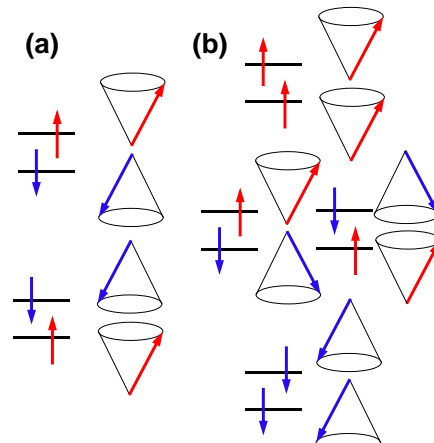


Figure 2.3. Schematic showing electron spin configurations in (a) singlet and (b) triplet excited state.

Organic Semiconductors

need not. This leads to different spin configurations in excited states, where the HOMO and LUMO electrons have different spin directions and phase. Phase is important, because the electron spin precession, represented by the cones in Figure 2.3, changes spin cancellation criteria. If the two spins cancel completely, as in Figure 2.3a, the state has zero net spin. These two states superimpose out of phase to form one state, denoted as $|S, M_S\rangle$, with S and M_S the spin quantum number and spin angular momentum, respectively.¹⁴¹

$$|0,0\rangle = \frac{1}{\sqrt{2}}(\uparrow\downarrow - \downarrow\uparrow) \quad (2.1)$$

There are $2S + 1 = 3$ cases where the spins have unity magnitude but different signs (Figure 2.3b), causing them to split energetically in a magnetic field (a partial example of the vectorial Russell-Saunders coupling that leads to the Zeeman effect¹⁴¹):

$$\begin{aligned} |1,1\rangle &= \uparrow\uparrow \\ |1,0\rangle &= \frac{1}{\sqrt{2}}(\uparrow\downarrow + \downarrow\uparrow) \\ |1,-1\rangle &= \downarrow\downarrow \end{aligned} \quad (2.2)$$

The multiplicity of these states gives rise to the singlet (Eqn. 2.1) and triplet (Eqn. 2.2) terminology. In general, triplet excited states are lower in energy than corresponding singlet states because electrons with like spins magnetically repel *via* the exchange interaction, increasing the orbital size and reducing electrical repulsion.¹⁴¹ This is also why triplet manifold centers often are located at larger molecular coordinates than singlet states; triplet states are not distinct orbitals, just alterations of the isoelectronic singlet state.

Converting between states (intersystem crossing) requires a spin flip, most often *via* spin-orbit coupling, electron spin coupled to the electrical current produced by its orbit.

Organic Semiconductors

This intermixes spin states and increases flip probability, influenced by charge in adjacent orbitals and scaling as Z^4 , where Z is the atomic number.¹⁴¹ For efficient coupling, molecular centers in OLED emitters often feature high- Z atoms (*e.g.*, Ir and Pt).^{13,142} More exotic modes like singlet fission are also observed,¹⁴³ often in organic crystals.^{144–148}

2.1.2. Optical Absorption and Emission

Electrons in the HOMO of a material can be promoted to the LUMO by the addition of energy, most commonly by absorption of a photon. This is most easily shown on a Jablonski diagram (Figure 2.4a). Molecules can absorb light of equal or greater energy than the difference between the available energy manifolds, shown in step (1). Often, this light has more energy than necessary to overcome the electronic difference, causing the electron to be promoted to a higher vibrational energy level within the upper manifold. Higher-energy vibrations readily couple to surrounding molecules, causing extremely fast

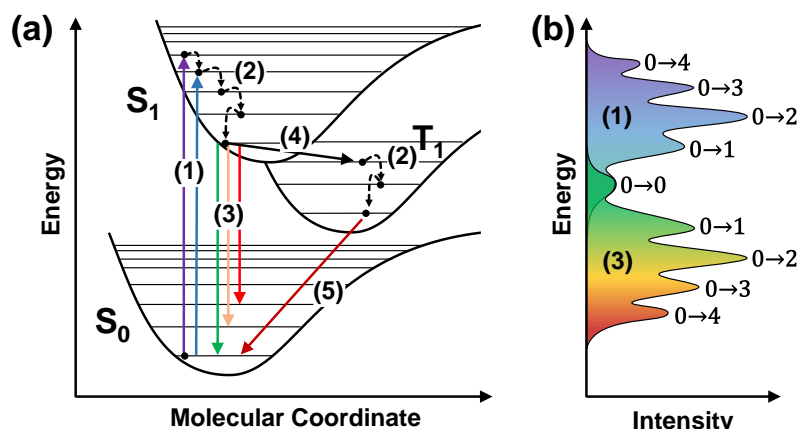


Figure 2.4. (a) Jablonski diagram showing excitonic processes in singlet (S_0 , S_1) and triplet (T_1) manifolds with approximate timescales: 1. Excitation (~1 fs) 2. Relaxation (10 fs-10 ps) 3. Fluorescence 1-100 ns 4. Intersystem crossing (10-1000 ps) 5. Phosphorescence (1 μ s-100 s). (b) Fictional absorption (1) and emission (3) spectra for an organic molecule, with the vibrational transitions labeled for (1) $S_0 \rightarrow S_1$ and (3) $S_1 \rightarrow S_0$. Spectral shape in real molecules would be determined by Franck-Condon factors.

relaxation to the fundamental harmonic (2). From there, the electron may transition to a lower-energy state, releasing the difference in energy by emission of a photon (3) or through non-radiative means.

Organic Semiconductors

Radiative singlet-singlet transitions are termed fluorescence, and are typically rapid owing to the fact that they are spin-allowed. Excited singlet states can also intersystem cross to form triplet states (4), which can be quite long-lived owing to the spin-disallowed nature of an optical transition to the ground singlet state and the fact that photons carry no momentum, making phosphorescence (5) considerably slower. The efficiency of light emission is the photoluminescence efficiency, η_{PL} , written as

$$\eta_{PL} = \frac{k_R}{k_R + k_{NR}} \quad (2.3)$$

where k_R and k_{NR} are the radiative and non-radiative exciton decay rates, respectively.

The process of relaxation (2) introduces a Stokes shift between absorption and emission (Figure 2.4b). Excitation photons must have energy greater than or equal to $S_0^0 \rightarrow S_1^0$ ($S_{e_B}^{n_B}$, e_B electronic level), which subsequently relax to S_1^0 . Optical emission occurs $S_1^0 \rightarrow S_0^{n_B}$, to any vibrational energy level, meaning that emitted photons will have energy less than or equal to $S_1^0 \rightarrow S_0^0$. This effectively inverts the absorption spectrum around $S_0^0 \rightarrow S_1^0$ to give the emission spectrum, and yields a very small amount of spectral overlap between each process; less once Coulombic charge interactions are included, as in Section 2.2.

2.1.3. Energy Level Determination Methods

Based on the physics of the previous sections, there are a few common techniques to measure the HOMO and LUMO energies, the levels relevant to most processes in organic electronics. These levels are most directly probed by photoemission, namely ultraviolet and inverse photoelectron spectroscopy (UPS and IPS or IPES, respectively).^{149,150} UPS probes electrons in the HOMO of a material *via* the photoelectric effect, in which a photon

Organic Semiconductors

of energy $h\nu_1$ ejects an electron (Figure 2.6a). The difference between the photon and electron energy is the ionization potential (IP) or HOMO energy.^{149,151,152} In IPES, the material is bombarded with electrons of known energy, some of which incorporate into the available LUMO (Figure 2.6b). This requires the release of energy by the electron,

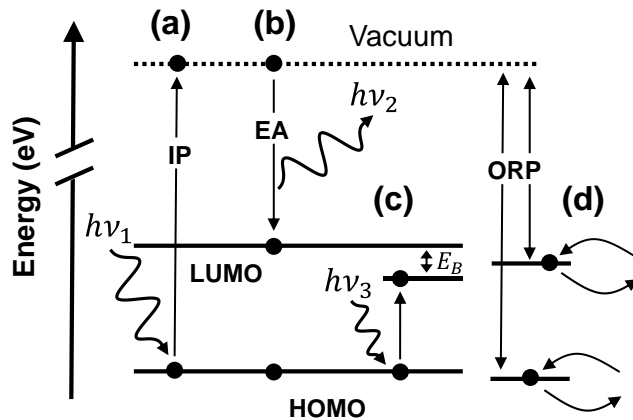


Figure 2.5. Methods of determining energy levels in organic semiconductors (a) ultraviolet photoelectron spectroscopy (UPS), (b) inverse photoelectron spectroscopy (IPES), (c) optical absorption, and (d) cyclic voltammetry. Other variables explained in the text.

gap is capable of promoting an electron and registers as an absorption onset (Figure 2.6c).^{153,154} However, this method can significantly underestimate the difference if the charges interact with a binding energy E_B ,^{78,136} as promotion is to the bound, not free, state. Finally, cyclic voltammetry (CV) probes dissolved material in an electrochemical cell by sweeping electrode voltages (Figure 2.5d).^{152–154} Peaks in electrode current are detected as the material gains or loses electrons to the electrolyte, giving the oxidation/reduction potential (ORP) of the material. In addition to the differences from the material being in solution rather than solid-state,^{151,152} there are variations in the calibration and interpretation of these values,¹³⁶ making CV values challenging to use consistently.

typically as light with a wavelength $h\nu_2$, which are detected and used to determine the material electron affinity (EA), or LUMO energy.^{150,151} An estimate of the HOMO-LUMO difference is sometimes measured using optical absorption, where light of energy $h\nu_3$ greater than the energy

2.2. Excitons

The optoelectronic character of organic electronic devices is defined by quasiparticles called excitons; Coulombically-bound, charge-neutral excited states comprised of an electron and hole. This Coulombic binding energy reduces the energy difference between the charges involved to less than the HOMO-LUMO energy gap, stabilizing the exciton relative to free carriers. The ubiquitous and defining nature of excitons in organic electronics has led to considerable work to better understand and manipulate their properties.^{78,155–163} In general, there are three main types of excitons which differ in binding energy and spatial position of charge, altering their properties and treatment in devices.

2.2.1. Wannier-Mott Excitons

Conventional inorganic semiconducting materials form excitons as a secondary photogeneration route, but the large dielectric constant of these materials screens the two carriers and reduces their binding energy to be comparable to available thermal energy.^{164,165} These excitons spontaneously dissociate without need for any special architectural or energetic considerations, which has allowed rather simple PV designs in existing solar cells,^{166–168} with excitons being little more than an afterthought.

2.2.2. Frenkel Excitons

Excitons in organic materials arise from the weak intermolecular bonds and low-mass atoms which comprise these molecules, resulting in low dielectric constants and poor charge-screening.^{18,156,169} In amorphous organic materials, excitons are thought of as largely residing on single molecules,¹⁷⁰ but in crystals, larger intermolecular coupling can

Organic Semiconductors

result in more delocalized excitons with lower exciton energies.^{171–174} Still, excitons are typically bound with sufficient strength (hundreds of meV) so as to prohibit their dissociation in bulk.^{18,38,175} Spontaneous dissociation thus requires available energy levels which have a net energy lower than that of the exciton. This is most often accomplished at heterojunctions of energetically dissimilar materials shown in Figure 2.6, however, the exciton may also be dissociated in strong electric fields, as in Schottky devices,^{176–180} or at defect sites such as free surfaces.^{181,182} Excitons may also dissociate into higher-energy states, but such an endothermic process is unfavorable. If dissociation does not occur within the finite exciton lifetimes listed in Figure 2.4, the exciton recombines.

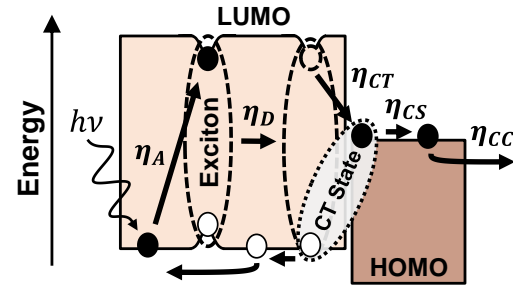


Figure 2.6. Photoconversion process in OPVs, showing the processes and efficiencies of absorption (η_A), exciton diffusion (η_D), charge transfer (η_{CT}), charge separation (η_{CS}), and charge collection (η_{CC}).

2.2.3. Charge-Transfer or Exciplex

A final type of excited state relevant in organic materials exists between spatially separated, but still interacting, charges. Charge-transfer states are formed as an intermediate between excitons dissociating into free carriers in OPVs,^{79,183,184} if injected carriers become bound on adjacent molecules, the state is termed an exciplex,^{185–187} common in OLEDs. CT states are often encountered in polycrystalline materials where additional delocalization is possible,^{184,188,189} are importantly correlated to the maximum operating voltage for OPVs,^{190,191} and affect the efficiency of the device as an energy loss pathway.⁷⁹

2.2.4. Exciton Recombination

An excited state is not a stable configuration, which drives rapid exciton recombination on time scales of 0.1-100 ns for singlet and 100 ps – 100 s for triplets.^{184,192–196} Radiative transitions are driven by the magnitude of the transition dipole moment, the degree of coupling between excited and ground states.¹⁹⁶ Although perhaps not surprising, this relationship means that the stronger the absorption for a material, the shorter the exciton lifetime – unfortunate for OPV materials. However, the limiting factor for many materials is nonradiative loss, inferred from the low η_{PL} in OPV materials.^{31,197,198} These transitions are difficult to identify because of the absence of any traceable ingredient or byproduct due to the charge-neutral nature of excitons and the absence of light or charge carriers. However, due to the quantitative nature of electronic transitions, exciton recombination must be coupled to processes which absorb and dissipate the exciton energy, such as phonon modes within the material or nearby excited states (exciton-exciton annihilation) and charge carriers. Annihilation and charge-based mechanisms are second-order processes and are thus highly sensitive to the density of each species, typically occurring under strong optical or electrical pumping.^{81,186,192,199,200} Alternatively, the exciton can also dissociate at defect sites with subsequent carrier recombination. These mechanisms are consistent with reports of exciton dissociation with dilution (solid and solution),^{192,198} purity,^{131,132} and defects,¹⁸¹ but remain challenging to directly visualize.

2.3. Exciton Motion

Excitons move by a quantitative transfer of energy between states. Energy transfer has

Organic Semiconductors

three primary manifestations in organic excitonic materials: Förster, Dexter, and Cascade energy transfer.^{78,156,160} Förster energy transfer is often considered dominant for thin films of molecules which emit light and couple *via* a dipole-dipole interaction. Dexter energy transfer relies on orbital overlap, does not require appreciable optical emission or absorption, and is often more favorable for less emissive triplet excitons or inefficient singlet materials. Cascade energy transfer features the long-range emission and absorption of a photon and requires strong luminescence and thick films or strong self-absorption in order to be efficient. In reality, each of these modes will occur to some extent in a given material, but, depending upon material properties, it may be possible to narrow the mechanism to one type of energy transfer and gain insight into underlying physics.^{170,201,202}

2.3.1. Cascade Energy Transfer

Excitons are capable of decaying radiatively, and if the resulting photon is of the correct energy to be absorbed by a second molecule, the exciton has effectively transferred energy mediated by a real photon. This type of energy transfer is termed “cascade” or “trivial” energy transfer since it resembles the basic photoexcitation process that can create excitons. The efficiency with which this process occurs is rather low, considering the low η_{PL} and relatively large Stokes shift of most materials as discussed in Section 2.1.2. For example, in the material boron subphthalocyanine chloride, η_{PL} is 1%, and the small overlap between fluorescence and absorption causes about 1.2 % of the photons emitted normal to the film surface to be absorbed in a 10 nm film, neglecting reflection. Coupling this with η_{PL} produces an energy transfer process that is less than 0.3 % efficient for SubPc films less

Organic Semiconductors

than 1 μm thick (see Table 2.1). However, excitons that are transferred do so over great distances, yielding an apparent L_D value which can be appreciable, but only for very thick films

Table 2.1. Cascade energy transfer efficiency (η_{CET} , %) and apparent cascade exciton diffusion length (L_D , nm) for films of different materials and thickness. η_{PL} values are given next to material names (%).

Film Thickness (nm)	SubPc (1.0) η_{CET}	Rubrene (2.8) L_D	Alq ₃ (14.5) η_{CET}	L_D
10	0.012	0.05	0.020	0.05
50	0.048	0.22	0.095	0.25
200	0.115	0.69	0.341	0.92
1000	0.252	3.03	1.052	3.45
			~ 0	4.61

which are typically much thicker than those used in devices. For these reasons, Cascade energy transfer is often neglected when other modes of transfer are possible.

2.3.2. Förster Energy Transfer

Förster energy transfer features intermolecular energy transfer through space and occurs *via* resonant dipole-dipole coupling.^{203–206} The Förster energy transfer rate between two point dipoles, k_F , separated by distance d is defined as

$$k_F = \frac{1}{\tau} \left(\frac{R_0}{d} \right)^6, \quad (2.4)$$

whereas for a point to a semi-infinite acceptor slab (k_{F_S}) or plane (k_{F_p}), the form is^{207–210}

$$k_{F_S} = \frac{\pi \rho_A R_0^6}{6\tau} \frac{1}{d^3} \quad (2.5)$$

$$k_{F_p} = \frac{\pi \rho_A R_0^6}{2\tau} \frac{1}{d^4} \quad (2.6)$$

where now d is the distance from the dipole to the acceptor slab or plane surface, and ρ_A is the number density of acceptors (per volume or area, respectively) within the acceptor material. The parameter R_0 is the Förster radius, the radius at which energy transfer is equally competitive with all other excited state decay pathways, described by

Organic Semiconductors

$$R_0^6 = \frac{9\eta_{PL}\kappa^2}{128\pi^5} \int \frac{\lambda^4 F_D(\lambda)\sigma_A(\lambda)}{[n(\lambda)]^4} d\lambda \quad (2.7)$$

For classical and quantum-mechanical derivations and discussion of this result, the reader is referred to Appendix G. Here, η_{PL} is the overall molecular photoluminescence efficiency or quantum yield, κ^2 is the orientation factor, n is the index of refraction for the surrounding medium, λ is the wavelength of light in nm, F_D is the area-normalized emission (fluorescence) spectrum of the excited state or donor, and σ_A is the absorption cross-section of the acceptor molecule under consideration,⁷⁸ related to the extinction coefficient k or absorption coefficient α by

$$\sigma_A(\lambda) = \frac{4\pi k(\lambda)}{\lambda \rho_A} = \frac{\alpha(\lambda)}{\rho_A} \quad (2.8)$$

In the event that energy transfer occurs in anisotropic crystals, the tensor dielectric properties (indicatrix and conductivity tensor) should be used: see Appendix G.4.

A common simplification is to use n at the wavelength of peak emission/absorption overlap and to remove it from the integral, which works well provided the donor material emits outside of the regions of rapid index dispersion common near absorption features. Since η_{PL} can also be written in terms of the rate of radiative and non-radiative exciton decay as shown in Eqn. 2.3, and τ written as

$$\tau = \frac{1}{k_R + k_{NR}} , \quad (2.9)$$

then the Förster rate can expressed in terms of the radiative exciton lifetime τ_{rad} as

$$k_F \propto \frac{\eta_{PL}}{\tau} = \left(\frac{k_R}{k_R + k_{NR}} \right) / \left(\frac{1}{k_R + k_{NR}} \right) = k_R = \frac{1}{\tau_{rad}} . \quad (2.10)$$

Eqn. 2.7 will sometimes include a factor of $(1000 \ln 10)/N_A$ (N_A is Avogadro's number);

Organic Semiconductors

that form uses the decadic (\log_{10}) molar absorption instead of σ_A .

By combination of Eqn. 2.4 with Eqns. 2.17 and 2.28 (discussed below), it may be shown that in a general isotropic Förster material,

$$L_D = \sqrt{\frac{R_0^6}{d^4}} = \frac{R_0^3}{d^2} \quad (2.11)$$

This leads to several interesting material trade-offs which are discussed in Section 2.3.4.

The orientation factor describing the molecular coupling in Förster energy transport has been the subject of much debate and confusion in the literature, especially as applied to biological probes.^{211–215} Examining the orientation factor in light of the provided derivations, the square of κ defined in Eqn. 14.30 is most commonly written

$$\kappa^2 = (\cos \gamma - 3 \cos \alpha \cos \beta)^2 \quad (2.12)$$

where α and β are the angles between the connecting vector \underline{r} and the dipole moments for the donor and acceptor molecules, and γ is the angle between the two dipoles shown in Figure 2.7a. An equivalent, and in many cases more direct, method of writing κ^2 is²¹⁶

$$\kappa^2 = (3 \cos^2 \psi + 1) \cos^2 \theta \quad (2.13)$$

The new variables ψ and θ represent the angle between excited state dipole and the connecting vector for the

donor-acceptor and the angle between the acceptor dipole and the electric field from the excited state at the

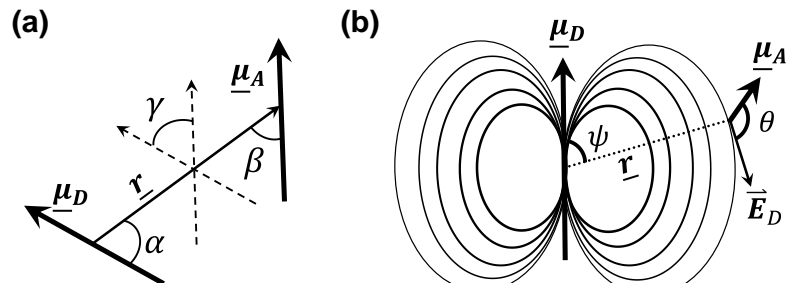


Figure 2.7. Diagrams showing different definitions of the orientation factor, with (a) purely geometric and (b) based on the donor electric field. Variables defined in the text.

Organic Semiconductors

acceptor center of mass, respectively, as shown in Figure 2.7b. Limiting cases of κ^2 are when the acceptor molecule is orthogonal to the donor electric field ($\theta = \pi/2$, $\kappa^2 = 0$) and when the two dipoles are collinear – not necessarily head-to-tail because of the oscillatory nature of the field – ($\psi, \theta = 0$ or 1 , $\kappa^2 = 4$).

More typically in disordered systems, the orientation factor is averaged for the static or dynamic limit. If the motion of the transition dipole is slow relative to the rate of energy transfer (e.g., frozen or viscous solutions, solids, thin films), the dipole orientation will be preserved while the excited state exists on a given molecule. Evaluation of the integral average of Eqn. 2.13 over all angles gives the “static limit” $\langle \kappa^2 \rangle = 0.476$.^{88,217,218} For the case of rapidly rotating dipoles (the “dynamic limit”) – common in solution or weakly bound biological probes – the orientation factor is evaluated as $\langle |\kappa| \rangle^2 = 2/3$.^{88,214,218}

Although the form in Eqn. 2.13 is more useful for evaluation of averages because ψ and θ are completely independent, calculations involving molecules oriented in a lattice are more easily performed using Eqn. 2.12, as the angles or vectors can be directly calculated if the transition dipole orientation is known. Visualizing transition dipoles is non-trivial, more so if the transition dipole on a molecule can assume multiple orientations, e.g., with n -fold symmetric molecules like phthalocyanines and porphyrins ($n \geq 3$). Dipole orientation varies greatly from along the short, long, or no molecular axis, as well as with different levels of excitation.^{200,219–222} In general, these dipoles must be calculated.

The case of degenerate dipoles requires a different calculation method. A common manner to do this is Jablonski’s method of a planar oscillator,^{218,223} explicitly varying κ

according to

$$\kappa(\nu_1, \nu_2) = \cos \gamma(\nu_1, \nu_2) - 3 \cos \alpha(\nu_1) \cos \beta(\nu_2) \quad (2.14)$$

Here, the angles ν_1 and ν_2 have been introduced to describe rotation of the donor and acceptor transition dipoles in the dipole plane, giving a dependence to all of the inter-dipole angles, as shown in Figure 2.8. These expressions can then be used in an integral average over all angles ν_1, ν_2 to calculate an average orientation factor for that molecule pair, taken here in the static limit.

$$\langle |\kappa| \rangle^2 = \left\{ \frac{1}{2\pi} \int_0^{2\pi} \left(\frac{1}{2\pi} \int_0^{2\pi} |\kappa(\nu_1, \nu_2)| d\nu_1 \right) d\nu_2 \right\}^2 \quad (2.15)$$

Since the orientation factor depends greatly on molecular position, it is sensitive to changes in the film structure, which can modulate its overall magnitude. Common methods to vary molecular arrangement include crystallization,^{109,224,225} molecular templating,²²⁶ film growth near the glass transition temperature,^{227,228} and ordering by targeted molecular design.^{229–231} Besides improvement of the orientation factor, such ordering is also targeted to enhance light absorption or emission by shaping the molecular interaction with the optical field.^{232–235}

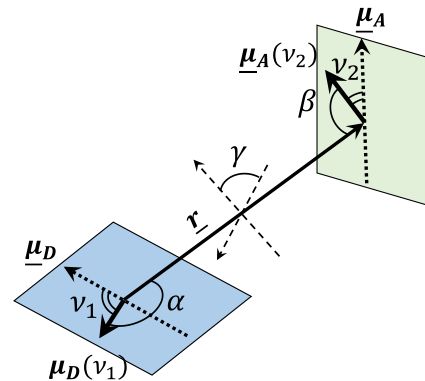


Figure 2.8. Diagram of rotating exciton donor $\underline{\mu}_D$ and acceptor $\underline{\mu}_A$ transition dipoles

2.3.3. Dexter Energy Transfer

When the exciton is unable to efficiently decay by radiative means, Förster energy transfer becomes prohibitive due to the η_{PL} dependence in Eqn. 2.7. However, the

Organic Semiconductors

impracticality of energy transmission by electrostatic coupling does not preclude the direct exchange of energy by molecules which overlap in orbital extent (or wavefunction), termed Dexter energy transfer or the “exchange” mechanism. This method of transfer was introduced by David L. Dexter in 1953 while studying sensitized luminescence in mixed solids incapable of Förster transfer due to the absence of spectral overlap between the energy donor (sensitizer) and acceptor (emitter).²³⁶ The Dexter energy transfer rate is

$$k_D = KJ \exp\left(-\frac{2d}{L}\right) \quad (2.16)$$

For a derivation of this result, the reader is encouraged to read Appendix G.5. Here, K accounts for all quantum-mechanical terms besides the normalized spectral overlap integral J , with the distance dependence scaling with L , the average Bohr radius of the excited donor state and the ground acceptor state. This sharp dependence with distance leads to a typical interaction volume of 2-3 molecular shells around the excited state.²³⁶

2.3.4. Comparison of Energy Transfer Methods

There are several factors which determine the efficiency of each energy transfer method, sometimes allowing for the isolation of one particular mode. Cascade energy transfer is rarely the sole diffusive mechanism because of its reliance on emission and absorption which also favor Förster transport. However, energy propagation *via* photon emission and absorption results in an extremely long-range process, despite being compromised in efficiency by large Stokes shifts in most materials. This makes Cascade energy transfer a secondary method of transfer at best, and is neglected in most cases.

Comparing between Dexter and Förster transport, the relatively long-distance (d^{-6})

Organic Semiconductors

dipole-dipole interaction (Figure 2.9a) and requirement of efficient luminescence for Förster transport contributes to an association of Förster transport with large diffusivities and predominantly fluorescent molecules.⁷⁸ Conversely, Dexter transport may be considered dominant in nearest-neighbor orbital overlap interactions (Figure 2.9b) in “dark” materials with extremely low η_{PL} , contributing to small diffusivities. Perhaps surprisingly, L_D need not decrease monotonically with molecular separation: the relationship of R_0^6/d^4 in Eqn. 2.11 coupled with the increase of η_{PL} upon dilution in many materials can lead to an increased L_D in dilute films despite larger d .^{237,238} However, the dependence of the exciton diffusion length on exciton lifetime differs significantly between the two transport modes, allowing diffusion by Dexter mechanisms to have comparable L_D values as Förster, even with significantly lower hopping rates (Figure 2.9c).

On a more fundamental level, this dependence implies finite limitations for Förster energy transport.^{156,196} The direct dependence of k_F on the radiative rate (Eqn. 2.10) means that the hopping rate and diffusivity are unbounded. However, the exciton diffusion length

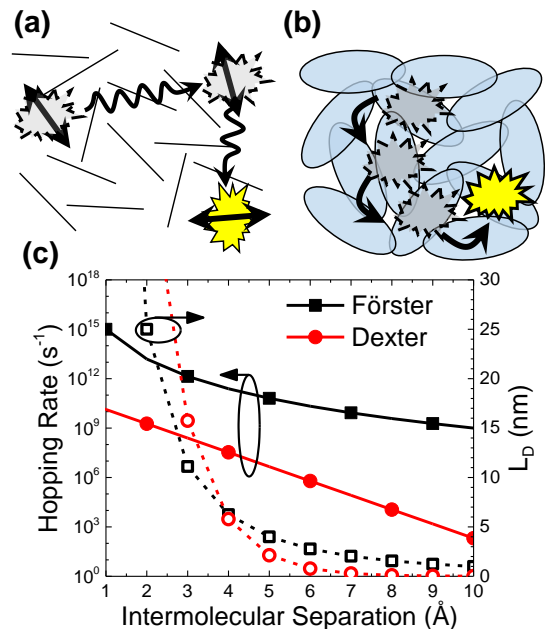


Figure 2.9. Schematics for (a) Förster and (b) Dexter energy transport, with the resulting distance dependence (c) for each style of motion. The calculations in (c) are for arbitrary molecules with $R_0 = 1$ nm and $\tau = 1$ ns (Förster) and $KJ = 10^{11} \text{ s}^{-1}$, $L = 1 \text{ \AA}$, and $\tau = 1 \mu\text{s}$ (Dexter).^{198,876}

scales according to their ratio owing to the dependence of k_F and τ on the magnitude of the excited state dipole moment:¹⁹⁶

$$L_D = \sqrt{D\tau} = \sqrt{k_F d^2 \tau} \propto \sqrt{\frac{k_R}{k_R + k_{NR}}} , \quad (2.17)$$

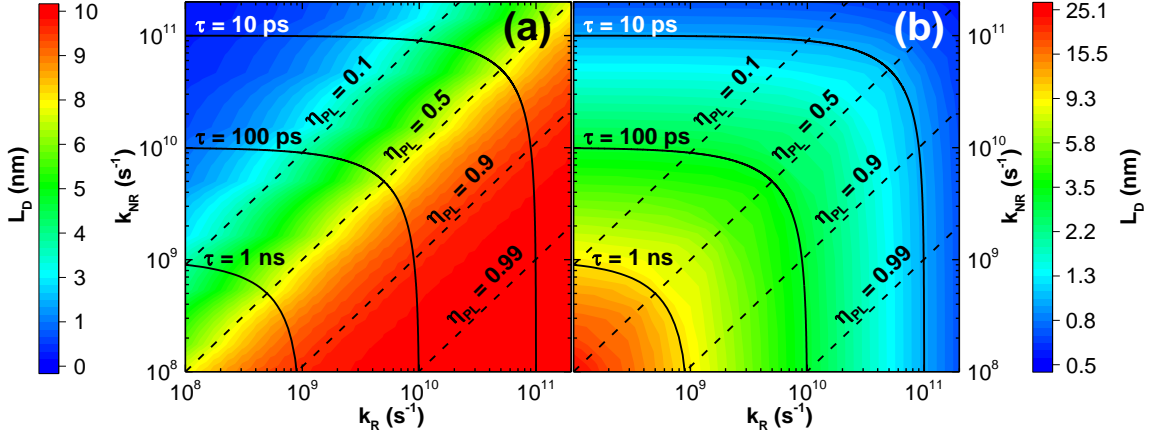


Figure 2.10. Exciton diffusion lengths as a function of k_R and k_{NR} for (a) Förster energy transfer, with $R_0^6/\eta_{PL} = 1$ nm and a cubic lattice of $a = 1$ nm, and (b) Dexter energy transfer, with $k_D = 10^9$ s $^{-1}$.

which means the diffusion length asymptotically approaches a fixed value as the radiative rate increases, as depicted in Figure 2.10a. In accordance with Eqn. 2.11, a variety of lifetimes are capable of producing large L_D values, but once an η_{PL} value is specified, the diffusion length is essentially determined. The Dexter rate does not depend on the exciton lifetime (Eqn. 2.16), making the diffusion length unbounded and only limited by the decay rate of the exciton (Figure 2.10b). As the decay rate decreases, the diffusion length diverges to infinity, which explains how the largest L_D values reported are for triplet excitons likely diffusing *via* Dexter transport.^{160,195,239} The spin-forbidden transition required for triplet exciton deactivation prolongs the exciton lifetime and allows the exciton to diffuse over a much larger distance than a comparable singlet exciton undergoing Förster energy transfer.

2.4. Polarons

Free, mobile charges in organic semiconductors exert a force on nearby molecular orbitals within a material, inducing partial charges which coordinate with the carrier and cause a distorted local environment.^{38,93} This net charge-lattice quasiparticle is a polaron, which moves through the material as the carrier pulls the lattice distortion along. Polarons differ fundamentally from excitons in that they are charged species, which means that they repel one another and are affected by the presence of an electric field. Their charged nature also enables direct recombination with polarons of opposite polarity, eliminating both polarons at once. The carriers comprising the polaron also possess spin, enabling tracking and manipulation of this spin in devices which further interest in spintronics.^{240–242} There are a finite number of polarons which exist in a material at room temperature, but the concentration is quite low and most likely arises from impurities or dopants.^{45,243}

2.5. Polaron Motion

Polaron movement in organic materials depends on the degree of intermolecular interaction: in the weak interaction limit (amorphous), carriers “hop” from molecule to molecule; for strong interactions (crystalline), the polaron is delocalized and motion is more “band-like”.¹⁴⁰ This means that amorphous semiconductors are governed by percolation-like behavior, where a continuous pathway must exist in order for the charge to pass through a material. In these cases, the hopping rate in the high-temperature limit is given by the Marcus electron transfer rate between molecules, k_M ,¹³⁸

Organic Semiconductors

$$k_M = \frac{2\pi}{h} |V_{ij}|^2 \sqrt{\frac{1}{4\pi k_B T \lambda_M}} \exp\left[-\frac{(\Delta G^\circ + \lambda_M)^2}{4\lambda k_B T}\right] \quad (2.18)$$

where k_B is Boltzmann's constant, λ_M is the molecular reorganizational energy (to account for polarization shift of the charged molecule and its surroundings), ΔG° is the change in the Gibbs free energy between initial and final states, and V_{ij} is the coupling between initial (ψ_i) and final (ψ_j) states, often called the transfer integral, given by

$$V_{ij} = \int \psi_i^* V \psi_j d\underline{x} \quad (2.19)$$

These transfer integrals are non-trivial and depend largely on the extent of orbital overlap between molecules, which can be determined by parameters such as the spacing, orientation, and offset (slip) between molecules.^{138,244–246} Eqn. 2.18 demonstrates the origin

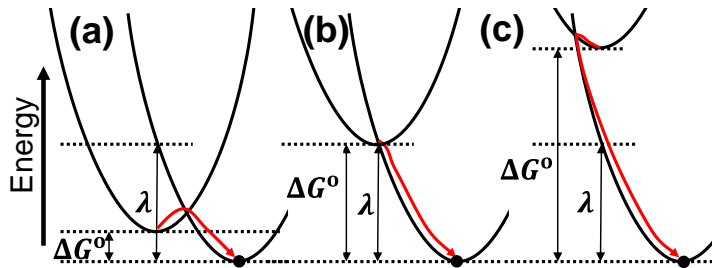


Figure 2.11. Marcus electron transfer diagram, showing (a) normal activated transfer ($|\Delta G^\circ| < \lambda$), (b) transfer with the minimum energy barrier ($|\Delta G^\circ| = \lambda$), and (c) inverted regime, where increased driving force causes an increase in the activation energy between states ($|\Delta G^\circ| > \lambda$).

of the “inverted Marcus regime”, where the application of a greater driving force ΔG° actually reduces the rate of transfer, as shown in Figure 2.11. Equally importantly,

polarons may become trapped in shallow energy wells within the material from defects (grain boundaries, impurities, disorder), which further reduces this rate.^{247–250} The hopping rate in Eqn. 2.18 decreases with temperature, since hopping is an activated process, but if the trapping rate decreases more quickly with temperature (from traps “freezing out”, becoming neutralized), the overall mobility of the polaron may effectively

Organic Semiconductors

increase.^{102,251,252} This behavior is observed in highly ordered and purified crystals, and is termed “band-like” for its resemblance to the inorganic case.¹⁴⁰

In stacks of heterogeneous materials, polarons transfer between dissimilar layers on the material HOMO and LUMO for holes and electrons, respectively. In the case of diffusion, as for OPVs, polarons move spontaneously to lower energy levels and eventually out of the device. OLEDs require polarons to be injected using an electric field, where they migrate (drift) with the field between different materials. The energetic offsets between layers leads to different barriers for polaron motion, as do the differing polaron mobilities in different materials.

2.6. Exciton and Polaron Transport Equations

Excitons move between molecules in a material at random, with calculable rates (or probabilities) as described in Section 2.3. In the absence of an electric field, polarons do the same. This behavior resembles diffusion, where a species (whether mass, heat, or momentum) is dispersed throughout a material by random motion and migration through collisions within the material, which proceeds until an equal potential (chemical, thermal, or force, respectively) is established throughout the accessible region.^{253,254} When there is a field, this imposes a gradient in the energy landscape, causing net polaron flow *via* drift or advection. Excitons may also migrate in non-uniform electric fields,^{255,256} but a more common drift-like mechanism is exciton gating.

2.6.1. Diffusion

Exciton motion can often successfully be described as diffusive because the excitons completely disorient upon transfer between sites and the length scales of motion are reasonably large compared to a single hop between sites. Polarons similarly move in random directions, covering large distances with many small movements. Something perhaps unusual about these quasiparticles is their ability to traverse many sites in a single hop, inconceivable for a physical species or thermal unit. Fortunately, the randomness of this motion cancels the size imbalance, except in the case of some motion-directing structures and fields, as will be discussed in Section 2.6.2. The net thermodynamic effect is for the species of interest to move into an area of lower chemical potential; Fermi energy for polarons and typically density or concentration for excitons. This motion can be highly anisotropic, especially in crystalline solids.^{88,239,257–263}

When diffusion is used and mapped in the literature, there is often misunderstanding over the origin of some factors associated with describing exciton diffusion and anisotropic diffusivity. As clarification and to provide a greater fundamental insight, a rigorous derivation of the exciton diffusion equation is provided here, written in general terms to include polaron motion as well.

In a given material, an exciton or polaron on molecule i moves by hopping to any surrounding molecule j with a rate k_{ij} , the rate of energy or electron transfer between molecules i and j (Figure 2.12a). In a uniform, isotropic material, this motion is random; mathematically, the particle has equal probabilities of moving in all directions. For

anisotropic materials, the rate k_{ij} will differ systematically as a function of direction. In the following derivation,^{253,264} let a quasiparticle be created on an arbitrary molecule D (particle donor) within the bulk of an excitonic material at time $t = 0$. The discrete site-to-site probability of the particle existing on this molecule at time t , $\rho_D(t)$, which corresponds to normalized concentration in classical diffusion, is unity upon creation but subsequently decreases at a rate proportional to net transfer (both to and from an acceptor molecule) and natural decay. Symbolically, this is²⁰⁴

$$\frac{\partial \rho_D(t)}{\partial t} = \sum_A [k_{AD}\rho_A(t) - k_{DA}\rho_D(t)] - \frac{1}{\tau} \rho_D(t) \quad (2.20)$$

where the sum is over all possible acceptor molecules A and τ is the natural particle lifetime of the material (carriers are typically much longer-lived than excitons), with the rate of transfer between a molecule and itself ($A = D$) set to zero. In classical diffusion, the typical length scale of movement per jump is considerably smaller than the total distance traveled from diffusion, allowing this probability to be converted to a continuous function of space $\rho(\underline{x}, t)$ rather than the discrete form written in Eqn. 2.20.²⁵⁴ This functional form allows expansion of the probability by a Taylor series as^{253,265}

$$\rho(\underline{x}_A t) = \rho(\underline{x}_D, t) + \underline{x}_A \cdot \underline{\nabla} \rho(\underline{x}_A t) + \frac{1}{2!} \underline{x}_A \underline{x}_A \cdot \underline{\nabla} \underline{\nabla} \rho(\underline{x}_A t) + \dots \quad (2.21)$$

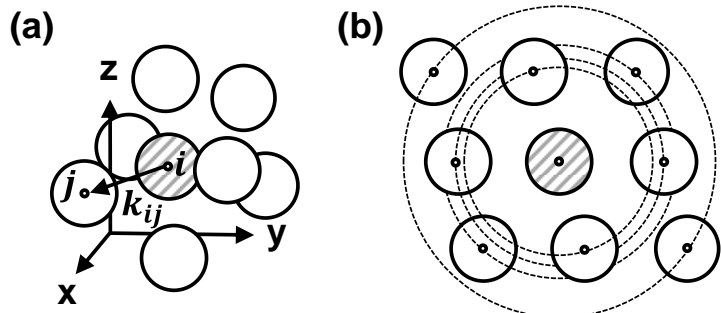


Figure 2.12. Diagram showing (a) energy or electron transfer from molecule i to j with rate k_{ij} and (b) the first four molecular shells for an arbitrary two-dimensional lattice.

Organic Semiconductors

written here for the first three series terms. Bolded variables with underscores are tensor quantities, with the tensor order given by the number of underbars: *e.g.*, \underline{x}_i is the first-order tensor $[x_i, y_i, z_i]$. Note that truncating Eqn. 2.21 to the second order term explicitly assumes that the distance between donor (\underline{x}_D) and acceptor (\underline{x}_A) positions, written as \underline{x} and $\underline{x} + \Delta\underline{x}$ in typical Taylor series, is small compared to the distance required for system non-linearity (*e.g.*, curvature in a concentration profile). In thin films relevant to organic electronic devices, the validity of this assumption depends upon the ratio of the diffusion length to a single hop or, alternatively, the particle lifetime relative to the transfer rate.

If the truncated form of Eqn. 2.21 is inserted into Eqn. 2.20, \underline{x}_D is set as the origin $\underline{0}$ (hop length = \underline{x}_A), and the transfer rate k_{ij} is expressed as $k_{ET}(\underline{x})$ (for transfer to position \underline{x}), the resulting equation is

$$\frac{\partial \rho(\underline{0}, t)}{\partial t} = \sum_A \left\{ [k_{ET}(-\underline{x}_A) - k_{ET}(\underline{x}_A)]\rho(\underline{0}, t) + k_{ET}(\underline{x}_A) \left[\underline{x}_A \cdot \nabla \rho(\underline{x}_A, t) + \frac{1}{2} \underline{x}_A \underline{x}_A : \nabla \nabla \rho(\underline{x}_A, t) \right] \right\} - \frac{1}{\tau} \rho(\underline{0}, t) \quad (2.22)$$

This is the general diffusion equation for temporally decaying species. The first zero-order terms describe transfer rate asymmetry, while the first-order term relies on a monotonic asymmetry in the rate-distance product as in a binned or gradient concentration architecture. Without this asymmetry, these odd terms cancel under summation. More direct interpretation of these terms is challenging, as discussed in Section 2.6.2. However, the second-order term can be recognized as diffusion by removing the zero- and first-order terms in Eqn. 2.22 and comparing to Fick's law for a general anisotropic medium:

Organic Semiconductors

$$\frac{\partial \rho}{\partial t} = \underline{\nabla} \cdot (\underline{\mathcal{D}} \cdot \underline{\nabla} \rho) \quad (2.23)$$

In Eqn. 2.22, the diffusivity tensor $\underline{\underline{\mathcal{D}}}$ is formulated by summation of transfer over all sites, as in Figure 2.12b, yielding a constant of

$$\underline{\underline{\mathcal{D}}} = \frac{1}{2} \sum_A k_{ET} \begin{bmatrix} x_A^2 & x_A y_A & x_A z_A \\ y_A x_A & y_A^2 & y_A z_A \\ z_A x_A & z_A y_A & z_A^2 \end{bmatrix} \quad (2.24)$$

Note that k_{ET} is still a function of direction and distance, detailed in Chapter 7. In an isotropic material, the off-diagonal elements of Eqn. 2.24 are cancelled because the material symmetry causes the odd terms to sum to zero, and the diagonal elements become equal, reducing the gradient dyad in Eqn. 2.22 to a Laplacian. For a cubic lattice (which is rare in organic crystal structures, but is often used to approximate a disordered film), Eqn. 2.22 may be further simplified by converting \underline{x} to d ($\underline{x} \cdot \underline{x} = d^2$), the distance between relevant sites. Then, the dyadic double-dot product in Eqn. 2.22 may be converted:

$$\sum_A \left(x_A^2 \frac{\partial^2}{\partial x^2} \rho + y_A^2 \frac{\partial^2}{\partial y^2} \rho + z_A^2 \frac{\partial^2}{\partial z^2} \rho \right) = \frac{1}{3} \sum_A (x_A^2 + y_A^2 + z_A^2) \nabla^2 \rho = \frac{1}{3} \sum_A d^2 \nabla^2 \rho \quad (2.25)$$

This isotropy introduces a factor of 1/3 into the equation, so that

$$\frac{\partial \rho(\underline{0}, t)}{\partial t} = \frac{1}{6} \sum_A \{k_{ET}(d) d^2 \nabla^2 \rho\} - \frac{1}{\tau} \rho(\underline{0}, t) \quad (2.26)$$

with the diffusivity expressed as

$$\mathcal{D} = \frac{1}{6} \sum_A k_{ET}(d) d^2 \quad (2.27)$$

The expression for \mathcal{D} in Eqn. 2.27 is still a summation over all sites, with the transfer rate now assumed to be isotropic and only dependent on distance. The factor of 1/6 present

Organic Semiconductors

in Eqn. 2.27 is only present for this isotropic, unbounded sum and is cancelled by a final, common approximation in exciton diffusion to only consider nearest neighbors in a simple cubic lattice, the six closest sites. This final step is valid for transfer events which are so localized that the probability of involvement of further molecular shells is insignificant, which may not be strictly valid for all modes of transport. For these six surrounding sites, d is a constant, the intermolecular lattice spacing a , allowing Eqn. 2.27 to be re-written as

$$\mathcal{D} = \frac{1}{6} \sum_{A=1}^6 k_{ET}(a)a^2 = k_{ET}(a)a^2 \quad (2.28)$$

Note the disappearance of the factor of $1/6$ in the final form, which is commonly used to describe energy transfer. Diffusivity values calculated assuming an isotropic cubic lattice are simply $k_{ET}(a)a^2$.

2.6.2. Drift (Advection) and Drift-Like Transport

Diffusion is spontaneous, random motion; advantageous in that such motion does not require the input of energy, but less so in the efficiency of said motion. Directed transport, classically termed advection (and colloquially convection) has precise analogs in polaron motion and somewhat looser comparisons in exciton transport.

Classical Advection

In classical systems,²⁶⁶ a particle density ρ being carried by an advective velocity \underline{v} travels a fixed distance per unit time, which can be written as

$$\rho(\underline{x}, t + \Delta t) = \rho(\underline{x} - \underline{v}\Delta t, t) \quad (2.29)$$

For a given time step, the density moves by a distance $\underline{v}\Delta t$. If each side is expanded with

Organic Semiconductors

a Taylor series in time and space, respectively, this yields

$$\rho(\underline{x}, t) + \Delta t \frac{\partial \rho(\underline{x}, t)}{\partial t} \approx \rho(\underline{x}, t) - \Delta t \underline{v} \cdot \nabla \rho(\underline{x}, t) \quad (2.30)$$

These approach equality for small Δt . Rearranging this equation gives

$$\frac{\partial \rho(\underline{x}, t)}{\partial t} + \underline{v} \cdot \nabla \rho(\underline{x}, t) = 0 \quad (2.31)$$

which must be modified to include effects of expansion and contraction of a volume element, $\rho(\underline{x}, t) \nabla \cdot \underline{v}$. The sum of terms and inverse product rule gives

$$\frac{\partial \rho(\underline{x}, t)}{\partial t} + \nabla \cdot [\underline{v} \rho(\underline{x}, t)] = 0, \quad (2.32)$$

the general advection equation. Advection and diffusion are independent processes, which means that their effects and functional forms are additive.

Polaron Drift

Directed transport in polarons is typically referred to as drift, where the polarons are thought of as drifting through a material from interacting with an applied electric field. In materials where scattering collisions dominate the carrier velocity, motion can be approximated as acceleration from the field with force $q\underline{E}$ punctuated by collisions every τ_q seconds (with q the polaron charge), resetting the velocity to zero. This gives an average momentum of $q\tau_q \underline{E}$, which can be put in terms of an average velocity by using the charge effective mass (m^*), giving the Drude equation for carrier velocity^{267,268}

$$\langle \underline{v} \rangle = \frac{q\tau_q}{m^*} \underline{E} \quad (2.33)$$

The proportionality between velocity and the field is called the carrier mobility, μ_q

Organic Semiconductors

$$\mu_q = \frac{q\tau_q}{m^*} \quad (2.34)$$

Using the polaron diffusivity and hopping rate results from Eqn. 2.18 and 2.22 combined with the Einstein relation for diffusivity allows for an alternate expression⁴⁵

$$\underline{\mu}_q = \frac{q}{k_B T} \underline{\underline{\mathcal{D}}} \quad (2.35)$$

which is most generally a tensor quantity, and can be highly anisotropic.^{269–271} This makes use of the fact that the same hopping processes responsible for diffusion allow carriers to move with an applied electric field, merely in a defined direction.

Exciton Gating

Excitons are charge-neutral, removing the practical possibility of a classical drift-like mechanism from an applied force (with the exception of non-uniform electric fields^{255,256}). However, it is still possible to create structures with directed exciton transport which mimic advection through systematic anisotropy in energy transfer rates.^{237,238}

Starting from the description of diffusion in the previous section, it is tempting to define the exciton drift velocity \underline{v} as the integral of the remaining terms in Eqn. 2.22

$$\underline{v} = - \sum_A \left\{ k_{ET}(\underline{x}_A) \underline{x}_A + \int k_{ET}(-\underline{x}_A) - k_{ET}(\underline{x}_A) d\underline{x}_A \right\}, \quad (2.36)$$

and use Eqn. 2.24 for the diffusivity constant to yield a more familiar transport equation for an exciton in an anisotropic homogeneous material²⁵³

$$\frac{\partial \rho}{\partial t} = -\underline{\nabla} \cdot (\underline{v}\rho - \underline{\underline{\mathcal{D}}} \cdot \underline{\nabla}\rho) - \frac{1}{\tau}\rho \quad (2.37)$$

However, this does not necessarily conserve the original form of Eqn. 2.22 because \underline{v} would almost never be spatially invariant, which prohibits the rearrangement of \underline{v} to within

Organic Semiconductors

the divergence of Eqn. 8.35. In Einstein or index notation,²⁵⁴ this is accomplished for the diffusive case by

$$\begin{aligned}
 k_{ET}(\underline{x}_A) \underline{x}_A \underline{x}_A : \underline{\nabla} \underline{\nabla} \rho(\underline{x}_A, t) &\equiv k_{ET} x_{Ai} x_{Aj} \partial_j \partial_i \rho = \partial_j k_{ET} x_{Aj} x_{Ai} \partial_i \\
 &\equiv \underline{\nabla} \cdot [k_{ET}(\underline{x}_A) \underline{x}_A \underline{x}_A \cdot \underline{\nabla} \rho(\underline{x}_A, t)] = \underline{\nabla} \cdot [\underline{\underline{\mathcal{D}}} \cdot \underline{\nabla} \rho(\underline{x}_A, t)] \\
 &= \underline{\underline{\mathcal{D}}} : \underline{\nabla} \underline{\nabla} \rho(\underline{x}_A, t)
 \end{aligned} \tag{2.38}$$

This is justifiable for normal diffusion, since bulk energy transfer varies with direction but not distance, making \underline{x}_A and k_{ET} a function of the molecular shell to which transfer is occurring, not position within a material, allowing the final simplifications in Eqn. 2.38. Contrast this to the case of gating, which requires rearrangement of $k_{ET} x_{Ai} \partial_i \rho$ and requires the product rule upon expansion

$$\partial_i (\rho k_{ET} x_{Ai}) = k_{ET} x_{Ai} \partial_i \rho + \rho \partial_i (k_{ET} x_{Ai}) \tag{2.39}$$

Only for the case of $k_{ET}(\underline{x}_A) = 1/\underline{x}_A$ does the last term drop out, which is not likely given the energy transfer rate equations in Section 2.3. However, there are methods around this challenge that are discussed further in Chapter 8.

Generalizing this behavior to a continuously graded asymmetric structure is non-trivial because the diffusion tensor necessarily also becomes asymmetric and spatially variant, with all nine elements location-dependent. In these cases, analytical solution of the general equation is not feasible.

2.7. Function and Characterization in Devices

Although the first organic semiconductors were initially studied as pigments,^{18,272,273} the real potential of the field lies in electronic devices. As such, understanding the optical and electric function of materials within devices is critical. This section describes the key features probed and measurements used for optoelectronic characterization.

In the dark, organic photovoltaic devices (OPVs) will conduct and partially rectify an applied current, giving a curve like that shown in Figure 2.13. Once illuminated, the current passing through the cell is offset by photogenerated current, requiring a larger voltage to achieve a given current (neglecting differences in device conductance due to photoconductivity). Negative current represents current produced by the cell at a given applied voltage; these conditions can be reproduced by dropping the cell voltage across a resistive load. The cell power conversion efficiency η_P at any point may be calculated from the produced voltage V , current density J , and incident optical power P_{opt} by

$$\eta_P = \frac{V \cdot J}{P_{opt}} \cdot 100\% \quad (2.40)$$

Typically, the maximum η_P is reported at the maximum power point (V_{MP}, J_{MP}) shown in Figure 2.13 for different illumination intensities. This point can be related to the maximum current (at short-circuit, J_{sc}) and the maximum voltage (at open circuit, V_{oc}) for a given

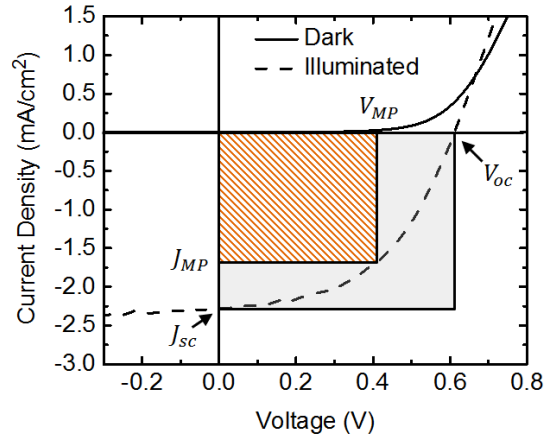


Figure 2.13. Electrical characterization of organic solar cells by sweeping the applied voltage (V) and measuring the resulting current (current density, J) passing through the device.

Organic Semiconductors

illumination condition by introducing a parameter called the fill factor FF ,

$$FF = \frac{V_{MP} \cdot J_{MP}}{V_{oc} \cdot J_{sc}}, \quad (2.41)$$

which represents the ratio of the colored to gray boxes in Figure 2.13. Care should be taken to correctly simulate or correct for the illumination source used in measurement to make measurements most applicable to the ultimate use for a given OPV.²⁷⁴⁻²⁷⁷ This is commonly achieved by using standardized “AM1.5G” illumination, the solar spectrum corrected for atmospheric absorption at mid-latitude locations applicable to most solar installations.

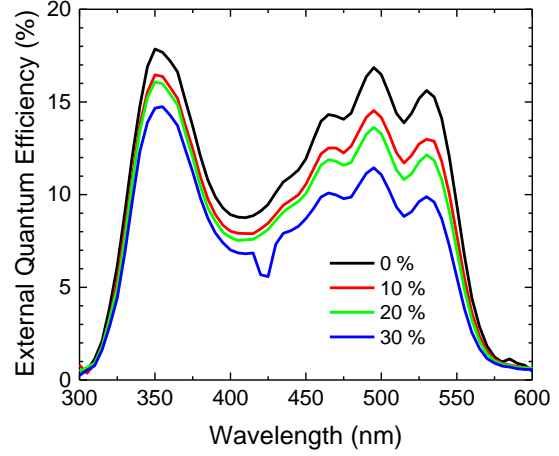


Figure 2.14. External quantum efficiency of rubrene: C_60 devices for different C_60 concentrations.

The other major characterization tool for OPVs is the device quantum efficiency, or the efficiency of carrier generation and subsequent harvesting from photons. The external quantum efficiency (η_{EQE}) may be calculated from the processes shown in Figure 2.6 as the product of each constitutive process efficiency

$$\eta_{EQE} = \eta_A \eta_D \eta_{CT} \eta_{CS} \eta_{CC} \quad (2.42)$$

and as such is a powerful tool for viewing the inner workings of an OPV if terms can be decoupled, calculated, or neglected. Experimentally, this is calculated from

$$\eta_{EQE}(\lambda) = \frac{hc}{e\lambda} \left(\frac{I_{Dev}(\lambda)}{I_{Det}(\lambda)} \right) \left(\frac{A_{TP}}{A_{Dev}} \right) R_{Det}(\lambda) \quad (2.43)$$

with I_{Dev} and I_{Det} the device and detector photocurrent, A_{TP} and A_{Dev} the testing plate hole and device area, and R_{Det} the detector responsivity.

Organic Semiconductors

Figure 2.14 is an example of this measurement, showing a broadband reduction with increasing C₆₀ content with an additional drop in the rubrene absorption region. This implies a decreasing η_{CC} for the device and dropping η_A for rubrene as its content is decreased.

2.8. Conclusions

Organic semiconductors are remarkable for the diverse functionalities made possible by the varied chemistry within each type of molecule. Such bonding interactions and energetics dictate optical and electronic properties which are useful for devices. In particular, the character and motion of quasiparticle excited states (excitons) and charge (polarons) are hallmark features which define the behavior of these materials. The physics introduced here will be useful for interpreting and understanding the optical and electrical results presented in later chapters.

3. PHASES AND CRYSTALLIZATION OF ORGANIC MATERIALS

The previous chapter described some of the underlying physics which govern electrical and optical properties of organic electronic devices. These properties can be greatly influenced by the phase of the material, especially considering a material that may transition between phases. In order to exploit this difference, an appreciation must be developed for the attributes of each type of phase with knowledge of methods to form and interconvert them. This chapter provides a discussion of common phases encountered in organic semiconductors and methods to form the crystalline phase, a focus of much of this thesis.

3.1. Bonding and Solid Phases

Organic semiconductors commonly exist in the three primary solid phases: amorphous, glass, and crystal. The differences between these phases are largely related to intermolecular interactions (bonding) and the opportunities given to create order within the material. Each phase has unique properties, benefits, and challenges which are briefly discussed below.

3.1.1. Intermolecular Bonding

There are three main types of intermolecular bonding, only two of which are commonly observed in organic semiconducting materials. These bonding interactions are classified by their directionality and symmetry, given here in decreasing bond strength: ionic, hydrogen, and van der Waals (Keesom, Debye, and London). Ionic interactions feature the near-total exchange of charge by an imbalance in electronegativity and a resulting Coulombic attraction between the charged species.^{278,279} Hydrogen bonding is an attraction between electron-rich (O, N, S) and electron-poor (H, C) regions of different molecules and has the directionality of the electron cloud.^{280–282} Van der Waals forces are due to charge density fluctuations on neighboring molecules with extending π systems, and arise from multipolar terms identical to those in Förster theory.²³⁶ Permanent dipole-dipole (Keesom), dipole-induced dipole (Debye), and induced dipole-induced dipole (London) interactions may all occur, each with an r^{-6} bond strength dependence. Hydrogen bonds and van der Waals interactions are responsible for the majority of interactions in organic materials,^{14,283–287} with hydrogen bonds playing an interesting role in film stability and crystal engineering.^{280,288–293}

3.1.2. Amorphous

A material which is classically amorphous (Greek: without form)²⁹⁴ has no long-range order and is thus isotropic, but need not be homogeneous. This isotropy does not preclude ordering on small length scales;²⁹⁵ even liquids show peaks in local distribution functions up to several molecular shells,²⁹⁶ and amorphous solids are approximated

Phases and Crystallization of Organic Materials

similarly.^{156,198,265,297} Given the mixed terminology used in the literature, a more representative definition may be simply a material which lacks a crystalline lattice. Amorphous materials have shown size-dependent orientation to preferentially align horizontally on substrates without crystallizing,^{229,231,298–301} leading to anisotropy especially in optical properties. Some amorphous solids also show optical behavior reminiscent of molecular dimers, but lack definitive crystalline signatures,^{297,302} suggesting that local ordering is highly specific, but rapidly deteriorates with distance.

Amorphous solids are useful especially for their isotropic, consistent properties, since by definition the properties are the same in all directions. This reduces the complexity of measuring parameters like charge or exciton transport and optical absorption, since such parameters need only be measured along one direction to capture the behavior in all. Further, amorphous films are simple to deposit as continuous layers, without voids or boundaries between regions common in crystallization. Also, despite reports on morphology and device variations with deposition conditions,^{116–118,303–305} amorphous films yield fairly repeatable properties because the stochasticity of deposition and film formation tend to average out variations.

Faults of this material class are film stability and less efficient transport than many crystals. Amorphous solids are prized for their high solubility and thus bioavailability in pharmaceuticals,^{306–308} but the same high-energy quality responsible for this rapid dissolution can also cause uncontrolled morphological changes in thin film, such as crystallization and rearrangement.^{59,309,310} This is especially accelerated by film heating,

Phases and Crystallization of Organic Materials

common in normal device operation. The buried nature of material within a device helps slow this transition,³¹¹ but the thermodynamic incentive provides a perpetual driving force.

Many organic semiconductors can form amorphous films when deposited.^{224,237,242,295,312–315} In general, these materials exhibit fairly rigid but bulky molecular structures and relatively weak intermolecular bonding motifs which allow for circumvention of crystallization pathways. In the organic electronics community, “amorphous” is sometimes distinguished as separate from “glassy”, but in reality, glasses are a subcategory of amorphous materials: all glasses are amorphous, but not *vice versa*.

3.1.3. Glass

Glasses are a subclass of amorphous materials and are defined by the presence of a glass transition, a transition marked by greatly enhanced material mobility as the material shifts from a solid glass to a supercooled liquid state. This is considered to be a material relaxation event, commensurate with the long-time liquid α relaxation.^{316–319} Glass transitions can be detected with rheological measurements or diffusivity measurements based on molecular motion,^{320–322} film roughening transitions in hot-stage AFM,^{323,324} heat capacity differences reflecting vibrational and rotational mode accessibility,^{325–330} and film thickness or density variation as the material expands faster in the more weakly bound supercooled liquid state.^{330–332} The glass transition temperature, T_g , represents the lowest energy which still allows a material to overcome intermolecular interactions and approach the equilibrium structure of the liquid during the observation time scale (sometimes defined as when the liquid viscosity equals 10^{12} Pa s),^{333–335} and is strictly a property of the

Phases and Crystallization of Organic Materials

liquid.^{317,336} The fictive temperature, T_f , is strictly a property of the glass and is the imaginary (fictive) temperature where an intensive quantity of the supercooled liquid (molar volume \tilde{V} , entropy \tilde{S} , enthalpy \tilde{H} , pressure P , etc.) would equal that of the glass upon heating.^{317,334,337}

The difference between T_g and T_f reflects additional relaxation and stabilization which occurs in the solid state, and depends strongly on the history of the material. The more relaxed and stable a glass is, the more energy will be required for it to overcome this stabilization and transition into the supercooled liquid state, represented by a higher transformation onset temperature T_O . The transition mechanisms also differ; normal glasses transform into a liquid in the bulk, while ultra-stable glasses appear to have a nucleated edge or front which moves through the sample.^{227,333,337} These can also be influenced by the substrate in films of thicknesses relevant to organic electronics,^{322,330–332,338} but with standardized thermal cycling and treatment, these temperatures are at least reproducible.^{322,339–341} Deposition conditions including rate and substrate temperature have been used extensively to study how glass stability and orientation can be influenced,^{228,321,326,342–345} an important area of work for OLEDs especially due to the predominance of glassy electron and hole transport layers.^{25,59,61,346}

The glass and fictive transitions may be understood graphically by comparing some intensive quantity across temperatures for different material phases and preparations as shown in Figure 3.1. Each of these points occurs at the glass-supercooled liquid intersection (Figure 3.1a). Cooling a melt can produce a glass, with slower cooling rates or aging

Phases and Crystallization of Organic Materials

producing glasses that are more stable and have a lower T_g .^{317,320,335} Vapor deposition onto

substrates near T_g can produce exceedingly stable glasses by allowing nearly unconstrained

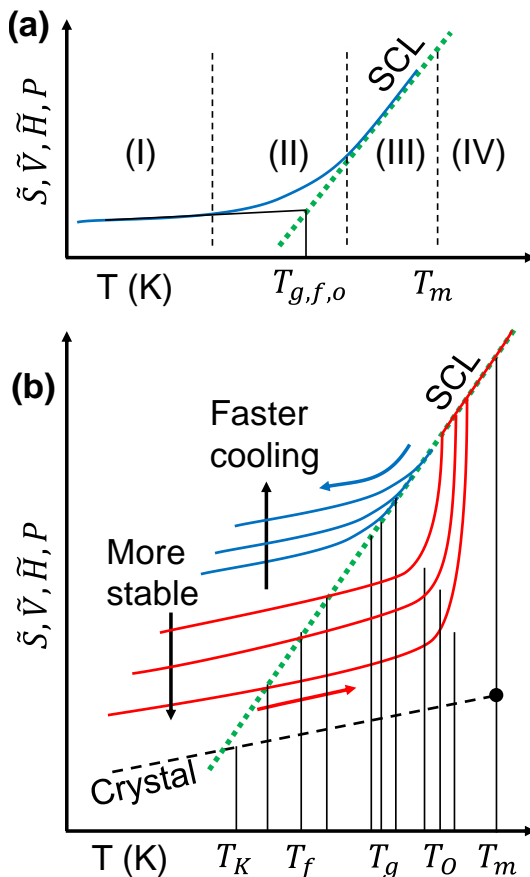


Figure 3.1. Example plots of transitions between liquid and solids, with (a) showing regions of (I) glass, (II) transition, (III) supercooled liquid (SCL), and (IV) equilibrium liquid. The glass transition, fictive, and onset temperatures (T_g , T_f , T_o) are identified by extrapolation of the glassy region to the liquid line (green dots). (b) shows the effects of cooling rate on liquid-glass transitions (blue lines) and film stability on glass-liquid transitions (red). Intersection of the liquid line with crystal leads to the paradoxical Kauzmann temperature, T_K .

amorphous films: T_g provides a convenient and simple method to compare thermodynamic stability of different molecular films. Preferential glass formation over crystallization

molecular motion on the free surface.^{227,228,333,344} However, eventually this energy minimization reaches a limit where the supercooled liquid intersects with the crystalline state, producing a liquid with the same (or lower) entropy as a crystalline solid. This seeming impossibility is termed the Kauzmann paradox,^{334,341} and is avoided by the liquid crystallizing or vitrifying at or before this point.

A number of organic semiconductors form glasses when deposited, and trends in synthesis of OLED materials have been towards molecules with ever higher T_g s in the hope that this will lead to more stable devices.^{11,12,61,315,346–349} This is perhaps an additional advantage of glasses over simple

Phases and Crystallization of Organic Materials

seems to be promoted by flexibility of the molecular core and functional groups, with stronger intermolecular bonds via hydrogen bonding or larger molecules yielding higher T_g s.^{347,349–351} Indeed, most glassy OLED materials feature polysubstituted core groups which are often coupled with somewhat flexible nitrogen σ bonds, compelling glass formation over amorphous or crystalline. One potential disadvantage of glassy materials is that they flow when heated above T_f , which can result in macroscopic film dewetting from capillarity.^{352–356}

3.1.4. Crystal

Molecules in a crystal assume a well-defined periodic lattice which often exhibits a preferential orientation (texturing) relative to the substrate. Any orientation is an optimization of interfacial and bulk forces, where hydrophobic molecules are driven to minimize interactions with typically polar, high surface energy substrates while simultaneously maximizing intermolecular interactions.^{357,358} This can lead to distinct thin-film phases during initial or few-layer growth, with molecules initially adopting a face-on configuration to maximize coordination of the electron density in the substrate with

molecular π -bonding orbitals (Figure 3.2a).^{359,360} As the films grow, the intermolecular interactions in the form of van der Waals bonds grow and can cause subsequent rearrangement of the

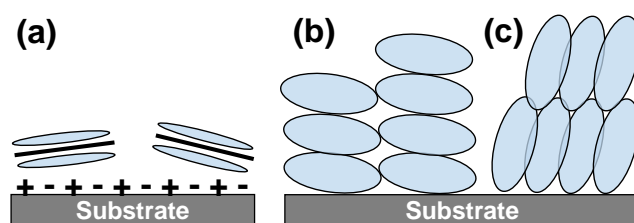


Figure 3.2. Interaction of molecules with a substrate in (a) very thin films, showing the conjugated molecular orbitals coordinating with a polar substrate in a face-on arrangement, (b) thick films where substrate interactions dominate, and (c) thick films where intermolecular interactions are dominant.

Phases and Crystallization of Organic Materials

initial layer and any additional material (Figure 3.2b-c).^{361–363} This resembles the behavior of glassy organic materials during vapor deposition as a function of deposition rate and temperature discussed above.^{227,228,345}

Structure resulting from molecular ordering and alignment will typically densify the material and present well-defined periodically repeating acceptor sites for energy and charge transfer, resulting in a dramatic increase in energy transfer rates and charge mobilities.^{246,258,270,314,364–368} Changes in the thin film morphology can also induce changes in the energetic landscape, with greater intermolecular coupling resulting in more delocalized excitons with lower exciton energies,^{171–174} increased efficiency of triplet formation,³⁶⁹ and longer,^{146,174,192,195,313,370} often anisotropic diffusion lengths.^{88,239,257–263}

In addition to altering the character of the excited state, crystals may also be able to improve the smoothness of the energy landscape in a material and thereby improve transport.¹⁹⁵ Excitons and hopping charges are sensitive to the energy levels of neighboring

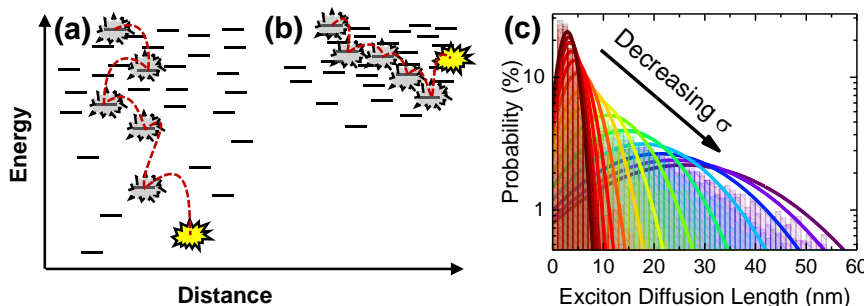


Figure 3.3. Effects of the excitonic density of states width σ on exciton diffusion. Schematics of (a) exciton trapping in the limit $\sigma > k_B T$ and (b) activated hopping when $\sigma \leq k_B T$, and (c) statistics of L_D as a function of σ , calculated using Kinetic Monte Carlo simulations for $5 \leq \sigma \leq 75$ meV and $T = 295\text{K}$.²⁹⁷ In both (a) and (b), the total number of sites are the same, but the number of deep ($>k_B T$) traps is lower in (b). The y-axis of (c) is the probability of each diffusion length occurring out of 10^4 trials, with each value of σ represented by a different color.

molecules, since the energy barrier of a transfer event acts to modulate the rate at which that event occurs. In the limit of a highly disordered

Phases and Crystallization of Organic Materials

film with a widely varying excitonic density of states (width σ meV), an exciton which transfers to a site with extremely low energy effectively becomes trapped, with energy transfer events away from the site probabilistically prohibitive (Figure 3.3a). In a wide distribution, these trap sites are also more prevalent, resulting in less variation in how far an exciton travels on average (Figure 3.3c). In more uniform bands, the available thermal energy $k_B T$ is sufficient to allow excitons to hop out of traps (Figure 3.3b), but this uniformity also increases the variability of when excitons encounter trap states, producing a wider distribution of exciton diffusion lengths with decreasing σ (Figure 3.3c).^{297,369,371,372} To probe the diffusive behavior of a given system from this method, either the diffusion length or diffusivity is measured.^{297,372}

The formation of crystals also introduces new types of energetic defects such as grain boundaries in polycrystalline films and even defects on the free surface capable of dissociating excitons and trapping carriers.^{182,271,365,373–375} Given the relevance of these findings to polycrystalline thin films, where the film nucleation site density may not allow for large single-crystalline grains,^{376,377} there has been much work to correlate grain size with the transport.^{373,378–380} It should be emphasized that although single crystals are often far superior to disordered phases, the single-crystal limit is not necessarily the fundamental upper limit for a given material, merely the limit with the resulting crystalline molecular orientation, intermolecular spacing, and so on.

Most organic semiconductors are capable of forming crystals under the correct conditions; for examples, see Appendix J. The lack of a solved crystal structure does not

mean that a given material will not crystallize, nor does a high T_g – see Appendix K. Depending on the driving force to form crystals, more or less manipulation during growth is necessary, as discussed in the following sections.

3.2. Crystal Growth Mechanisms

Much of this thesis discusses crystal growth and applications of crystals in organic semiconducting materials. This section describes how crystals fundamentally grow, and is followed by common techniques which make use of these physics.

3.2.1. Theory of Crystal Nucleation, Growth, and Shape

After much philosophical speculation about the structure and formation of crystals, it was some time before semi-quantitative and qualitatively accurate theories were devised to describe how crystals grow, notably by Gibbs (1875),³⁸¹ Wulff (1901),³⁸² and Burton, Cabrera, and Frank (1951).³⁸³ These authors correctly deduced that the surface energy of the growing crystal and the material available for attachment drive the rate and shape of the growing crystal. Gibbs in particular defined the process of nucleation, recognizing that the stabilization derived from the Gibbs energy of a bulk crystal lattice (G_c) is offset by the destabilization of growth units on the crystal surface from the crystal surface energy γ , leading to an expression for the Gibbs energy G with nucleus radius r :³⁸⁴

$$\frac{dG}{dr} = \frac{4\pi}{3}r^3G_c + 4\pi r^2\gamma \quad (3.1)$$

Solving for the critical radius r_c at which this crystal nucleus becomes stable ($dG/dr = 0$) gives $r_c = -2\gamma/G_c$, where G_c is assumed to be negative and stabilizing. This criterion

Phases and Crystallization of Organic Materials

changes in two-dimensional systems and when surface curvature effects on vapor pressure are accounted for (the Gibbs-Thomson effect).^{357,384–386} In real systems, homogeneous nucleation occurs by density fluctuations, which have been observed experimentally.^{387–390}

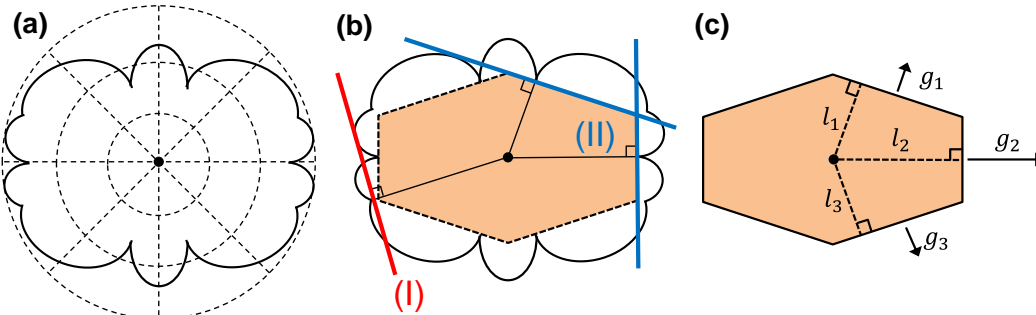


Figure 3.4. Crystal shape determination (a) polar plot of crystal surface energy as a function of crystal surface normal direction $\gamma(\hat{n})$, (b) a growing crystal with (I) invisible and (II) observed planes, and (c) growing crystal with growth rates g_i and distances l_i from the crystal center to plane normal.

Once a crystal nucleus is established, the planes which grow exist as minima in the surface energy (Figure 3.4a), since these result in a minimum in the overall crystal energy. The planes which grow have surfaces normal to a line drawn from the energetic center of the crystal (the Wulff point) to the surface energy cusp, shown in Figure 3.4b. The relative energy of each plane dictates where it intersects with other planes, causing most planes to be eliminated from the growing crystal habit and only the lowest-energy planes to survive. This faceting creates the Wulff shape, the lowest-energy crystal habit, and is responsible for the spectacular natural and industrial crystals which grow with beautiful, distinctive shapes and facets. In effect, the crystal habit is a partial look into the surface energy and growth conditions for that particular crystal. This shape can be realized mathematically by evaluating the change in Gibbs free energy for creating the surface of a crystal from N facets with surface area A_i relative to material at the stable center of the crystal.³⁹¹

$$\Delta G = \sum_i^N \gamma(\underline{\hat{n}}_i) A_i \quad (3.2)$$

For this energy to be minimized, the derivative with surface area must be zero. If the crystal shape change changes slightly at constant volume, then

$$\partial V = \frac{1}{3} \sum_i^N \partial(A_i l_i) = \frac{1}{3} \sum_i^N (l_i \partial A_i + A_i \partial l_i) = 0 \quad (3.3)$$

The term $A_i \partial l_i$ does not conserve volume and is eliminated. If Eqn. 3.3 and the minimum criterion of Eqn. 3.2 are combined with a proportionality constant C , the result is

$$\sum_i^N (l_i + C \gamma_i(\underline{\hat{n}}_i)) \partial A_i = 0 \quad (3.4)$$

This result holds for any crystal volume, making the sum arbitrary and yielding

$$\frac{l_i}{\gamma_i(\underline{\hat{n}}_i)} = C \quad (3.5)$$

that is, any ratio of crystal dimension and planar surface energy observed in a growing crystal must be equivalent, giving a shape like that shown in Figure 3.4c.

Planes which are not observed are higher energy and effectively “grow out” of the crystal as material continues to accumulate on the crystal surface, as shown in Figure 3.5. Counterintuitively, it is these high-energy planes which greatly facilitate crystallization, making this process faster and allowing the planes to grow much more quickly when conditions dictate.^{391–393} However, as the faster-growing plane evolves, it becomes limited by material attachment to the slower-

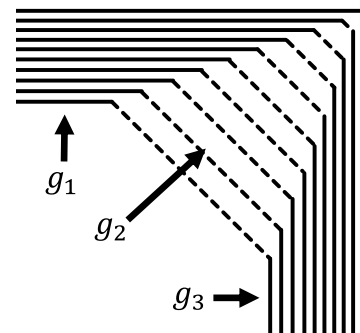


Figure 3.5 Diagram of plane 2 “growing out” of a crystal. In this case, $g_2 \approx g_1 + g_3$.

Phases and Crystallization of Organic Materials

growing neighboring planes, trimming off available growth area from the edges. In Figure 3.5, each line represents the growth progress of the three planes at different time steps. For each step of growth for plane 2, planes 1 and 3 gain additional area and dictate growth over a larger fraction of the facets. Eventually, the faster-growing facet disappears altogether from the crystal habit.

Factors determining growth rates of specific polymorphs and crystal planes are complex,^{357,391,394,395} but a number of methods have been developed to perform these calculations.^{292,396–405} Most simply, the relative growth rate of planes within one molecular crystal structure can be related by the planar density and interplanar spacing,^{391,392} conceptually based on the strength of each bond at a lattice site. Sites in sparsely packed planes have a stronger total bond energy (same charge density spread among fewer neighbors); similarly, planes with small interplanar spacing interact more strongly with freshly added layers, increasing the bond strength (the Bravais relationship^{392,406}). As material is added to the crystal, it will do so fastest in these high-energy regions.^{392,403} However, material dissolving or desorbing will do so from the weakest bound planes, which happen to also be the slowest-growing and determine the Wulff-shape. In this manner, the slowest, most weakly bound planes dictate crystal shape during growth and dissolution. The growth rates of these and other planes in a crystal can be related to the planar density ρ_{hkl} and interplanar spacing d_{hkl} by³⁹¹

$$g_{hkl} \propto \frac{1}{\rho_{hkl}} \propto \frac{1}{d_{hkl}} \quad (3.6)$$

Since the volume per molecule is constant in all planes, $\tilde{V} = d_{hkl}/\rho_{hkl}$, making these

Phases and Crystallization of Organic Materials

quantities roughly equivalent in predicting relative planar growth rates.

The actual growth of a crystal in solution, melt, and vapor most often takes place through addition to step edges and kink sites on the crystal surface (Figure 3.6), and has

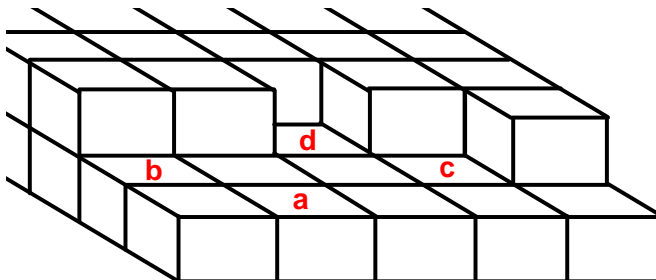


Figure 3.6 Attachment sites for material adding to a growing crystal with coordination number 1 (a), 2 (b), 3 (c), and 4 (d).

become known as BCF theory.^{383,401,407} All real crystal surfaces contain a series of steps which cover the surface, an integer number of molecules tall – real

examples are given later in Figure 9.3. Molecules deposit on the crystal surface from the liquid driven by a difference in chemical potential, which is correlated to supersaturation or temperature, and diffuse around the crystal surface. Diffusing molecules face a thermodynamic barrier for going over a step edge (Figure 3.6a), the Schwoebel-Erlich barrier,^{408–413} and are sometimes observed accumulating at these edges.^{122,127,414} Edge (Figure 3.6b) or corner (also called a kink, Figure 3.6c) sites of the steps coordinate with diffusing molecules on two or three sides instead of the one side that a flat surface does, increasing the sticking probability considerably.^{383,415–418} As a result, most molecules add to these step edges rather than nucleate a new region of material elsewhere on the crystal. The crystal grows through the perceived motion of these step edges, with the edge moving each time more material adds. New step edges are nucleated at a rate related to the supersaturation to replace those that grow off the crystal edge, except for a specific type of step nucleated by a screw dislocation, which grows as a never-ending vertical spiral.

Phases and Crystallization of Organic Materials

In the solid-state, crystals grow by rearranging and realigning neighboring amorphous material. At the temperatures involved in crystal growth, molecules have considerable thermal energy which activates translational and rotational diffusion. Molecules are constantly moving, even in the solid state (Figure 3.7), allowing a constant sampling of their surroundings through surface and bulk diffusion.^{122,322,419–434} Once a nucleation event occurs, material impinging on the edge of the crystal is likely to become energetically bound to the growing crystal, whether that requires molecular conformation changes or diffusion. In some two-dimensional cases, rapid binding causes the formation of an empty diffusive boundary layer,⁴³⁵ but in others growth is surprisingly fast (glass-crystal growth),^{307,318,436–439} suggesting potentially different mechanisms.^{318,337}

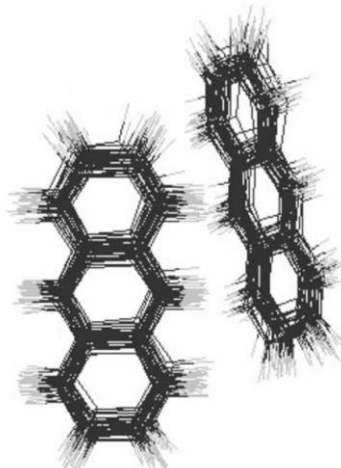


Figure 3.7. Thermal motion in an anthracene crystal, adapted from Sleigh *et al.*⁴¹⁹

3.2.2. Types of Growth and Transitions

The most interesting type of growth for many applications is single-crystal growth,^{102,279,440–442} where the advancing growth front progresses as a single interface with uniform crystallographic orientation across the crystal.^{318,443–446} In this type of growth, the diffusive mobility of the adding material is such that the crystal front is able to successfully realign added material to incorporate seamlessly into the crystal structure. Depending on the growth conditions and energetics, faceting may or may not be observed; kinetic and thermodynamic factors will further dictate which planes are present (not necessarily those

Phases and Crystallization of Organic Materials

which predict the Wulff shape).^{392,394,395,397,398,447–449} Single crystals in film are commonly smooth and continuous,^{442,450–452} making them attractive for electronics (Figure 3.8a, c).

Above a temperature known as the roughening temperature related to the plane bonding

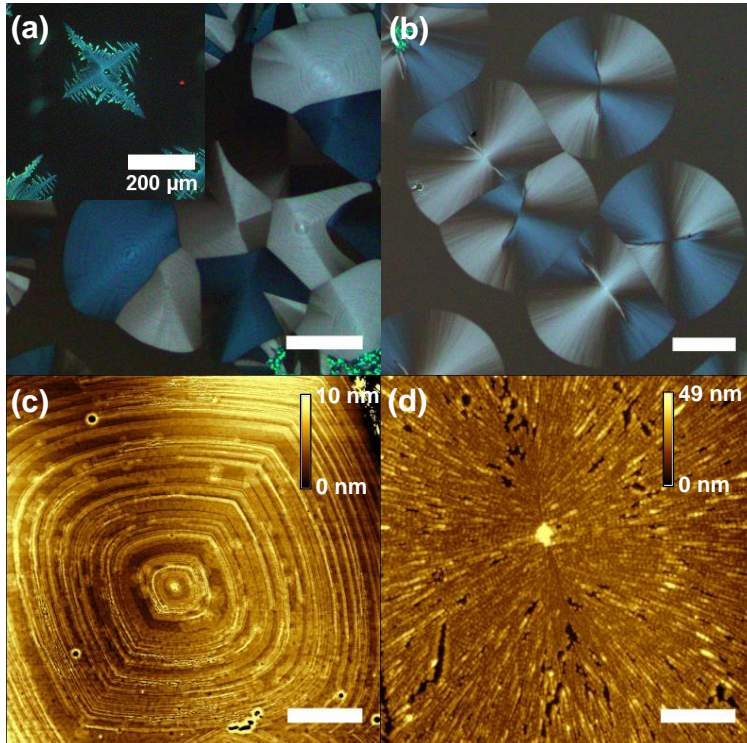


Figure 3.8. Examples of (a), (c) single crystal growth, (b), (d) spherulite growth, and dendritic growth in the inset of (a). Scale bars in (a)-(b) 100 μm , (c)-(d) 10 μm . For more information about these images, see (a)-(b) Figure 4.11, (c)-(d) Figure 4.12, and inset of (a) Figure 5.8.

When the material encountered by the crystal is sufficiently misoriented such that the planar energy or diffusivity is insufficient to allow it to incorporate, that material may nucleate a new crystal at the growth front with a different orientation, effectively forming a new grain across a grain boundary. Recurrence of these non-crystallographic branching events forms a spherically symmetric crystal morphology in three dimensions known as a spherulite (Figure 3.8b, d).^{455–458} Depending on the rapidity of branching at the nucleation site, spherulites can be further classified as Category I (complete, microscopic branching

energy, crystal planes will cease to be faceted and instead take on a rounded appearance,^{392,399,418,453,454} similar to crystals grown out of a melt where surface tension effects are non-negligible.⁴⁴⁸

When the material encountered by the crystal is sufficiently misoriented such that the planar energy or

Phases and Crystallization of Organic Materials

starting from nucleation) or Category II (initial growth as a needle, followed by branching of the ends).⁴⁵⁶ The only difference is the initial crystal morphology; at long times and large distances from the nucleation site, both types are radially symmetric. With crystals often defined by a single dominant growth direction, spherulites consist of a network of neighboring needles and can be very rough in thin film.^{459–461} Spherulitic growth should not be confused with dendritic growth (Figure 3.8a inset), which is a diffusion-limited growth mode featuring branching that preserves crystallographic orientation.^{458,462,463}

3.3. Crystal Growth Techniques

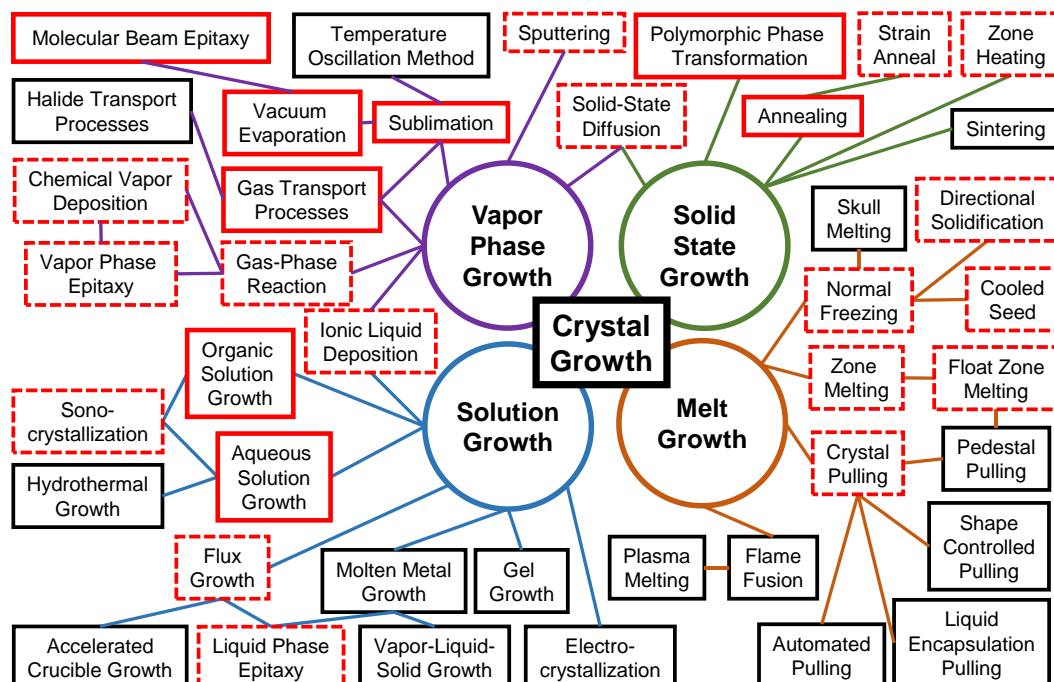


Figure 3.9. General classes of crystal growth, with those in red boxes applicable to organic semiconductors, and those in solid red boxes common in organic semiconductors. Based on a figure in Pamplin *et al.*²⁷⁹

As suggested in Figure 3.9, there are a multitude of methods to produce crystals, a number of which are applicable to organic semiconductors. This section briefly defines some of the key features, advantages, and disadvantages of a few common crystallization

techniques for organic molecules.

3.3.1. Vapor-Solid

The general process of converting a gas directly to a solid is not always conducive to crystal growth, but these cases are most applicable to organic electronic materials which are to be deposited as crystalline films.

Physical Vapor Deposition

Physical vapor deposition is a high-vacuum ballistic process, where molecules have a direct path from the source to substrate (Figure 3.10).⁴⁶⁴⁻⁴⁶⁶

In some situations, films grown directly from vapor will crystallize on a cold substrate, and even allow for patterning of crystal growth.⁴⁶⁷ These materials are typically strongly interacting, with large planar

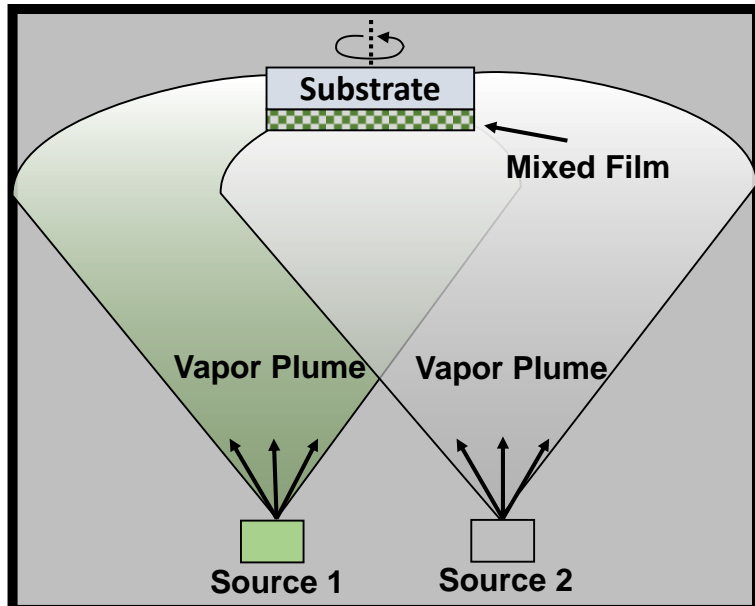


Figure 3.10. Example of a physical vapor deposition system. Within an evacuated high-vacuum chamber, sources containing the deposition material are heated resistively, subliming material into a vapor plume which condenses onto a substrate to form a film.

shapes allowing maximal π electron interactions and self-assembly.⁴⁶⁸⁻⁴⁷⁰ Grain size can be manipulated by variation of deposition rate and temperature, presenting an area of ongoing research.^{357,377,471} However, the substrate plays a key role in film quality and can introduce a defective interface,^{360,379,472} and in molecules which change conformation in

Phases and Crystallization of Organic Materials

vapor or crystal or have weak intermolecular bonding, simply depositing onto a cold, low-energy surface may not be sufficient to reorganize the molecules into a crystal.^{473–477}

Physical Vapor Transport

Instead of being directly evaporated onto a substrate, molecules may be transported there or grown on free-standing crystals by a stream of inert gas near room pressure (Figure 3.11).⁴⁷⁸ When carried out inside of a furnace or heated tube with a slowly decreasing axial

temperature gradient,

this creates a very short

molecular mean-free-

path and near-

equilibrium crystal

growth conditions,

allowing the molecules

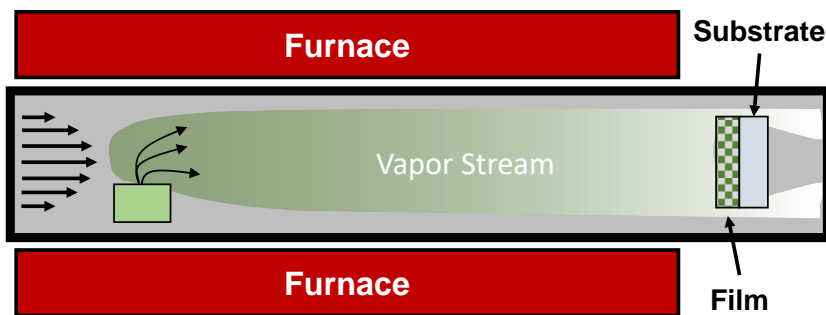


Figure 3.11. Schematic of a physical vapor transport system. A carrier gas enters on the left (laminar flow velocity profile shown) and blows over a source holding the deposition material. Heat from the surrounding furnace evaporates or sublimes the material into a plume which is conveyed to the right by the carrier gas, condensing onto a substrate to form a film. Excess gas exits the tube, typically to a low-vacuum pump to maintain a desired chamber pressure.

to collide many times with a crystal surface before depositing onto it.^{465,478} The temperature

gradient also has the effect of purifying the material as it is deposited,^{479–481} and as a result,

this creates some of the highest-quality organic crystals for devices.^{102,251,482,483}

Interestingly, the gas properties appear to influence the resulting crystal properties, with

less massive gasses such as helium producing higher quality (less defective) crystals.³⁷⁰

Epitaxy and Molecular Template Growth

Molecular template growth and epitaxy are terms for the use of a structured film (the template) to induce ordering in subsequently deposited layer(s) (overlayer(s)).^{226,484} In

Phases and Crystallization of Organic Materials

contrast to inorganic materials,^{485,486} this takes place by weak physisorption, not chemisorption, and cannot typically sustain high strains.¹⁰⁹ Whether by variations in overall surface energy,^{487,488} site energies,^{430,433} or even interlocking crystalline motifs,^{225,489,490} the

template causes reorientation and very often crystallization of the overlayer.

Templating is a subclass of epitaxy, the

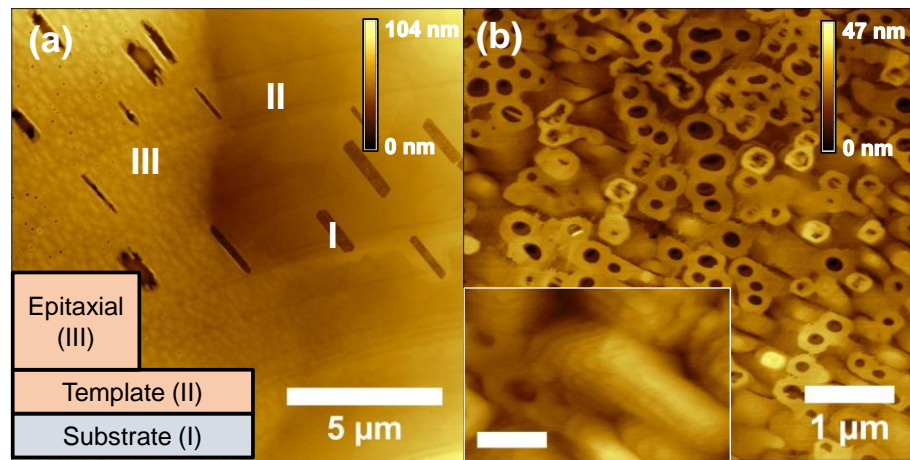


Figure 3.12. Examples of homoepitaxial growth, showing (a) regions of substrate, template, and epitaxial layer, (b) magnified view of the epitaxial region showing screw dislocation sites, and molecular terraces in the inset of (b). Inset scale bar is 300 nm. For additional information on these images, see Figure 9.2.

precise arrangement of dissimilar materials at a heterojunction typically achieved at ultrahigh vacuum to circumvent surface contamination.^{109,476,491–494} Homoepitaxy, growth featuring the same material as template and overlayer, can be advantageous when a material crystallizes in thin film but exhibits thickness-dependent crystallization which requires the use of a suboptimal film thickness.^{114,174,376}

Heteroepitaxy, the more general combination of dissimilar template and overlayer materials, can be useful to induce materials which do not crystallize well in thin film or feature polymorphism that is difficult to control using other methods.^{495–499} This is most similar to molecular template growth or weak epitaxial growth, which use dissimilar organic or inorganic molecules to order overlayers.^{226,484} There are other names used for

Phases and Crystallization of Organic Materials

organic epitaxy, including weak,^{484,500–503} van der Waals,^{284,285,504} quasiepitaxy,^{284,504,505} and inverse quasi-epitaxy,²⁸⁷ but these typically arise due to ambiguity in the template-overlayer interaction and spatial relationship.

The important features of a template layer depend on the application. In all cases, the template must present a consistent, regular surface for the overlayer to grow upon. Initially, this was accomplished with salt crystals,^{496,506–509} but can also include polymers.^{299,510} Candidate template molecules are those with significant $\pi - \pi$ interaction in crystal, usually linear, planar, highly conjugated molecules. For OPV and OLED, the template must also conduct carriers, typically holes, and not absorb light as a parasitic loss. In OFET applications, the template need only exclude carriers, as the overlayer material of interest is typically of much higher mobility than the template.^{226,501} These demands lead to selection of small molecules with large electronic energy gaps for OFETs and conductive p-type materials with minimal absorption for OPV. Interestingly, the criteria for OPV also fits some thin films of metal halides, especially CuI and CuBr, both of which can be vacuum-deposited and have been used to induce crystallization of subsequent organic materials. This is especially true for molecules with considerable π electron density, such as planar phthalocyanines.^{305,363,511–513} These alternative materials give another avenue for exploration of methods to promote crystallinity in organic thin films.

3.3.2. Liquid-Solid

If a material is soluble or liquefiable, a crystal may be produced by driving it from liquid into the solid phase; especially convenient for soluble, printable materials.

Phases and Crystallization of Organic Materials

Solution

For organic materials which are soluble or can be made soluble by functionalization, the material can continue to dissolve into a solvent until the solvent is saturated, or at equilibrium with the solid material. Reversing this process requires that the solution become supersaturated, driving material in the liquid to form or add to a solid phase. This is accomplished in a number of ways, including reducing the solution temperature,^{514–517} injecting a poor solvent (antisolvent),^{120,518,519} evaporating solvent,^{478,517,520} and even vacuum deposition into an ultra-low vapor pressure liquid.^{521,522} Novel concepts have also been introduced to tailor crystal orientation,⁵²³ structure,⁵²⁴ polymorph composition,⁵²⁵ and location,^{8,112,124,526,527} as well as enabling solution-based epitaxial growth.^{495,496,499,528–531} It can be challenging to create multilayer crystalline stacks with this method due to mutual solubility (solvent orthogonality) issues which can mix materials between layers.^{532–534}

Melt

If a molecule is thermally stable at temperatures required for its liquefaction, a liquid melt may be prepared. Cooling this melt (and often seeding growth with a pre-grown crystal from one end) can cause solidification and crystallization to occur, producing crystalline material.^{318,440,449,478,535–542} The melting point of a material may also be reduced by confinement or solvation effects through microscopic substrate patterning or alloying.^{543–549} Besides thermal decomposition, a challenge of melting many small organic molecules is the high evaporation rate from their large vapor pressure. Furthermore, uniform thin films with an exposed free surface can be problematic, leading to limited

Phases and Crystallization of Organic Materials

practical usage in the organic electronics field.

3.3.3. Solid-Solid

Transformations of an amorphous solid into a crystalline solid are usually achieved after deposition, and allows use of primary deposition techniques which do not always produce crystalline films, such as PVD.

Annealing

When a film is heated, the molecules comprising the film are imparted thermal energy, which may allow them to diffuse (translate and rotate) or even sublime.^{106,118,453,550} The inclusion of solvent or polymer further plasticizes the material and enhances molecular mobility in a wide array of materials.^{104,119,224,307,461,546,551,552} This additional motion enables molecules to sample a considerably larger conformation space, increasing the probability of crystal nucleation and growth, making it a popular choice for transformation of amorphous thin films for devices.^{105,106,111,426,432,553–560} In thin films, film evolution is sensitive to the substrate, enabling *in situ* or post-annealing patterning of crystalline and amorphous regions for electronic devices.^{113–115,224,526,561} Choosing an annealing temperature and duration requires optimization:^{106,560,562} too long or hot and the films may majorly phase-segregate or dewet; too short or cold and the transformation may be incomplete. In the long-term limit, annealing can also result in (typically undesirable) Ostwald ripening, the process where large, strain-free grains consume smaller or strained grains through material migration.^{516,563}

Phase Transitions

Phases and Crystallization of Organic Materials

Materials are also capable of transforming into new states or structures from pressure and electromagnetic fields. Pressure-induced phase transitions are much less commonly used in organic electronic devices because compressibility in a material is often reversible; once pressure is removed, the material reverts to its low-density stable structure.^{564–567} However, in low-density, polycrystalline materials, compression is capable of plastic and permanent deformation which affects film properties including carrier mobility.⁵⁶⁸ Similarly, annealing combined with an applied field has been shown to alter material properties,⁵⁶⁹ but not as much as when applied during deposition.^{270,508,527,570–572}

3.4. Material Deposition

Organic electronics revolve around extremely thin (1-100 nm) films and interfaces. Creation of these films requires well-defined deposition techniques which commonly utilize vapor- or liquid-phase processing to achieve uniform material profiles.

3.4.1. Vapor-Phase

Evaporation or sublimation of material produces a vapor cloud which grows more uniform as it spreads from the source, and can be condensed onto a substrate to create a film with exquisite control and repeatability. Primary techniques include physical vapor transport (organic vapor phase deposition),^{465,466,483,573–575} hot-wall deposition,^{475,575} physical vapor deposition (thermal evaporation),^{464,561,576,577} and organic molecular beam deposition.^{476,505} The primary differences between these methods are the system pressure (decreases as listed) and that PVT uses a carrier gas. The majority of the films in this thesis

Phases and Crystallization of Organic Materials

were deposited using physical vapor deposition, which typically uses pressures on the order of 10^{-7} - 10^{-6} torr (10^{-10} - 10^{-9} atm; “high vacuum”), achievable with relatively durable cryogenic pumps. This results in a molecular mean-free-path length λ_{MFP} on the order of the distance from the source to substrate:

$$\lambda_{MFP} = \frac{k_B T}{\sqrt{2}\pi\phi^2 P}, \quad (3.7)$$

where ϕ is the molecular diameter. For 10^{-7} torr, λ_{MFP} is 3.1 m with 1 nm diameter molecules at 200 °C. This allows molecules a line-of-sight path during deposition, reducing scatter and film roughness. Lower pressure also reduces secondary molecules adsorbed onto the surface of the growing film, since the time to adsorb a monolayer of ambient molecules t_{ML} with sticking coefficient ζ onto N_s sites per area also scales with pressure⁵⁷⁸

$$t_{ML} = \frac{N_s \sqrt{2\pi m k_B T}}{\zeta P} \quad (3.8)$$

For nitrogen at typical deposition pressures of 5×10^{-7} torr, this time is about 2 seconds.¹⁰⁹ This suggests an optimum lower limit for deposition rates on the order of 1 Å/s.

The deposition system used in this thesis is an eight-source Angstrom Engineering® Evovac chamber (Figure 3.13) allowing simultaneous deposition at variable rates from up to four sources. Source material can include organics, metals, metal oxides, and metal halides, allowing complete device fabrication with only one vacuum break (to mask cathode active areas). Each source is a resistively heated container (boat) of tantalum-

Phases and Crystallization of Organic Materials

doped tungsten capable of repeatedly sustaining high currents (~100 A) and powers (300-400 W). The source temperature determines the vapor pressure of the compound and thus the evaporation rate. This rate is measured by the resonance shift with increasing mass of electrically driven, actively cooled quartz crystal monitors (QCMs) positioned near the source and controlled *via* a closed-loop PID software control. When the desired rate(s) are established, a shutter is opened to allow deposition onto the substrates, which are rotated to further improve uniformity and can be heated to > 300 °C. Typical thickness uniformity is better than ± 1 nm across a 4" substrate, with exquisite precision in multilayer stacks.

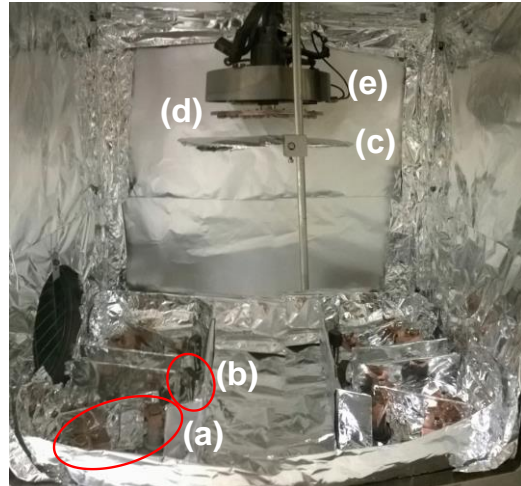


Figure 3.13. Deposition chamber used for this thesis, with (a) source, (b) QCM, (c) shutter, (d) substrate holder, and (e) substrate heater.

3.4.2. Liquid-Phase

Along with a variety of printing techniques,^{9,120,579,580} organic films are commonly cast from solvents using spin coating.^{112,581-584} In this approach, a substrate is spun at 100-5000 rotations per minute (RPM) after or during application of a solution containing the material of interest (Figure 3.14). The applied liquid is typically a dilute aqueous or organic solution with viscosities on the order of 1-100 cP, between water and a light oil. Large inertial forces from spinning equilibrate with capillary and viscous forces as the solution is flung off the edges and the solvent evaporates,^{581,583} yielding a radially symmetric film. Since the films

Phases and Crystallization of Organic Materials

are subjected to liquid-phase diffusion and flow during deposition, they are excellent for planarizing rough surfaces or edges prior to depositing films *via* techniques like PVD. The solution vapor pressure, viscosity, and concentration can all be manipulated to vary film properties. Although cheaper than PVD in terms of capital costs, spin coating is inherently challenging to scale up, with the added issue of mutual solubilities for previously deposited materials, requiring orthogonal solvents or intermediate crosslinking steps for multilayer stacks. Solvent recovery and moving towards “green” solvents also are problematic in practice.

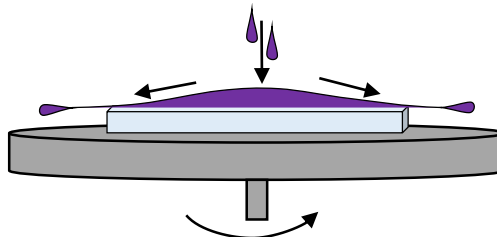


Figure 3.14. Example spin coating process.

3.5. Conclusions

Organic semiconductors exist in a variety of phases owing to the relatively flexible molecules and bonding methods. These phases each have benefits and disadvantages in terms of stability and optoelectronic properties, but often allow for interconversion *via* glass transitions, melting, and crystallization. As a relatively understudied but important crystallization method in organic materials, annealing will be the focus of the following three chapters. Research efforts in this thesis are in general directed towards understanding and engineering crystallization by annealing to exploit unique aspects of this film transformation technique.

4. CRYSTALLIZATION OF ANNEALED RUBRENE FILMS

With a thorough background in crystallization methods and underlying physics from the previous chapter, this chapter describes work towards understanding the crystallization processes in thin films of the organic semiconductor rubrene. Films relevant to organic electronic devices often can be amorphous or glassy in nature,^{12,349,473} as discussed in Chapter 3. However, as also discussed, transitioning from poorly ordered to crystalline films can bring about effective charge and exciton transport, as well as enhanced optical absorption.^{195,361,445,585,586} These potential improvements brought about by transforming the material structure make crystalline films highly desirable, and incentivize understanding and development of more effective crystallization techniques. The goals of this chapter are to characterize rubrene films as they crystallize and demonstrate methods by which to control polymorph composition and crystal morphology to enable further film structure engineering.

4.1. Introduction

The ability to precisely order and crystallize organic semiconductor thin films has been widely exploited to realize the available improvements due to molecular orientation. Such

Crystallization of Annealed Rubrene Films

enhancement may be manifested in greater orbital overlap to aid charge transfer,²⁴⁴ reduced film disorder to improve energy transfer,³⁷³ and alignment of more strongly absorbing molecular axes with optical stimuli,⁵⁸⁷ each of which has practical implications for electronic devices. In addition to literature showing the efficacy of crystalline films as transistors,^{55,367,554} recent work has also demonstrated the ability to grow highly crystalline thin films using a template layer for use in organic photovoltaic cells.^{174,484,502,588,589} For materials which are amorphous or glassy upon deposition, it is essential to devise processing approaches that induce crystallinity in a controlled and predictable manner.

As discussed previously, one route to the realization of crystalline thin films is thermal annealing, wherein the film is heated to allow molecules sufficient time and energy to reorder into an energetically favored structure. Previous work in the solid phase crystallization of small molecular weight organic semiconductors has characterized *in situ* film and powder annealing behavior using x-ray diffraction (XRD) and differential scanning calorimetry, respectively. These techniques elucidate crystallization progress and thermodynamic information regarding the phase transition, but yield limited insight into the spatial evolution of thin-film crystal growth because of the relatively large sample volumes of these techniques.^{451,532,590} Polarized optical microscopy (POM) has been demonstrated to be a valuable technique for quantifying micron-scale crystal growth,^{318,591,592} however POM studies have been largely confined to melts of insulating polymers or pharmaceuticals with a few exceptions.⁴⁶¹ Applying this technique to study crystal growth in small molecule organic semiconductor thin films allows facile *in situ*

Crystallization of Annealed Rubrene Films

observation of quantitative and qualitative effects of temperature, time, and other film perturbations. In this work, the roles of these factors are elucidated for rubrene.

4.1.1. Rubrene

Rubrene is a tetraphenyl-substituted tetracene, as shown in Figure 4.1, giving it similar properties to the acenes including absorption shape and charge carrier mobility. In syntheses documented earlier than 1936,⁵⁹³ rubrene is colloquially named for its reddish-orange color in powders or thick crystals. Although it absorbs weakly, the strongest transition exists along the axis of the phenyl sidegroups, in the plane of the tetracene backbone and perpendicular to its axis.⁵⁹⁴ Rubrene is best known for its high, anisotropic hole mobility in OFETs and extremely long exciton diffusion lengths in the crystalline state.^{174,195,239,246,367,595,596} It is also infamous for its photooxidative behavior to form an endoperoxide through the reaction scheme depicted in Figure 4.2.^{597–600} The reversion from (2) to (1) requires heating to above 180 °C in the presence of light with sufficient energy, and can progress in solution irreversibly to compound (3) through loss of phenol.^{601–603} However, since this is a photooxidation, the reaction rate can be significantly reduced by elimination of light or oxygen.^{599,600} For this reason, annealed films of rubrene were kept in a nitrogen glove box and covered by

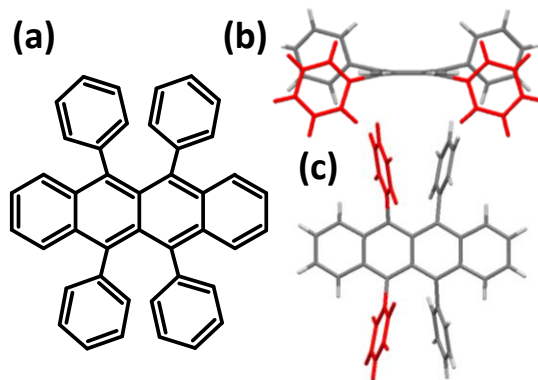


Figure 4.1. Rubrene molecule as (a) chemical structure, and in solid phase viewed (b) along and (c) perpendicular to the tetracene backbone, phenyl rings colorized to emphasize staggering. Images generated using Mercury 3.3 software.⁷⁸⁹

Crystallization of Annealed Rubrene Films

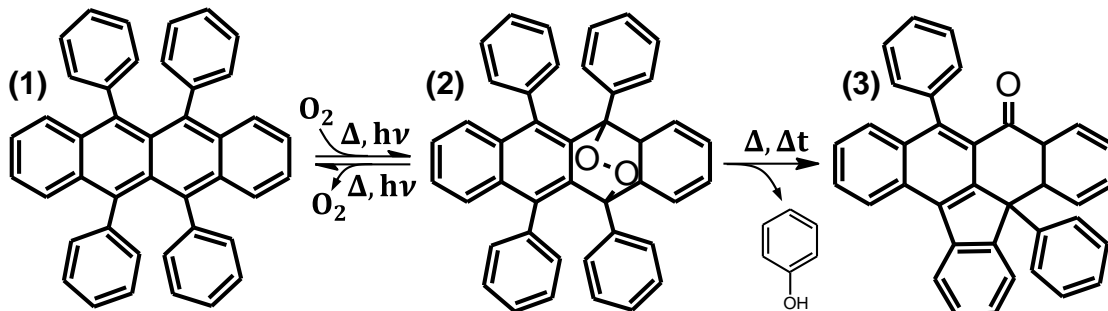


Figure 4.2. The reversible oxidation and cycloreversion of rubrene (1) to an endoperoxide (2), followed by irreversible pyramidalization by loss of phenol to (3).

aluminum foil until immediately before use, at which point the annealing procedure described in the appendix was followed to reduce oxygen exposure as much as possible.

Annealing rubrene thin films presents an intriguing case study since these initially amorphous films are known to crystallize upon annealing, yet little is documented about what happens as crystals grow in terms of nucleation, growth mode, and morphology evolution, making it an ideal candidate for *in situ* exploration. Because of its polymorphism and relatively simple molecular structure (Figure 4.1), information gained from studying this archetypical organic semiconductor may lend insight to the wider class of small organic molecules, both semiconducting and otherwise. Furthermore, due to its anisotropic field-effect mobility,⁶⁰⁴ simple determination of grain orientation is key to more accurate quantification of thin film transistor performance limits in crystalline rubrene and other molecular thin films, providing impetus for development of more facile crystal orientation determination techniques.

4.2. Polymorphs and Selection Methods

Many organic materials exhibit polymorphism because of the molecular flexibility

Crystallization of Annealed Rubrene Films

which enables a variety of energetically permissible conformations.^{291,292,605–608} For some materials, these polymorphs can have large discrepancies in optical or electronic character, which suggests that identification and control of polymorphs is critical to the further development of crystalline organic electronic devices.

4.2.1. Rubrene Polymorphs

Rubrene has three known polymorphs belonging to the triclinic,⁶⁰⁹ monoclinic,⁶¹⁰ and orthorhombic crystal systems.^{482,611} The triclinic and monoclinic forms are observed in solution-grown crystals,⁶¹² orthorhombic in vapor-grown,⁴⁷⁸ and orthorhombic and triclinic in annealed thin films,⁴⁵¹ with lattice parameters tabulated in Table 4.1 and structures shown in Figure 4.3b-d. The molecules generally display a herringbone structure in thin film, with the large skew in the alignment of the molecular backbone in the triclinic and monoclinic structures. In the case of orthorhombic rubrene, the molecules have a slip stacking which

Figure 4.3. Rubrene molecular and crystal structures: (a) solid phase rubrene molecule, (b) triclinic, (d) orthorhombic, and (e) monoclinic crystal structures. For clarity, only the tetracene backbone of rubrene is shown in the crystal structures. (c) shows the appearance of (I) amorphous, (II) orthorhombic, and (III) triclinic regions between crossed polarizers.

Crystallization of Annealed Rubrene Films

Table 4.1. Rubrene crystal structures, lattice parameters, and crystallization conditions. An asterisk next to a reference denotes the source of the listed lattice parameters for each crystal system. X = not observed.

Crystal	a (Å)	b (Å)	c (Å)	α (°)	β (°)	γ (°)	Solution	Vapor	Anneal
Triclinic	7.02	8.54	11.95	93.04	105.58	96.28	612†	X	451
Monoclinic	8.74	10.13	15.64	90	90.98	90	612†	X	X
Orthorhombic‡	14.43	7.19	26.86	90	90	90	443	482	451

†In solution recrystallization, greater supersaturation favors formation of the monoclinic phase

‡Using axes defined in the majority of OFET literature.

neatly overlaps the molecular orbitals and allows for a reasonably large transfer integral in neat and deuterated crystals.^{251,595,613} This means that the orthorhombic phase of rubrene is preferred for device applications due to its large hole mobility, with the added benefit of lower roughness than the thin film triclinic phase.^{246,366} However, during the transition from amorphous to crystalline film, there is competition between the triclinic and orthorhombic phases as each grows, consuming the finite amorphous material. This underscores the importance of directing which type of polymorph will actually grow in films intended for a given purpose.

In the majority of this chapter, the polymorph composition is inferred from the crystal growth mode and coloration. The orthorhombic and triclinic polymorphs differ significantly in crystal coloration and shape as shown in Figure 4.3e, which makes this analysis somewhat simpler. These crystal shape

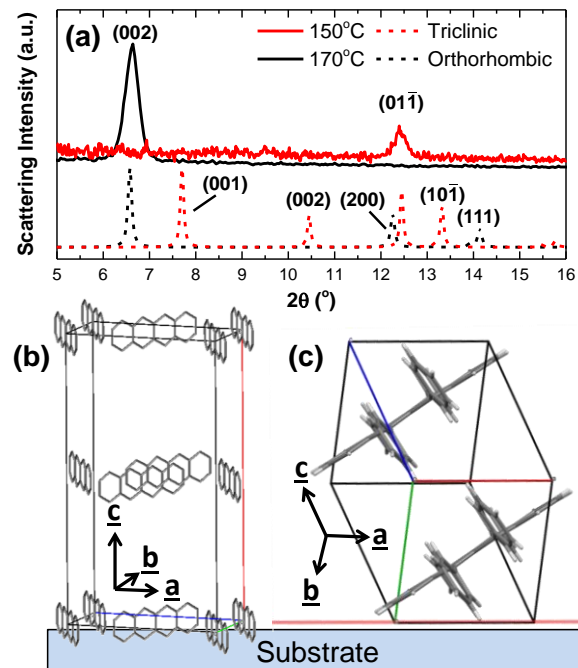


Figure 4.4. (a) XRD spectra of annealed films containing orthorhombic and triclinic rubrene, with unit cell orientations of the orthorhombic⁴⁸² (b) and triclinic⁶⁰⁹ (c) unit cell inferred from 2D XRD with samples grown, annealed, and measured on silicon.

Crystallization of Annealed Rubrene Films

and coloration observations are drawn from phase pure samples on which x-ray diffraction had confirmed polymorph type and orientation, as shown in Figure 4.4. Interestingly, the two thin-film polymorphs fundamentally differ in how the rubrene molecule is oriented with respect to the substrate, which also changes the exposed crystal planes that are able to efficiently propagate in the plane of the film. This has an effect on the crystal shape and methods used to identify crystallographic orientation, as described in Section 4.3.

4.2.2. Heating Rate Effects

In thin film, the polymorphs can be favored by choice of heating rate, with rapid heating and the resulting kinetic constraints yielding phase-pure orthorhombic films.⁴⁵¹ This was first demonstrated by Lee *et al.*⁴⁵¹ through differential scanning calorimetry (DSC) and concluded to be an effect of heating rate alone, affecting the length of time amorphous

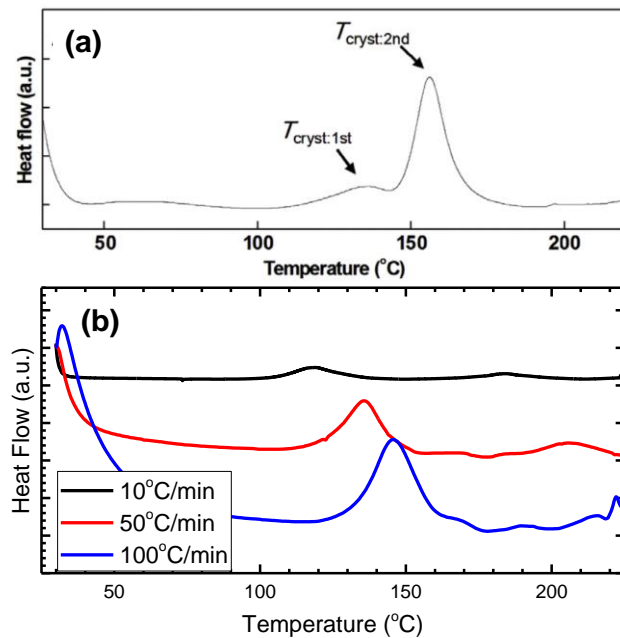


Figure 4.5. (a) DSC heating trace for amorphous rubrene, 80 °C/min adapted from Lee *et al.*⁴⁵¹ (b) Comparison DSC traces for vapor-deposited rubrene at different heating rates. Both plots are exothermic heat flow upward.

material spends in the range for each type of polymorph growth. As shown in Figure 4.5a, these temperatures roughly coincide with the temperature ranges over which the authors suspect each polymorph to grow, the first being triclinic and second orthorhombic. An attempt to reproduce this bimodal trend by this author failed, as shown in Figure

Crystallization of Annealed Rubrene Films

4.5b. To create this figure, rubrene was grown onto aluminum foil positioned around the deposition boat (approx. 100 nm reading on the QCM), then scraped into an air-tight vial to be characterized *via* DSC. All curves shown are the first heating of approximately 5 mg and show a continuous variation in one main crystallization peak, as opposed to two distinct peaks corresponding to individual polymorphs. Furthermore, XRD performed on powder extracted from the sealed DSC pans showed the occurrence of both polymorphs in samples quenched at the exotherm peak for 10 °C/min and 100 °C/min, at ~120 °C and ~140 °C, respectively (Figure 4.6). Even though the range of heating rates accessible to conventional DSC is far below what is achieved in thin-film annealing experiments (200 °C in ~10 sec, or >1000 °C/min), there are clearly other factors affecting polymorphic composition than simply heating rate. Also, although selection by heating rate may be useful in techniques such as DSC or rapid thermal annealing, varying heating rate controllably in this range is difficult without specialized equipment.

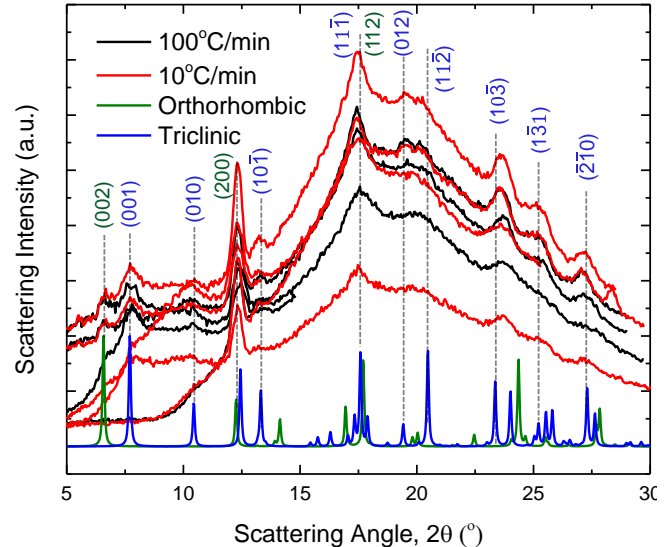


Figure 4.6. Cu K_{α} XRD on rubrene powders scraped from DSC pans heated at different rates, then scraped onto double-sided tape on a silicon wafer piece. Both polymorphs appear prominently, regardless of heating rate, implying that heating rate alone is insufficient to control polymorph composition.

4.2.3. Annealing Temperature Effects

If the goal of using a large heating rate is merely to bypass a low-temperature growth

Crystallization of Annealed Rubrene Films

regime, a similar effect may be achieved by varying the annealing temperature for fixed heating rate. To our knowledge, there has not been a report pertaining to the situation where only the temperature of the heated surface is varied, a configuration that is more applicable to a typical laboratory annealing experiment for thin-film polymorph selection.

Figure 4.7a shows the crystalline phase composition for a 20-nm-thick film of rubrene as a function of annealing temperature. As before, this composition was measured by optical microscopy, where the identifying characteristics of each crystal type were first correlated to a polymorph by x-ray diffraction (XRD) on phase-pure films as shown in Figure 4.4a.

The film consists predominantly of triclinic phase at low temperatures ($<150^{\circ}\text{C}$), with the slowly growing orthorhombic phase resulting in negligible coverage. At intermediate temperatures ($150\text{-}170^{\circ}\text{C}$), the growth of the triclinic phase slows and is eventually truncated by nucleation of the orthorhombic phase, allowing orthorhombic crystals which have nucleated in the bulk and on triclinic crystals to consume the film, albeit at a slower rate than that observed for the triclinic phase. At high temperatures ($>170^{\circ}\text{C}$), this triclinic truncation occurs sooner, resulting in a progressively larger fraction of orthorhombic crystals. This implies a potential interplay of kinetic and

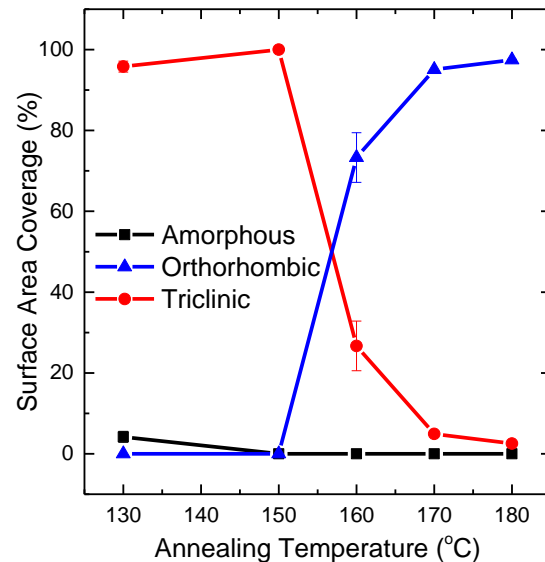


Figure 4.7. (a) Polymorph selection by choice of annealing temperature. Each temperature represents three 20-nm films on ITO annealed for three minutes.

Crystallization of Annealed Rubrene Films

thermodynamic factors, similar to what has been observed in thin films of α,ω -dioctylterthiophene.⁵⁴⁰

4.2.4. Film Thickness Effects

Other factors may also contribute to polymorphic selection in parallel with temperature, including film thickness. As the film thickness increases, the onset of orthorhombic crystallization shifts to slightly higher temperatures, with the area fraction largely dictated by the perseverance of the triclinic polymorph, as shown in Figure 4.8a. The triclinic growth mode densifies (Figure 4.8b), as may be expected from transformation from a film with considerably more material, but still is extremely rough and spherulitic.

The orthorhombic polymorph also changes growth mode, with radially symmetric periodic undulations in height observed at high temperatures and extremely smooth crystals at lower temperatures. The high temperature mode may be an extension of the height oscillations

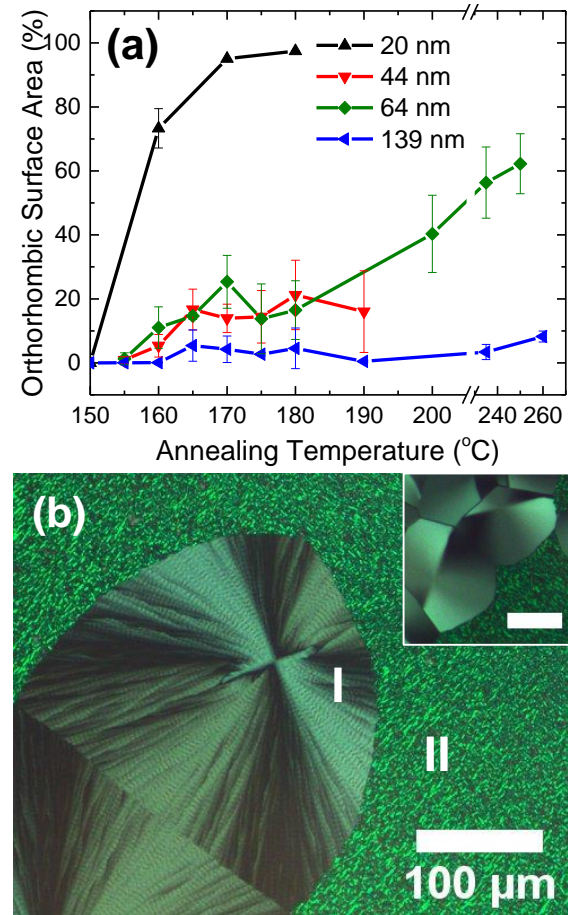


Figure 4.8. (a) Polymorphic composition of completely annealed rubrene films as a function of annealing temperature. Each data point represents multiple films on ITO, with the error bars describing the standard deviation between films. (b) Appearance of (I) orthorhombic and (II) triclinic rubrene grown at 200 °C (inset at 160 °C, 100 μm scale) in a 64 nm film.

Crystallization of Annealed Rubrene Films

observed in thin films at high temperatures, discussed below and shown in Figure 4.12b-c.

These effects imply that thin (20 nm) films are necessary in order to create smooth, orthorhombic, device-relevant films, important for additional work discussed in Chapter 7.

4.2.5. Effects of Light

Light is known to enable polymorphic control and patterning in some organic systems,^{614,615} but has not been explored for rubrene. It became apparent that light has an effect on rubrene crystallization during initial experiments upon comparison of the illuminated region to the surrounding area (Figure 4.9a-b). Not only does the composition vary, the growth mode of the triclinic polymorph appears to change: with increasing illumination power, the triclinic polymorph shifts from a coarse structure with birefringent Maltese crosses to one which is less ordered (finer branches with no hierarchical structure) that is also a more uniform green. This has the effect of increasing the amount of the orthorhombic

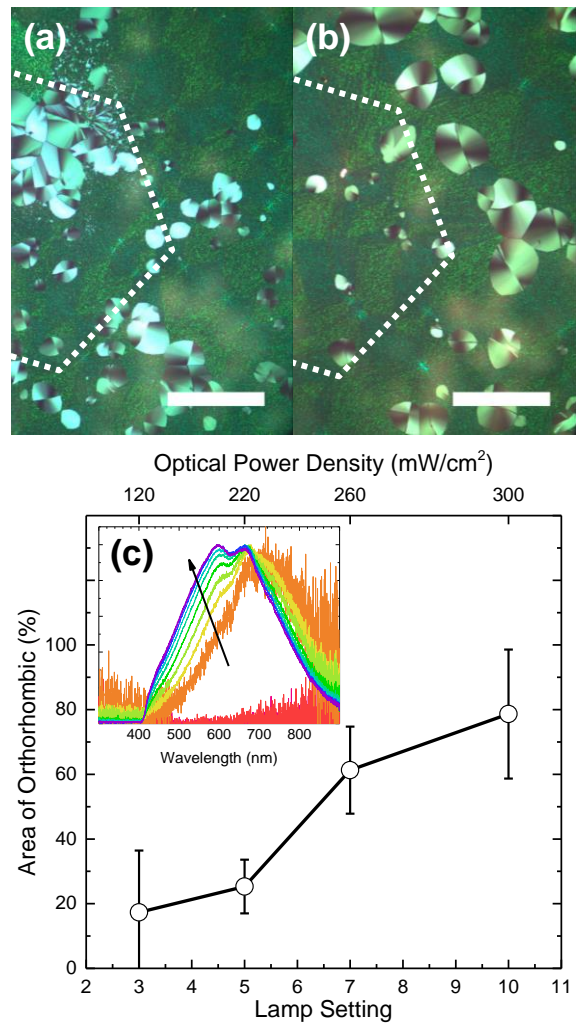


Figure 4.9. Polarized optical micrographs of 64 nm rubrene films annealed at 170 °C with (a) 300 and (b) 120 mW/cm² of light during annealing. The area illuminated during annealing is the dotted hexagon. (c) Film composition as a function of illumination power, inset showing the incandescent tungsten microscope lamp spectrum with increasing power.

Crystallization of Annealed Rubrene Films

polymorph to levels even higher than can be achieved strictly thermally, but at the expense of sometimes ablating or evaporating material in the region of interest. The total absence of material in some cases of high lamp power suggests that this may be driven by molecular heating by light absorption within the film,⁶¹⁵ substrate, or heating surface. In the case of heating by film absorption, the orthorhombic polymorph benefits in two ways: the higher temperature enhances the fraction evolved according to Figure 4.8a, and the orientation of the molecule in the unit cell prevents coupling of the strongest transition dipole to the incident light,¹⁷⁴ slowing further heating and sublimation. The different orientations of molecules in the triclinic and orthorhombic unit cells (Figure 4.4b) would cause more light to be absorbed by triclinic crystals and material most amenable to joining the crystal, slowing their growth in similar fashion to Figure 4.8a.

It is important to note that with increased light flux comes an increased risk of oxidation according to Figure 4.2; however, the conditions which allow favorable viewing (Lamp Setting of 5) are also those which appear to be considerably less susceptible to oxidation and also coincide with the polymorphic composition and growth of much lower light intensities (Figure 4.9c) which also closely match rubrene crystals grown without light.

4.2.6. Selection Mechanisms

The trends of composition with temperature may be explained with the reasoning previously applied to abrupt annealing.⁴⁵¹ As the surface temperature is increased, there is no sharp cutoff for the observation of each type of crystal; instead, the films appear to display a continuum of compositions consistent with a sequential increase in the substrate

Crystallization of Annealed Rubrene Films

temperature upon heating. Immediately after the substrate is placed on the heated surface, the film is relatively cool and there is no observed growth as the molecules lack sufficient energy to reorganize. Crystal growth then follows as the film is heated, with triclinic nucleation and growth occurring first and most rapidly but gradually slowing, followed by orthorhombic nucleation and growth, often from the leading edges of triclinic crystals (Figure 4.10). This nucleation of the orthorhombic phase is consistent with reports of cross-nucleation in other organic materials, wherein the faster growing polymorph is observed to nucleate on the slower via similarities in lattice parameters and other factors, though rubrene thin films may be the first observation of this behavior in thin-film annealing.^{591,616,617}

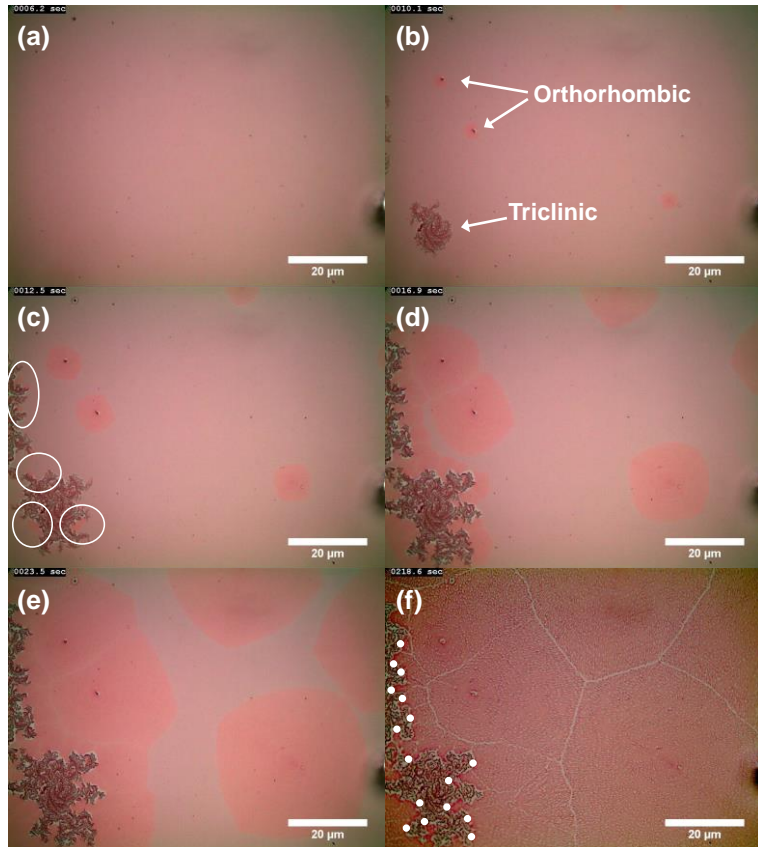


Figure 4.10. Unpolarized episcopic optical micrographs showing the process of rubrene cross-nucleation and grain ripening on ITO at 170°C as a function of time after annealing begins. (a) Amorphous film at $t = 6.2$ s; (b) triclinic and orthorhombic nuclei at $t = 10.1$ s; (c) cross-nucleation of orthorhombic grains on triclinic spherulites at $t = 12.5$ s, highlighted in white ovals; (d) continuing cross-nucleation and growth of orthorhombic rubrene at $t = 16.9$ s; (e) complete truncation of triclinic growth at $t = 23.5$ s; (f) grain ripening ($t = 218.6$ s), showing grain boundaries between different orthorhombic regions and cross-nucleation sites extracted from these boundaries depicted by white dots.

Crystallization of Annealed Rubrene Films

Theoretical predictions and density-based arguments show that the triclinic polymorph is slightly more thermodynamically stable at room temperature,⁶¹⁸ so the prevalence of each phase must be influenced by the relative roles of the surface versus bulk effects (film thickness) in determining growth mode and rate. Furthermore, the fact that no polymorph interconversion between triclinic and orthorhombic is observed at times relevant for film annealing implies that the crystal structures become kinetically trapped upon formation. This polymorph progression and substrate heating rate give rise to the sigmoidal curve shape in Figure 4.7b, which is compounded with additional molecular energy from illumination in the case of Section 4.2.5.

In considering the origin of this polymorphic transition with temperature and thickness, it is important to weigh the influence of substrate, bulk, and surface effects.^{360,619} Film confinement effects on polymorphism have been observed in solution-processed films,⁵²⁵ but these are largely facilitated by a “crust” of equilibrium crystal forming on the film top surface which strains the material beneath and nucleates the metastable polymorph. Although the effects of temperature are not clear in this mode, confinement would result in coexistence of polymorphs at all points in confined films, which is not observed in rubrene films. The substrate is invariant with annealing temperature, which leaves the free surface and film bulk as contributing factors to define the polymorphic growth modes.^{311,540} This may imply a transition in the film bulk (such as a glass transition with thickness sensitivity) which changes material attachment to the growing crystal as with glass-crystal growth.^{308,318,330,331} Alternatively, new modes of material transport, such as sublimation,

Crystallization of Annealed Rubrene Films

could become increasingly important as the film temperature changes. The shift in film composition with increasing thickness (Figure 4.8) implies a stronger bulk effect, but each of these could discriminate between polymorphs.

A final consideration in the polymorphic transformation of rubrene is the effect of strain on crystallization and polymorphism. Thin organic films on the order of 10-20 nm are typically the lowest thickness that would be expected to relax in terms of (pseudo-)epitaxial strain,¹⁰⁹ which proceeds through a variety of growth modes which include Stranski-Krastanov and Frank-van der Merwe.³⁵⁷ The absence of these regimes in amorphous rubrene implies that the film is not likely significantly strained upon deposition, which could be expected for an amorphous solid on a weakly interacting, disordered substrate like SiO₂ or ITO. With the rapid application of heat, thermal stress, σ_T , is rapidly developed in the film according to^{620,621}

$$\sigma_T = \frac{(\alpha_f - \alpha_s)(T_D - T_F) E_f}{1 - \nu_f} \quad (4.1)$$

where α_i is the thermal expansion coefficient for the film or substrate, T_F is the film temperature relative to the deposition temperature T_D , E_f is the film elastic modulus, and ν_f is Poisson's ratio for the film. Note that it is possible for the film to be under compressive (negative) or tensile (positive) strain depending on the deposition temperature and the relative thermal expansion coefficients. This is also only the thermal component; other residual stresses may exist within the film,^{357,622-625} and can impact device performance.⁶²⁶ For crystalline orthorhombic rubrene, $\alpha_f = (10 - 80) \times 10^{-6}/^\circ\text{C}$, compared to that of silicon or glass of $(3 - 4) \times 10^{-6}/^\circ\text{C}$ ppm.⁶²⁷ When coupled with the mechanical properties

Crystallization of Annealed Rubrene Films

of orthorhombic rubrene ($E_f = 10 - 15$ GPa, $\nu_f \approx 0.067$)⁶²⁸, this gives an in-plane compressive stress of 11-120 MPa for a temperature rise of 150 °C. Considering that the tensile yield strain ϵ_Y of orthorhombic rubrene appears to be ~0.05%⁶²⁷ (achievable with an applied stress of $\sigma_Y = E_f \epsilon_Y = 5 - 8$ MPa), the calculated thermal stress is significant in terms of the rubrene intermolecular bonding, even in the crystal. An amorphous or glassy film likely has weaker intermolecular bonding (*e.g.*, glass transitions and crystallization events observed below the melting point), but much higher α_f . This may mean that even in compression, perhaps this force is enough to alter molecular orientation on the substrate or densify the film to restrict the growth of the triclinic polymorph.

4.3. Crystal Growth Mode and Shape

Assessment of crystal morphology *in situ* allows simple tracking of feature evolution with time and temperature. This allows for the identification of crystal shapes, with the ability to examine films *ex situ* with other techniques after quenching or completing crystallization. The optical appearance of crystals can also be highly useful for distinguishing between different modes of crystal growth, the method by which the crystalline growth front propagates.

4.3.1. Crystal Growth Mode

The triclinic polymorph grows as a spherulite, wherein the growth front of the crystal undergoes non-crystallographic branching during growth, typically evolving a polycrystal which is macroscopically spherical in three dimensions and circular in two.^{455,456} This

Crystallization of Annealed Rubrene Films

represents the general shape of fully developed triclinic crystals, though deviations are observed on small length scales, especially near the beginning of growth. The overall effect is a disorganized polycrystal with limited long-range order because of the relatively low density of branches and surface diffusion of material to existing branches.

The orthorhombic polymorph shows two growth modes which appear to be thermally activated, shown in Figure 4.11.

At low temperatures, the orthorhombic crystals grow with a growth front propagating as a single continuous boundary with consistent crystallographic orientation across each crystallite, while at higher temperatures the growth transitions to a more radially symmetric spherulite growth pattern. Several key features of these optical

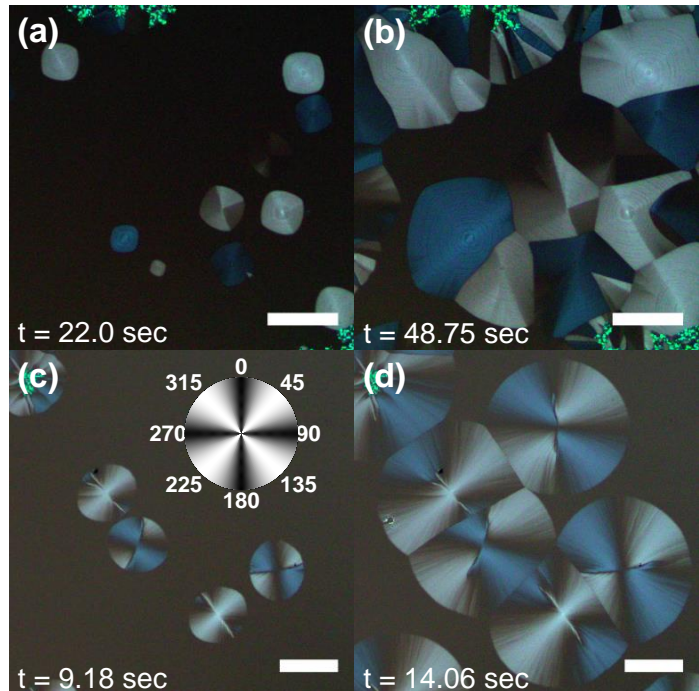


Figure 4.11. Polarized optical micrographs of orthorhombic rubrene growth on ITO viewed at (a), (b) 162°C and (c), (d) 179°C (scale bar 100 μm). The inset of (c) is the calculated intensity of an ideal, radially symmetric birefringent polycrystal.

micrographs allow a more detailed description of crystal character: first, the optical extinction in Figure 4.11a and Figure 4.11b is largely uniform across individual crystals. This, coupled with the observation of continuous, faceted growth rings within each crystal, suggests that each is a single crystal. The opposite can be said for those crystals in Figure

Crystallization of Annealed Rubrene Films

4.11c and Figure 4.11d: these crystals show alternating bright and dark regions under polarized light. This implies a continuously changing crystallographic orientation, which gives rise to an intensity profile similar to that shown in the inset of Figure 4.11c,⁶²⁹ but with notable differences that are discussed in the following section.

The occurrence of rings within the growing single crystals is curious, especially since they neatly follow the perimeter of the growing crystal and are unique to each crystal within the film. The uniqueness is demonstrable by examination of the crystal rings across grain boundaries: at a grain boundary, both crystals must simultaneously have grown into one another. If the effect were related to a substrate-wide change, all crystal growth rings should have formed at the same time and should thus align across grain boundaries. This is not observed in these films. There appear to be few classical analogues on these spatiotemporal scales: the feature size is far too small for gravity-driven assembly;^{630,631} the Grinfeld instability results in periodic oscillations and requires the presence of a volatile or liquid phase for mass transport;⁶³² Liesengang ring formation from reaction-diffusion crystallization requires a spatial inhomogeneity of species,⁶³³ and enthalpy-driven crystallization waves in “explosive” crystallization do not necessarily yield rate instabilities or surface topography.⁶³⁴ One explanation of such formations is a variation in the crystal growth rate, where the crystal growth periodically slows and accelerates, accumulating more and less material moving across the surface from the amorphous region. An example of this could be in response to an increase or decrease in film temperature; however, variations in the net film temperature should give simultaneous rings across all

Crystallization of Annealed Rubrene Films

crystals (with rings matching across grain boundaries), disqualifying it as a mechanism. If the crystals were to speed or slow from dissipation of the enthalpy of crystallization (exothermic for rubrene, as shown in Figure 4.5), the result should be a continuous increase in the crystallization rate to a steady-state value; unlike supersaturated liquid or melt where a reduction in temperature provides the chemical potential to incorporate into the solid, solid-phase crystallization is driven by an enhancement in molecular diffusivity. As more and more enthalpy was released, the crystallization rate would continue to increase until the substrate could sufficiently dissipate or absorb the enthalpy release.⁶³⁴ A final proposal is a modulation of the crystallization rate by stress buildup and release, as demonstrated in metal alloys.⁶³⁵ In this scenario, the release of strain energy from the amorphous phase would affect the relative attachment rate for molecules onto the crystal. This release could be sudden and would be a property of the crystal and amorphous matrix, convoluted with the thermal conditions when it nucleated. This could yield a well-defined height difference upon release (growth ring) and unique features related to the build-up for each crystal in time.

4.3.2. Crystal Shape

In order to more quantitatively probe changes in film morphology and phase composition, annealed films were examined using AFM and XRD. In particular, the orthorhombic crystals were found to be oriented with the c axis orthogonal to the substrate (Figure 4.4a),^{174,451} which permits correlation of the measured angle between the growth front facets with crystal planes to visually assign individual crystallite orientation.

Crystallization of Annealed Rubrene Films

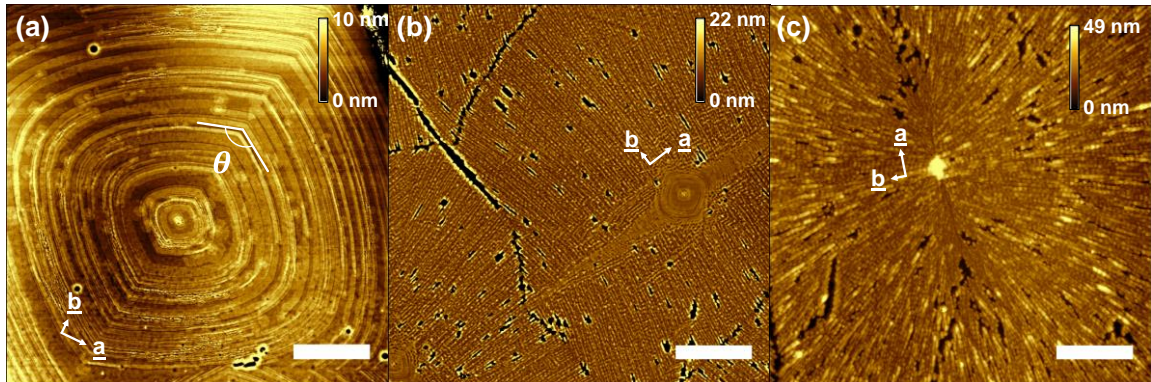


Figure 4.12. Atomic force micrographs of orthorhombic rubrene films grown on silicon and annealed at (a) 160°C, (b) 170°C, and (c) 200°C. Scale bars 10 μm . Growth on silicon reduces the triclinic-orthorhombic transition temperature by approximately 10°C but does not change the observed morphology trend.

With the c axis orthogonal to the plane in a typical grain, the a and b axes are left in plane. Measurement of the angle θ in Figure 4.12a averaged over many growth fronts gives a value of $(128 \pm 4)^\circ$, which agrees well with the calculated angle between the (110) and $(1\bar{1}0)$ planes (127.0°). In addition to this measurement, the crystal facets in the bulk of the grains can be measured by allowing the film to remain at its annealing temperature for an extended period of time past that required for complete crystallization. This results in a loss of material around film irregularities, crystal and substrate defects, and other perturbations with subsequent material rearrangement so that the spaces which appear are faceted (Figure 4.13). These measurements yield $(100)\cap\{110\}$ equal to $(118 \pm 5)^\circ$ and $(110)\cap(1\bar{1}0)$ equal to $(128 \pm 5)^\circ$, compared to 116.6° and 127.0° , respectively. A complete comparison of the angles formed at 170 °C and

180 °C is given in Table 4.2.

The growing crystal

Table 4.2. Comparison of calculated and measured facet angles corresponding to those measured in Figure 4.13a-b.

Plane Intersection (Interior Angle)	Calculated	Measured	
		170°C	180°C
$(100)\cap\{110\}$	116.6°	$118 \pm 5^\circ$	$116.2 \pm 0.9^\circ$
$(110)\cap(1\bar{1}0)$	127.0°	$128 \pm 5^\circ$	$127.1 \pm 0.8^\circ$

shape of Figure 4.12 can be understood by considering the relative growth rates of

Crystallization of Annealed Rubrene Films

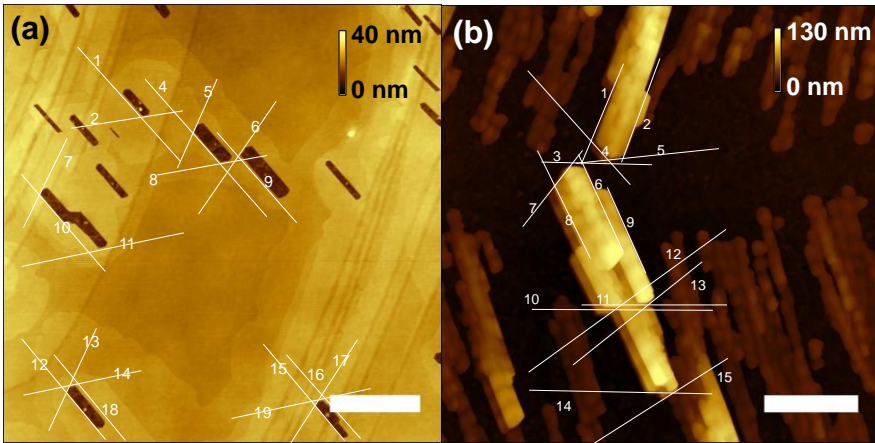


Figure 4.13. Determination of crystallographic axes and correspondence to grain location at high temperature. (a) and (b) AFM images of rubrene on ITO, annealed at (a) 170°C for 180 seconds and (b) 180°C for 600 seconds, scale bars 3 μm.

individual crystal planes, as per the Wulff formalism.³⁹¹ Low-density planes with small spacing have the highest surface attachment energy

and thus largest growth rate, which results in those planes “growing out” of the crystal.

Such a case occurs with the (010) plane and the {110} family of orthorhombic rubrene.

The (010) has a much smaller spacing and density than {110}, causing it to disappear from the crystal shape, leaving the facets to

be defined by the {110}

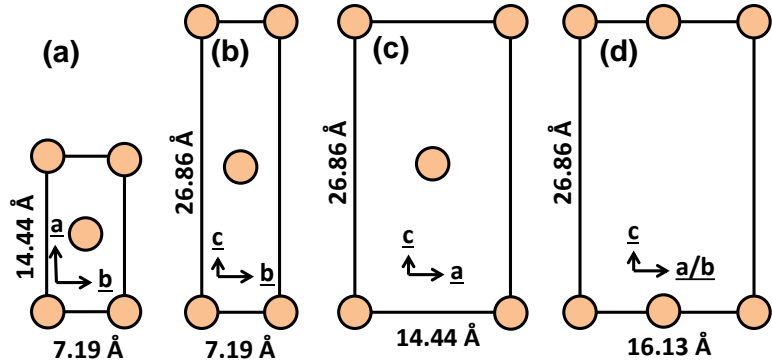


Figure 4.14. Planar density diagrams for orthorhombic rubrene planes: (a) (001), (b) (100), (c) (010), and (d) {110}. Diagrams to scale.

planes. In contrast, because the planar density and spacing of the {110} planes are comparable to those of the (100), there is competition for the observed plane. This results in the curved growth front perpendicular to the a axis. Similar arguments using the relative surface energies of the exposed planes (Figure 4.14) explain the faceting observed at long times, with planes showing well-defined intersections because of equilibration allowed by

Crystallization of Annealed Rubrene Films

the considerably slower evolution of the crystal surface. The planar density and spacing together combine to give considerably lower growth rates for the (001), (100), and {110} planes, shown in Table 4.3. These results are in accordance with Eqn. 3.6.

Table 4.3. Planar densities, spacing, and growth rates for orthorhombic rubrene.

Plane	(001)	(100)	(010)	(110)	(120)	(210)
ρ_{hkl} (#/ \AA^2)	0.01926	0.01036	0.00516	0.00692	0.0043	0.0025
d_{hkl} (\AA)	13.43	7.217	3.597	6.438	3.49	5.09
$(\rho_{hkl} d_{hkl})^{-1}$ (\AA)	3.866	13.37	53.87	22.44	66.64	78.58
Relative Rate	0.049	0.170	0.686	0.286	0.848	1

4.3.3. Proposed Growth Mechanism

As the annealing temperature increases, there is a breakdown of this orderly growth pattern, shown schematically in Figure 4.15. Each orthorhombic nucleation site typically originates one single crystal structure, meaning all locations within that crystallite share the same crystallographic orientation. As time elapses (Figure 4.15b), the growth front at the intersection of the (110) and (1̄10) planes devolves into individual crystalline rays with propagation in the direction of the b axis, as determined from crystal facets observed in long-term ripening experiments (Figure 4.13). The slightly larger growth rate of these crystal planes as compared to that of the a axis leads to the characteristic crystal ellipticity in early stages of growth (Figure 4.15c), which increases with increasing misorientation between the growing grains until single crystal growth along the a axis is terminated by growth of b axis oriented crystals. After this point (Figure 4.15d), the growing crystals are increasingly centrosymmetric with time. As this transition occurs sooner at higher temperatures, the final crystals are also more circular at higher temperatures, reinforcing

Crystallization of Annealed Rubrene Films

the idea of a breakdown into a rapidly branching spherulite growth mode at high

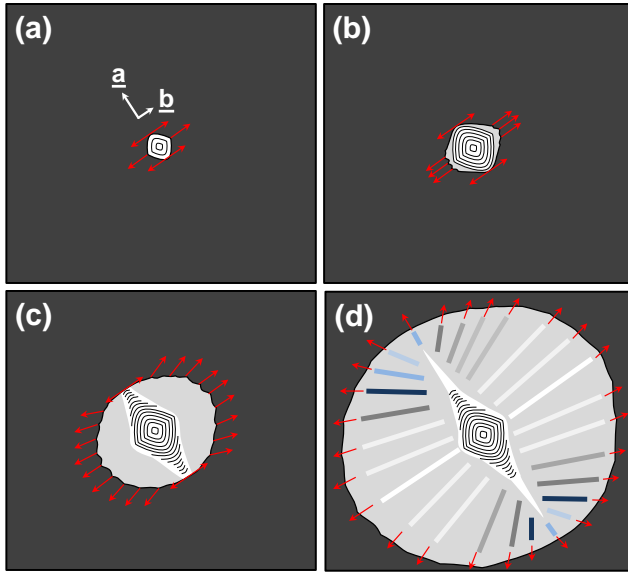


Figure 4.15. Diagram of the orthorhombic growth transitions during rubrene thin film annealing, showing (a) nucleation of the orthorhombic polymorph, with the red arrows denoting the local direction of the b axis, (b) growth front of the $\{110\}$ devolving into individual rays of crystalline material, (c) continued disorientation of branching crystals, and (d) termination of the core single crystal growth.

temperatures (Figure 4.16). In addition, the crystalline material formed after this point displays the full coloration of a circularly distributed spherulite between crossed polarizers; however, the core of these crystals does not always display the expected Maltese cross-shaped extinction pattern because of the local ordering of the undeviated b axis growth about the single crystal center.

This results in an area centered about the nucleation site which displays similar coloration and intensity without a cross because of a lack of material with the extinction orientation.

The single-to-polycrystal transition may be in part due to the thermal stress discussed in Section 4.2.6. As the stress continues to increase with increasing annealing temperature, the stress relief mechanism increasingly becomes the densification and reorganization (material diffusion) which occurs as the growth front passes through. If this stress is non-normal to the growth direction, there could be a shear stress which develops at the growth front, *e.g.*, along the faceted direction corresponding to the $[010]$ direction. This non-normal strain could be responsible for periodically changing truncating or shifting the

Crystallization of Annealed Rubrene Films

growing crystal front, resulting in discontinuous crystallinity which is largely radially symmetric. This would also preserve the [100] axis for somewhat longer, as that rounded crystal direction neatly navigates the burgeoning

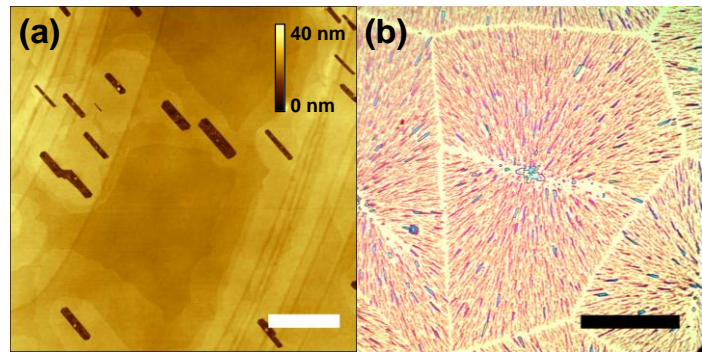


Figure 4.16. Contrast between films on ITO annealed past complete crystallization at (a) 170°C, 180 seconds and (b) 210°C, 300 seconds. (a) is an atomic force micrograph, scale bar 3 μ m; (b) is an optical micrograph, scale bar 50 μ m. At low temperature, the holes which appear in the ripening crystal are faceted and aligned across the crystal, whereas the high temperature crystals show a more centrosymmetric deterioration.

polycrystalline growth, preserving a single-crystalline spire which grows from the nucleation site. Alternatively, the crystal growth may simply proceed at different rates along these different axes, yielding a higher rate of growth-front nucleation along the [010] and thus a greater propensity for polycrystallinity. This situation seems strange when viewed through the lens of supercooled liquids where dynamic and particulate heterogeneity culminate in growth front instabilities,^{456,636,637} and even from a thin-film standpoint where the orthorhombic polymorph of rubrene is known to grow as a spherulite in thick film at low temperature;^{488,558,638} however, the arguments for rate-limiting species diffusivity inherent in these approaches still hold true.

The type of growth mechanism proposed in Figure 4.15 is further corroborated by the nanostructures observed in AFM images of high-temperature grains, such as Figure 4.12b and Figure 4.12c. These images show alternating rays of accumulation and depletion which radiate out from the nucleation site and are oriented with the b axis parallel to the long axis

Crystallization of Annealed Rubrene Films

of the ray. It is conceivable that even in this heavily branched growth regime, the growth rate of the b axis exceeds that of the a axis, which would result in a crystalline “wake” with an angle given by the arctangent of the b/a axis growth rate ratio. This wake follows the leading crystal tips, depicted by the arrows in Figure 4.15c. Rubrene molecules undergoing lateral transport across the surface (surface diffusing or depositing from vapor) will experience a different energy of interaction with the growing crystal facet *versus* the surrounding amorphous material. The relative order of this energy of interaction can be deduced from the relative sublimation rates of material from rubrene films during annealing. During these experiments, amorphous material develops circular holes which continue to grow until the material is incorporated into an orthorhombic grain, at which point the material loss appears frozen. From this, we can deduce that the orthorhombic phase is more stable than amorphous, as expected. This then leads to the existence of anisotropic transport preferentially to the crystallized region, resulting in vertical accumulation manifested in the observed ridges.

4.4. Crystal Growth Rate and Activation Energy

The identification of crystallite orientation and growth mode permits quantification of the growth rates and activation energy of crystallization for the various growth directions nucleated in a rubrene thin film annealed at 160°C. As shown in Figure 4.7e, a temperature of 160°C is within the transition range between the two polymorphs for a 20 nm film, meaning that each exists and grows during some point in the annealing process. The triclinic polymorph starts growing first and shows a linear increase in radius until bulk

Crystallization of Annealed Rubrene Films

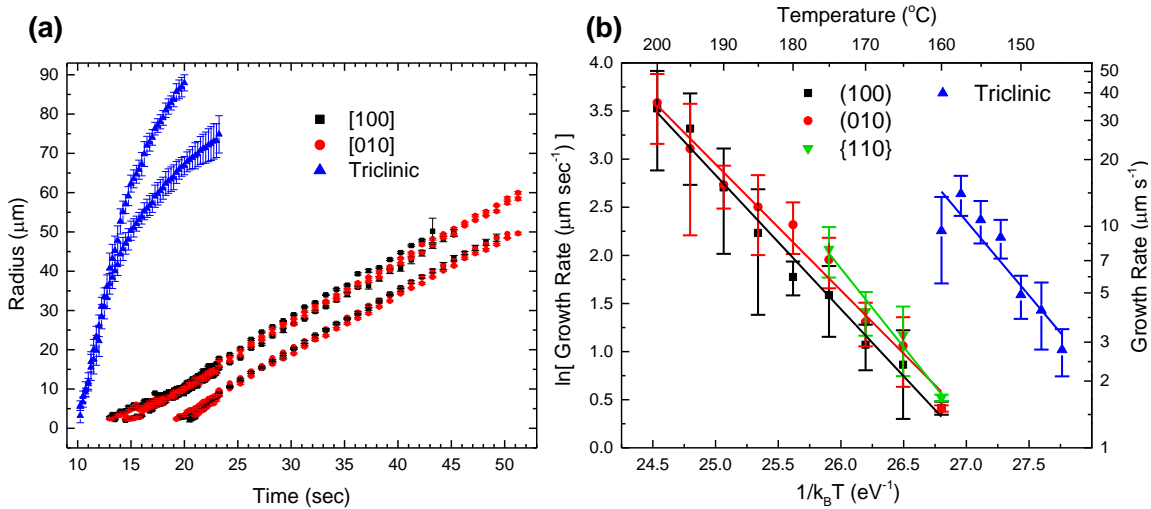


Figure 4.17. (a) Plot of crystal dimensions as a function of time at 160°C, showing the average radius of triclinic spherulites and crystal radius along the [100] and [010] directions of orthorhombic grains. All crystals shown nucleated in the bulk. (b) Plot of the growth rates of the identified crystal planes for the orthorhombic polymorph and the average growth rate of triclinic spherulites, where the {110} growth is calculated from the measured growth along [010]. All films are 20-nm-thick on ITO-coated glass substrates.

nucleation of the orthorhombic and polymorphs. Figure 4.17a shows an example set of growth curves for crystals which polymorph, at which point the growth rate begins to decrease. The orthorhombic grains show no such behavior, nor do triclinic crystals grown well below this transition temperature. This correspondence suggests that conditions favorable for orthorhombic growth reduce the growth rate and branching of the triclinic polymorph, which is consistent with the theory that the film may be undergoing a glass transition which favors the orthorhombic growth. The change in the polymorphic composition of the observed nuclei with temperature and the presence of cross nucleation further reinforces this transformation as a kinetic transition, with growth rates of the polymorphs additionally altered by film thickness effects.³¹⁸

To determine the crystallization activation energy (E_a) and Arrhenius prefactor (crystallization rate at infinite temperature, r_o) for growth of these crystal planes, the

Crystallization of Annealed Rubrene Films

dependence of growth rate ($\frac{dr}{dt}$) on temperature is fit according to the linearized Arrhenius expression,

$$\ln\left(\frac{dr}{dt}\right) = \ln(r_o) - E_a \frac{1}{k_B T} \quad (4.2)$$

where k_B is the Boltzmann constant and T is absolute temperature. These data and fits are presented in Figure 4.17b, and the fit parameters are given in Table 4.4.

Interestingly, the activation energies are all within error of one another, which implies that rubrene

Table 4.4. Measured activation energy E_a , Arrhenius prefactor r_o , and interpolated growth rate at 160°C $r|_{160^\circ\text{C}}$ for orthorhombic (O) and triclinic (T) rubrene on ITO.

Crystal Plane	E_a (eV)	r_o ($\mu\text{m s}^{-1}$)	$r _{160^\circ\text{C}}$ ($\mu\text{m s}^{-1}$)
O (100)	1.39 ± 0.06	$(2 \pm 8) \times 10^{16}$	1.4 ± 1.6
O (010)	1.31 ± 0.06	$(3 \pm 12) \times 10^{15}$	1.8 ± 1.7
O {110}	1.6 ± 0.2	$(2 \pm 20) \times 10^{19}$	2 ± 5
T	1.5 ± 0.3	$(1 \pm 28) \times 10^{19}$	14 ± 9

molecules face similar barriers when attaching to all facets and polymorphs. The difference in growth rate is instead found in the offsets between lines, which are compared by the crystal plane growth rate at 160°C ($r|_{160^\circ\text{C}}$) and are related to the prefactor r_o term. For analogous first-order chemical reactions, this prefactor is sometimes called the “Arrhenius frequency factor” and interpreted as the number of molecular collisions with favorable orientation for reaction.⁶³⁹ The Boltzmann probability factor $\exp\left(-\frac{E_a}{k_B T}\right)$ is multiplied by this parameter to give the reaction rate. The large error bars on r_o and $r|_{160^\circ\text{C}}$ are compounded by the slope uncertainty and distance from the y-intercept, though the r_o difference may imply a difference in event frequency or molecular orientation specificity between polymorphs.

It is also interesting that the extracted activation energies are comparable to the

Crystallization of Annealed Rubrene Films

sublimation enthalpy of rubrene of 157 kJ/mol,⁴⁷⁵ or 1.6 eV/molecule. This implies that among the factors relevant for thin-film crystal growth, including surface diffusion, molecular rearrangement, and sublimation/deposition, sublimation cannot be immediately discounted in this temperature range. Without dramatically changing the film architecture to, e.g., assess the wavelength dependence of the transport phenomenon,⁶¹⁹ it is difficult to further characterize the transport; however, film restructuring at long times after the completion of crystal growth is heavily influenced by loss due to sublimation, as evidenced by depletion in long-time annealing images (Figure S5b).

The measured activation energies are approximately twice that previously measured for rubrene (0.74 eV),⁴³⁵ but are comparable in magnitude to the crystallization and even surface diffusion activation energy of other organic compounds.^{471,536,640} It is also worth noting that our film thickness (20 nm) and substrate (ITO/glass) differ substantially from the layer measured previously (80 nm on silicon), which changes the relative magnitude of the substrate, bulk, and free surface effects on the crystallization behavior.

4.5. Conclusions

In summary, the defining crystal planes for annealed rubrene thin films have been identified optically, rationalized energetically, and coupled with *in situ* optical measurements to quantify growth rates of the dominant crystal polymorphs and directions observed during thin-film rubrene crystallization. This crystallization includes a thermally activated transition between the triclinic and orthorhombic polymorph with cross-nucleation, which has been explored as a function of temperature and film thickness, and

Crystallization of Annealed Rubrene Films

suggests a bulk film effect responsible for the transition. Additionally, a transition between the single-crystalline and spherulitic growth mode of the orthorhombic polymorph is reported. This spherulitic growth mode differs from the orthorhombic single-crystal low-temperature growth mode and yields b axis-oriented crystals aligned radially about the nucleation site. The activation energies for the growth of all observed crystals compare well with other organic systems and fall between (1.31 ± 0.06) and (1.6 ± 0.2) eV.

5. MANIPULATING RUBRENE CRYSTAL SHAPE AND GROWTH

With a better understanding of how thin organic films crystallize and change over time, the perspective changes to more applied effects such as controlling crystal shape and growth rate. One method to do this is by inclusion of a secondary species which disrupts molecular attachment to the growing crystal. In films which are sufficiently dilute, this disruption is severe enough to severely slow crystal growth and shut off growth along specific crystal directions. The degree to which this disruption occurs varies across different molecular additives, with multiple co-additives producing a hybrid crystal behavior with crystal shape between that corresponding to each component additive.

5.1. Introduction

Solid-state mixtures of organic molecules are found in a wide variety of applications including organic electronic devices and pharmaceuticals.^{12,641,642} In addition to sought-after mixture effects such as enhanced excited state dissociation,^{96,643} charge conduction,⁶⁴⁴ or drug bioavailability,^{645,646} mixtures can alter the fundamental behavior of their constituents in unforeseen ways, including their crystallization.^{307,391,647} Directed control of crystal size and shape has been well-characterized in solution-grown inorganic

Manipulating Rubrene Crystal Shape and Growth

nanoparticles^{648–650} and nanowires³⁹⁸ and has been described in organic crystals grown from solution.^{392,394,612} However, this manipulation remains elusive in the solid state, where the ability to direct crystal shape is highly desirable for patterning organic field-effect transistors (OFETs).^{526,527} Similarly, the effects of macromolecular additives, *e.g.*, polymer excipients, on crystal growth rates in pharmaceutical solids and melts are well-known,^{307,651–653} if still not fully understood, but studies of facet-dependent growth or mixtures of small-molecular-weight species are lacking. These conditions, relevant to drug mixtures and organic light-emitting devices (OLEDs), are important to gain additional understanding of methods to halt crystallization for enhanced stability of pharmaceuticals and OLEDs,^{58,346,654} each of which are often comprised of highly conjugated organic molecules in amorphous mixtures. The present work reports tunable crystal shape from discs to needles and conditions to stifle crystal growth in annealed solids *via* simple mixing, demonstrated here using thin films of two archetypal small-molecular-weight organic semiconductors.

The molecules used in this study are rubrene (5,6,11,12-tetraphenyltetracene), a common channel material in OFETs,⁶⁰⁴ and 2,2',2''-(1,3,5-benzinetriyl)-tris(1-phenyl-1-H-benzimidazole) (TPBi), a common electron transport material in OLEDs.¹² The high hole mobility of rubrene has driven exhaustive research into understanding its crystallization in thin film, where rubrene exhibits complicated thickness- and temperature-dependent transitions in polymorph composition and growth mode.^{376,435,451,475}

5.2. Additive Concentration Effects

The molecules used in this study are rubrene (5,6,11,12-tetraphenyltetracene), a common active material in OFETs,⁶⁰⁴ and 2,2',2''-(1,3,5-benzinetriyl)-tris(1-phenyl-1-H-benzimidazole) (TPBi), a common electron transport material in OLEDs.¹² The high hole mobility of rubrene has driven exhaustive research into understanding its crystallization in thin film, where rubrene exhibits complicated thickness- and temperature-dependent transitions in polymorph composition and growth mode.^{376,435,451,475} In particular, pure rubrene grows in equiaxed, single-crystalline grains of the orthorhombic polymorph at temperatures $160\text{ }^{\circ}\text{C} < T < 180\text{ }^{\circ}\text{C}$ as shown in Figure 5.1a. These crystals are characterized by two-fold symmetry, featuring a faceted vertex defined by the {110} planes along the [010] direction and a rounded edge formed by competition between the (100) and {110} planes intersecting the [100] direction.³⁷⁶ TPBi is a

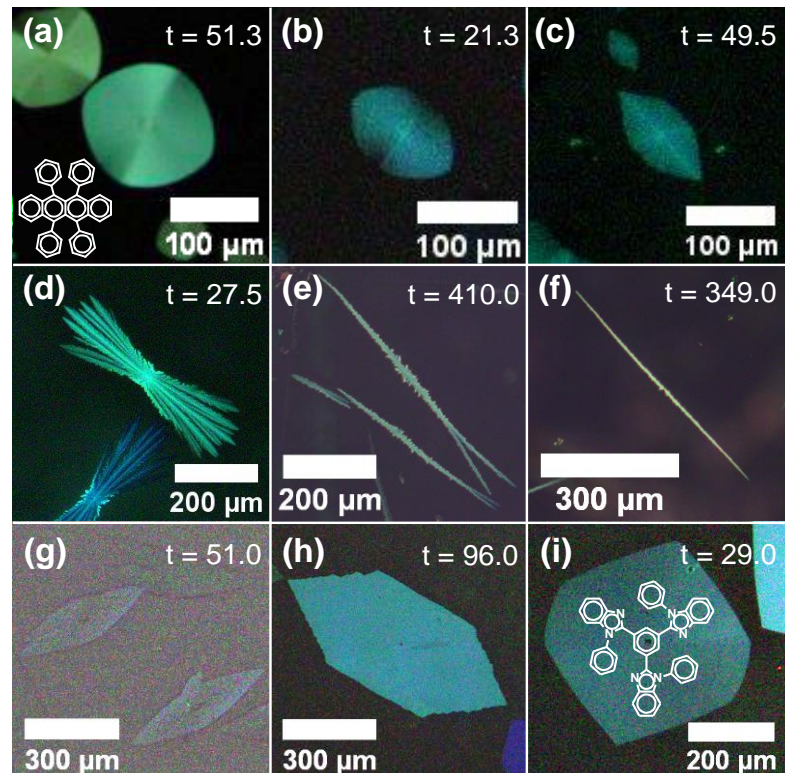


Figure 5.1. . Crystal shapes at different compositions (vol% TPBi) and annealing temperatures: (a) 0, 160 °C (b) 10, 170 °C (c) 15, 170 °C (d) 15, 190 °C (e) 20, 170 °C (f) 25, 170 °C (g) 80, 200 °C (h) 90, 190 °C and (i) 100, 190 °C. The inset molecular structures are (a) rubrene and (i) TPBi. Annealing times in seconds are inset in the upper-right corner of each image, and all images are polarized optical micrographs.

Manipulating Rubrene Crystal Shape and Growth

glass-forming molecule which crystallizes upon annealing and has greater steric bulk than rubrene, making it ideal for studying the disruption of rubrene crystal growth and *vice versa*. With the inclusion of TPBi, the rubrene crystal shape changes dramatically: as the concentration of TPBi is increased, the crystals show pronounced elongation along the [010] direction, effectively becoming microwires at concentrations above 20 vol% TPBi (Figure 5.1b-f). The transition in shape between 15 and 20 vol% TPBi is preceded by the change observed in 15 vol% films at high temperature (Figure 5.1d), where growth proceeds primarily along the [010] direction, resulting in many narrow crystals. Note that the [010] direction is also the direction of highest hole mobility in rubrene,⁶⁰⁴ convenient for possible use as microwire transistors. A shape change is also observed in TPBi-rich crystals, where the neat films show equiaxed, hexagonal grains which become elongated along the acutely faceted direction with the addition of rubrene (Figure 5.1g-i). For films in which each species has sufficiently diluted the other (between 40-60 vol% TPBi), neither crystal type is able to efficiently nucleate or grow, causing crystal growth to be stunted.

5.3. Additive Location Effects

To assess where this shape changing effect originates, the relative placement of the additive within the film was varied by growing films of graded composition shown in Figure 5.2. Interestingly, the shape produced does not depend strongly on additive location. Regardless of whether the TPBi-rich interface is at the substrate (Figure 5.2a) or top film surface (Figure 5.2b), the crystal shapes resemble the case of uniformly mixed films with the average gradient composition. This suggests that bulk diffusion, albeit considerably

Manipulating Rubrene Crystal Shape and Growth

slower than surface diffusion,³¹¹ is significant for these films at the annealing temperature.

A complication of this is that films may change in composition over time as the more volatile species (*i.e.* rubrene) sublimes from the film surface, as in highly concentrated but majority-rubrene films at relatively high temperatures. These films exhibit slow, stagnating rubrene needle growth at short times (Figure 5.2c), followed by secondary growth of TPBi-rich domains at considerably longer times (Figure 5.2d-e). This implies that at long times, there is appreciable evaporation of rubrene during annealing at high temperatures, effectively concentrating the films to the point that TPBi crystals may grow. Films with high concentrations of TPBi also show the effects of rubrene sublimation, with the crystal aspect ratio plateauing between 60-80 vol% TPBi and correspondingly longer times required for crystals to nucleate and grow (Figure 5.4a-b), presumably delayed by the loss of rubrene to a critical concentration. Majority rubrene films instead show a reduction in aspect ratio at high concentrations since the crystals are unable to grow quickly enough before the surrounding film sublimes. In addition to these observations,

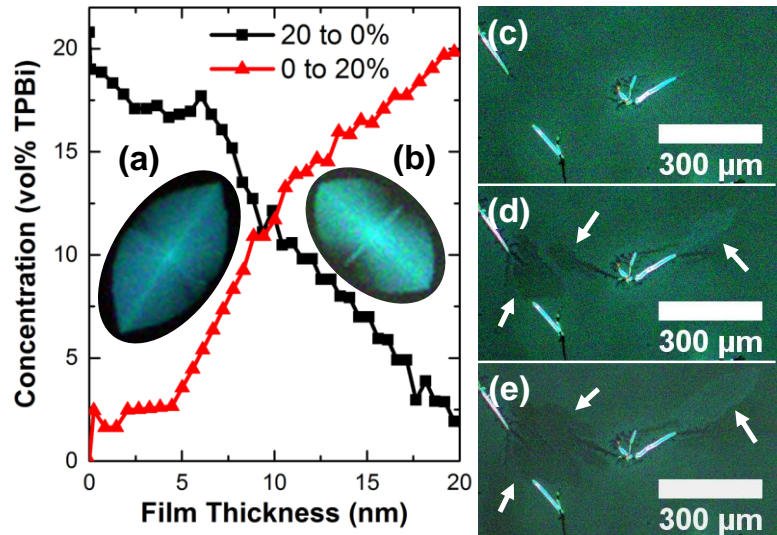


Figure 5.2. Effects of additive location on crystal shape in annealed rubrene films, including linearly graded films with the composition varied from (a) 20-0 vol% TPBi, (b) 0-20 vol% annealed at 180 °C, and uniformly mixed 35 vol% TPBi films at (c) 53, (d) 71, and (e) 75 sec and 210 °C. White arrows highlight the new growth of dark and light TPBi-rich phases. All images are polarized optical micrographs.

stagnating rubrene needle growth at short times (Figure 5.2c), followed by secondary growth of TPBi-rich domains at considerably longer times (Figure 5.2d-e). This implies that at long times, there is appreciable evaporation of rubrene during annealing at high temperatures, effectively concentrating the films to the point that TPBi crystals may grow. Films with high concentrations of TPBi also show the effects of rubrene sublimation, with the crystal aspect ratio plateauing between 60-80 vol% TPBi and correspondingly longer times required for crystals to nucleate and grow (Figure 5.4a-b), presumably delayed by the loss of rubrene to a critical concentration. Majority rubrene films instead show a reduction in aspect ratio at high concentrations since the crystals are unable to grow quickly enough before the surrounding film sublimes. In addition to these observations,

Manipulating Rubrene Crystal Shape and Growth

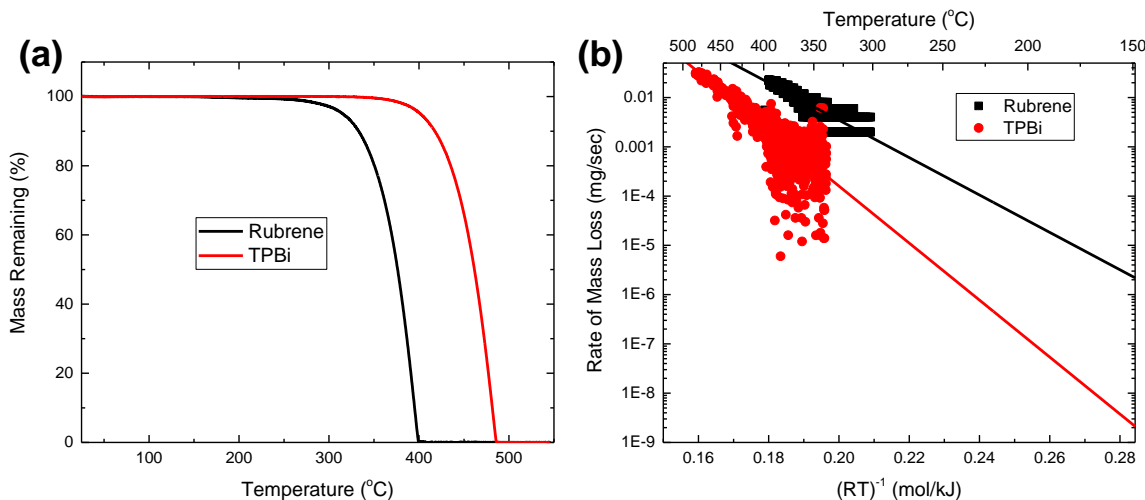


Figure 5.3. Thermogravimetric data for rubrene and TPBi showing (a) percent mass loss with temperature and (b) mass loss rate with temperature, plotted on an Arrhenius plot.

thermogravimetric data demonstrate that rubrene is considerably more volatile than TPBi (Figure 5.3),⁶⁵⁵ which reinforces the proposal of significant mass loss of primarily rubrene with annealing. If developed further, these observations may provide a unique method to determine the relative rates of diffusion and sublimation for a material within a crystallizing film.

5.4. Crystal Growth Rate and Aspect Ratio

Elongation of crystal shape represents an alteration in crystal planar growth rates from the pure film case, with possible causes including facilitated growth of the long axis,^{656–658} impeded growth of the short axis,^{648,649} or some combination thereof. Examination of the crystal growth rate with concentration and temperature (Figure 5.4c) shows there is a decrease in growth rate of the elongated axis with mixing, but an even more pronounced reduction in growth rate along the short axis, as can be inferred from the increase in crystal aspect ratio. Figure 3c implies that the crystal shape is governed by secondary molecules

Manipulating Rubrene Crystal Shape and Growth

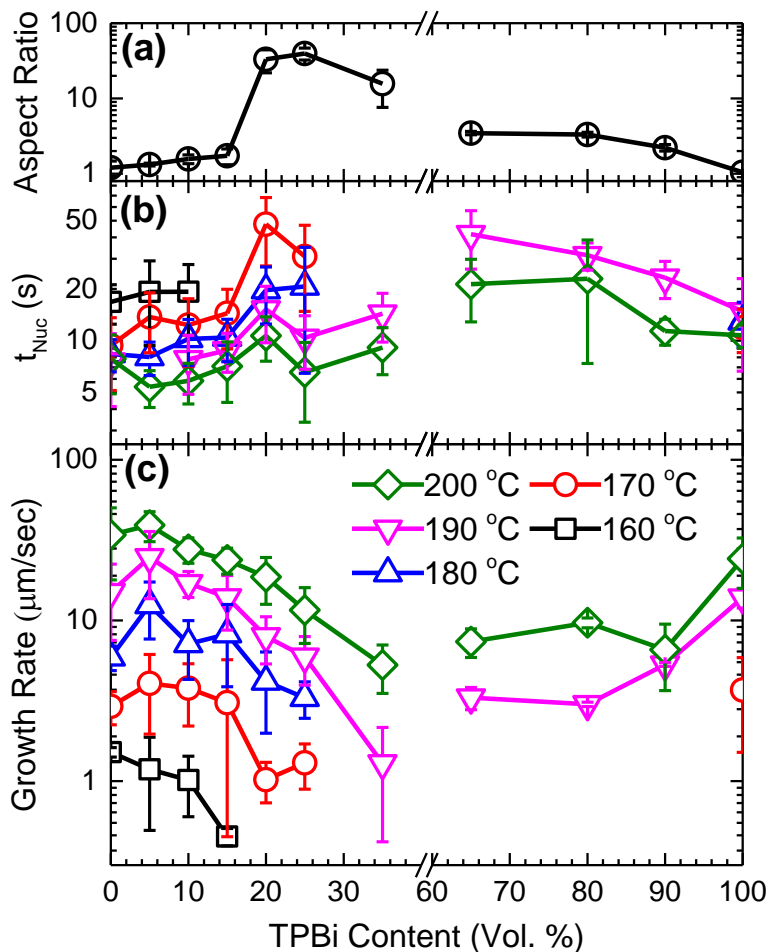


Figure 5.4. Properties of rubrene films with varying TPBi concentration: (a) maximum crystal aspect ratio, (b) nucleation time, t_{Nuc} , and (c) growth rate along the elongated crystal axis.

impeding the attachment of primary, crystal-forming molecules rather than enhancing their attachment, very similar to what is observed in the shape-controlled synthesis of solution-grown nanoparticles.^{648,649} It is unclear whether this change of rate corresponds to growth delay from additive exclusion, lattice disruption

by inclusion of additive pockets, or other

mechanisms previously discussed.^{652,653} If the growing crystal excludes material, as with rigorously stoichiometric inorganic mixtures,^{658–660} the minority species could be expected to partition to the crystal surfaces or become included in the bulk as a concentrated additive cluster. Despite the multiple molecular conformations and weak van der Waals bonds common in polymorphic organic crystals, perhaps increasing susceptibility to additive incorporation, all collected X-ray diffraction (XRD) patterns on mixed films do not deviate

Manipulating Rubrene Crystal Shape and Growth

from pure-material spectra (Figure 5.5). This suggests that the crystalline lattice is unaltered by the additive, but does not preclude either of the proposed mechanisms.

5.5. Film Morphology Effects

As the TPBi content increases in majority-rubrene films, the rubrene attachment rate is significantly slowed along both crystal directions, but especially along the [100] direction. Eventually, the rate of [100] growth becomes unable to compete with that of sublimation from the film, causing material near the crystal edge to move preferentially via a vapor cloud over the film and deposit on the top surface of the crystal edge rather than continue lateral growth. This leads to a trough-like appearance of the needles with atomic force microscopy (AFM, Figure 5.6a), as well as the formation of a material depletion region along the resulting (100) sides of the crystals, essentially ceasing growth and preventing other crystals from growing in the vicinity (Figure 5.6b). Due to the higher rate of [010] growth, the [010] direction stays competitive material diffusion, allowing growth to continue. Examination of quenched films shows no visible gap at the needle tip ([010]), with marked depletion of material along the needle sides ([100]).

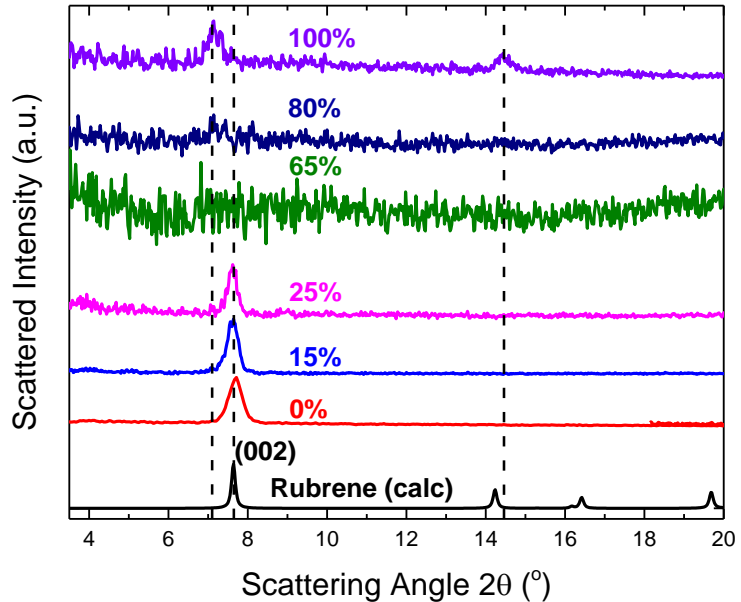


Figure 5.5. X-ray diffraction patterns for films of varying TPBi compositions (vol% TPBi) on ITO.

preferentially via a vapor cloud over the film and deposit on the top surface of the crystal edge rather than continue lateral growth. This leads to a trough-like appearance of the needles with atomic force microscopy (AFM, Figure 5.6a), as well as the formation of a material depletion region along the resulting (100) sides of the crystals, essentially ceasing growth and preventing other crystals from growing in the vicinity (Figure 5.6b). Due to the higher rate of [010] growth, the [010] direction stays competitive material diffusion, allowing growth to continue. Examination of quenched films shows no visible gap at the needle tip ([010]), with marked depletion of material along the needle sides ([100]).

Manipulating Rubrene Crystal Shape and Growth

frustrating lateral crystal growth. This process may be examined for formation of depleted areas and height differences by quenching films during annealing (Figure 5.7). Profiles show a depleted region along the needle edge which grows in depth and lateral extent farther from the needle tip. The crystal tip appears slightly raised from the

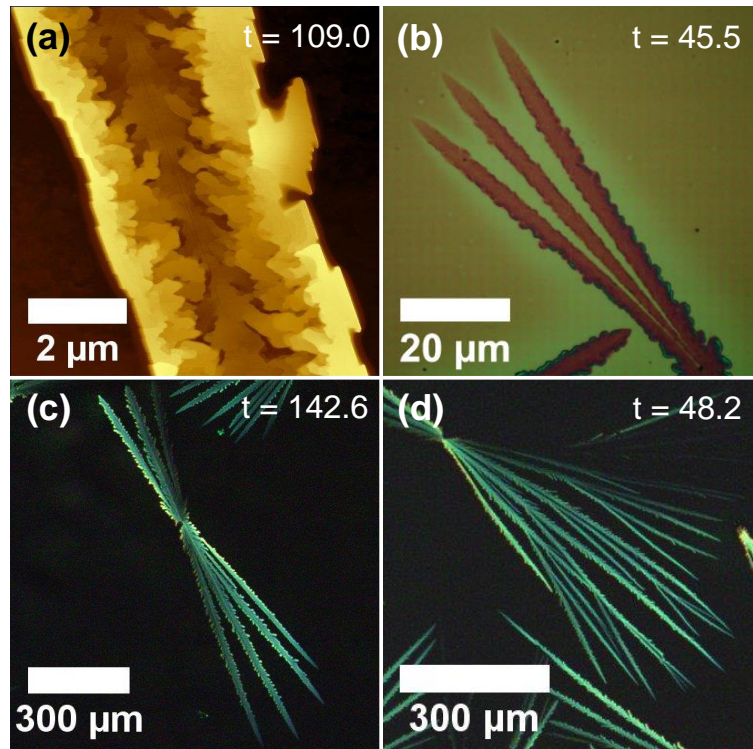


Figure 5.6. Topography and temperature dependence of 20 vol% TPBi films. (a) Atomic force micrograph of a crystal grown at 190 °C, (b) unpolarized optical micrograph of light-colored depleted regions around growing crystals in a film quenched after annealing at 180 °C, and polarized optical micrographs showing branching of crystals grown at (c) 185 and (d) 200 °C.

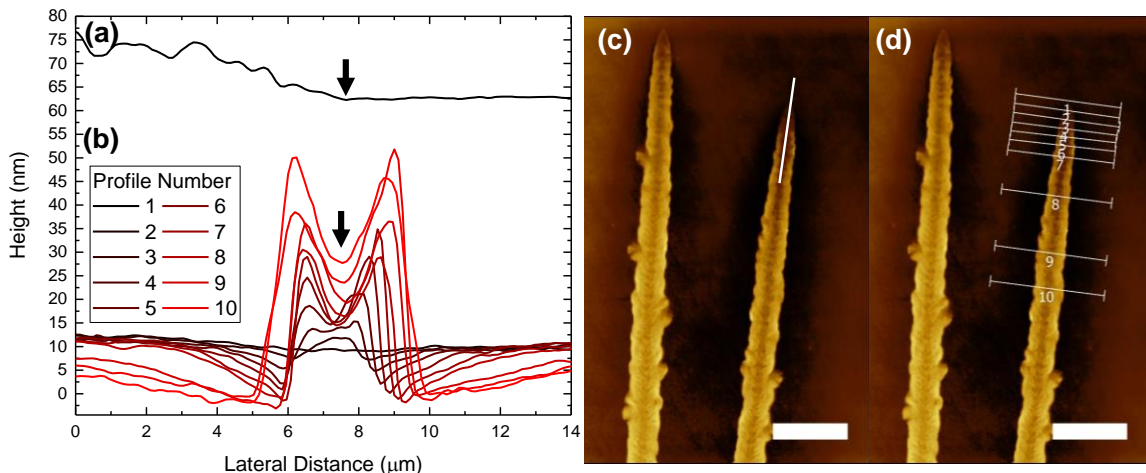


Figure 5.7. AFM profiles and corresponding micrographs for a 25 vol% TPBi film annealed for 30 seconds at 190 °C: (a) profile along the needle length shown in (c); (b) profiles perpendicular to the needle length as shown in (d). The profile in (a) is offset from (b) by +50 nm. Arrows denote the (a) needle tip and (b) needle center. Scale bars in (c)-(d) are 10 μm with a logarithmic height scale of 156 nm.

Manipulating Rubrene Crystal Shape and Growth

surrounding amorphous film with no discernable gap. This growth asymmetry causes the crystals to continuously elongate until the ultimate stagnation of the [010] direction, likely after TPBi concentration from rubrene sublimation slows lateral growth below that of vapor transport.

5.6. Varying Additive Type

The effects described thus far show the interaction of rubrene and TPBi, but other molecules also have an effect on the crystal growth of rubrene, as shown in Figure 5.8. From the selection of molecules presented, it is apparent that the axis of influence for TPBi is not universal; however, inducing shape change in rubrene crystals is. That similar

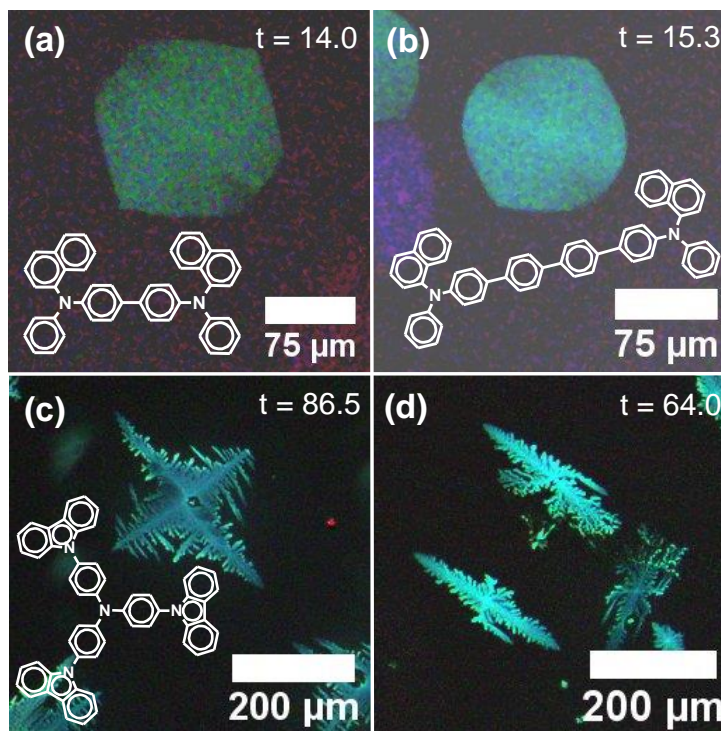


Figure 5.8. Polarized optical micrographs of crystal shapes of rubrene doped with (a) 30 vol% α -NPD at 190 °C, (b) 15 vol% 4p-NPD at 180 °C, (c) 10 vol% TCTA at 180 °C, and (d) 10 vol% TCTA and 10 vol% TPBi at 180 °C.

molecules like α -NPD (N,N' -Di(1-naphthyl)- N,N' -diphenyl-

(1,1'-biphenyl)-4,4'-diamine,

Figure 5.8a) and 4p-NPD (N,N' -di-1-naphthalenyl- N,N' -

diphenyl-[1,1':4',1":4",1'''-
quaterphenyl]-4,4'''-diamine,

Figure 5.8b) produce similar
shape modifications in rubrene
suggests perhaps shape
manipulation is related to the
molecular functional units (e.g.,

Manipulating Rubrene Crystal Shape and Growth

binding or miscibility) or rigidity rather than strictly molecule size. Either parameter could influence how an additive molecule hinders lattice site attachment in a growing crystal or diffuses to aggregate elsewhere. If the determining factor were strictly size, a bulky molecule like TCTA (tris(4-carbazoyl-9-ylphenyl)amine) might be expected to behave more similarly to TPBi than α -NPD, which is not obvious from the collected data (Figure 5.8c). A final dimension to these alternative additives is the incorporation of multiple species, such as TCTA and TPBi, as shown in Figure 5.8d. In this example, the crystal shape appears to resemble an elongated cross-shaped structure; a hybrid between the shapes observed in Figure 5.1b and Figure 5.8c. This adds another axis by which to customize crystal shape selection in thin organic films. Further work more closely examining crystal growth with a series of impurities systematically varied in stiffness, size, and intermolecular interaction would be helpful in elucidating the underlying mechanism.

5.7. Directions of Interest

This work opens or furthers several avenues of research. First, the ability to create precisely defined regions of crystalline material with depleted regions on either side could aid in developing OFETs with low degrees of conduction between separate transistors, crucial for scaling down devices. Second, monitoring crystal shape and growth rate allows for optical measurement of molecular concentrations in thin films. This presents a new method to study solid-state diffusion of molecular species through thick or buried layers, using materials which are relevant for electronic devices with device-relevant geometries and spatial scales. This approach could also be applied to study pharmaceutical compounds

Manipulating Rubrene Crystal Shape and Growth

when deposited in thin-film geometries.^{337,344} Finally, building on work with polymer additives in pharmaceuticals,^{307,651,652} using mixed films of small molecules to understand and control crystallization can be further quantified and exploited to improve the stability of drugs and electronic devices. With these possibilities come challenges, such as controlling crystal nucleus location and orientation in OFETs, ensuring crystal growth of a layer deposited atop an arbitrary material stack, and maintaining optoelectronic and medical properties of a material while incorporating increasing amounts of a secondary species; however, these opportunities are enticing.

5.8. Conclusions

In conclusion, mixed thin films of small organic molecules, specifically rubrene and TPBi, produce dramatically varying crystal shapes and growth rates when annealed. This variation results from the impediment of crystal growth by the film minority species to differing degrees for different crystallographic axes, with additional effects due to film sublimation yielding surprisingly elongated crystals for films with a high loading of additive. The resulting crystal shape varies depending upon the additive type, with cumulative shape-changing properties for ternary films.

6. HIGHLY PERIODIC SMALL-MOLECULAR WEIGHT ORGANIC FILMS BY ANNEALING

This chapter showcases work towards understanding the periodicity achieved in annealed thin organic films which are originally glassy in nature. The project described here grew out of an accidental discovery of light diffraction by an annealed organic film that was being removed from a heated microscope stage, exposing it to the direct microscope illumination and producing the rainbow effect shown in Figure 6.7. When these thin films are heated, a melting and crystallization front propagates across the substrate surface, producing useful optical-wavelength diffraction gratings. This is explained as film wrinkling, a relaxation mode for in-plane stresses that develop from a mismatch in thermal expansion between the film and substrate. This effect is common, but the spontaneous production of aligned wrinkles is not, making this an interesting example system.

6.1. Introduction

The spontaneous production of highly periodic structures is a hallmark of block polymer films and has received considerable attention for use in lithography and other pattern formation techniques.^{661–665} Spontaneity of feature formation is highly attractive

Highly Periodic Small-Molecular Weight Organic Films by Annealing

for the ease and control afforded by the material itself controlling periodicity rather than requiring highly accurate and sometimes tedious external manipulation of a material.^{661,666} Block polymers remain the frontrunner for alternative pattern formation on nanoscopic scales,^{663,665} but are less able to create features with wavelengths on the length scale of light, such as what may be useful for in-plane lasing applications or the manufacture of optical diffraction gratings.^{667–669} Block copolymer films are also necessarily comprised of at least two blocks, with the block polydispersity affecting pattern uniformity.⁶⁶³ Single-component films with large-wavelength features circumvent this challenge.

There has been considerable work to study spontaneous pattern formation as driven by strain differences across heterointerfaces in elastic and viscoelastic materials,^{356,670–673} and work to understand the structure and evolution in vapor-deposited glassy films.^{227,333,344} However, these properties have not yet been observed in tandem. The present work demonstrates exquisite topographical periodicity in homogeneous thin films comprised of a small-molecular weight organic semiconductor achieved simply by annealing as-deposited films at elevated temperature for a short time.

This work uses the electron-transporting organic semiconductor 2,2',2''-(1,3,5-benzinetriyl)-tris(1-phenyl-1-H-benzimidazole) (TPBi), which was purchased from Luminescent Technologies and used as received (sublimed grade). As before, annealing was initiated by dropping a substrate onto a pre-heated homebuilt heated microscope stage held at the annealing temperature. Films used in this chapter were manufactured using high-vacuum ($< 10^{-6}$ torr) thermal evaporation at deposition rates of 1 Å/s for TPBi and 3

Highly Periodic Small-Molecular Weight Organic Films by Annealing

Å/s. Silicon substrates were maintained at ambient (25 °C) temperature during deposition and exposed to a UV-ozone ambient for 10 minutes prior to deposition.

6.2. Film Transformation

As-deposited films of TPBi appear smooth and featureless, typical of glassy vapor-

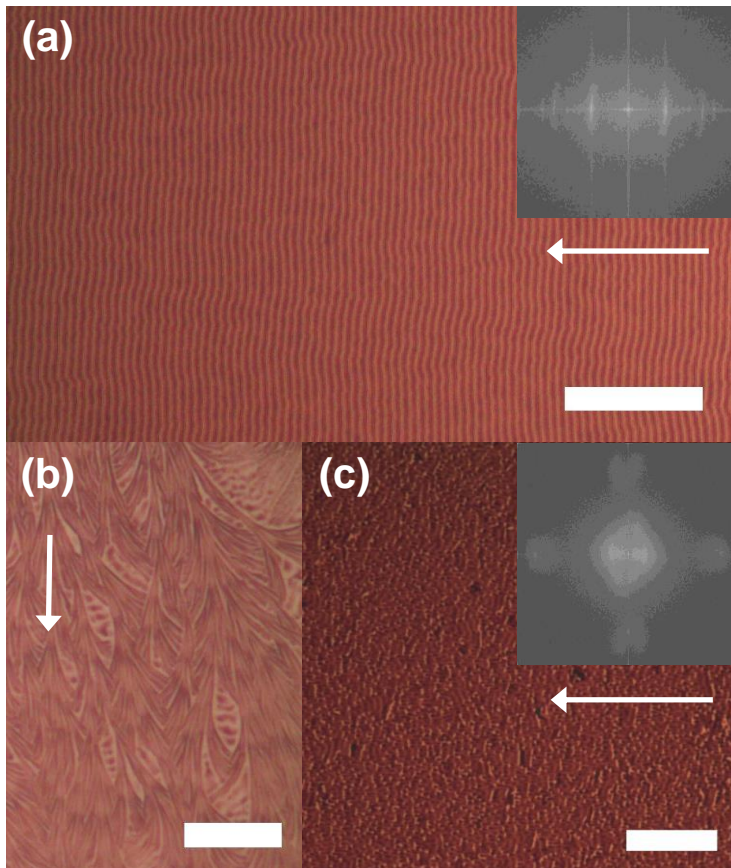


Figure 6.1. Unpolarized optical micrographs of TPBi films annealed at different temperatures: (a) 180 °C, (b) 175 °C, (c) 190 °C. Arrows depict the direction of crystal growth, and the insets of (a) and (c) are Fast Fourier Transforms (FFTs) of the images, showing periods centered at (a) 1.23, 0.73, 0.6, and 0.53 μm , and (c) 1.2-1.3 and 0.25-0.3 μm . Films are 30 nm with a 60 nm epitaxial TPBi layer deposited after annealing to improve visibility. All scale bars are 20 μm .

undulations in the region trailing the front. In these films, x-ray diffraction from a previous chapter shows two peaks orthogonal to the substrate corresponding to d_{hkl} spacings of

deposited films. TPBi has a bulk glass transition temperature of 124 °C,¹² and begins to rapidly crystallize in thin films starting ~ 170 °C. Crystallization at these relatively low temperatures occurs via spherulitic growth (Figure 6.1b) with long, finely branched domains. As the annealing temperature is increased to 180 °C (Figure 6.1a), the crystal growth front becomes smooth and continuous, forming periodic

Highly Periodic Small-Molecular Weight Organic Films by Annealing

14.25 Å and 7.12 Å (Figure 5.5). Neat TPBi has no solved crystal structure, but it is interesting that the larger dimension corresponds almost exactly to the molecular diameter (14.57 Å) as measured in a methanol solvate,²⁹⁰ suggesting that the molecules stand on edge, consistent with the behavior of many other organic molecules in thin films.³⁶⁰ At higher temperatures (190 °C, Figure 6.1c), the film transformation changes from evolving along a smooth interface to a more rough, fluid

interface. This produces poorly defined periodic structures with little long-range order. Interestingly, similar results are obtained along the transformation front for the faster-growing facet of TPBi crystals even at 180 °C (Figure 6.2), implying that the breakdown in order may be related to annealing temperature through the velocity of the transformation front.

To study the formation of these features, films were imaged *in situ* during annealing using a home-built heated microscope stage and a high-speed camera capturing at 50

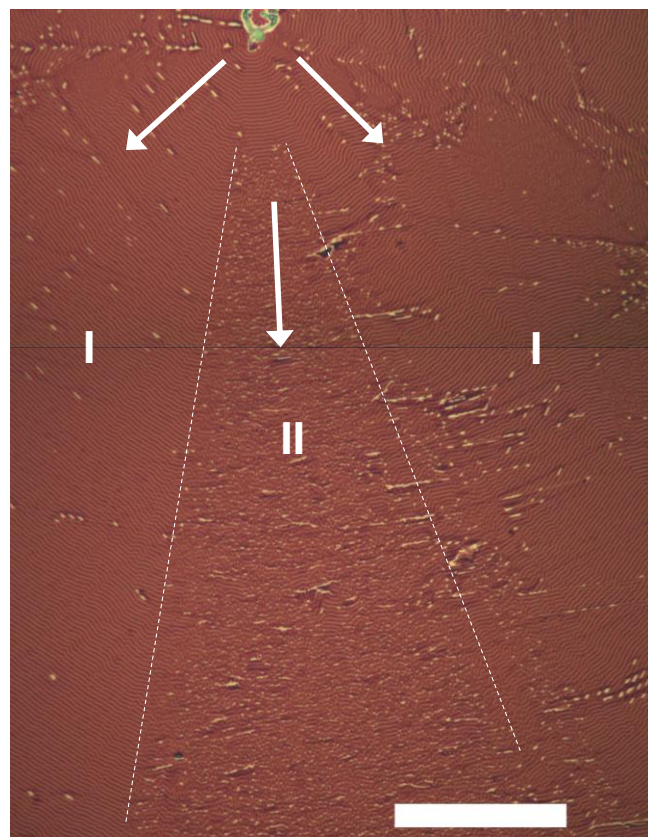


Figure 6.2. Unpolarized optical micrograph of a TPBi film annealed at 180 °C, showing growth from the nucleation site (arrows) and areas of periodic (I) and aperiodic (II) domains. Films are 30 nm with a 60 nm epitaxial TPBi layer deposited after annealing to improve visibility. Scale bar 50 μm.

Highly Periodic Small-Molecular Weight Organic Films by Annealing

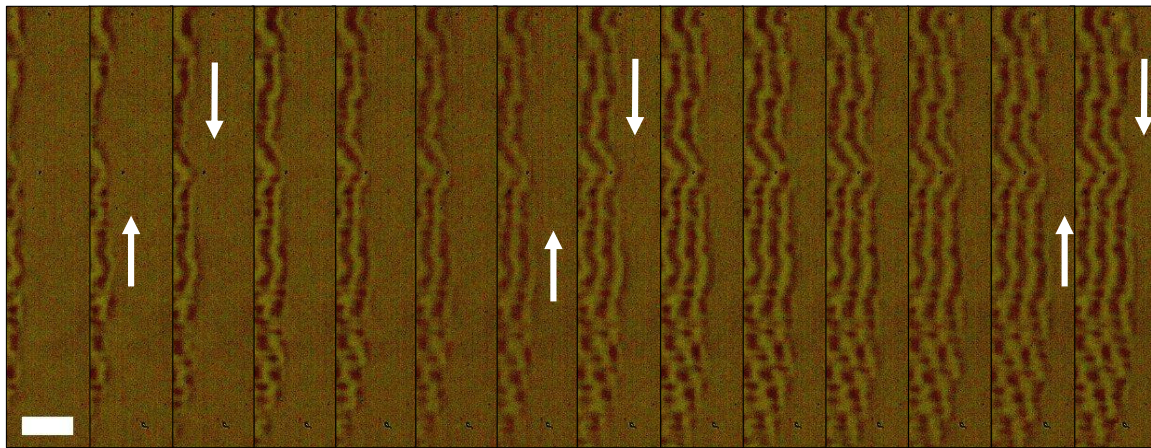


Figure 6.3. Time series during annealing 30-nm-thick films at 180 °C, showing growth of aperiodic and periodic regions in the films. Arrows highlight the propagation of undulations along the growth interface. Time between frames is 200 ms, scale bar is 5 μm.

frames per second with 1 ms exposures. The evolution of a growth front showing both periodic and aperiodic structures is shown in Figure 6.3. The primary difference in growth mode is the continuity of the interface. Where the interface remains contiguous (as obviated by new undulations traveling continuously along the interface until reaching a kink), the undulations are maintained parallel and periodic in an oscillatory but stable configuration. When the interface breaks up, the features divide into globular domains which separate from the transformation front, independently forming unique undulating features. Feature proximity can allow parts of the front to meld together again before repeating the process.

Slightly thicker films (40 nm, Figure 6.4a) show similar behavior with comparable feature wavelengths, but at higher thickness (50 nm, Figure 6.4b) the transformation front is unable to remain straight, giving circularly symmetric crystals with bands of periodic structures. The similarity in periodicity is initially surprising, given that thicker films would be expected to be more resistant to deformation and yield larger feature wavelengths; however, the wavelength is dictated by a balance of factors described below.

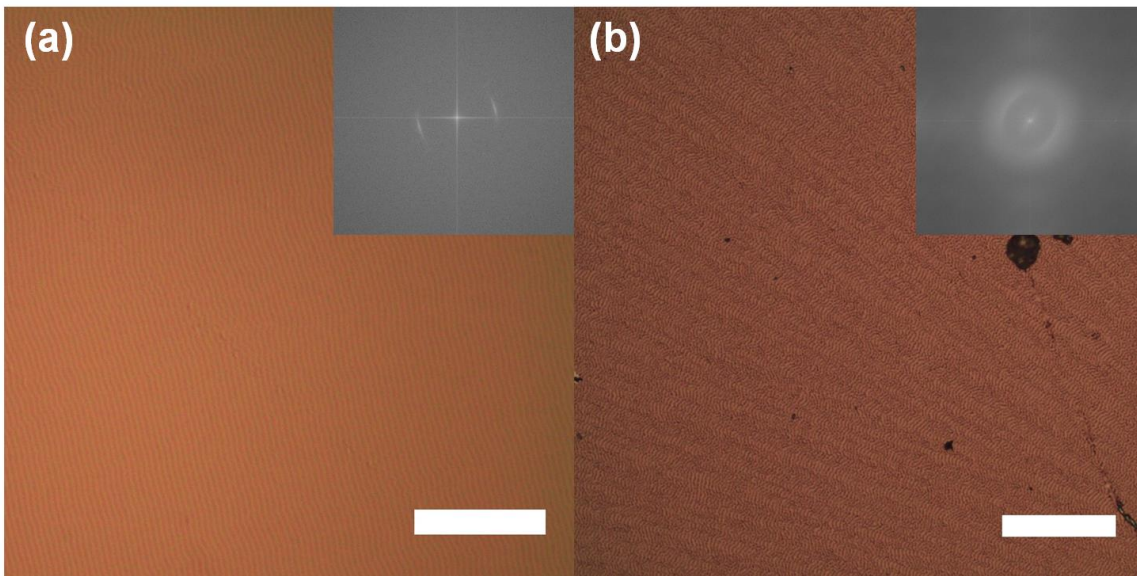


Figure 6.4. Morphology of TPBi films annealed at 180 °C of thickness (a) 40 nm and (b) 50 nm. Insets are FFTs showing periods centered at (a) 1.35 μm and (b) 1.02 μm . Scale bars are 30 μm .

6.3. Surface Morphology

When these films are examined *ex situ* with atomic force microscopy (AFM), the depth and waveform of the pattern becomes apparent. The films show well-defined periodicity which is nearly sinusoidal, with a wavelength of $(1.3 \pm 0.1) \mu\text{m}$ (Figure 6.5a,e). Surprisingly, in these 30-nm films, the film surface fluctuates $\pm 7 \text{ nm}$, achieving a total feature depth which is almost half of the film thickness. Figure 6.5a also demonstrates a type of defect which can occur at the valley of every other waveform, giving a secondary 2λ periodicity. Films annealed at 190 °C show globular, melted surfaces (Figure 6.5b) with abrupt edges in the direction of the remaining amorphous material (Figure 6.5c), as if a solid sheet were broken off during bending to form these periods. The cantilever phase image around the growth front (Figure 6.5d) implies less energy dissipation in the transformed material,⁶⁷⁴ providing a method to distinguish between topography and

Highly Periodic Small-Molecular Weight Organic Films by Annealing

mechanical properties. The boundary between transformed and untransformed material (light and dark) is sharp and coincides well with the onset of undulations. Because these images are taken *ex situ* on thermally quenched films, we cannot definitively conclude whether these mechanics correspond to conditions in growth, but the sudden birefringence observed in *in situ* polarized optical micrographs suggest that the growth transition is similarly sharp.

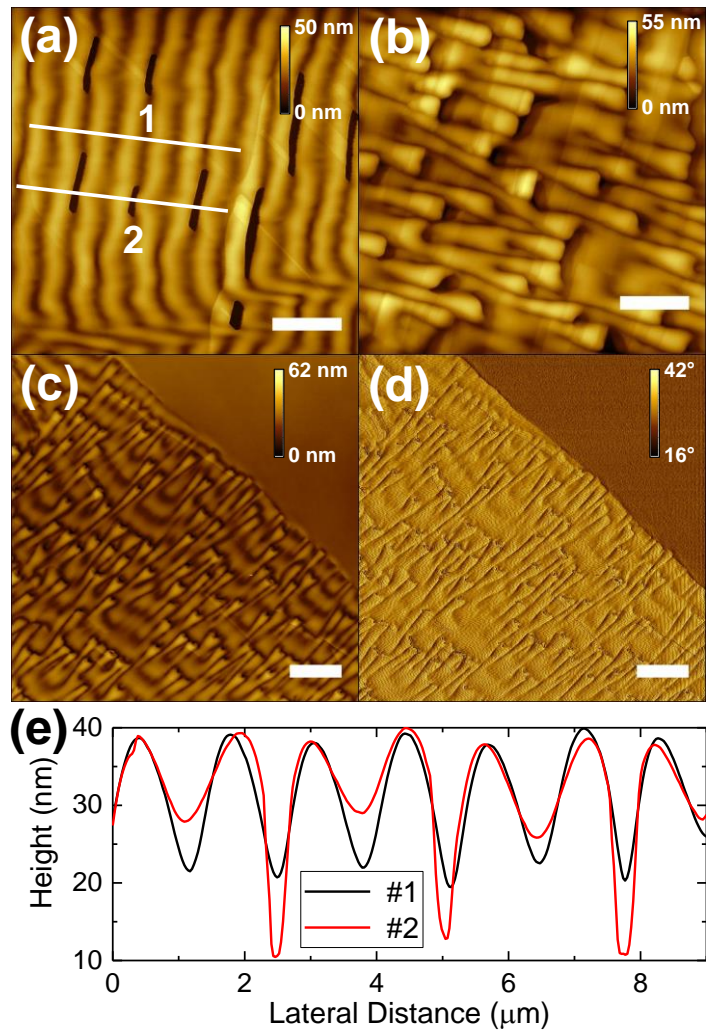


Figure 6.5. Surface morphology of 30-nm TPBi films annealed at (a) 180 °C, (b)-(d) 190 °C. (a)-(c) are height images, with (d) the phase image of (c). Plotted in (e) are height profiles shown in (a). Scale bars are (a), (c), (d) 3 μm , (b) 2 μm .

6.4. Proposed Mechanism

As discussed in Chapter 3, glasses deposited by thermal evaporation are known to transform from a glassy to supercooled liquid state by a transformation front which sweeps through the material, typically beginning at the substrate and other interfaces.^{227,333} We propose that in this system, the transformation which occurs nucleates and spreads

Highly Periodic Small-Molecular Weight Organic Films by Annealing

laterally, directly in front of a crystallization front. The dissimilar thermal expansion coefficients for the film and substrate produce a compressive stress on the film which is

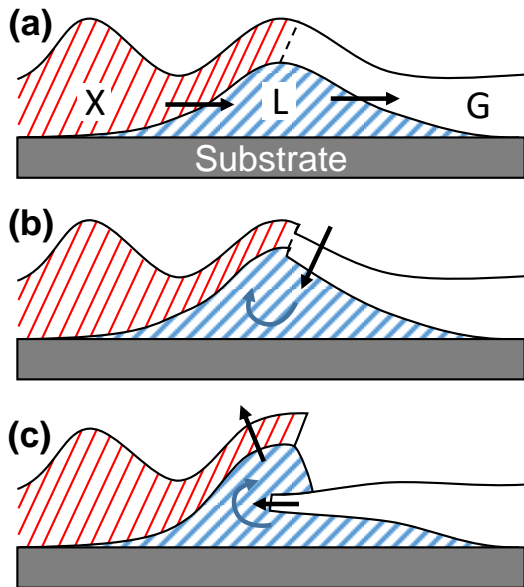


Figure 6.6. Mechanism of pattern formation in annealed TPBi films showing motion of the crystal (X), liquid (L), and glass (G) phases. (a) 180 °C, where the top solid layer remains continuous and deforms into a sinusoid. The top layer at higher growth rates (b), causing the glassy solid to relax towards the substrate (black arrow) and producing motion in the supercooled liquid (blue arrow). This pushes the crystalline solid away from the substrate (c) and forces the glassy solid towards the substrate as it relaxes laterally. Image not to scale.

relieved by wrinkling of a thin, solid layer which sits on a viscoelastic supercooled liquid as shown schematically in Figure 6.6. In the lower-temperature growth mode (180 °C), this solid layer remains continuous, and the undulations assume a parallel, periodic pattern in accordance with torsional strain minimization in the solid along the transformation front. At higher annealing temperatures (190 °C), the solid layer may thin irregularly due to more rapid melting, leading to fracture. When it fractures near the waveform peak, possibly due to the more extreme film curvature, there evolves a

discontinuity in the surface morphology as the solid layer on the amorphous side subducts beneath the solid layer on the crystalline side. The lateral slip of the amorphous side causes strain to be released in the solid layer, causing the next feature to appear farther away than in the continuous case. The increased importance of the melt at 190 °C is corroborated by the existence of smooth features reminiscent of flow and viscous relaxation. Unlike

Highly Periodic Small-Molecular Weight Organic Films by Annealing

previous results on intentionally oxidized polydimethylsiloxane (PDMS),⁶⁷⁰ this solid layer is probably not a surface reaction product with oxygen or water, since annealing inside of a nitrogen-filled glovebox produces identical structures.

The temperature range for this phenomenon is well above the bulk T_g of TPBi (124 °C), implying that the film should be entirely liquid. However, film thickness and heating rate have both been shown to have an appreciable effect on observed values of T_g ,^{330,331,675} and in-plane stress may further increase this value.^{676,677} Furthermore, vapor-deposited glassy films are significantly relaxed relative to melt-quenched glasses, yielding a melting onset temperature which is commonly 10-20 °C higher than the observed thin-film T_g .^{227,228}

The observed undulations and proposed mechanism are analogous to wrinkling in systems comprised of a strained elastic solid layer on top of a viscoelastic material which sits on a substrate.^{673,678,679} In these systems, the intrinsic wavelength λ_i formed as the strained system relaxes is related to the mechanical properties of the adjoined solid and viscoelastic layers, and can be approximated as⁶⁷⁹

$$\lambda_i = 2\pi h_e \left[\frac{(1 + \nu_e)(1 - 2\nu_v)E_e h_v}{12(1 - \nu_v)(1 - \nu_e^2)E_v h_e} \right]^{1/4} \quad (6.1)$$

where h_i , ν_i , and E_i are the thickness, Poisson's ratio, and elastic modulus for the solid elastic ($i = e$) and viscoelastic ($i = v$) layers. This is in contrast to the equilibrium wavelength λ_e for buckling of an elastic film on an elastic surface substrate ($i = s$):⁶⁸⁰

$$\lambda_e = 2\pi h_e \left[\frac{(1 - \nu_s^2)E_e}{3(1 - \nu_e^2)E_s} \right]^{1/3} \quad (6.2)$$

There is limited date for most of these parameters for amorphous organic semiconductors.

Highly Periodic Small-Molecular Weight Organic Films by Annealing

Using values close to amorphous polystyrene above its glass transition for the viscoelastic supercooled liquid ($E_v \sim 10$ kPa, $\nu_v = 0.35$)⁶⁷⁹ and the lower reported values for crystalline rubrene as the thin solid ($E_e \sim 10$ GPa, $\nu_e \sim 0.3$)⁶²⁸ together with the experimental wavelength of 1.22 ± 0.03 μm gives a thickness for the thin solid layer $h_e = 14.6 \pm 0.7$ nm out of a 30 nm film. These solid thicknesses are surprisingly reasonable given the observed height variation and approximate nature of Eqn. 6.1. Using $\lambda_i = 1.35$ μm from Figure 6.4a for a 40-nm film yields a very similar $h_e = 14.1$ nm. When the film thickness increases, the wavelength does not necessarily need to increase if the viscoelastic region becomes significantly thicker. For example, using Eqn. 6.1 with the same parameters as above but for a 50-nm film and $\lambda_i = 1000$ μm gives $h_e \sim 8$ nm. For comparison, an elastic film with the above mechanical properties on bare silicon requires a film of $h_e \sim 1$ nm thick by Eqn. 6.2, a non-physical result.

What is particularly noteworthy about this system is that the stress relaxation can occur along a smooth transformation front. In contrast to other systems exhibiting spontaneous spinodal decomposition^{356,672,681,682} and wrinkling,^{673,678,683,684} this induces unidirectional, aligned periodic structure without requiring secondary patterning, light-induced^{679,685} or otherwise.⁶⁸⁴ Spontaneous, strain-driven formation of aligned highly periodic structures could facilitate development of organic lasers and simple diffraction gratings.

6.5. Optical Properties

Since these films are periodic on the length scales of the wavelength of light, it is convenient to characterize them also with optical diffraction measurements. Indeed, the optical appearance of these films was what first prompted their further investigation (Figure 6.7). Diffraction from a periodic surface satisfies the grating equation relating the period spacing d , the angle of the incident beam θ_i and diffracted beam θ_d relative to the period normal, the diffraction order m , and the

light wavelength λ according to⁶⁶⁷

$$d(\sin \theta_i + \sin \theta_d) = m\lambda \quad (6.3)$$

which reduces to Bragg's law of diffraction for $\theta_i = \theta_d$. It should be emphasized that the diffraction order is positive for diffracted beams closer to the period normal, regardless of

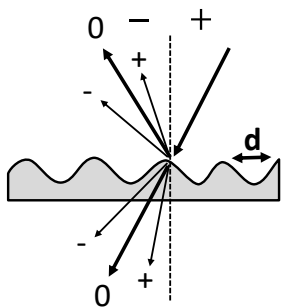


Figure 6.8. Diagram of the diffraction order sign convention.

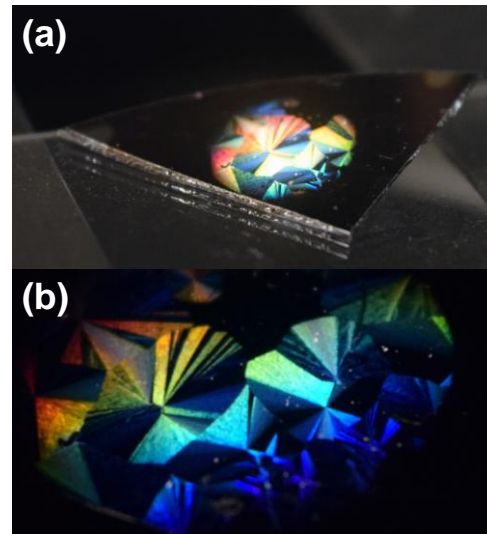


Figure 6.7. Diffraction from 30 nm annealed TPBi films on silicon showing (a) the whole sample and (b) just the illuminated region. Spot size is approximately 1 cm diameter, unpolarized light.

if the mode is transmitted or reflected. This is shown pictorially in Figure 6.8, with the dashed line representing the period normal. The $m = 0$ mode is simply specular reflection which is independent of the grating spacing ($\theta_i = \theta_d$), and in normal transmission or reflection measurements, the mode spacing is symmetric as $\sin \theta_i = 0$. Waves with $m\lambda/d > 2$ have complex diffraction

Highly Periodic Small-Molecular Weight Organic Films by Annealing

angles, and are evanescent, non-propagating waves.

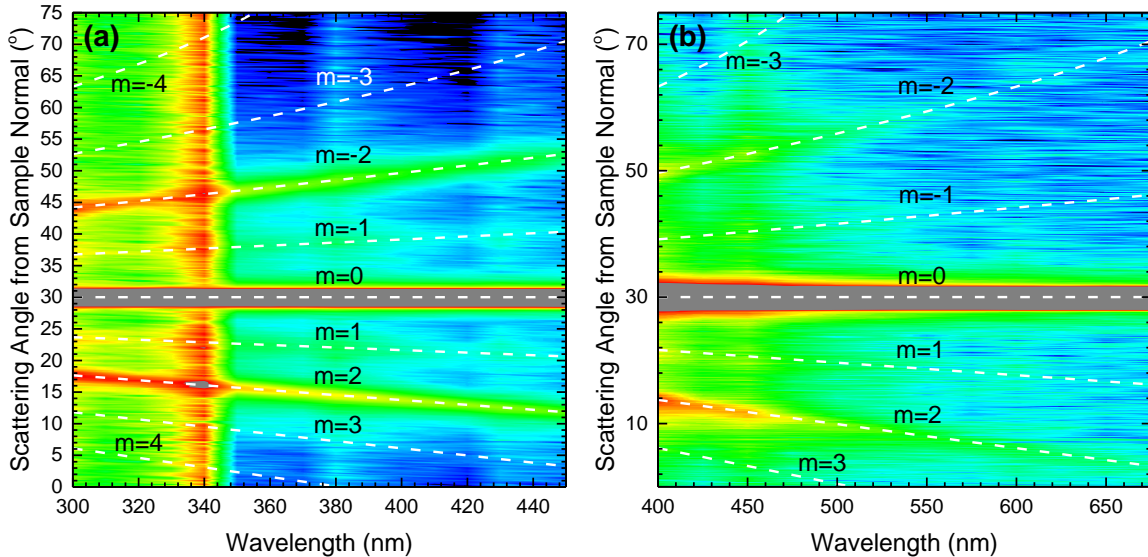


Figure 6.9. Diffraction of p-polarized light ($\theta_i = 30^\circ$) from a 30 nm TPBi grating coated with 50 nm aluminum (a) 300–450 nm, (b) 400–675 nm. Diffraction orders shown correspond to $d = 3.05 \mu\text{m}$. The change in the background of (a) at 350 nm is due to the insertion of a long-pass filter in the monochromator. Color scale is logarithmic to bring out the weak diffraction features.

The light source used to characterize these films was not intense enough to observe diffraction from bare TPBi films annealed at 180°C due to their poor reflectivity. However, TPBi films with 50 nm vapor-deposited aluminum reflected sufficient light for optical characterization, yielding the intensity plots shown in Figure 6.9. Surprisingly, there are weak peaks observed for a d spacing of $3.05 \mu\text{m}$, approximately twice that observed with the morphological characterization. This is most likely a ghost effect from the defects which form between waves shown in Figure 6.5a and the consequent imperfect pattern depth with period 2λ .⁶⁶⁷ However, the strongest peak in positive and negative orders ($m = \pm 2$) corresponds to both the second harmonic of the fundamental mode and a d spacing of $1.525 \mu\text{m}$, much closer to the values of $1.3 \pm 0.1 \mu\text{m}$ measured with AFM. These values are not within measurement error or observed sample deviation of one other, and reasons

Highly Periodic Small-Molecular Weight Organic Films by Annealing

for this discrepancy are unclear.

The low vertical feature height in Figure 6.5 contributes to relatively inefficient optical gratings across all observed wavelengths, calculated to have peak efficiency near $\lambda = 300$ nm and decreasing asymptotically at larger wavelengths.⁶⁶⁷ The maximum measured grating efficiency at $\lambda = 300$ nm, $m = 2$ (relative to $d = 3.05\text{ }\mu\text{m}$) is 0.06%, likely also due to slight non-idealities in the periodicity which may be also observed in Figure 6.5.

6.6. Conclusions

This chapter has described the discovery and characterization of spontaneous formation of highly periodic and aligned structures in annealed thin films of the organic semiconductor TPBi. These features evolve during annealing from a stress-driven mechanical instability and undergo simultaneous wrinkling and crystallization, producing a sinusoidal surface topography. The periodic film features are shown to diffract light, which provides a second method to characterize the feature spacing and demonstrates one possible application for such films. When annealed above of a specific temperature, the periodic structures lose alignment as the transformation front fractures and liquefies.

7. ENGINEERING EXCITON DIFFUSION WITH CRYSTALLIZATION

The inherent tradeoff between the exciton diffusion length (L_D) and absorption length in most organic semiconductors demands a rational approach to further understand and improve solar cell efficiencies. This chapter discusses the effects of crystallization on the archetypal organic photovoltaic cell material boron subphthalocyanine chloride (SubPc), which shows an increased in L_D of >80% from (11.3 ± 0.7) nm to $(21.2. \pm 0.6)$ nm when crystallized. This improvement is rationalized by an enhanced exciton diffusivity owing to favorable molecular proximity and orientation (17% increase), increased molecular coupling from improved spectral overlap (31% increase), and a reduction in the width of the excitonic density of states upon templating (15-25% increase). The effects of film roughness are also quantitatively simulated and found to be negligible for the grain sizes and film morphology used in this work. The physical factors and techniques presented here to interpret exciton diffusion in crystalline solids should be universally applicable to other amorphous and crystalline spin-singlet excitonic materials.

7.1. Introduction

The efficiency of organic photovoltaic cells (OPVs) is dictated by the efficiency of

Engineering Exciton Diffusion with Crystallization

photon absorption, exciton diffusion, exciton dissociation, and charge collection within the cell.^{38,175} In typical organic semiconductors, the characteristic length scales for absorption (≥ 100 nm) and exciton diffusion (L_D , 1-10 nm) are disparate.^{365,686,687} Although the exciton diffusion efficiency can be improved by using a bulk heterojunction instead of planar heterojunction architectures, increasing L_D would enable more complex bulk heterojunction morphologies between materials of varying miscibilities.^{532,688,689} Ideally, L_D would be increased enough to be commensurate with the absorption length, enabling simple yet efficient planar architectures in terms of exciton and charge carrier harvesting. Recently, such planar heterostructure OPVs have experienced renewed interest, further motivating work to improve L_D .^{174,198,690} Indeed, there have been several noteworthy studies that have sought to engineer L_D via crystallization.^{260,369,373,470} While successful in increasing L_D , these works do not quantitatively consider changes in the physical factors that lead to the enhancement. The goal of the present work is to examine such physical factors and their effects on L_D upon crystallization using an archetypal OPV material as a model system.

7.2. Exciton Diffusion Length Measurement

This paper focuses on the three-fold symmetric, highly non-planar molecule boron subphthalocyanine chloride (SubPc), noted for its high open circuit voltage (V_{OC}) and strong photovoltaic performance in a variety of cell architectures.^{98,100,690,691} SubPc shows absorption properties similar to other phthalocyanines,^{692,693} with a Soret band resonance near $\lambda = 300$ nm and a Q-band transition peaked at $\lambda = 575$ nm in amorphous thin films

Engineering Exciton Diffusion with Crystallization

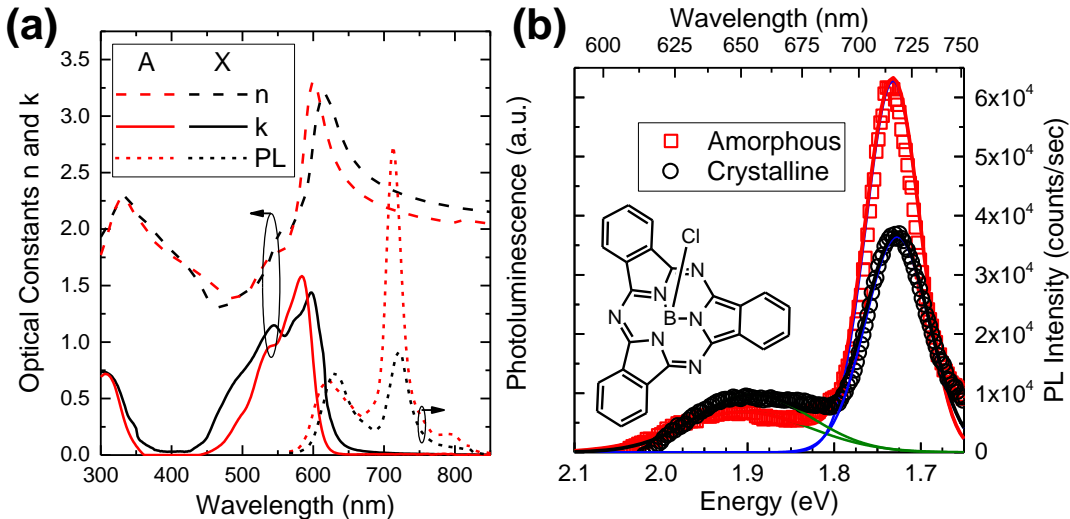


Figure 7.1. Optical properties of amorphous (A) and crystalline (X) SubPc: (a) refractive index n , extinction coefficient k , and photoluminescence PL, (b) PL spectra deconvoluted into two gaussian features. The high- and low-energy features yield 0.5% and 2.5% η_{PL} for amorphous, and 0.6% and 1.7% η_{PL} for crystalline, respectively, with the remainder in the low-energy tail.

(Figure 7.1). The photoluminescence (PL) is peaked at $\lambda = 625$ nm, with a lower-energy feature centered at $\lambda = 710$ nm suspected to be emission from a molecular aggregate owing to its disappearance with dilution.¹⁹⁸ Upon crystallization, both absorption and PL display a marked red-shift of 15-20 nm, with the absorption and emission intensity reduced. Deconvolution of the PL (Figure 7.1b) shows a majority of excitons are emitting from the low-energy feature, with an overall PL efficiency (η_{PL}) of $(3.4 \pm 0.3)\%$ for amorphous and $(2.5 \pm 0.3)\%$ for crystalline films.

In order to determine the change in L_D upon crystallization, thin (40-nm) films of SubPc were manufactured on cleaned glass slides without UV-ozone treatment using high-vacuum thermal evaporation and annealing ($< 10^{-6}$ Torr) at 1 \AA s^{-1} and 25°C . Crystalline films used 20 nm SubPc annealed for 3 minutes at 175°C in nitrogen atmosphere as a template for an additional 20 nm SubPc in an effort to improve film coverage. These films were then measured using steady-state, spectrally resolved PL quenching (SR-PLQ)

Engineering Exciton Diffusion with Crystallization

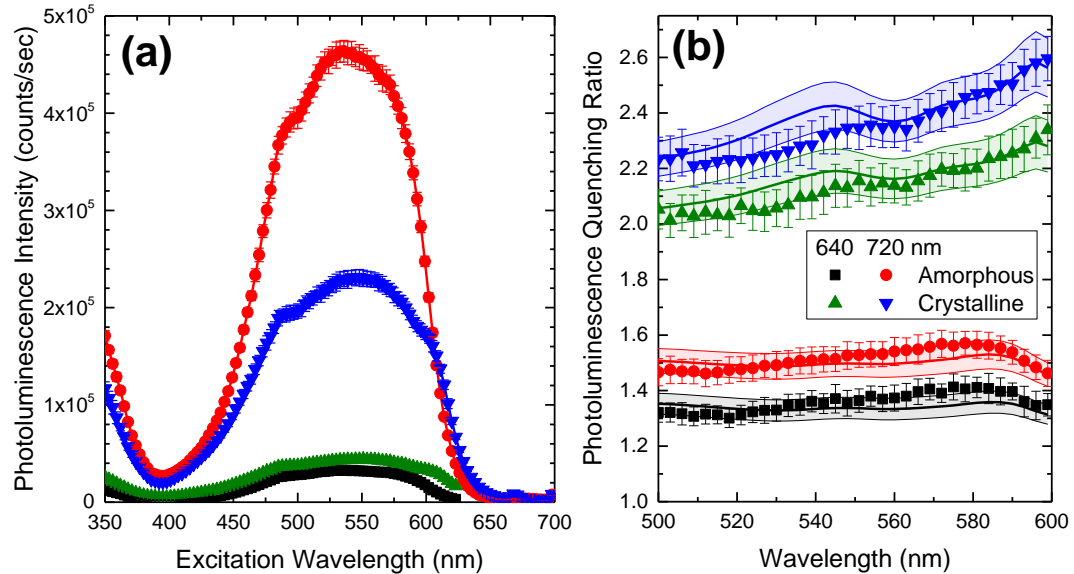


Figure 7.2. . (a) Unquenched excitation spectra and (b) quenching ratios as measured at $\lambda = 640$ nm and $\lambda = 720$ nm for the amorphous and crystalline SubPc films used in this work. The solid lines and shaded regions in (b) represent the transfer matrix fits and fit uncertainty ranges.

measurements,³⁶⁵ yielding the excitation spectra shown in Figure 7.2a. Consistent with k and η_{PL} of Figure 1, the crystalline films show less intense light emission and a red-shift of the absorption edge. When these amorphous and crystalline thin films of SubPc are either capped with the exciton quencher 1,4,5,8,9,11-hexaazatriphenylene hexacarbonitrile (HATCN) or left bare, the quenching ratios (unquenched to quenched PL intensity) may be determined, and are plotted in Figure 7.2b. The crystalline films show considerably larger quenching ratios than amorphous, suggesting more efficient exciton quenching. When these data are fit using a transfer matrix formalism,⁶⁹⁴ the extracted L_D increases upon crystallization from (11.3 ± 0.7) nm, in good agreement with previous work,¹⁹⁸ to (21.2 ± 0.6) nm for the 625-nm peak and (14.1 ± 0.7) nm to (22.3 ± 0.9) nm for the 710-nm peak. Interestingly, the discrepancy in improvement between the two peaks implies a difference in quenching for excitons occupying each state in crystalline and amorphous

SubPc, likely from differences in aggregate distribution within the film as discussed below.

7.3. Enhancements in Excitonic Energy Transfer

To understand this enhancement, we consider the possible mechanisms for exciton migration. Exciton diffusion in organic materials occurs *via* three mechanisms: cascade or “trivial,” Dexter, and Förster energy transfer.^{78,203} The contribution of each type depends on factors including film thickness and radiative efficiency, and for fluorescent materials with a spin singlet excited state, Förster energy transfer is commonly considered as the dominant energy transfer process. In the limit of coupling between point dipoles, the energy transfer rate, k_F , can be expressed as described in Chapter 2:

$$k_F = \frac{1}{\tau} \left(\frac{R_0}{|\underline{d}|} \right)^6 \quad (7.1)$$

with τ the exciton lifetime, \underline{d} the vector connecting the energy donor and acceptor molecules, and R_0 the Förster radius with the functional form

$$R_0 = \left(\frac{9\eta_{PL}\kappa^2}{128\pi^5} \frac{\int \lambda^4 F_D(\lambda) \sigma_A(\lambda) d\lambda}{[n(\lambda)]^4} \right)^{\frac{1}{6}} \quad (7.2)$$

Recall that F_D is the area-normalized fluorescence spectrum of the excited state, σ_A is the absorption cross-section of the acceptor molecule, n is the index of refraction of the surrounding medium, λ is the wavelength, and κ^2 is the dipole orientation factor expressing the orientation-depending electrostatic coupling between the donor and acceptor molecules. Increases in L_D are driven by an enhancement of R_0 through higher η_{PL} (*via* an increase in the radiative decay rate, k_R ¹⁹⁶), favorable molecular orientation (κ^2), or greater

Engineering Exciton Diffusion with Crystallization

emission-absorption overlap by reduction of the Stokes shift.^{78,156} Since $L_D \propto R_0^3/d^2$, engineering molecular proximity also affords methods to improve L_D .¹⁹⁸ Each of these effects are discussed in the following sections.

7.4. Effects of Changes in Optical Properties

When SubPc is crystallized, there is an enhancement in the overlap integral from the absorption red-shift and slight increase in the monomer peak intensity (625 nm), which counters the observed overall reduction in η_{PL} . In this system, it is important to consider the wavelength dependence of n within the integral, since SubPc shows very strong refractive index dispersion at the point of maximum overlap in both crystalline and amorphous films. These combined effects yield an overall increase in R_0 from $1.732\sqrt[3]{\kappa}$ nm to $1.823\sqrt[3]{\kappa}$ nm, corresponding to an increase in L_D of 17% of the monomer peak before κ^2 effects ($L_D \propto R_0^3$).

7.5. Molecular Aggregation

The above mechanism cannot account for improvements observed in the low-energy peak (710 nm), since Förster energy transfer requires overlap of emission and absorption spectra and SubPc has no measurable absorption in this region. If this feature is considered a dilute excitonic trap state such as a molecular aggregate, it will be populated from mobile excitons on the monomer. As such, the observed emission and quenching ratio will closely follow that of the monomer peak, but may vary more dramatically in a quenching geometry depending on spatial distribution of the aggregate. These two peaks (625 and 710 nm)

Engineering Exciton Diffusion with Crystallization

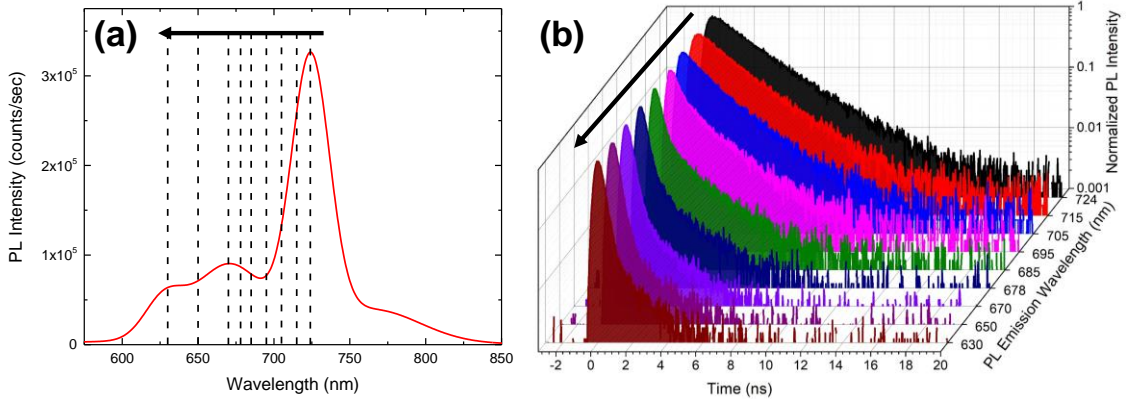


Figure 7.3. Exciton lifetime histograms for ~400 nm crystalline SubPc films on glass grown on a 20-nm crystalline template by attaching the substrate to the deposition shield near the source. (a) Emission spectrum for very thick crystalline film with lines showing the location of the lifetime measurements in (b).

ascribed to monomer and aggregate emission correspond to distinct states, as evidenced by lifetime measurements conducted across the emission spectrum (Figure 7.3). There is steady growth of a short lifetime feature as the emission wavelength is decreased, with two distinct decay times observed (constant slopes) at intermediate wavelengths. This implies that there are two distinct states, such as a monomer and aggregate, rather than a continuum

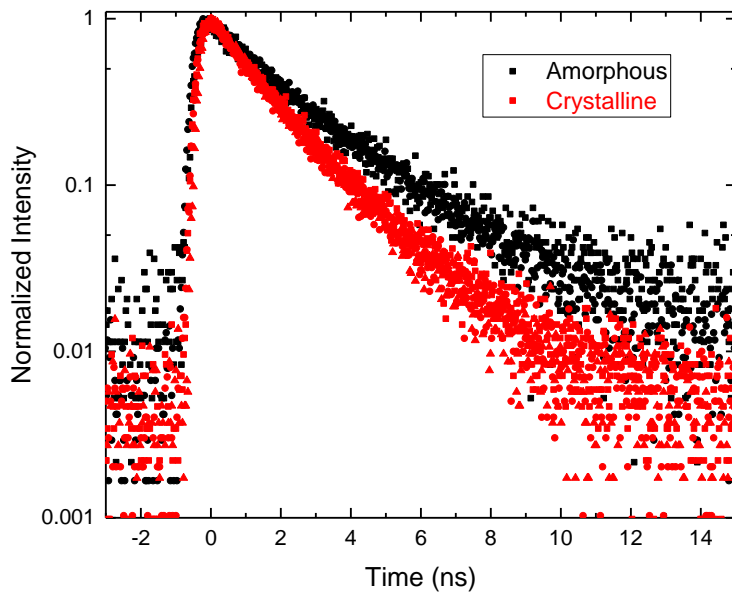


Figure 7.4. Exciton lifetime histograms for amorphous and crystalline SubPc films.

of mixed-lifetime states.

The additional quenching observed in the aggregate state could have two origins: energy transfer between aggregates or non-uniform aggregate distribution within the film. Although the crystalline films show weaker

Engineering Exciton Diffusion with Crystallization

light emission (Figure 7.1b), this change originates entirely from an increased non-radiative decay rate (Figure 7.4, Table 7.1), not a difference in the number of aggregates. The extracted lifetime values from Figure 7.4 are (2.1 ± 0.2) ns for amorphous and (1.5 ± 0.2) ns for crystalline SubPc. Using the definition of η_{PL} from Eqn. 2.3 and that of τ from Eqn. 2.9 allows evaluation of the radiative and non-radiative decay rates (k_R and k_{NR} , respectively) as

$$k_{NR} = \frac{1 - \eta_{PL}}{\tau} \quad (7.3)$$

$$k_R = \frac{1 - k_{NR}\tau}{\tau} \quad (7.4)$$

Combining the measurements of η_{PL} and τ (and assuming that these states are formed comparably from the 0.5 ns monomer lifetime in amorphous and crystalline films) gives the values shown in Table 7.1. These data suggest that the reduction in peak intensity upon crystallization is due to an increased number of non-radiative loss pathways which increase k_{NR} .

Since a Dexter exchange mechanism with exponential dependence on distance should be favored by a denser crystal medium and yield a longer diffusion length in crystal, we instead propose that the observed increase in film quenching ratio comes from a difference in aggregate distribution within the film thickness. Such a distribution could form by favored molecular mobility and aggregate formation near the free film surface in amorphous films, with less surface rearrangement in the crystalline case.

Table 7.1. Radiative and non-radiative exciton decay rates for the 710-nm (aggregate) peak

Phase	$k_R (\mu s^{-1})$	$k_{NR} (\mu s^{-1})$
Amorphous	16 ± 2	650 ± 70
Crystalline	17 ± 2	460 ± 50

7.6. Effects of Changes in Molecular Configuration

It follows from Eqn. 7.1 and 7.2 that film transformations which reduce the intermolecular spacing or increase the orientation factor are beneficial for exciton transport through increase of the energy transfer rate. One method in particular to target this enhancement is through crystallization, especially in the cases where the orientation of the unit cell may be controlled via epitaxy or molecular templating.^{109,226,695} Crystals are denser than amorphous or glassy films of the same composition,³⁴¹ meaning that d will generally decrease along at least one direction upon crystallization. The orientation factor is considerably more variable, as there exist molecular configurations which yield $\kappa^2 = 0$; thus, the overall diffusivity must be calculated as described below and evaluated to assess desirability. Recall from Chapter 2 that one method of expressing κ^2 is

$$\kappa^2 = (\cos \gamma - 3 \cos \alpha \cos \beta)^2 \quad (7.5)$$

with α the angle between the donor transition dipole and the vector connecting the donor and acceptor molecules, β the equivalent angle for the acceptor, and γ the angle between the donor and acceptor molecule transition dipoles shown in Figure 7.5a. Since γ is coupled to α and β , κ^2 is rigorously bounded between 0 and 4, with an average of 0.476 for dipoles which do not re-orient between absorption and emission.²¹⁶

Calculation of κ^2 is somewhat more complicated in phthalocyanines because of the high molecular symmetry, which makes multiple transition dipole configurations possible. For SubPc, the transition dipole has been calculated to exist in the plane defined by the three *meso*-nitrogen atoms, perpendicular to the B-Cl bond as shown in Figure 7.5b,^{222,696}

Engineering Exciton Diffusion with Crystallization

which can be accounted for by averaging the transition dipole over all geometric configurations.²²³ Practically, this is accomplished by the square of the integral average of $|\kappa(\nu_1, \nu_2)| = |\cos \gamma(\nu_1, \nu_2) - \cos \alpha(\nu_1) \cos \beta(\nu_2)|$ over all possible orientation angles of the transition dipoles of the donor (ν_1) and acceptor (ν_2) within their characteristic planes:²¹⁸

$$\langle \kappa \rangle^2 = \left\{ \frac{1}{2\pi} \int_0^{2\pi} \left(\frac{1}{2\pi} \int_0^{2\pi} |\kappa(\nu_1, \nu_2)| d\nu_1 \right) d\nu_2 \right\}^2 \quad (7.6)$$

Use of the absolute value of κ represents the static limit, wherein the reorientation of the transition dipoles is slow compared to the energy transfer rate.⁸⁸ The implementation of this dependence is somewhat involved, and, thus, an outline is given here.

Energy transfer between two dipoles is normally evaluated using the orientation factor κ^2 calculated as detailed in Eqn. 7.5; however, when considering energy transfer between two planar species with three-fold or higher symmetry, κ^2 is evaluated as in Eqn. 7.6 with κ given by

$$\kappa(\nu_1, \nu_2) = \cos \gamma(\nu_1, \nu_2) - 3 \cos \alpha(\nu_1) \cos \beta(\nu_2) \quad (7.7)$$

where now the intermolecular angles depend on the orientation of the donor (ν_1) and acceptor (ν_2) transition dipole within their characteristic planes, denoted in blue and tan in

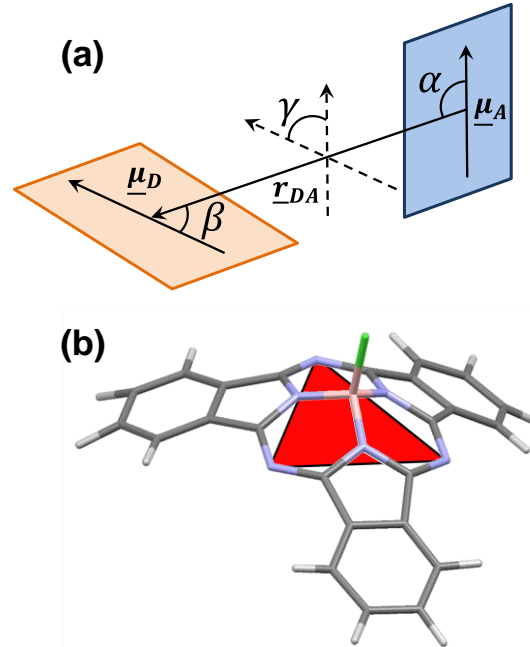


Figure 7.5. (a) Orientation of two molecular dipoles with angles used to calculate the orientation factor, κ^2 . (b) Depiction of the plane which contains the transition dipole on a SubPc molecule (red).

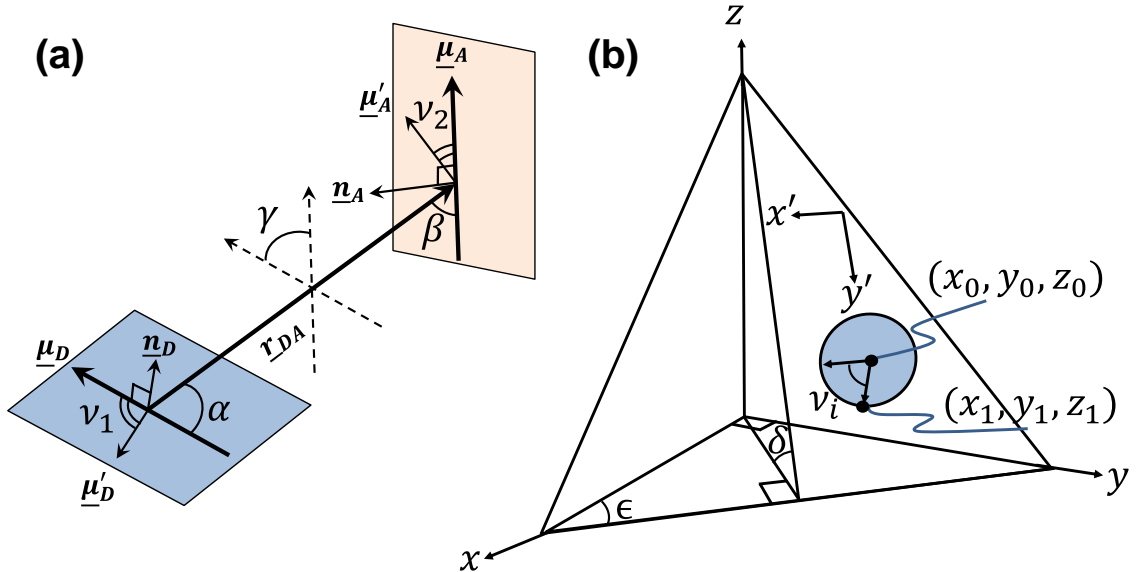


Figure 7.6. (a) Diagram of an exciton donor $\underline{\mu}_D$ and acceptor $\underline{\mu}_A$ transition dipole, with other variables defined in the text. (b) Schematic of the coordinate system used to rotationally average degenerate transition dipoles.

Figure 7.6a. These transition dipoles rotate about the plane normal vectors \underline{n}_D and \underline{n}_A . For ease of notation, the expression for Eqn. 7.7 can be rewritten in terms of vectors, with $\hat{\underline{\mu}}_D$ and $\hat{\underline{\mu}}_A$ unit vectors describing the transition dipoles of the energy donor and acceptor molecules, respectively, and $\hat{\underline{r}}_{DA}$ the unit vector connecting their centers:

$$\kappa(\nu_1, \nu_2) = \hat{\underline{\mu}}_A \cdot \hat{\underline{\mu}}_D - 3 (\hat{\underline{\mu}}_A \cdot \hat{\underline{r}}_{DA}) (\hat{\underline{\mu}}_D \cdot \hat{\underline{r}}_{DA}) \quad (7.8)$$

The next step is to express $\hat{\underline{\mu}}_D$ and $\hat{\underline{\mu}}_A$ as a function of ν_1 and ν_2 . For this work, this is accomplished by independently considering the donor and acceptor transition dipoles and how they change in space, shown in Figure 7.6b. First, the equation for the dipole plane, given by

$$ax + by + cz + d = 0 \quad (7.9)$$

where a , b , c , and d are scalars multiplied by the cardinal directions x , y , and z , and are

Engineering Exciton Diffusion with Crystallization

calculated according to the cross product of two vectors in the dipole plane. For an n -fold degenerate molecule ($n \geq 3$), there are at least three points on the molecule which describe the transition dipole plane. If the positions of these points are denoted by $\underline{e}_i = [x_i, y_i, z_i]$, then the coefficients in Eqn. 7.9 may be calculated using a vector cross product to find the normal

$$[a, b, c] = (\underline{e}_1 - \underline{e}_2) \times (\underline{e}_1 - \underline{e}_3) \quad (7.10)$$

and inserting these values into Eqn. 7.6 to give

$$d = -[a, b, c] \cdot \underline{e}_i^T \quad (7.11)$$

Now that the equation for the dipole plane is known with respect to fixed axes, the vector coordinates in the plane can be calculated, depicted in Figure 7.6b as the blue circle centered at (x_0, y_0, z_0) , the center of the molecular transition dipole plane in real space, or $(x'_0, y'_0, z'_0) = (0, 0, 0)$ in the transposed coordinates in the plane. The equation relating the relative position of the vector endpoint (x_1, y_1, z_1) after rotation by the angle v_i from the horizontal is

$$[x', y', z'] = [\cos(v_i), \sin(v_i), 0] \quad (7.12)$$

What remains is the transposition of these coordinates into real space, which requires definition of the angles ϵ and δ . Solving Eqn. 7.9 for the axis intercepts shows $x = -d/a$, $y = -d/b$, and $z = -d/c$, which means that $\epsilon = \tan^{-1} \left(\frac{a}{b} \right)$ and $\delta = \tan^{-1} \left(\frac{a}{c \sin \epsilon} \right)$. The transposition can be written as

$$\begin{bmatrix} x_1 \\ y_1 \\ z_1 \end{bmatrix} = \begin{bmatrix} x_0 + x' \cos \epsilon + y' \cos \delta \sin \epsilon \\ y_0 - x' \sin \epsilon + y' \cos \delta \cos \epsilon \\ z_0 - y' \sin \delta \end{bmatrix} \quad (7.13)$$

Engineering Exciton Diffusion with Crystallization

The final result of the vector endpoint as a function of the dipole rotation angle is obtained by substituting Eqn. 7.12 into 7.13 to yield

$$\begin{bmatrix} x_1 \\ y_1 \\ z_1 \end{bmatrix} = \begin{bmatrix} x_0 + \cos \nu_i \cos \epsilon + \sin \nu_i \cos \delta \sin \epsilon \\ y_0 - \cos \nu_i \sin \epsilon + \sin \nu_i \cos \delta \cos \epsilon \\ z_0 - \sin \nu_i \sin \delta \end{bmatrix} \quad (7.14)$$

This means that $\underline{\hat{\mu}}_D$, $\underline{\hat{\mu}}_A$, and \underline{r}_{DA} from Eqn. 7.8 can be expressed by

$$\underline{\hat{\mu}}_D(\nu_1) \text{ or } \underline{\hat{\mu}}_A(\nu_2) = \begin{bmatrix} \cos \nu_i \cos \epsilon + \sin \nu_i \cos \delta \sin \epsilon \\ -\cos \nu_i \sin \epsilon + \sin \nu_i \cos \delta \cos \epsilon \\ -\sin \nu_i \sin \delta \end{bmatrix} \quad (7.15)$$

$$\underline{r}_{DA} = [x_{0,D}, y_{0,D}, z_{0,D}] - [x_{0,A}, y_{0,A}, z_{0,A}] \quad (7.16)$$

These expressions can be used in Eqn. 7.8 to evaluate $\kappa(\nu_1, \nu_2)$, which can then be used in the integral average (Eqn. 7.6) over all angles ν_1, ν_2 to calculate an average orientation factor for that molecule pair. This process is repeated over multiple molecules in many molecular shells to give an aggregate Förster energy transfer rate.

The exciton diffusion length along a direction of interest (denoted as the unit row vector $\underline{\hat{x}}$) is related to k_F through the diffusivity $\underline{\underline{D}}$ ($L_D = \sqrt{(\underline{\hat{x}}^T \underline{\hat{x}} : \underline{\underline{D}})} \tau$), which is most generally a tensor quantity in anisotropic media. SubPc crystallizes in an orthorhombic lattice,⁶⁹⁷ so the anticipated tensor along its principal axes is diagonal with no more than three components unique. However, the presence of κ^2 introduces a direction-dependent R_0 which can cause non-diagonal elements to remain. The diffusivity is evaluated by the sum of energy transfer over all relevant molecular sites N

Engineering Exciton Diffusion with Crystallization

$$\underline{\underline{D}} = \frac{1}{2} \sum_{i=1}^N \left(k_{F,i} \begin{bmatrix} d_x^2 & d_x d_y & d_x d_z \\ d_x d_y & d_y^2 & d_y d_z \\ d_x d_z & d_y d_z & d_z^2 \end{bmatrix} \right) = \frac{1}{2} \sum_{i=1}^N (k_{F,i} \underline{d}_i^T \underline{d}_i) \quad (7.17)$$

where $k_{F,i}$ is the Förster rate to molecule i , and \underline{d}_i is the vector $[d_{x,i}, d_{y,i}, d_{z,i}]$ connecting the excited state to molecule i . When considering changes in \underline{d} and κ^2 , $\underline{\underline{D}} \propto \kappa^2 / |\underline{d}|^4$.

The results of calculating Eqn. 7.17 only considering changes in κ^2 and d are shown in Figure 7.7a as a ratio of the crystalline diffusivity to that of amorphous SubPc. Surprisingly, the diffusivity increases along all directions by a factor of 1.4 to 3 times. Although the orientation factor is enhanced somewhat along specific directions, the primary difference between amorphous and crystalline SubPc lies in the intermolecular spacing reduction from the amorphous Wigner-Seitz radius of 0.48 nm (an example of the

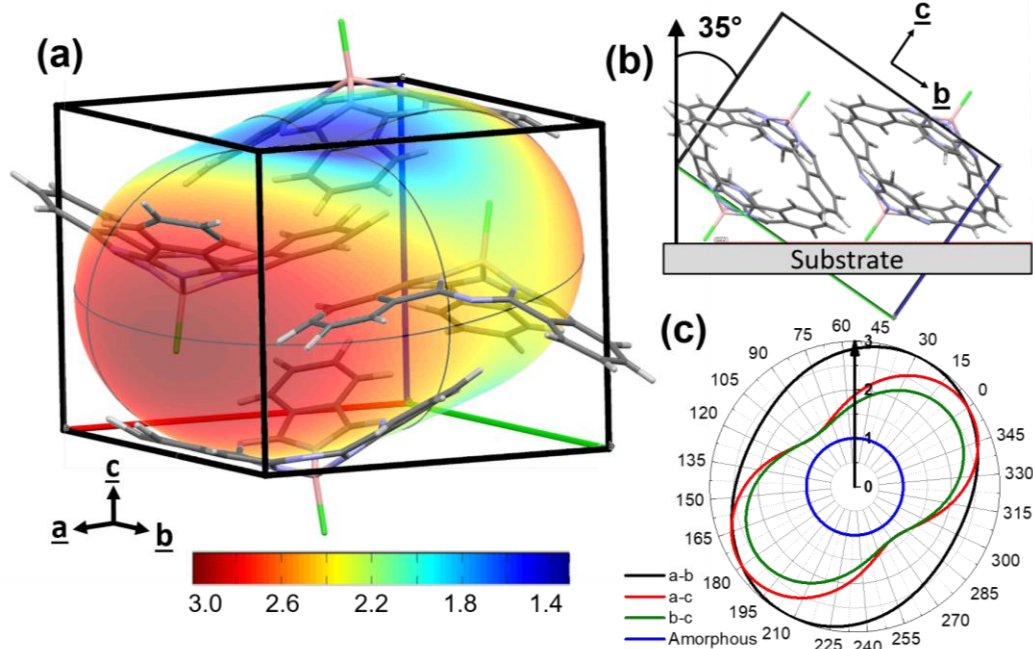


Figure 7.7. (a) SubPc density-based exciton diffusivity enhancement ellipsoid (crystalline over amorphous values). (b) Orientation of SubPc lattice on the substrate. (c) Corresponding diffusivity ellipses in planes along primary crystal planes ($a-b$, $a-c$, and $b-c$, where the first axis is at 0° , the second at 90°). The arrow is a projection along the direction orthogonal to the substrate for the $b-c$ plane.

Engineering Exciton Diffusion with Crystallization

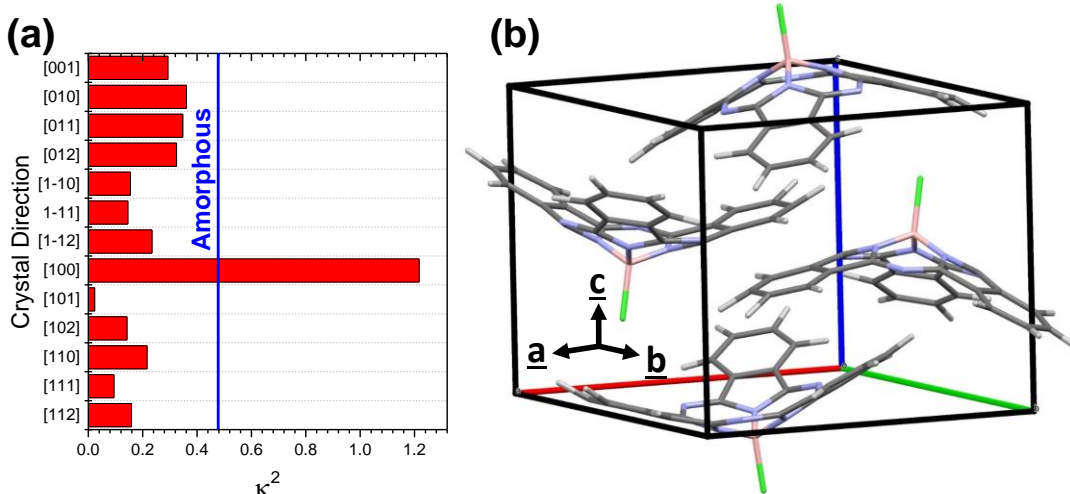


Figure 7.8. Variation in κ^2 along selected crystal directions compared to the amorphous orientation factor. Selected values of κ^2 are shown in (a), the SubPc unit cell in (b).

variation of κ^2 along sample crystal directions in given in Figure 7.8). The orientation factor averaging in Eqn. 7.6 reduces variation in κ^2 somewhat; in molecules with nondegenerate transition dipoles, the orientation factor will be more influential in selecting exciton propagation directions. That the difference is due to density is further evidenced by the dramatic enhancement specifically along periodic chains of neighboring molecules which are favorably aligned, in this case slightly skewed from along the a -axis. Previous authors have demonstrated that care is required when assessing interactions of molecules which may form dimer states,^{259,698} as rapid energy transfer between isolated dimers is not representative of overall energy transfer that leads to exciton diffusion. However, in SubPc, the use of an averaged center comprising the transition dipole plane of Figure 7.5 results in an approximately constant bond spacing along the a -axis bond chain, the direction most likely to be calculated as a dimer state. This implies that the calculated transfer rates are representative of macroscopic exciton diffusion.

Application of these results to extract L_D requires projecting the direction of interest onto the ellipsoid.

Figure 7.7b shows the orientation of the

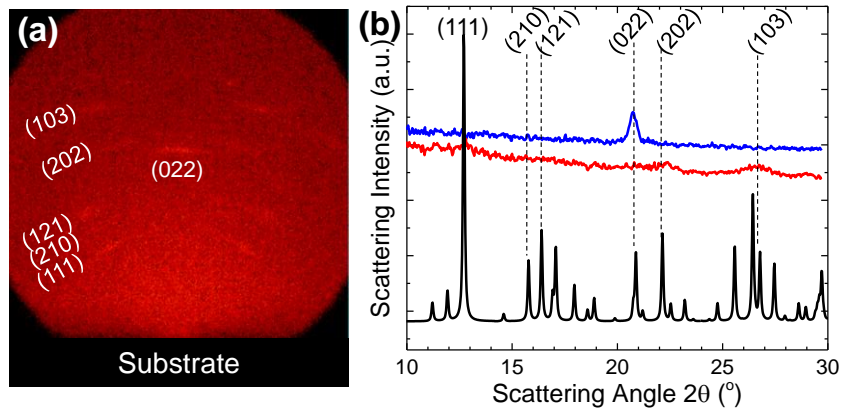


Figure 7.9. X-Ray diffraction of 70 nm crystalline SubPc films on Si: (a) 2D diffraction pattern with peaks labeled; (b) integrated pattern (red and blue) compared to simulated (black).⁶⁹⁷

SubPc unit cell as determined by two-dimensional X-ray diffraction (XRD) measurements (Figure 7.9). This orientation implies that the b-c plane of the ellipsoid of Figure 7.7a is the relevant ellipse, and that the direction orthogonal to the substrate plane is 35° from that of the c-axis. Overlaying this direction on the b-c ellipse in Figure 3c yields a density-based diffusivity enhancement of 1.71 times, or a possible L_D increase of 31%. If the crystalline lattice were optimally oriented for exciton diffusion (ellipsoid maximum normal to the substrate), an L_D increase of 71% is possible, potentially increasing L_D to 28 nm.

7.7. Effects of Film Roughness

When SubPc films are crystallized, there is also a topographical change which occurs. SubPc crystals in annealed thin films grow as Category II spherulites,⁴⁵⁶ rapidly branching with a characteristic angle of $(36 \pm 3)^\circ$. Based on the in-plane crystal structure of these films (Figure 7.10), this implies a possible fast growth axis of the [100] with branches along molecular bond chains, but without ultrahigh-resolution AFM or STM on facets or SAED

Engineering Exciton Diffusion with Crystallization

along individual spherulite arms, this is strictly speculative.

As-deposited SubPc is amorphous,

(Figure 7.11)

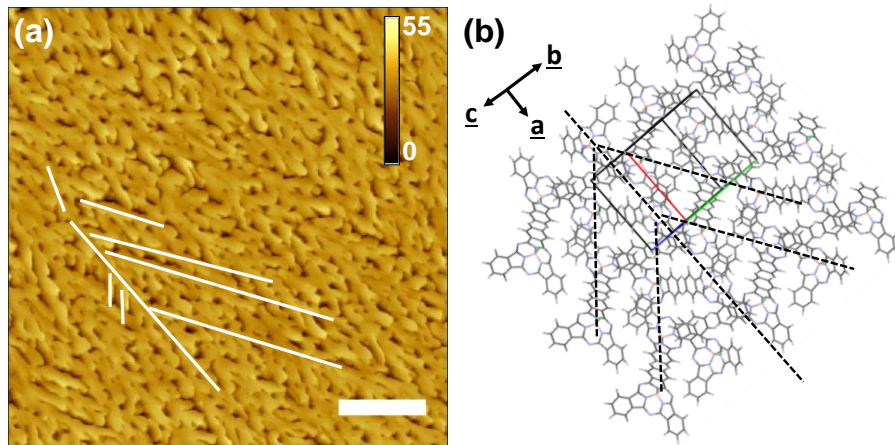


Figure 7.10. Determination of branching angles for SubPc spherulite growth: (a) lines tracing branches of SubPc crystals from Figure 7.11b and (b) lines of the same angles overlaid on SubPc crystal structure viewed orthogonal to the (022) plane, implying the primary growth direction is along [100].

yielding very smooth films. Close examination of Figure 7.11c shows molecular terraces and spiral growth consistent with observations of growth around screw dislocations. This

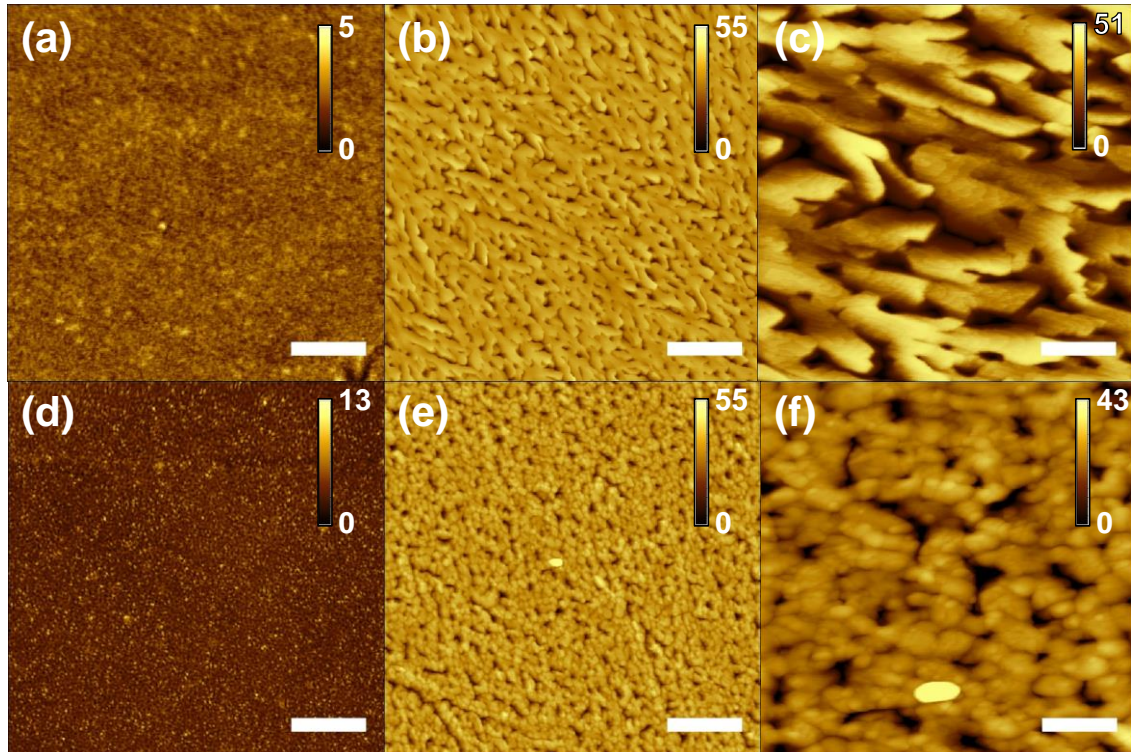


Figure 7.11. Film morphology changes upon crystallization and with a quenching layer. Films are 40 nm SubPc (a), (d) amorphous, (b), (c), (d), (e) crystalline, with (a)-(c) bare SubPc and (d)-(f) SubPc with 13 nm HATCN deposited on top. Scale bars 1 μ m, except (c), (d) which are 200 nm; height scales in nm.

Engineering Exciton Diffusion with Crystallization

growth mode occurs during the deposition of the second 20 nm of SubPc onto the crystalline template, similar to the type of growth observed in Section 9.2.1. Growth of these spherulites also causes substantial roughening of the top film interface at which

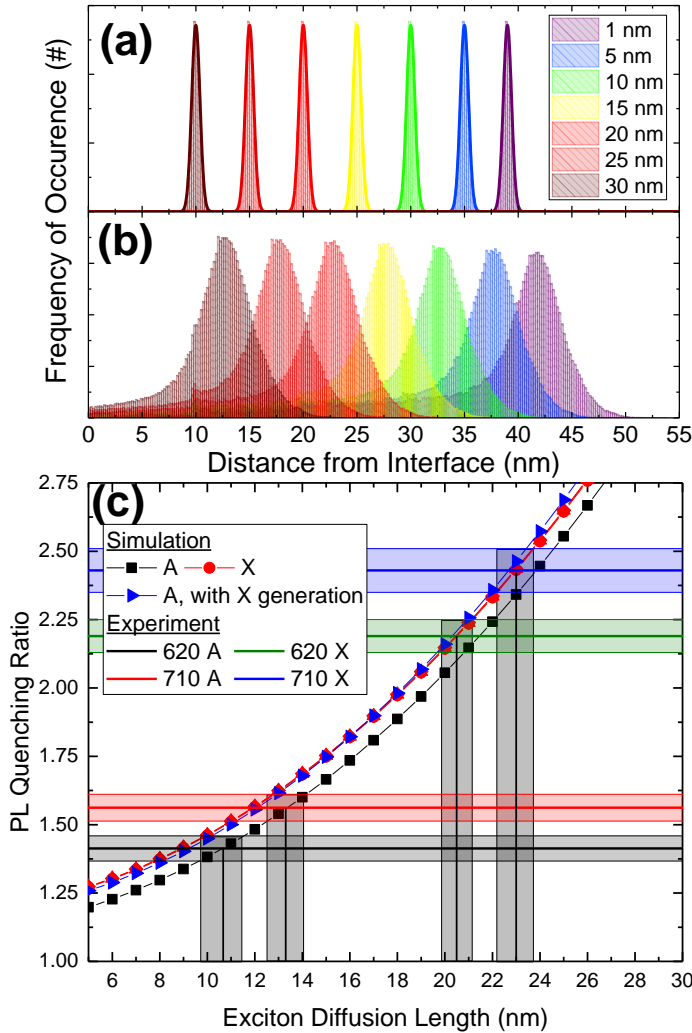


Figure 7.12. Effects of film roughness on exciton diffusion. Histograms of distance distributions from points in a plane xx nm from the substrate to the nearest interface in (a) the amorphous film of Figure 4a and (b) the crystalline film of Figure 4b. (c) Simulated PL quenching ratio for amorphous (A) and crystalline (X) films compared to the experimentally measured ratios excited at $\lambda = 575$ nm and measured at $\lambda = 640$ nm or 720 nm.

form valleys and areas of low thickness, other regions in the film must necessarily

excitons dissociate in a quenched architecture, yielding a $(5 \pm 3)\%$ increase in interface area from atomic force microscopy (AFM) measurements. Examining the distribution of distances to an interface for different planes within a given material shows a considerably larger spread for the case of a crystalline film (Figure 7.12a-b), implying that there are locations which more rapidly reach the surface to dissociate. However, equally important are

the locations which become farther from an interface due to material conservation: in order to

Engineering Exciton Diffusion with Crystallization

accumulate additional material. This is manifested in the considerable skew towards zero exhibited by the crystalline distributions, reducing the effective interface distance close to the substrate and increasing it farther from the substrate compared to the smooth amorphous case. The relative contributions of thickness and roughness depend on the domain size and diffusion length, which determines the extent of lateral exciton diffusion. To quantitatively assess the effects of this in-plane diffusion, numerical simulations of steady-state, three-dimensional diffusion were carried out on geometries created using parametric fits of experimental film morphologies. These results are shown in Figure 7.12c. Surprisingly, there is little difference between the simulated quenching ratio of the crystalline and amorphous films, and most of this difference can be accounted for simply by a change in optical exciton generation rate from film properties. Simulating a smooth, amorphous film with the crystalline exciton generation profile yields quenching ratios almost identical to the crystalline films. These ratios give the exciton diffusion lengths

presented in Table 7.2, which compare favorably to those measured with SR-PLQ.

The similarity of these values implies that

Table 7.2. Simulated and experimental L_D values (nm) for amorphous (A) and crystalline (X) films.

Wavelength	Experimental	Simulated
640 nm, A	11.3 ± 0.7	10.7 ± 0.8
720 nm, A	14.1 ± 0.7	13.3 ± 0.8
640 nm, X	21.2 ± 0.6	20.5 ± 0.6
720 nm, X	22.3 ± 0.9	23.0 ± 0.5

any non-normal diffusion is minimal and causes SR-PLQ to yield the intrinsic diffusion length of the material for these topographies and diffusion lengths.

7.8. Effects of Site Energy Distribution

It is also important to consider the effects of increasing the homogeneity of the energetic landscape upon molecular ordering. Previous work has suggested that molecules

Engineering Exciton Diffusion with Crystallization

in films may display excitonic energies which are perturbed by the local environment of the molecule, through deformation or impingement by other molecules, the substrate, etc.³⁷⁵ Because exciton motion is largely diffusive and proceeds via activated hopping at room temperature, the presence of deep energetic trap states is detrimental to this motion.^{372,699} The energetic sites which are accessible to an exciton can be represented by a band with a Gaussian tail and standard deviation σ , which results in a modified expression for Eqn. 7.1:²⁹⁷

$$k_F = \frac{1}{\tau_{rad}} \left(\frac{R_{0,C}}{|\underline{d}|} \right)^6 \exp \left(-\frac{E_A}{k_B T} \right) \times \begin{cases} \exp \left(-\frac{E' - E}{k_B T} \right), & E < E' \\ 1, & E > E' \end{cases} \quad (7.18)$$

This is simply the Förster rate with a temperature-invariant radiative lifetime τ_{rad} and Förster radius $R_{0,C}$, modified by the Arrhenius activation energy E_A describing the temperature dependence of the overlap integral in Eqn. 7.2 and a Boltzmann factor for the probability of transfer from a site of energy E to a site energy E' , which are in turn affected by the absolute temperature T and Boltzmann factor k_B . These parameters have been previously tabulated for SubPc,²⁹⁷ which makes exploration of the dependence of L_D on σ straightforward.

The chosen method for this investigation was Kinetic Monte Carlo simulation for its transparent evolution of an exciton diffusion length from energy transfer rates. These simulations were performed using in-house software written for Matlab. Simulations employed a cubic lattice of 50^3 molecules with periodic boundary conditions and a Gaussian normal site energy distribution, with energy transfer rates calculated to a cube of

Engineering Exciton Diffusion with Crystallization

17 molecules around the excited molecule. An exciton was randomly generated within the lattice and allowed to hop through sites according to the probabilities of Eqn. 7.18 until decaying, at which point its mean squared displacement was calculated. Values of L_D were calculated by averaging 10^4 excitons, with error bars derived from the standard deviation of the population. This yielded the results shown in Figure 7.13. As shown, reducing σ increases the average number of sites an exciton samples, with a correspondingly larger

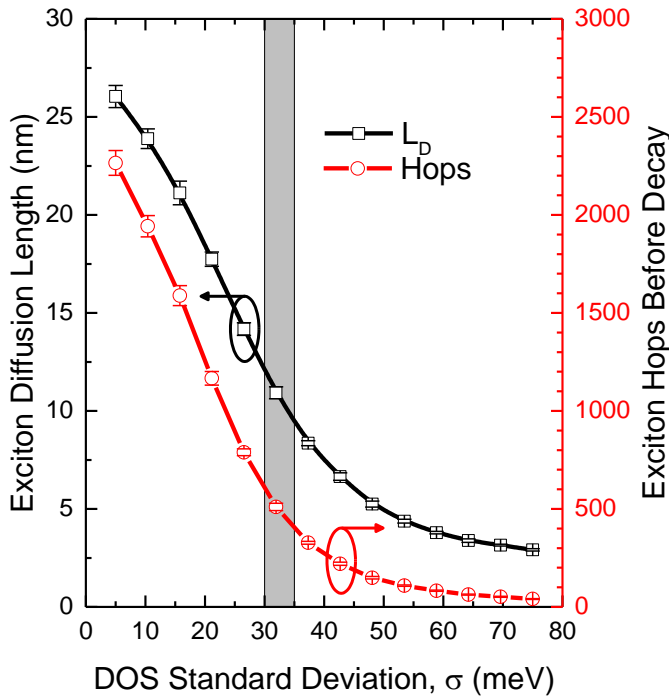


Figure 7.13. Exciton diffusion length (L_D) and number of hops before decay as a function of the width of the excitonic density of states, σ . The gray region shows the narrowing of σ required to account for the additional diffusion length increase due to crystallization.

exciton makes and L_D . As this bandwidth is narrowed, the probability of hopping is sufficiently high so as to allow a large number of hops to occur, increasing L_D . Interestingly, L_D exhibits a nonzero plateau for large σ . This can be rationalized by

L_D . Narrowing the bandwidth reduces the probability of an exciton encountering a prohibitively deep energetic trap from which emission is unlikely. At very large σ , excitons routinely encounter such states, where they ultimately decay because of the magnitude of the barrier relative to available thermal energy. This reduces both the number of hops the

Engineering Exciton Diffusion with Crystallization

considering that an exciton typically must hop to reach its ultimate trap site; as σ increases, there are always states which are lower in energy than that where the exciton was generated on average. The exciton then undergoes a certain number of hops to irreversibly sample increasingly lower-energy sites, similar to the low-temperature limit of narrow bands. The finite, nonzero number of sites fixes both the number of hops and average diffusion length. At the other extreme, a band with no width ($\sigma = 0$) does not diverge but is bounded due to the limiting case of the Boltzmann factor of Eqn. 7.18 going to unity. As shown in Figure 7.13, there is considerable room for improvement of SubPc L_D by merely manipulating the excitonic density of states.

The density and optical improvements discussed earlier can account for a 52% increase in L_D , from (11.3 ± 0.7) nm to (17 ± 1) nm; the remaining 15-25% can be described by a reduction of σ by 3-5 meV from the original value of 35 meV, shown in the grey region of Figure 7.13. There is little work comparing σ for exciton transport in amorphous *versus* crystalline organic materials, and without supporting temperature measurements it is important to consider the presence of an estimated 10-20 meV of broadening due to thermal fluctuations.^{375,419}

7.9. Theoretical Limitations

Finally, there are limitations to consideration of SubPc as a strictly dipole-dipole Förster energy transfer system.^{170,202} Owing to its high symmetry, molecular SubPc possesses an electromagnetic octupole,²²² suggesting that these resonances may require consideration of higher-order terms typically omitted in Förster energy transfer. The

Engineering Exciton Diffusion with Crystallization

distance dependence of these energy transfer rates scales with $d^{-2(D+A+1)}$,⁷⁰⁰ where D and A are the dipole order of donor and acceptor, respectively. For dipole-dipole coupling, $D = A = 1$ and the d^{-6} dependence is recovered; for dipole-quadrupole, d^{-8} , and so on. Although calculation of the rate coefficients in this limit is non-trivial,⁷⁰¹ these terms will be considerably more sensitive to densification of the solid, implying that fully quantitative, quantum-mechanical assessment of more complicated molecules should consider their evaluation.

There are other considerations which are detailed more completely in the appendices, including anisotropy in optical constants (Appendix G.4.) and limitations to the point-dipole approximation (Appendix G.3.). A full density functional quantum-mechanical simulation would be useful to lend insight into the actual roles of these additional factors.

7.10. Conclusions

All combined, the crystallization of SubPc is shown to yield an apparent L_D increase from (11.3 ± 0.7) nm to (21.2 ± 0.6) nm which is explained here in terms of the contributions from film densification, changes in optical properties, film roughness, and exciton energetics. Density-driven changes in intermolecular transfer rates are responsible for a 31% improvement, optical properties yield a 16% enhancement, and exciton energetics can account for the remainder. Despite the relatively large roughness values, for crystal grains and diffusion lengths of this magnitude, lateral diffusion is negligible, causing the experimentally measured diffusion length to correspond to the intrinsic L_D . Further improvement of L_D in this system should be possible by orienting the crystal lattice

Engineering Exciton Diffusion with Crystallization

along directions of maximal diffusivity, presenting opportunities for future work.

8. DESCRIBING EXCITON TRANSPORT IN ENERGY-CASCADE STRUCTURES

With an understanding of factors which can enhance the exciton diffusion length in organic semiconductors from the previous chapter, this chapter revisits an alternative method for improving exciton diffusion posed in Chapter 2: exciton transport across anisotropic interfaces. Such interfaces are exploited in energy-cascade OPVs to form high-efficiency devices, making it imperative that a simple, effective modeling method be developed to direct future efforts. This chapter describes different thermodynamic and formulaic constructs for viewing and solving equations of exciton motion in these energy-cascade structures.

8.1. Introduction

Exciton transport occurs in excitonic materials as a means of energy migration in devices including OPVs and organic photodetectors,^{18,86,159,163,588} and is generally diffusive and isotropic in nature owing to the energy transfer mechanisms and material symmetry.^{78,156,203,236,702} However, when this symmetry is broken, as in graded-concentration systems or heterostructures with interfaces with differing rates of forward and reverse transfer, it is possible to unilaterally direct exciton transport and achieve super-

Describing Exciton Transport in Energy-Cascade Structures

diffusive behavior.^{198,237,238,690,703,704} Though the high demonstrated power conversion efficiencies in these systems incentivize modeling efforts to better understand mechanisms and methods of improvement,^{17,237,690,703,705} there have been few studies which quantitatively probe the underlying physical parameters to gain insight into tailororable trends.^{209,237,238,703} Of these studies, simulations clearly elucidating parameter interactions have relied on Kinetic Monte Carlo methods,^{209,238} which tend to be time-consuming to create and run, limiting general use in the field. Simple, efficient mathematical approaches could greatly expand the use of simulations in energy cascade architectures to drive forward progress.

Towards this goal, an approximate analytical approach is first discussed to show exact parameter functionality, then expanded to the general numerical case. Finally, general trends and suggestions for construction and optimization of energy cascade architectures are given. To establish the conceptual framework for these studies, a discussion of interface effects and diffusion in exciton transport is given first.

8.2. The Validity of Exciton Motion as Diffusive

The approximation of exciton motion as diffusive is commonly used because this formalism simply and elegantly describes measured results,^{78,156,706} providing useful insight into underlying physics.^{87,373,707} However, there are some unconventional aspects of diffusion which become relevant in exciton gating. Particularly poignant are the roles of interfaces and rate anisotropy, which are the subject of this section. In classical systems, interfaces are infinitesimally thin and typically defective, resulting in sufficiently rapid

Describing Exciton Transport in Energy-Cascade Structures

exchange to equilibrate at the nanoscopic level and a system response dictated by spatial extent and diffusivity. Anisotropy in rate often occurs between immiscible phases or membranes, which leads naturally to partition coefficients and membrane solubilities.

Organic semiconducting systems differ in the aspects of size and exchange rate. The relative size of the interface and its effects are now non-zero, so much so that direct exchange can occur between non-contacting layers. Although multiple site jumps are not problematic for the concept of diffusion, the fact that this greatly enlarges the region of influence for the interface is. This becomes obvious when evaluating different methods to include excitonic interface effects. A common method of modifying the exciton diffusion equation to include additional Förster energy transfer is as a sink and source term:^{703,707}

$$\frac{\partial n}{\partial t} = \mathcal{D} \frac{\partial^2 n}{\partial x^2} - \frac{n}{\tau_i} + k_F n + G(x) \quad (8.1)$$

more precisely written for each layer i surrounded by layers j as

$$\frac{\partial n_i}{\partial t} = \mathcal{D}_{x,i} \frac{\partial^2 n_i}{\partial x^2} - \frac{n_i}{\tau_i} + \sum_{j \neq i} k_{F,ji} n_j - n_i \sum_{i \neq j} k_{F,ij} + G_i(x) \quad (8.2)$$

This is merely a variant of Eqn. 2.22, keeping the zeroth-order terms. Consider a hypothetical interface where $k_{F,ij} = k_{F,ji} = k_{F,ii}$, such as an interface between two layers of the same material. For any exciton profile with nonzero slope, the summations remain, introducing an additional flux across the interface. This is only noticeable in the limit of similar Förster radii; many systems studied with this approximation have interface terms which dominate over diffusion, with interfacial Förster radii 2-3 times the self-Förster radius.⁷⁰⁷ Since $\mathcal{D} \propto k_{F,ii} \propto R_{0,ii}^6$, such ratios allow direct transfer to the interface to

Describing Exciton Transport in Energy-Cascade Structures

dominate, significantly reducing the diffusive flux. Direct energy transfer may not appear in an interfacial flux balance depending on the chosen form of k_F , as these source and sink terms are body variables, not surface. This can make it challenging to calculate real fluxes at all points in space. The form most consistent with Eqn. 2.22,

$$\frac{\partial n_i}{\partial t} = \mathcal{D}_{x,i} \frac{\partial^2 n_i}{\partial x^2} - \frac{n_i}{\tau_i} + n_i \sum_{i \neq j} (k_{F,ji} - k_{F,ij}) + G_i(x) \quad (8.3)$$

is also problematic in that it allows for the extraction of excitons from a layer j which has none, doing so at a rate proportional to the population in the i th layer.

The effect of energy transfer rates also manifests in the system steady-state. When the rate imbalance between interfaces is large, commonly by diminishing one rate, the bulk exciton diffusion rates may be comparably small relative to one interfacial rate, but large compared to the other. Contrary to classical interfaces, the population of excitons in the preferential acceptor will never be as large as predicted by an equilibrium concentration ratio because transfer away from the interface is much faster than the rate-limiting step of back transfer. In these cases, a more general flux or advective condition, rather than interface equilibrium, argument must be used.

8.3. Exciton Gates as Advection Transport

In a diffusive system, the primary methods to introduce directional transport are through boundary conditions, bulk source/sink terms, and advection. This is apparent mathematically from the ∇^2 dependence on n : transient diffusion responds to the system concavity, whereas simple steady-state diffusion seeks to establish an even gradient of

Describing Exciton Transport in Energy-Cascade Structures

chemical potentials. This means that irregularities are smoothed by motion of particles in all directions, with net motion simply due to more particles exploring regions where there were fewer before.

8.3.1. Derivation of an Exciton Velocity

Although an exciton drift velocity \underline{v} is unconventional, the resemblance of exciton gates to advective transport is striking. In gating architectures, interlayer transport results in highly unequal interface concentrations. In these highly dilute systems (parts per trillion) with no auxiliary species or solubilities, diffusion yields a continuous concentration profile. The additional driving force for motion is provided by highly asymmetric energy transfer, which can be mapped to an average velocity using the first-order term of Eqn. 2.22:

$$\underline{v} = \sum_{j \neq i} \underline{x}_{ij} k_F(\underline{x}_{ij}) \quad (8.4)$$

The exciton velocity is dictated by the rate at which it transfers and the distance traveled in each transfer event. In the event that there are equal rates in either direction, $\underline{v} = 0$.

This result may also be derived from classical diffusion assuming a biased random walk.⁷⁰⁸ For the classical result, this begins with a definition of the average velocity from equating thermal and kinetic energy in one dimension,

$$\langle v \rangle = \frac{k_B T}{m} \quad (8.5)$$

then defining the probabilities of stepping to the right (p) and left (q) with step size δ as

$$p = \frac{1}{2} + \frac{F_x \delta}{4k_B T} \quad (8.6)$$

Describing Exciton Transport in Energy-Cascade Structures

$$q = \frac{1}{2} - \frac{F_x \delta}{4k_B T} \quad (8.7)$$

Note that the probabilities are defined such that if the applied force F_x equals the thermal energy, $p \rightarrow 1$ and $q \rightarrow 0$. These may then be used to calculate an average displacement for the population $\langle x \rangle$ after n steps according to a binomial distribution:

$$\langle x(n) \rangle = (2\langle k \rangle - n)\delta \quad (8.8)$$

where k is the number of steps taken to the right,

$$\langle k \rangle = np \quad (8.9)$$

Using the definition of a time between hops $t/\tau = n$ and step length in terms of the diffusivity $\delta = \sqrt{2D\tau}$ gives the result

$$\langle x\left(\frac{t}{\tau}\right) \rangle = \left(\frac{2t}{\tau} \left[\frac{1}{2} + \frac{F_x \sqrt{2D\tau}}{4k_B T} \right] - \frac{t}{\tau} \right) \sqrt{2D\tau} = \frac{F_x D}{k_B T} t \quad (8.10)$$

that is, there is only net displacement under the influence of an applied force, with an average velocity equal to $\frac{F_x D}{k_B T}$.

Compare this to the case for excitons. Now, the probabilities can be defined as the probabilities of energy transfer in each direction in terms of the forward, reverse, and total transfer rates k_f , k_r , and k_{tot} , respectively, where

$$p = \frac{1}{2} + \frac{\sum_{+x} k_{ET}(x) - \sum_{-x} k_{ET}(x)}{2 \sum_x k_{ET}(x)} = \frac{1}{2} + \frac{k_f - k_r}{2k_{tot}} \quad (8.11)$$

As with Eqn. 8.7, the probability of extra transfer is bounded by $\pm 1/2$, since $0 \leq p \leq 1$.

Inserting this into Eqn. 8.8 but not substituting for δ yields

$$\langle x\left(\frac{t}{\tau}\right) \rangle = \left(\frac{2t}{\tau} \left[\frac{1}{2} + \frac{k_f - k_r}{2k_{tot}} \right] - \frac{t}{\tau} \right) \delta = \delta \frac{k_f - k_r}{\tau k_{tot}} t \quad (8.12)$$

Describing Exciton Transport in Energy-Cascade Structures

A final substitution of the inverse total hopping rate for τ yields the velocity

$$\underline{v} = (k_f - k_r) \underline{\delta} = \sum_{j \neq i} \underline{x}_{ij} k_F(\underline{x}_{ij}) \quad (8.13)$$

which is consistent with the velocity defined in Eqn. 8.4.

8.3.1. Velocity Edge Effects

The subtle difference between Eqn. 8.14 and 8.15 lies in the normalization of isotropic transport. Use of the Förster rate as a body term (Eqn. 8.14) requires subtraction of backwards energy transfer because k_F is a scalar quantity and thus lacks direction. Accounting for interface anisotropy as an advective velocity (Eqn. 8.15) naturally cancels isotropic transport, but requires a correction for edge effects.

To understand the reason for these edge effects, consider the sphere of sites available

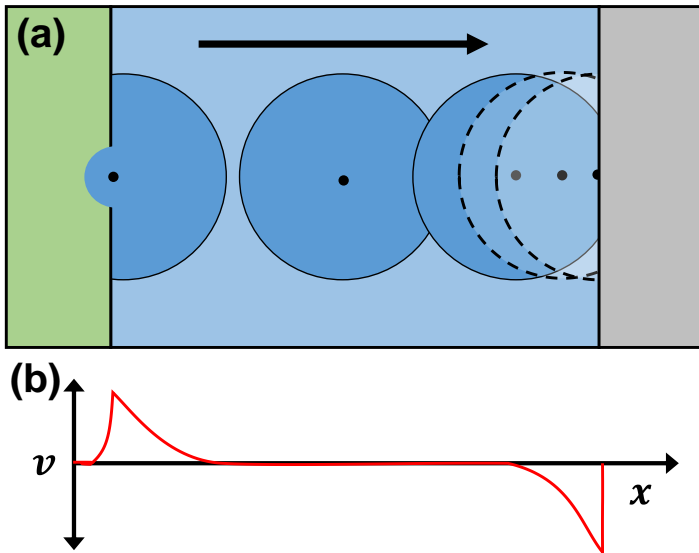


Figure 8.1. Diagram of exciton convection, showing (a) the sphere of available energy acceptors at different locations and (b) the calculated advective velocity.

different sizes, but this describes real transport phenomena within the film. Near the film edges, such as near a substrate or air interface, a similar effect occurs with fewer acceptors

for energy transfer from an excited donor, shown in Figure 8.1a. An exciton at different points a given structure has different quantities of energy acceptors available for transfer. Near an interface with a rate imbalance (left), the available spheres may be considerably

but yields a negative apparent velocity step at the interface (Figure 8.1b) and nonphysical negative exciton densities in extreme cases. To account for these effects, an additional layer of the same material may be added to the edge during computation of the velocity.

8.4. Posing the Problem

In energy cascade architectures such as that shown in Figure 8.2, excitons enter and subsequently diffuse according to the diffusivity defined in Eqn. 2.24. At the interfaces between layers, the energy transfer rates $k_{i,i+1}$ and $k_{i+1,i}$ may differ from bulk values. In one dimension, the exciton diffusion equation for each layer can be written with a layer-specific generation rate G_i as

$$\frac{\partial n_i}{\partial t} = \mathcal{D}_{x,i} \frac{\partial^2 n_i}{\partial x^2} - \frac{n_i}{\tau_i} + G_i \quad (8.14)$$

Note that variables and constants are indexed by layer. This equation has a general steady-state solution of

$$n_i(x) = C_{2i-1} \exp\left(-\frac{x}{L_{D,i}}\right) + C_{2i} \exp\left(\frac{x}{L_{D,i}}\right) + G_i \tau_i \quad (8.15)$$

with an equivalent solution using hyperbolic transcendental functions

$$n_i(x) = C'_{2i-1} \sinh(x/L_{D,i}) + C'_{2i} \cosh(x/L_{D,i}) + G_i \tau_i \quad (8.16)$$

Next, the integration constants C_{2i-1} and C_{2i} must be solved using boundary conditions. In accordance with previous work,²³⁸ an exciton flux F at $x = 0$ and dissociation at $x = L$ are specified according to

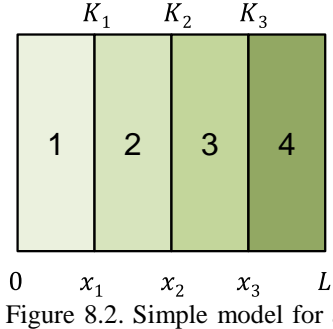


Figure 8.2. Simple model for a 4-layer gated structure, showing rate anisotropy (top) and spatial positions (bottom).

$$-\mathcal{D}_{x,i} \frac{\partial n_i}{\partial x} |_{x=0} = F \quad (8.17)$$

$$n_i |_{x=L} = 0 \quad (8.18)$$

At all times, the flux across interfaces must be conserved (neglecting decay within the infinitely thin interface), yielding $N - 1$ equations of

$$-\mathcal{D}_{x,i} \frac{\partial n_i}{\partial x} |_{x_i} = -\mathcal{D}_{x,i+1} \frac{\partial n_{i+1}}{\partial x} |_{x_i} \quad (8.19)$$

The remaining $N - 1$ equations must be provided by approximations for the gating interfaces as discussed in the following sections.

8.5. Equilibrium Conditions

If the interfaces themselves are considered to impose an anisotropic flux on the system (rather than bulk transfer within the layer, as discussed below) and transfer across the interface is comparably fast relative to transfer to the interface, then the concentrations across the interface may be approximated as an equilibrium reaction. In this limit, the exciton concentration ratio will be dictated by the rate ratio according to the law of Mass Action used in pseudo-equilibrium reactions.²⁵³



As these populations approach equilibrium, their concentrations will be dictated by

$$\frac{n_2}{n_1} = \frac{k_{12}}{k_{21}} \equiv K_1 \quad (8.21)$$

This means that concentration boundary conditions for the structure can be written as

Describing Exciton Transport in Energy-Cascade Structures

$$n_{i+1}|_{x_i} = K_i n_i|_{x_i} \quad (8.22)$$

Eqns. 8.21 and 8.22 effectively equate proportional quantities on either side of an interface, with only defined values at the ends of the layer stack. This requires solving a system of equations for the coefficients, which can be written as a linear system

$$\underline{\underline{c}} \cdot \underline{\underline{C}} = \underline{\underline{b}} \quad (8.23)$$

with $\underline{\underline{c}}$ and $\underline{\underline{b}}$ defined as (using $n(x)$ as defined in Eqn. 8.15)

$$\underline{\underline{c}} = \begin{bmatrix} L_{D1}/\tau_1 & -L_{D1}/\tau_1 & 0 & 0 & 0 & \cdots & 0 & 0 \\ K_1 e^{-\frac{x_1}{L_{D1}}} & K_1 e^{\frac{x_1}{L_{D1}}} & -e^{-\frac{x_1}{L_{D2}}} & -e^{\frac{x_1}{L_{D2}}} & 0 & \cdots & 0 & 0 \\ L_{D1}/\tau_1 e^{-\frac{x_2}{L_{D1}}} & -L_{D1}/\tau_1 e^{\frac{x_2}{L_{D1}}} & -L_{D2}/\tau_2 e^{-\frac{x_2}{L_{D2}}} & L_{D2}/\tau_2 e^{\frac{x_2}{L_{D2}}} & 0 & \cdots & 0 & 0 \\ 0 & 0 & K_2 e^{-\frac{x_2}{L_{D2}}} & K_2 e^{\frac{x_2}{L_{D2}}} & -e^{-\frac{x_2}{L_{D2}}} & \cdots & 0 & 0 \\ \vdots & \vdots & \vdots & \vdots & \vdots & \ddots & \vdots & \vdots \\ 0 & 0 & 0 & 0 & \cdots & 0 & e^{-\frac{L}{L_{DN}}} & e^{\frac{L}{L_{DN}}} \end{bmatrix} \quad (8.24)$$

$$\underline{\underline{b}}^T = [F \quad K_1 G_2 \tau_2 - G_1 \tau_1 \quad 0 \quad K_2 G_3 \tau_3 - G_2 \tau_2 \quad 0 \quad \cdots \quad 0 \quad -G_N \tau_N] \quad (8.25)$$

with dimension $2N$, where N is the number of total layers calculated.

If the stack shown in Figure 8.2 is simulated with a constant ratio of rate imbalance equal to 3, the resulting exciton concentration profiles are reasonably consistent with expectation. As the rate imbalance between layers increases, the concentration difference across the interface also increases (Figure 8.3a). The diffusion efficiency η_D , the efficiency with which excitons reach the dissociating interface at $x = L$, also trends with rate imbalance (Figure 8.3b) and the number of layers (Figure 8.3c) within a given film thickness. It should be emphasized that the number of layers can easily be increased beyond

Describing Exciton Transport in Energy-Cascade Structures

physical values; the sizes of molecules impose very real constraints on the lower bound for layer thicknesses, no smaller than ~ 3.5 Å for, *e.g.*, the π -stacking direction in phthalocyanines (see Appendix J.3.).

If the diffusion efficiency is explicitly defined in terms of the flux entering and leaving

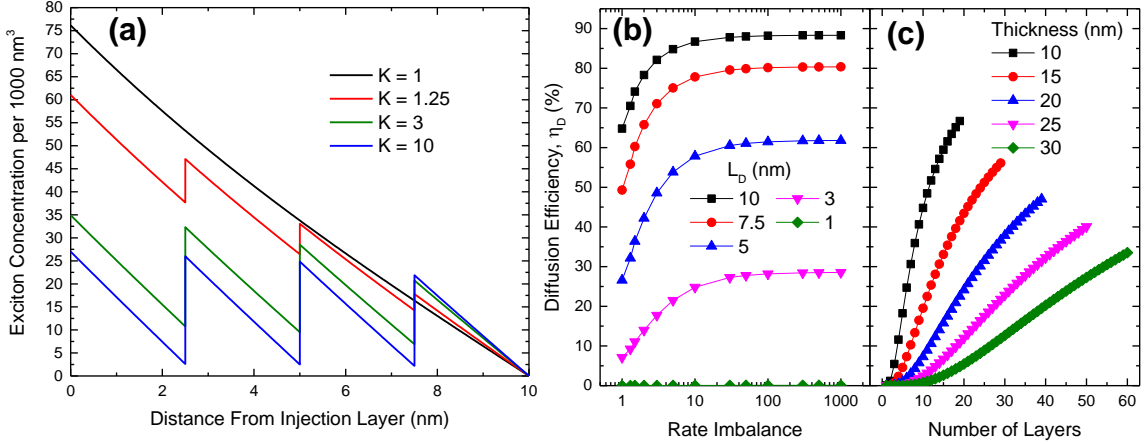


Figure 8.3. (a) Exciton concentration in a 10 nm, 4-layer stack for different rate imbalances, and exciton diffusion efficiency (a) in a 10 nm, 4-layer stack for different L_D and (c) stacks of different thickness and numbers of layers for L_D linearly interpolated between 1-10 nm and $K= 5$. In all simulations, $F=1$ exciton/nm² ns and $\tau = 1$ ns.

the stack, this yields

$$\eta_D = \left(-\mathcal{D}_{x,N} \frac{\partial n_N}{\partial x} |_L \right) / \left(F + \sum_{\text{Layers}} G_i \right) \quad (8.26)$$

This allows for the evaluation of this quantity in terms of experimental, measurable variables. Evaluating Eqn. 8.26 symbolically yields a completely intractable (enormous) expression for η_D for all but the simplest case, a two-layer stack:

$$\eta_D = \frac{2K_1\tau_1e_{12}e_{22}(e_{11}^2 + e_{21}^2)}{\tau_2 \left(\frac{L_{D1}}{L_{D2}} \right) e_{11}(e_{12}^2 - e_{22}^2 - e_{12}^2e_{21}^2 + e_{21}^2e_{22}^2) + 2\tau_1K_1e_{12}e_{21}e_{22}(1 + e_{11}^2)} \quad (8.27)$$

where the exponential terms have been substituted according to

Describing Exciton Transport in Energy-Cascade Structures

$$e_{ij}^{\pm k} = \exp\left(\pm \frac{kx_i}{L_{Dj}}\right) \quad (8.28)$$

This at least qualitatively explains some of the trends of Figure 8.3. As the rate imbalance increases, only terms with K_1 survive, asymptotically approaching the limit of

$$\eta_D = \frac{e_{22}(e_{11}^2 + e_{21}^2)}{e_{21}e_{22}(1 + e_{11}^2)} \quad (8.29)$$

The dependence on L_D and thickness enter through the exponential terms, since the expression has an overall e_{ij}^{-k} dependence. This gives exponentially decaying efficiency with decreasing L_D or increasing thickness, as might be expected from the classical case.

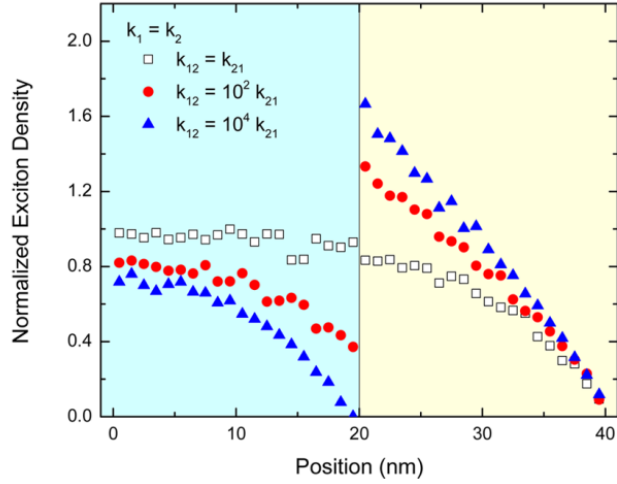


Figure 8.4. Plot from Menke *et al.*²³⁸ showing exciton concentration varying with anisotropic transport.

Finally, in the limit of a bulk material, the diffusion efficiency

$$\eta_D = \frac{2e_{22}}{(1 + e_{21}^2)} \quad (8.30)$$

is recovered, which may be confirmed analytically.

In reality, the interface rarely approaches equilibrium because transport to and from the interface occurs by the same processes (energy transfer) as for transport across the interface, and will therefore have similar rates. There is then no step which limits diffusion to or from the interface more than the interface itself, which can be inferred from the exciton concentration ratios shown in Figure 8.4; a rate imbalance of 10^2 produces a

exciton density ratio which is clearly not of that magnitude.

8.6. Non-Equilibrium Conditions

Although the interface is not at equilibrium, the relative fluxes on either side are at steady state and are calculable from the exciton concentration and energy transfer rate. This means that rather than using a Dirichlet boundary condition (Eqn. 8.22), a Neumann condition describing the net flux through each side of the interface may be constructed as

$$-\mathcal{D}_{x,i||i+1} \frac{\partial n_{i||i+1}}{\partial x} |_i = j_{x,i \rightarrow i+1} - j_{x,i+1 \rightarrow i} \quad (8.31)$$

Here, \parallel is used as “or.” The net flux across the interface at a point has to be equal to the difference of the fluxes from either direction. Representing these fluxes as a function of measureable parameters requires recognition of the mechanism behind exciton motion. The rates used by Menke *et al.*²³⁸ are of the form for energy transfer to a semi-infinite slab²⁰⁷

$$k_{F,S} = \frac{\rho_A \pi R_0^6}{6\tau d^3} \quad (8.32)$$

where ρ_A is the density of energy acceptors within the slab. In their paper, Menke *et al.* assume excitons transfer from the middle of a given molecular “bin” to the interface; thus,

$$d = t_{bin} \left(N_{bin} + \frac{1}{2} \right) \quad (8.33)$$

This volumetric rate is properly converted to a flux by integration to give a net rate²⁵³

$$-\mathcal{D}_{x,i||i+1} \frac{\partial n_{i||i+1}}{\partial x} |_i = \int_{x_{i-1}}^{x_i-a_i} \frac{\rho_{i+1} \pi R_{0,i \rightarrow i+1}^6}{6\tau_i (x_i - x)^3} n_i dx - \int_{x_i+a_{i+1}}^{x_{i+1}} \frac{\rho_i \pi R_{0,i+1 \rightarrow i}^6}{6\tau_{i+1} (x - x_i)^3} n_{i+1} dx \quad (8.34)$$

The form of these integrals is cumbersome and numerical in nature due to the integration of $e^{\pm x}/x^3$, but can be approached using integral average exciton densities around the

interface.

8.7. Numerical Solution for the General Case

The diffusion equation in general requires numerical solution, especially when coupled to experimental generation profiles and a spatially varying velocity. The chosen numerical method was a finite differences scheme for its relative simplicity and flexibility. A discussion of the implementation and considerations for the finite differences code used in this section is given in Appendix Q.

The equation that is modeled is that of a steady-state convection in an anisotropic homogeneous material²⁵³

$$\frac{\partial n}{\partial t} = -\underline{\nabla} \cdot (\underline{v}n - \underline{\underline{D}} \cdot \underline{\nabla}n) - \frac{1}{\tau}n + G(x) = 0 \quad (8.35)$$

with the velocity defined in Eqn. 8.4. Note that this velocity expression is discrete, requiring normalization from the continuous space of finite differences to a molecular basis by the factor $\Delta x/a_i$, where a_i is the molecular spacing in layer i . Two sets of flux continuity equations are used as boundary conditions, with the approximation that three points will be approximately collinear if taken over a sufficiently small interval.

For a comparison of speed, many of the simulations in previous work required hours or days to run. Typical simulations in this work require 5-60 seconds, a dramatic savings in computation time. The code for this work is also simpler (~100 lines for solving each case), and is given in Appendix R.9.

8.8. Model Validation

Existing cases and analytical solutions allow for comparison to and validation of the convective transport model. This section explores these comparisons.

8.8.1. Boundary Layer Effects in Neat Film

Use of advection with a corrective boundary layer works well to describe simple diffusion in an ungated stack, as shown in Figure 8.5. With no boundary layers, the velocity

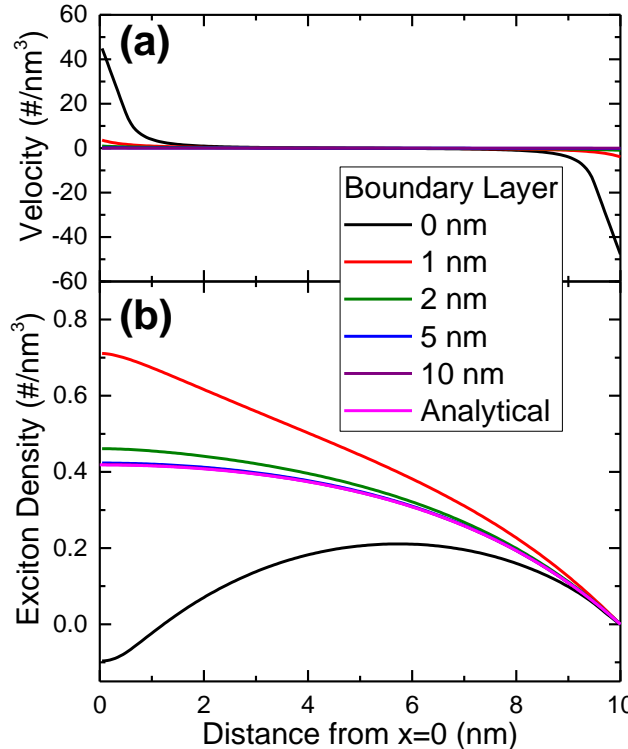


Figure 8.5. Effects of boundary layer thickness on (a) exciton velocity and (b) density in a two-layer stack, each layer 5 nm with $R_0 = 1$ nm. The data in (b) also include the results for an analytical calculation of the exciton density. $G = 1/\text{nm}^3 \text{ ns}$.

density profiles compatible with the analytical solution are obtained, as expected by the definition of the Förster radius – the distance at which energy transfer is equally competitive with all other forms of decay. At R_0 , half of the excitons will transfer

tends to push excitons towards the center of the stack (Figure 8.5a), producing a negative exciton concentration at $x = 0$ as a byproduct of establishing an opposing steady-state concentration gradient. for this generation rate. Unless noted otherwise in this chapter, $\tau = 0.5$ ns, $d = 0.5$ nm, $R_0 = 1$ nm, and $F = 0$. Increasing the boundary layer

thickness to $2R_0$ sufficiently reduces the edge velocity so that exciton

Describing Exciton Transport in Energy-Cascade Structures

successfully; at $2R_0$, that fraction is much smaller. Increasing the boundary layer thickness does nothing to further alter the velocity, although in a system with significant interlayer transfer through thin films, the boundary layers could have appreciable effects. Although this is the approximation used when describing point-to-slab energy transfer (Eqn. 8.32), to avoid overestimation of transfer rates to the edges of finite slabs, the boundary layers are only included in the velocity calculations for the layer physically in contact with the boundary layer. This allows for recovery of the neat-film diffusive behavior near the system perimeter. Unless noted, all boundary layers in this chapter are 5 nm.

8.8.2. Comparison to Monte Carlo Simulations

Existing results have shown consistency with experimental performance in devices and films. If accurate, the convective transport model should yield the same results.

The system chosen for comparison is an arbitrary multilayer stack with interpolated physical and transport properties which approximate a system of diluted materials. In such a system, the diffusion lengths and volume fractions X_i are linearly interpolated, allowing the new intermolecular spacing d_i to be calculated by

$$d_i = \sqrt[3]{d^3/X_i} \quad (8.36)$$

and the Förster rate by Eqn. 2.11

$$R_{0,ii}^6 = L_{D,i}^2 d_i^4 \quad (8.37)$$

A final approximation is that the energy transfer rates to neighboring layers are the same as transfer rates within each layer:

$$\underline{\underline{R}}_0 = \begin{bmatrix} R_{0,11} & R_{0,12} & \dots \\ R_{0,21} & R_{0,22} & \dots \\ \vdots & \ddots & \ddots \end{bmatrix} \equiv \begin{bmatrix} R_{0,11} & R_{0,11} & \dots \\ R_{0,22} & R_{0,22} & \dots \\ \vdots & \ddots & \ddots \end{bmatrix} \quad (8.38)$$

This introduces anisotropy at each interface towards the layer with lower diffusivity.

8.9. Model Results

This formalism can now be used to probe underlying physics of gated interfaces. An example of the effects of interface anisotropy is given in Figure 8.6. Something not revealed by earlier simulations is the role of the magnitudes of the transfer rates responsible for interface asymmetry. In Figure 8.6b, there is clearly a difference between the 2:1 and 1:0.5 $R_{0,12}:R_{0,21}$ cases in the advective model, even though they yield identical asymmetry ratios and similar equilibrium densities. This discrepancy is more obvious if the exciton diffusion efficiency is examined as a function of rate asymmetry (Figure 8.7). Anisotropy arising from slower backwards energy transfer does not produce nearly as strong of an effect as that arising from enhanced forward transfer. These results can be understood completely from a convective view: enhanced forward transfer causes a much larger advective velocity pushing excitons towards the interface, whereas a lower rate of

backwards transfer only reduces the backwards components in the velocity sum (Eqn. 8.4). Translated to energy transfer, there is simply more change possible by increasing $R_{0,ij}$ on an unbounded domain than there is by reducing it towards zero.

Figure 8.7 also highlights the ability of the interface to approach equilibrium under different conditions. For

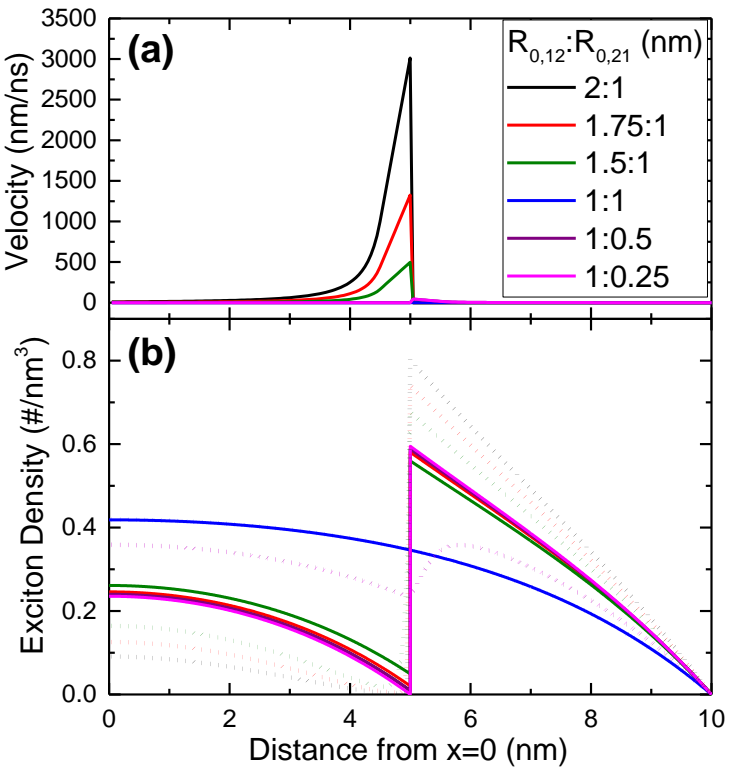


Figure 8.6. The effects of energy transfer rate anisotropy in a two-layer gating stack on (a) exciton velocity and (b) exciton density. Each layer is 5 nm thick. In (b), solid lines are the equilibrium model, dots are the non-equilibrium advection model.

interface transfer rates that are competitive with bulk transport ($x:1$, low anisotropy), the analytical equilibrium model compares well with the numerical solution. When the forward transfer rate is large enough that the backwards transfer across the interface is unable to compete with transfer away from the interface, the system transitions to a kinetics dominated steady state, rather than one dictated by thermodynamic equilibrium. Nonetheless, the analytical equilibrium model is acceptable for describing weakly anisotropic interfaces, provided that both interfacial rates are competitive with the bulk transport properties.

8.10. Conclusions

The description of exciton motion as diffusive is often adequate for explaining experimental results, and can be successfully adapted to describe transport across anisotropic interfaces. In describing these systems, an analytical model based on interface equilibrium works well in weakly anisotropic regimes where both forward and backwards transfer across the interface are competitive with transport to the interface. A more general approach utilizing advective motion provides a different formalism with which to view exciton motion. This approach can successfully duplicate experimentally observed trends across a range of conditions much more rapidly than existing simulation strategies, facilitating further investigation.

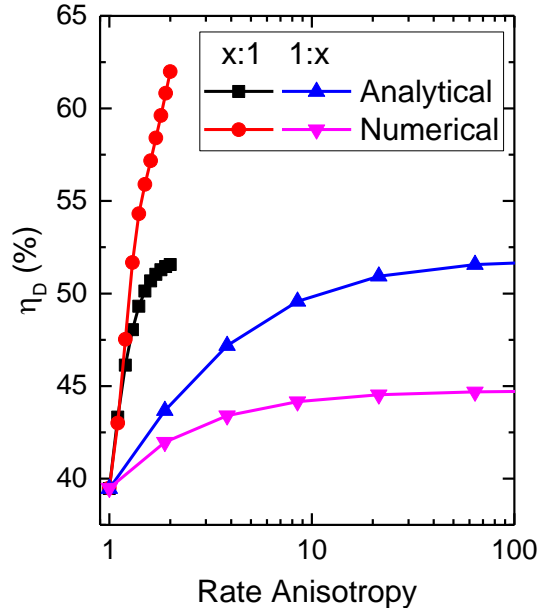


Figure 8.7. The effects of energy transfer rate anisotropy on the exciton diffusion efficiency, η_D in a two-layer gating stack. The legend shows the origin of the anisotropy, with x:1 arising from a larger forward transfer rate and 1:x from a smaller backward transfer rate.

9. HOMOEPIТАXY AND MIXTURE EPITAXY IN OPVs

Epitaxy is an excellent method to induce crystallization when a template can be successfully produced, as discussed in Section 3.3. This is particularly desirable for OPVs when crystalline films have properties which enable the active layers to be thicker and thus absorb more light. The work in this chapter highlights the use of rubrene in crystalline OPVs in neat planar devices *via* simple homoepitaxy and in planar-mixed devices, which involves templating a mixture. Overall, crystalline devices show high photocurrent due to the increased charge collection efficiency and active layer thickness, but are somewhat limited in efficiency by a reduction in V_{oc} commensurate with a change in the HOMO level of rubrene upon crystallization. Building from work in the previous chapter, mixture devices show a reasonable tolerance for impurities during crystallization, which improves photocurrent in the case of an optically active additive.

9.1. Introduction

Epitaxy allows for the crystallization and texturing of materials through interactions with an underlying material, as discussed in Section 3.3. As a crystallization technique, it is particularly interesting for vapor-deposited samples because subsequent morphologies may be significantly modified through the introduction of a simple layer with crystalline

properties. Relatively efficient homo-, hetero- and mixture-epitaxial devices have been previously demonstrated;^{287,500,507,513,588,709,710} however, these devices use materials which already tend to form microcrystalline domains when vapor deposited on arbitrary substrates. Many materials of relevance to organic electronics are not crystalline and require a transformative technique to become so, suggesting that expansion of this knowledge into generally amorphous materials would enable better understanding of limiting factors for this technique and methods to perhaps circumvent this loss. As demonstrated through several chapters in this thesis, rubrene is an ideal molecule by which to study this effect because of its amorphous nature and various polymorphic and growth transitions, giving it a variety of challenges that could be associated with other arbitrary organic electronic materials.

9.2. Homoepitaxy

Homoepitaxy of rubrene has been previously documented in the case of single crystals and thin films.^{174,711} This technique is particularly useful in rubrene and other materials which display film thickness-dependent polymorphism or growth modes, as discussed in Section 4.2. In these cases, thicker crystalline films with a desired morphology may not be directly accessible from the amorphous phase due to thermodynamic or kinetic constraints

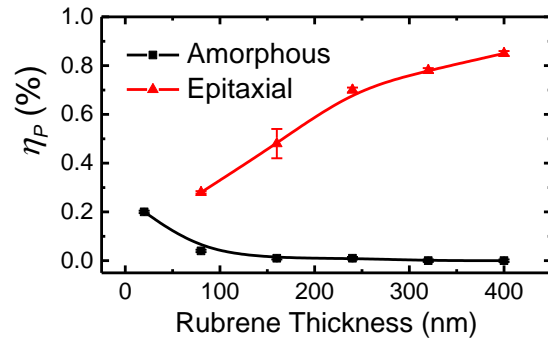


Figure 9.1. Data published by Verreet *et al.*¹⁷⁴ showing an increased device efficiency for crystalline rubrene OPVs with increasing rubrene thickness starkly contrasted to amorphous.

Homoepitaxy and Mixture Epitaxy in OPVs

which favor formation of an undesirable phase. Rubrene in particular transitions to increasingly growth of the triclinic polymorph with an extremely rough growth mode as film thickness is increased. In addition to the triclinic polymorph exhibiting poor charge conduction relative to orthorhombic,³⁶⁶ the large film roughness renders this type of growth unacceptable for thin-film devices. The primary purpose of this portion of the chapter was to replicate literature results, primarily those in Verreet *et al.* shown in Figure 9.1.¹⁷⁴

9.2.1. Film Growth and Characterization

Films grown on rubrene single crystals show very smooth surfaces for thin (3 nm) films,⁷¹¹ and well-defined faceting if grown slowly on other templates consistent with those defined in earlier chapters.⁵⁰¹ Thick epitaxial films which use a template film appear considerably more defective, possibly pointing to defect incorporation in the growing crystal during annealing, leftover material on the template surface, or accumulated defects as the film grows which serve as a nucleation site for multiple small domains on top of each grain. Unless noted, all templates are 20-nm thick rubrene films annealed at 170 °C for 45 seconds. Examples of these films are given in Figure 9.2, with Figure 9.2a showing the optical characterization which is used to screen films for templating behavior. POM is a fast, large-scale characterization technique which relies on the in-plane material birefringence to yield greater light transmittance to the camera with thicker (crystalline) films, courtesy of the greater optical rotation with greater path length discussed in Appendix D.2. This quickly suggests that the additional material deposited through a circular shadow mask (circle in center) did in fact crystallize as deposited. More convincing

Homoepitaxy and Mixture Epitaxy in OPVs

are the XRD patterns shown in Figure 9.2b, where the epitaxial region shows significantly greater diffraction intensity than the bare template layer. Closer investigation of the material morphology of the epitaxial region across the mask boundary is shown in Figure

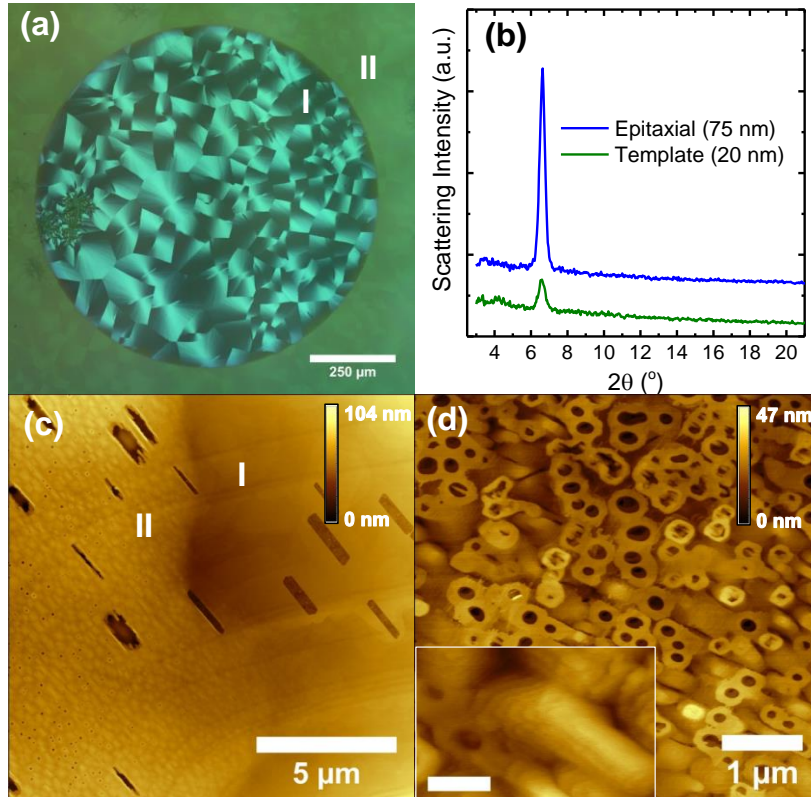


Figure 9.2. Comparison of epitaxial films (I) and templates (II): (a) POM image of 100 nm epitaxial rubrene film on a template, (b) X-ray scattering intensity for epitaxial and template films, (c) atomic force micrograph of the border for a 100 nm epitaxial film, and (d) close-up of a 100 nm epitaxial rubrene film, with inset showing molecular terraces, scale bar 200 nm.

9.2c, and suggests not only vertical ordering but also lateral, with crystalline material projecting from the edges of the faceted defect sites. Much of the epitaxial region is composed of a gently mounded and rolling surface, but some domains show considerable pitting, as

shown in Figure 9.2d. The circularity of these regions has been suggested to correspond to screw dislocations which nucleate on the surface of the template layer,¹⁸⁹ and the exceptional flatness of the top-most surface and molecular terraces descending from the edges of the features in the inset of Figure 9.2d support this assessment. The presence of these defects and the line defects manifested as diagonal fissures in Figure 9.2d appear to

Homoepitaxy and Mixture Epitaxy in OPVs

be related to epitaxial film thickness and deposition rate and temperature.⁷¹² These lines form parallel to the [100] direction and are reported to be a result of strain relaxation.⁷¹²

Closer examination of templating behavior on rubrene single crystals shows some degree of surface diffusion of material deposited upon the surface. Figure 9.3a shows the pristine surface of an orthorhombic rubrene single crystal, showing molecular terraces 13.5 Å tall spaced approximately 2 μm. The step height implies that the c axis is vertically oriented, while the step spacing suggests that the crystal may have been grown at relatively high temperatures, resulting in average crystal quality.^{126,478,711} These step edges typically form parallel to the (100) plane of rubrene (the slow in-plane growth direction),¹²⁶ further allowing identification of the crystal direction in these samples.

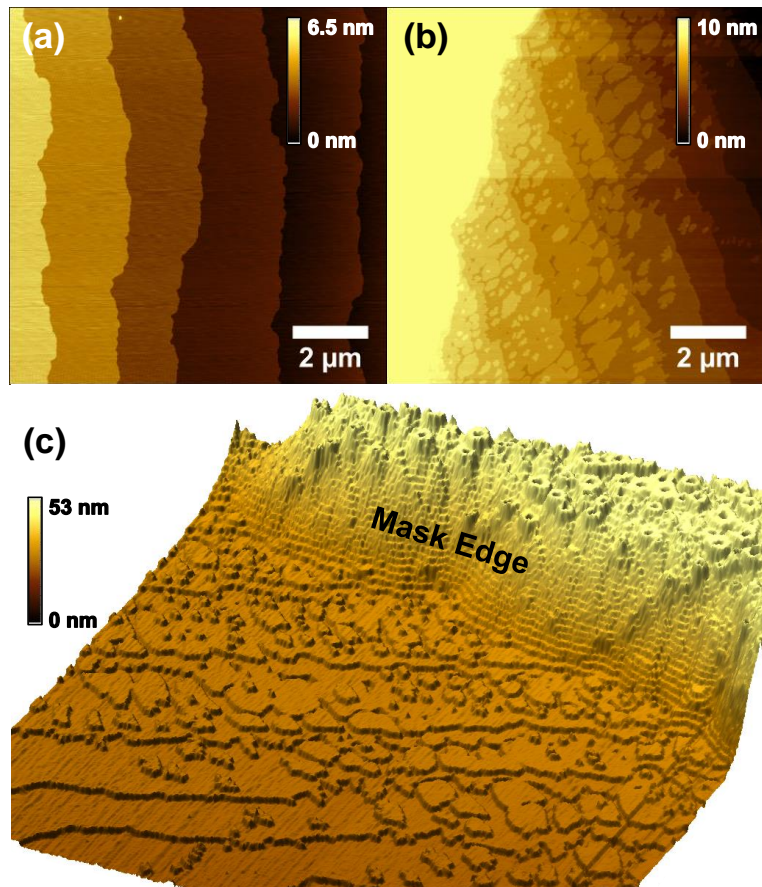


Figure 9.3. Homoepitaxial rubrene films on single crystals (a) single crystal surface, (b) homoepitaxy of 50 nm rubrene grown at 1 Å/s onto single crystal using a cleaved silicon edge as a mask, and (c) trimmed 3D rendering of (b), showing molecular steps and diffusing islands.

When additional material is deposited on the crystal, it displays mound-like morphologies

Homoepitaxy and Mixture Epitaxy in OPVs

consistent with Figure 9.2c-d in the thick, unmasked region, and flat islands one molecule tall in regions which have diffused away from the masked area or perhaps diffused in during deposition (Figure 9.3b-c). The morphology of the masked edge as a function of thickness supports the bulk development of screw dislocations responsible for the pitting and cylinder formation in Figure 9.2d. Irregularities in the layer-by-layer growth do not appear until the fourth or fifth layer along the edge, with increasing occurrence as the film grows thicker. These defects likely reach a critical density where they become self-inhibiting, yielding a relatively constant density above a certain film thickness and unifying Figure 9.2d and Figure 9.3c. It is also interesting to note the excessive formation of screw dislocations where the intrinsic molecular terraces pass under the epitaxial layer in Figure 9.3c, implying that an irregular template surface also plays a role in defect formation.

9.2.2. Homoepitaxial Devices

With the successful demonstration of epitaxial templating and morphology in films, this technique was generalized to device manufacture. This required the addition of an electron acceptor (C_{60}), an exciton blocking layer (bathocuproine, BCP), and a cathode (silver, Ag) in order to function (Figure 9.4). Silver was used as a cathode based on previous work in the literature, but tends to oxidize in air in conjunction with rubrene, making it somewhat problematic for devices. For future devices, aluminum (which is similar in workfunction to silver) should be explored as a cathode option. Note the difference in BCP thickness between thick and thin rubrene devices. For thicker epitaxial layers, the increased active layer roughness requires a thicker BCP layer to prevent

Homoepitaxy and Mixture Epitaxy in OPVs

shorting, optimized at 20 nm.

Using the architectures in Figure 9.4a-b, the devices show performance consistent with previously reported work (Figure 9.4c).¹⁷⁴ Initially, crystalline cells suffer from a low V_{oc} and reduced J_{sc} , but these parameters recover with thicker films. The lower V_{oc} has two

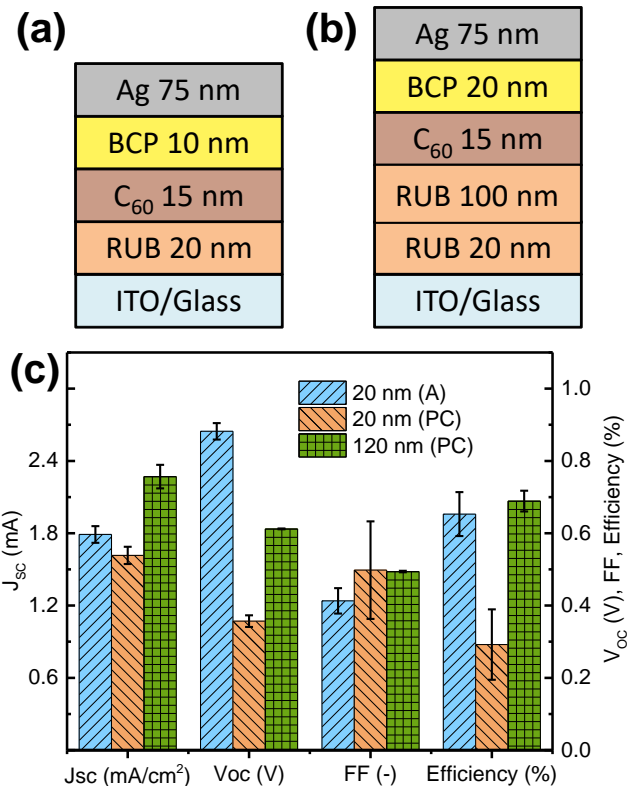


Figure 9.4. Homoepitaxial rubrene (RUB) devices, showing the architectures used for (b) 20 nm and (c) 120 nm devices and (c) resulting optoelectronic performance.

origins, energy level rearrangement and film roughness or defects. The HOMO of rubrene has been reported to decrease by (450 ± 50) meV upon crystallizing,⁷¹³ which would reduce the energy level offset which produces V_{oc} .¹⁷⁴ This would explain a drop in V_{oc} from 0.9 to 0.45 V upon crystallizing, but not to the observed 0.35 V. The remaining difference is likely due to shunts within the devices from C_{60} contacting or nearing ITO at

grain boundaries, nucleation sites, and thermally ripened defects which increases the device dark current. Indeed, when additional material is deposited, these shunts are likely covered and may even contribute to a higher, more amorphous V_{oc} . The difference in device J_{sc} is due to the loss of the longest-wavelength absorption feature from the orientation of the molecule within the orthorhombic unit cell, causing that absorption direction to be

Homoepitaxy and Mixture Epitaxy in OPVs

perpendicular to the incident light field.^{174,594} The absence of this feature is notable in the device η_{EQE} plots shown in Figure 9.5 (there are no 20 nm crystalline devices because of high leakage currents). Further, a trend in photocurrent with thickness is apparent, with the total η_{EQE} increasing, then decreasing with thickness (Figure 9.5b) and the rubrene contribution steadily increasing (Figure 9.5c). The increased absorption of thicker rubrene films explains the latter result, while it is suspected that materials purity plays a role in the former. With increasing thickness, responsivity and fill factor each initially increase through 114 nm, then decrease. Even though sublimed-grade materials from Luminescent Technology were used in this study, for additional improvement, triple purification of materials as listed in Verreet *et al.* would be a viable path to pursue.¹⁷⁴

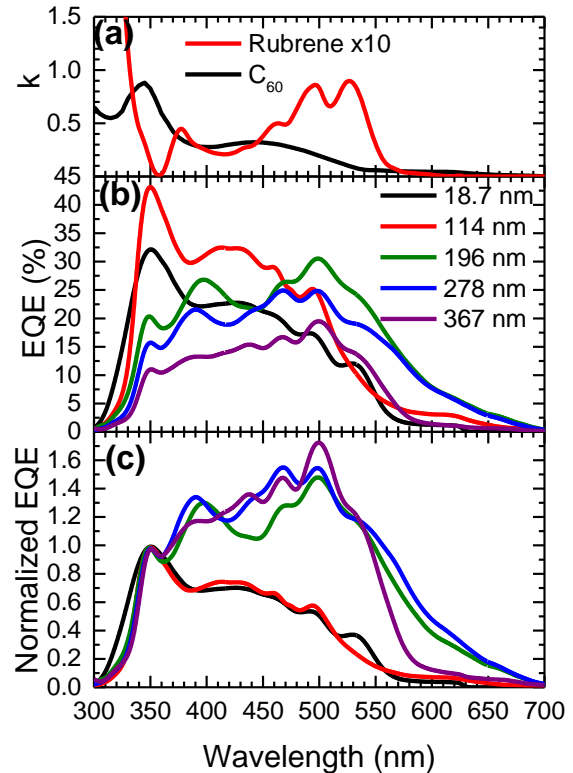


Figure 9.5. (a) Extinction coefficient k for rubrene and C_{60} for comparison to the external quantum efficiencies of crystalline rubrene epitaxial devices varying with rubrene thickness (18.7 nm is an amorphous comparison) (b) as collected and (c) normalized to the C_{60} peak at 350 nm.

9.3. Mixture Epitaxy

The concept of mixture epitaxy is essentially the same as homoepitaxy, but with deposition of a mixed overlayer instead of neat overlayer. This allows the epitaxial layer to take on the additional features of the mixture while ideally still preserving the benefits

of the crystalline matrix.

9.3.1. Mixture Epitaxy with an Inert Additive

Rubrene is a poorly absorptive material, as may be inferred by the lack of photoresponse and low extinction coefficient in Figure 9.5. However, rubrene has favorable charge and exciton transport properties, which suggests that it would be beneficial to incorporate a second, highly absorptive material within the established rubrene matrix. In testing this hypothesis, a control experiment with the optically and

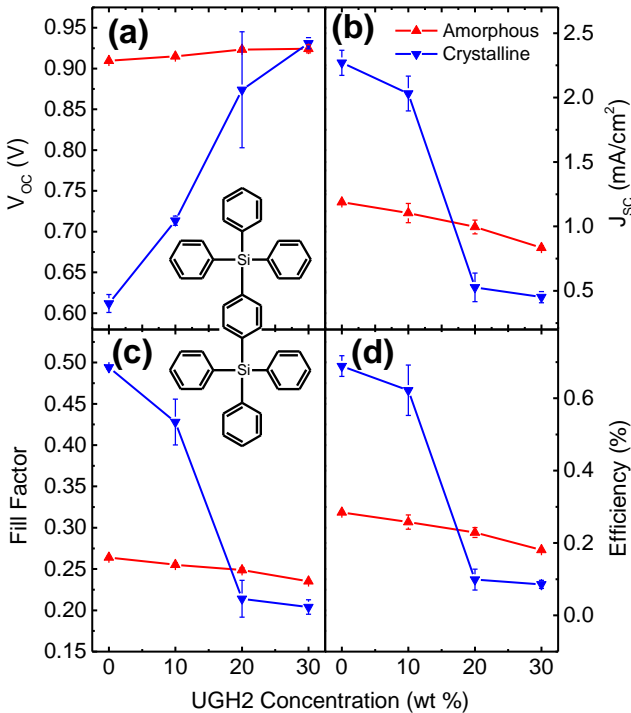


Figure 9.6. Device parameters for rubrene planar devices as a function of epitaxial layer UGH2 concentration: (a) V_{oc} , (b) J_{sc} , (c) fill factor, and (d) power conversion efficiency. Device architectures: ITO // Rubrene 20 nm (1 Å/s, anneal 45 sec at 170 °C) // Rubrene:UGH2 55 nm (2 Å/s) // C_60 15 nm (2 Å/s) // BCP 20 nm (2 Å/s) // Ag 75 nm (0.5 Å/s).

electrically inert molecule UGH2 (Benzene, 1,4-bis(triphenylsilyl)-;1,4-Phenylenebis(triphenylsilane)) was performed.

UGH2 has a very large HOMO-LUMO gap, making it non-absorptive in the spectral regions of interest and causing it to exclude carriers energetically, and has been used in solid-state dilution studies with other compounds.^{198,237,238} In amorphous devices (Figure 9.6), increasing UGH2 concentration increases V_{oc}

slightly (possibly due to a solid-state solvation effect),¹⁹⁸ decreases photocurrent due the

Homoepitaxy and Mixture Epitaxy in OPVs

replacement of photoactive material with one which is inert, and causes a reduction in fill factor, possibly implying a more resistive active layer with increasing UGH2 concentration. Crystalline devices respond much differently, with precipitous changes in all parameters. With increasing UGH2 concentration, V_{oc} increases steadily from the crystalline value to that of amorphous, implying a steady transformation between totally crystalline and

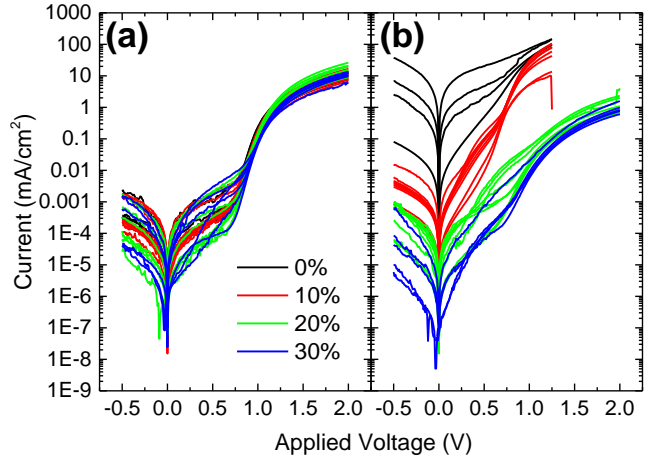


Figure 9.7. Dark currents of rubrene devices with increasing UGH2 content for (a) amorphous and (b) polycrystalline template films.

majorly amorphous within the active layer. This is also manifested in the device dark currents, which show dramatic reductions with increasing volume fraction of UGH2 (Figure 9.7). As the impurity concentration increases, this transformation (or breakdown of crystalline growth) likely occurs earlier, giving a greater amount of amorphous material. This threshold is most pronounced in J_{sc} and fill factor, each of which fall off sharply after 10 % UGH2, suggesting disruption of crystallinity at critical interfaces which dictate dissociation and recombination, like the donor-acceptor interface.

These observations are corroborated by the device η_{EQE} , shown in Figure 9.8. The amorphous devices show a steady reduction in photoresponse across the full spectrum, supporting the concept of an increasingly resistive active layer hindering charge collection, as well as a larger drop in the rubrene region from UGH2 substitution for rubrene.

Homoepitaxy and Mixture Epitaxy in OPVs

Crystalline devices are particularly notable for the disappearance of the absorption feature at 540 nm for pure crystalline devices, followed by partial recovery of the feature for 10 %

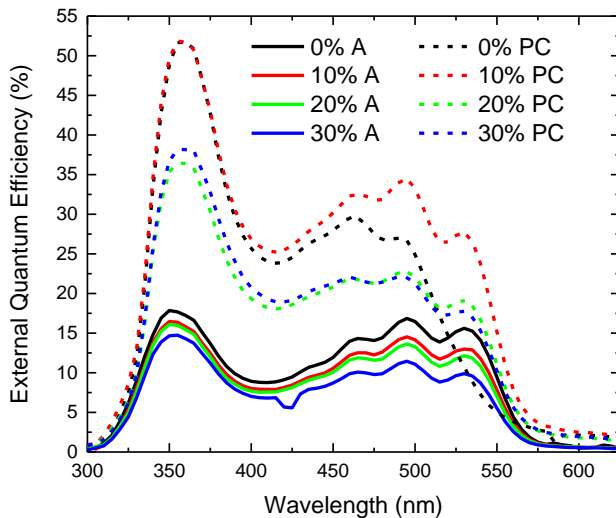


Figure 9.8. η_{EQE} for rubrene devices with increasing UGH2 content. A = amorphous, PC = polycrystalline template.

UGH2, then identical rubrene spectra for 20-30%. Using the presence of this feature and the photoresponse of C_60 as indicators of amorphous material present, this trend implies that there is considerable reversion of the epitaxial material with increasing UGH2, especially above 10 %. The absolute

shift in response is likely from increased charge conduction in crystalline material, with the residual difference in 20-30% arising from the crystalline template layer, which is unchanged by additional depositions.

Morphological characterization yields a rather pronounced change with increasing UGH2 content, as shown in Figure 9.9. Neat layers appear as described earlier (Figure 9.2c, Figure 9.3c), but the crystalline

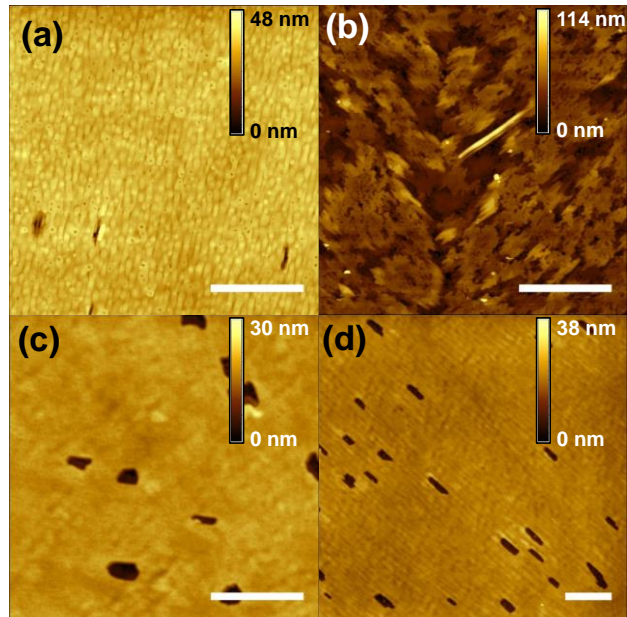


Figure 9.9. AFM images of the epitaxial rubrene:UGH2 active layer on crystalline template, with UGH2 content (a) 0, (b) 10, (c) 20, (d) 30 vol%. All scale bars 3 μ m.

order is considerably disrupted by the inclusion of even 10 vol% UGH2 and appears generally featureless at higher concentrations, reminiscent of amorphous films. This matches the electrical trends, although the roughness of Figure 9.9b may be somewhat problematic for devices with a very thin acceptor and blocking layer and may explain the relatively high photocurrent in Figure 9.6b as deriving from higher interfacial area for exciton dissociation.

9.3.2. Mixture Epitaxy with C₆₀

The results with UGH2 suggest that mixed devices using an electron acceptor may expect perseverance of crystallinity to useful acceptor levels (10 vol%), with a potentially beneficial interface structure simply by incorporation of a small concentration of acceptor. To test this, a series of devices were grown with architectures of the previous section, but with a 45 nm epitaxial layer and C₆₀ substituted for UGH2.

These devices differ somewhat from the

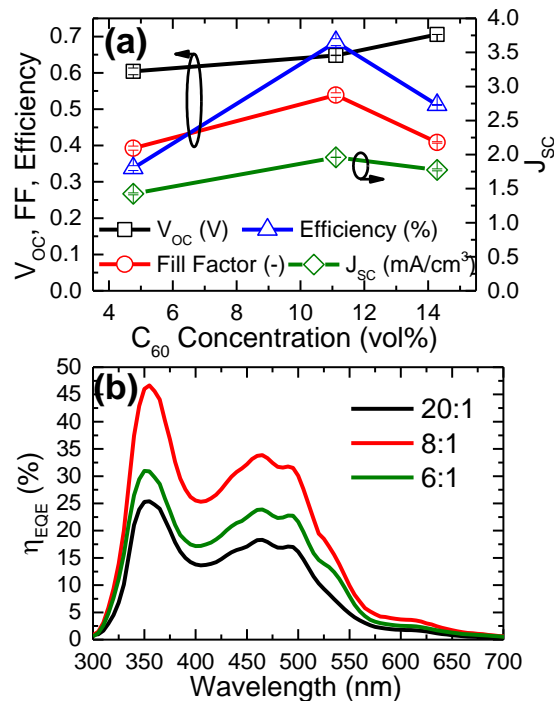


Figure 9.10. Performance of mixture epitaxy devices with C₆₀ as the impurity and a crystalline template: (a) device parameters and (b) η_{EQE} with the rubrene:C₆₀ ratio. Architecture: ITO // Rubrene 20 nm (1 Å/s, anneal 45 sec at 170 °C) // Rubrene:C₆₀ 45 nm (2 Å/s) // C₆₀ 15 nm (2 Å/s) // BCP 20 nm (2 Å/s) // Ag 75 nm (0.5 Å/s).

rubrene:UGH2 case, as shown in Figure 9.10. V_{oc} continues to increase with impurity, but with a weaker dependence. J_{sc} increases, but does not fall off entirely after reaching the 10

Homoepitaxy and Mixture Epitaxy in OPVs

vol% point critical to UGH2, likely because C₆₀ is considerably more absorptive than rubrene and UGH2, allowing the devices to absorb more incident light and dissociate excitons at the multitude of interfaces formed throughout the bulk film. At high enough concentrations, the crystallinity is likely breaking down, evidenced by the drop in fill factor and presence of the 540 nm rubrene feature in η_{EQE} plots, Figure 9.10b.

These mixed rubrene:C₆₀ solar cells also emit visibly bright yellow-orange light when driven at high enough forward bias (~8-9 V), yielding spectra shown in Figure 9.11. Rubrene is known to electroluminesce in OLED structures,^{714,715} so it is perhaps not

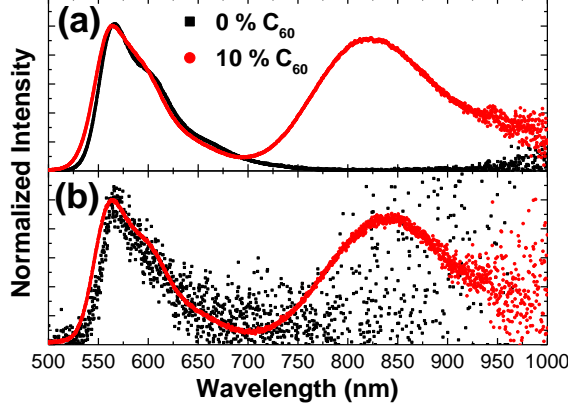


Figure 9.11. Electroluminescence of mixed rubrene:C₆₀ devices with an (a) amorphous and (b) crystalline template layer.

nm in PL,⁷¹⁶ compared to 565 and 610 nm in EL), with a long-wavelength feature (~850 nm) in mixed films which is likely emission of a charge-transfer state of energy ~1.5 eV,¹⁹⁰ significantly less than the HOMO-LUMO offset of rubrene and C₆₀ of 2.7 eV and 1.9 eV for amorphous and crystalline rubrene, respectively. Neat crystalline rubrene shows similar signatures, but considerably less emission in neat films. Crystals of rubrene photoluminesce quite efficiently,^{147,195,370} so perhaps this significant reduction is instead

surprising that this emission occurs in an OPV materials stack, however inefficiently. Amorphous rubrene displays a single, bright emission feature with 2-3 vibronic states which are red-shifted relative to those observed in photoluminescence (peaks at 540 and 580

Homoepitaxy and Mixture Epitaxy in OPVs

due to carriers more efficiently finding and deactivating excitons due to the higher carrier mobility. With the incorporation of C₆₀ into the epitaxial layer (and disruption of the crystallinity), this emission becomes much stronger and the CT state is again observed. The observed difference in peak energies is ~30 meV, but this could be due to a number of factors including spectrometer baseline fluctuation and device burn-out.

What is perhaps more striking is the morphological differences with the incorporation of C₆₀ (Figure 9.12). Unlike UGH2, where the crystal lattice is slightly disrupted at 10 vol% and then amorphized at 20 vol%, C₆₀ shows more destructive behavior: even at 5 vol%, the film is considerably roughened and small domains begin to appear (Figure 9.12a, d). When this concentration is increased to 12.5 vol%, dendritic regions of rubrene appear fractured

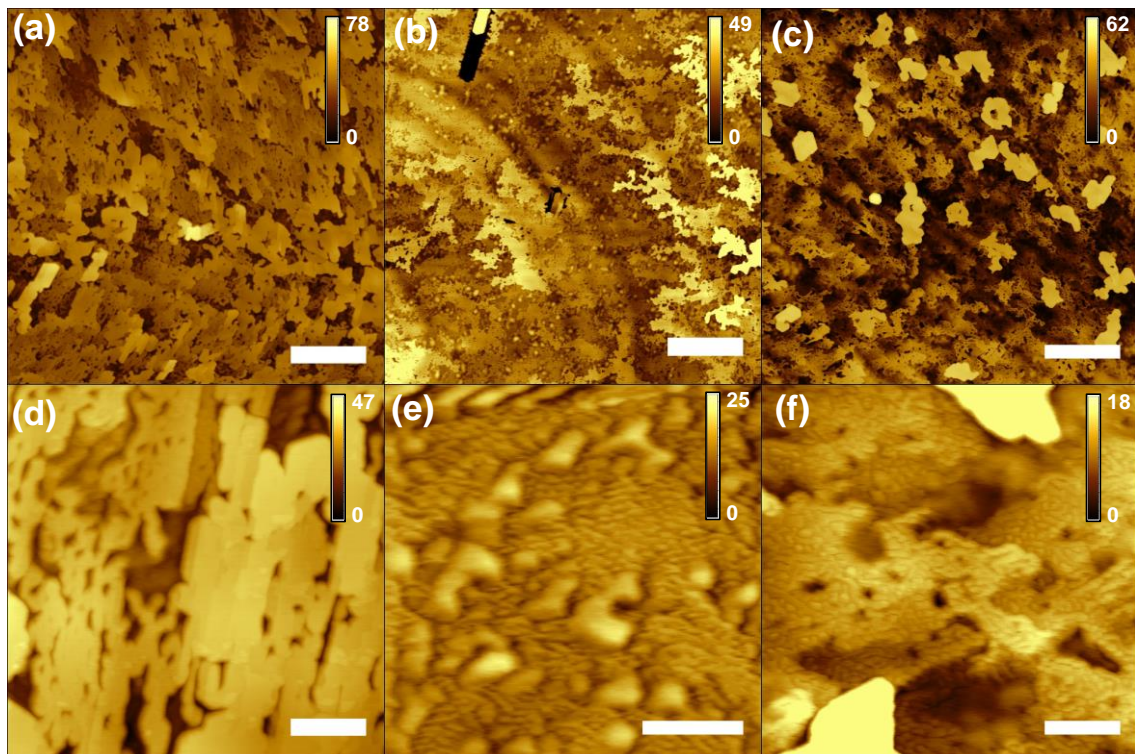


Figure 9.12. AFM images of the epitaxial rubrene:C₆₀ active layer on crystalline template, with rubrene:C₆₀ ratios (a), (d) 20:1; (b), (e) 8:1, (c), (f) 6:1. Scale bars (a)-(c) 1 μm, (d)-(f) 200 nm.

Homoepitaxy and Mixture Epitaxy in OPVs

across the surface of crystals, with even more pronounced and smaller domains (Figure 9.12b, e). At higher concentration still, the rubrene crystals effectively grow as islands with size perhaps limited by the maximum distance C_{60} can diffuse before becoming buried (Figure 9.12c). Between these crystalline islands, the underlying film displays even more finely textured regions, potentially due to phase separation of rubrene and C_{60} (Figure 9.12f).

9.4. Discussion of Mixture Epitaxial Growth

Inclusion of an impurity in the growing matrix of an epitaxial film disrupts crystallization and the propagation of crystallinity from the template layer. The dominant morphological effect studied here was that of concentration, where at large C_{60} concentrations, deposited rubrene is reasonably likely to encounter a C_{60} molecule (at 10 vol% impurity, each surface lattice site will on average touch one impurity molecule), reducing conformation forces that would normally adapt it into the crystal structure (Figure 9.13a-b). In reality, these molecules likely phase-separate into microscopic regions which slightly improve the perseverance of crystallinity,^{118,688,717} but only within diffusive limits. The total distance that molecules can diffuse after deposition depends on the substrate temperature, interaction strength and roughness of the underlying layers, and deposition rate.^{109,357,445,718–723} The diffusivity of a material increases exponentially with temperature, typically yielding larger grains at higher substrate temperatures.³⁵⁷ A slower deposition rate allows a molecule greater time on the film surface before becoming buried, prolonging the extent of diffusion (Figure 9.13c-d). This should be counterbalanced with the impingement

Homoepitaxy and Mixture Epitaxy in OPVs

of other contaminating or disruptive molecules on the surface which can become problematic at extremely low deposition rates;¹⁰⁹ thus, there exists an optimum rate as compromise in these parameters to minimize total defect incorporation (Figure 9.13e-f).

The deposition rate and substrate temperature dependence of this system were not studied

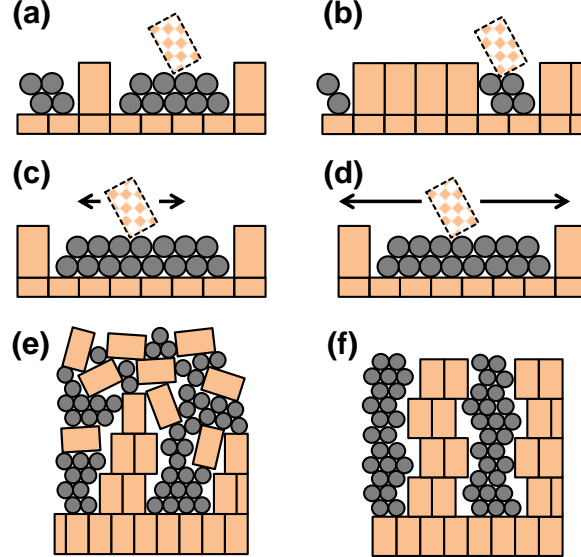


Figure 9.13. Models for mixture epitaxy: concentration effects for (a) low and (b) high host fraction; diffusivity effects showing (c) low and (d) high diffusivity; and defect accumulation (e) dominant and (f) minor.

in this study, presenting an opportunity for future exploration.

The incorporation of an absorptive material within the crystalline rubrene matrix did not significantly improve device efficiency despite anticipation from rubrene:UGH2 devices. Even in comparison to the crystalline control device, the rubrene:C₆₀ mixtures show reduced efficiency. What is surprising is

that V_{oc} , a harbinger of lattice disruption, does not increase remarkably (100 mV) for rubrene:C₆₀ stoichiometry up to 6:1, whereas the rubrene:UGH2 case increases almost twice that over the same range despite having less visible morphology changes. Part of this may be related to recombination of photogenerated charges on electrically isolated C₆₀ molecules within the bulk of rubrene, manifested in a change in the dark current of these devices. In this regard, it would be especially useful to vary deposition rate and substrate temperature in an attempt to create the idealized columnar morphology shown in Figure

9.13f.

In terms of generalizing these results, it would be naïve to assume that rubrene:UGH2 will perfectly mimic rubrene: C_{60} interactions, since the size and shape of the molecules and orbitals differ substantially. However, there appear to be hallmark morphology changes which occur within 10 vol% of impurity and initiate electrical changes that should be observable in other systems. Furthermore, this work shows that it is possible to propagate crystallinity in mixed epitaxial films of normally amorphous materials, albeit at lower mixture concentrations than in cases using microcrystalline materials.^{588,724} This range may be broadened through the variation of substrate temperature and deposition rate, increasing the viability of this technique in general OPV materials.

9.5. Conclusions

Functional crystalline rubrene OPVs were successfully manufactured using both homoepitaxy and mixture epitaxy. Crystallinity allows for more efficient thick devices, but these are ultimately limited by low fill factor potentially related to materials purity. With the introduction of additional materials into epitaxial rubrene films, the films undergo remarkable morphological changes, with roughening and a breakdown of crystallinity above approximately 10 vol% for UGH2 and C_{60} , characterized by a recovery of the amorphous V_{oc} . Although C_{60} is absorptive and exciton-dissociating, mixed devices performed poorly, suggesting additional work is necessary to optimize growth conditions.

10. MOLECULAR TEMPLATING IN SUBPC OPVS

Homoepitaxy is useful in situations when film crystallization processes changes with thickness, as discussed in Chapter 7. To achieve morphologies that are not possible for a particular material, heteroepitaxy or templating by a different material may be suitable. Annealed films of SubPc are rough and defect-ridden, which complicates their use in OPVs, but growth on a template material is a method to circumvent this roughness. The template layer studied likely dissociates excitons and was not sufficient to induce crystallization in room-temperature depositions (and is not true molecular template growth for that reason), but provides an insightful counterexample to that presented in Chapter 7.

10.1. Introduction

As discussed in Chapter 2, the efficiency of organic photovoltaic cells (OPVs) is dictated by the efficiency of photon absorption, exciton diffusion and dissociation, and charge collection within the cell.^{38,175} To circumvent the disparate length scales for absorption (≥ 100 nm) and exciton diffusion (1-10 nm),^{365,686,687} modern high-efficiency devices often feature bulk heterojunction instead of planar heterojunction architectures,^{552,560,588,725,726} but many bulk heterojunctions suffer from a low charge collection efficiency compared to planar cells.^{100,727} Alternatively, an increase in the

Molecular Templating in SubPc OPVs

exciton diffusion length to be commensurate with that of absorption could enable efficient planar architectures in terms of exciton and charge carrier harvesting. Recently, OPVs based on planar heterojunction architectures have experienced renewed research interest, further motivating work to improve L_D .^{174,198,690} One method in particular towards this goal is molecular templating, the use of a crystalline template layer to induce crystallization in materials which do not crystallize or crystallize in detrimental ways (uncontrolled polymorphism, roughness, dewetting, etc.). This work highlights the interactions between boron subphthalocyanine chloride (SubPc) and 5,5'-bis(4-biphenylyl)-2,2'-bithiophene (BP2T) in planar photovoltaic cells.

SubPc is interesting as a photovoltaic material for its ability to produce OPVs with remarkably high V_{oc} (> 1 V) and also high efficiency.^{100,704,728} The cupped molecular conformation arising from missing one of the phthalocyanine arms also means that SubPc does not crystallize during deposition onto substrates not actively heated.¹⁰⁰ Although some non-planar molecules have been explored (vanadyl phthalocyanine, VOPc),⁷²⁹ SubPc remains interesting for its strong device performance which could be improved with an enhanced exciton diffusion length and hole mobility.^{100,198}

10.2. Template Optimization

The optimal template film would be molecularly flat, high mobility, and energetically resonant with the electrode and organic overlayer. The template used in this work, BP2T, has been shown to form very smooth, high-(hole)-mobility thin films which have a low injection barrier to an ITO electrode.^{588,730} After obtaining this material, the first step was

Molecular Templating in SubPc OPVs

to optimize the film morphology in terms of smoothness and crystallinity. In this space, there are three primary ways to manipulate morphology: deposition rate, substrate temperature during deposition, and substrate type. These effects are shown for varying growth rate and substrate at fixed temperature in Figure 10.1. For a complete data set across all three parameters (including high-resolution AFM), the reader is referred to Appendix

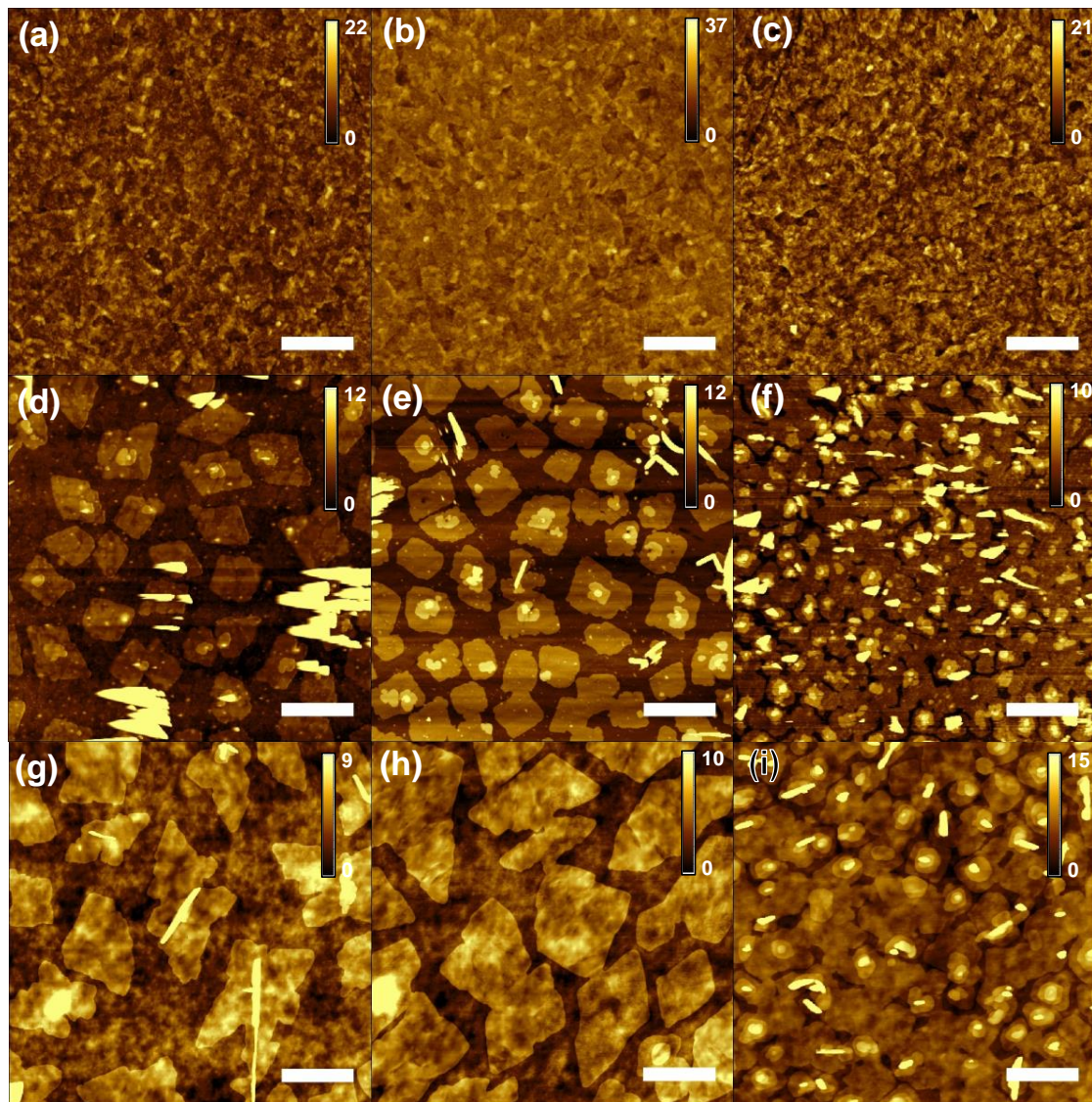


Figure 10.1. Effects of substrate type and growth rate of 10-nm BP2T films grown at 100 °C on (a)-(c) bare ITO, (d)-(f) quartz, and (g)-(i) ITO spin-coated with 50 nm PEDOT:PSS. The film deposition rate increases across columns left to right: 0.1 Å/s, 0.3 Å/s, and 1.0 Å/s. AFM scale bars 1 μm, height in nm.

H. In general, BP2T on ITO displays a film-like morphology with localized regions on the tips and edges of ITO flakes, with little morphological trend across the rates probed here. For a comparison to neat ITO, the reader is referred to Appendix O. This contrasts starkly with the layer-by-layer type growth observed on smooth substrates such as quartz and PEDOT:PSS planarized ITO, where BP2T forms islands of material punctuated by intermittent spikes of material. These islands increase in density and coverage with increasing deposition rate, suggesting a diffusion-limited aggregation type of growth on these smooth substrates.^{357,388,418,471,472,487,731,732} On bare ITO, BP2T may not have enough mobility or planarity to coalesce into ordered monolayers.

10.3. Heterostructure Morphology Characterization

To elucidate the morphological variation of device-relevant films which include SubPc and other device layers, a number of techniques were employed to study the film surface and structural properties, including AFM, XRD, and TEM. These tests and results are presented in the following sections.

10.3.1. Surface Characterization

When this template is used with a SubPc overlayer, there is subsequent ordering which occurs, as shown in Figure 10.2. Without BP2T, these films are relatively featureless, with any morphology from the underlying ITO layer. Similarly, the cathode over the device stack shows only a granular metal morphology. When BP2T is included, the films on untreated ITO show some roughening which mimics the underlying BP2T observed in

Molecular Templating in SubPc OPVs

Figure 10.1b, while there is significantly more restructuring on the smooth, planarized BP2T films (Figure 10.2c, f). These films show small grains of organic collected on the surface surrounded by a ring of material. This likely represents the bulk and edge of the BP2T grains,

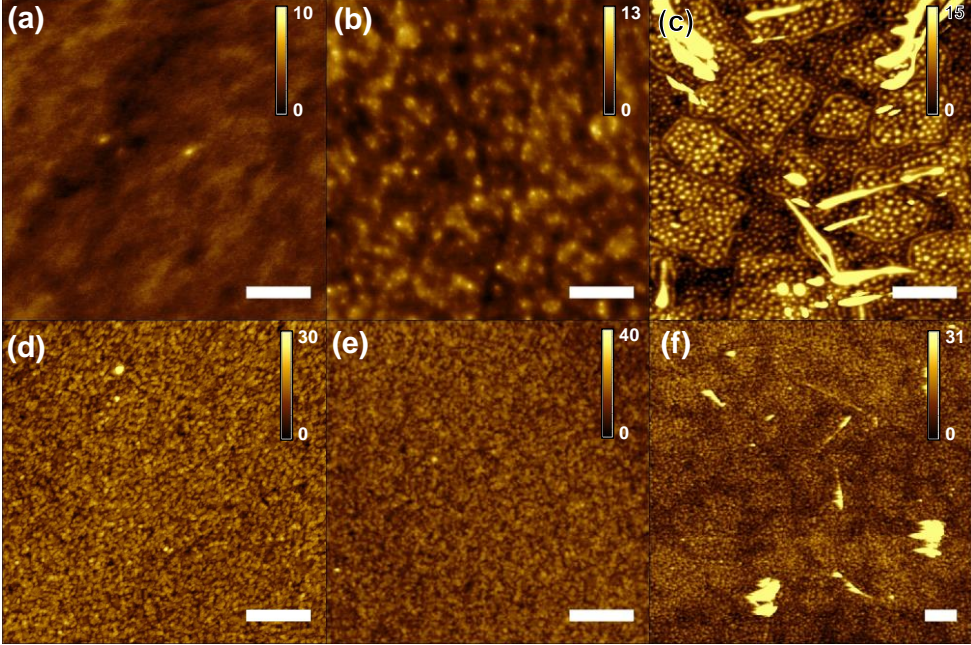


Figure 10.2. The morphology of SubPc planar device stacks grown on top of (a), (d) bare ITO, (b), (e) ITO with BP2T 8 nm, 0.3 Å/s, 100 °C, and (c), (f) ITO planarized with 50 nm PEDOT-PSS, then with BP2T 8 nm, 0.3 Å/s, 100 °C. (a)-(c) are the top-most organic surface, (d)-(f) are the aluminum cathode surface. AFM scale bars 1 μm, height in nm. Device structure: ITO//SubPc 13 nm//C₆₀ 35 nm//BCP 10 nm//Al.

respectively, with ring formation as a result of the Schwoebel barrier hindering molecular diffusion over the lower-coordination molecular terrace edge and causing material pile-up at the edge,^{408–411} similar to what has been observed in the past with deposition of thin organic films onto crystalline terraces.¹²² Material stranded in the center of BP2T grains simply aggregate into domains, the size of which is related to the diffusion length of the depositing molecules. This has the unfortunate property of preserving the tall structures of BP2T observed on very smooth substrates, even to the extent of causing their appearance through the cathode surface in Figure 10.2f, causing blurring of the image from tip fouling on those features. This morphology greatly reduces the chance of manufacturing a

Molecular Templating in SubPc OPVs

functional device without shunts, and was thus investigated minimally.

Somewhat more promising are the films grown on BP2T on bare ITO, as these present evidence of possible secondary reconstruction of the overlayer and simultaneous low film roughness, possibly more amenable to device operation. A logical comparison of this morphology is as a function of SubPc deposition rate, which influences the amount of time available for deposited molecules to diffuse about the surface before being buried by additional material. If the behavior observed in Figure 10.2 is actually due to molecular diffusion, these domains might be expected to increase in size at lower growth rates to the extent permitted by the substrate roughness or the underlying BP2T grain size. As shown in Figure 10.3, the SubPc domains simply become better-defined with slower deposition rates. This is likely due to the limiting size of the small BP2T grains on ITO. At faster deposition rates, these domains still form, but less completely, giving the appearance of increasing domain size at faster deposition rates. This is strictly an effect of SubPc on BP2T, since films on bare ITO show no difference at different rates.

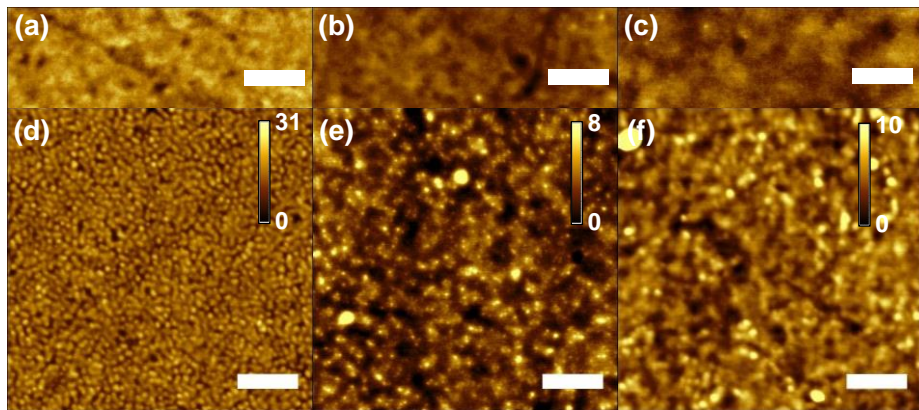


Figure 10.3. The morphology of 13 nm SubPc grown on (a)-(c) bare ITO, and (d)-(f) 8 nm BP2T, with BP2T grown at 0.3 Å/s, 100 °C. SubPc growth rates are (a), (d) 0.1 Å/s, (b), (e) 1.0 Å/s, and (c), (f) 10.0 Å/s. All scale bars 1 μ m, height scales in nm.

diffusion, these domains might be expected to increase in size at lower growth rates to the extent permitted by the substrate roughness or the underlying BP2T grain size. As shown in Figure 10.3, the SubPc domains simply become better-defined with slower deposition rates. This is likely due to the limiting size of the small BP2T grains on ITO. At faster deposition rates, these domains still form, but less completely, giving the appearance of increasing domain size at faster deposition rates. This is strictly an effect of SubPc on BP2T, since films on bare ITO show no difference at different rates.

10.3.2. Structural Characterization

Though the film reorganization observed on the surface is suggestive, true molecular templating is demonstrable by crystallization of the overlayer, typically with a specific orientation relative to the template. This can be proven by the existence of diffraction features with electron, x-ray, or other forms of radiation of suitable wavelength. Being comprised of low-atomic number atoms, many organic thin films are challenging to scatter from with average x-ray diffractometers because the signal can be barely above the noise.

For this reason, it was not necessarily surprising to not observe x-ray diffraction of SubPc grown on top of BP2T since SubPc diffracts weakly even in neat crystalline films, with thickness under ~50 nm registering no signal above the background noise on a lab-based diffractometer (Figure 10.4). However, crystalline

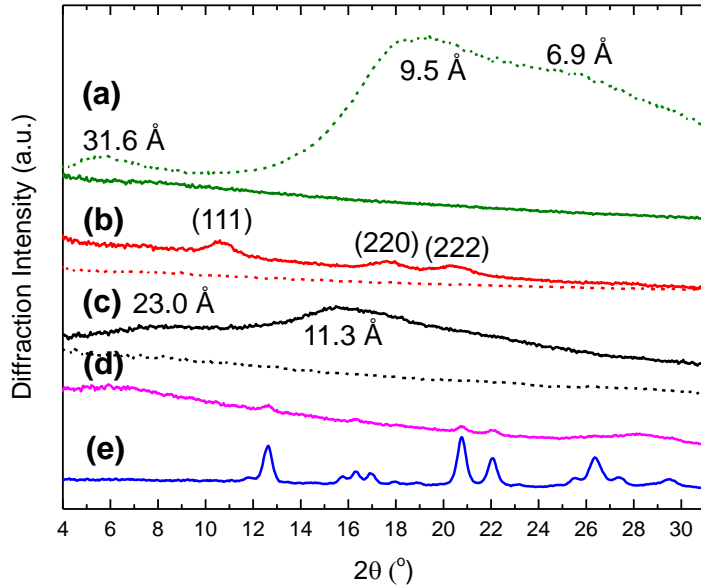


Figure 10.4. X-ray diffraction patterns with a lab-based Cu K_α source for (a) SubPc/C₆₀, (b) C₆₀, and (c) SubPc grown on silicon with (dashed) and without (solid) an 8 nm BP2T layer on silicon grown at 0.3 Å/s, 100 °C. SubPc 13 nm, C₆₀ 35 nm. (d) 75 nm and (e) ~700 nm SubPc films on silicon annealed at 150 °C for 30 min. Distances near peaks represent the interplanar spacing for that diffraction angle.

SubPc films yield well-defined patterns when measured at a synchrotron, giving an unambiguous crystallite orientation with the (022) plane parallel to the substrate, as shown in Appendix H.2.

Molecular Templating in SubPc OPVs

Without ready access to a synchrotron, the next best diffraction technique available for organic thin films may actually be transmission electron microscopy. The fluence, energetic uniformity, and wavelength are all sufficient to probe organic samples at reasonable time and length scales in thin films especially. A selection of grid types also enables film morphologies which are consistent with devices or films. The samples discussed here (Figure 10.5) closely mimic the results for SubPc grown on BP2T on smooth

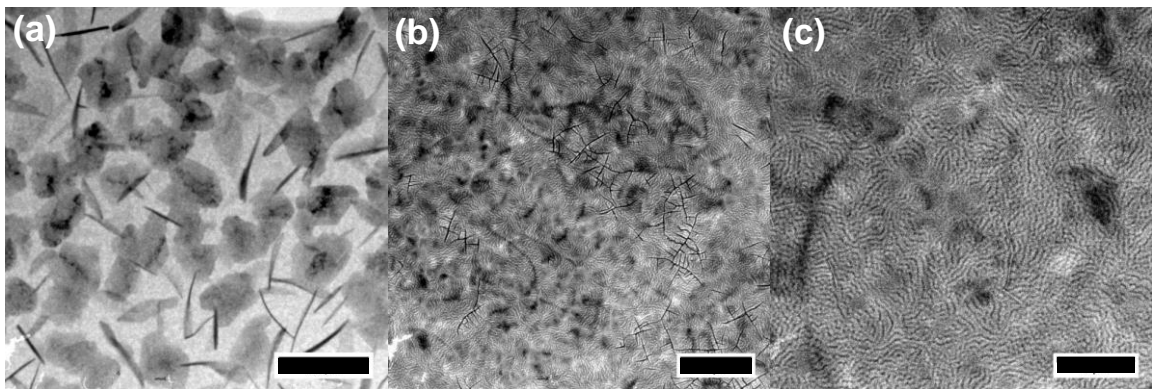


Figure 10.5. Brightfield TEM images of (a) 25 nm BP2T (0.3 Å/s, 100 °C) on Quantifoil and (b), (c) 25 nm SubPc (1 Å/s, 25 °C) on 25 nm BP2T (0.3 Å/s, 100 °C) deposited onto SiO₂ window TEM grids. Scale bars (a) 0.5, (b) 5, and (c) 2 μm. Images captured by Dan Cremons, processing by the author.

or planarized substrates (Figure 10.2c), as may be expected from the smoothness of the TEM grids. Material domains show in these brightfield images through thickness contrast,⁷³³ where additional material scatters more electrons from the primary electron beam which forms the image, similar to rough films scattering light in an optical microscope. In Figure 10.5a, BP2T domains are evident as dark disks and narrow wires, while in Figure 10.5b-c the contrast arises largely from variations in the SubPc film which change transmission of the beam. These samples display layer-by-layer growth, with similar SubPc patterning and rippling from molecular diffusion. With a large aperture, these films show well-defined polycrystalline, textured BP2T diffraction (Figure 10.6),

Molecular Templating in SubPc OPVs

with BP2T orienting with the (001) plane parallel to the surface, as is expected from the substantial in-plane π -stacking and electrophilic hydrogens exposed on the outside edge of the molecule. This gives diffraction peaks which share the [001] zone axis.

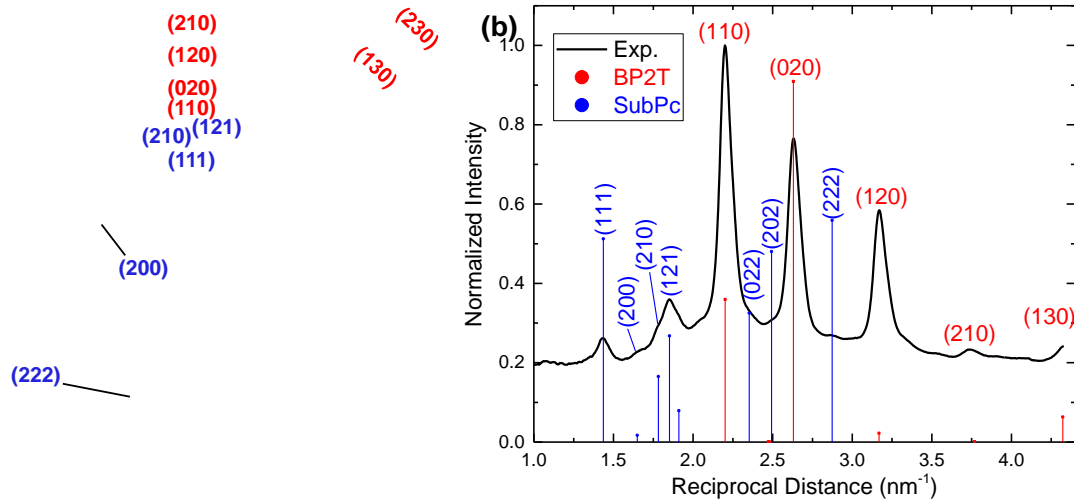


Figure 10.6. Electron diffraction on a $\sim 32 \mu\text{m}$ diameter area of a 25 nm SubPc (1 $\text{\AA}/\text{s}$, 25 $^\circ\text{C}$) on 25 nm BP2T (0.3 $\text{\AA}/\text{s}$, 100 $^\circ\text{C}$) deposited onto Quantifoil TEM grids. (a) 2D pattern and (b) integrated data compared to calculated peaks. Films with no BP2T show only amorphous rings. Pattern in (a) captured by Dan Cremons, analysis by the author.

SubPc is less distinct, showing planes which correspond to both the $[01\bar{1}]$ and $[10\bar{1}]$ zone axes. The crystallographic orientation observed before on inorganic substrates with the (022) plane parallel to the substrate is actually contained in the $[01\bar{1}]$ axis, suggesting that either the crystals are adopting a very different orientation on BP2T or they are much less textured. The 11° full width at half the maximum height (FWHM) in crystal orientation observed in Figure 14.17 is not enough to bring the (022) parallel to the substrate or to explain the coexistence of the two zone axes, implying instead that the crystals which grew are in two distinct regions of BP2T, less textured, or are randomly oriented. The absence of the strongly diffracting (022) peak in the diffraction pattern of Figure 10.6b would suggest that the crystals are probably not randomly oriented, leading to the conclusion that

Molecular Templating in SubPc OPVs

there are distinct regions of BP2T which nucleate SubPc. Considering the presence of vertical BP2T spikes and molecular terraces observed with AFM and in Figure 10.5, this is not necessarily a surprising result.

The existence of crystallites themselves is encouraging, but orientation between heteroepitaxial layers would be firm proof of molecular templating. Examining the samples with a smaller aperture produced diffraction patterns which were considerably more single-

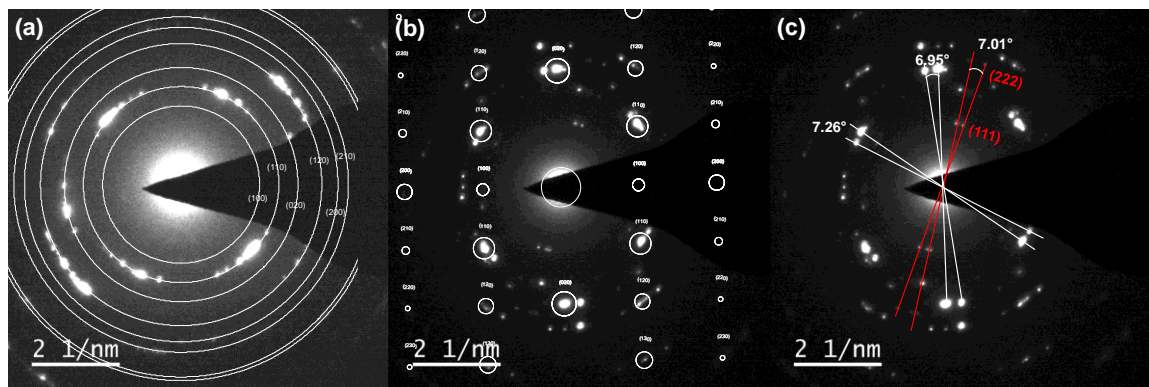


Figure 10.7. Selected area electron diffraction of a $\sim 1.6 \mu\text{m}$ diameter area of a on 25 nm SubPc (1 \AA/s , 25°C) on 25 nm BP2T (0.3 \AA/s , 100°C) deposited onto Quantifoil TEM grids. (a) example BP2T pattern showing similar grain orientation among neighboring grains compared to a simulated BP2T pattern along the [001] zone axis. A possible epitaxial relationship is shown in (b), with the BP2T pattern overlaid and the SubPc spots identified in (c). A similarity in the misorientation angle between the two BP2T and SubPc grains suggests a possible alignment between layers. Patterns captured by Dan Cremons, analysis by the crystalline in nature, but the majority contained only BP2T peaks (Figure 10.7). Of the few

that also showed SubPc, the only SubPc peaks which were present were the (111) and (222), which does not allow determination of the zone axis. Nonetheless, the misorientation between BP2T and SubPc peaks seems consistent between two sets of grains.

The presence of SubPc diffraction in Figure 10.6 and the lack of regions which produced SubPc diffraction in Figure 10.7 could be attributed to sample damage or simply a lack of regions with SubPc crystals. The diffracted intensity appeared stable over at least 120 seconds from SubPc and BP2T in all cases except convergent beam electron diffraction

Molecular Templating in SubPc OPVs

(CBED), where signal would disappear on the order of 60 seconds, even for BP2T. It is probable that there are simply few regions of material which diffract electrons, especially given that fresher films show even less SubPc diffraction. In spite of this scarcity, images were captured showing evidence for SubPc crystallizing on BP2T and showing the $[01\bar{1}]$ and $[10\bar{1}]$ zone axes (Figure 10.8), with slightly different crystallographic orientation of SubPc on BP2T for the $[10\bar{1}]$ zone (rotated 47.2° relative to Figure 10.7). This could perhaps be explained by the somewhat four-fold symmetry in the (001) plane of BP2T, where the unit cell axes are similar (5.7 \AA vs. 7.6 \AA) and molecules pack in a herringbone structure, but even so, it seems more likely that SubPc molecules crystallize with a textured out-of-plane axis (thus the two dominant zone axes observed), but randomly in-plane on the smooth BP2T planes.

If additional characterization to establish any epitaxial relationship were desired, a recommended next step would be to deposit SubPc at elevated substrate temperatures and slower growth rates for characterization by TEM. Alternatively, single crystals of BP2T could be grown out of vapor or solution and SubPc deposited on them for testing with a

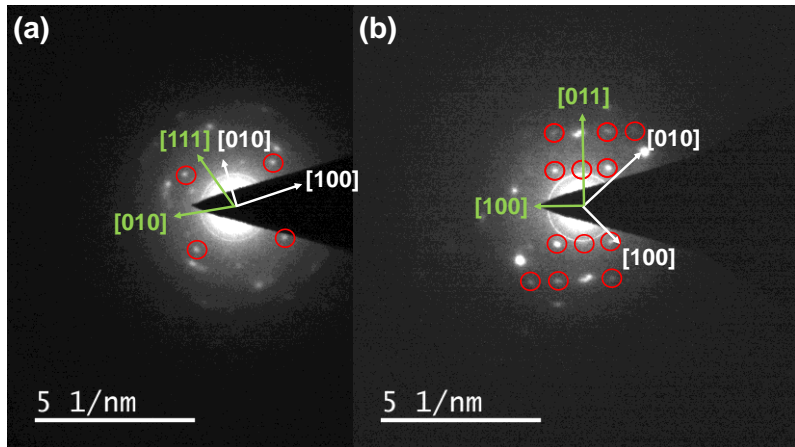


Figure 10.8. Selected area electron diffraction of a $\sim 1.6 \mu\text{m}$ diameter area of a 25 nm SubPc (1 \AA/s , 25°C) on 25 nm BP2T (0.3 \AA/s , 100°C) deposited onto Quantifoil TEM grids. SubPc shows (a) and $[10\bar{1}]$ and (b) $[01\bar{1}]$ zone axes on BP2T $[001]$. Green arrows denote directions of the SubPc unit cell, white of BP2T. Red circles correspond to SubPc peaks, with additional images provided in Appendix H.3. Patterns captured by Dan Cremons, analysis by the author.

Molecular Templating in SubPc OPVs

GIWAXS system with substrate rotation for in-plane alignment.

Despite the lack of proof for crystallinity in the SubPc overlayer, exciton diffusion may be enhanced by densifying or ordering the film according to the inverse dependence on distance discussed in Eqns. 2.4 and 2.16, which would not necessarily be detectable in diffraction studies. Ellipsometry is one technique to extract relative density changes by comparing the thickness of films deposited simultaneously but subject to different substrate or post-deposition conditions. The results of comparing multiple points on such samples are shown in Figure 10.9. As fit by Cauchy dispersion models, there is no observable difference in film thickness (and thus density) between SubPc grown on bare silicon or silicon with BP2T.

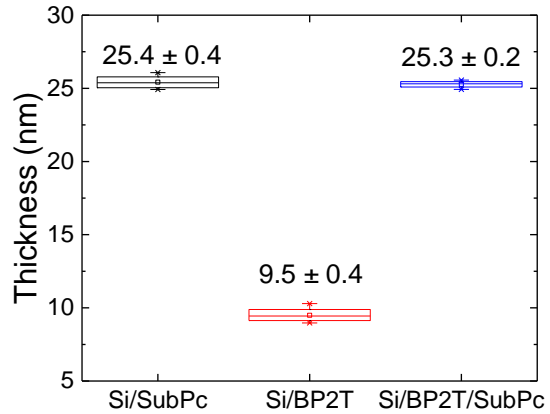


Figure 10.9. Comparison of organic film thicknesses by ellipsometry, including SubPc (1.0 Å/s, 25 °C) on silicon, BP2T on silicon (0.3 Å/s, 100 °C), and SubPc on BP2T on silicon (just SubPc component).

Ellipsometry is not the only method to measure film thickness: x-ray reflectivity (XRR) also allows for determination of thickness (and theoretically density independently), given relatively smooth films with reasonable electron density contrast between layers. Films of neat SubPc on silicon give pronounced interference patterns extending to 6 orders of magnitude above the noise floor (Figure 10.10a), implying well-defined parallel interfaces with reasonable dielectric contrast. When SubPc is evaluated on BP2T, this changes dramatically (Figure 10.10b). Though the films are comparable in thickness, films on BP2T

Molecular Templating in SubPc OPVs

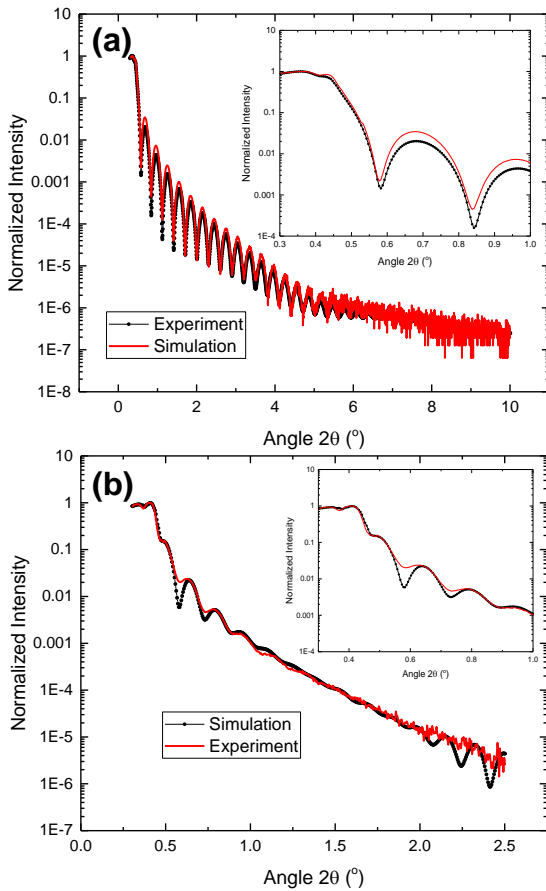


Figure 10.10. XRR on (a) 25 nm SubPc on Si (1.0 Å/s, 25 °C), and (b) 50 nm SubPc on 8 nm BP2T on silicon (0.3 Å/s, 100 °C). The first several interference features are shown in the inset plots. Data in (a) collected by Mike Manno and (b) by Javier Garcia-Barriocanal. Analysis by the author.

supposition of a rougher interface, particularly between BP2T and SubPc, where the surface roughness is comparable to the fitted BP2T thickness. Both cases yield densities which are less than the calculated

show only the first 5 interference fringes with considerably less definition over about 3 orders of magnitude. This is most likely due to the roughness of the surfaces reducing the scattering intensity. A summary of the fit parameters is given in Table 10.1. In both cases, the SubPc film was modeled as containing a thin substrate-induced layer (bottom) with different properties than the bulk layer (top). In both cases, this low-density surface layer extends approximately 3 SubPc monolayers into the film before bulk properties are achieved, perhaps similar to what is observed in CuPc thin films.⁷³⁴ The fitted roughness values reinforce the

Table 10.1. Fitted parameters for the XRR measurements shown in Figure 10.10, including film thickness, density (ρ), and roughness (σ_R) for the different layers and stacks.

Layer	Thickness (nm)	σ_R (nm)	ρ (g/cm ³)
Figure 10.10a			
SubPc (top)	27.34	0.44	1.47
SubPc (bottom)	1.75	0.13	1.24
SiO ₂	3.90	0.05	2.64
Figure 10.10b			
SubPc (top)	44.89	1.03	1.40
SubPc (bottom)	1.27	1.19	1.25
BP2T	4.16	2.59	2.00
SiO ₂	2.91	0.38	2.23

crystal (1.534 g/cm^3), with the SubPc film on BP2T marginally *less* than that on silicon. If there is a change in density, it is likely hindering diffusion rather than enhancing it. It should be emphasized that the multiple parameters allowed to vary within these fits leads to a rather broad solution criteria with a range of equally likely values. Thus, while these fitted values do not have confidence limits, the 5% deviation in density between the top SubPc layers is well within the observed margin for error of the fit.

10.4. Optical Characterization

The photoluminescence spectra for SubPc deposited on glass with and without BP2T are shown in Figure 10.11. Surprisingly, there is no change observed in the spectra of SubPc deposited on BP2T (Figure 10.11a), whether the BP2T is has been deposited at low or high temperature. Since crystallization has been shown to change the HOMO and LUMO levels for organic semiconductors,^{735,736} this implies that BP2T is either poorly dissociating when deposited at these temperatures or a serendipitous change in other

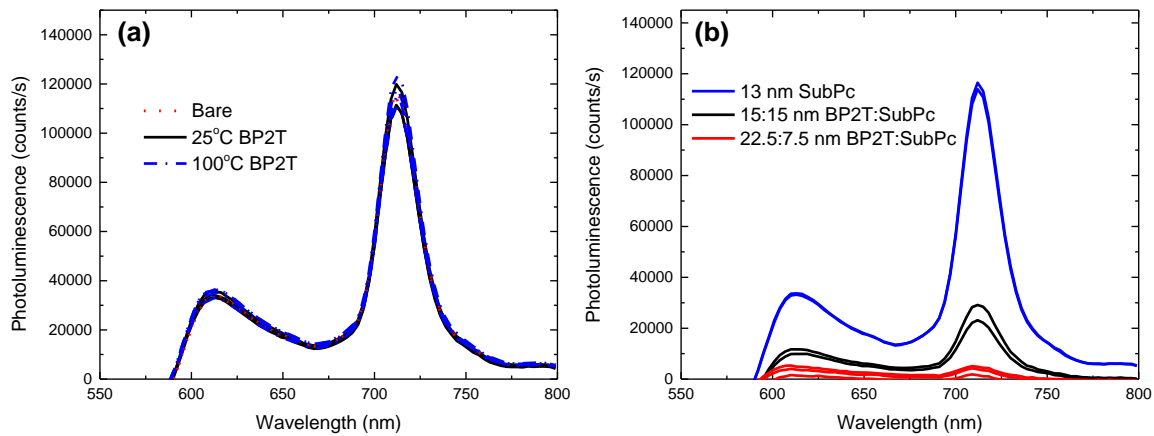


Figure 10.11. Photoluminescence emission spectra of SubPc films excited at 525 nm. (a) SubPc (13 nm, 1.0 Å/s, 25 °C) on glass previously deposited with different BP2T films (8 nm, 0.3 Å/s). (b) SubPc uniformly mixed with BP2T (net rate 1.0 Å/s, 25 °C) with thicknesses given in the legend. Films deposited on glass.

Molecular Templating in SubPc OPVs

properties cancels the exciton quenching effects by this interface. For comparison, a 13 nm SubPc film with an L_D of 10 nm which is completely quenched on one side should show over 50% reduction in photoluminescence from loss of dissociated excitons, so any dissociation would require significant changes in other film properties to compensate. From UV-Vis, the absorption of these films is unchanged, and transfer matrix modeling (Appendix R.1.) predicts almost identical optical fields within the SubPc layer. Measurements of η_{PL} also suggest that these values are within error for the bare and BP2T-coated glass. It is surprising, then, to see a reduction in photoluminescence when BP2T is uniformly mixed with SubPc, as shown in Figure 10.11b. These data show a steady reduction in photoluminescence with increasing BP2T concentration, even more than would be expected from loss of SubPc content. This would imply perhaps that BP2T is

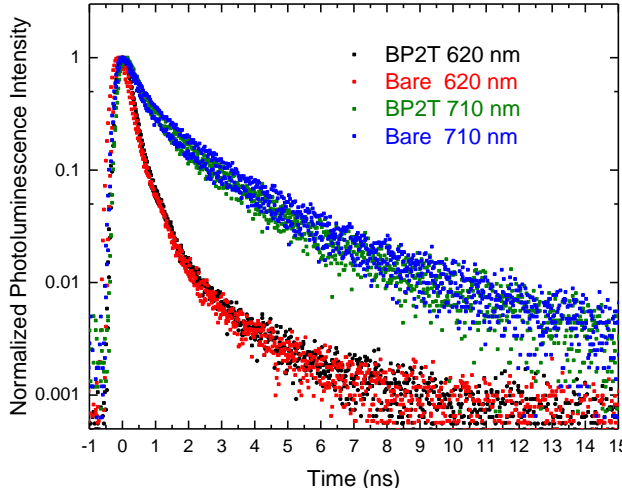


Figure 10.12. Time-correlated single photon counting measurement of SubPc (25 nm, 1.0 Å/s, 25 °C) exciton lifetime on bare glass and glass with BP2T (8 nm, 0.3 Å/s, 100 °C) as measured from the photoluminescence emission peaks at 620 nm and 710 nm from Figure 10.11.

such as C₆₀ or HATCN quench emission completely at concentrations as low as 25 vol%.

capable of dissociating excitons, albeit with poor efficiency. The difference between the mixture and neat planar layer results could simply be due to a difference in molecule coupling along different directions of BP2T molecules, though these differences must be fairly small. For comparison, known quenching materials for SubPc

Molecular Templating in SubPc OPVs

Measurements of the exciton lifetime of SubPc (Figure 10.12) corroborate the observation from Figure 10.11a that BP2T is not dissociating excitons efficiently in a heterojunction architecture, as lifetime measurements are immune to differences in η_{PL} and instead elucidate the magnitude of k_R+k_{NR} .

10.5. Planar Heterojunction Devices

With these films now characterized morphologically and optically, the remaining step is to probe their optoelectronic properties in OPV architectures. Since an improvement in the exciton diffusion length and charge transport would be most evident (and easily measured) in a planar heterojunction, these devices were investigated first.

10.5.1. Device Parameters

Planar heterojunction OPVs were constructed with SubPc as the electron donor at varying SubPc deposition rates, with the results shown in Figure 10.13. Contrary to previously published device structures, these devices do not feature MoO_x because the combination of BP2T deposited over MoO_x is highly resistive and produces devices with low responsivity and fill factor. Most parameters display slight trends with deposition rate, with more quickly deposited films showing higher V_{oc} but lower fill factor due to the maximum power point not shifting. Devices which are very slowly deposited show high dark currents, possibly due to leaks (shunts) or increased recombination from the effective SubPc thickness reduction caused by the film roughness shown in Figure 10.3, though this only explains the BP2T-templated case. Other possible causes include impurity

incorporation within the layer during deposition or molecular ordering in a manner which

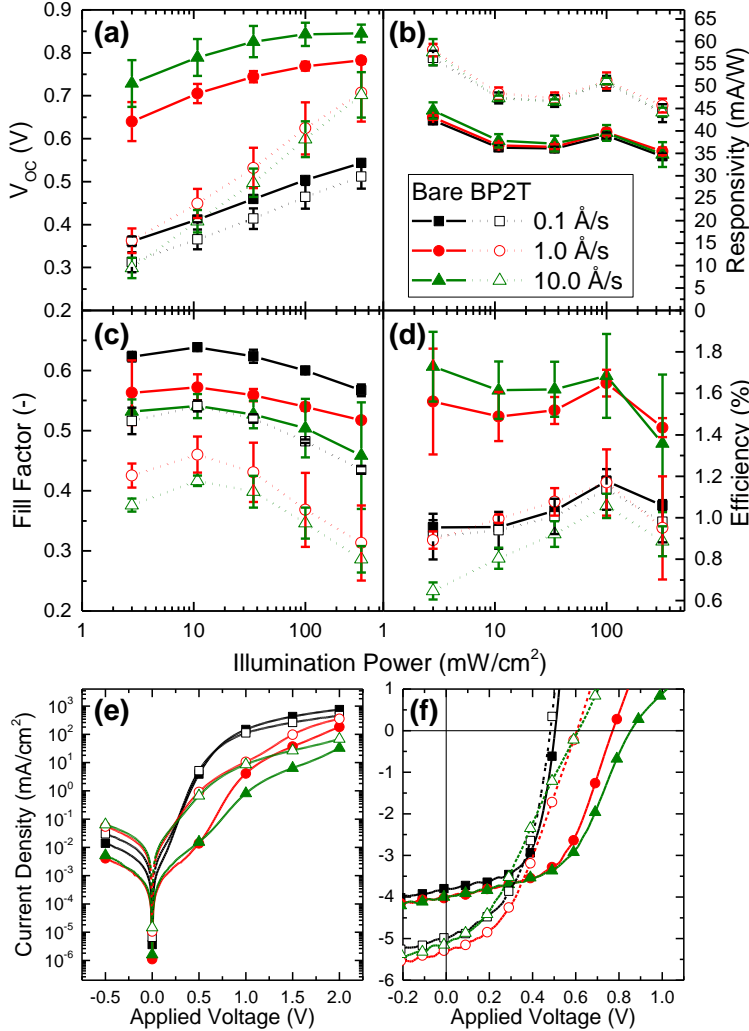


Figure 10.13. Device parameters for SubPc planar heterojunctions, including (a) V_{oc} , (b) responsivity, (c) fill factor, (d) power conversion efficiency, and current-voltage characteristics at (e) 0 and (f) 1 sun AM1.5G illumination. Device architecture: ITO // [BP2T 8 nm (0.3 Å/s, 100 °C)] // SubPc 13 nm (1 Å/s) // C₆₀ 35 nm (2 Å/s) // BCP 10 nm (2 Å/s) // Al 100 nm (3 Å/s). All layers other than BP2T deposited at 25 °C.

without illumination, which is not sufficient time for full characterization. However, this effect is only a property of the BP2T-polymer interface, as polymer-SubPc devices did not degrade (Figure 10.14b). This may imply increased water or oxygen absorption in these

increases charge mobility, though the lack of an absorption change with treatment precludes large-scale molecular rearrangement.

The intriguing molecularly smooth BP2T terrace morphology obtained by planarizing substrates as shown in Figure 10.1 results in very unstable devices, as shown in Figure 10.14. These devices significantly degraded on the time scale of 30 seconds with and

Molecular Templating in SubPc OPVs

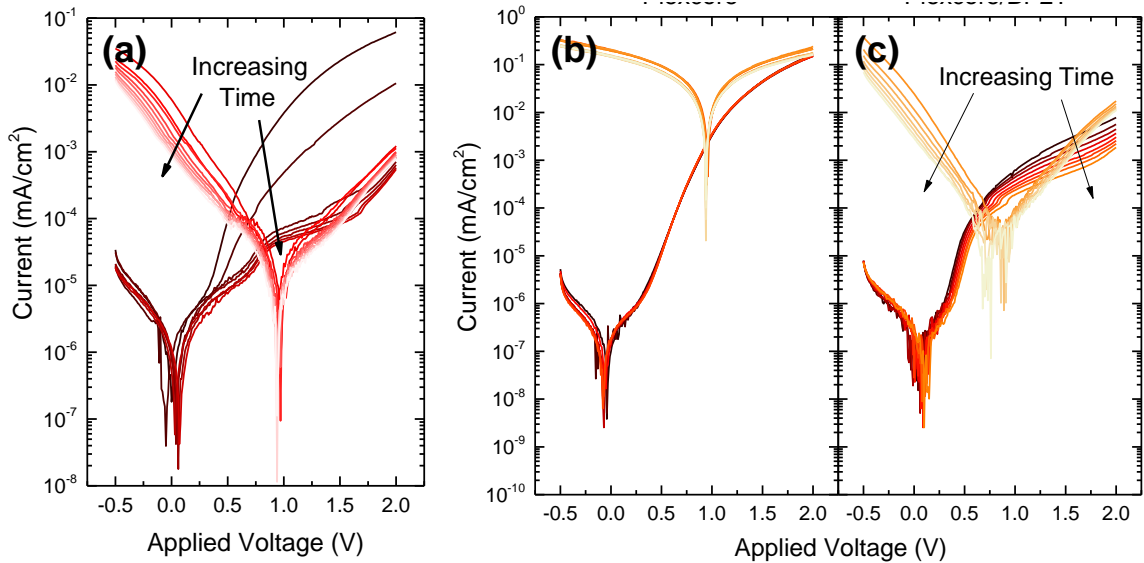


Figure 10.14. Current-voltage characteristics of planar SubPc devices over time. Architecture as described in Figure 10.13, except (a) has 50 nm PEDOT:PSS planarizing the ITO, (b) has 50 nm AQ1200 planarizing the ITO with no BP2T, and (c) has 50 nm AQ1200 planarizing the ITO with BP2T. Each scan spaced approximately 5 seconds, with devices first exposed to dark, then 0.03 suns AM1.5G illumination.

roughened films or through cathode voids. Degradation due to air exposure can be largely circumvented with packaging the devices in epoxy-sealed glass, but even with packaging, these devices were characterized by a lower fill factor and slightly higher V_{oc} likely brought about by additional series resistance in the planarizing layer which lowers the device dark current. For these reasons, devices with planarizing ITO layers were not used for the remainder of this chapter.

Perhaps most remarkably, V_{oc} in non-planarized templated devices is significantly reduced (15-25%) while responsivity is increased by 25%. The change in V_{oc} may be explained by increased dark current, but the responsivity shift implies a change in photon harvesting. Indeed, a plot of η_{EQE} for these devices shows that a greatly enhanced SubPc photoresponse is responsible for the responsivity change, with the response of C₆₀

essentially identical across different architectures (Figure 10.15). Templated devices also show a slight trend in the SubPc peak response, with increasing photoresponse correlated with a higher SubPc deposition rate; however, this difference is offset somewhat by a slight decrease in the C₆₀ response, giving essentially unchanged responsivity across these architectures.

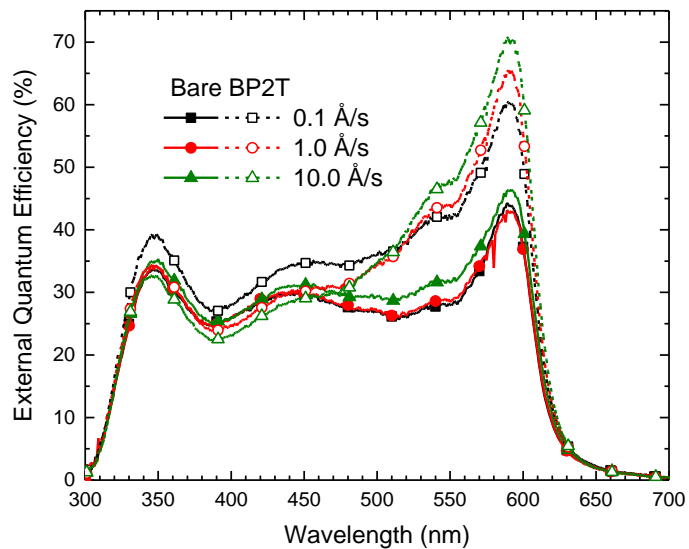


Figure 10.15. External quantum efficiencies of the planar SubPc devices described in Figure 10.13.

This result implies enhanced photon harvesting, specifically from SubPc. Since the absorption of SubPc is unchanged (from UV-Vis measurements and optical simulations) and η_{CC} is similar (from the unchanged C₆₀ response), there must be an improvement in exciton diffusion and/or dissociation, each of which are considered separately here. In particular, exciton diffusion and the energy of the charge transfer state are addressed.

10.5.2. Charge-Transfer State Energy

One method to evaluate the differences in exciton dissociation is through device electroluminescence, looking specifically for CT state emission. The CT state energy for SubPc:C₆₀ has been previously measured in this manner, with a value of 1.55 eV reported.¹⁹⁰ However, measurements carried out on planar and mixture devices with and without BP2T show only SubPc emission (Figure 10.16), with no noticeable feature

Molecular Templating in SubPc OPVs

changes from the photoluminescence spectrum other than an enhancement of the 710 nm peak in BP2T-templated devices, possibly from favorable injection from BP2T and

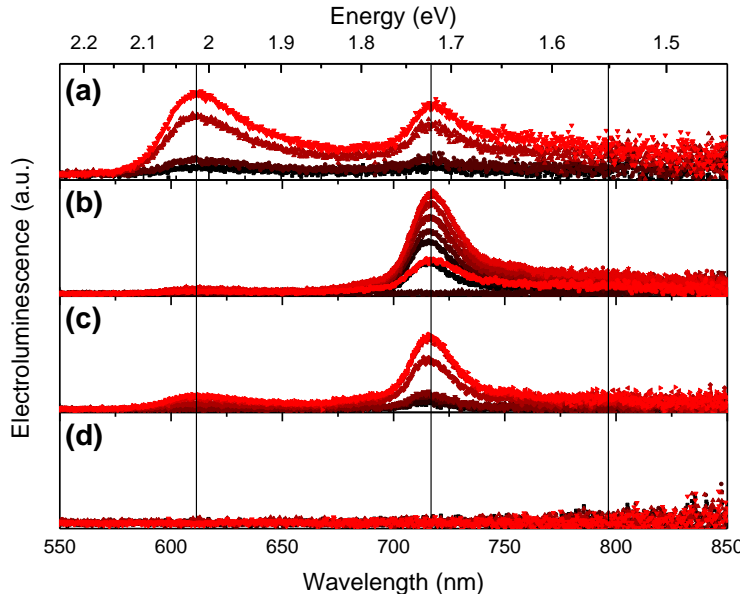


Figure 10.16. Electroluminescence of SubPc/C₆₀ planar (a), (c) and mixture (b), (d) devices without (a)-(b) and with (c)-(d) BP2T. Applied voltage increases from black to red. Vertical lines show the positions of the 620 nm and 710 nm SubPc photoluminescence peaks and the anticipated 1.55 eV SubPc-C₆₀ CT state peak. Planar architectures the same as Figure 10.13; mixture architecture ITO // [BP2T 8 nm (0.3 Å/s, 100 °C)] // SubPc 12 nm : C₆₀ 48 nm (net 2 Å/s) // BCP 10 nm (2 Å/s) // Al 100 nm (3 Å/s). All layers other than BP2T deposited at 25 °C.

between polaron mobilities in the neighboring layers, and would be expected for SubPc and C₆₀ from their disparate mobilities, given in Appendix K. What is perhaps more remarkable is that CT state emission is observed with a MoO_x interlayer. Unfortunately, without CT state emission, it impossible to quantify the CT state energy from these measurements.

The final method used to explore the CT state difference in BP2T-SubPc planar devices was examining the change in device parameters, namely V_{oc} , with temperature. As Zou *et*

recombination on the aggregates. The lack of CT state emission implies that polarons are recombining in SubPc rather than at the interface, which signifies an accumulation of electrons at the donor-acceptor interface, some of which are injected onto SubPc and recombine radiatively. This can be caused by a discrepancy

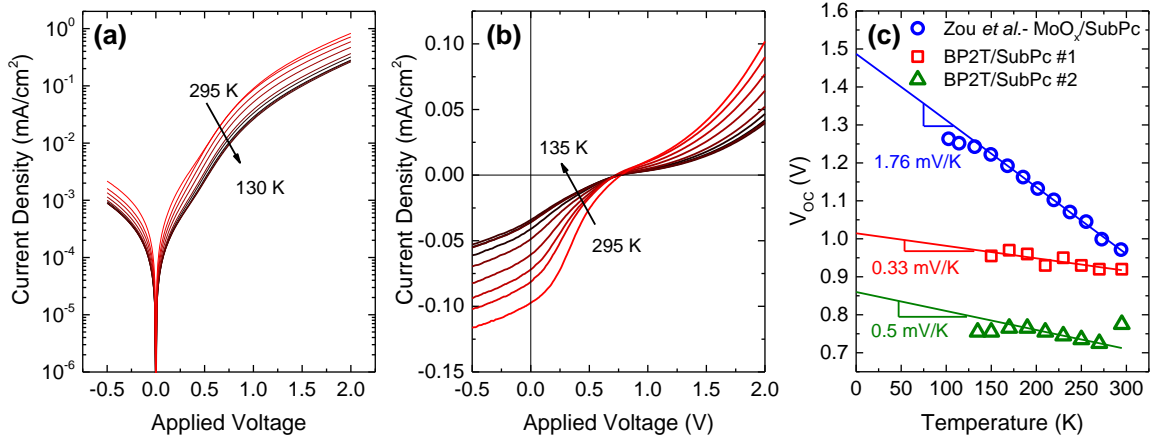


Figure 10.17. Temperature-dependent device performance for BP2T-SubPc planar devices, including current-voltage properties at (a) 0 and (b) 1 sun AM1.5G and (c) V_{oc} with temperature compared to Zou *et al.*⁷³⁷ Planar device architecture is the same as that in Figure 10.13, with the curves in (a) and (b) corresponding to device #2 in (c). Maximum V_{oc} in (c) from top to bottom are 1.49 V, 1.01 V, and 0.86 V.

al. showed,¹⁹⁰ the maximum achievable V_{oc} at 0 K can be directly related to the CT state energy. As shown in Figure 10.17, BP2T-SubPc devices show high dark current which decreases with temperature, commensurate with an overall reduction in device current from falling carrier mobility. However, the device V_{oc} increases much less rapidly with decreasing temperature, leading to a considerably lower maximum V_{oc} , and also varies significantly between different devices. In such devices that are limited by dark current, the linear region increasingly deviates from that which gives the true maximum V_{oc} describing the CT state,⁷³⁷ meaning that this measurement is also not insightful. Other measurements that could be potentially useful would be direct assessment of any changes in the SubPc HOMO with templating, such as with KPFM, STM, or UPS. KPFM measurements on these films are briefly detailed in Appendix H.4.

10.5.3. Exciton Diffusion Length Measurement

If changes in the CT state are neglected, then the observed improvement in SubPc

Molecular Templating in SubPc OPVs

response must instead come from an increase in the exciton diffusion efficiency, η_D . This can arise from an increase in the exciton diffusivity or proximity to a dissociating interface. In the case of BP2T/SubPc, neither option can be excluded, since the presence of BP2T may cause SubPc to transform in a manner which increases the diffusivity or, equivalently, BP2T may serve as a second exciton dissociation interface, even if partially dissociating.

One method to measure L_D in a device setting is to fit η_{EQE} with known absorption efficiency. The exciton generation and diffusion profile can be calculated analytically, then used to predict the wavelength-dependent photocurrent given values of L_D in the absorbing materials.⁶⁹⁴ This fitting yields an exciton diffusion length for all absorbing materials (assume distinct spectral features), in this case SubPc and C₆₀. The partial results of these calculations are shown in Figure 10.18, with the full set of plots given in Appendix H.5.. Since $\eta_{EQE} = \eta_A \eta_D \eta_{CT} \eta_{CS} \eta_{CC}$, these fits require assumptions about other parameters involved, namely η_{CC} and $\theta = \eta_{CT} \eta_{CS}$ at any potential exciton-dissociating interfaces.

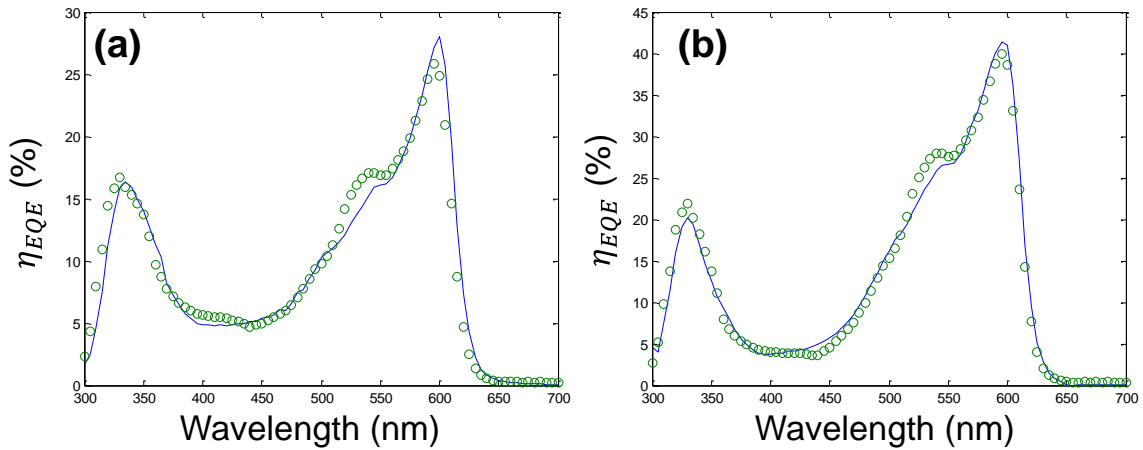


Figure 10.18. Fitted η_{EQE} for (a) bare and (b) BP2T SubPc planar devices, with experiment as a blue line and fit in green circles ($\eta_{CC} = 0.99$). Device architectures are: Bare = ITO // SubPc 28 nm (1 Å/s) // C₆₀ 10 nm (2 Å/s) // BCP 10 nm (2 Å/s) // Al 100 nm (3 Å/s); BP2T = same as bare, but with BP2T 16 nm (0.3 Å/s, 100 °C) between ITO and SubPc. All layers besides BP2T deposited at room temperature.

Molecular Templating in SubPc OPVs

Absorption can be measured independently, accounting for η_A , and η_D is fit for L_D , but η_{CC} and θ must be globally optimized or estimated. Here, fits are reported for extreme values of θ and $\eta_{CC} = 1$ vs. an optimized fit bounded by 0.5. As the C₆₀ acceptor was very thin for these devices, the fit C₆₀ L_D is probably not significant.

Not surprisingly, the diffusion length is inversely related to η_{CC} , as shown in Table 10.2 (plots of all fits given in

Figure 14.24): the fewer polarons are collected, the more excitons must be dissociated to achieve the same photocurrent.

Table 10.2. Fitted η_{EQE} parameters for the devices in Figure 10.18.

Device	θ	η_{CC}	SubPc L_D (nm)	C ₆₀ L_D (nm)	ITO Thick. (nm)
Bare	0	1.000	9.0	2.2	95.0
Bare	0	0.935	9.3	2.4	96.7
BP2T	0	1.000	13.6	2.0	90.1
BP2T	0	0.500	42.9	3.2	91.3
BP2T	1	1.000	6.3	2.0	91.4
BP2T	1	0.500	20.7	3.2	91.3

This causes a variance of 0.3 nm in SubPc L_D for the bare case, but significantly more for the BP2T cases, with additional variation due to θ . Clearly, a defined value for η_{CC} would greatly improve the accuracy of these fits.

One such method of evaluating η_{CC} is by measuring photocurrent at reverse bias, where charge extraction barriers are reduced, increasing η_{CC} towards 1.⁷²⁷ Comparison of the device photoresponse at unity charge collection to that at short-circuit yields η_{CC} at the relevant device operating point. Measured data for SubPc planar heterojunctions with and without BP2T are shown in Figure 10.21 (biased full η_{EQE} plots given in Figure 14.25).

The overall voltage range was somewhat limited by device leakage current and shorting, but yielded a plateau region for the BP2T devices, giving a range of $0.45 < \eta_{CC} < 0.58$ for 13 nm SubPc and $0.35 < \eta_{CC} < 0.50$ for 20 nm (depending on absorption feature). The

Molecular Templating in SubPc OPVs

continuing upward trend of bare devices only gives an upper limit on η_{CC} of $\eta_{CC} < 0.63$

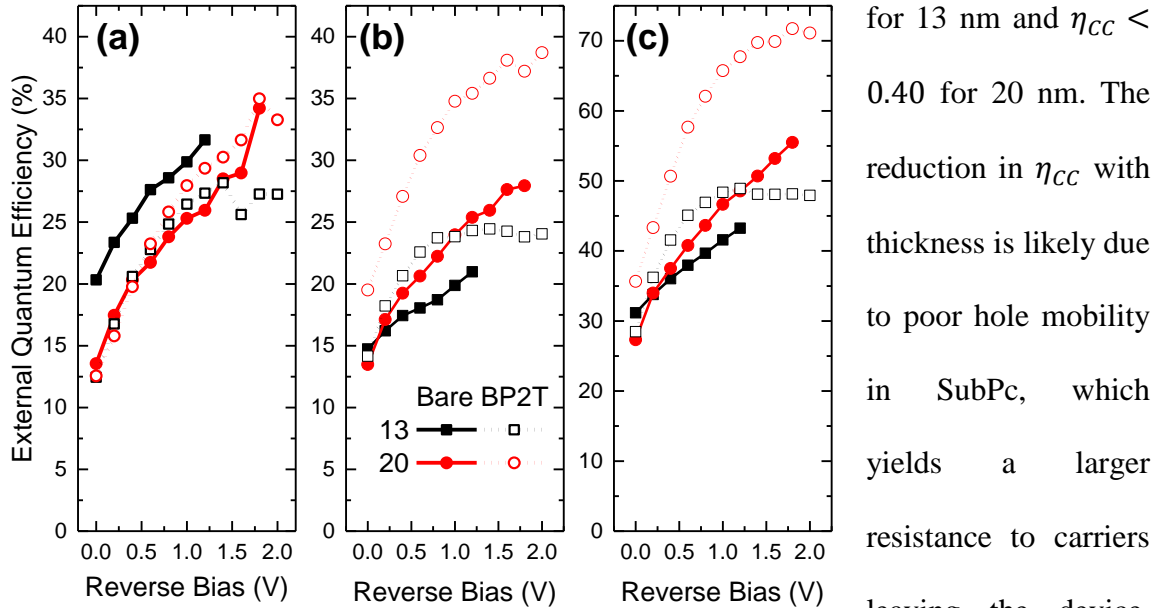


Figure 10.19. Measured η_{EQE} as a function of applied reverse bias and SubPc thickness (nm) at (a) 335, (b) 545 and (c) 595 nm, corresponding to (a) SubPc Soret band, (b) SubPc Q-band vibronic, and (c) SubPc Q-band main peak absorption. Device architectures are: Bare = ITO // SubPc XX nm (1 Å/s) // C₆₀ 5 nm (2 Å/s) // BCP 10 nm (2 Å/s) // Al 100 nm (3 Å/s); BP2T = same as bare, but with BP2T 8 nm (0.3 Å/s, 100 °C) between ITO and SubPc. XX = 13 or 20 nm, as given in the legend. All layers besides BP2T deposited at room temperature.

(higher dark current), giving somewhat higher collection efficiency, especially at high SubPc thicknesses. Unfortunately, this range in η_{CC} gives a wide range of extracted L_D , as already shown in Table 10.2. A technique which circumvents charge collection would theoretically be able to overcome this challenge.

One such technique is photoluminescence quenching, but this technique is often performed with multiple film thicknesses or in very thick films.^{78,365} As the templating effects of SubPc on BP2T with thickness may vary, a single, device-comparable measurement is desirable. This can be achieved by monitoring the photovoltage rise of a

for 13 nm and $\eta_{CC} < 0.40$ for 20 nm. The reduction in η_{CC} with thickness is likely due to poor hole mobility in SubPc, which yields a larger resistance to carriers leaving the device.

Similarly, the BP2T devices likely show higher conduction

device under illumination, then correlating this voltage to a carrier population within it.⁷³⁸

To evaluate this possibility, charge extraction and transient photovoltage measurements in conjunction with optical field and exciton diffusion simulations were conducted as described elsewhere.⁷³⁸

Briefly, charge extraction from an OPV switched from an illuminated open-circuit to a dark short-circuit state allows calibration of the carrier population within a device at a particular V_{oc} (Figure 10.20a). This can then be used to determine the number of carriers present in a device for a given photovoltage rise (Figure 10.20b),

which, when related to the incident photon flux and device optical field, gives the number of excitons which produced polarons relative to the total number of excitons that were generated. It is then trivial to evaluate the exciton diffusivity with simple diffusion models.⁶⁹⁴

Since variations in the acceptor diffusion efficiency can influence the donor measurements, planar heterojunctions with a thin (10 nm) C₆₀ acceptor layer were manufactured and measured using transient photovoltage. The results of these

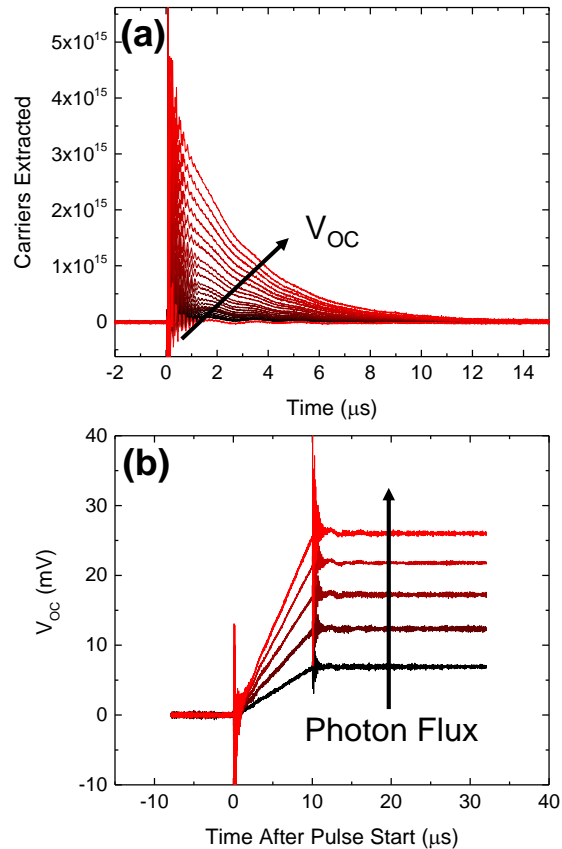


Figure 10.20. Example (a) charge extraction and (b) transient photovoltage curves for the SubPc planar architecture in Figure 10.13.

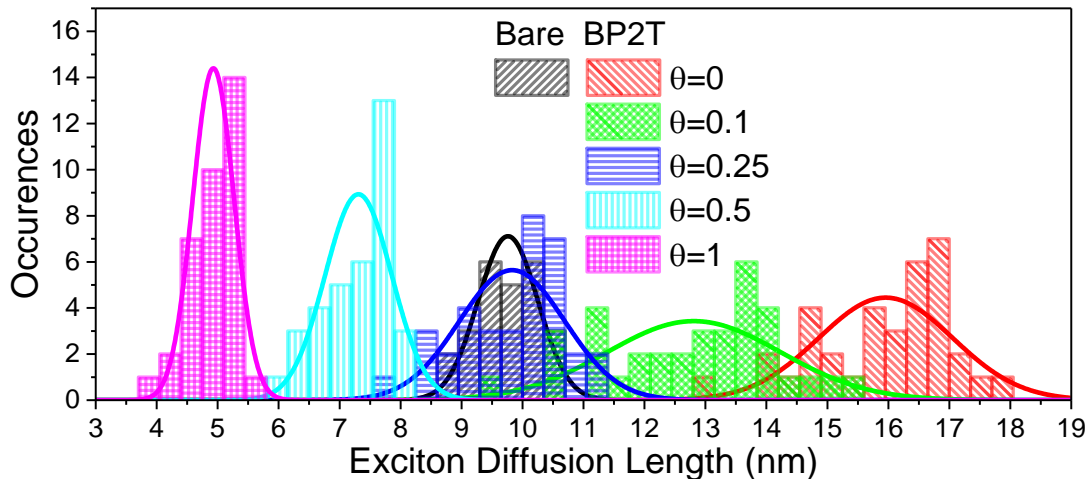


Figure 10.21. SubPc exciton diffusion lengths in a planar heterojunction extracted using a photovoltage-based measurement. Diffusion lengths are fit with a variable exciton dissociation efficiency (θ) at the BP2T-SubPc interface, with $C_{60} L_D = 16$ nm. Device architectures are: Bare = ITO // SubPc 25 nm (1 Å/s) // C_{60} 10 nm (2 Å/s) // BCP 10 nm (2 Å/s) // Al 100 nm (3 Å/s); BP2T = same as bare, but with BP2T 8 nm (0.3 Å/s, 100 °C) between ITO and SubPc. All layers besides BP2T deposited at room temperature.

measurements and simulations are shown in Figure 10.21. The diffusion length for the case of SubPc on bare ITO (9.8 ± 0.5 nm) agree with previous photoluminescence-based measurements,^{198,365} although the varied nature of exciton and polaron loss processes in a device *vs.* film architecture would perhaps argue that they should not. Devices with a BP2T interlayer were evaluated by varying the efficiency of exciton dissociation at the BP2T-SubPc interface through the diffusive boundary condition, with $\theta = \eta_{CT}\eta_{CS}$ accounting for the total efficiency of polaron formation from excitons. If the BP2T-SubPc interface is approximated as exciton reflecting ($\theta = 0$), the exciton diffusion length is calculated as 16 ± 1 nm, yielding an increase of over 60% from the bare case. However, as θ increases, the diffusion length is correspondingly decreased due to the accessibility of a secondary dissociating surface,

Table 10.3. Calculated exciton diffusion lengths for the devices in Figure 10.21.

Device	θ	L_D (nm)
Bare	0.0	9.8 ± 0.5
BP2T	0.0	16 ± 1
BP2T	0.1	13 ± 1
BP2T	0.25	9.8 ± 0.9
BP2T	0.5	7.3 ± 0.5
BP2T	1.0	4.9 ± 0.3

with a minimum of 4.9 ± 0.3 nm for a totally dissociating interface ($\theta = 1$; summary of all values given in Table 10.3). Depending on which trend of photoluminescence quenching in Figure 10.11 is to be believed, the quenching efficiency is bounded between $0 \leq \theta \leq 0.85$, since a planar BP2T/SubPc interface shows no quenching, while a uniformly dispersed equichoric mixture of BP2T:SubPc reduces the photoluminescence by ~85%. This leaves considerable room for variation of L_D from much higher to much lower than the bare case; not helpful for determination of a single value of L_D .

10.5.4. Alternative Electron Acceptors

If the arrangement of SubPc on top of BP2T were somehow favorably affecting exciton dissociation at the donor-acceptor heterojunction, then changing the electron acceptor should affect the device parameters negatively. This was tested by comparing C₆₀ to PTCDA, PTCDI, and a 1:1 mixed film of BP2T:SubPc (Figure 10.22). Most notably, the responsivity of all devices (except for the 1:1 mixture) show an increase in responsivity, with the improvement approximately proportional to the responsivity without templating. It is probable that the BP2T:SubPc mixture was highly crystalline, rough, and air sensitive, since device performance was extremely poor and appeared to degrade throughout device testing. However, all other acceptors showed significant improvement of responsivity when BP2T was included. Such a generic effect suggests it is not unique to C₆₀ and thus probably not related to the donor-acceptor interface, reinforcing the idea that a change in the CT state may not be responsible for the increased responsivity. However, an improvement in photocurrent for all acceptors with BP2T is also consistent with BP2T

dissociating excitons, since the SubPc-BP2T interface would be strictly additive in its contribution to photocurrent.

The η_{EQE} plots confirm that the increased responsivity is from SubPc excitons (Figure

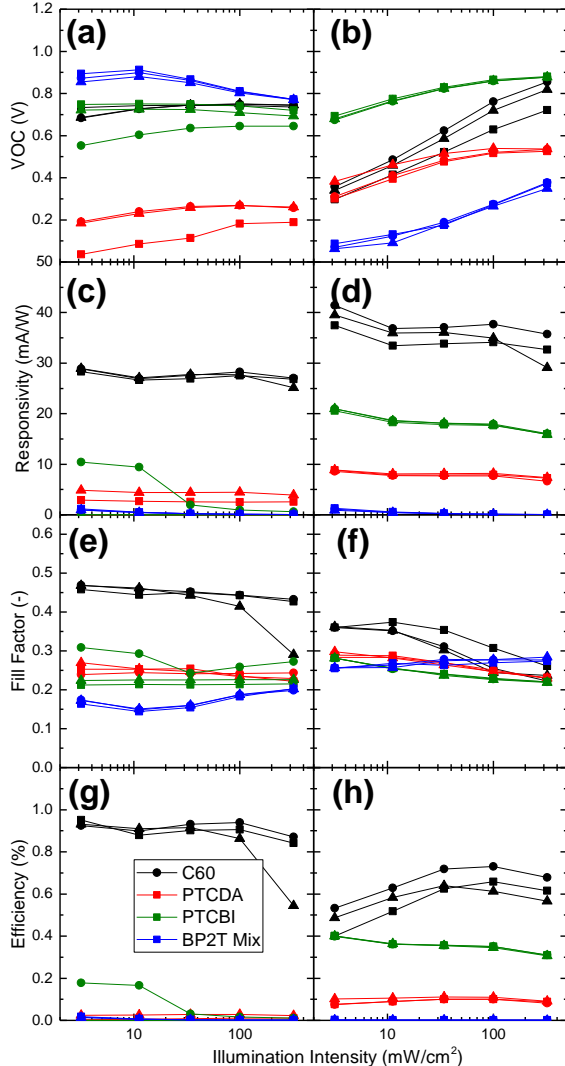


Figure 10.22. SubPc planar heterojunction device parameters without (left) and with (right) BP2T. (a)-(b) V_{oc} , (c)-(d) responsivity, (e)-(f) fill factor, (g)-(h) η_P . Device architectures: ITO // [BP2T 8 nm (0.3 Å/s, 100 °C)] // SubPc 25 nm (1.0 Å/s) // Acceptor 20 nm (1 Å/s) // BCP 10 nm (2.0 Å/s) // Al 100 nm (3.0 Å/s). Acceptor layer specified in legend; all layers besides BP2T deposited at room temperature.

10.23a-b). With templating, the acceptor absorption (350-450 nm for C₆₀, >600 nm for PTCBI, and not appreciable for PTCDA or BP2T) stays consistent, with only the SubPc peak increasing in response. The dark currents in Figure 10.23c-d also explain the V_{oc} and fill factor trends observed with templating: higher dark current for templated cells with PTCBI, C₆₀, and BP2T leads to lower V_{oc} and *vice versa* for PTCDA. The greater slope of the dark current for templated C₆₀ devices reduces the fill factor, while most other cells show a rough vertical translation of the dark current and comparable fill factors.

Given these trends in L_D measurement and photoluminescence, it is highly likely that BP2T is not actually increasing the

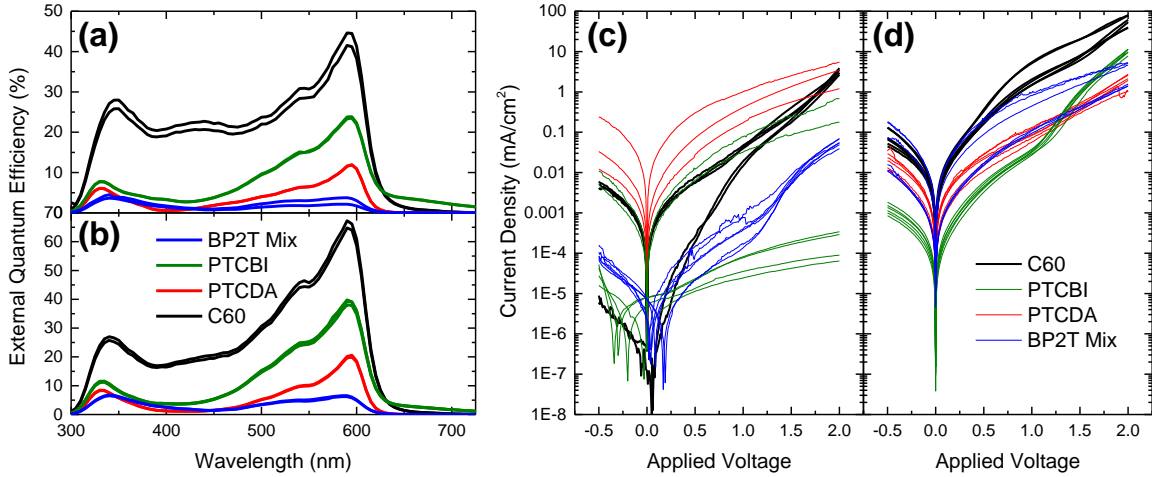


Figure 10.23. η_{EQE} and dark current for the devices with architectures given in Figure 10.22. (a), (c) are on bare ITO, (b), (d) have a BP2T interlayer.

exciton diffusion length but instead dissociating a small fraction (~25%) of the excitons which reach the BP2T-SubPc interface. By providing an available HOMO level which is between ITO and SubPc, BP2T may also reduce the hole injection barrier in these devices, yielding higher dark current. This effect probably occurs in tandem with an increase in film roughness from SubPc deposition onto the roughened BP2T surface. Though the increase in surface area is negligible, material interpenetration and shunts between layers are increasingly likely with phase segregation at low deposition rates, lending a deposition rate dependence to the device parameters.

10.6. Alternate Device Architectures

Although the effects of BP2T on SubPc in planar devices is predominantly to dissociate excitons and roughen subsequently deposited films, this may not necessarily be the case in (typically much thicker) mixture or gradient composition OPVs, or in Schottky cells which rely on the built-in field to dissociate excitons. Furthermore, if BP2T is actually

Molecular Templating in SubPc OPVs

dissociating excitons, the responsivity improvement should decrease as the exciton-generating molecule (SubPc) is diluted with optically inactive materials or materials which have different energy levels, such as UGH₂ or boron subnaphthalocyanine (SubNc). In environments where SubPc excitons may also dissociate on nearby acceptor molecules (*e.g.*, C₆₀), the presence of a BP2T-SubPc interface should also have less of an impact on exciton dissociation. To better understand the effects of BP2T on SubPc in these alternate architectures, such devices were manufactured and characterized, and are described below.

10.6.1. Mixture and Gradient Heterojunction Devices

SubPc:C₆₀ mixtures and gradient architecture devices have been previously proven to be higher efficiency than planar heterojunctions due to their increased η_D from a larger, more dispersed dissociating interface,^{98,100,728} making them of interest for investigation. Demonstrated crystalline heteroepitaxial mixture devices require the use of a neat donor layer between the template and mixture in order to achieve favorable epitaxy,^{588,724} which would likely also be true for BP2T-SubPc devices if there is epitaxial templating. Furthermore, if the material is deposited in a crystalline state, a graded donor-acceptor (gradient) composition should be ideal for producing interpenetrating conical, columnar regions of neat materials for efficient η_D and η_{CC} .

The results from characterization of mixture and gradient devices support the role of BP2T as strictly an exciton-dissociating interface (Figure 10.24). The inclusion of BP2T has no impact on the device responsivity in gradient or mixture devices, although the inclusion of a neat SubPc layer does improve the performance of the mixture devices. This

Molecular Templating in SubPc OPVs

is probably an effect of limiting electron leakage through the device to the ITO anode, reducing carrier recombination and increasing both V_{oc} and responsivity by a small amount. Since the gradient architecture already features a much higher SubPc concentration at the anode, inclusion of the neat layer makes much less of an impact on device performance, slightly improving V_{oc} and fill factor. Overall, however, templated devices remain limited by low V_{oc} , obviated by the sharp turn-on present at relatively low voltages in the current-voltage characteristics (Figure 10.25c-d).

The behavior of these devices in η_{EQE} also points to BP2T as dissociating excitons, with templated devices with neat material at the anode showing a stronger SubPc response coupled with a comparable or slightly weaker C₆₀ response (Figure 10.25a-b). Even though the neat layer is thin (5 nm) and the gradient devices still have C₆₀ present to dissociate excitons near

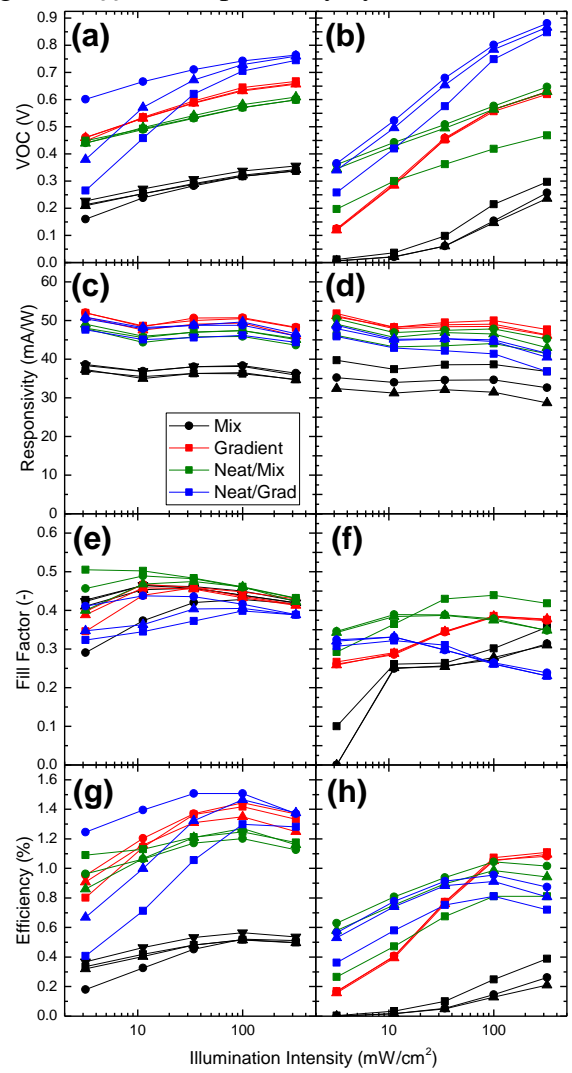


Figure 10.24. SubPc bulk heterojunction device parameters without (left) and with (right) BP2T. (a)-(b) V_{oc} , (c)-(d) responsivity, (e)-(f) fill factor, (g)-(h) η_P . Device architectures: ITO // [BP2T 8 nm (0.3 Å/s, 100 °C)] // [SubPc 5 nm (1.0 Å/s)] // BHJ XX nm (1 Å/s) // BCP 10 nm (2.0 Å/s) // Al 100 nm (3.0 Å/s). BHJs are: gradient 1:4 SubPc:C₆₀ nonzero endpoint graded composition cells (66 nm),⁹⁸ mixture 1:4 SubPc:C₆₀ (60 nm).⁷²⁸ Neat/BHJ devices include the 5 nm SubPc layer beneath the BHJ. All layers besides BP2T deposited at room temperature.

Molecular Templating in SubPc OPVs

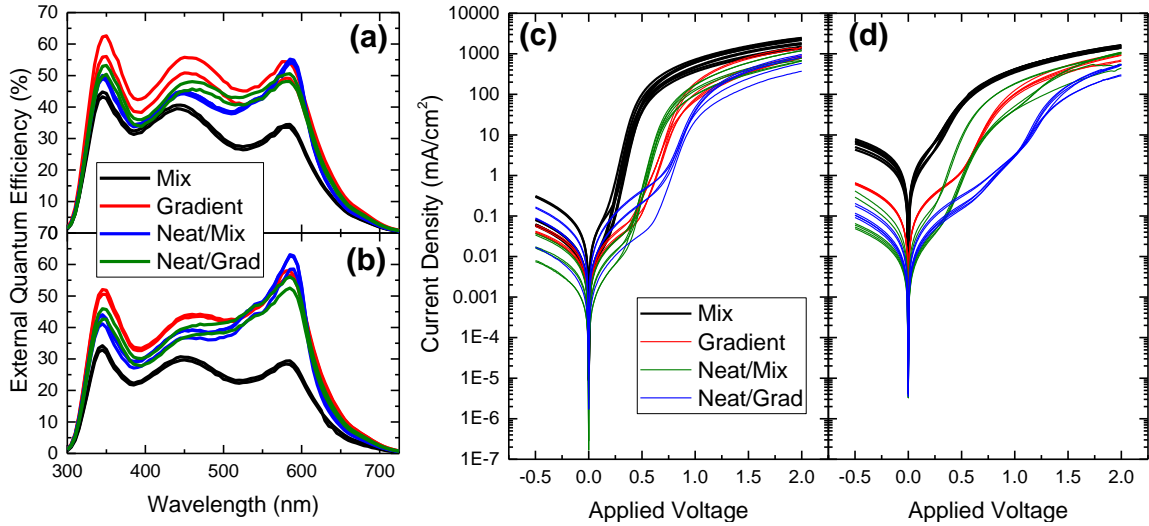


Figure 10.25. η_{EQE} and dark current for the mixture and gradient devices, with architectures given in Figure 10.24. (a), (c) are on bare ITO, (b), (d) have a BP2T interlayer.

ITO (1:1 SubPc:C₆₀), the addition of BP2T must facilitate this dissociation by proximity, allowing excitons that would otherwise recombine near ITO to contribute polarons. C₆₀ is known to segregate into nanocrystalline domains in other materials,^{576,717,724} perhaps something similar is happening near the anode to further reduce exciton dissociation (and electron leakage) in the gradient case. The contrasting case for this is that of the mixture device, which has sufficient C₆₀ near the anode and throughout the device to optimally dissociate all excitons. This device shows a slight overall reduction in η_{EQE} with templating, probably from increased injection or recombination evidenced by a much higher dark current.

10.6.2. Dilute Donor Devices

For similar reasons to the previous section, diluting the SubPc donor with an inert material presents an opportunity to study exciton dissociation at the anode. The dilute devices in this section were constructed according to previous results,¹⁹⁸ but include

Molecular Templating in SubPc OPVs

optional layers of neat SubPc and BP2T at the anode. Although the inclusion of a neat

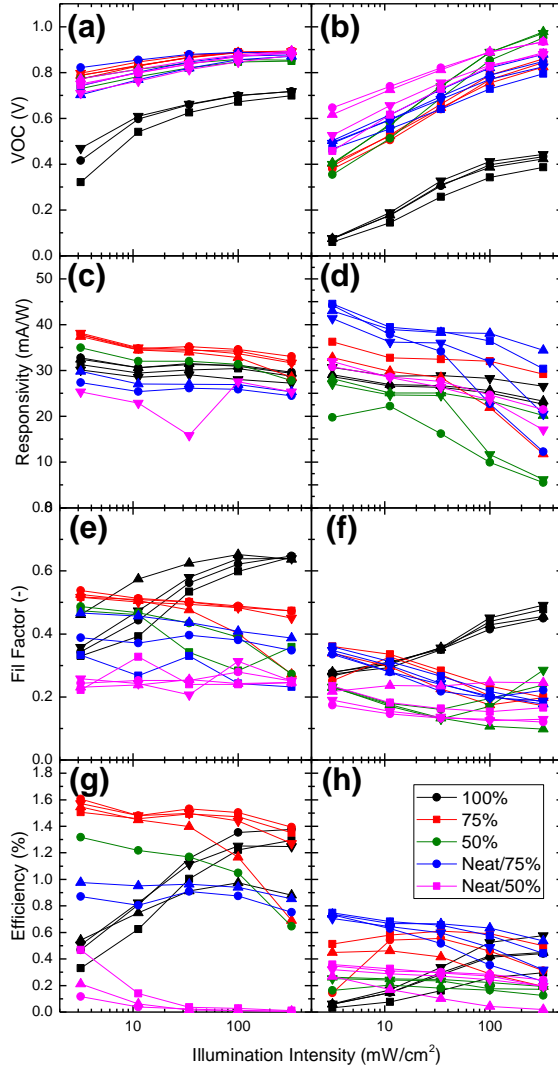


Figure 10.26. Dilute-donor SubPc devices without (left) and with BP2T (right). Schottky device parameters. (a)-(b) V_{oc} , (c)-(d) responsivity, (e)-(f) fill factor, (g)-(h) η_P . Device architectures: ITO // [BP2T 8 nm (0.3 Å/s, 100 °C)] // [SubPc 5 nm (1.0 Å/s)] // SubPc:UGH2 XX% 12 nm (1.0 Å/s) // SubPc 5 nm (1.0 Å/s) // C₆₀ 35 nm (2.0 Å/s) // BCP 10 nm (2.0 Å/s) // Al 100 nm (3.0 Å/s). Bracketed layers are only present when specified in legend; all layers besides BP2T deposited at room temperature.

this dark current, allowing reasonable conclusions to be drawn.

SubPc layer at the anode counters or even reverses much of the exciton gating effect that makes these devices interesting, this allows for testing of dissociation at the anode (and increases the probability of mixture templating if BP2T were acting as a template of crystallinity).

The optoelectronic performance of these devices is shown in Figure 10.26. Of note is the particularly poor performance of templated 100% devices; this is due to extremely high dark current which overwhelms the photocurrent to give a low V_{oc} and even reduces the responsivity at short circuit. This would happen occasionally (< 10% of device growths) in BP2T device batches at random, with no discernable cause. However, the inclusion of UGH2 in the device architecture controls

With the dark current reduction, the device V_{oc} is higher for diluted devices, with a slight enhancement with the inclusion of a neat SubPc layer at the anode from a more efficient electron blocking, which in this case also increases the device resistance and yields a lower fill factor. In bare ITO devices, this SubPc anode layer is also not contributing to photocurrent, and may actually be extracting excitons from the dilute layer. However, devices with BP2T show an improvement with the neat anode layer, which must be from dissociation. This is also evident in the η_{EQE} plots (Figure 10.27), though the templated device trends are less clear than those in Figure 10.26.

All dilute devices show an increase in SubPc response with the inclusion of BP2T (with a slight reduction in C_{60}), though the neat layer inclusion changes device response. Although the responsivity trends appear similar at low illumination levels, it is possible that devices with no neat SubPc layer have a higher response than observed in the broadband results of Figure 10.26.

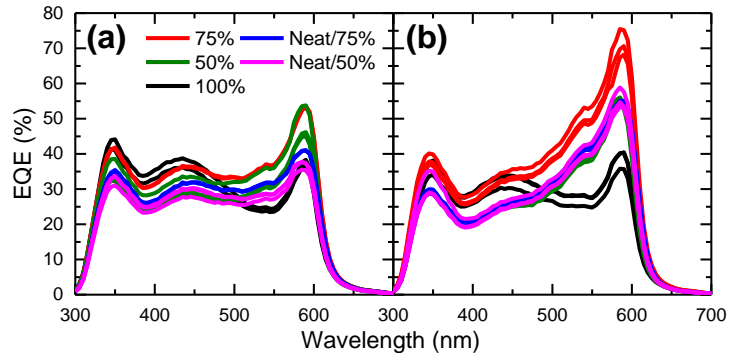


Figure 10.27. η_{EQE} for dilute donor devices, with architectures given in Figure 10.26. Devices are on (a) bare ITO, (b) BP2T interlayer.

10.6.3. Schottky Devices

Schottky devices rely on the built-in electric field from the electrode work function to dissociate excitons, commonly producing low photocurrent and fairly high V_{oc} . More importantly for this study, these devices can show the presence of a dissociating interface (or additional band bending) through enhanced photocurrent in the same active layer with

Molecular Templating in SubPc OPVs

the inclusion of a secondary material. As a final test of the exciton-dissociation abilities of BP2T, SubPc and SubNc Schottky devices were constructed, with device performance given in Figure 10.28. Despite their similar molecular structures, BP2T influences SubNc differently than SubPc, with a more consistent V_{oc} with different substrate treatments and a net reduction in responsivity with BP2T and MoO_x; surprising when compared to SubPc. In SubPc devices, MoO_x tends to reduce the dark current and increase V_{oc} through the formation of a secondary Schottky junction,⁷³⁷ which explains the increased V_{oc} with the addition of MoO_x. However, the increase in responsivity with BP2T inclusion implies that the excitons are either being dissociated at the BP2T interface or are easier to dissociate in the field, perhaps through a more weakly bound excitonic state. The interface of SubPc-BP2T possesses a 300 meV offset between HOMO levels (BP2T shallower) which

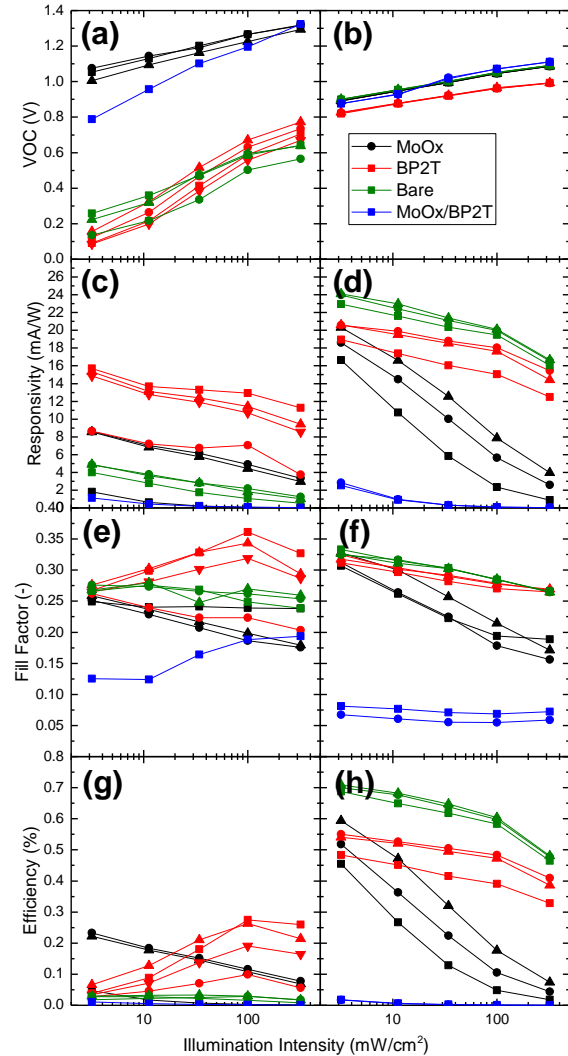


Figure 10.28. SubPc (left) and SubNc (right) Schottky device parameters. (a)-(b) V_{oc} , (c)-(d) responsivity, (e)-(f) fill factor, (g)-(h) η_P . Device architectures: ITO // [MoO_x 10 nm (0.5 Å/s)] // [BP2T 8 nm (0.3 Å/s, 100 °C)] // SubPc or SubNc 25 nm (1.0 Å/s) // BCP 10 nm (2.0 Å/s) // Al 100 nm (3.0 Å/s). Bracketed layers only present when specified in legend; all layers besides BP2T deposited at room temperature.

is likely sufficient to act as a secondary dissociation mechanism in addition to the field.⁷³⁹

SubNc-BP2T has a 50-200 meV HOMO offset,^{237,705} approaching typical exciton binding energies for these materials and the variance between different experimental groups which measure HOMO levels. This offset reduction is consistent with the observed trend of responsivity with BP2T inclusion for SubNc, and further confirms the theories presented in this chapter that BP2T is effective at improving responsivity only in systems where the energetics allow favorable exciton dissociation.

10.7. Conclusions

BP2T has been successfully used as a template of crystal growth for many other OPV electron donor materials, but when used with SubPc, its primary advantageous role appears to be to dissociate excitons. This gives a rather interesting responsivity increase across a variety of device architectures with sufficient SubPc at the device anode, but this increase is insufficient to overcome consequent losses in V_{oc} and fill factor due to increased film roughness and a reduction of the hole injection barrier, ultimately yielding similar or slightly lower efficiency devices. Depending on the efficiency of exciton dissociation at the BP2T-SubPc interface, the simulated exciton diffusion length of templated SubPc varies significantly around non-templated, but a dissociation efficiency of 25% gives an identical diffusion length to that of amorphous SubPc. The topographical morphology of SubPc on BP2T varies with deposition rate, but given that the film optical absorption and emission together with internal structure do not change in any meaningful way, BP2T is likely only changing where SubPc molecules partition on the surface. This eliminates any

Molecular Templating in SubPc OPVs

significant bulk property change in crystallinity or density and leaves exciton dissociation as the only appreciable effect.

11. FUTURE WORK

With the bulk of the impactful work conducted during this thesis presented, this chapter proposes areas and methods to direct future research efforts along related topics. The focus of this thesis was largely on methods and effects of inducing order, thus the future work continues to focus on these areas. First, projects are proposed to expand the crystal shape engineering discussed in Chapter 5, followed by work to more closely examine the role of mechanical stress in thin organic films to better understand the mechanism presented in Chapter 6. Building on work with mixed crystals, mixed glassy films are next discussed to explore their thermodynamic and electroluminescent properties in OLEDs. Finally, the crystallization processes studied in this thesis allow for preparation of novel specimens for studies with ultrafast electron microscopy. Work is proposed to use these specimens to examine mechanical, exciton, and polaron dynamics. These proposals are intended to stimulate thoughts of future researchers.

11.1. Shape Selection in Thin Films

The novel aspect of the crystal shape selection in annealed organic films discovered during this thesis (Chapter 5.) begs additional work to better elucidate the mechanism(s) responsible and possible applications, discussed below.

Future Work

11.1.1. Mechanism Determination and Generalization

Even with the limited assortment of additive molecules and molecule combinations surveyed, it is apparent that additives can have very different effects on crystal growth that appear relatively uncorrelated with molecule size. Previous work has shown effects on pharmaceutical crystallization from polymer excipients,^{307,653} with increased crystallization rates associated with lower- T_g excipients, presumably from their greater diffusivity facilitating crystal growth. It may be instructive to systematically correlate rubrene crystal growth rates in the single crystal and polycrystalline temperature range with dopants of vastly differing T_g , such as UGH1 (26 °C), UGH2 (< 50 °C), TPD (60 °C), NPD (95 °C), TPBi (122 °C), and TCTA (151 °C). Convolved with this trend will be differences in volatility from the dissimilar molecular masses, but those differences should be quantifiable using TGA to map mass loss with temperature, then extrapolating back to a mass loss rate at the annealing temperature as in Figure 5.3. If the shape selection is dictated by the rate at which an additive can leave or be excluded from a film, such vapor pressure data in neat powders and alloyed (homogeneous, melted) slugs should be insightful. In this case, the rate of mass loss could be correlated to growth rate, potentially a transient growth rate like majority TPBi-rubrene films, to observe growth rate differences as a function of film composition in real time. Measurements on a heated quartz crystal monitor could provide such information, provided the crystal was stable enough and the heating rate could be high enough. Although intriguing, correlating rate with composition in real-time should provide similar data to the simpler growth rate with composition experiments already

Future Work

performed in this thesis.

Other potential variables include additive flexibility and miscibility with rubrene. Molecular flexibility is related somewhat to T_g with other parameters and is thus partially accounted for,³⁵¹ but extreme examples might include solution-cast rubrene films mixed with polymer or highly solubilized organic molecules to study the effects of solubilizing chains and polymer conjugation. Miscibility is more challenging to measure, but if the precursor powders (rubrene and additive) could be finely ground and well-mixed, the enthalpy of mixing may be apparent upon heating the mixture through the melting point of both materials as the difference in the area of the melting endotherm.

There are also open questions about additive exclusion which will require high-resolution and likely energy-sensitive imaging, such as STM or energy-filtered TEM (EF-TEM). In these experiments, the characteristic HOMO level of the additive or elemental energy signature would be tracked while rastering across a mixed crystal. Additive exclusion to the crystal surface would be especially visible with surface techniques like STM (or even KPFM); incorporated additive pockets would be best observed in transmission with EF-TEM. An alternative method to exposing surface or bulk defects would be by immersing the sample for short periods (minutes) in a solvent like ethanol to preferentially etch defect sites. These etch pits could be compared in size and density to other films grown without additives to determine the prevalence of mechanical and chemical defects. Presumably, samples with pockets of additive would show as more defective than those without. A final method to study additive inclusion would be

Future Work

examination of the optical absorption and emission for confinement or other environmental effects that might be expected in very small additive pockets. For these experiments, the additive must have nested HOMO-LUMO levels for a non-quenching host-guest relationship with the majority species. Such an example would be rubrene in TPBi, TCTA, or NPD, or perhaps an inclusion of SubNc or red OLED emitters in rubrene.

A further step would be to generalize shape selection to other host molecules. Rubrene and TPBi are not the only materials to grow as relatively single crystals in annealed thin film; other examples include NPD, TCTA, 4CzIPN, and DPDCPB. The low-symmetry crystal systems of each of these molecules should allow for comparable studies to those presented in this thesis for rubrene and TPBi on facet-specific growth rate effects.

11.1.2. As a Means to Detect Molecular Concentration and Diffusion

Mapping chemical concentrations in thin films is challenging because of the extremely small material volumes and corresponding masses. The pronounced shape change observed in response to additive incorporation in rubrene films implies that crystal shape could be used to detect concentrations of different species within or adjoining to rubrene films. Recent work in solution-grown plasmonic particles has demonstrated similar sensing abilities applied to a biological assay,⁷⁴⁰ and generalization to the solid state could prove useful as an inexpensive method to probe film compositions.

Implementation of this technique would involve growing or acquiring a film of mixed composition, depositing a neat rubrene film on top of it, then annealing to create crystals. The resulting crystal shape could be compared to rubrene intentionally mixed with the

Future Work

unknown grown on a pure film of the majority mixture species. This could be expanded to test for molecular diffusion using an architecture like Figure 11.1, where a bilayer stack of materials is deposited, then aged at a desired temperature for a period of time, then tested by growing and annealing a rubrene film on the surface. With different ageing temperatures and times, the concentration at the film surface could be used with the diffusion equation

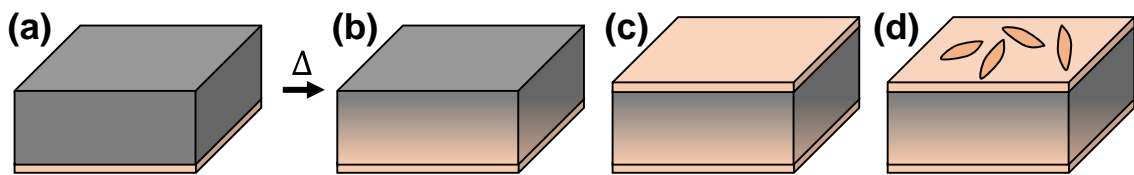


Figure 11.1. Proposed architecture for determination of material diffusivities. (a) Bilayer stack of two materials, with the material on bottom (orange) of interest for determining molecular diffusivity within the top material (black). After ageing (b), the bottom material has diffused into the top, which can then be capped with a rubrene film (c) and annealed (d) to form crystals, the shape of which are correlated to the surface composition of the diffusing molecule.

to determine the diffusivity of the additive through the majority mixture species. Care must be taken to account for molecular motion during the rubrene annealing step, ideally by studying motion in materials with high T_g values for proof of concept.

11.1.3. Optoelectronic Properties of Mixed Crystals

The most promising area for this technique is in the formation of crystalline needle-like domains for transistors, but electrical and optical properties of these structures are currently unknown because of their novelty. It will be enlightening to determine the field-effect mobilities in these structures, since the elongated axis is along the direction of highest mobility in rubrene. The size and isolation of the needles, coupled to their compatibility with oxidized silicon substrates should facilitate testing of isolated needles. Concurrent with mechanistic investigations described above, optoelectronic measurements

Future Work

may also reveal where the additive sits in these likely highly impure crystals. TPBi is an electron-transporting material, while rubrene preferentially transports holes. Will the mixed crystal be somewhat ambipolar, or will rubrene isolate TPBi domains and act as an electron trap? A useful counterexample here is rubrene mixed with TCTA, a hole-transporting material, especially since rubrene is nested within the energy levels of TCTA.

Such films could also be tested in an OPV geometry. If rubrene microwires were grown mixed with C₆₀ or UGH2, capped with a C₆₀ layer, and tested under illumination with

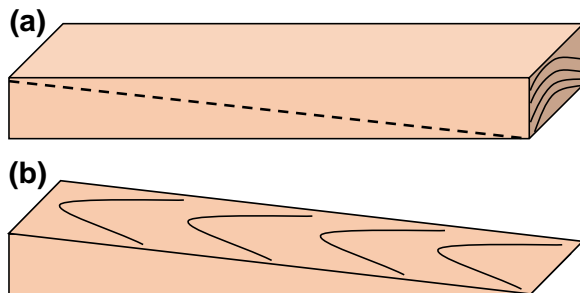


Figure 11.2. Method of etching a rubrene microwire (a) with possible vertical variations in composition or properties into a wedge (b), where the vertical variation is now spread laterally and resolvable by KPFM.

conducting AFM, the optoelectronic performance could be compared to the mixed epitaxy films presented in Chapter 8. The results for V_{oc} and J_{sc} would clearly demonstrate the degree of crystallinity. Alternatively, the

rubrene wires could be etched with focused ion beam milling or an AFM tip to expose the vertical composition of the microwire, which could be imaged using KPFM to observe changes in surface potential from defects and additives (Figure 11.2). Crystalline rubrene films have been intentionally doped before to increase charge carrier density, but only at relatively low concentrations (parts per thousand);⁷⁴¹ the proposed work is anticipated to be at considerably higher additive concentrations.

11.2. Role of Mechanical Strain on Ordering

As recently emphasized in the organic electronics community,⁷⁴² mechanical strain in

Future Work

organic thin films and even laminated single crystals is significantly understudied. Although the effects to-date have only correlated work function and transistor performance with strain (crystals nucleate dislocations upon cooling or heating when the organic-substrate thermal expansion mismatch is too great),^{627,742} such forces must also be expected to be present in annealed films during annealing (compressive) and after cooling (tensile). Experiments testing the impact of these forces could include x-ray scattering at grazing incidence or electron diffraction while heating and cooling a film, specifically looking at in-plane lattice spacing (or, by Poisson's ratio and wide-angle scattering, the out-of-plane lattice spacing). If crystals annealed on highly mismatched substrates show increased numbers of defects, these could be correlated to slip planes for additional information on the film/crystal mechanical properties. Finally, films on various substrates could be tested in transistor geometries for impacts on electrical properties.

11.3. Ordered Glasses in OLEDs

Existing work has proven the benefits of order in OLEDs to improve charge conduction and light outcoupling from the device,^{231,234,743–746} albeit for relatively specific systems. Considerable work exists on understanding thin-film glasses, with general applicability, as discussed in Section 3.1.3. What is lacking is the connection of these studies to device-relevant mixed films, followed by studies of the effects on device efficiency and lifetime

11.3.1. Film Thermodynamics, Kinetics, and OLED Performance

With others, the research group led by Mark Ediger has done excellent work to

Future Work

understand the kinetic and thermal stability of glassy films prepared by vapor deposition discussion in Section 3.1.3. They argue that an improvement in device stability can result from improved film stability, which is corroborated in the limited number of studies available.⁷⁴⁷ The proprietary nature of this work in OLEDs does not lend itself well to generalizable conclusions, incentivizing further study. In addition, many transport layers and nearly all emissive layers in OLEDs are comprised of mixtures, which demands that this work be expanded to include relevant material mixtures.

The proposed studies are straightforward: a combination of thoughtfully chosen material mixtures are to be deposited as thin films and then evaluated on a heated ellipsometry stage to determine T_o , T_f , and T_g at different compositions. What is not obvious is the interaction between dissimilar molecules. Using a molecule from a set of archetypal OLED glassformers (TPD, TPBi, TCTA), how will the listed transformations change with different alloys? Once these trends are established, how do the kinetics of transformation change with heating rate? Examples of additives with different properties include salts or metals (LiF, Al) for small size, acenes (tetracene, pentacene) for largely multipolar C-H interactions in a relatively small molecule, fullerenes (C_{60} , C_{70}) for van der Waals bonding, then OLED materials in order of increasing size (mCP, CBP, TPBi, 3TPYMB, etc.). The film density should be correlated with the molecular free volume and the meshing of steric groups, while the film stability as assessed by T_o should be more related to the intermolecular interactions in solid state. If the two components remain miscible and do not sublime above T_o , variations in T_g may be closest to what is expected

Future Work

for different thermodynamic mixture models.

Once these studies are completed, it would be highly relevant to correlate this work with OLED performance, both in terms of efficiency parameters and device lifetime. Depositing glassy films at varying substrate temperatures has been shown to cause ordering in the film,²²⁸ which has in turn been shown to influence the orientation of some emitters in OLEDs.⁷⁴⁴ Connecting these two areas for the first time could drastically change the way that processing steps are viewed in OLED manufacture.

A final area of investigation could include comparing molecules which can be deposited both from solution and vapor to examine how variables for the vapor (growth rate, substrate temperature, thickness, etc.) correlate with those of the liquid phase (solution loading, spinning speed, solvent volatility/polarity, etc.) in terms of film stability. This could be particularly interesting to explain discrepancies between devices manufactured from different approaches.

11.3.2. Crystallization

An alternative method of inducing order in OLEDs is through crystallization.

There have been numerous attempts

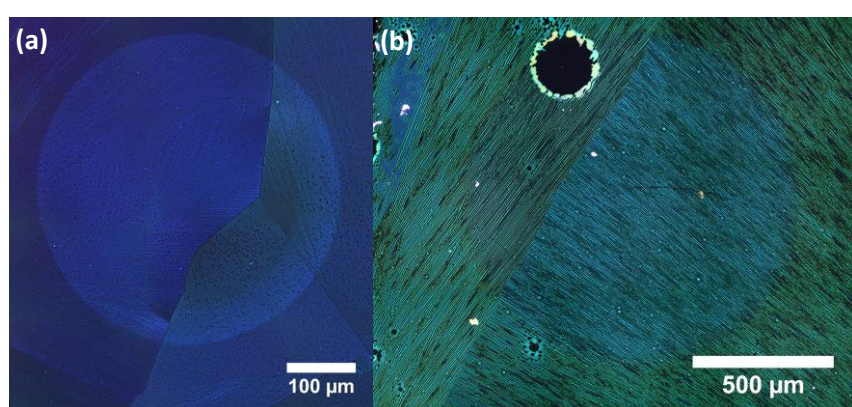


Figure 11.3. 40-nm epitaxial layers (highly birefringent center circles) on 20-nm crystalline templates on ITO. (a) NPD, (b) TCTA. Template treatments were (a) 220 °C for 5 min, (b) 240 °C for 6 min.

Future Work

towards this goal, starting with laminated single crystal devices,^{51,233,748–751} then post-deposition annealed devices,^{111,747} and culminating in templated crystalline OLEDs and OLEDs with a crystalline emissive layer.^{235,300,752} Crystalline OLEDs would be a natural extension of the homoepitaxial and heteroepitaxial work presented in this thesis, especially considering preliminary work on epitaxy in NPD and TCTA showing successful propagation of crystallinity in homoepitaxial films (Figure 11.3).

11.4. Imaging Ultrafast Organic Semiconductor Dynamics

Electron microscopy and diffraction allow visualization of material phenomena on length scales smaller than the molecules used in organic electronic devices. Electron microscopy has been utilized to characterize spatial ordering in heterogeneous mixtures,^{724,753} map crystallographic alignment of epitaxial layers,^{226,754} and identify unique crystalline phases in organic devices,¹⁰⁰ among many other studies. The field of organic electronics may benefit enormously from the incorporation of recent advances in ultrafast electron microscopy (UEM)^{755,756} to spatially visualize coupled exciton, polaron, and phonon dynamics and better understand fundamental processes and limits in electronic materials. The crystal growth techniques studied and applied in this thesis serve as useful methods by which to prepare novel specimens for investigation.

11.4.1. Structural Dynamics

Ultrafast mechanical studies of organic materials could shed light on behavior relevant to electronic devices while simultaneously allowing for the exploration of new classes of

Future Work

physics, as with work on inorganic systems.^{757–759} Organic systems feature both van der Waals interactions and excitons, similar to two-dimensional transition metal dichalcogenides (TMDCs);^{760–763} however, organics bond almost exclusively through van der Waals forces and the excitons have several unique properties.

The van der Waals bonds, coupled with the low-symmetry space groups of most organic crystal lattices, lead to substantial anisotropy in mechanical and optoelectronic properties.⁶²⁸ Such systems as TTF-TCNQ (ionic), C₆₀ (van der Waals spheres), H₂Pc or coronene (van der Waals plates), and tetracene (multipolar) afford ample variation. All may also be readily grown as single crystals with simple PVT growth, discussed in Section 3.3.1. A study of bond type and anisotropy effects on phonon launch location, propagation, and decay pathways could be highly interesting to determine the effects of defects and impurities, where phonon modes depend on scattering or reflection directions. Single crystals may already contain defects in significant numbers,¹²⁶ and homoepitaxial rubrene films show differing amounts of mechanical defects depending on film preparation,⁷¹² giving a simple method to manipulate defect concentration. These results, coupled with a comparison to isotopic crystals²⁵¹ or bulk phonon measurements,⁷⁶⁴ would be useful for modeling the effects of processing and purity upon parameters like charge-carrier mobility.⁷⁶⁵ Observations at low temperature may also explain the existence of an anomalous transition in the field-effect mobility of, *e.g.*, rubrene, which does not originate from a crystallographic change in the material.⁴⁸²

There are also open questions about coupling mechanisms of “hot” excitons to the

Future Work

lattice and exciton decay through non-radiative pathways,^{255,766} which are often dismissed as a change in the coupling of excitons to the phonon bath.^{170,173,200,373} It is of fundamental interest to experimentally observe such coupling *via* exciton decay and phonon launch in a spatially varying medium. This would allow identification of mechanisms for the initial launch and implications for device performance. The different exciton spin states (and their interconversion, which depends on crystallinity)¹⁴³ also provide different temporal and spatial scales for the role of excitons in the formation of phonons, which may be externally validated using photoluminescence lifetime measurements.

11.4.2. Exciton and Polaron Dynamics

UEM has the potential to answer questions that affect much of the organic electronics community: what do the transient and steady-state exciton and polaron populations look like within a given architecture? The answers to these questions impact such diverse areas as charge balance, recombination zone size, and lifetime in OLEDs; carrier and exciton recombination mechanisms and dynamics in OPVs; and mobility and switching frequency in OFETs. Direct visualization of polaron and exciton dynamics would be strongly complementary to existing simulation- and fitting-based methods.

Detecting polaron populations and motion could be conducted in an OPV architecture such as that shown in Figure 11.4. In this scheme, an organic single crystal would have an exciton-quenching material deposited on a desired facet, noting that different facets and thus diffusion directions should show different behavior.^{195,604} The quencher thickness is irrelevant for the following experiments, but could be modified if dynamics in the quencher

Future Work

were also of interest. The crystal would then be sliced perpendicular to the quencher-crystal interface to produce a thin slab, positioned on a grid with the interface parallel to the electron beam. Upon laser excitation, excitons will be generated throughout the crystal and diffuse to be dissociated at the quenching interface, producing carriers which will also diffuse to establish an equilibrium population. Rubrene, the focus of much of this thesis, is an example material that may be ideal for proof-of-concept experiments: $L_D \sim 5 \mu\text{m}$ (triplet), $\tau \sim 1 \mu\text{s}$ (triplet), and $\mu_h \sim 20 \text{ cm}^2/\text{V s}$.^{195,604} These length and time scales allow for exciton and polaron migration well within the spatiotemporal scales of UEM. The relatively low absorption coefficient of rubrene also allows for excitation through the bulk of a specimen, since the absorption length is approximately 1 μm .⁵⁹⁴ Furthermore, if the outer edges of the crystals are grounded or shorted together, the polaron and exciton populations will decay on similar timescales ($\sim 1 \mu\text{s}$), allowing for $\sim 100 \text{ kHz}$ repetition rates if electronic processes are limiting. Unfortunately, the low thermal conductivity of organic materials ($\sim 0.5 \text{ W/m K}$)^{764,767,768} and interface resistance may well limit repetition rates to below this value.

Efficiently detecting generated polarons and excitons may be more challenging. There is work demonstrating imaging of charge carrier dynamics in inorganic systems,^{769–771} but

Future Work

these studies detect emitted secondary electrons, the energies of which are highly sensitive to electronic excitation of the material. However, disparities in carrier populations have been shown to produce an electromagnetic plasma lensing effect in TEM,^{772,773} so with a relatively high laser fluence (and potentially lower accelerating voltage), a sufficient population of charge carriers could be generated to deflect a measureable amount of the electron beam. Simulations have suggested that a 2.5 pC charge plasma spread over a 30 μm disc is capable of producing lensing;⁷⁷³ this equates to 2.21×10^{16} carriers/cm³ for a 1- μm -thick specimen, a dimension which is likely attainable for such low-Z organic materials.⁷³³ Extracted photoinduced carrier densities in OPVs easily reach this value,⁷³⁸ implying that such visualization is possible in these or thinner geometries. The low-Z atoms comprising most organic molecules may further aid in the detection of excess charge. In this system, owing to the large μ_h , steady-state results could be compared with carrier populations in the same sample under illumination measured by KPFM. This could form the basis for measurement of spatial dynamics in systems below the resolution of other techniques, such as crystalline SubPc.

Excitons could be detected using one of two methods: lattice distortion (reciprocal space) and molecular energy state (electron energy loss spectroscopy, EELS). Excitons (or even CT states) are charge-neutral quasiparticles which distort the surrounding lattice and exist as excited molecular (or bimolecular) states. At high enough exciton densities, this distortion could manifest similarly to the Debye-Waller effect,⁷⁷⁴ where the measured diffraction intensity varies inversely with average spatial perturbation. This could be

Future Work

deconvoluted from confounding factors like specimen tilt and a heat-induced Debye-Waller effect by measuring sample regions with and without an exciton-quenching interface. Otherwise, excitons may be detectable by energy loss of the electron beam, since excitonic energies commonly range from 1-5 eV, resolvable from ground-state electronic transitions by modern electron spectrometers.⁷³³ For these experiments, it may be best to use crystals of a wider energy gap material than rubrene (optical $E_g \sim 1.5$ eV),^{713,735} such as anthracene (optical $E_g \sim 4$ eV,¹⁵⁰ $L_D \sim 50$ nm²⁵⁹), to increase the magnitude of the exciton energy. If carrier dynamics confound exciton measurements, an exciton-quenching and carrier recombination layer, such as a metal or doped organic, could be used to significantly reduce the polaron population.^{709,775,776} At an appropriately chosen interface (*e.g.*, anthracene-tetracene), the energetics of the CT state may also be distinguishable from those of the excitons (HOMO-HOMO $E_{CT} \sim 3.4$ eV¹⁵⁰), affording study of their dynamics and motion.

If the visualization of excitons in a slab geometry is successful, probing anisotropic exciton transport at low-symmetry interfaces (exciton gating) could be used to experimentally test existing theoretical work.²³⁸ This could be accomplished by heteroepitaxial growth of a material which undergoes preferential energy transfer to or from rubrene, such as DBP.⁷⁰³ This materials system is capable of forming high efficiency OPVs,⁷⁰³ making it an interesting case study. Such systems should also show exciton concentration discontinuities consistent with the work presented in Chapter 8.

Finally, direct visualization of exciton dynamics would elucidate the role of defects and

Future Work

impurities on exciton recombination dynamics, including fission and fusion. Defect states are suspected to be responsible for a majority of light emission in some single-crystal systems,³⁷⁰ which suggests that there should be spatial variation in exciton populations corresponding to such defects. UEM is an ideal tool to probe these defects, with molecular-level spatial and elemental resolution to identify defects, followed by spatiotemporal resolution to elucidate their impacts on dynamics. Interconversion of spin-singlet and triplet excitons through fission and fusion (common in rubrene and other organic crystals¹⁴³) with corresponding effects on phonon and polaron evolution could be mapped across laser fluences and specimen temperatures to further demonstrate the role of different types of defect states in exciton and polaron dynamics. These observations could lead to feedback for optimizing purification and crystal growth schemes to produce faster and more efficient devices.

12. CONCLUSIONS

This thesis explores fundamental questions related to the mechanisms of crystallization in thin films, how a greater understanding can lead to thoughtfully designed film and device architectures, and ultimately how this knowledge can be used to build more efficient electronic devices. Significant results and novel aspects of this work are summarized in this chapter.

12.1. Annealing-Induced Crystallization in Organic Films

The majority of work on annealing thin organic films focused on the archetypal organic semiconductor rubrene. Rubrene is useful as a model system in that it deposits as an amorphous film but readily undergoes crystallization to form a variety of polymorphs and growth habits that must be identified and selected. This work was able to confirm the existence of the two polymorphs reported in thin film (triclinic and orthorhombic) and also report on other methods to select for each polymorph. Consistent with existing literature,⁴⁵¹ the orthorhombic phase is favored by thin (20 nm) films, relatively bright illumination, higher annealing temperatures, and potentially high heating rate for the rapidity of attaining a high annealing temperature. However, the additional factors here allow some speculation on the mechanisms of polymorph selection. In addition to known heating rate effects, the

Conclusions

changing composition with thickness implies a transition from substrate-dominated to bulk-dominated behavior. Possible mechanisms include thermally-induced mechanical strain and relaxation of the film as well as a thickness-dependent glass transition.

Rubrene also exhibits a variety of previously undescribed crystal growth modes and regimes. With increasing temperature, the films display spherulitic growth of the triclinic polymorph, then single-crystal growth and finely branched polycrystalline spherulitic growth of the orthorhombic polymorph. Each of the higher-temperature modes appears to nucleation from the lower-temperature modes. These transitions are essential to note for construction of devices, given the differences in optoelectronic properties between polymorphs and differences in crystal quality between growth modes.^{366,488} The spherulite growth mode inevitably includes grain boundaries, which are particularly potent in that they exist near substrate, in the volume transporting the majority of charge in conventional bottom-gated transistors. Each consecutive boundary hinders charge and exciton motion within a device constructed on such films.^{373,374} This work clearly identifies an ideal temperature range of 170-180 °C and film thickness of 20 nm for producing the highest quality crystalline films.

The crystals within these thin films can also be tuned in shape, which was hitherto unknown in the field of solid-phase organic crystallization before this thesis. Contrary to existing solid-state inorganic examples,^{656–658,660} additives slow the growth of crystal planes and do so anisotropically in low-symmetry crystal systems, more analogous to the directed growth of nanowires in solution by ligand attachment.^{648,649} By simple

Conclusions

incorporation of auxiliary species (additives), the crystal shape of rubrene may be manipulated from equiaxed, circular grains to crystalline wires with an aspect ratio over 50. The effect varies strongly with different types of additives, presenting several avenues for future work which have been discussed. It is anticipated that such growth could lead to novel ways to manufacture organic conductors, transistors, and lasers, while also creating a new method to measure concentrations and motion of molecules in multilayer stacks.

Finally, annealing thin organic films can yield useful surface topography, as evidenced by the formation of an optical grating by simply annealing thin films of TPBi. Although the proposed mechanism of mechanical strain relaxation has been previously observed and utilized in polymer-metal and all-polymer systems,^{670,671,684} this work is the first demonstration of such an effect in glassy films comprised of small molecules, with useful directing of pattern formation by the involved transformation mechanisms. This work is also interesting in that it affords a completely different method by which to observe the lateral transformation of a solid film into a supercooled liquid followed immediately by crystallization. Such behavior has previously only been observed vertically, and on much slower time scales.^{227,333}

12.2. Epitaxial Growth of Crystalline Organic Films

In this thesis, efforts were also directed towards applying crystallization to device-relevant geometries in order to study the effects of crystallization on device parameters. Again, rubrene provided an ideal platform for this study owing to its compatibility with multiple device and architecture types as well as its amorphous character when deposited

Conclusions

onto a bare substrate. Rubrene homoepitaxial layers matched the literature,⁷¹² with the appearance of numerous screw and edge dislocations. When these epitaxial layers were mixed with dissimilar species (C₆₀ and UGH2), the films preserved their crystallinity to approximately 10 vol% additive, after which point the films displayed significant roughening, with tall, faceted, and smooth domains surrounded by lower-lying smooth regions. With increasing amount of additive, the faceted domains (assumed to be nearly pure rubrene) were reduced in size and overall film area, becoming narrower and wire-like. At high enough additive concentrations (>20 vol%), the films again became smooth, suggesting a total loss of crystallinity.

When this work was expanded to heteroepitaxial growth of SubPc on BP2T, BP2T was rigorously determined to not serve as an epitaxial template for room-temperature growth of SubPc. The possible reasons for this include the very small BP2T grains size on ITO confounding contiguous growth, insufficient thermal energy for rearrangement of SubPc on BP2T, and poorly-defined interactions of SubPc with crystalline BP2T leading to poor order. SubPc crystallizes well in a homoepitaxial geometry, so the problem is clearly at the BP2T-SubPc interface. Suggestions for future work in this area include the use of a heated substrate during SubPc deposition and exploration of substrate planarization effects concurrent with heated SubPc deposition onto BP2T.

The results from these studies are valuable in providing counterexamples to other demonstrations of mixed epitaxial growth in systems which crystallize more easily, even when deposited onto an untreated substrate.^{588,724} Progress in generalizing such mixed

Conclusions

epitaxial growth to a naturally amorphous system provides insight into the pathways for breakdown of a crystalline lattice and how such pathways vary across different types of additives. Coupled with device measurements as performed here, these results will serve as a point of comparison for others seeking to grow mixed crystalline systems.

12.3. Optoelectronic Properties of Crystalline Organic Films

The first parameter exploration presented in this thesis is the exciton diffusion length of SubPc, which increases dramatically upon crystallization. Although interesting in itself, the work more broadly focuses on the various contributions of underlying parameters to this enhancement. The results show the largest increase along directions of closest molecular proximity which lie in the substrate plane, presenting an opportunity for improvement with film texturing. While not surprising, the treatment of this change in exciton diffusion within an anisotropic crystalline lattice is non-trivial and had not been previously presented or used. Other effects are discussed, including the increased electronic coupling in the crystalline state, film roughness, and excitonic band structure, where this work is also among the first to quantitatively simulate and suggest changes in the excitonic band structure as a means for improvement in exciton diffusion.

When crystalline rubrene devices were constructed, V_{oc} is reduced, but photocurrent increases for thick films, indicative of improved carrier and exciton harvesting. With an incorporation of an inert additive (UGH2), V_{oc} increases, eventually reaching the

Conclusions

amorphous value, while other properties suffer from increased series resistance. With an optically and electrically active additive (C_{60}), trends are more complicated, since now the additive can both contribute to photocurrent and facilitate carrier recombination. Overall, incorporation of C_{60} does not cause a marked increase in measurable device parameters, likely because of charge trapping and recombination.

When crystalline devices are constructed using SubPc templated by BP2T, the primary contribution of BP2T is to dissociate excitons and thereby improve the photocurrent while reducing V_{oc} , likely from leakage and altered injection barriers. The as-constructed devices show no signs of crystallinity in the SubPc layer, suggesting that the changes in electronic properties stem from energetic changes between ITO and SubPc.

12.4. Outlook

After being introduced in studies of photosynthesis and since used as pigments, optical filters, and various other products, organic semiconductors have finally grown to assume a respectable position in the electronics market. OLEDs are stronger than ever, having met and surpassed quality benchmarks to find use in a plethora of display and lighting applications. OFETs are increasingly viable in flexible and inexpensive circuitry, such as RFID tags and other ubiquitous tools. Even OPV companies have found ways to continually rebrand themselves to take advantage of some of the niche applications that OPVs excel at, such as building-integrated PV and ultra-portable PV. While OPVs will likely be eclipsed by other upcoming technologies such halide perovskite solar cells, such technologies still face significant technical challenges including stability and toxicity. Even

Conclusions

so, much of the underlying work in OPVs affects other areas of organic electronics and *vice versa*, making contributions to any field useful in some degree for all. It is hoped that this thesis allows others to continue progressing towards building devices which are newer, better, less expensive, and enhance lives.

13. BIBLIOGRAPHY

- (1) Gaj, M. P. High-Performance Organic Light-Emitting Diodes for Flexible and Wearable Electronics, Georgia Institute of Technology, 2016.
- (2) Kaduwal, D.; Zimmermann, B.; Würfel, U. *Sol. Energy Mater. Sol. Cells* **2014**, *120*, 449.
- (3) Briseno, A. L.; Tseng, R. J.; Ling, M.-M.; Falcao, E. H. L.; Yang, Y.; Wudl, F.; Bao, Z. *Adv. Mater.* **2006**, *18* (17), 2320.
- (4) Pop, S. D.; Kate, S. P.; Rappich, J.; Hinrichs, K. *Sol. Energy Mater. Sol. Cells* **2014**, *127*, 169.
- (5) Sun, Y.; Zhu, X.; Chen, Z.; Zhang, Y.; Cao, Y. *J. Org. Chem.* **2006**, *71*, 6281.
- (6) Yoon, M.-H.; Facchetti, A.; Stern, C. E.; Marks, T. J. *J. Am. Chem. Soc.* **2006**, *128* (17), 5792.
- (7) Sun, Z.; Wu, J. **2011**, No. 2, 519.
- (8) Briseno, A. L.; Mannsfeld, S. C. B.; Ling, M. M.; Liu, S.; Tseng, R. J.; Reese, C.; Roberts, M. E.; Yang, Y.; Wudl, F.; Bao, Z. *Nature* **2006**, *444* (December), 913.
- (9) Søndergaard, R. R.; Hösel, M.; Krebs, F. C. *J. Polym. Sci. Part B Polym. Phys.* **2013**, *51* (1), 16.
- (10) Hecker, K. *Organic Electronics Association*. Frankfurt/Main, Germany 2011.,
- (11) Strohriegl, P.; Wagner, D.; Schrögel, P.; Hoffmann, S. T.; Köhler, A.; Heinemeyer, U.; Münster, I. *Proc. SPIE* **2013**, 8829, 882906.
- (12) Tao, Y.; Yang, C.; Qin, J. *Chem. Soc. Rev.* **2011**, *40*, 2943.
- (13) Kalyani, N. T.; Dhoble, S. J. *Renew. Sustain. Energy Rev.* **2012**, *16*, 2696.
- (14) Sirringhaus, H. *Adv. Mater.* **2014**, *26* (9), 1319.
- (15) Yun, M.; Sharma, A.; Fuentes-Hernandez, C.; Hwang, D. K.; Dindar, A.; Singh, S.; Choi, S.; Kippelen, B. *Appl. Mater. Interfaces* **2014**, *6*, 1616.
- (16) Dimitrakopoulos, C. D.; Malenfant, P. R. L. *Adv. Mater. (Weinheim, Ger.)* **2002**, *14* (2), 99.
- (17) Schlenker, C. W.; Barlier, V. S.; Chin, S. W.; Whited, M. T.; McAnally, R. E.; Forrest, S. R.; Thompson, M. E. *Chem. Mater.* **2011**, *23* (18), 4132.
- (18) Gregg, B. A. *J. Phys. Chem. B.* **2003**, *107*, 4688.
- (19) Peumans, P.; Yakimov, A.; Forrest, S. R. *J. Appl. Phys.* **2003**, *93* (7), 3693.
- (20) Dolcourt, J.; Bennett, B. We tried on Lenovo's bendable phone that you can wear like a watch <https://www.cnet.com/pictures/flexible-tech-lets-you-wear-your-phone-literally-pictures/5/>.

Bibliography

- (21) Philips. Lumiblade OLEDs <http://www.lighting.philips.com/main/products/oled> (accessed Apr 4, 2017).
- (22) Katzmaier, D. LG rolls up OLED TV, smokes my mind (hands-on) <https://cnet2.cbsistatic.com/img/afU5XBniEEilurzU21B2564e1NY=/770x433/2016/01/07/5a1a0ed1-b958-46f2-878c-09e0cb5ad374/ces2016lgrollable.jpg> (accessed Jan 3, 2017).
- (23) Fu, H.; Cheng, Y.-M.; Chou, P.-T.; Chi, Y. *Mater. Today* **2011**, *14* (10), 472.
- (24) Kido, J. *Soc. Inf. Disp.* **2008**, *39* (1), 931.
- (25) Triambulo, R. E.; Park, J. W. *Org. Electron. physics, Mater. Appl.* **2016**, *28*, 123.
- (26) Asadpoordarvish, A.; Sandström, A.; Larsen, C.; Bollström, R.; Toivakka, M.; Österbacka, R.; Edman, L. *Adv. Funct. Mater.* **2015**, n/a.
- (27) Obama, B. *Science* **2017**, *355* (6321), 126.
- (28) Barbose, G.; Darghouth, N. R.; Weaver, S.; Feldman, D.; Margolis, R.; Wiser, R. *Prog. Photovoltaics Res. Appl.* **2014**, *23* (6), 692.
- (29) Nayak, P. K.; Cahen, D. *Adv. Mater.* **2014**, *26* (10), 1622.
- (30) Lewis, N. S. *Science* **2016**, *351* (6271), aad1920.
- (31) Rand, B. P.; Genoe, J.; Heremans, P.; Poortmans, J. *Prog. Photovolt Res. Appl.* **2007**, *15* (July 2015), 659.
- (32) Isabella, O.; Smets, A. H. M.; Zeman, M. *Sol. Energy Mater. Sol. Cells* **2014**, *1*.
- (33) Green, M. A.; Emery, K.; Hishikawa, Y.; Warta, W.; Dunlop, E. D. *Prog. Photovoltaics Res. Appl.* **2014**, *22*, 701.
- (34) Leong, W. L.; Ooi, Z.-E.; Sabba, D.; Yi, C.; Zakeeruddin, S. M.; Graetzel, M.; Gordon, J. M.; Katz, E. A.; Mathews, N. *Adv. Mater.* **2016**, n/a.
- (35) Heliatek. Asia's largest Building Integrated Organic PV (BIOPV) First installation of HeliaFilm® completed in Singapore <http://www.heliatek.com/en/press/press-releases/details/asias-largest-building-integrated-organic-pv-biopv-first-installation-of-helialfilm-completed-in-singapore>.
- (36) InfinityPV. Flexible solar cell https://infinitypv.com/images/infinityPV_OPV_organic_solar-DSC_4013.jpg (accessed Jan 3, 2017).
- (37) OPVIus. Transparent OPV rooftop powers African Union lighting <http://www.opvius.com/africa-supplies-opv-electricity.html> (accessed Mar 15, 2017).
- (38) Hains, A. W.; Liang, Z.; Woodhouse, M. A.; Gregg, B. A. *Chem. Rev.* **2010**, *110* (11), 6689.
- (39) Printz, A. D.; Savagatrup, S.; Rodriguez, D.; Lipomi, D. J. *Sol. Energy Mater. Sol. Cells* **2015**, *134*, 64.
- (40) Gaudiana, R.; Brabec, C. *Nat. Photonics* **2008**, *2* (May), 287.
- (41) Siciliano, A. The future is clear <http://msutoday.msu.edu/feature/2015/the-future-is-clear/> (accessed May 1, 2017).
- (42) CES 2017: Heliatek exhibits building integrated PV <http://www.solarnovus.com/ces-2017-heliatek-exhibits-building-integrated->

Bibliography

- pv_N10563.html.
- (43) Pandey, R.; Kerner, R. A.; Menke, S. M.; Holst, J.; Josyula, K. V. B.; Holmes, R. J. *Org. Electron.* **2013**, *14* (3), 804.
- (44) Young, M.; Traverse, C. J.; Pandey, R.; Barr, M. C.; Lunt, R. R. *Appl. Phys. Lett.* **2013**, *103* (13), 133304.
- (45) Neaman, D. A. *Semiconductor Physics and Devices*, 4th ed.; McGraw-Hill: New York, NY, 2012.
- (46) PolyIC. Printed electronics on roll http://www.polyic.com/fileadmin/images/content-images/presse_news_events/Pictures_for_the_Press/28.jpg (accessed Mar 15, 2017).
- (47) PolyIC. Model of a polymer flexible RFID tag http://www.polyic.com/fileadmin/images/content-images/presse_news_events/Pictures_for_the_Press/55.jpg (accessed Mar 14, 2017).
- (48) Someya, T.; Pal, B.; Huang, J.; Katz, H. E. *MRS Bull.* **2008**, *33*, 690.
- (49) Mabeck, J. T.; Malliaras, A. G. *Anal. Bioanal. Chem.* **2006**, *384*, 343.
- (50) Campana, A.; Cramer, T.; Simon, D. T.; Berggren, M.; Biscarini, F. *Adv. Mater.* **2014**, n/a.
- (51) Nakanotani, H.; Kabe, R.; Yahiro, M.; Takenobu, T.; Iwasa, Y.; Adachi, C. *Appl. Phys. Express* **2008**, *1*, 91801.
- (52) Lee, B. H.; Hsu, B. B. Y.; Patel, S. N.; Labram, J.; Luo, C.; Bazan, G. C.; Heeger, A. J. *Nano Lett.* **2015**, acs.nanolett.5b03868.
- (53) Braga, D.; Erickson, N. C.; Renn, M. J.; Holmes, R. J.; Frisbie, C. D. *Adv. Funct. Mater.* **2012**, *22* (8), 1623.
- (54) Yokoyama, T.; Park, C. B.; Nishimura, T.; Kita, K.; Toriumi, A. *Jpn. J. Appl. Phys.* **2008**, *47* (5), 3643.
- (55) Qian, X.; Wang, T.; Yan, D. *Org. Electron.* **2013**, *14* (4), 1052.
- (56) Giebink, N. C.; Andrade, B. W. D.; Weaver, M. S.; Mackenzie, P. B.; Brown, J. J.; Thompson, M. E.; Forrest, S. R.; Giebink, N. C.; Andrade, B. W. D.; Weaver, M. S.; Mackenzie, P. B.; Brown, J. J.; Thompson, M. E.; Forrest, S. R. *J. Appl. Phys.* **2008**, *103*, 44509.
- (57) McCulloch, I.; Heeney, M.; Bailey, C.; Genevicius, K.; Macdonald, I.; Shkunov, M.; Sparrowe, D.; Tierney, S.; Wagner, R.; Zhang, W.; Chabinyc, M. L.; Kline, R. J.; McGehee, M. D.; Toney, M. F. *Nat. Mater.* **2006**, *5* (4), 328.
- (58) Tyagi, P.; Srivastava, R.; Giri, L. I.; Tuli, S.; Lee, C. *Synth. Met.* **2015**, *216*, 40.
- (59) Smith, P. F.; Gerroir, P.; Xie, S.; Hor, A. M.; Popovic, Z.; Hair, M. L. *Langmuir* **1998**, *14* (20), 5946.
- (60) Wang, C.-H.; Jian, S.-D.; Chan, S.-W.; Ku, C.-S.; Huang, P.-Y.; Chen, M.-C.; Yang, Y.-W. *J. Phys. Chem. C* **2012**, *116* (1), 1225.
- (61) Baek, H.-I.; Lee, H.-K.; Lee, C. *Proc. SPIE* **2006**, *6333*, 63331B.
- (62) Balderrama, V. S.; Estrada, M.; Han, P. L.; Granero, P.; Pallarés, J.; Ferré-Borrull,

Bibliography

- J.; Marsal, L. F. *Sol. Energy Mater. Sol. Cells* **2014**, *125*, 155.
- (63) Feldman, A.; Ahrenkiel, R.; Lehman, J. *Sol. Energy Mater. Sol. Cells* **2013**, *117*, 408.
- (64) Yuen, A. P.; Bamsey, N. M.; Hor, A.-M.; Preston, J. S.; Klenkler, R. a.; Jovanovic, S. M.; Loutfy, R. O. *Sol. Energy Mater. Sol. Cells* **2011**, *95* (11), 3137.
- (65) Street, R. A.; Davies, D. M. *Appl. Phys. Lett.* **2013**, *102* (4), 43305.
- (66) Bastos, P.; Voroshazi, E.; Fron, E.; Brammertz, G.; Vangerven, T.; Auweraer, M. Van Der; Poortmans, J.; Cheyns, D. *Appl. Mater. INterfaces* **2016**, *8*, 9798.
- (67) Glen, T. S.; Scarratt, N. W.; Yi, H.; Iraqi, a.; Wang, T.; Kingsley, J.; Buckley, a. R.; Lidzey, D. G.; Donald, a. M. *Sol. Energy Mater. Sol. Cells* **2015**, *140*, 25.
- (68) Gong, J.; Wan, L.; Lei, S.; Bai, C.; Lee, S. **2005**, 1675.
- (69) D'Andrade, B. W.; Forrest, S. R.; Chwang, A. B. *Appl. Phys. Lett.* **2003**, *83* (19), 3858.
- (70) Culligan, B. S. W.; Chen, A. C.; Wallace, J. U.; Klubek, K. P.; Tang, C. W.; Chen, S. H. *Adv. Funct. Mater.* **2006**, *16*, 1481.
- (71) Sapkota, S. B.; Spies, A.; Zimmermann, B.; Dürr, I.; Würfel, U. *Sol. Energy Mater. Sol. Cells* **2014**, *130*, 144.
- (72) Gevorgyan, S. A.; Jørgensen, M.; Krebs, F. C.; Sylvester-Hvid, K. O. *Sol. Energy Mater. Sol. Cells* **2011**, *95* (5), 1389.
- (73) Chung, Y.-H.; Sheng, L.; Xing, X.; Zheng, L.; Bian, M.; Chen, Z.; Xiao, L.; Gong, Q. *J. Mater. Chem. C* **2015**, *3*, 1794.
- (74) El Chaar, L.; Lamont, L. a.; El Zein, N. *Renew. Sustain. Energy Rev.* **2011**, *15* (5), 2165.
- (75) Narendran, N.; Gu, Y.; Freyssinier, J. P.; Yu, H.; Deng, L. *J. Cryst. Growth* **2004**, *268*, 449.
- (76) Borkar, S. *IEEE Micro* **2005**, *25* (6), 10.
- (77) Vissenberg, M. C. J. M.; Matters, M. *Phys. Rev. B* **1998**, *57* (20), 964.
- (78) Menke, S. M.; Holmes, R. J. *Energy Environ. Sci.* **2013**, *7*, 499.
- (79) Street, R. a.; Schoendorf, M. *Phys. Rev. B* **2010**, *81* (20), 1.
- (80) Ray, B.; Lundstrom, M. S.; Alam, M. A. *Appl. Phys. Lett.* **2012**, *100* (1), 13307.
- (81) Tzabari, L.; Zayats, V.; Tessler, N. *J. Appl. Phys.* **2013**, *114* (15), 154514.
- (82) Wu, Y.; Zhou, Y. C.; Wu, H. R.; Zhan, Y. Q.; Zhou, J.; Zhang, S. T.; Zhao, J. M.; Wang, Z. J.; Ding, X. M.; Hou, X. Y. *Appl. Phys. Lett.* **2005**, *87* (4), 44104.
- (83) Burin, A. L.; Ratner, M. A. *J. Phys. Chem. A* **2000**, *104* (20), 4704.
- (84) Voz, C.; Puigdollers, J.; Asensi, J. M.; Galindo, S.; Cheylan, S.; Pacios, R.; Ortega, P.; Alcubilla, R. *Org. Electron.* **2013**, *14* (6), 1643.
- (85) Forrest, S. R. *MRS Bull.* **2005**, *30* (January), 28.
- (86) Janssen, R. A. J.; Nelson, J. *Adv. Mater.* **2013**, *25* (13), 1847.
- (87) Mikhnenko, O. V.; Kuik, M.; Lin, J.; van der Kaap, N.; Nguyen, T.-Q.; Blom, P. W. M. *Adv. Mater.* **2014**, *26*, 1912.
- (88) Baumann, J.; Fayer, M. D. *J. Chem. Phys.* **1986**, *85*, 4087.
- (89) Obara, S.; Itabashi, M.; Okuda, F.; Tamaki, S.; Tanabe, Y.; Ishii, Y.; Nozaki, K.;

Bibliography

- Haga, M.-A. *Inorg. Chem.* **2006**, *45* (22), 8907.
- (90) Sancho-García, J. C.; Pérez-Jiménez, a J.; Olivier, Y.; Cornil, J. *Phys. Chem. Chem. Phys.* **2010**, *12* (32), 9381.
- (91) Sonar, P.; Lim, J. P. F.; Chan, K. L. *Energy Environ. Sci.* **2011**, *4* (5), 1558.
- (92) Wu, W.; Liu, Y.; Zhu, D. *Chem. Soc. Rev.* **2010**, *39*, 1489.
- (93) Bredas, J.-L.; Norton, J. E.; Cornil, J.; Coropceanu, V. *Acc. Chem. Res.* **2009**, *42* (11), 1691.
- (94) Tang, C. W.; Vanslyke, S. a. *Appl. Phys. Lett.* **1987**, *51* (1987), 913.
- (95) Tang, C. W. *Appl. Phys. Lett.* **1986**, *48* (2), 183.
- (96) Hiramoto, M.; Fujiwara, H.; Yokoyama, M. *Appl. Phys. Lett.* **1991**, *58* (10), 1062.
- (97) Xiao, X.; Bergemann, K. J.; Zimmerman, J. D.; Lee, K.; Forrest, S. R. *Adv. Energy Mater.* **2014**, *4* (7), 1.
- (98) Pandey, R.; Holmes, R. J. *Adv. Mater.* **2010**, *22* (46), 5301.
- (99) Erickson, N. C.; Holmes, R. J. *Appl. Phys. Lett.* **2010**, *97* (8), 83308.
- (100) Pandey, R.; Gunawan, A. A.; Mkhoyan, K. A.; Holmes, R. J. *Adv. Funct. Mater.* **2012**, *22* (3), 617.
- (101) Cui, S.; Hu, Y.; Lou, Z.; Yi, R.; Hou, Y.; Teng, F. *Org. Electron.* **2015**, *22*, 51.
- (102) Hasegawa, T.; Takeya, J. *Sci. Technol. Adv. Mater.* **2009**, *10*, 24314.
- (103) Liao, H.-C.; Ho, C.-C.; Chang, C.-Y.; Jao, M.-H.; Darling, S. B.; Su, W.-F. *Mater. Today* **2013**, *16* (9), 326.
- (104) Grob, S.; Bartynski, A. N.; Opitz, A.; Gruber, M.; Grassl, F.; Meister, E.; Linderl, T.; Hörmann, U.; Lorch, C.; Moons, E.; Schreiber, F.; Thompson, M. E.; Brütting, W. *J. Mater. Chem. A* **2015**, 15700.
- (105) Dang, E.; Gooding, R. *Phys. Rev. Lett.* **1995**, *74* (19), 3848.
- (106) Kirsch, C.; Mitran, S. *J. Appl. Phys.* **2012**, *112* (5), 54502.
- (107) Ameri, T.; Li, N.; Brabec, C. J. *Energy Environ. Sci.* **2013**, *6* (8), 2390.
- (108) Itaka, K.; Yamashiro, M.; Yamaguchi, J.; Yaginuma, S.; Haemori, M.; Koinuma, H. *Appl. Surf. Sci.* **2006**, *252* (7), 2562.
- (109) Forrest, S. R. *Chem. Rev.* **1997**, *97* (6), 1793.
- (110) Kang, R.; Oh, S.-H.; Na, S.-I.; Kim, T.-S.; Kim, D.-Y. *Sol. Energy Mater. Sol. Cells* **2014**, *120*, 131.
- (111) Osipov, K. a.; Pavlovskii, V. N.; Lutsenko, E. V.; Gurskii, A. L.; Yablonskii, G. P.; Hartmann, S.; Janssen, A.; Johannes, H.-H.; Caspary, R.; Kowalsky, W.; Meyer, N.; Gersdorff, M.; Heukens, M.; van Gemmern, P.; Zimmermann, C.; Jessen, F.; Kalisch, H.; Jansen, R. H. *Thin Solid Films* **2007**, *515* (11), 4834.
- (112) Li, Y.; Sun, H.; Shi, Y.; Tsukagoshi, K. *Sci. Technol. Adv. Mater.* **2014**, *15* (2), 24203.
- (113) Zhu, J.; Wang, W.; Zhong, Q.; Li, L.; Du, C.; Lv, A.; Wang, H.; Fuchs, H.; Chi, L. *J. Mater. Chem. C* **2014**, *2*, 9359.
- (114) Lee, H. M.; Kim, J. J.; Choi, J. H.; Cho, S. O. *ACS Nano* **2011**, *5* (10), 8352.
- (115) Kim, J. J.; Lee, H. M.; Park, J. W.; Cho, S. O. *J. Mater. Chem. C Mater. Opt. Electron. devices* **2015**, *3*, 2650.

Bibliography

- (116) Bordo, K.; Rubahn, H. *Mater. Sci.* **2012**, *18* (4), 313.
- (117) Cheng, L. F.; Liao, L. S.; Lai, W. Y.; Sun, X. H.; Wong, N. B.; Lee, C. S.; Lee, S. T. *Chem. Phys. Lett.* **2000**, *319*, 418.
- (118) Adams, C. D.; Srolovitz, D. J. *J. Appl. Phys.* **1993**, *74* (3), 1707.
- (119) Chen, H.; Hsiao, Y.-C.; Hu, B.; Dadmun, M. *Adv. Funct. Mater.* **2014**, n/a.
- (120) Noda, Y.; Minemawari, H.; Matsui, H.; Yamada, T.; Arai, S.; Kajiya, T.; Doi, M.; Hasegawa, T. *Adv. Funct. Mater.* **2015**, n/a.
- (121) Kim, H.; Boulogne, F.; Um, E.; Jacobi, I.; Button, E.; Stone, H. A. **2016**, *124501* (March), 1.
- (122) Breuer, T.; Witte, G. *ACS Appl. Mater. Interfaces* **2013**, *5*, 9740.
- (123) Aizenberg, J.; Black, a J.; Whitesides, G. M. *Nature* **1999**, *398* (1971), 495.
- (124) Briseno, A. L.; Aizenberg, J.; Han, Y.-J.; Penkala, R. a; Moon, H.; Lovinger, A. J.; Kloc, C.; Bao, Z. *J. Am. Chem. Soc.* **2005**, *127* (35), 12164.
- (125) Feron, K.; Nagle, T. J.; Rozanski, L. J.; Gong, B. B.; Fell, C. J. *Sol. Energy Mater. Sol. Cells* **2013**, *109*, 169.
- (126) Chapman, B. D.; Checco, a.; Pindak, R.; Siegrist, T.; Kloc, C. *J. Cryst. Growth* **2006**, *290* (2), 479.
- (127) Koelling, S.; Richard, O.; Bender, H.; Uematsu, M.; Schulze, A.; Zschaetzsch, G.; Gilbert, M.; Vandervorst, W. *Nano Lett.* **2013**, *13* (6), 2458.
- (128) Forrest, S. R. *Nature* **2004**, *428*, 911.
- (129) Lei, Y.-L.; Jin, Y.; Zhou, D.-Y.; Gu, W.; Shi, X.-B.; Liao, L.-S.; Lee, S.-T. *Adv. Mater.* **2012**, *24* (39), 5345.
- (130) Ding, L.; Dong, S.-C.; Jiang, Z.-Q.; Chen, H.; Liao, L.-S. *Adv. Funct. Mater.* **2015**, *25*, 645.
- (131) Curtin, I. J.; Blaylock, D. W.; Holmes, R. *J. Appl. Phys. Lett.* **2016**, *108*, 163301.
- (132) Salzman, R.; Xue, J.; Rand, B.; Alexander, A.; Thompson, M.; Forrest, S. *Org. Electron.* **2005**, *6*, 242.
- (133) Ko Ko Kyaw, A.; Hwan Wang, D.; Tseng, H.-R.; Zhang, J.; Bazan, G. C.; Heeger, A. *J. Appl. Phys. Lett.* **2013**, *102* (16), 163308.
- (134) Tiana, D.; Hendon, C. H.; Walsh, A.; Vaid, T. P. *Phys. Chem. Chem. Phys.* **2014**, *16*, 14463.
- (135) Tang, M. L.; Reichardt, A. D.; Wei, P.; Bao, Z. *J. Am. Chem. Soc.* **2009**, *131* (14), 5264.
- (136) Bredas, J. *Mater. Horizons* **2014**, *1*, 17.
- (137) Morse, G. E.; Helander, M. G.; Stanwick, J.; Sauks, J. M.; Paton, A. S.; Lu, Z.-H.; Bender, T. P. *J. Phys. Chem. C* **2011**, *115* (23), 11709.
- (138) Li, H.; Brédas, J.-L.; Lennartz, C. *J. Chem. Phys.* **2007**, *126* (16), 164704.
- (139) Pope, M.; Swenberg, C. E. *Electronic processes in organic crystals*; Oxford University Press: New York, NY, 1982.
- (140) Bredas, J.; Beljonne, D.; Coropceanu, V.; Cornil, J. *Chem. Rev.* **2004**, *104*, 4971.
- (141) McQuarrie, D. A.; Simon, J. D. *Physical Chemistry: A molecular approach*; University Science Books: Sausalito, CA, 1997.

Bibliography

- (142) Roberts, S. T.; Schlenker, C. W.; Barlier, V.; Mcanally, R. E.; Zhang, Y.; Mastron, J. N.; Thompson, M. E.; Bradforth, S. E. *J. Phys. Chem. Lett.* **2011**, 2, 48.
- (143) Smith, M. B.; Michl, J. *Chem. Rev.* **2010**, 110, 6891.
- (144) Lin, Y. L.; Fusella, M. A.; Kozlov, O. V; Lin, X.; Kahn, A.; Pshenichnikov, M. S.; Rand, B. P. *Adv. Funct. Mater.* **2016**.
- (145) Jia, W.; Chen, Q.; Chen, L.; Yuan, D.; Xiang, J.; Cheng, Y.; Xiong, Z. *Jounral Phys. Chem.* **2016**.
- (146) Wan, Y.; Guo, Z.; Zhu, T.; Yan, S.; Johnson, J.; Huang, L. *Nat. Chem.* **2015**, 7 (September), 1.
- (147) Ma, L.; Zhang, K.; Kloc, C.; Sun, H.; Michel-Beyerle, M. E.; Gurzadyan, G. G. *Phys. Chem. Chem. Phys.* **2012**, 14 (23), 8307.
- (148) Pensack, R. D.; Tilley, A. J.; Parkin, S. R.; Lee, T. S.; Payne, M. M.; Gao, D.; Jahnke, A. a; Oblinsky, D.; Li, P.-F.; Anthony, J. E.; Seferos, D. S.; Scholes, G. D. *J. Am. Chem. Soc.* **2015**, 150506174105009.
- (149) Krause, S.; Casu, M. B.; Schöll, a; Umbach, E. *New J. Phys.* **2008**, 10 (8), 85001.
- (150) Djurovich, P. I.; Mayo, E. I.; Forrest, S. R.; Thompson, M. E. *Org. Electron.* **2009**, 10 (3), 515.
- (151) Hwang, J.; Kim, E.; Liu, J.; Bre, J.; Duggal, A.; Kahn, A. *J. Phys. Chem. C* **2007**, 111, 1378.
- (152) Andrade, B. W. D. Ó.; Datta, S.; Forrest, S. R.; Djurovich, P.; Polikarpov, E.; Thompson, M. E. *Org. Electron.* **2005**, 6, 11.
- (153) Leonat, L.; Sbarcea, G.; Branzoi, I. V. *UPB Sci. Bull. Ser. B* **2013**, 75 (3), 111.
- (154) Pruneanu, S.; Veress, E.; Marian, I.; Oniciu, L. *J. Mater. Sci.* **1999**, 34, 2733.
- (155) Ward, A. J.; Ruseckas, A.; Samuel, I. D. W. *J. Phys. Chem. C* **2012**, 116, 23931.
- (156) Mikhnenko, O. V; Blom, P. W. M.; Nguyen, T. Q. *Energy Environ. Sci.* **2015**, 8, 1867.
- (157) Athanasopoulos, S.; Emelianova, E. V; Walker, A. B.; Beljonne, D. *Phys. Rev. B* **2009**, 80, 195209.
- (158) Haugeneder, A.; Neges, M.; Kallinger, C.; Spirkl, W.; Lemmer, U.; Feldmann, J. **1999**, 59 (23), 346.
- (159) Tamai, Y.; Ohkita, H.; Benten, H.; Ito, S. *J. Phys. Chem. Lett.* **2015**, 6, 3417.
- (160) Akselrod, G. M.; Deotare, P. B.; Thompson, N. J.; Lee, J.; Tisdale, W. A.; Baldo, M. A.; Menon, V. M.; Bulović, V. *Nat. Commun.* **2014**, 5, 3646.
- (161) Gosele, U.; Hauser, M.; Klein, U. K. A.; Frey, R. *Chem. Phys. Lett.* **1975**, 34 (3), 519.
- (162) Klein, U. K. A.; Frey, R.; Hauser, M.; Gosele, U. *Chem. Phys. Lett.* **1976**, 41 (1), 139.
- (163) Lin, J. D. A.; Mikhnenko, O. V; Chen, J.; Masri, Z.; Ruseckas, A.; Mikhailovsky, A.; Raab, R. P.; Liu, J.; Blom, P. W. M.; Loi, M. A.; Garcia-Cervera, C. J.; Samuel, I. D. W.; Nguyen, T.-Q. *Mater. Horizons* **2014**, 1, 280.
- (164) Hsiao, Y.-C.; Wu, T.; Li, M.; Liu, Q.; Qin, W.; Hu, B. *J. Mater. Chem. A* **2015**, 3, 15372.

Bibliography

- (165) Wheeler, D. A.; Zhang, J. Z. *Adv. Mater.* **2013**, 1.
- (166) Ingenito, A.; Isabella, O.; Solntsev, S.; Zeman, M. *Sol. Energy Mater. Sol. Cells* **2014**, 123, 17.
- (167) Glunz, S. W. *Adv. Optoelectron.* **2007**, 2007, 1.
- (168) Zhao, H.; Ozturk, B.; Schiff, E. a.; Sivec, L.; Yan, B.; Yang, J.; Guha, S. *Sol. Energy Mater. Sol. Cells* **2014**, 1.
- (169) Street, R. A. **2016**, 3814.
- (170) Beljonne, D.; Curutchet, C.; Scholes, G. D.; Silbey, R. J. *J. Phys. Chem. B* **2009**, 113 (19), 6583.
- (171) Haskal, E.; Shen, Z.; Burrows, P.; Forrest, S. *Phys. Rev. B. Condens. Matter* **1995**, 51 (7), 4449.
- (172) Huijser, J. M. Energy transfer dynamics in molecular layers of porphyrin derivatives, Delft University of Technology, 2008.
- (173) Silbey, R. *Annu. Rev. Phys. Chem.* **1976**, 27, 203.
- (174) Verreet, B.; Heremans, P.; Stesmans, A.; Rand, B. P. *Adv. Mater.* **2013**, 25 (38), 5504.
- (175) Kippelen, B.; Brédas, J.-L. *Energy Environ. Sci.* **2009**, 2 (3), 251.
- (176) Wang, X.; Li, H.; Su, Z.; Fang, F.; Zhang, G.; Wang, J.; Chu, B.; Fang, X.; Wei, Z.; Li, B.; Li, W. *Org. Electron.* **2014**, 15 (10), 2367.
- (177) Yang, D.; Zhou, X.; Ma, D. *Org. Electron.* **2013**, 14 (11), 3019.
- (178) Karak, S.; Lim, J. A.; Ferdous, S.; Duzhko, V. V; Briseno, A. L. *Adv. Funct. Mater.* **2014**, 24 (8), 1039.
- (179) Lim, J. A.; Ferdous, S.; Briseno, A. L. *Polym. Prepr.* **2010**, 51 (1), 3096.
- (180) Videlot, C.; Kassmi, A. El; Fichou, D. *Sol. Energy Mater. Sol. Cells* **2000**, 63, 69.
- (181) Najafov, H.; Biaggio, I.; Podzorov, V.; Calhoun, M.; Gershenson, M. *Phys. Rev. Lett.* **2006**, 96 (5), 56604.
- (182) Najafov, H.; Lyu, B.; Biaggio, I.; Podzorov, V. *Appl. Phys. Lett.* **2010**, 96 (18), 183302.
- (183) Bao, Q.; Sandberg, O.; Dagnelund, D.; Sandén, S.; Braun, S.; Aarnio, H.; Liu, X.; Chen, W. M.; Österbacka, R.; Fahlman, M. *Adv. Funct. Mater.* **2014**, 1.
- (184) Deotare, P.; Chang, W.; Hontz, E.; Congreve, D.; Shi, L.; Reusswig, P.; Modtland, B.; Bahlke, M.; Lee, C.; Willard, V.; Bulović, V.; Van Voorhis, T.; Baldo, M. *Nat. Mater.* **2015**, 14, 1130.
- (185) Lee, J.; Cheng, S.; Yoo, S.; Shin, H.; Chang, J.; Wu, C.; Wong, K.; Kim, J. *Adv. Funct. Mater.* **2015**, 25, 361.
- (186) Xiang, J.; Chen, Y.; Jia, W.; Chen, L.; Lei, Y.; Zhang, Q.; Xiong, Z. *Org. Electron. physics, Mater. Appl.* **2016**, 28, 94.
- (187) Seino, Y.; Sasabe, H.; Pu, Y.-J.; Kido, J. *Adv. Mater.* **2014**, 26 (10), 1612.
- (188) Zheng, Z.; Tummala, N. R.; Fu, Y.; Coropceanu, V.; Bredas, J.-L. *ACS Appl. Mater. Interfaces* **2017**.
- (189) Rand, B. P. In *Fall MRS Z5.07*; Boston, MA, 2015.
- (190) Zou, Y.; Holmes, R. J. *ACS Appl. Mater. Interfaces* **2015**, 7, 118306.

Bibliography

- (191) Vandewal, K.; Widmer, J.; Heumueller, T.; Brabec, C. J.; McGehee, M. D.; Leo, K.; Riede, M.; Salleo, A. *Adv. Mater.* **2014**, 3839.
- (192) Burdett, J. J.; Müller, A. M.; Gosztola, D.; Bardeen, C. J. *J. Chem. Phys.* **2015**, 144506 (2010), 144506.
- (193) Kroese, J. E.; Savenije, T. J.; Vermeulen, M. J. W.; Warman, J. M. *J. Phys. Chem. B* **2003**, 107, 7696.
- (194) Caplins, B. W.; Mullenbach, T. K.; Holmes, R. J.; Blank, D. A. *J. Phys. Chem. C* **2015**, acs.jpcc.5b09817.
- (195) Najafov, H.; Lee, B.; Zhou, Q.; Feldman, L. C.; Podzorov, V. *Nat. Mater.* **2010**, 9 (11), 938.
- (196) Yost, S. R.; Hontz, E.; Yeganeh, S.; Voorhis, T. Van. *J. Phys. Chem. C* **2012**, 116, 17369.
- (197) Lee, C.; Liu, S.; Cheng, C.; Su, W.; Chou, C.; Lin, C.; Chen, C. *Int. J. Photoenergy* **2013**, 2013, 1.
- (198) Menke, S. M.; Luhman, W. A.; Holmes, R. J. *Nat. Mater.* **2013**, 12 (2), 152.
- (199) Engel, E.; Leo, K.; Hoffmann, M. *Chem. Phys.* **2006**, 325 (1), 170.
- (200) Marciak, H.; Fiebig, M.; Huth, M.; Schiefer, S.; Nickel, B.; Selmaier, F.; Lochbrunner, S. *Phys. Rev. Lett.* **2007**, 99 (17), 1.
- (201) Hennebicq, E.; Pourtois, G.; Scholes, G. D.; Herz, L. M.; Russell, D. M.; Silva, C.; Setayesh, S.; Grimsdale, A. C.; Mullen, K.; Bredas, J.-L.; Beljonne, D. *J. Am. Chem. Soc.* **2005**, 127, 4744.
- (202) Scholes, G. D. *Annu. Rev. Phys. Chem.* **2003**, 54, 57.
- (203) Förster, T. *Discuss. Faraday Soc.* **1959**, 27 (10), 7.
- (204) Förster, T. *Ann. Phys.* **1948**, 2, 55.
- (205) Förster, T. *Zeitschrift für Naturforsch.* **1949**, 4a, 321.
- (206) Powell, R. C.; Soos, Z. G. *J. Lumin.* **1975**, 11, 1.
- (207) Scully, B. S. R.; Armstrong, P. B.; Edder, C.; Fréchet, J. M. J.; McGehee, M. D. *Adv. Mater.* **2007**, 19, 2961.
- (208) Kuhn, H. *J. Chem. Phys.* **1970**, 53 (1), 101.
- (209) Reid, O. G.; Rumbles, G. *J. Phys. Chem. C* **2016**, 120, 87.
- (210) Haynes, D. R.; Tokmakoff, A.; George, S. M. *J. Chem. Phys.* **1993**, 100 (3), 1968.
- (211) Loura, L. M. S. **2012**, 15252.
- (212) Yang, J.; Winnik, M. A. *J. Phys. Chem. B* **2005**, 109 (39), 18408.
- (213) Clegg, R. M. *Reviews in Fluorescence 2006*; Geddes, C. D., Lakowicz, J. R., Eds.; Springer Science + Business Media, LLC: New York, NY, 2006.
- (214) Dale, R. E.; Eisinger, J.; Blumberg, W. E. *Biophys. J.* **1979**, 26 (2), 161.
- (215) Song, H. J.; Kim, D. H.; Lee, E. J.; Haw, J. R.; Moon, D. K. *Sol. Energy Mater. Sol. Cells* **2014**, 123, 112.
- (216) Steinberg, I. Z. *J. Chem. Phys.* **1968**, 48 (6), 2411.
- (217) Menke, S. M. Exciton Transport in Organic Semiconductors, University of Minnesota, 2015.
- (218) Mårtensson, J. *Chem. Phys. Lett.* **1994**, 229, 449.

Bibliography

- (219) Scholes, G. D.; Ghiggino, K. P.; Oliver, A. M.; Paddon-Row, M. N. *J. Phys. Chem.* **1993**, 97, 11871.
- (220) Penick, M. A.; Mahindaratne, M. P. D.; Brancaleon, L. In *International Electronic Conference on Synthetic Organic Chemistry*; Seijas, J. A., Vazquez, T. M. P., Eds.; MDPI: Basel, Switzerland, 2011; p a13/1–a13/9.
- (221) Hinderhofer, A.; Heinemeyer, U.; Gerlach, A.; Kowarik, S.; Jacobs, R. M. J.; Sakamoto, Y.; Suzuki, T.; Schreiber, F. *J. Chem. Phys.* **2007**, 127 (19), 194705.
- (222) Martín, G.; Rojo, G.; Agulló-López, F.; Ferro, V. R.; De La Vega, J. M. G.; Martínez-Díaz, M. V.; Torres, T.; Ledoux, I.; Zyss, J. *J. Phys. Chem. B* **2002**, 106 (51), 13139.
- (223) Jablonski, A. *Zeitschrift für Phys.* **1935**, 96, 236.
- (224) Mascaro, D. J.; Thompson, M. E.; Smith, H. I.; Bulović, V. *Org. Electron.* **2005**, 6 (5–6), 211.
- (225) Raimondo, L.; Moret, M.; Campione, M.; Borghesi, A.; Sassella, A. *J. Phys. Chem. C* **2011**, 115, 5880.
- (226) Yang, J.; Yan, D.; Jones, T. S. *Chem. Rev.* **2015**, 150514144417003.
- (227) Walters, D. M.; Richert, R.; Ediger, M. D. *J. Chem. Phys.* **2015**, 142 (13), 134504.
- (228) Dalal, S. S.; Walters, D. M.; Lyubimov, I.; de Pablo, J. J.; Ediger, M. D. *Proc. Natl. Acad. Sci.* **2015**, 201421042.
- (229) Yokoyama, D.; Sakaguchi, A.; Suzuki, M.; Adachi, C. *Org. Electron.* **2009**, 10 (1), 127.
- (230) Frischeisen, J.; Yokoyama, D.; Adachi, C.; Brütting, W. *Appl. Phys. Lett.* **2010**, 96 (7), 73302.
- (231) Kim, J. Y.; Yokoyama, D.; Adachi, C. *J. Phys. Chem. C* **2012**, 116 (15), 8699.
- (232) Kawamura, Y.; Goushi, K.; Brooks, J.; Brown, J. J.; Sasabe, H.; Adachi, C. *Appl. Phys. Lett.* **2005**, 86 (7), 71104.
- (233) Nakanotani, H.; Adachi, C. *Appl. Phys. Lett.* **2010**, 96 (5), 53301.
- (234) Lampe, T.; Schmidt, T. D.; Jurow, M. J.; Djurovich, P. I.; Thompson, M. E.; Brütting, W. *Chem. Mater.* **2016**, acs. chemmater.5b04607.
- (235) Kim, K.; Liao, J.; Lee, S. W.; Sim, B.; Moon, C.; Kim, H. J.; Chi, Y.; Kim, J. *Adv. Mater.* **2016**, 1.
- (236) Dexter, D. L. *J. Chem. Physics* **1953**, 21 (5), 836.
- (237) Menke, S. M.; Holmes, R. J. *ACS Appl. Mater. Interfaces* **2015**, 7 (4), 2912.
- (238) Menke, S. M.; Mullenbach, T. K.; Holmes, R. J. *ACS Nano* **2015**, 9 (4), 4543.
- (239) Irkhin, P.; Biaggio, I. *Phys. Rev. Lett.* **2011**, 107 (1), 17402.
- (240) Fratini, S.; Mayou, D.; Ciuchi, S. *Adv. Funct. Mater.* **2016**, n/a.
- (241) Yang, L.; Yi, D.; Han, S.; Xie, S. *Org. Electron.* **2015**, 23, 39.
- (242) Shim, J.; Raman, K.; Park, Y.; Santos, T.; Miao, G.; Satpati, B.; Moodera, J. *Phys. Rev. Lett.* **2008**, 100 (22), 226603.
- (243) Xie, W.; Menke, S. M.; Frisbie, C. D.; Holmes, R. J. In *The WSPC Reference on organic electronics: organic semiconductors: basic concepts*; 2016; pp 231–291.
- (244) Moon, H.; Zeis, R.; Borkent, E.-J.; Besnard, C.; Lovinger, A. J.; Siegrist, T.; Kloc,

Bibliography

- C.; Bao, Z. *J. Am. Chem. Soc.* **2004**, *126* (47), 15322.
- (245) Yamada, T.; Sato, T.; Tanaka, K.; Kaji, H. *Org. Electron.* **2010**, *11* (2), 255.
- (246) Takeya, J.; Yamagishi, M.; Tominari, Y.; Hirahara, R.; Nakazawa, Y.; Nishikawa, T.; Kawase, T.; Shimoda, T.; Ogawa, S. *Appl. Phys. Lett.* **2007**, *90* (10), 102120.
- (247) Gorgolis, S.; Giannopoulou, A.; Kounavis, P. *J. Appl. Phys.* **2013**, *113*, 123102.
- (248) Nicolai, H. T.; Kuik, M.; Wetzelaer, G. a H.; de Boer, B.; Campbell, C.; Risko, C.; Brédas, J. L.; Blom, P. W. M. *Nat. Mater.* **2012**, *11* (10), 882.
- (249) Barnes, P. R. F.; Miettunen, K.; Li, X.; Anderson, A. Y.; Bessho, T.; Gratzel, M.; O'Regan, B. C. *Adv. Mater.* **2013**, *25* (13), 1881.
- (250) Dürr, a. C.; Schreiber, F.; Münch, M.; Karl, N.; Krause, B.; Kruppa, V.; Dosch, H. *Appl. Phys. Lett.* **2002**, *81* (12), 2276.
- (251) Xie, W.; Mcgarry, K. A.; Liu, F.; Wu, Y.; Ruden, P. P.; Douglas, C. J.; Frisbie, C. D. *J. Phys. Chem. C* **2013**, *117*, 11522.
- (252) Cheng, Y. C.; Silbey, R. J.; da Silva Filho, D. A.; Calbert, J. P.; Cornil, J.; Brédas, J. L. *J. Chem. Phys.* **2003**, *118* (8), 3764.
- (253) Deen, W. M. *Analysis of Transport Phenomena*, 2nd ed.; Oxford University Press: New York, NY, 2012.
- (254) Panton, R. L. *Incompressible Flow*, 3rd ed.; John Wiley & Sons, Inc: Hoboken, New Jersey, 2005.
- (255) Yang, F.; Meng, R.; Zhang, G.; Gao, K.; Xie, S. *Org. Electron. physics, Mater. Appl.* **2016**, *30*, 171.
- (256) Pope, M.; Braams, B. J.; Brenner, H. C. *Chem. Phys.* **2003**, *288*, 105.
- (257) Markov, D.; Blom, P. *Phys. Rev. B* **2006**, *74* (8), 85206.
- (258) Mulder, B. J. *Philips Res. Rep* **1967**, *22*, 142.
- (259) Stehr, V.; Engels, B.; Deibel, C.; Fink, R. F. *J. Chem. Phys.* **2014**, *140*, 24503.
- (260) Xie, X.; Ma, H. *ChemistryOpen* **2016**, *5*, 201.
- (261) Kawka, S.; La Rocca, G. C. *Phys. Rev. B* **2012**, *85*, 115305.
- (262) Gosele, U. *Chem. Phys. Lett.* **1976**, *43* (I), 61.
- (263) Ern, V. *Phys. Rev. Lett.* **1969**, *22* (8), 343.
- (264) Mullenbach, T. K. Energy flow in organic thin films - from excitons to polarons, University of Minnesota, 2016.
- (265) Knox, R. S. "Intermolecular Energy Migration and Fluorescence" (translation) in *Biological Physics*; American Institute of Physics: New York, NY, 1993.
- (266) Socolofsky, S. A.; Jirka, G. H. *Environmental Fluid Mechanics 1: Mixing and Transport Processes in the Environment*; Texas A&M University, 2005.
- (267) Kasap, S. O. *Principles of electronic materials and devices*, 3rd ed.; McGraw-Hill Education: New York, NY, 2005.
- (268) Kittel, C. *Introduction to solid state physics*, 8th ed.; John Wiley & Sons, Inc: Hoboken, New Jersey, 2005.
- (269) Ling, M. M.; Reese, C.; Briseno, A. L.; Bao, Z. *Synth. Met.* **2007**, *157*, 257.
- (270) Shklyarevskiy, I. O.; Jonkheijm, P.; Stutzmann, N.; Wasserberg, D.; Wondergem, H. J.; Christianen, P. C. M.; Schenning, A. P. H. J.; Leeuw, D. M. De; Wu, J.; Mu,

Bibliography

- K.; Maan, J. C. **2005**, No. 8, 16233.
- (271) Lee, B.; Chen, Y.; Fu, D.; Yi, H. T.; Czelen, K.; Najafov, H.; Podzorov, V. *Nat. Mater.* **2013**, 12 (October), 1125.
- (272) Kearns, D.; Calvin, M. *J. Chem. Phys.* **1958**, 29 (4), 950.
- (273) Bradley, D. F.; Calvin, M. *Proc. Natl. Acad. Sci.* **1955**, 41 (8), 563.
- (274) Editorial. *Nat. Mater.* **2015**, 14, 1073.
- (275) Timmreck, R.; Meyer, T.; Gilot, J.; Seifert, H.; Mueller, T.; Furlan, A.; Wienk, M. M.; Wynands, D.; Hohl-Ebinger, J.; Warta, W.; Janssen, R. a. J.; Riede, M.; Leo, K. *Nat. Photonics* **2015**, 9 (8), 478.
- (276) Riede, M.; Mueller, T.; Tress, W.; Schueppel, R.; Leo, K. *Nanotechnology* **2008**, 19 (42), 424001.
- (277) Gevorgyan, S. a.; Eggert Carlé, J.; Søndergaard, R.; Trofod Larsen-Olsen, T.; Jørgensen, M.; Krebs, F. C. *Sol. Energy Mater. Sol. Cells* **2013**, 110, 24.
- (278) Rubbo, M.; Aquilano, D. *J. Cryst. Growth* **1998**, 194, 156.
- (279) *Crystal Growth*, 2nd ed.; Pamplin, B. R., Ed.; Pergamon Press: New York, NY, 1980.
- (280) Bishop, R. *CrystEngComm* **2015**, 17 (39), 7448.
- (281) Shewmon, N. T.; Watkins, D. L.; Galindo, J. F.; Zerdan, R. B.; Chen, J.; Keum, J.; Roitberg, A. E.; Xue, J.; Castellano, R. K. *Adv. Funct. Mater.* **2015**, n/a.
- (282) Enengl, C.; Enengl, S.; Havlicek, M.; Stadler, P.; Glowacki, E. D.; Scharber, M. C.; White, M.; Hingerl, K.; Ehrenfreund, E.; Neugebauer, H.; Sariciftci, N. S. *Adv. Funct. Mater.* **2015**, n/a.
- (283) Tkatchenko, A. *Adv. Funct. Mater.* **2014**, 25 (13), 2054.
- (284) Forrest, S.; Burrows, P.; Haskal, E.; So, F. *Phys. Rev. B. Condens. Matter* **1994**, 49 (16), 11309.
- (285) Huang, H.; Huang, Y.; Wang, S.; Zhu, M.; Xie, H.; Zhang, L. 1.
- (286) Zhang, Y.; Luo, Z.; Hu, F.; Nan, H.; Wang, X.; Ni, Z.; Xu, J.; Shi, Y.; Wang, X. **2016**, 1.
- (287) Zimmerman, J. D.; Lassiter, B. E.; Xiao, X.; Sun, K.; Dolocan, A.; Gearba, R.; Bout, D. A. Vanden; Stevenson, K. J.; Wickramasinghe, P.; Thompson, M. E.; Forrest, S. R. *ACS Nano* **2013**, 7 (10), 9268.
- (288) Bruni, F.; Sassi, M.; Campione, M.; Giovanella, U.; Ruffo, R.; Luzzati, S.; Meinardi, F.; Beverina, L.; Brovelli, S. **2014**, 7410.
- (289) Chen, Y.; Zhang, W.; Yu, L. **2016**.
- (290) Song, W.-F.; Wu, Y.; Fan, Y.; Wang, Y.; Liu, Y. *Acta Crystallogr. Sect. E, Struct. reports* **2009**, E65, o2461.
- (291) Nangia, A. *Acc. Chem. Res.* **2008**, 41 (5), 595.
- (292) Price, S. L. *Acc. Chem. Res.* **2009**, 42 (1), 117.
- (293) Duong, A.; Thierry, M.; Wuest, J. D. *Cryst. Eng. Commun.* **2011**, 13 (18), 5571.
- (294) *Webster's Seventh New Colegiate Dictionary*, 7th ed.; Merriam Co., G. & C., Ed.; H. O. Houghton & Co., The Riverside Press: Cambridge, MA, 1963.
- (295) Baldo, M. a.; Soos, Z. G.; Forrest, S. R. *Chem. Phys. Lett.* **2001**, 347 (4–6), 297.

Bibliography

- (296) Kaznessis, Y. N. *Statistical Thermodynamics and Stochastic Kinetics: An introduction for Engineers*; Cambridge University Press: New York, NY, 2012.
- (297) Menke, S. M.; Holmes, R. J. *J. Mater. Chem. C* **2016**, *4*, 3437.
- (298) Yokoyama, D.; Qiang Wang, Z.; Pu, Y.-J.; Kobayashi, K.; Kido, J.; Hong, Z. *Sol. Energy Mater. Sol. Cells* **2012**, *98*, 472.
- (299) Matsushima, T.; Matsuo, H.; Yamamoto, T.; Nakao, A.; Murata, H. *Sol. Energy Mater. Sol. Cells* **2014**, *123*, 81.
- (300) Frischeisen, J.; Yokoyama, D.; Endo, A.; Adachi, C.; Brüting, W. *Org. Electron.* **2011**, *12* (5), 809.
- (301) Kim, S.-Y.; Jeong, W.-I.; Mayr, C.; Park, Y.-S.; Kim, K.-H.; Lee, J.-H.; Moon, C.-K.; Brüting, W.; Kim, J.-J. *Adv. Funct. Mater.* **2013**, *23*, 3896.
- (302) Heumueller, T.; Mateker, W. R.; Distler, A.; Fritze, U. F.; Cheacharoen, R.; Nguyen, W. H.; Biele, M.; Salvador, M.; von Delius, M.; Egelhaaf, H.-J.; McGehee, M. D.; Brabec, C. J. *Energy Environ. Sci.* **2015**, *9* (1), 247.
- (303) Pratontep, S.; Brinkmann, M.; Nüesch, F.; Zuppiroli, L. *Phys. Rev. B* **2004**, *69* (16), 1.
- (304) Lee, C.-C.; Liu, S.-W.; Chung, Y.-T. *J. Phys. D. Appl. Phys.* **2010**, *43* (7), 75102.
- (305) Vasseur, K.; Broch, K.; Ayzner, A. L.; Rand, B. P.; Cheyns, D.; Frank, C.; Schreiber, F.; Toney, M. F.; Froyen, L.; Heremans, P. *ACS Appl. Mater. Interfaces* **2013**, *5* (17), 8505.
- (306) Roberts, C. J.; Debenedetti, P. G. *AIChE J.* **2002**, *48* (6), 1140.
- (307) Sun, Y.; Zhu, L.; Wu, T.; Cai, T.; Gunn, E. M.; Yu, L. *Am. Assoc. Pharm. Sci. J.* **2012**, *14* (3), 380.
- (308) Yu, L. *Adv. Drug Deliv. Rev.* **2016**, 1.
- (309) Çelikbilek, M.; Ersundu, A. E.; Ayd, S. **2009**.
- (310) Sun, Y.; Zhu, L.; Cai, T.; Gunn, E.; Hasebe, M.; Powell, T.; Wu, T.; Xi, H.; Villliers, M. De; Ediger, M. Amorphous Organic Solids and Their Crystallization http://www.icdd.com/ppxrd/11/presentations/tuesday/lian_yu-amorphous_solids.pdf.
- (311) Zhu, L.; Brian, C. W.; Swallen, S. F.; Straus, P. T.; Ediger, M. D.; Yu, L. *Phys. Rev. Lett.* **2011**, *106*, 256103.
- (312) Giebink, N. C.; Sun, Y.; Forrest, S. R. **2006**, *7*, 375.
- (313) Hofberger, W.; BAssler, H. *Phys. Status Solidi* **1975**, *725*, 725.
- (314) Park, S. W.; Hwang, J. M.; Choi, J. M.; Hwang, D. K.; Oh, M. S.; Kim, J. H.; Im, S. *Appl. Phys. Lett.* **2007**, *90* (2007), 2005.
- (315) Ma, X.; Wang, S.; Li, X.; Xiao, Y. *Org. Electron. physics, Mater. Appl.* **2014**, *15* (8), 1876.
- (316) Karmakar, S.; Dasgupta, C.; Sastry, S. *Phys. Rev. Lett.* **2016**, *116*, 85701.
- (317) Loucks, R. Lecture 13: The Fictive and Glass Transition Temperatures <https://www.google.com/url?sa=t&rct=j&q=&esrc=s&source=web&cd=1&cad=rj&uact=8&ved=0ahUKEwjWIJu1qNvSAhVE7YMKHXO2AZAQFggcMAA&url=https%3A%2F%2Fwww.lehigh.edu%2Fimi%2Fteched%2FRelax2010%2FLect>

Bibliography

- ure13_loucks.pdf&usg=AFQjCNGhyH9OUbnBtUOZGxqZeypYn7ZIPA&sig2=Ja
tmp3pJqz7r8aNi1RlkAA.
- (318) Sun, Y.; Xi, H.; Chen, S.; Ediger, M. D.; Yu, L. *J. Phys. Chem. B* **2008**, *112* (18), 5594.
- (319) Brian, C. W.; Yu, L. *J. Phys. Chem. A* **2013**, *117* (50), 13303.
- (320) Ediger, M. D.; Inoue, T.; Cicerone, M. T.; Blackburn, F. R. *Macromol. Symp.* **1996**, *101*, 139.
- (321) Swallen, S.; Bonvallet, P.; McMahon, R.; Ediger, M. *Phys. Rev. Lett.* **2003**, *90* (1), 1.
- (322) Tseng, K.; Turro, N.; Durning, C. *Phys. Rev. E. Stat. Phys. Plasmas. Fluids. Relat. Interdiscip. Topics* **2000**, *61* (2), 1800.
- (323) Schmidt, R. H.; Haugstad, G.; Gladfelter, W. L. *Langmuir* **2003**, *19*, 10390.
- (324) Haugstad, G. In *Atomic Force Microscopy: Understanding Basic Modes and Advanced Applications*; John Wiley & Sons, Inc: Hoboken, New Jersey, 2012; pp 211–258.
- (325) Gill, P. S.; Sauerbrunn, S. R.; Reading, M. *J. Therm. Anal.* **1993**, *40*, 931.
- (326) Capaccioli, S.; Ngai, K. L.; Paluch, M.; Prevosto, D. *Phys. Rev. E* **2012**, *86* (5), 51503.
- (327) Meyers, G. F.; Dekoven, B. M.; Dineen, M. T.; Strandjord, A.; Connor, P. J. O.; Hu, T.; Chiao, Y.; Pollock, H. M.; Hammiche, A. **2000**, *190*.
- (328) Meyers, G.; Pastzor, A.; Kjoller, K. **2007**, *39* (20), 9.
- (329) Pollock, H. M.; Hammiche, A. *J. Phys. D. Appl. Phys.* **2001**, *34*, R23.
- (330) Fryer, D. S.; Nealey, P. F.; De Pablo, J. J. *Macromolecules* **2000**, *33* (17), 6439.
- (331) Kim, J. H.; Jang, J.; Zin, W. C. *Langmuir* **2001**, *17* (9), 2703.
- (332) Priest, J. **2011**.
- (333) Swallen, S. F.; Kearns, K. L.; Satija, S.; Traynor, K.; McMahon, R. J.; Ediger, M. D. *J. Chem. Phys.* **2008**, *128* (21).
- (334) Kearns, K. L.; Swallen, S. F.; Ediger, M. D.; Wu, T.; Sun, Y.; Yu, L. *J. Phys. Chem. B* **2008**, *112* (16), 4934.
- (335) Brian, C. W.; Zhu, L.; Yu, L.; Brian, C. W.; Zhu, L.; Yu, L. *J. Chem. Phys.* **2014**, *140*, 54509.
- (336) Badrinarayanan, P.; Zheng, W.; Li, Q.; Simon, S. L. *J. Non. Cryst. Solids* **2007**, *353*, 2603.
- (337) Rodríguez-Tinoco, C.; Gonzalez-Silveira, M.; Ràfols-Ribé, J.; Lopeandia, A.; Rodriguez-Viejo, J. *Phys. Chem. Chem. Phys.* **2015**, *17*, 31195.
- (338) Keddie, J. L.; Jones, R. A. L.; Cory, R. A. *Europhys. Lett.* **1994**, *27*, 59.
- (339) Meyeis, G. F.; Dekoven, B. M.; Seitzj, J. T. **1992**, 2330.
- (340) Van den Brande, N.; Van Assche, G.; Van Mele, B. *Cryst. Growth Des.* **2015**, *15* 1014090453004.
- (341) Stillinger, F. H. *J. Chem. Phys.* **1988**, *88* (12), 7818.
- (342) Gujral, A.; O'Hara, K. a.; Toney, M. F.; Chabinyc, M. L.; Ediger, M. D. *Chem. Mater.* **2015**, *27* (9), 3341.

Bibliography

- (343) Gujral, A.; Gomez, J.; Jiang, J.; Huang, C.; O'Hara, K. A.; Toney, M. F.; Chabinyc, M. L.; Yu, L.; Ediger, M. D. *Chem. Mater.* **2017**, *29*, 849.
- (344) Swallen, S. F.; Kearns, K. L.; Mapes, M. K.; Kim, Y. S.; McMahon, R. J.; Ediger, M. D.; Wu, T.; Yu, L.; Satija, S. *Science* **2007**, *315*, 353.
- (345) Sepúlveda, A.; Swallen, S. F.; Ediger, M. D. *J. Chem. Phys.* **2013**, *138* (12).
- (346) Fenter, P.; Schreiber, F.; Bulovic, V.; Forrest, S. R. *Chem. Phys. Lett.* **1997**, *277*, 521.
- (347) Plante, A.; Palato, S.; Lebel, O.; Soldera, A. *J. Mater. Chem. C* **2013**, *1* (5), 1037.
- (348) Han, E.; Do, L.; Niidome, Y.; Masamichi, F. *Chem. Lett.* **1994**, 969.
- (349) Shirota, Y.; Kageyama, H. *Chem. Rev.* **2007**, *107* (4), 953.
- (350) Kalra, A.; Tishmack, P.; Lubach, J. W.; Taylor, L. S.; Byrn, S. R.; Li, T. **2017**.
- (351) Laventure, A.; Maris, T.; Pellerin, C.; Lebel, O. *Cryst. Growth Des.* **2017**.
- (352) Topple, J. M.; Burke, S. A.; Ji, W.; Fostner, S.; Tekiel, A.; Gru, P. *J. Phys. Chem. C* **2011**, *115*, 217.
- (353) Becker, J.; Grün, G.; Seemann, R.; Mantz, H.; Jacobs, K.; Mecke, K. R.; Blossey, R. *Nat. Mater.* **2003**, *2* (1), 59.
- (354) Redon, C.; Brochard-Wyart, F.; Rondelez, F. *Phys. Rev. Lett.* **1991**, *66* (6), 715.
- (355) Reiter, G. *Eur. Phys. J. E* **1992**, *68* (1), 75.
- (356) Kargupta, K.; Sharma, A. *J. Colloid Interface Sci.* **2002**, *245* (1), 99.
- (357) Venables, J. A.; Spiller, G. D. T.; Hanbucken, M. *Reports Prog. Phys.* **1984**, *47*, 399.
- (358) Witte, G.; Woll, C. *J. Mater. Res.* **2004**, *19* (7), 1889.
- (359) Bayliss, S. M.; Heutz, S.; Rumbles, G.; Jones, T. S. *Phys. Chem. Chem. Phys.* **1999**, *1*, 3673.
- (360) Jones, A. O. F.; Chattopadhyay, B.; Geerts, Y. H.; Resel, R. *Adv. Funct. Mater.* **2016**, n/a.
- (361) Kim, H. J.; Lee, H. H.; Kim, J. W.; Jang, J.; Kim, J.-J. *J. Mater. Chem.* **2012**, *22* (18), 8881.
- (362) Evans, D. A.; Roberts, O. R.; Vearey-Roberts, A. R.; Williams, G. T.; Brieva, A. C.; Langstaff, D. P. *Appl. Phys. Lett.* **2013**, *102* (2), 21605.
- (363) Cheng, C. H.; Wang, J.; Du, G. T.; Shi, S. H.; Du, Z. J.; Fan, Z. Q.; Bian, J. M.; Wang, M. S. *Appl. Phys. Lett.* **2010**, *97* (8), 83305.
- (364) Yang, J.; Zhu, F.; Yu, B.; Wang, H.; Yan, D. *Appl. Phys. Lett.* **2012**, *100* (10), 103305.
- (365) Lunt, R. R.; Giebink, N. C.; Belak, A. A.; Benziger, J. B.; Forrest, S. R. *J. Appl. Phys.* **2009**, *105* (5), 53711.
- (366) Yassar, A. *Polym. Sci. Ser. C* **2014**, *56* (1), 4.
- (367) Yoon, Y.; Kim, S.; Lee, H.; Kim, T.; Babajanyan, A.; Lee, K.; Friedman, B. *Thin Solid Films* **2011**, *519* (16), 5562.
- (368) Sakai, S.; Soeda, J.; Häusermann, R.; Matsui, H.; Mitsui, C.; Okamoto, T.; Ito, M.; Hirose, K.; Sekiguchi, T.; Abe, T.; Uno, M.; Takeya, J. *Org. Electron.* **2015**, *22*, 1.
- (369) Pinto, R. M.; Macoas, E. M. S.; Neves, A. I. S.; Raja, S.; Baleizão, C. M.; Santos, I.

Bibliography

- C.; Alves, H. *J. Am. Chem. Soc.* **2015**, 150520072059007.
- (370) Chen, Y.; Lee, B.; Fu, D.; Podzorov, V. *Adv. Mater.* **2011**, 23 (45), 5370.
- (371) Mladenovic, M.; Stankovic, I. *Serbian J. Electr. Eng.* **2013**, 10 (1), 125.
- (372) Schönherr, G.; Eiermann, R.; Bässler, H.; Silver, M. *Chemical Phys.* **1980**, 52, 287.
- (373) Lunt, R. R.; Benziger, J. B.; Forrest, S. R. *Adv. Mater.* **2010**, 22 (11), 1233.
- (374) Chwang, A. B.; Frisbie, C. D. *J. Appl. Phys.* **2001**, 90 (3), 1342.
- (375) Kalb, W. L.; Haas, S.; Krellner, C.; Mathis, T.; Batlogg, B. **2010**, 1.
- (376) Fielitz, T. R.; Holmes, R. *J. Cryst. Growth Des.* **2016**, 16 (8), 4720.
- (377) Pratontep, S.; Brinkmann, M.; Nüesch, F.; Zuppiroli, L. *Synth. Met.* **2004**, 146 (3), 387.
- (378) Wan, J.; Li, Y.; Ulbrandt, J. G.; Smilgies, D.-M.; Hollin, J.; Whalley, A. C.; Headrick, R. L. *APL Mater.* **2016**, 4 (1), 16103.
- (379) Lee, H. H.; Kim, H. J.; Kim, J. W.; Jang, J.; Kim, J.-J. *Org. Photovoltaics XIII* **2012**, 8477, 84771O.
- (380) Lee, S. S.; Kim, C. S.; Gomez, E. D.; Purushothaman, B.; Toney, M. F.; Wang, C.; Hexemer, A.; Anthony, J. E.; Loo, Y. L. *Adv. Mater.* **2009**, 21, 3605.
- (381) Gibbs, J. W. *Trans. Connect. Acad. Arts Sci.* **1875**, 3 (1), 108.
- (382) Wulff, G. *Zeitschrift für Krist. - Cryst. Mater.* **1901**, 34 (1), 449.
- (383) Burton, W. K.; Cabrera, N.; Frank, F. C. *Philos. Trans. R. Soc. A* **1951**, 243 (866), 299.
- (384) Lewis, B. In *Crystal Growth*; Pamplin, B. R., Ed.; Pergamon Press: New York, NY, 1980; pp 23–63.
- (385) Perez, M. *Scr. Mater.* **2005**, 52 (8), 709.
- (386) Gommes, C. J. 2013; pp 1–29.
- (387) Toxvaerd, S. *J. Chem. Phys.* **2015**, 143, 1540705.
- (388) Lee, I. J.; Yun, M. *Macromolecules* **2010**, 43 (12), 5450.
- (389) Qi, W.; Peng, Y.; Han, Y.; Bowles, R. K.; Dijkstra, M. *Phys. Rev. Lett.* **2015**, 115 (18), 185701.
- (390) Song, P.; Wang, Y.; Wang, Y.; Hollingsworth, A. D.; Weck, M.; Pine, D. J.; Ward, M. D. *J. Am. Chem. Soc.* **2015**.
- (391) Winn, D.; Doherty, M. F. *AIChE J.* **2000**, 46 (7), 1348.
- (392) Lovette, M. A.; Browning, A. R.; Griffin, D. W.; Sizemore, J. P.; Snyder, R. C.; Doherty, M. F. *Ind. Eng. Chem. Res.* **2008**, 47 (24), 9812.
- (393) Kim, S. H.; Dandekar, P.; Lovette, M. a.; Doherty, M. F. *Cryst. Growth Des.* **2014**, 14, 2460.
- (394) Borsos, A.; Majumder, A.; Nagy, Z. K. *Cryst. Growth Des.* **2015**, 16, 555.
- (395) Tilbury, C. J.; Green, D. A.; Marshall, W. J.; Doherty, M. F. *Cryst. Growth Des.* **2016**, 16 (5), 2590.
- (396) Drummy, L. F.; Miska, P. K.; Alberts, D.; Lee, N.; Martin, D. C. *J. Phys. Chem. B* **2006**, 110, 6066.
- (397) Schorsch, S.; Hours, J.-H.; Vetter, T.; Mazzotti, M.; Jones, C. N. *Comput. Chem. Eng.* **2015**, 75, 171.

Bibliography

- (398) Salvalaglio, M.; Backofen, R.; Bergamaschini, R.; Montalenti, F.; Voigt, A. *Cryst. Growth Des.* **2015**, *15*, 2787.
- (399) Xiao, R.-F.; Alexander, J. I.; Rosenberger, F. *Phys. Rev. A* **1991**, *43* (6), 2977.
- (400) Li, R.; Zhang, X.; Dong, H.; Li, Q.; Shuai, Z.; Hu, W. *Adv. Mater.* **2015**, *1*.
- (401) Bennema, P. *J. Cryst. Growth* **1967**, *1*, 278.
- (402) Han, G.; Chow, P. S.; Tan, R. B. H. *Cryst. Growth Des.* **2015**, *150129114741009*.
- (403) Hartman, P.; Perdok, W. G. *Acta Crystallogr.* **1955**, *8*, 49.
- (404) Hartman, P.; Perdok, W. G. *Acta Crystallogr.* **1955**, *8*, 525.
- (405) Spackman, M. a.; Jayatilaka, D. *CrystEngComm* **2009**, *11*, 19.
- (406) Bravais, A. E. *Etudes Crystallographique*; Gauthier-Villars: Paris, France, 1866.
- (407) Li, J.; Tilbury, C. J.; Joswiak, M. N.; Peters, B.; Doherty, M. F. *Cryst. Growth Des.* **2016**, *16*, 3313.
- (408) Liu, S. J.; Huang, H.; Woo, C. H. *Appl. Phys. Lett.* **2002**, *80* (18), 3295.
- (409) Schwoebel, R. L.; Shipsey, E. J. *J. Appl. Phys.* **1966**, *37* (1966), 3682.
- (410) Schwoebel, R. L. *J. Appl. Phys.* **1969**, *40* (2), 614.
- (411) Hlawacek, G.; Puschnig, P.; Frank, P.; Winkler, A.; Ambrosch-Draxl, C.; Teichert, C. *Science* **2008**, *321* (5885), 108.
- (412) Stephan, J.; Brehmer, L. *Synth. Met.* **2000**, *109* (1–3), 333.
- (413) Cantrell, R. a; James, C.; Clancy, P. *Langmuir* **2011**, *27* (16), 9944.
- (414) Smerdon, J. a; Young, K. M.; Lowe, M.; Hars, S. S.; Yadav, T. P.; Hesp, D.; Dhanak, V. R.; Tsai, a P.; Sharma, H. R.; McGrath, R. *Nano Lett.* **2014**, *14* (3), 1184.
- (415) Ribič, P. R.; Bratina, G. *Surf. Sci.* **2007**, *601*, 1.
- (416) Thompson, R. J.; Yadin, B.; Grout, Z. J.; Hudziak, S.; Kloc, C. L.; Mitrofanov, O.; Curson, N. *J. Appl. Phys. Lett.* **2011**, *98* (2011), 11.
- (417) Goose, J. E.; Clancy, P. *J. Phys. Chem. C* **2007**, *111*, 15653.
- (418) Evans, J. W.; Thiel, P. a.; Bartelt, M. C. *Surf. Sci. Rep.* **2006**, *61* (1–2), 1.
- (419) Sleigh, J. P.; McMahon, D. P.; Troisi, A. *Appl. Phys. A* **2009**, *95* (1), 147.
- (420) Tumbek, L.; Winkler, A. *Surf. Sci.* **2012**, *606* (15–16), L55.
- (421) Ngai, K. L.; Magill, J. H.; Plazek, D. J. *J. Chem. Phys.* **2000**, *112* (4), 1887.
- (422) Weckesser, J.; Barth, J. V.; Kern, K. *J. Chem. Phys.* **1999**, *110* (11), 5351.
- (423) Gomer, R. *Reports Prog. Phys.* **1990**, *53*, 917.
- (424) Malshe, R.; Ediger, M. D.; Yu, L.; Pablo, J. J. De; Malshe, R.; Ediger, M. D.; Yu, L.; Pablo, J. J. De. *J. Chem. Phys.* **2011**, *134*, 194704.
- (425) Jensen, P.; Barabasi, A.-L.; Arralde, H. L.; Havlin, S.; Stanley, H. E. *Phys. Rev. B* **1994**, *50* (20), 316.
- (426) Reucroft, P. J.; Kevorkian, H. K.; Labes, M. M. *J. Chem. Phys.* **1966**, *44* (12), 4416.
- (427) Otero, R.; Hümmelink, F.; Sato, F.; Legoas, S. B.; Thostrup, P.; Laegsgaard, E.; Stensgaard, I.; Galvão, D. S.; Besenbacher, F. *Nat. Mater.* **2004**, *3*, 779.
- (428) Berner, S. Molecular Diffusion and Self-Organization on Metal Surfaces: Sub-Phthalocyanine on Ag (111), Universitat Basel, 2002.
- (429) Tsong, T. T. *Prog. Surf. Sci.* **2001**, *67*, 235.
- (430) Campoy-Quiles, M.; Ferenczi, T.; Agostinelli, T.; Etchegoin, P. G.; Kim, Y.;

Bibliography

- Anthopoulos, T. D.; Stavrinou, P. N.; Bradley, D. D. C.; Nelson, J. *Nat. Mater.* **2008**, 7, 158.
- (431) Berkebile, S.; Koller, G.; Hlawacek, G.; Teichert, C.; Netzer, F. P.; Ramsey, M. G. *Surf. Sci.* **2006**, 600 (24), L313.
- (432) Watts, B.; Belcher, W. J.; Thomsen, L.; Ade, H.; Dastoor, P. C. *Macromolecules* **2009**, 42 (21), 8392.
- (433) Antczak, G.; Ehrlich, G. *Surf. Sci. Rep.* **2007**, 62, 39.
- (434) Lee, C. H.; Kevorkian, H. K.; Reucroft, P. J.; Labes, M. M. *J. Chem. Phys.* **1965**, 42 (4), 1406.
- (435) Park, S.-W.; Choi, J.-M.; Lee, K. H.; Yeom, H. W.; Im, S.; Lee, Y. K. *J. Phys. Chem. B* **2010**, 114 (17), 5661.
- (436) Nascimento, M. L. F.; Zanotto, E. D. *J. Chem. Phys.* **2010**, 133, 174701.
- (437) Cullinan, T. E.; Cullinan, T. E. **2015**.
- (438) Sun, Y.; Zhu, L.; Kearns, K. L.; Ediger, M. D.; Yu, L. *Proc. Natl. Acad. Sci. U. S. A.* **2011**, 108 (15), 5990.
- (439) Shtukenberg, A.; Freundenthal, J.; Gunn, E.; Yu, L.; Kahr, B. *Cryst. Growth Des.* **2011**, 11 (10), 4458.
- (440) Kéna-Cohen, S.; Forrest, S. R. *Nat. Photonics* **2010**, 4 (6), 371.
- (441) Zheng, Q.; Huang, J.; Cao, S.; Gao, H. *J. Mater. Chem. C* **2015**, 3 (28), 7469.
- (442) Kwon, S.; Kim, J.; Kim, G.; Yu, K.; Jo, Y.-R.; Kim, B.-J.; Kim, J.; Kang, H.; Park, B.; Lee, K. *Adv. Mater.* **2015**, n/a.
- (443) Zhang, P.; Zeng, X.; Deng, J.; Huang, K.; Bao, F.; Qiu, Y.; Xu, K.; Zhang, J. *Jpn. J. Appl. Phys.* **2010**, 49 (9), 95501.
- (444) Su, J.; Chen, D. P.; Lin, C. T. *J. Cryst. Growth* **2015**, 422, 75.
- (445) Virkar, A.; Mannsfeld, S.; Bao, Z.; Stingelin, N. *Adv. Mater.* **2010**, 22 (34), 3857.
- (446) Liu, C.-Y.; Bard, A. J. *Chem. Mater.* **2000**, 12 (8), 2353.
- (447) Canbek, Z. C.; Cortes-Huerto, R.; Testard, F.; Spalla, O.; Moldovan, S.; Ersen, O.; Wisnet, A.; Wang, G.; Goniakowski, J.; Noguera, C.; Menguy, N. *Cryst. Growth Des.* **2015**, 150702145906006.
- (448) Yang, X.; Fujiwara, K.; Maeda, K.; Nozawa, J.; Koizumi, H.; Uda, S. *Prog. PHOTOVOLTAICS Res. Appl.* **2014**, 22, 574.
- (449) Liu, S. **2004**, 214103, 1.
- (450) Moret, M.; Campione, M.; Borghesi, A.; Miozzo, L.; Sassella, A.; Trabattoni, S.; Lotz, B.; Thierry, A. *J. Mater. Chem.* **2005**, 15 (25), 2444.
- (451) Lee, H. M.; Moon, H.; Kim, H.-S.; Kim, Y. N.; Choi, S.-M.; Yoo, S.; Cho, S. O. *Org. Electron.* **2011**, 12, 1446.
- (452) Takemura, Y. Method of making thin film transistor using lateral crystallization, 1997.
- (453) Xiao, R.-F.; Alexander, J. I. D.; Rosenberger, F. *J. Cryst. Growth* **1990**, 100, 313.
- (454) Gilmer, G. H. *J. Cryst. Growth* **1980**, 49, 465.
- (455) Shtukenberg, A. G.; Punin, Y. O.; Gunn, E.; Kahr, B. *Chem. Rev.* **2012**, 112, 1805.
- (456) Gránásy, L.; Pusztai, T.; Tegze, G.; Warren, J.; Douglas, J. *Phys. Rev. E* **2005**, 72

Bibliography

- (1), 11605.
- (457) Granasy, L.; Pusztai, T.; Borzsonyi, T. **2007**, 48.
- (458) Gránásy, L.; Pusztai, T.; Börzsönyi, T.; Warren, J. a; Douglas, J. F. *Nat. Mater.* **2004**, 3 (9), 645.
- (459) Luo, Y.; Brun, M.; Rannou, P.; Grevin, B. *Phys. Status Solidi* **2007**, 204 (6), 1851.
- (460) Yoo, H.; Choi, H. H.; Shin, T. J.; Rim, T.; Cho, K.; Jung, S.; Kim, J.-J. *Adv. Funct. Mater.* **2015**, n/a.
- (461) Zheng, L.; Liu, J.; Sun, Y.; Ding, Y.; Han, Y. *Macromol. Chem. Phys.* **2012**, 213, 2081.
- (462) Dougherty, a.; Kaplan, P. D.; Gollub, J. P. *Phys. Rev. Lett.* **1987**, 58 (16), 1652.
- (463) Caginalp, G.; Socolovsky, E. *SIAM J. Sci. Comput.* **1994**, 15 (1), 106.
- (464) Cho, J.; Terry, S. G.; LeSar, R.; Levi, C. G. *Mater. Sci. Eng. A* **2005**, 391 (1–2), 390.
- (465) Laudise, R. A.; Kloc, C.; Simpkins, P. G.; Siegrist, T. *J. Cryst. Growth* **1998**, 187 (December 1997), 449.
- (466) Baldo, M.; Deutsch, M.; Burrows, P.; Gossenberger, H.; Gerstenberg, M.; Ban, V.; Forrest, S. *Adv. Mater.* **1998**, 10 (18), 1505.
- (467) Mannsfeld, S. C. B.; Briseno, a. L.; Liu, S.; Reese, C.; Roberts, M. E.; Bao, Z. *Adv. Funct. Mater.* **2007**, 17 (17), 3545.
- (468) Holzmueller, F.; Wilde, L.; Wölzl, F.; Koerner, C.; Vandewal, K.; Leo, K. *Org. Electron.* **2015**, 27, 133.
- (469) Brieva, A. C.; Jenkins, T. E.; Jones, D. G.; Strössner, F.; Evans, D. A.; Clark, G. F. *J. Appl. Phys.* **2006**, 99 (7), 73504.
- (470) Kurrle, D.; Pflaum, J. *Appl. Physics Lett.* **2008**, 92, 133306.
- (471) Ribič, P.; Kalihari, V.; Frisbie, C.; Bratina, G. *Phys. Rev. B* **2009**, 80 (11), 115307.
- (472) Verlaak, S.; Steudel, S.; Heremans, P.; Janssen, D.; Deleuze, M. *Phys. Rev. B* **2003**, 68 (19), 1.
- (473) Käfer, D.; Ruppel, L.; Witte, G.; Wöll, C. *Phys. Rev. Lett.* **2005**, 95 (16), 166602.
- (474) Wang, L.; Kong, H.; Song, X.; Liu, X.; Wang, H. *Phys. Chem. Chem. Phys.* **2010**, 12 (44), 14682.
- (475) Käfer, D.; Witte, G. *Phys. Chem. Chem. Phys.* **2005**, 7, 2850.
- (476) Udhardt, C.; Forker, R.; Gruenewald, M.; Watanabe, Y.; Yamada, T.; Ueba, T.; Munakata, T.; Fritz, T. *Thin Solid Films* **2016**, 598, 271.
- (477) Kytka, M.; Gisslen, L.; Gerlach, a.; Heinemeyer, U.; Kováč, J.; Scholz, R.; Schreiber, F. *J. Chem. Phys.* **2009**, 130 (2009), 0.
- (478) Kloc, C. *Proc. SPIE* **2006**, 6336, 633606.
- (479) Morgan, N. T.; Zhang, Y.; Grandbois, M. L.; Bell, B. M.; Holmes, R. J.; Cussler, E. L. *Org. Electron.* **2015**, 24, 212.
- (480) Morgan, N. T.; Zhang, Y.; Molitor, E. J.; Bell, B. M.; Holmes, R. J.; Cussler, E. L. *AIChE J.* **2014**, 60 (4), 1374.
- (481) Podzorov, V.; Sysoev, S. E.; Loginova, E.; Pudalov, V. M.; Gershenson, M. E. *Appl. Phys. Lett.* **2003**, 83 (17), 3504.
- (482) Jurchescu, O. D.; Meetsma, A.; Palstra, T. T. M. *Acta Crystallogr. B* **2006**, 62 (Pt

Bibliography

- 2), 330.
- (483) Voloshenko, A.; Tan, K. J.; Kloc, C.; Lev, O.; Shelkov, M.; Sladkevich, S.; Prikhodchenko, P. V.; Gun, J. *Org. Electron. Mater. Appl.* **2013**, *14* (1), 378.
- (484) Yang, J.; Yan, D. *Chem. Soc. Rev.* **2009**, *38*, 2634.
- (485) Kühnapfel, S.; Gall, S.; Rech, B.; Amkreutz, D. *Sol. Energy Mater. Sol. Cells* **2015**, *140*, 86.
- (486) Kim, Y.; Cruz, S. S.; Lee, K.; Alawode, B. O.; Choi, C.; Song, Y.; Johnson, J. M.; Heidelberger, C.; Kong, W.; Choi, S.; Qiao, K.; Almansouri, I.; Fitzgerald, E. A.; Kong, J.; Kolpak, A. M.; Hwang, J.; Kim, J. *Nat. Publ. Gr.* **2017**, *544*, 340.
- (487) Northrup, J.; Tiago, M.; Louie, S. *Phys. Rev. B* **2002**, *66* (12), 1.
- (488) Choi, J.; Jeong, S.; Hwang, D.; Im, S.; Lee, B.; Sung, M. *Org. Electron.* **2009**, *10* (1), 199.
- (489) Fumagalli, E.; Campione, M.; Raimondo, L.; Sassella, A.; Moret, M.; Barba, L.; Arrighetti, G. *J. Synchrotron Radiat.* **2012**, *19* (Pt 5), 682.
- (490) Raimondo, L.; Fumagalli, E.; Moret, M.; Campione, M.; Borghesi, A.; Sassella, A. *J. Phys. Chem. C* **2013**, *117*, 13981.
- (491) Hooks, D. E.; Fritz, T.; Ward, M. D. *Adv. Mater.* **2001**, *13* (4), 227.
- (492) Sassella, A. *Cryst. Res. Technol.* **2013**, *48* (10), 840.
- (493) Trelka, M.; Medina, A.; Écija, D.; Urban, C.; Gröning, O.; Fasel, R.; Gallego, J. M.; Claessens, C. G.; Otero, R.; Torres, T.; Miranda, R. *Chem. Commun. (Camb.)* **2011**, *47* (36), 9986.
- (494) Fritz, T.; Hara, M.; Knoll, W.; Sasabe, H. In *Atomic Force Microscopy/Scanning Tunneling Microscopy 2*; 1997; pp 99–106.
- (495) Mitchell, C. A.; Yu, L.; Ward, M. D. *J. Am. Chem. Soc.* **2001**, *123* (44), 10830.
- (496) Bonafede, S. J.; Ward, M. D. *J. Am. Chem. Soc.* **1995**, *117* (30), 7853.
- (497) Krause, B.; Dürr, A.; Ritley, K.; Schreiber, F.; Dosch, H.; Smilgies, D. *Phys. Rev. B* **2002**, *66* (23), 235404.
- (498) Lee, C.-H.; Schiros, T.; Santos, E. J. G.; Kim, B.; Yager, K. G.; Kang, S. J.; Lee, S.; Yu, J.; Watanabe, K.; Taniguchi, T.; Hone, J.; Kaxiras, E.; Nuckolls, C.; Kim, P. *Adv. Mater.* **2014**, *26* (18), 1.
- (499) Wu, J.; Li, Q.; Xue, G.; Chen, H.; Li, H. *Adv. Mater.* **2017**, *29*, 1606101.
- (500) Yan, D.; Yu, B.; Huang, L.; Chen, W.; Qiao, X. Organic solar cell adopting weak epitaxial growth film as donor. 200910067006, 2009.
- (501) Chang, H.; Li, W.; Tian, H.; Geng, Y.; Wang, H.; Yan, D.; Wang, T. *Org. Electron.* **2015**, *20*, 43.
- (502) Wang, H.; Zhu, F.; Yang, J.; Geng, Y.; Yan, D. *Adv. Mater.* **2007**, *19* (16), 2168.
- (503) Yang, J.; Wang, T.; Wang, H.; Zhu, F.; Li, G.; Yan, D. *J. Phys. Chem. B* **2008**, *112*, 3132.
- (504) Forrest, S.; Zhang, Y. *Phys. Rev. B. Condens. Matter* **1994**, *49* (16), 11297.
- (505) So, F. F.; Forrest, S. R.; Shi, Y. Q.; Steier, W. H. *Appl. Phys. Lett.* **1990**, *56* (7), 674.
- (506) Huang, M.; Antonietti, M.; Cölfen, H. *APL Mater.* **2016**, *4* (1), 15705.

Bibliography

- (507) Toda, Y.; Yanagi, H. *Appl. Phys. Lett.* **1996**, *69* (16), 2315.
- (508) Hayashi, K.; Kawato, S.; Fujii, Y.; Horiuchi, T.; Matsushige, K. *Appl. Phys. Lett.* **1997**, *70* (11), 1384.
- (509) Copel, M.; Kaxiras, E.; Tromp, M.; Stranski-krastanov, T. *Phys. Rev. Lett.* **1989**, *63* (6), 632.
- (510) Müller, C.; Aghamohammadi, M.; Himmelberger, S.; Sonar, P.; Garriga, M.; Salleo, A.; Campoy-Quiles, M. *Adv. Funct. Mater.* **2013**, *23* (19), 2368.
- (511) Peng, Y.; Yaacobi-Gross, N.; Perumal, A. K.; Faber, H. A.; Vourlias, G.; Patsalas, P. A.; Bradley, D. D. C.; He, Z.; Anthopoulos, T. D. *Appl. Phys. Lett.* **2015**, *106* (24), 243302.
- (512) Bernède, J. C.; Cattin, L.; Makha, M.; Jeux, V.; Leriche, P.; Roncali, J.; Froger, V.; Morsli, M.; Addou, M. *Sol. Energy Mater. Sol. Cells* **2013**, *110*, 107.
- (513) Kim, T.; Shim, H.; Choi, M.; Kim, H. J.; Kim, J. *ACS Appl. Mater. Interfaces* **2014**, *6*, 4286.
- (514) Tummala, N. R.; Mehraeen, S.; Fu, Y.-T.; Risko, C.; Brédas, J.-L. *Adv. Funct. Mater.* **2013**, *23* (46), 5800.
- (515) Manetta, S.; Ehrenspurger, M.; Bosshard, C.; Günter, P. *Comptes Rendus Phys.* **2002**, *3*, 449.
- (516) Vetter, T.; Igglund, M.; Ochsenbein, D. R.; Hänseler, F. S.; Mazzotti, M. *Cryst. Growth Des.* **2013**, *13*, 4890.
- (517) Matsukawa, T.; Takahashi, Y.; Tokiyama, T.; Sasai, K.; Murai, Y.; Hirota, N.; Tominari, Y.; Mino, N.; Yoshimura, M.; Abe, M.; Takeya, J.; Kitaoka, Y.; Mori, Y.; Morita, S.; Sasaki, T. *Jpn. J. Appl. Phys.* **2008**, *47*, 8950.
- (518) Bhangu, S. K.; Ashokkumar, M.; Lee, J. *Cryst. Growth Des.* **2016**, *16* (4), 1934.
- (519) El Helou, M.; Medenbach, O.; Witte, G. *Cryst. Growth Des.* **2010**, *10* (8), 3496.
- (520) Kim, J.; Park, C.; Choi, H. C. *Chem. Mater.* **2015**, *27* (7), 2408.
- (521) Horike, S.; Koshiba, Y.; Misaki, M.; Ishida, K. *3*, 1.
- (522) Ishii, Y.; Shimada, T.; Okazaki, N.; Hasegawa, T. *Langmuir* **2007**, *23* (12), 6864.
- (523) Wu, K.-Y.; Wu, T.-Y.; Chang, S.-T.; Hsu, C.-S.; Wang, C.-L. *Adv. Mater.* **2015**, *1*, n/a.
- (524) Giri, G.; Verploegen, E.; Mannsfeld, S. C. B.; Atahan-Evrenk, S.; Kim, D. H.; Lee, S. Y.; Becerril, H. a; Aspuru-Guzik, A.; Toney, M. F.; Bao, Z. *Nature* **2011**, *480* (7378), 504.
- (525) Giri, G.; Li, R.; Smilgies, D.-M.; Li, E. Q.; Diao, Y.; Lenn, K. M.; Chiu, M.; Lin, D. W.; Allen, R.; Reinschach, J.; Mannsfeld, S. C. B.; Thoroddsen, S. T.; Clancy, P.; Bao, Z.; Amassian, A. *Nat. Commun.* **2014**, *5*, 3573.
- (526) Briseno, A. L.; Roberts, M.; Ling, M.-M.; Moon, H.; Nemanick, E. J.; Bao, Z. *J. Am. Chem. Soc.* **2006**, *128*, 3880.
- (527) Liu, S.; Wang, W. M.; Briseno, A. L.; Mannsfeld, S. C. B.; Bao, Z. *Adv. Mater.* **2009**, *21*, 1217.
- (528) Ward, M. D. .
- (529) Carter, P. W.; Ward, M. D. *J. Am. Chem. Soc.* **1993**, *115* (24), 11521.

Bibliography

- (530) Guo, S.; Ward, M. D.; Wesson, J. A. *Langmuir* **2002**, *18*, 4284.
- (531) Olmsted, B. K.; Ward, M. D. *CrystEngComm* **2011**, *13* (4), 1070.
- (532) Brady, M. A.; Su, G. M.; Chabinyc, M. L. *Soft Matter* **2011**, *7* (23), 11065.
- (533) Treat, N. D.; Brady, M. a.; Smith, G.; Toney, M. F.; Kramer, E. J.; Hawker, C. J.; Chabinyc, M. L. *Adv. Energy Mater.* **2011**, *1* (1), 82.
- (534) Meng, B.; Wang, Z.; Ma, W.; Xie, Z.; Liu, J.; Wang, L. *Adv. Funct. Mater.* **2015**, *22*.
- (535) Mora, S.; Tavazzi, S.; Spearman, P. *Synth. Met.* **2012**, *162* (19–20), 1737.
- (536) Liu, S. L.; Chung, T. S. *Polymer (Guildf.)* **2000**, *41* (8), 2781.
- (537) Chen, L.; Dong, G.; Duan, L.; Wang, L.; Qiao, J.; Zhang, D.; Qiu, Y. **2009**, *16549*.
- (538) Skrypnychuk, V.; Boulanger, N.; Yu, V.; Hilke, M.; Toney, M. F.; Barbero, D. R. *J. Mater. Chem. C* **2016**.
- (539) Hibino, R.; Nagawa, M.; Hotta, S.; Ichikawa, M.; Koyama, T.; Taniguchi, Y. *Adv. Mater.* **2002**, *14* (2), 119.
- (540) Lercher, C.; Resel, R.; Balandier, J. Y.; Niebel, C.; Geerts, Y. H.; Sferrazza, M.; Gbabode, G. *J. Cryst. Growth* **2014**, *386*, 128.
- (541) Kéna-Cohen, S.; Davanço, M.; Forrest, S. *Phys. Rev. Lett.* **2008**, *101* (11), 116401.
- (542) Kéna-Cohen, S.; Davanço, M.; Forrest, S. *Phys. Rev. B* **2008**, *78* (15), 153102.
- (543) Christenson, H. K. *J. Phys. Condens. Matter* **2001**, *13* (11), R95.
- (544) Stingelin-Stutzmann, N.; Smits, E.; Wondergem, H.; Tanase, C.; Blom, P.; Smith, P.; de Leeuw, D. *Nat. Mater.* **2005**, *4* (8), 601.
- (545) Jo, P. S.; Duong, D. T.; Park, J.; Sinclair, R.; Salleo, A. *Chem. Mater.* **2015**, *150519131253001*.
- (546) Su, Y.; Liu, J.; Zheng, L.; Ding, Z.; Han, Y. *RSC Adv.* **2012**, *2* (13), 5779.
- (547) Ciciora, F.; Miwa, J. a; Perepichka, D. F.; Rosei, F. *J. Phys. Chem. A* **2007**, *111* (49), 12674.
- (548) Ho, C.; Tao, Y. *Chem. Commun.* **2014**.
- (549) Chung, J.; Hyon, J.; Park, K.; Cho, B.; Baek, J.; Kim, J. *Nat. Publ. Gr.* **2016**, No. February, 1.
- (550) Yang, F.; Sun, K.; Forrest, S. R. *Adv. Mater.* **2007**, *19* (23), 4166.
- (551) Fischer, F. S. U.; Trefz, D.; Back, J.; Kayunkid, N.; Tornow, B.; Albrecht, S.; Yager, K. G.; Singh, G.; Karim, A.; Neher, D.; Brinkmann, M.; Ludwigs, S. **2014**, *1*.
- (552) Zimmerman, J. D.; Xiao, X.; Renshaw, C. K.; Wang, S.; Diev, V. V; Thompson, M. E.; Forrest, S. R. *Nano Lett.* **2012**, *12* (8), 4366.
- (553) Winkel, a. K.; Hobbs, J. K.; Miles, M. J. *Polymer (Guildf.)* **2000**, *41*, 8791.
- (554) Park, S.-W.; Jeong, S. H.; Choi, J.-M.; Hwang, J. M.; Kim, J. H.; Im, S. *Appl. Phys. Lett.* **2007**, *91* (3), 33506.
- (555) Regimol, C.C., C. S. M. *Sci. Mater.* **2007**, *25* (3).
- (556) Oklobia, O.; Shafai, T. S. *Sol. Energy Mater. Sol. Cells* **2013**, *117*, 1.
- (557) Sakai, J.; Taima, T.; Yamanari, T.; Saito, K. *Sol. Energy Mater. Sol. Cells* **2009**, *93*, 1149.
- (558) Du, C.; Wang, W.; Li, L.; Fuchs, H.; Chi, L. *Org. Electron. physics, Mater. Appl.*

Bibliography

- 2013, 14 (10), 2534.
- (559) Kim, K.; Liu, J.; Namboothiry, M. a. G.; Carroll, D. L. *Appl. Phys. Lett.* **2007**, 90 (16), 163511.
- (560) Wei, G.; Lunt, R. R.; Sun, K.; Wang, S.; Thompson, M. E.; Forrest, S. R. *Nano Lett.* **2010**, 10, 3555.
- (561) Haemori, M.; Yamaguchi, J.; Yaginuma, S.; Itaka, K.; Koinuma, H. *Japanese J. Appl. Physics, Part 1 Regul. Pap. Short Notes Rev. Pap.* **2005**, 44, 3740.
- (562) Ray, B.; Nair, P. R.; Alam, M. A. *Sol. Energy Mater. Sol. Cells* **2011**, 95 (12), 3287.
- (563) Tang, Y.; Wang, Y.; Wang, X.; Xun, S.; Mei, C.; Wang, L.; Yan, D. *J. Phys. Chem. B* **2005**, 109, 8813.
- (564) Bergantin, S.; Moret, M.; Buth, G.; Fabbiani, F. P. a. *J. Phys. Chem. C* **2014**, 140603132134007.
- (565) Ostrowska, K.; Kropidlowska, M.; Katrusiak, A. *Cryst. Growth Des.* **2015**, 150210115452007.
- (566) Hernández, I.; Gillin, W. P. *J. Phys. Chem. B* **2009**, 113 (43), 14079.
- (567) Fabbiani, F. P. a; Allan, D. R.; Parsons, S.; Pulham, C. R. *Acta Crystallogr. B* **2006**, 62 (Pt 5), 826.
- (568) Matsushima, T.; Esaki, Y.; Adachi, C.; Matsushima, T.; Esaki, Y.; Adachi, C. *Appl. Phys. Lett.* **2014**, 105, 243301.
- (569) Padinger, B. F.; Rittberger, R. S.; Sariciftci, N. S. *Adv. Funct. Mater.* **2003**, 13 (1), 85.
- (570) Schuster, B.-E.; Basova, T. V; Peisert, H.; Chassé, T. *Chemphyschem* **2009**, 10 (11), 1874.
- (571) Basova, T. V.; Kiselev, V. G.; Plyashkevich, V. a.; Cheblakov, P. B.; Latteyer, F.; Peisert, H.; Chassè, T. *Chem. Phys.* **2011**, 380 (1–3), 40.
- (572) Potticary, J.; Terry, L. R.; Bell, C.; Papanikolopoulos, A. N.; Christianen, P. C. M.; Engelkamp, H.; Collins, A. M.; Fantanesi, C.; Kociok-Kohn, G.; Crampin, S.; Da Como, E.; Hall, S. R. *Nat. Commun.* **2016**, 7, 11555.
- (573) Zeis, R.; Besnard, C.; Siegrist, T.; Schlockermann, C.; Chi, X.; Kloc, C. *Chem. Mater.* **2006**, 18 (2), 244.
- (574) Podzorov, V. *MRS Bull.* **2013**, 38 (1), 15.
- (575) Wada, T.; Ueda, N. *J. Appl. Phys.* **2013**, 113 (15), 154503.
- (576) Song, B.; Forrest, S. R. *Nano Lett.* **2016**.
- (577) Donhauser, D.; Pfannmöller, M.; Dieterle, L.; Schultheiß, K.; Schröder, R. R.; Kowalsky, W.; Kröger, M. *Adv. Funct. Mater.* **2013**, 23 (17), 2130.
- (578) Weston, G. F. *Ultrahigh vacuum practice*; Butterworths: London, England, 1985.
- (579) Minemawari, H.; Yamada, T.; Matsui, H.; Tsutsumi, J.; Haas, S.; Chiba, R.; Kumai, R.; Hasegawa, T. *Nature* **2011**, 475 (7356), 364.
- (580) Liu, F.; Ferdous, S.; Wang, C.; Hexamer, A.; Russell, T. *Bull. Am. Phys. Soc.* **2014**, Volume 59, 886.
- (581) Xu, Y.; Zhu, L.; Shi, J.; Xu, X.; Xiao, J.; Dong, J.; Wu, H.; Luo, Y.; Li, D.; Meng, Q. *ChemPhysChem* **2016**, 17 (1), 112.

Bibliography

- (582) McNeill, C. R.; Watts, B.; Thomsen, L.; Belcher, W. J.; Greenham, N. C.; Dastoor, P. C. *Nano Lett.* **2006**, 6 (6), 1202.
- (583) Toolan, D. T. W.; Pullan, N.; Harvey, M. J.; Topham, P. D.; Howse, J. R. *Adv. Mater.* **2013**, 25 (48), 7033.
- (584) Deng, W.; Zhang, X.; Wang, L.; Wang, J.; Shang, Q.; Zhang, X.; Huang, L.; Jie, J. *Adv. Mater.* **2015**, 27 (45), 7305.
- (585) Rand, B. P.; Cheyns, D.; Vasseur, K.; Giebink, N. C.; Mothy, S.; Yi, Y.; Coropceanu, V.; Beljonne, D.; Cornil, J.; Brédas, J.-L.; Genoe, J. *Adv. Funct. Mater.* **2012**, 22 (14), 2987.
- (586) Mönch, T.; Guttmann, P.; Murawski, J.; Elschner, C.; Riede, M.; Müller-Meskamp, L.; Leo, K. *Org. Electron.* **2013**, 14 (11), 2777.
- (587) Sakurai, T.; Fukasawa, R.; Kawai, S.; Akimoto, K. *Japanese J. Appl. Physics, Part 1 Regul. Pap. Short Notes Rev. Pap.* **2006**, 45, 397.
- (588) Yu, B.; Wang, H.; Yan, D. *Nanotechnology* **2013**, 24 (48), 484006.
- (589) Li, Z.; Du, J.; Tang, Q.; Wang, F.; Xu, J.-B.; Yu, J. C.; Miao, Q. *Adv. Mater.* **2010**, 22 (30), 3242.
- (590) Chen, W.; Nikiforov, M. P.; Darling, S. B. *Energy Environ. Sci.* **2012**, 5 (8), 8045.
- (591) Chen, S.; Xi, H.; Yu, L. *J. Am. Chem. Soc.* **2005**, 127 (13), 17439.
- (592) Fischer, F.; Hahn, T.; Bässler, H.; Bauer, I.; Strohriegl, P.; Köhler, A. *Adv. Funct. Mater.* **2014**, 24 (39), 6172.
- (593) Allen, C. F. H.; Gilman, L. **1936**, 1322 (1), 937.
- (594) Irkhin, P.; Ryasnyanskiy, A.; Koehler, M.; Biaggio, I. *Phys. Rev. B* **2012**, 86, 85143.
- (595) Ding, H.; Gao, Y. *Proc. SPIE* **2010**, 7778, 77780J.
- (596) Williams, W. G. *Discuss. Faraday Soc.* **1971**, 51, 61.
- (597) Bowen, E. J.; Steadman, F. *J. Chem. Soc.* **1932**, No. 1098, 1098.
- (598) Fumagalli, E.; Raimondo, L.; Silvestri, L.; Moret, M.; Sassella, A.; Campione, M. *Chem. Mater.* **2011**, 23 (13), 3246.
- (599) Kytka, M.; Gerlach, a.; Schreiber, F.; Kováč, J. *Appl. Phys. Lett.* **2007**, 90 (2007).
- (600) Thompson, R. J.; Fearn, S.; Tan, K. J.; Cramer, H. G.; Kloc, C. L.; Curson, N. J.; Mitrofanov, O. *Phys. Chem. Chem. Phys.* **2013**, 15 (14), 5202.
- (601) Briseno, A. L. In *Fall MRS EM4.4.07*; Boston, MA, 2016.
- (602) Brauer, H. D.; Schmidt, R. *J. Photochem.* **1984**, 27, 17.
- (603) Katscher, U.; Schmidt, R.; Brauer, H. *Chem. Phys. Lett.* **1993**, 205 (1), 75.
- (604) Sundar, V. C.; Zaumseil, J.; Podzorov, V.; Menard, E.; Willett, R. L.; Someya, T.; Gershenson, M. E.; Rogers, J. A. *Science* **2004**, 303, 1644.
- (605) Nyman, J.; Day, G. M. *Phys. Chem. Chem. Phys.* **2016**, 18, 31132.
- (606) Nyman, J.; Day, G. M. *CrystEngComm* **2015**, 17, 5154.
- (607) Nangia, A.; Guru Row, T. N. *CrystEngComm* **2015**, 17 (28), 5128.
- (608) Chung, H.; Diao, Y. *J. Mater. Chem. C* **2016**, 4, 3915.
- (609) Akopyan, Z. A.; Avoyan, R. L.; Struchkov, Y. T. *Zhurnal Strukt. Khimif* **1962**, 3 (5), 602.
- (610) Taylor, W. H. *Zeitschrift für Krist. - Cryst. Mater.* **1936**, 93 (1), 151.

Bibliography

- (611) Henn, D. E.; Williams, W. G.; Gibbons, D. J. *J. Appl. Crystallogr.* **1971**, *4* (3), 256.
- (612) Huang, L.; Liao, Q.; Shi, Q.; Fu, H.; Ma, J.; Yao, J. *J. Mater. Chem.* **2010**, *20*, 159.
- (613) da Silva Filho, D. A.; Kim, E.-G.; Bredas, J.-L. *Adv. Mater.* **2005**, *17* (8), 1072.
- (614) Pithan, L.; Cocchi, C.; Zschiesche, H.; Weber, C.; Zykov, A.; Bommel, S.; Leake, S. J.; Schäfer, P.; Draxl, C.; Kowarik, S. *Cryst. Growth Des.* **2015**, *15* (10), 150211145859005.
- (615) Pithan, L.; Beyer, P.; Bogula, L.; Zykov, A.; Schäfer, P.; Rawle, J.; Nicklin, C.; Opitz, A.; Kowarik, S. *Adv. Mater.* **2017**, *29*, 1604382.
- (616) Yu, L. *J. Am. Chem. Soc.* **2003**, *125*, 6380.
- (617) Cavallo, D.; Gardella, L.; Portale, G.; Müller, A. J.; Alfonso, G. C. *Macromolecules* **2014**, *47*, 870.
- (618) Obata, S.; Miura, T.; Shimoi, Y. *Jpn. J. Appl. Phys.* **2014**, *53*.
- (619) Mullins, W. W. *J. Appl. Phys.* **1959**, *30* (1), 77.
- (620) Freund, L. B.; Suresh, S. *Thin film materials: stress, defect formation, and surface evolution*; University Press: Cambridge, UK, 2003.
- (621) Thornton, J. A.; Hoffman, D. W. *Thin Solid Films* **1989**, *171*, 5.
- (622) Chowdhury, M.; Sheng, X.; Ziebert, F.; Sepe, A.; Steiner, U.; Reiter, G. *Macromolecules* **2016**, *49*, 9060.
- (623) Hutchinson, J. W. *Stresses and Failure Modes in thin films and multilayers*; Cambridge, MA, 1996.
- (624) Kumar, A.; Widenborg, P. I.; Dalapati, G. K.; Ke, C.; Subramanian, G. S.; Aberle, A. *Cryst. Growth Des.* **2015**, *15*, 1067.
- (625) Spaepen, F. *Acta Mater.* **2000**, *48*, 31.
- (626) Zhou, H.; Park, J.-W. *Org. Electron.* **2015**, *24*, 272.
- (627) Wu, Y.; Chew, A. R.; Rojas, G. A.; Sini, G.; Haugstad, G.; Belianinov, A.; Kalinin, S. V.; Li, H.; Risko, C.; Brédas, J.-L.; Salleo, A.; Frisbie, C. D. *Nat. Commun.* **2016**, *7*, 10270.
- (628) Reyes-Martinez, M. A.; Ramasubramaniam, A.; Briseno, A. L.; Crosby, A. J. *Adv. Mater.* **2012**, *24* (c), 5548.
- (629) Wolf, E.; Born, M. *Principles of Optics: Electromagnetic Theory of Propagation Interference and Diffraction of Light*, 6th ed.; Pergamon Press, Ltd: London, England, 1980.
- (630) Bundgaard, F.; Ellegaard, C.; Scheibye-Knudsen, K.; Bohr, T.; Sams, T. *Phys. Rev. E* **2004**, *70* (6), 06207.
- (631) Scheibye-Knudsen, K.; Ellegaard, C.; Bundgaard, F.; Sams, T. *Phys. Rev. E* **2005**, *72* (1), 016209.
- (632) Müller, J.; Grant, M. *Phys. Rev. Lett.* **1999**, *82* (8), 1736.
- (633) Cartwright, J. H. E.; García-Ruiz, J. M.; Villacampa, A. I. *Comput. Phys. Commun.* **1999**, *121*, 411.
- (634) Buchner, C.; Schneider, W. *Proc. Appl. Math. Mech.* **2010**, *10* (1), 493.
- (635) Telang, A. U.; Bieler, T. R.; Zamiri, A.; Purboghrat, F. *Acta Mater.* **2007**, *55*, 2265.
- (636) Mullins, W. W.; Sekerka, R. F. *J. Appl. Phys.* **1963**, *34* (1963), 323.

Bibliography

- (637) Mullins, W. W.; Sekerka, R. F. *J. Appl. Phys.* **1964**, *35* (1964), 444.
- (638) Seo, J. H.; Park, D. S.; Cho, S. W. J.; Kim, C. Y.; Jang, W. C.; Whang, C. N.; Yoo, K.-H.; Chang, G. S.; Pedersen, T.; Moewes, A.; Chae, K. H.; Cho, S. W. *J. Appl. Phys. Lett.* **2006**, *89* (16), 163505.
- (639) Gowenlock, B. G. *Q. Rev. Chem. Soc.* **1960**, *14* (2), 133.
- (640) van der Wielen, M. W.; Cohen Stuart, M. A.; Fleer, G. J.; Schlatmann, A. R.; de Boer, D. K. *Phys. Rev. E. Stat. Phys. Plasmas. Fluids. Relat. Interdiscip. Topics* **1999**, *60* (4 Pt B), 4252.
- (641) Byrn, S.; Pfieffer, R.; Ganey, M.; Hoiberg, C.; Poochikian, G. *Pharm. Res.* **1995**, *12* (7), 945.
- (642) Peumans, P.; Uchida, S.; Forrest, S. R. *Nature* **2003**, *425*, 158.
- (643) Yu, G.; Gao, J.; Hummelen, J. C.; Wudl, F.; Heeger, A. J. *Science* **1995**, *270* (5243), 1789.
- (644) Schubert, S.; Kim, Y. H.; Menke, T.; Fischer, A.; Timmreck, R.; Müller-Meskamp, L.; Leo, K. *Sol. Energy Mater. Sol. Cells* **2013**, *118*, 165.
- (645) Vasconcelos, T.; Sarmento, B.; Costa, P. *Drug Discov. Today* **2007**, *12* (23/24), 1068.
- (646) Serajuddin, A. T. M.; Sheen, P.-C.; Augustine, M. A. *J. Pharm. Sci.* **1990**, *79* (5), 463.
- (647) Zhang, J.; Li, C.-Z.; Williams, S. T.; Liu, S.; Zhao, T.; Jen, A. K.-Y. *J. Am. Chem. Soc.* **2015**, *137*, 2167.
- (648) Guo, S.; Fidler, A. F.; He, K.; Su, D.; Chen, G.; Lin, Q.; Pietryga, J. M.; Klimov, V. I. *J. Am. Chem. Soc.* **2015**, *137*, 15074.
- (649) Xia, Y.; Xia, X.; Peng, H.-C. *J. Am. Chem. Soc.* **2015**, *137*, 7947.
- (650) Polavarapu, L.; Mourdikoudis, S.; Pastoriza-Santos, I.; Pérez-juste, J. *CrystEngComm* **2015**, *17*, 3727.
- (651) Cai, T.; Zhu, L.; Yu, L. *Pharm. Res.* **2011**, *28*, 2458.
- (652) Kestur, U. S.; Lee, H.; Santiago, D.; Rinaldi, C.; Won, Y.; Taylor, L. S. *Cryst. Growth Des.* **2010**, *10* (8), 3585.
- (653) Aso, Y.; Yoshioka, S.; Kojima, S. *J. Pharm. Sci.* **2004**, *93* (2), 384.
- (654) Lee, E. H. *Asian J. Pharm. Sci.* **2014**, *9* (4), 1.
- (655) Price, D. M. *Thermochim. Acta* **2000**, *367–368*, 253.
- (656) Hempel, T.; Schoenfeld, O.; Syrowatka, F. *Solid State Commun.* **1993**, *85* (11), 921.
- (657) Nygren, E.; McCallum, J. C.; Thornton, R.; Williams, J. S.; Olson, G. L. *Mater. Res. Soc. Symp. Proc.* **1988**, *100*, 405.
- (658) Nygren, E.; Williams, J. S.; Pogany, A.; Elliman, R. G.; Olson, G. L.; McCallum, J. C. *Mater. Res. Soc. Symp. Proc.* **1987**, *74*, 307.
- (659) Jacobson, D. C.; Elliman, R. G.; Gibson, J. M.; Olson, G. L.; Poate, J. M.; Williams, J. S. *Mater. Res. Soc. Symp. Proc.* **1987**, *74*, 327.
- (660) Radnóczki, G. Z.; Knez, D.; Hofer, F.; Frangis, N.; Vouroutzis, N.; Stoemenos, J.; Pecz, B. *J. Appl. Phys.* **2017**, *121*, 145301.
- (661) Kim, S. O.; Solak, H. H.; Stoykovich, M. P.; Ferrier, N. J.; De Pablo, J. J.; Nealey,

Bibliography

- P. F. *Nature* **2003**, *424* (6947), 411.
- (662) Chavis, M. a.; Smilgies, D.-M.; Wiesner, U. B.; Ober, C. K. *Adv. Funct. Mater.* **2015**, n/a.
- (663) Bates, C. M.; Maher, M. J.; Janes, D. W.; Ellison, C. J.; Willson, C. G. *Macromolecules* **2014**, *47*, 2.
- (664) Park, M.; Harrison, C.; Chaikin, P. M.; Register, R. A.; Adamson, D. H. *Science* **1997**, *276*, 1401.
- (665) Baruth, A.; Rodwgin, M. D.; Shankar, A.; Erickson, M. J.; Hillmyer, M. A.; Leighton, C. *Appl. Mater. Interfaces* **2011**, *3*, 3472.
- (666) Bates, F. S.; Fredrickson, G. H. *Annu. Rev. Phys. Chem.* **1990**, *41*, 525.
- (667) Palmer, C.; Loewen, E. *Diffraction Grating Handbook*, 6th ed.; Newport Corporation: Rochester, NY, 2005.
- (668) Baldo, M. A.; Holmes, R. J.; Forrest, S. R. **2002**, *1*.
- (669) Samuel, I. D. W.; Turnbull, G. A. **2007**, 1272.
- (670) Bowden, N.; Huck, W. T. S.; Paul, K. E.; Whitesides, G. M. *Appl. Phys. Lett.* **1999**, *75* (17), 2557.
- (671) Suh, K. Y.; Seo, S. M.; Yoo, P. J.; Lee, H. H. *J. Chem. Phys.* **2006**, *124*, 24710.
- (672) Muller-Wiegand, M.; Georgiev, G.; Oesterschulze, E.; Fuhrmann, T.; Salbeck, J. *Appl. Physics Lett.* **2002**, *81* (26), 4940.
- (673) Huang, R. *J. Mech. Phys. Solids* **2005**, *53*, 63.
- (674) Haugstad, G. *Atomic Force Microscopy: Understanding Basic Modes and Advanced Applications*; John Wiley & Sons, Inc: Hoboken, New Jersey, 2012.
- (675) Moynihan, C. T.; Easteal, A. J.; Wilder, J.; Tucker, J. *J. Phys. Chem.* **1974**, *78* (26), 2673.
- (676) Atake, T.; Angell, C. A. *J. Phys. Chem.* **1979**, *83* (25), 3218.
- (677) Casalini, R.; Roland, C. M. *Phys. Rev. E* **2004**, *69*, 62501.
- (678) Harrison, C.; Stafford, C. M.; Zhang, W.; Karim, A. *Appl. Phys. Lett.* **2004**, *85* (18), 4016.
- (679) Guo, C. F.; Nayyar, V.; Zhang, Z.; Chen, Y.; Miao, J.; Huang, R.; Liu, Q. *Adv. Mater.* **2012**, *24*, 3010.
- (680) Stafford, C. M.; Vogt, B. D.; Harrison, C.; Julthongpiput, D.; Huang, R. *Macromolecules* **2006**, *39*, 5095.
- (681) Kotni, T. R.; Khanna, R.; Sarkar, J. *J. Phys. Condens. Matter* **2017**, *29*, 175001.
- (682) Seeman, R.; Herminghaus, S.; Neto, C.; Schlagowski, S.; Podzimek, D.; Konrad, R.; Mantz, H.; Jacobs, K. *J. Phys. Condens. Matter* **2005**, *17*, S267.
- (683) Mei, H.; Huang, R.; Chung, J. Y.; Yu, C. M. S.; Yu, H.-H. *Appl. Physics Lett.* **2007**, *90*, 151902.
- (684) Bowden, N.; Brittain, S.; Evans, A. G.; Hutchinson, J. W.; Whitesides, G. M. *Nature* **1998**, *393*, 146.
- (685) Gruner, P.; Arlt, M.; Fuhrmann-lieker, T. *ChemPhysChem* **2013**, *14*, 424.
- (686) Madigan, C.; Bulovic, V. **2006**, 46404 (February), 1.
- (687) Yang, F.; Forrest, S. R. *ACS Nano* **2008**, *2* (5), 1022.

Bibliography

- (688) Chintala, R.; Tait, J. G.; Eyben, P.; Voroshazi, E.; Surana, S.; Fleischmann, C.; Conard, T.; Vandervorst, W. *Nanoscale* **2016**.
- (689) Do, K.; Risko, C.; Anthony, J. E.; Amassian, A.; Bredas, J.-L. *Chem. Mater.* **2015**, 151022104025003.
- (690) Cnops, K.; Rand, B. P.; Cheyns, D.; Verreet, B.; Empl, M. A.; Heremans, P. *Nat. Commun.* **2014**, 5, 3406.
- (691) Mutolo, K. L.; Mayo, E. I.; Rand, B. P.; Forrest, S. R.; Thompson, M. E. *J. Am. Chem. Soc.* **2006**, 128 (25), 8108.
- (692) Lucia, E. A. *J. Chem. Phys.* **1968**, 48 (6), 2674.
- (693) El-Nahass, M. M.; Bahabri, F. S.; Al-Harbi, R. *Egypt. J. Solids* **2001**, 24 (1), 11.
- (694) Pettersson, L. A. A.; Roman, L. S.; Inganäs, O. *J. Appl. Phys.* **1999**, 86 (1), 487.
- (695) Hinderhofer, A.; Schreiber, F. *Chemphyschem* **2012**, 13 (3), 628.
- (696) Fukuda, T.; Olmstead, M. M.; Durfee, W. S.; Kobayashi, N. *Chem. Commun.* **2003**, 1, 1256.
- (697) Kietabl, H. *Monatshefte fur Chemie* **1974**, 105, 405.
- (698) Stehr, V.; Fink, R. F.; Engels, B.; Jens, P.; Deibel, C. *J. Chem. Theory Comput.* **2014**, 10, 1242.
- (699) Meskers, S. C. J.; Hübner, J.; Oestreich, M.; Bässler, H. *J. Phys. Chem. B* **2001**, 105, 9139.
- (700) Andrews, D. L. In *Tutorials in Complex Photonic Media*; Noginov, M. A., Dewar, G., McCall, M. W., Zheludev, N. I., Eds.; SPIE Press, 2009; pp 439–470.
- (701) Salam, A. *J. Chem. Phys.* **2005**, 112, 44112.
- (702) Akselrod, G. M.; Deotare, P. B.; Thompson, N. J.; Lee, J.; Tisdale, W. A.; Baldo, M. A.; Menon, V. M.; Bulovic, V. *Nat. Commun.* **2014**, 5, 3646.
- (703) Griffith, O. L.; Forrest, S. R. *Nano Lett.* **2014**, 14 (5), 2353.
- (704) Verreet, B.; Cnops, K.; Cheyns, D.; Heremans, P.; Stesmans, A.; Zango, G.; Claessens, C. G.; Torres, T.; Rand, B. P. *Adv. Energy Mater.* **2014**, 4, 1301413.
- (705) Endres, J.; Pelczer, I.; Rand, B. P.; Kahn, A. *Chem. Mater.* **2016**, 28, 794.
- (706) Xu, G.; Lu, N.; Wang, W.; Gao, N.; Ji, Z.; Li, L.; Liu, M. *Org. Electron.* **2015**, 23, 53.
- (707) Luhman, W. A.; Holmes, R. J. *Adv. Funct. Mater.* **2011**, 21 (4), 764.
- (708) Berg, H. C. *Random Walks In Biology*; Princeton University Press: Princeton, NJ, 1983.
- (709) Chen, W.; Huang, L.; Qiao, X.; Yang, J.; Yu, B.; Yan, D. *Org. Electron.* **2012**, 13 (13), 1086.
- (710) Lassiter, B. E.; Lunt, R. R.; Renshaw, C. K.; Forrest, S. R. *Opt. Express* **2010**, 18 (S3), 444.
- (711) Zeng, X.; Wang, L.; Duan, L.; Qiu, Y. *Cryst. Growth Des.* **2008**, 8 (5), 1617.
- (712) Fusella, M. A.; Schreiber, F.; Abbasi, K.; Kim, J. J.; Briseno, A. L.; Rand, B. P. *Nano Lett.* **2017**, 17, 3040.
- (713) Nakayama, Y.; Machida, S.; Minari, T.; Tsukagishi, K.; Noguchi, Y.; Ishii, H. *Appl. Phys. Lett.* **2008**, 93 (17), 173305.

Bibliography

- (714) Saxena, K.; Mehta, D. S.; Rai, V. K.; Srivastava, R.; Chauhan, G.; Kamalasan, M. N.; Jain, V. K. *Phys. Status Solidi* **2009**, *206* (7), 1660.
- (715) Huang, H.-H.; Chu, S.-Y.; Kao, P.-C.; Chen, Y.-C. *Thin Solid Films* **2008**, *516* (16), 5669.
- (716) Mullenbach, T. K.; McGarry, K. A.; Luhman, W. A.; Douglas, C. J.; Holmes, R. J. *Adv. Mater.* **2013**, *1*.
- (717) Mönch, T.; Sherkar, T. S.; Anton Koster, L. J.; Friederich, P.; Riede, M.; Formanek, P.; Koerner, C.; Vandewal, K.; Wenzel, W.; Leo, K. *Org. Electron.* **2015**, *27*, 183.
- (718) Goose, J. E.; Killampalli, A.; Clancy, P.; Engstrom, J. R. *J. Phys. Chem. C* **2009**, *113* (15), 6068.
- (719) Keblinski, P.; Maritan, A.; Toigo, F.; Banavar, J. R. *Phys. Rev. Lett.* **1995**, *74* (10), 1783.
- (720) El-nashar, H. F. *Egypt. J. Solids* **2002**, *25* (2), 191.
- (721) Schreiber, F. *Phys. Status Solidi* **2004**, *201* (6), 1037.
- (722) Lehnens, C.; Lu, T.-M. *Phys. Rev. B* **2010**, *82* (8), 85437.
- (723) Mal, B.; Ray, S.; Shamanna, J. *Eur. Phys. J. B* **2011**, *82* (3–4), 341.
- (724) Zhou, Y.; Taima, T.; Miyadera, T.; Yamanari, T.; Kitamura, M.; Nakatsu, K.; Yoshida, Y. *Appl. Phys. Lett.* **2012**, *100* (23), 233302.
- (725) Zheng, Y.; Potscavage, W. J.; Komino, T.; Hirade, M.; Adachi, J.; Adachi, C. *Appl. Phys. Lett.* **2013**, *102* (14), 143304.
- (726) Zheng, Y.; Potscavage, W. J.; Komino, T.; Adachi, C. *Appl. Phys. Lett.* **2013**, *102* (15), 153302.
- (727) Pandey, R.; Holmes, R. J. *Appl. Phys. Lett.* **2012**, *100* (8), 83303.
- (728) Pandey, R.; Zou, Y.; Holmes, R. J. *Appl. Phys. Lett.* **2012**, *101* (3), 33308.
- (729) Huang, L.; Zhu, F.; Liu, C.; Treske, U.; Grobosch, M.; Tian, H.; Zhang, J.; Geng, Y.; Knupfer, M.; Yan, D. *Adv. Funct. Mater.* **2012**, *22* (21), 4598.
- (730) Huang, L.; Liu, C.; Yu, B.; Zhang, J.; Geng, Y.; Yan, D. *J. Phys. Chem. B* **2010**, *114*, 4821.
- (731) Meyer zu Heringdorf, F. J.; Reuter, M. C.; Tromp, R. M. *Nature* **2001**, *412* (6846), 517.
- (732) Killampalli, A. S.; Schroeder, T. W.; Engstrom, J. R. *Appl. Phys. Lett.* **2005**, *87* (2005), 85.
- (733) Williams, D. B.; Carter, C. B. *Transmission Electron Microscopy*, 2nd ed.; Springer Science + Business Media, LLC: New York, NY, 2009.
- (734) Wang, L.; Qi, D.; Liu, L.; Chen, S.; Gao, X.; Wee, A. T. S. *J. Phys. Chem. C* **2007**, *111* (8), 3454.
- (735) Takenobu, T.; Takahashi, T.; Takeya, J.; Iwasa, Y. *Appl. Phys. Lett.* **2007**, *90* (1), 13507.
- (736) Ding, H.; Gao, Y. *Appl. Phys. A* **2009**, *95* (1), 89.
- (737) Zou, Y.; Holmes, R. J. *Appl. Phys. Lett.* **2013**, *103* (5), 53302.
- (738) Mullenbach, T. K.; Curtin, I. J.; Zhang, T.; Holmes, R. J. *Nat. Commun.* **2017**, *8*, 14215.

Bibliography

- (739) Chandran, H. T.; Ng, T.; Foo, Y.; Li, H.; Qing, J.; Liu, X.; Chan, C.; Wong, F.; Zapien, J. A.; Tsang, S.; Lo, M.; Lee, C. *Adv. Mater.* **2017**, 1606909.
- (740) Soh, J. H.; Lin, Y.; Thomas, M. R.; Todorova, N.; Kallepitidis, C.; Yarovskiy, I.; Ying, J. Y.; Stevens, M. M. *Adv. Funct. Mater.* **2017**, 1700523.
- (741) Ohashi, C.; Izawa, S.; Shinmura, Y.; Kikuchi, M.; Watase, S.; Izaki, M.; Naito, H.; Hiramoto, M. *Adv. Mater.* **2017**, 29 (23), 1605619.
- (742) Jurchescu, O. D. In *Fall MRS EM4.6.10*; Boston, MA, 2016.
- (743) Yokoyama, D.; Park, Y.; Kim, B.; Kim, S.; Pu, Y.-J.; Kido, J.; Park, J. *J. Appl. Phys. Lett.* **2011**, 99 (12), 123303.
- (744) Yokoyama, D. *J. Mater. Chem.* **2011**, 21 (48), 19187.
- (745) Graf, A.; Liehm, P.; Murawski, C.; Hofmann, S.; Leo, K.; Gather, M. C. *J. Mater. Chem. C* **2014**, 2 (48), 10298.
- (746) Liehm, P.; Murawski, C.; Furno, M.; Lüssem, B.; Leo, K.; Gather, M. C. *Appl. Phys. Lett.* **2012**, 101 (25), 253304.
- (747) Kearns, K. L.; Na, H.-Y.; Froese, R. D.; Mukhopadhyay, S.; Woodward, H.; Welsh, D.; De Vries, T.; Devore, D.; Trefonas, P.; Hong, L. In *Proceedings of SPIE*; So, F., Ed.; 2014; Vol. 9183, pp 1–12.
- (748) Li, X.; Xu, Y.; Li, F.; Ma, Y. *Org. Electron.* **2012**, 13 (5), 762.
- (749) Bisri, S. Z.; Takenobu, T.; Yomogida, Y.; Shimotani, H.; Yamao, T.; Hotta, S.; Iwasa, Y. *Adv. Funct. Mater.* **2009**, 19 (11), 1728.
- (750) Yomogida, Y.; Takenobu, T.; Shimotani, H.; Sawabe, K.; Bisri, S. Z.; Yamao, T.; Hotta, S.; Iwasa, Y. *Appl. Phys. Lett.* **2010**, 97 (17), 173301.
- (751) Takenobu, T.; Bisri, S.; Takahashi, T.; Yahiro, M.; Adachi, C.; Iwasa, Y. *Phys. Rev. Lett.* **2008**, 100 (6), 66601.
- (752) Zhou, Y.; Wang, L.; Chen, S.; Qin, S.; Liu, X.; Chen, J.; Xue, D.-J.; Luo, M.; Cao, Y.; Cheng, Y.; Sargent, E. H.; Tang, J. *Nat. Photonics* **2015**, 9 (May), 409.
- (753) He, Z.; Li, D.; Hensley, D. K.; Rondinone, A. J.; Chen, J. *Appl. Phys. Lett.* **2013**, 103 (11), 113301.
- (754) Yu, B.; Huang, L.; Wang, H.; Yan, D. *Adv. Mater.* **2010**, 22 (9), 1017.
- (755) Lobastov, V. A.; Srinivasan, R.; Zewail, A. H. *Proc. Natl. Acad. Sci.* **2005**, 102 (20), 7069.
- (756) Flannigan, D. J.; Zewail, A. H. *Acc. Chem. Res.* **2012**, 45 (10), 1828.
- (757) McKenna, A. J.; Eliason, J. K.; Flannigan, D. J. *Nano Lett.* **2017**, 17 (6), 3952.
- (758) Cremons, D. R.; Plemmons, D. A.; Flannigan, D. J. *Nat. Commun.* **2016**, 7, 1.
- (759) Cremons, D. R.; Plemmons, D. A.; Flannigan, D. J. In *Microscopy and Microanalysis*; 2016; Vol. 22, pp 1632–1633.
- (760) Rezk, A. R.; Carey, B.; Chrimes, A. F.; Lau, D. W. M.; Gibson, B. C.; Zheng, C.; Fuhrer, M. S.; Yeo, L. Y.; Kalantar-zadeh, K. *Nano Lett.* **2016**, acs.nanolett.5b02826.
- (761) Hill, H. M.; Rigosi, A. F.; Roquelet, C.; Chernikov, A.; Berkelbach, T. C.; Reichman, D. R.; Hybertsen, M. S.; Brus, L. E.; Heinz, T. F. *Nano Lett.* **2015**, 150327160959000.

Bibliography

- (762) Rigosi, A. F.; Hill, H. M.; Li, Y.; Chernikov, A.; Heinz, T. F. *Nano Lett.* **2015**, 150717105243008.
- (763) Zhang, X.; Meng, F.; Christianson, J. R.; Arroyo-Torres, C.; Lukowski, M. a; Liang, D.; Schmidt, J. R.; Jin, S. *Nano Lett.* **2014**, 14 (6), 3047.
- (764) Okada, Y.; Uno, M.; Nakazawa, Y.; Sasai, K.; Matsukawa, K.; Yoshimura, M.; Kitaoka, Y.; Mori, Y.; Takeya, J. *Phys. Rev. B* **2011**, 83, 113305.
- (765) Schweicher, G.; Olivier, Y.; Lemaur, V.; Henri, Y. *Isr. J. Chem.* **2014**, 54, 595.
- (766) Zhang, X.; Li, Z.; Lu, G. *Phys. Rev. B* **2011**, 84, 235208.
- (767) Kim, N.; Christensen, A.; Kippelen, B. *Appl. Phys. Lett.* **2013**, 87, 241908.
- (768) Yao, Y.; Shahi, M.; Payne, M. M.; Anthony, J. E.; Brill, J. W. *J. Mater. Chem. C* **2016**, 4 (1), 8817.
- (769) Sun, J.; Adhikari, A.; Shaheen, B. S.; Yang, H.; Mohammed, O. F. *J. Phys. Chem. Lett.* **2016**, 7, 985.
- (770) Sun, J.; Melnikov, V. A.; Khan, J. I.; Mohammed, O. F. *J. Phys. Chem. Lett.* **2015**, 6, 3884.
- (771) Najafi, E.; Ivanov, V.; Zewail, A.; Bernardi, M. *Nat. Commun.* **2017**, 8, 15177.
- (772) Plemmons, D. A.; Flannigan, D. J. *Chem. Phys. Lett.* **2017**, 683, 186.
- (773) Scoby, C. M.; Li, R. K.; Musumeci, P. *Ultramicroscopy* **2013**, 127, 14.
- (774) Cremons, D. R.; Flannigan, D. J. *Ultramicroscopy* **2016**, 161, 10.
- (775) Lee, Y.-E.; Kim, S.-Y.; Jeong, W.-I.; Kim, J.-J. *Sol. Energy Mater. Sol. Cells* **2013**, 114, 59.
- (776) Gao, Y.; Jin, F.; Li, W.; Su, Z.; Chu, B.; Wang, J. **2016**, No. April, 1.
- (777) Slawinski, M. A.; Slawinski, R. A.; Brown, R. J.; Parkin, J. M. *Geophysics* **2000**, 65 (2), 632.
- (778) *Guide to using WVASE spectroscopic ellipsometry data acquisition and analysis software*; J. A. Woollam Co., Inc.: Lincoln, NE, 2012.
- (779) Jezierski, K. *Br. J. Appl. Phys.* **1965**, 16, 1119.
- (780) Sanders, S. Kramers Kronig Lecture Notes
https://homepages.cae.wisc.edu/~ssanders/me_770/supplemental_material/kramers-kronig/kramers_kronig_lecture_notes_UCF.pdf.
- (781) Dressel, M.; Gompf, B.; Faltermeier, D.; Tripathi, A. K.; Pflaum, J.; Schubert, M. *Opt. Express* **2008**, 16 (24), 19770.
- (782) Faltermeier, D.; Gompf, B.; Dressel, M.; Tripathi, A. K.; Pflaum, J. *Phys. Rev. B* **2006**, 74, 125416.
- (783) O'Connor, D. V; Phillips, D. *Time-correlated single photon counting*; Academic Press: London, England, 1984.
- (784) Wan, Y.; Stradomska, A.; Knoester, J.; Huang, L. *J. Am. Chem. Soc.* **2017**, 139, 7287.
- (785) Kolosov, D.; English, D. S.; Bulovic, V.; Barbara, P. F.; Forrest, S. R.; Thompson, M. E. *J. Appl. Phys.* **2001**, 90 (7), 3242.
- (786) Aziz, H.; Popovic, Z.; Tripp, C. P.; Hu, N.; Hor, A.; Xu, G. *Appl. Phys. Lett.* **1998**, 72 (21), 2642.

Bibliography

- (787) Schindelin, J.; Arganda-Carreras, I.; Frise, E.; Kaynig, V.; Longair, M.; Pietzsch, T.; Preibisch, S.; Rueden, C.; Saalfeld, S.; Schmid, B.; Tinevez, J.-Y.; White, D. J.; Hartenstein, V.; Eliceiri, K.; Tomancak, P.; Cardona, A. *Nat. Methods* **2012**, *9* (7), 676.
- (788) Necas, D.; Klapetek, P. *Cent. Eur. J. Phys.* **2012**, *10* (1), 181.
- (789) Macrae, C. F.; Bruno, I. J.; Chisholm, J. A.; Edgington, P. R.; McCabe, P.; Pidcock, E.; Rodriguez-Monge, L.; Taylor, R.; van de Streek, J.; Wood, P. A. *J. Appl. Crystallogr.* **2008**, *41*, 466.
- (790) Bjorck, M.; Andersson, G. *J. Appl. Crystallogr.* **2007**, *40*, 1174.
- (791) Thomas, L. C. *Am. Lab.* **2001**, *33* (1).
- (792) Mathot, V.; Pyda, M.; Pijpers, T.; Vanden, G.; Kerkhof, E. Van De; Herwaarden, S. Van; Herwaarden, F. Van; Leenaers, A. *Thermochim. Acta* **2011**, *522* (1–2), 36.
- (793) Schick, C. 6.
- (794) Bar, G. K.; Meyers, G. F. **2004**, No. July, 464.
- (795) Hobbs, J. K.; Vasilev, C.; Humphris, A. D. L. *Polymer (Guildf.)* **2005**, *46* (23), 10226.
- (796) Gasperino, D.; Yeckel, A.; Olmsted, B. K.; Ward, M. D.; Derby, J. J. *Langmuir* **2006**, *22* (15), 6578.
- (797) Ward, M. D. *Science* **2005**, *308* (5728), 1566.
- (798) Dora, S. K. *World J. Nano Sci. Eng.* **2017**, *7*, 1.
- (799) Garcia, R.; San Paulo, A. *Phys. Rev. B* **2000**, *61* (20), 381.
- (800) Yildiz, A. Classical derivation of r_0 of Förster transfer <http://research.physics.berkeley.edu/yildiz/Teaching/PHYS250/SupplementaryFile s/ClassicalFRETderivation2008.pdf> (accessed Jan 7, 2017).
- (801) Ketskemeti, I. *Naturforsch* **1954**, *17A*, 666.
- (802) Scholes, G. D.; Rumbles, G. *Nat. Mater.* **2006**, *5*, 683.
- (803) Curutchet, C.; Mennucci, B.; Scholes, G. D.; Beljonne, D. *J. Phys. Chem. B* **2008**, *112*, 3759.
- (804) Eisfeld, A.; Briggs, J. S. *Chem. Phys.* **2006**, *324*, 376.
- (805) Nguyen, T.; Wu, J.; Doan, V.; Schwartz, B.; Tolbert, S. *Science* **2000**, *288* (5466), 652.
- (806) Markov, D.; Tanase, C.; Blom, P.; Wildeman, J. *Phys. Rev. B* **2005**, *72* (4), 45217.
- (807) Scully, S. R.; Mcgehee, M. D.; Scully, S. R.; Mcgehee, M. D. **2006**, 34907.
- (808) Saleh, B. E. A.; Teich, M. C. In *Fundamentals of Photonics*; John Wiley & Sons, Inc: Hoboken, New Jersey, 1991; Vol. 5, pp 193–237.
- (809) Wooten, F. *OPTICAL PROPERTIES of solids*; Academic Press: New York, NY, 1972.
- (810) Davids, C. C. *Lasers and electro-optics: fundamentals and engineering*; Cambridge University Press: Cambridge, UK, 2014.
- (811) Tropf, W. J.; Thomas, M. E.; Harris, T. J. In *Handbook of Optics: Devices, measurements, and properties, Volum II*; Bass, M., Ed.; McGraw-Hill: New York, NY, 1995.

Bibliography

- (812) Dresselhaus, M. S. In *Proceedings of the International School of Physics*; Fermi, E., Tau, J., Eds.; Academic Press: New York, NY, 1966.
- (813) *The ARRL Antenna Handbook*, 22nd ed.; Hall, G. L., Ed.; Amateur Radio Relay League, Inc.: Newington, CT, 2015.
- (814) Zhang, W.; Brian, C. W.; Yu, L. *J. Phys. Chem. B* **2015**, *119*, 5071.
- (815) Münch, A. *J. Phys. Condens. Matter* **2005**, *17*, S309.
- (816) Meredith, J. C.; Smith, A. P.; Karim, A.; Amis, E. J. *Macromolecules* **2000**, *33*, 9747.
- (817) Family, F. *J. Phys. A Math. Gen.* **1986**, *19*, 441.
- (818) Jung, T. A. *Molecular Surface Diffusion*; 1999.
- (819) Ruan, S.; Zhang, W.; Sun, Y.; Ediger, M. D.; Yu, L.; Ruan, S.; Zhang, W.; Sun, Y.; Ediger, M. D.; Yu, L. **2016**, *64503*.
- (820) Sun, Q.; Zhang, C.; Li, Z.; Sheng, K.; Kong, H.; Wang, L.; Pan, Y.; Tan, Q.; Hu, A.; Xu, W. *Appl. Phys. Lett.* **2013**, *103* (1), 13103.
- (821) Rajeswaran, M.; Blanton, T. N. *J. Chem. Crystallogr.* **2005**, *35* (1), 71.
- (822) Cheng, J.-A.; Cheng, P.-J. *J. Chem. Crystallogr.* **2010**, *40* (6), 557.
- (823) Zhang, Z.; Burkholder, E.; Zubieta, J. *Acta Crystallogr. C* **2004**, *60* (Pt 6), o452.
- (824) Kennedy, A. R.; Smith, W. E.; Tackley, D. R.; David, W. I. F.; Shankland, K.; Brown, B.; Teat, S. J. *J. Mater. Chem.* **2002**, *12* (2), 168.
- (825) McGarry, K. A.; Xie, W.; Sutton, C.; Risko, C.; Wu, Y.; Young, V. G.; Brédas, J.-L.; Frisbie, C. D.; Douglas, C. *J. Chem. Mater.* **2013**, *25* (11), 2254.
- (826) Campbell, R. B.; Robertson, J. M.; Trotter, J. *Acta Crystallogr.* **1961**, *14*, 705.
- (827) Sakamoto, Y.; Suzuki, T.; Kobayashi, M.; Gao, Y.; Fukai, Y.; Inoue, Y.; Sato, F.; Tokito, S. *J. Am. Chem. Soc.* **2004**, *126* (26), 8138.
- (828) Salzmann, I.; Duhm, S.; Heimel, G.; Rabe, J. P.; Koch, N.; Oehzelt, M.; Sakamoto, Y.; Suzuki, T. *Langmuir* **2008**, *24* (14), 7294.
- (829) Holmes, D.; Kumaraswamy, S.; Matzger, A. J.; Vollhardt, K. P. C. *Chem. - A Eur. J.* **1999**, *5* (11), 3399.
- (830) Cruickshank, D. W. J. *Acta Crystallogr.* **1956**, *9* (11), 915.
- (831) Gould, R. G. *Coord. Chem. Rev.* **1996**, *156*, 237.
- (832) Hoshino, A.; Takenaka, Y.; Miyaji, H. *Acta Crystallogr. Sect. B Struct. Sci.* **2003**, *59* (3), 393.
- (833) Brown, C. *J. J. Chem. Soc. A* **1968**, 2488.
- (834) Erk, P.; Hengelsberg, H.; Haddow, M. F.; van Gelder, R. *CrystEngComm* **2004**, *6* (78), 474.
- (835) Janczak, J.; Kubiak, R. *J. Alloys Compd.* **1992**, *190*, 121.
- (836) Zugenmaier, P. *J. Mater. Sci.* **1997**, *32*, 5561.
- (837) Robertson, J. M. *J. Chem. Soc.* **1934**, 615.
- (838) Fulford, M. V.; Jaidka, D.; Paton, A. S.; Morse, G. E.; Brisson, E. R. L.; Lough, A. J.; Bender, T. P. *J. Chem. Eng. Data* **2012**, *57* (10), 2756.
- (839) Liu, S.; Lu, Y. J.; Kappes, M. M.; Ibers, J. a. *Science* **1991**, *254* (5030), 408.
- (840) David, W. I. F.; Ibberson, R. M.; Matthewman, J. C.; Prassides, K.; Dennis, T. J. S.;

Bibliography

- Hare, J. P.; Kroto, H. W.; Taylor, R.; Walton, D. R. M. *Nature* **1991**, *353*, 147.
- (841) Verheijen, M. A.; Meekes, H.; Meijer, G.; Bennema, P.; de Boer, J. L.; van Smaalen, S.; van Tendeloo, G.; Amelinckx, S.; Muto, S.; van Landuyt, J. *Chem. Phys.* **1992**, *166*, 287.
- (842) Chen, Q.; Rada, T.; McDowall, a.; Richardson, N. V. *Chem. Mater.* **2002**, *14* (2), 743.
- (843) Camerman, a.; Trotter, J. *Acta Crystallogr.* **1965**, *18* (4), 636.
- (844) Guillermet, O.; Mossoyan-Déneux, M.; Giorgi, M.; Glachant, a.; Mossoyan, J. C. *Thin Solid Films* **2006**, *514* (1–2), 25.
- (845) Chen, Y.-H.; Lin, L.-Y.; Lu, C.-W.; Lin, F.; Huang, Z.-Y.; Lin, H.-W.; Wang, P.-H.; Liu, Y.-H.; Wong, K.-T.; Wen, J.; Miller, D. J.; Darling, S. B. *J. Am. Chem. Soc.* **2012**, *134* (33), 13616.
- (846) Hotta, S.; Goto, M.; Azumi, R.; Inoue, M. *Chem. Mater.* **2004**, *16*, 237.
- (847) Horowitz, G.; Bachet, B.; Yassar, A.; Lang, P.; Demanze, F.; Fave, J.; Garnier, F. *Chem. Mater.* **1995**, *7* (15), 1337.
- (848) Okada, Y.; Tokumaru, Y. *J. Appl. Phys.* **1984**, *56* (2), 314.
- (849) Hom, T.; Kiszenick, W.; Post, B. *J. Appl. Crystallogr.* **1975**, *8*, 457.
- (850) Kim, H.; Piqué, C. M. G.; Pique, A.; Horwitz, J. S.; Matoussi, H.; Murata, H.; Kafafi, Z. H.; Chrisey, D. B. *J. Appl. Phys.* **1999**, *86* (11), 6451.
- (851) Ohta, H.; Orita, M.; Hirano, M.; Hosono, H. *J. Appl. Phys.* **2002**, *91* (6), 3547.
- (852) Zachariasen, W. *Nor. Geol. Tidsskr.* **1927**, *9*, 310.
- (853) Le Page, Y.; Donnay, G. *Acta Crystallogr. Sect. B Struct. Sci.* **1976**, *32*, 2456.
- (854) Brill, R.; Hermann, C.; Peters, C. *Naturwissenschaften* **1939**, *40*, 676.
- (855) Goushi, K.; Yoshida, K.; Sato, K.; Adachi, C. *Nat. Photonics* **2012**, *6* (4), 253.
- (856) Baldo, M. A.; Forrest, S. R. *Phys. Rev. B* **2000**, *62* (16), 958.
- (857) Gao, Z. Q.; Luo, M.; Sun, X. H.; Tam, H. L.; Wong, M. S.; Mi, B. X.; Xia, P. F.; Cheah, K. W.; Chen, C. H. *Adv. Mater.* **2009**, *21* (6), 688.
- (858) Kanno, H.; Holmes, R. J.; Sun, Y.; Kena-Cohen, S.; Forrest, S. R. *Adv. Mater.* **2006**, *18*, 339.
- (859) Sugiyama, K.; Ishii, H.; Ouchi, Y.; Seki, K. *J. Appl. Phys.* **2000**, *87* (1), 295.
- (860) Chou, H.; Shih, H.; Cheng, C. *J. Mater. Chem.* **2010**, *20*, 798.
- (861) Pandey, A. K.; Nunzi, J.-M. *Appl. Phys. Lett.* **2007**, *90* (26), 263508.
- (862) Ding, J.; Wang, Q.; Zhao, L.; Wang, L.; Jing, X.; Wang, F. *J. Mater. Chem.* **2010**, *20*, 8126.
- (863) Holmes, R. J.; D'Andrade, B. W.; Forrest, S. R.; Ren, X.; Li, J.; Thompson, M. E. *Appl. Phys. Lett.* **2003**, *83* (18), 2001.
- (864) Chang, C.-H.; Ding, Y.-S.; Hsieh, P.-W.; Chang, C.-P.; Lin, W.-C.; Chang, H.-H. *Thin Solid Films* **2011**, *519* (22), 7992.
- (865) Schon, J. H.; Kloc, C.; Dodabalapur, A.; Batlogg, B. *Science* **2002**, *289*, 599.
- (866) Kozlov, V. G.; Bulovic, V.; Burrows, P. E.; Forrest, S. R. *Nature* **1997**, *389*, 362.
- (867) Holmes, R. J. *Nat. Nanotechnol.* **2007**, *2* (March), 7.
- (868) Kozlov, V. G.; Parthasarathy, G.; Burrows, P. E.; Khalfin, V. B.; Wang, J.; Chou,

Bibliography

- S. Y.; Forrest, S. R. *IEEE J. Quantum Electron.* **2000**, *36* (1), 18.
- (869) Qin, L.; Lv, L.; Ning, Y.; Li, C.; Lu, Q.; Zhu, L.; Hu, Y.; Lou, Z.; Teng, F.; Hou, Y. *RSC Adv.* **2015**, *5* (125), 103674.
- (870) Flannigan, D. J.; Suslick, K. S. *Nature* **2005**, *434*, 52.
- (871) Kim, H. N.; Sander, J. R. G.; Zeiger, B. W.; Suslick, K. S. *Cryst. Growth Des.* **2015**, *15* 0312140300003.
- (872) Vig, J. R. *Ultraviolet-Ozone cleaning of Semiconductor Surfaces*; Fort Monmouth, NJ, 1992.
- (873) Clark, M. D.; Leever, B. J. *Sol. Energy Mater. Sol. Cells* **2013**, *116*, 270.
- (874) Kato, Y.; Jung, M.-C.; Lee, M. V.; Qi, Y. *Org. Electron.* **2014**, *15* (3), 721.
- (875) Chen, A.; Zhu, K.; Zhong, H.; Shao, Q.; Ge, G. *Sol. Energy Mater. Sol. Cells* **2013**.
- (876) You, Z.; Hsu, C. *J. Chem. Phys.* **2010**, *133*, 74105.

14. APPENDICES

As with any project that extends over many years, there are pieces that are supportive or complementary in nature but do not fit the scope or theme of the project bulk. To give a more complete perspective and clarity to others, those pieces are included here.

Some of the fragments included are supplementary, like the derivations of energy transfer, investigation of scan rate limitations in AFM, and extra images from Chapter 10. Some are intended for those new to the field or researchers interested in this work, like the computer codes, analytical techniques, lattice constants, and material properties. Everything else is here because it would not fit elsewhere or was strongly recommended to be included here. It is hoped that this extra information will be helpful.

Appendix B. Publications

1. Fielitz, T. R., Holmes, R. J. Crystal growth and morphology in annealed rubrene thin films. *J. Crys. Gr. Des.* **2016**, *16* (8), 4720-4726
2. Fielitz, T. R., Menke, S. M., Holmes, R. J. Correction: Evaluating the role of energetic disorder and thermal activation in exciton transport. *J. Mater. Chem. C* **2016**, *4*, 7508
3. Do, Q. H., Fielitz, T. R., Zeng, C., Vanli, O. A., Zhang, C., Zheng, J. P. Vanadium oxide-carbon nanotube composite electrodes for energy storage by supercritical fluid deposition: experiment design and device performance. *Nanotech.* **2013**, *24*, 315401
4. Lin, R., Ma, X., Fielitz, T. R., Obare, S. O., Ofoli, R. Y. Facile hydrogenation of carbon-carbon double bonds using catalytic noble nanoparticles immobilized in microfluidic reactors. *Catalysis Comm.* **2012**, *18*, 168-175
5. Lin, R., Freemantle, R. G., Kelly, N. M., Fielitz, T.R., Obare, S. O., Ofoli, R. Y. *In situ* immobilization of palladium nanoparticles in microfluidic reactors and assessment of their catalytic activity. *Nanotech.* **2010**, *21*, 325605

Appendix B. Presentations

B.1. Oral Presentations

1. Fielitz, TR, Holmes, RJ. Enhancing exciton diffusion via molecular templating. [Materials Research Society](#), Boston, MA, November 27-December 2, 2016
2. Fielitz, TR, Holmes, RJ. Templating molecular order in organic solar cells. [Industrial Partnership for Research in Interfacial Materials and Engineering](#), Minneapolis, MN, June 1, 2016
3. Fielitz, TR, Holmes, RJ. In situ visualization of crystallization dynamics in annealed rubrene thin films. [Materials Research Society](#), Boston, MA, December 1, 2015
4. Fielitz, TR, Holmes, RJ. Engineering crystallinity in organic semiconductor thin films. [Industrial Partnership for Research in Interfacial Materials and Engineering](#), Minneapolis, MN, May 27, 2015

B.2. Poster Presentations

1. Fielitz, TR, Holmes RJ. Crystal shape manipulation in annealed organic thin films. [Industrial Partnership for Research in Interfacial Materials and Engineering](#), Minneapolis, MN, May 31, 2017
2. Fielitz, TR, Holmes, RJ. Templating molecular order in organic solar cells. [3M Poster Symposium](#), St. Paul, MN, October 14, 2016
3. Fielitz, TR, Holmes, RJ. Templating molecular order in organic solar cells. [3M Tech Forum](#), St. Paul, MN, July 11, 2016
4. Fielitz, TR, Holmes, RJ. Templating molecular order in organic solar cells. [Industrial Partnership for Research in Interfacial Materials and Engineering](#), Minneapolis, MN, June 1, 2016
5. Fielitz, TR, Holmes, RJ. Engineering crystallinity in organic semiconductor thin films. [3M Poster Symposium](#), St. Paul, MN, November 13, 2015
6. Fielitz, TR, Holmes, RJ. Engineering crystallinity in organic semiconductor thin films. [Industrial Partnership for Research in Interfacial Materials and Engineering](#), Minneapolis, MN, May 27, 2015
7. Fielitz, TR, Holmes, RJ. Organic thin-film annealing: effects on morphology and epitaxial OPV function. [Industrial Partnership for Research in Interfacial Materials and Engineering](#), Minneapolis, MN, May 27, 2014

8. Fielitz, TR, Lin, R, Ofoli, RY. Measurement of reactivity of Pd, Pt, and Ru nanocatalysts in hydrogenation reactions. [University Undergraduate Research and Arts Forum](#), East Lansing, MI, April 8, 2011

B.3. Awards

1. “Best Poster”, Flexible Electronics and Photovoltaics section of 2017 Industrial Partnership for Research in Interfacial Materials and Engineering.
2. Poster Award, 1st Place, 2011 University Undergraduate Research and Arts Forum

Appendix C. Copyright Permissions

1. Figure 1.1a reproduced with permission from CNET. Photo by James Martin/CNET.
2. Figure 1.1b reproduced with permission from OLEDworks and partner Carl Stahl Architektur.
3. Figure 1.1c reproduced with permission from CNET. Photo by: Sarah Tew/CNET.
4. Figure 1.2a reproduced with permission from Heliatek, GmbH. © Heliatek: Covered Walkway with HeliaFilm® at the Seletar Airport Singapore.
5. Figure 1.2b reproduced with personal permission from InfinityPV.
6. Figure 1.2c reproduced with permission from OPVIus, GmbH. Source: OPVIus GmbH.
7. Figure 1.3a-b reproduced with permission from PolyIC GmbH & Co.
8. Figure 1.4a reprinted from “Intrinsic luminance loss in phosphorescent small-molecule organic light-emitting devices due to bimolecular annihilation reactions,” Giebink, N. C., D’Andrade, B. W., Weaver, M. S., Mackenzie, P. B., Brown, J. J., Thompson, M. E., Forrest, S. R. *Journal of Applied Physics*, **2008**, 103, 044509 with the permission of AIP Publishing.
9. Figure 1.4b adapted with permission from “Oxygen-Induced Degradation in C60-Based Organic Solar Cells: Relation Between Film Properties and Device Performance,” Bastos, J. P., Voroshazi, E., Fron, E., Brammertz, G., Vangerven, T., Van der Auweraer, M., Poortmans, J., Cheyns, D. *Applied Materials & Interfaces*, **2016**, 8, 9798-9805. Copyright 2016 American Chemical Society.
10. Figure 1.4c adapted with permission from “Stable Organic Field-Effect Transistors for Continuous and Nondestructive Sensing of Chemical and Biologically Relevant Molecules in Aqueous Environment,” Yun, M., Sharma, A., Fuentes-Hernandez, C., Hwang, D. K., Dindar, A., Singh, S., Choi., Kippelen, B. *Applied Materials and Interfaces*, **2014**, 6, 1616-1622. Copyright 2014, American Chemical Society.
11. Figure 1.5 adapted with permission from “Degradation of Organic Electroluminescent Devices. Evidence for the Occurrence of Spherulitic Crystallization in the Hole Transport Layer,” Smith, P. F., Gerroir, P., Xie, S., Hor, A. M., Popovic, Z., Hair, M. L. *Langmuir*, **1998**, 14 (20), 5946-5950. Copyright 1998 American Chemical Society.
12. Parts of Chapter 2. were adapted from... (book chapter)

Appendix C. Copyright Permissions

13. Figure 3.7 was adapted from “Effect of the intermolecular thermal motions on the tail of the electronic density of states in polyacene crystals”, Sleigh, J. P., McMahon, D. P., Troisi, A. *Applied Physics A*. **2009**, *95* (1), 147-152 © Springer-Verlag 2008, with permission of Springer.
14. Much of Chapter 4. was adapted with permission from “Crystal morphology and growth in annealed rubrene thin films,” Fielitz, T. R., Holmes, R. J. *Crystal Growth and Design*, **2016**, *16* (8) 4720-4726. Copyright 2016 American Chemical Society.
15. Figure 4.5a was reprinted from “Abrupt heating-induced high-quality crystalline rubrene thin films for organic thin-film transistors,” Lee, H. M., Moon, H., Kim, H.-S., Kim, Y. N., Choi, S.-M., Yoo, S., Cho, S. O. *Organic Electronics*, **2011**, *12* (8), 1446-1453, with permission from Elsevier.
16. Figure 8.4 adapted with permission from “Directing energy transport in organic photovoltaic cells using interfacial exciton gates,” Menke, S. M., Mullenbach, T. K., Holmes, R. J. *ACS Nano*, **2015**, *9* (4), 4543-4552. Copyright 2015 American Chemical Society.

Appendix D. Characterization Techniques

The films and devices manufactured in this thesis are not intrinsically capable of demonstrating their capabilities or properties, which requires considerable characterization in order to better understand properties including surface and bulk, optical and electrical, and morphological and energetic. Some of the key features of these techniques, including specific equipment and limitations are presented here.

D.1. Optical Spectroscopy

Examining light which is reflected, transmitted, and emitted by a sample can be very useful to characterize light-matter interactions and deduce populations of species within a material.

Ultraviolet-Visible Spectroscopy (UV-Vis)

Spectroscopy measures the intensity of light which passes through or is reflected from a sample to calculate absorption and reflection processes occurring within it. When light passes through a material with an absorption coefficient $\underline{\alpha}$, where $\underline{\alpha} = 4\pi\underline{k}/\lambda$ and the extinction coefficient may be a vector quantity \underline{k} , the light is absorbed incrementally as it passes through, giving an exponentially decaying electric field with material thickness through the total thickness \underline{L}

$$|\underline{E}(\underline{x})| = |\underline{E}(0)| \exp\left(-\frac{|\underline{x}|}{\underline{\alpha} \cdot \hat{\underline{x}}}\right) \quad (14.1)$$

Note that in simulation \underline{x} must be corrected for any off-normal wave propagation angles according to Snell's Law, which is non-trivial for anisotropic media.⁷⁷⁷ The intensity may

Appendix D. Characterization Techniques

be used to derive expressions for the transmission, absorption, and reflection coefficients for light passing from material 0 into 1 and then 2,

$$|T| = \frac{|\underline{\mathbf{E}}(\underline{\mathbf{L}})|_{+\underline{x}_0}}{|\underline{\mathbf{E}}(0)|_{+\underline{x}_2}} \quad (14.2)$$

$$|R| = \frac{|\underline{\mathbf{E}}(0)|_{-\underline{x}_0}}{|\underline{\mathbf{E}}(0)|_{+\underline{x}_0}} \quad (14.3)$$

$$|A| = \frac{|\underline{\mathbf{E}}(0)|_{+\underline{x}_1} - |\underline{\mathbf{E}}(\underline{\mathbf{L}})|_{+\underline{x}_1}}{|\underline{\mathbf{E}}(0)|_{+\underline{x}_1}} = 1 - |T| - |R| \quad (14.4)$$

The identity in Eqn. 14.4 uses $T + R + A = 1$ by conservation of energy; useful since it is impossible to measure the field in a material without perfectly index-matching the material and detection system. Eqn. 14.4 should not be confused with the decadic *absorbance*, given by $-\log_{10}|T|$.

Practically, this is accomplished by either neglecting reflection at normal incidence to deduce the absorbance from a transmission measurement or by quantitatively measuring transmission and reflection at the same angle.

Equipment used for these measurements in this thesis include an Agilent CARY-6000, a Milton Roy/Thermo Fischer Spectronic Genesys 5, and a Woollam VASE ellipsometer.

Ellipsometry

Ellipsometry measures the polarization of light before and after interacting with a sample to extract the sample interaction from the difference. The polarization of light can be quantified using two parameters, Ψ and Δ , defined as⁷⁷⁸

Appendix D. Characterization Techniques

$$\Psi = \tan^{-1}(E_p/E_s) \quad (14.5)$$

$$\Delta = \delta_p - \delta_s \quad (14.6)$$

where E_i and δ_i are the amplitude (electric field intensity) and absolute phase of transverse waves oscillating along axis i of p- or s-polarized light. Ψ is related to the orientation (angle) of the polarization ellipse relative to the y axis, while Δ describes its ellipticity, varying between linearly polarized ($\Delta = 0^\circ$) to circularly polarized ($\Delta = 90^\circ$), with elliptical polarization at all other values. These can be used to define the ellipsometric parameter $\tilde{\rho}$ as the ratio of the complex sample Fresnel reflection coefficients \tilde{R}_i

$$\tilde{\rho} = \frac{\tilde{R}_p}{\tilde{R}_s} = \tan(\Psi) \exp(i\Delta) \quad (14.7)$$

The electric field incident on the detector E_D can then be expressed in terms of the transfer matrices of the individual components before the detector using Jones matrices, with A and P the analyzer and polarizer angle relative to the plane of incidence, given here for p-polarized input light on an isotropic, smooth sample (diagonalized sample Jones matrix):

$$\begin{aligned} E_D &= [\quad \text{Analyzer} \quad][\text{Sample}][\quad \text{Polarizer} \quad][\text{In}] \\ &= [1 \quad 0] \begin{bmatrix} \cos(A) & \sin(A) \\ -\sin(A) & \cos(A) \end{bmatrix} \begin{bmatrix} \tilde{R}_p & 0 \\ 0 & \tilde{R}_s \end{bmatrix} \begin{bmatrix} \cos(P) & -\sin(P) \\ \sin(P) & \cos(P) \end{bmatrix} [1] \\ &= \begin{bmatrix} \tilde{R}_p \cos(P) \cos(A) + \tilde{R}_s \sin(P) \sin(A) \\ 0 \end{bmatrix} \end{aligned} \quad (14.8)$$

The intensity of the field at the detector I_D is the magnitude of electric field, which after rearranging Eqn. 14.30 and substituting 14.29 is given by

$$I_D \propto 1 + \alpha' \cos(2A) + \beta' \sin(2A) \quad (14.9)$$

where the coefficients α' and β' are equal to

Appendix D. Characterization Techniques

$$\alpha' = \frac{\tan^2 \Psi - \tan^2 P}{\tan^2 \Psi + \tan^2 P} \quad (14.10)$$

$$\beta' = \frac{2 \tan \Psi \cos \Delta \tan P}{\tan^2 \Psi + \tan^2 P} \quad (14.11)$$

Since the ellipsometer has a rotating analyzer, the analyzer angle is a continuous function of time, allowing it to be eliminated with a Fourier transform of the data, which yields the coefficients α' and β' . These can then be used to calculate Ψ and Δ from Eqns. 14.10-14.11:

$$\tan \Psi = \sqrt{\frac{1 + \alpha'}{1 - \alpha'}} |\tan P| \quad (14.12)$$

$$\cos \Delta = \frac{\beta'}{\sqrt{1 - \alpha'^2}} \frac{\tan P}{|\tan P|} \quad (14.13)$$

These values can then be used to fit for the sample Jones matrix, thereby fitting for sample thickness, index, composition, etc.

The most common modeling approach for isotropic, non-absorbing films uses Cauchy's equation for the dispersion of refractive index with wavelength:

$$n(\lambda) = A_n + \frac{B_n}{\lambda^2} + \frac{C_n}{\lambda^4} + \dots \quad (14.14)$$

This can in turn be used to calculate the film thickness from the \tilde{R}_i s in the sample Jones matrix. Obviously, the film must be optically transparent and not depolarizing. To fit n and k , the Cauchy model varies their value iteratively at each wavelength to produce the measured signal. This implies that there can be variation in optical constants with this fitting method depending on the initial guess, as n and k contribute in a similar manner to light propagation. Although simple and often physical, these values should be checked for consistency with the Kramers-Kronig relations, which relate the phase and intensity of the

Appendix D. Characterization Techniques

real and imaginary components of an oscillator response function, $a = a' + ia''$:²⁶⁸

$$a'(\omega) = \frac{2}{\pi} P \int_0^\infty \frac{a''(\omega')}{\omega'^2 - \omega^2} d\omega' \quad (14.15)$$

$$a''(\omega) = -\frac{2\omega}{\pi} P \int_0^\infty \frac{a'(\omega')}{\omega'^2 - \omega^2} d\omega' \quad (14.16)$$

where P is the Cauchy principal value integral²⁶⁸ (necessary for asymptotic functions, but generally not n or k). These can also be calculated from reflection data⁷⁷⁹ or checked in terms of known absorption data,⁷⁸⁰

$$n(\omega) = 1 + \frac{c}{\pi} \int_0^\infty \frac{\alpha(\omega')}{\omega'^2 - \omega^2} d\omega' = 1 + \frac{2}{\pi} \int_0^\infty \frac{k(\omega')\omega}{\omega'^2 - \omega^2} d\omega' \quad (14.17)$$

Note that the integral requires a constant be added when starting at any frequency greater than zero; this is generally the static index of refraction which may be obtained in the transparent near-infrared region for most materials. These relations also only hold along principle optic axes in anisotropic materials,^{781,782} requiring use of Euler angles depending on sample orientation. Alternatively, the anticipated absorption spectrum, *e.g.*, from UV-Vis, may be assembled using any of a number of oscillator models (GenOsc, etc.) and then used to fit the ellipsometric data for the exact oscillator strength, position, and width.

Ellipsometric data in this thesis were collected using a Woollam VASE VB-400 with AutoRetarder and x-y translation stage. Data analyzed with WVASE32 software.

Fluorimetry

Fluorimetry measures the light absorption and emission properties of a sample. This is accomplished by simply exciting the sample with light of a known wavelength and measuring its emission at a desired wavelength. As such, fluorimeters feature a light

Appendix D. Characterization Techniques

source, a sample compartment, a detector and monochromators for selecting excitation and emission wavelengths. Sweeping either (or both) of these wavelengths gives information about sample absorption and processes which occur before radiative decay of the excited state. This can include measurements of exciton diffusion as well as determining the ratio of radiative to non-radiative decay rates (η_{PL}).

Sample emission and excitation data in this thesis were collected using a Photon Technology International QuantaMaster spectrofluorimeter with a xenon lamp source, single monochromators on the input and output, and a photomultiplier tube or InGaAs detector for visible or infrared, respectively.

Time-Correlated Single Photon Counting

Time correlated single photon counting (TCSPC) registers the optical decay of single excited states relative to the excitation pulse by means of extremely fast electronic detection and correlation, which are accumulated into a histogram to give the overall temporal decay of the excited state.⁷⁸³ To ensure that individual photons are being counted, detector count rates should be kept below 5% of the excitation pulse rate. Temporal limits of this technique are dictated by the excitation pulse and detection electronics. For most of this thesis, a realistic lower bound of measurable lifetimes was ~0.5 ns.

TCSPC data in this thesis were collected using a PicoQuant PDL800-B laser pulse driver for a 470 nm pulsed diode laser, collected using PicoQuant NanoHarp250 software with 31 ps temporal resolution. The total histograms were fit with single exponential decays convoluted with instrument response measured on a scratched glass surface at the

Appendix D. Characterization Techniques

laser wavelength. Sample emission was monochromated by a Horiba H10 monochromator and fed into a silicon avalanche photodiode detector. The typical lower-bound system response was ~400 ps and is likely detection-limited.

D.2. Microscopy

Perhaps one of the more commonly known characterization techniques, microscopy allows direct visualization of features of interest within a sample. The particular subset used within this field depends on the sample type and desired information.

Optical Microscopy

Optical microscopy (OM) uses light to visualize the spatial arrangement of matter on the microscale. This can be light which is polarized, transmitted through a sample, or reflected, scattered, or emitted from a sample, making it an exquisitely powerful technique for features which are optically resolvable. Ernst Abbe's diffraction relation imposes a finite lower limit for optical resolution of

$$d_R = \frac{\lambda}{2n \sin \theta} = \frac{\lambda}{2(NA)} \quad (14.18)$$

where light from a feature converging at half-angle θ will resolve a feature of minimum size d_R . This can also be expressed in terms of the lens numerical aperture (NA), which for the 50x objective lens used in this thesis of numerical aperture 0.75 gives a feature size limit of $\lambda/1.5$, or about 330 nm for green light.

If the sample is comprised of a birefringent material, one which differs in refractive index along at least two optic axes, then polarized optical microscopy (POM) can be highly instructive. This is because light which enters the crystal is forced to oscillate along these

Appendix D. Characterization Techniques

axes, which causes some amount of this light to take on a component normal to the original

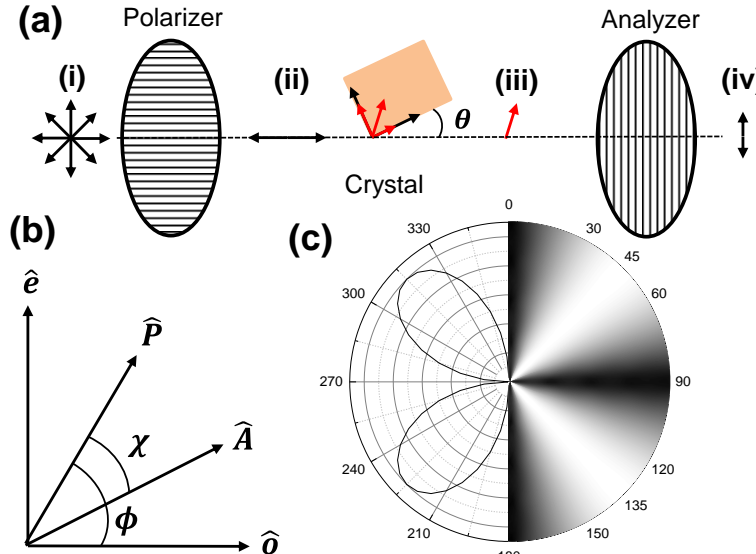


Figure 14.1. Polarized light passing through a birefringent material. (a) polarization state from (i) unpolarized, (ii) after the polarizer, (iii) after the birefringent material, and (iv) after the analyzer. (b) shows the vector analysis of polarized light with variables defined in text. The result of (b) for perpendicular polarizer and analyzer is shown in (c), with the polar intensity plot on the left and a visual representation of the intensity on the right (white = more intense).

encounters a crystal with orthogonal extraordinary (\hat{e}) and ordinary (\hat{o}) axes before passing through an analyzer with axis \hat{A} (Figure 14.1b). The component of \hat{P} which oscillates along \hat{e} and \hat{o} is given by their dot product⁶²⁹

$$\underline{e} = \hat{e}(\hat{e} \cdot E\hat{P}) = E\hat{e} \cos \phi \quad (14.19)$$

$$\underline{o} = \hat{o}(\hat{o} \cdot E\hat{P}) = E\hat{o} \sin \phi \quad (14.20)$$

Similarly, the component which is transmitted through the analyzer is also a dot product:

$$\underline{A}_e = \hat{A}(\hat{A} \cdot \hat{e})(\hat{e} \cdot E\hat{P}) = E\hat{A} \cos \phi \cos(\phi - \chi) \quad (14.21)$$

$$\underline{A}_o = \hat{A}(\hat{A} \cdot \hat{o})(\hat{o} \cdot E\hat{P}) = E\hat{A} \sin \phi \sin(\phi - \chi) \quad (14.22)$$

Because of the difference in refractive index along the two material axes, there will be a phase delay Δ between the waves when they emerge from the material which depends on

polarization direction, which can be detected by passing the resulting light through an analyzer which is perpendicular to the original polarized beam (Figure 14.1a). Written mathematically, consider the case of polarized light vibrating along the polarizer axis \hat{P} which

Appendix D. Characterization Techniques

the thickness h and index difference:

$$\Delta = \frac{2\pi}{\lambda} (n_o - n_e) h \quad (14.23)$$

where the difference $|n_o - n_e|$ is the material birefringence. The intensity is then the sum of the modulus of these two waves plus any interference, or

$$I = I_e + I_o + 2\sqrt{I_e I_o} \cos \Delta = E^2 \left[\cos^2 \chi - \sin 2\phi \sin 2(\phi - \chi) \sin^2 \frac{\Delta}{2} \right] \quad (14.24)$$

after trigonometric identity substitutions. Thus, for a sample with no birefringence,

$$I = E^2 \cos^2 \chi \quad (14.25)$$

e.g., there is no transmitted intensity for perpendicular analyzer and polarizer ($\chi = 90^\circ$). This is highly useful for distinguishing birefringent regions from amorphous because for a birefringent sample viewed with perpendicular analyzer and polarizer,

$$I = E^2 \sin^2 2\phi \sin^2 \frac{\Delta}{2} \quad (14.26)$$

This gives the distinct “Maltese cross” appearance of spherulites, as shown mathematically in Figure 14.1c. The intensity and coloration can also be used to determine the relative orientation of different crystallites within a sample. Alternatively, different regions of a crystal may be viewed by rotating the microscope stage. The wavelength dependence of refraction and extinction means that films of different thicknesses and materials are different colors under polarized light from Δ and film absorption, which can be incorporated in a somewhat more complicated form of Eqn. 14.24.⁶²⁹

Fluorescence (or alternatively electroluminescence) microscopy can be useful in organic electronic materials research to examine the origin of light emission within a film or device structure.^{239,784–786} Lateral variations in light emission due to exciton defects at

Appendix D. Characterization Techniques

grain boundaries or material aggregation are readily apparent with this technique, which relies on excitation (typically by a laser for the high optical power monochromaticity, enhancing sample visibility and allowing simple spectral notch filtering of the excitation), followed by collection of the sample emission through the normal microscope objectives and capture either with a camera or a scanned pinhole detector. Although simple in principle, care must be taken with alignment, power, and filtering of the excitation to limit damage to the microscope, camera, and user.

There are many other capabilities of optical microscopes, including dark field viewing for scattered light, differential interference contrast (DIC) for using index changes within a sample, scanning FTIR microscopy for visualizing chemical composition and uniformity within a sample, and confocal microscopy to examine vertical dimensionality of samples, but these techniques were not used in this thesis and are not addressed further here.

The majority of optical microscopy data presented in this thesis were collected using a Nikon CSi Eclipse with LV-UEPi-N episcopic illumination attachment equipped with plan objectives and a Lumenera Infinity 1.0 digital 3.1 megapixel color camera. Images were captured with Infinity Analyze 6.3.0 software or Fiji macro and analyzed with ImageJ (Fiji).⁷⁸⁷ High-speed data in Chapter 6. were collected using a Nikon Eclipse with a Vision Research Phantom Miro Ex2-4096MC camera with a Zeiss Makro-Planar 2/100 ZF.2 lens aimed through the microscope ocular (to compensate for the lower camera resolution) and captured and analyzed with the supplied Vision Research software. Camera and software courtesy of the Paul Dauenhauer research group. Some preliminary data were also collected

Appendix D. Characterization Techniques

using an AmScope ME520TC equipped with an AmScope 3 megapixel color camera, courtesy of the Dave Flannigan research group. Rudimentary fluorescence microscopy measurements were conducted by illuminating the sample from above with a 405 nm diode laser approximately 70° from the sample normal, with a 405 nm notch filter inserted between the objectives and viewing ports through the analyzer port.

Transmission Electron Microscopy

Transmission electron microscopy (TEM) images materials on the micro- to nanoscale with an electron beam which is transmitted through the specimen and focused onto a detector.⁷³³ Although similar to optical microscopes in many respects, TEM is noteworthy for the incredibly small deBroglie wavelength of the accelerated electrons, which greatly improves image resolution and enables diffraction from molecular or atomic structural features within the film. This allows for highly localized measurement of material properties such as crystallinity, composition, and even bonding state. However, exposure to the highly focused electron beam can damage samples, particularly weakly bonded and poorly conductive organic materials, requiring low beam fluence or cryogenically cooled samples to mitigate these effects.

TEM measurements performed for this thesis were conducted on an FEI Tecnai Femto ultrafast electron microscope at room temperature by Dan Cremons of the Dave Flannigan research group. Samples were vapor deposited onto either silicon grids with SiO₂ windows or Quantifoil holey carbon grids. Data was analyzed using Digital Micrograph 2.12.1579.0 of the Gatan Microscopy Suite in tandem with ImageJ/Fiji, with Matlab used to simulate

Appendix D. Characterization Techniques

diffraction patterns, given in Appendix R.6.

Scanning Probe Microscopy

Scanning probe microscopy scans an extremely small, sharp cantilever tip over a sample surface in a raster pattern while monitoring and modulating the tip-sample interaction to build an image of a sample property(s) of interest on the micro- to nanoscale. This allows for, *e.g.*, direct and simultaneous topographic and energetic measurements on samples. The subcategories of this technique are differentiated by the tip-sample interaction which is being probed.⁶⁷⁴ Since the tip directly interacts with the sample, scan rates are limited by the tip-sample equilibration time (~8 minutes per image) and any tip contamination will adversely affect image quality. Interestingly, reasonably high frame rates can be achieved in specific situations, as discussed in Appendix E.

Atomic force microscopy (AFM) monitors cantilever deflection in response to the force the sample exerts on the tip as it is scanned over the sample surface and adjusts the tip height to bring the deflection to a specified value. To cover the sample surface, this scan will usually use a raster pattern

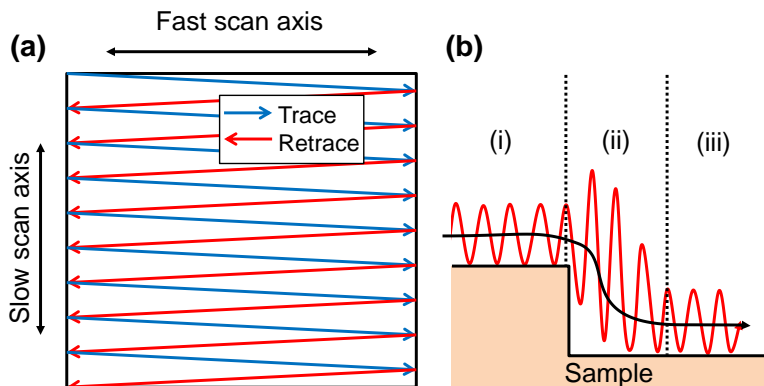


Figure 14.2. (a) Raster pattern, showing the fast and slow scan axes with the data collected on trace and retrace. (b) Response of a tapping mode cantilever to changing sample topography. (i) Oscillations are at specified setpoint, until a sample edges is reached (ii), allowing the cantilever to oscillate more freely, increasing its amplitude. The system then corrects the tip height until the amplitude setpoint is again reached (iii).

(Figure 14.2a), allowing data collection as the tip is scanned left-to-right (trace) and again

Appendix D. Characterization Techniques

right-to-left (re-trace). While scanned, the tip is most often either in one of two modes: constant contact with the surface (contact mode) or alternating between contact and free oscillation (alternating contact, AC, mode or tapping mode). Contact mode is a direct probe of the sample surface, but can dull tips and damage samples from the constant abrasion. For soft organic films, contact mode can be challenging because of the delicacy of the material, causing sample scratching or etching during scanning. AC mode is often preferred for these delicate films because of the lower force exerted on the sample. This technique works by driving a cantilever to oscillate, then approaching the sample surface until this oscillation is reduced to a fixed value, the amplitude setpoint (Figure 14.2b). Depending on the driving frequency and force, the tip-sample interaction can be adjusted so that the tip is sensing the attractive force field directly above the sample surface (the attractive regime), sensing the repulsive force as the tip collides with the physical sample surface (the repulsive regime), or even probing mechanical properties beneath the surface.

There is little difference in the resolution between these techniques if done properly, but slightly different information is obtained from each regime. In particular, information from the tip phase relative to the driving force differs significantly between the attractive and repulsive regimes. In the attractive regime, the tip responds to electrostatic, van der Waals, and other localized forces, the changes of which over small distances from the sample surface are described by the Hamaker constant. These forces do not vary as significantly across different materials as deformation or adhesion, leading to small variations in phase across a sample measured in the attractive regime. Tip phase relative to

Appendix D. Characterization Techniques

the driving force does vary appreciably in the repulsive regime, with stronger tip-surface interactions (“stickier”) shifting the phase to lower values. Interpreting this data to yield elastic modulus or adhesion requires considerably more knowledge about tip and sample properties and is best done in PeakForce or PeakVolume scans. Material regions may be identified as different from phase information, but generally only qualitatively so. One must also be careful with AC mode to establish a regime of operation, as bistability (intermittent switching between regimes) may occur with improper tuning or dirty tips, leading to poor-quality phase data and artifacts in the topographical data.

To sense the electric field and thus surface potential of a sample, an AFM can be used as a Kelvin probe with Kelvin probe force microscopy (KPFM). In this mode, the tip is first physically driven and scanned over the sample (usually in the attractive regime) to establish the surface topography. Then, using the topographic information, the tip is lifted from the surface by a specified “liftoff height” of 10-50 nm and scanned over the same area while being electrically driven. By adjusting the potential on the tip to null the interaction force with the sample, the sample surface potential may be detected. This is useful to detect material differences, strains within a material, free carriers, etc., but is somewhat less spatially sensitive due to the long-range

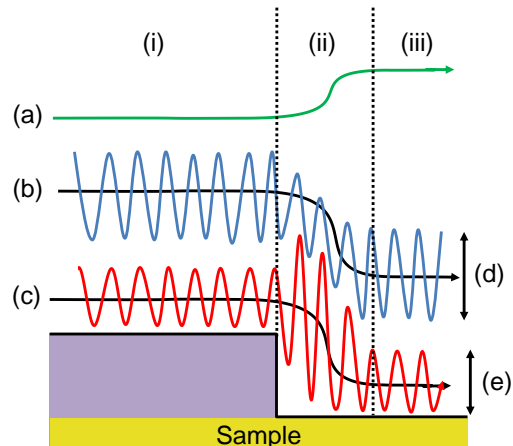


Figure 14.3. Diagram of KPFM operation, showing the first topographic scan (c) and amplitude setpoint (e), followed by a second scan with electrical excitation (b) at that setpoint (d), and the resulting surface potential detected (a). All curves display the transitions in behavior described in Figure 14.2b for regions (i)-(iii).

Appendix D. Characterization Techniques

nature of the electrostatic forces being probed.

A final SPM variant of interest here is scanning tunneling microscopy (STM), where a conductive tip is scanned across a surface and the tip-sample interaction is measured by the tip-sample tunneling current at a specified tip voltage. By varying the tip voltage, different sample energy levels (*e.g.*, HOMO, LUMO, LUMO + 1) may be directly probed and spatially visualized.

AFM and KPFM measurements for this thesis were conducted between three Bruker Nanoscope V Multimode 8s, with one inside an argon-filled glovebox owned by the C. Dan Frisbie research group used for the majority of this thesis and all KPFM work. Aluminum-coated SiN cantilevers with nominal spring constant of 40 N/m were used for AC and contact mode measurements, with PtIr-coated cantilevers with a nominal spring constant of 2.8 N/m used for KPFM. Images were analyzed with Gwyddion 2.44.⁷⁸⁸ The AFMs in ambient were operated in the Characterization Facility, University of Minnesota, a member of the NSF-funded Materials Research Facilities Network (www.mrfn.org) via the MRSEC program.

D.3. Structural and Energetic

Techniques which are capable of visualizing material morphology and phase through bulk characterization are especially useful for work with thin films, as discussed below.

X-Ray Scattering

Scattering measurements use constructive interference to characterize distances between repeating units in a material in terms of their spatial frequency, which may be

Appendix D. Characterization Techniques

easily magnified by changing the radiation wavelength or distance between the sample and detector. Radiation sources include atomic nuclei (usually metals) which are ionized with high-energy electrons and then undergo radiative transitions and synchrotron radiation, where beams of high-energy electrons are decelerated and release radiation. Synchrotron radiation has the advantage of extremely high brightness, coherence, and energy uniformity, which leads to very high signal to noise ratios. This allows for successful diffraction from thin films of low atomic number materials, like organic semiconductors. Though they have much lower signal to noise ratios, lab-scale diffractometers are much more readily available for rapid and inexpensive characterization, making them the standard characterization tool for regular analysis.

X-ray reflectivity measurements are confined to extremely low angles of incidence (almost parallel to the substrate), where the beam can be totally externally reflected from the sample surface at small angles and experience constructive and destructive interference conditions at higher angles. These interference features may be fit to determine layer thickness, roughness, and density from the scattering intensity and peak location.

Wide-angle x-ray diffraction measurements for this thesis were conducted on a Bruker AXS Microdiffractometer with Cu K α source or a Bruker D8 Advance 2D with Cu K α or Mo source. WAXS data were processed using Mercury 3.8 from the Cambridge Crystallographic Data Centre.⁷⁸⁹ Grazing incidence wide-angle x-ray scattering was conducted at the Stanford Synchrotron Radiation Lightsource using Beamline 11-3 and was analyzed with WXDiff software by Stefan C. B. Mannsfeld of SSRL

Appendix D. Characterization Techniques

(<http://code.google.com/p/wxdiff>). XRR measurements were conducted by Mike Manno and Javier Garcia Barriocanal on a Panalytical X'Pert Diffractometer. XRR data was analyzed using GenX software.⁷⁹⁰ XRR and WAXS data were collected in the Characterization Facility, University of Minnesota, a member of the NSF-funded Materials Research Facilities Network (www.mrfn.org) via the MRSEC program.

Thermal Characterization

Most thermal measurements performed on samples assess heat flow, mass loss, and structural changes to or from a sample with changing temperature and time. Differential scanning calorimetry (DSC) measures the differential (additional) heat flux required to heat a sample at the same rate as a standard reference, collecting information on parameters including heat capacity and glass, crystallization, and melting transitions.^{325,791–793} Similar information can be collected on thin films using an ellipsometer with a heated stage (see Appendix L.3.) and heated AFM tips.^{328–330,794} Thermogravimetric analysis (TGA) analyzes sample mass loss (or gain) as a function of temperature, enabling quantification of evaporative and degradation processes.

TGA measurements in this thesis were performed on a TA Instruments TGA Q500 purged with nitrogen and heated at a 10 °C/min ramp rate. DSC measurements were conducted on 5-10 mg samples using a TA Instruments Discovery DSC with hermetically sealed aluminum pans with an empty pan as reference.

D.4. Optoelectronic

Optoelectronic measurements probe the optical and electronic properties of material(s)

Appendix D. Characterization Techniques

of interest by application or detection of light and voltage from a properly configured device. These measurements can be steady-state or transient and conducted at different temperatures, depending on the information which is desired.

Organic solar cells are typically illuminated with a light source of some spectral power composition and probed by measuring the current flowing through the device as a function of the voltage applied to opposing electrodes. Most device parameters (V_{oc} , responsivity, J_{sc} , fill factor, and η_P) are assessed under a broadband illumination source which mimics solar irradiance at the surface of the earth mid-hemisphere (AM1.5G), although the device properties in the dark allow characterization of underlying diode behavior. Assessing η_{EQE} merely requires a monochromatic light source which is typically chopped and tracked with a lock-in amplifier to isolate the weak signal only due to the light source, which can be compared to the fluence of the light source to determine the electron yield per photon.

OPV power conversion efficiency was measured in ambient using a 150 W Oriel xenon arc lamp equipped with an AM1.5G corrective filter. The incident optical power was varied 0.06-10 suns modulated with neutral density filters. This intensity was calibrated with a Newport 818P-010-2 photodetector. Device response was probed with an Agilent Technologies 4155C semiconductor parameter analyzer.

OPV η_{EQE} was measured with a 300 W Oriel xenon arc lamp monochromated by a Newport 7400 Cornerstone 130 1/8 m monochromator fed to the sample through a liquid light guide. This illumination was chopped by a Stanford Research Systems SR540 optical chopper and tracked with a Stanford Research Systems SR810 lock-in amplifier. Raw

Appendix D. Characterization Techniques

spectral power was assessed with a Newport 818-UV calibrated silicon detector. Biased η_{EQE} measurements were carried out by inserting a Stanford Research Systems SR570 low-noise preamplifier between the OPV and lock-in amplifier.

Charge extraction measurements were carried out with collimated fiber-coupled M445F1, M530F1, or M625F1 LEDs from Thorlabs as the excitation source. These LEDs and OPV leads were simultaneously switched (from on to off, and open to closed circuit, respectively) with an Agilent 33220A pulse generator. The switching MOSFETs were n-channel STMicroelectronics STP27N3LH5, which for the LEDs were driven by a Microchip Technology TC4421AVPA inverting gate driver, while the OPVs were driven by a Microchip Technology TC4422AVPA noninverting gate driver. Current transients from the OPV were measured using a Tektronix TDS5104B oscilloscope.

Voltage transients, used for calibration of the charge extraction measurement, utilized the same LEDs as above, but were powered directly by a Hewlett-Packard 8114A pulse generator. OPV voltage transients were measured using a Tektronix TDS5104B oscilloscope. The LEDs intensities and spectra were separately calibrated using a Thorlabs PDA36A amplified silicon photodetector and an Ocean Optics HR4000 spectrometer, respectively.

Device electroluminescence spectra were measured using an Ocean Optics HR4000 fiber-coupled spectrometer. Electroluminescence power was measured using a Hamamatsu S3584-08 large-area photodetector.

Cryogenic device properties were assessed inside of a Janis Research ST-500 optical

Appendix D. Characterization Techniques

cryogenic probe station illuminated with a 300 W Oriel xenon arc lamp.

Laser excitation of films and devices was conducted with an Optical Building Blocks OL-4300 nitrogen laser (337 nm) optionally fed into an Optical Building Blocks OL-401 dye laser (360-980 nm).

Appendix E. AFM Scan Rate Limitations

Prior to the development of alternate *in situ* imaging solutions for organic crystal growth in thin films (see Appendix L.1.), hot-stage atomic force microscopy (AFM) was considered and investigated. The UMN Characterization Facility has an Agilent 5500 environmental AFM with variable sample temperatures of -30 °C to 250 °C. Although organic crystal growth in film and solution has been observed with AFM (often “movie-mode” AFM),^{553,563,795–798} the organic films investigated in this thesis present several challenges to this approach: air sensitivity, variable roughness, softness, and rapid crystal growth. Air sensitivity can be mitigated by transportation in a sealed container and immediate insertion into an environmental chamber, but the remainder pose significant problems as a combination. Rapid crystal growth requires that the sample be heated quickly and imaged quickly so as to explore the growth regime of interest in sufficient detail. The heated stage is capable of heating 25-150 °C in approximately 30 seconds; impressive, but not fast enough for some of the fastest-growing crystals, especially for polymorph selection. Thermal expansion of the stage and sample in the z-direction also complicates rapid heating, requiring a constant re-scaling of the z stepper motor so as to keep the z piezo in range. Image frame rates sufficient to image a process occurring on the order of 60 seconds requires frame rates on the order of 50 mHz minimum, which can cause the tip to insufficiently correct for sample surface perturbations (especially in rough samples), damaging the sample and potentially damaging or contaminating the tip.

Despite all of these challenges, meaningful data could likely be de-convoluted from

Appendix E. AFM Scan Rate Limitations

images captured in an inert atmosphere with a 30-second heating rate, given sufficiently high frame rates to make useful observations. This motivated the investigation of frame rate effects on image quality and sample damage as discussed in this section.

All experiments in this section were conducted using a Bruker Nanoscope V Multimode 8 in an argon-filled glovebox with aluminum-coated SiN cantilevers with a nominal spring constant of 40 N/m for AC and contact mode.

E.1. Fundamental Limitations of Scan Rate

The concept of AFM requires detection of a change in sample-tip interaction, typically followed by alteration of the tip in some way to recover the original interaction strength in a continuous feedback loop. In this, there are three main limiting steps which come into play: tip response to the sample, detection of that response, and recovery of the original interaction. These all operate in parallel owing to their similar time scales.

The tip dynamics are dictated by inertial and external forces, approximated by:⁷⁹⁹

$$m \frac{\partial^2 z}{\partial t^2} = -k_c z - \frac{m\omega_o}{Q} \frac{\partial z}{\partial t} + F_{ts} + F_o \cos(\omega t) \quad (14.27)$$

Here, m , k_c , Q , and ω_o are the mass, force constant, quality factor, and angular resonance frequency of the free cantilever, z is the tip height above the sample surface, F_o and ω are the driving force and angular frequency, and F_{ts} is the tip-surface interaction force:

$$F_{ts}(z_o, z) = \begin{cases} \frac{HR}{6d^2} & a \leq z + z_o \\ \frac{HR}{6a^2} + \bar{E}\sqrt{R(a-d)^3} & a > z + z_o \end{cases} \quad (14.28)$$

with H the Hamaker constant (van der Waals interaction at small separations), R is the tip

Appendix E. AFM Scan Rate Limitations

radius, \bar{E} is the reduced elastic modulus of the tip and sample, and d is the tip-sample distance given by $d = z_o + z$, where z_o is the equilibrium tip-surface separation. In Eqn. 14.27, most parameters are dictated by the tip. In particular, the equilibration time of the tip is roughly proportional to Q : the larger the quality factor (necessary for extremely high-resolution measurement), the slower the tip response to changing stimuli, as shown in

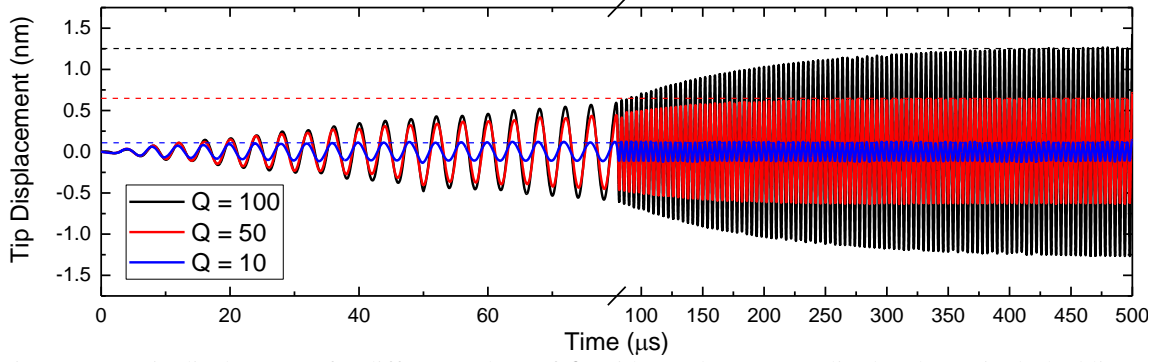


Figure 14.4. Tip displacement for different values of Q , with steady-state amplitudes shown in dashed lines. Simulations conducted with $\omega_o = \omega = 2\pi(250 \text{ kHz})$, $k_c = 40 \text{ N/m}$, $F_o = 0.1 \text{ nN}$, $R = 10 \text{ nm}$, $H = 6.4 \times 10^{-20} \text{ J}$, $\bar{E} = 1.51 \text{ GPa}$, $z_o = 15 \text{ nm}$, and $a = 5 \text{ \AA}$. Parameters are taken from experiment or Garcia *et al.*⁷⁹⁹ (except F_o , to which the simulations are not very sensitive) and simulated with Eqns. 14.27–14.28. Code given in Sec. R.8.

Figure 14.4. The tip essentially behaves as a driven, underdamped oscillator, with larger Q further reducing the damping coefficient. This equilibration time can be tied to the number of oscillations required for the tip to stabilize by the resonant frequency, giving approximately Q cycles (“taps”) for a tip to stabilize. Typical tip Q values range from 100–1000 – a tip with $Q = 500$ requires (minimum) 2 ms per pixel, or 8.7 min (1.9 mHz) for a 512 × 512 image and 2.2 min (7.6 mHz) for a 256 × 256. It would seem that Q could be offset by larger ω_o , but Q and ω_o tend to be coupled. One possible solution is to use software “ Q enhancement” in reverse to de-tune the cantilever, but this was not investigated here. Obviously, contact modes are largely immune to this effect.

Appendix E. AFM Scan Rate Limitations

The process of detecting and modulating this tip response is also non-trivial. Response rates of the quadrant photodiode as well as stray inductance and capacitance in cables slow the signal detection, which is just the laser reflection moving about on the photodiode array. This response time in typical systems has been estimated as on the order of 0.1 ms,⁷⁹⁹ implying that contact mode operation may be approximately ten times faster than AC mode, enabling proportionally faster frame rates.

E.2. Alternating Contact (Tapping) Mode

In spite of the simulation results, AC mode is still of interest for its sensitivity and (optional) non-contact imaging of the sample surface. Surprisingly, this mode works remarkably well up to scan rates which are considerably higher than those anticipated by the model when the tip does not foul (Figure 14.5). Imaging of features parallel to the scan

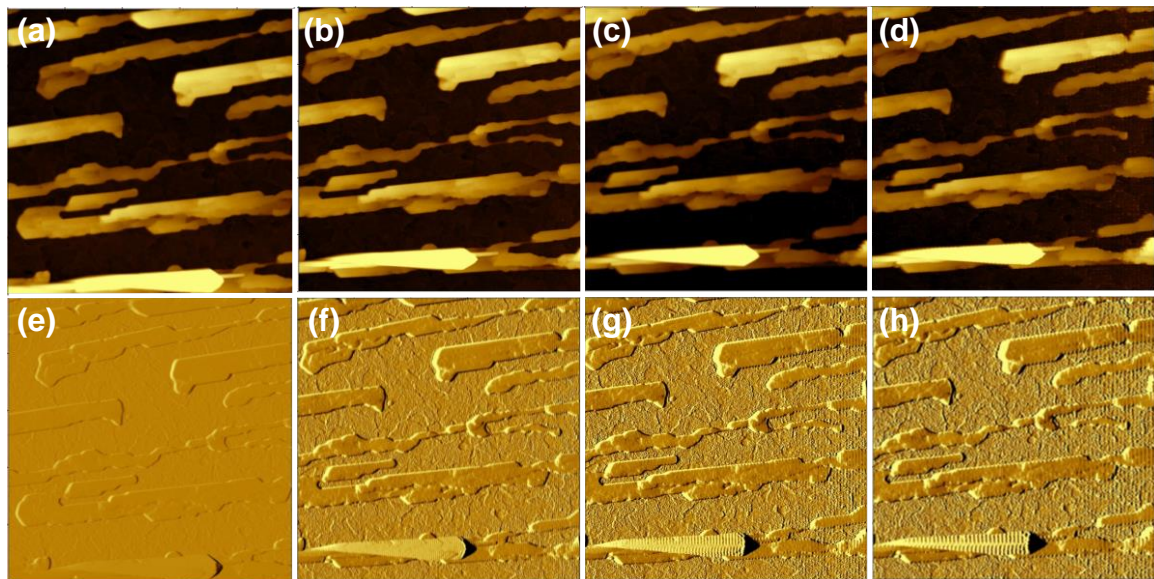


Figure 14.5. $5 \times 5 \mu\text{m}$ 512×512 pixel height (top row) and error (bottom row) images of an annealed rubrene film on ITO imaged at (a), (e), (b), (f) 3.5, (c), (g) 5.4, and (d), (h) 7 Hz line rates, corresponding to 1.9-13.7 mHz frame rates. Height scale 110 nm for height images, images collected on tip retrace.

direction effectively slows the rate of change, reducing the visibility of some tip-induced

Appendix E. AFM Scan Rate Limitations

artifacts. However, there is noticeable tip “hangliding” from the feature edges at high scan

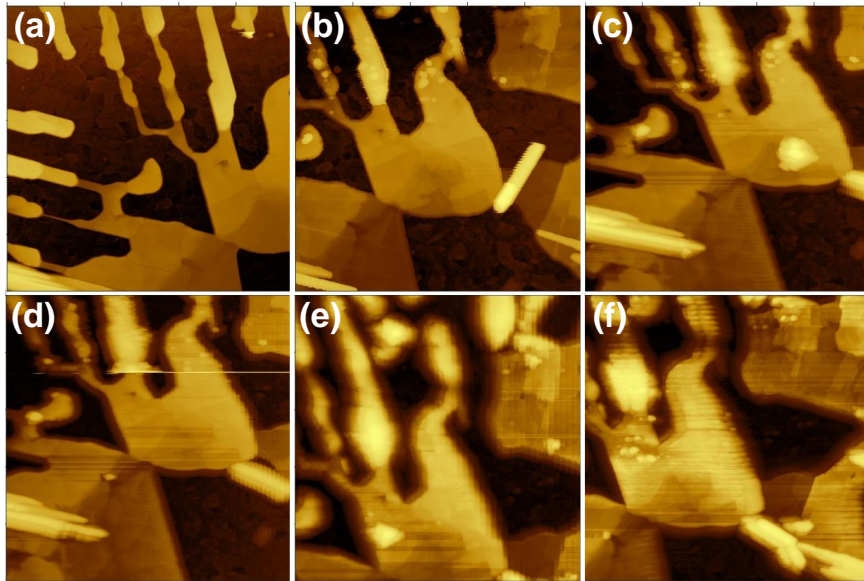


Figure 14.6. $5 \times 5 \mu\text{m}$ 512×512 height images of an annealed rubrene film on ITO imaged at (a) 1, (b) 3, (c) 5.4, (d) 7.5, (e) 9.8, and (f) 1 (after) Hz line rates. All height scales approximately 130 nm.

rates, in addition to oscillatory feedback observed trailing after sharp feature edges at high scan rates. The failure of the tip to accurately track

these edges is even

more noteworthy in regions of flat material, where noticeable damage can occur during the scanning process (Figure 14.6). Also noticeable is a loss of resolution, which is especially problematic as the tip becomes contaminated from colliding with material. At much larger

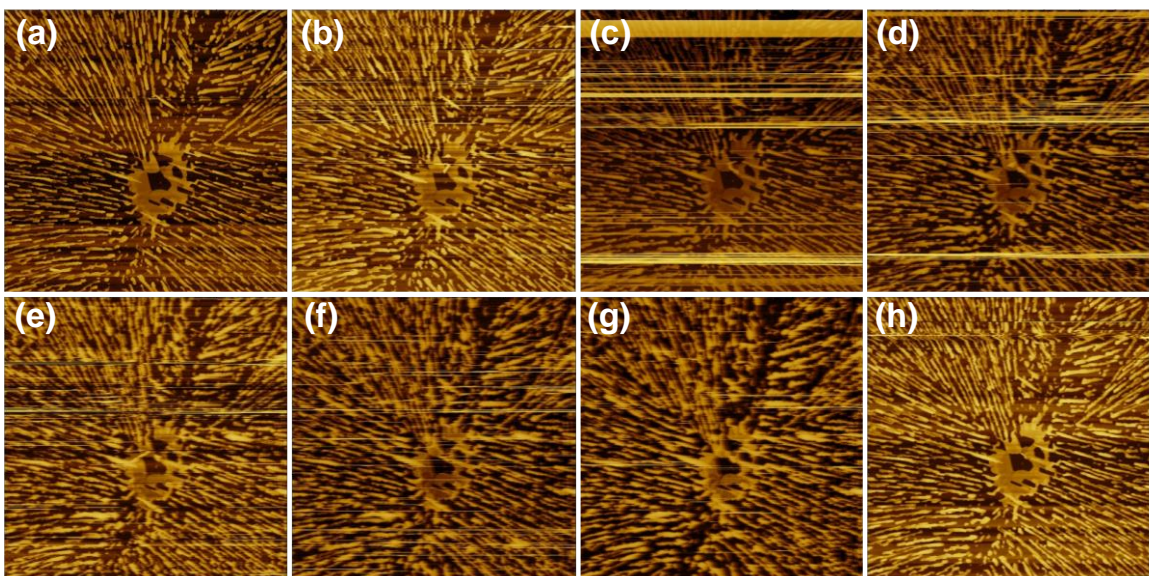


Figure 14.7. $40 \times 40 \mu\text{m}$ 512×512 height images of an annealed rubrene film on ITO imaged at (a) 1, (b) 2, (c) 3, (d) 4, (e) 5.4, (f) 7.5, (g) 9.8, and (h) 1 (after) Hz line rates. All height scales approximately 700 nm.

Appendix E. AFM Scan Rate Limitations

scan sizes (and thus even higher scanning speeds), tip contamination is more problematic, and leads to blurring of sample features (Figure 14.7). These images suggest a reasonable upper limit of approximately 3.5 Hz line scan rates for AC mode on a standard AFM so as to not damage the sample, and perhaps 5 Hz rates for smooth samples before significant loss of resolution.

E.3. Contact Mode

Contact mode is less susceptible to resonance and attraction changes from tip contamination, making it potentially more suited for high-speed imaging. Simple testing

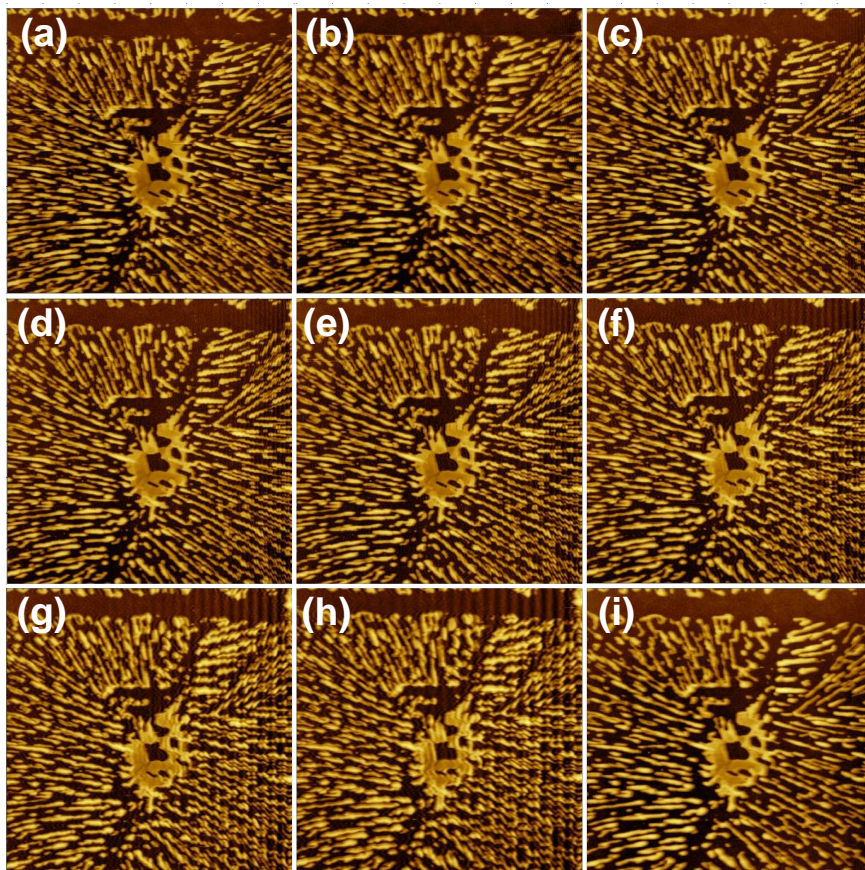


Figure 14.8. $40 \times 40 \mu\text{m}$ 512×512 height images of an annealed rubrene film on ITO imaged at (a) 3, (b) 4, (c) 5.4, (d) 7.5, (e) 9.8, and (f) 12.2 (g) 16.3, (h) 19.5, and (i) 3 (after) Hz line rates. All height scales approximately 190 nm.

supports this conclusion (Figure 14.8), with suitable images obtained at line scan speeds up to 10 Hz and useful data collected even as high as almost 20 Hz (38 mHz frame rate for 512×512 ; 76 mHz for 256×256). The considerably higher

Appendix E. AFM Scan Rate Limitations

force applied to the sample surface was also apparent when organic material was completely scraped from the surface before the tip amplitude setpoint was correctly adjusted (three horizontal streaks in Figure 14.8). The sample also appears to coarsen with scanning, with a number of smaller features eliminated between Figure 14.8a and Figure 14.8i, probably from the tip simply eroding them over time.

Interestingly, a new form of artifact occurs at very high scan rates, which appears to be an oscillatory feedback issue initiated by a sudden change in tip direction. Whether this was caused by poor substrate adhesion to the magnetic puck, a piezo artifact, or an instability in the control loop, it appears to be present at many speeds with the wavelength inversely proportional to the scan speed. This could be due to the sampling rate approaching the system response time, as the time per pixel at 20 Hz line rate in a 512 pixel image is ~0.1 ms, close to the example response time given earlier. However, this effect should be present at all points in the image and would likely depend on height, proved false by the occurrence of periodic waves in the smooth scraped regions.

Fortunately, this artifact can be largely eliminated by superimposing the trace and retrace images upon one another, as shown in Figure 14.9. In this manner,

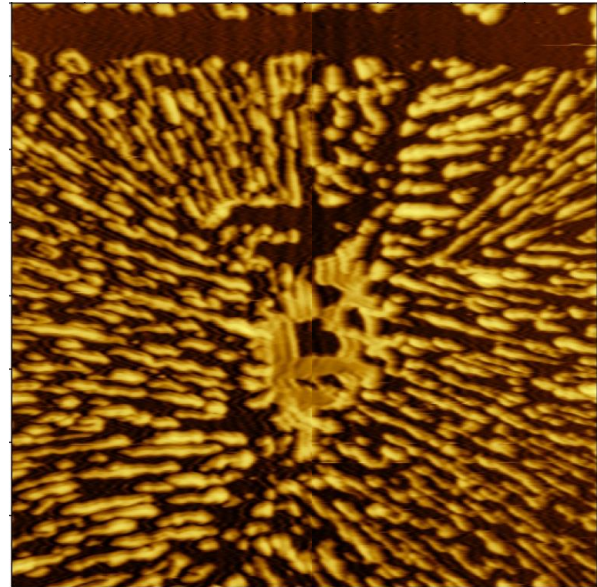


Figure 14.9. 40 x 40 μm 512 x 512 height image of an annealed rubrene film on ITO imaged 19.5 Hz line rate. Image is a composite of retrace (left) and trace (right) scans to eliminate oscillations. Height scale 180 nm.

Appendix E. AFM Scan Rate Limitations

acceptable images may be obtained even at almost 20 Hz and likely higher. Perhaps short, low-loss cables and connectors between the instrument and controller would further improve this range.

E.4. Conclusions

The primary breakdown modes in the high-speed regime occurs by loss of equilibrium with the sample surface and tip fouling in AC mode and an oscillatory direction-change induced artifact in contact mode. In AC mode, this cripples imaging observation with streaking and eventual sample erosion, leading to a maximum non-destructive line scan rate of about 3 Hz. Contact mode exhibits no streaking (perhaps by virtue of re-scanning the region from the AC mode study, but height scales are still similarly large) and reasonable resolution up to 10 Hz, with acceptable composite images up to at least 20 Hz, almost ten times greater than AC mode as suggested by simple calculations based on a harmonic oscillator.

These imaging rates are acceptable for phenomena which occur over time scales of at least 30 seconds, with an image captured every 12 seconds at 20 Hz and 256 x 256 resolution. Apart from secondary challenges including using a non-coated cantilever (to relieve cantilever strain) and accounting for rapid thermal expansion of the substrate and sample during heating, this implies that it would be fundamentally possible, albeit tedious, to image crystallization of thin films of typical organic semiconductors on a conventional AFM.

Appendix F. Photovoltage L_D Measurement V_{oc} Effects

Photovoltage combined with charge extraction as a technique to measure the exciton diffusion length in device-relevant geometries and conditions is especially useful in materials which are poorly emissive or are not otherwise amenable to thickness-based photoluminescence quenching measurements.⁷³⁸ Something surprising about this technique is its relative insensitivity to V_{oc} : OPVs will often give fairly consistent

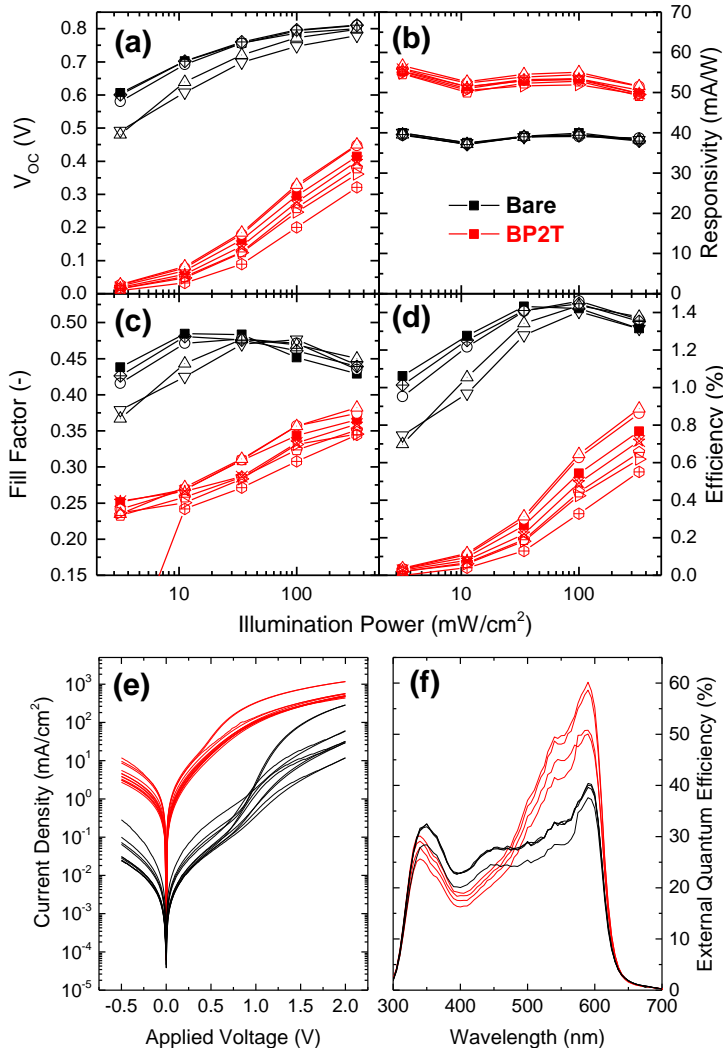


Figure 14.10. Optoelectronic performance for the devices used in this section, including (a) V_{oc} , (b) responsivity, (c) fill factor, (d) η_P , (e) dark current, and (f) η_{EQE} . Architectures are the same as Figure

measurements of L_D despite having greatly disparate V_{oc} s, provided the photovoltage rise is large enough to be discernable. To explain the origin of this robustness, a set of planar SubPc devices with and without BP2T were investigated.

The devices used in this study are unremarkable in most respects (Figure 14.10), but the BP2T-interlayer devices exhibit extremely low V_{oc} compared to typical

Appendix F. Photovoltage LD Measurement V_{oc} Effects

performance. When these devices are probed with charge extraction, linear relations for the number of electrons at a given V_{oc} are recovered (Figure 14.11a). This shows a perhaps non-surprising systematic difference between devices with and without a BP2T interlayer, implying that BP2T devices have fewer carriers extracted at a given V_{oc} . If this V_{oc} is instead plotted with the photon flux required to establish it, an almost quadratic relationship appears, with the two devices significantly offset (Figure 14.11b). A greater photon flux is required to establish a given V_{oc} in BP2T devices, similar to what is observed as a function of device dark current, where the larger the dark current, the higher the photocurrent required to offset it. This can be directly compared to the dark current by calculating an equivalent photon flux

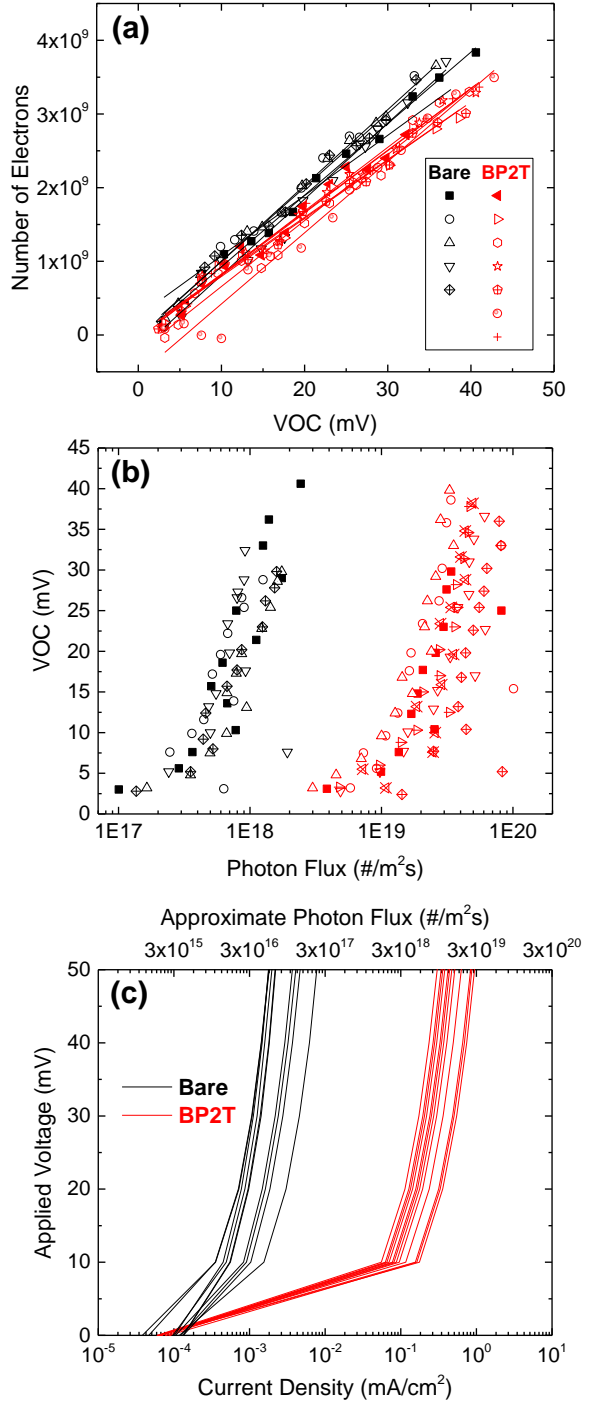


Figure 14.11. (a) Electrons extracted as a function of V_{oc} , (b) established V_{oc} as a function of incident photon flux, and (c) device dark voltage, plotted *vs.* current density and an estimated photon flux equivalent.

Appendix F. Photovoltage LD Measurement V_{oc} Effects

that would be required to create a photocurrent equal to the current density, with the proportionality given by η_{EQE} . This result, for an average η_{EQE} of 50% over the LED wavelength range (peak at 530 nm), is plotted in Figure 14.11c. In reality, this amount is the minimum current required, and a direct conversion between current density and photon flux requires conversion for each device. Each of these which would tend to shift the curves in Figure 14.11c to higher photon fluxes, with the bare devices shifted by an additional η_{EQE} factor of almost two, but comparison between Figure 14.11b and Figure 14.11c provides compelling evidence for the cause of the curve collapse in Figure 14.11a.

Dark current represents leakage and recombination pathways which are available from shunts, thermally generated carriers, etc. that are also present under illumination. For a given material (in this case SubPc), this rate of carrier loss must be supplemented by photogenerated carriers. This requires a proportionally higher photon flux to create the carrier population necessary to establish V_{oc} . Although these photon fluxes can differ considerably, the effect is largely cancelled out in the “calibration” plots, such as that in Figure 14.11a.

Appendix G. Derivations and Discussion of Energy Transfer

These derivations are provided to give additional insight into the underlying physics, approximations, and limitations of Förster and Dexter energy transfer. The original approaches of Förster and Dexter were through quantum mechanics, so those derivations draw mostly from their original work. Förster energy transfer can also (more physically) be explained and visualized in terms of classical electrodynamics, so that derivation is also included for comparison.

G.1. Classical Derivation of Förster Energy Transfer

Being a dipole-dipole mediated energy transfer event, the Förster rate includes electrostatic components and resonant states components, each of which gives the Förster rate dependence on molecular parameters. The following discussion describes the rates of energy exchange relative to decay of the donor and how R_0 results naturally when these quantities are equated, following from other available derivations.^{208,213,218,800,801}

First, the spatially distinct charges of the exciton on the donor molecule establish a transition dipole moment $\underline{\mu}_D$ and corresponding oscillating electric field \underline{E}_D , which may be approximated in the near field close to the molecule as

$$\underline{E}_D(\underline{r}, t) = \frac{1}{4\pi\epsilon_0|\underline{r}|^3} [3(\underline{\mu}_D \cdot \hat{\underline{r}})\hat{\underline{r}} - \underline{\mu}_D] \cos\left(\frac{2\pi c}{n(\lambda)\lambda}t\right) \quad (14.29)$$

where \underline{r} is the vector connecting the donor to a point in space at time t , ϵ_0 is the vacuum permittivity, c is the speed of light in vacuum, and λ is the wavelength of light creating the field. Any vector with a caret (*e.g.* $\hat{\underline{r}}$) is a unit vector along the associated direction (*e.g.*

Appendix G. Derivations and Discussion of Energy Transfer

\underline{r}). The interaction energy of the donor with an acceptor molecule (U_{DA}) is equal to the negative dot product of Eqn. 14.29 with the induced acceptor dipole moment ($\underline{\mu}_A$), which gives

$$\begin{aligned} U_{DA}(\underline{r}, t) &= \frac{|\underline{\mu}_D| |\underline{\mu}_A|}{4\pi\epsilon_0 |\underline{r}|^3} [\hat{\underline{\mu}}_D \cdot \hat{\underline{\mu}}_A - 3(\hat{\underline{\mu}}_D \cdot \hat{\underline{r}})(\hat{\underline{\mu}}_A \cdot \hat{\underline{r}})] \cos\left(\frac{2\pi c}{n(\lambda)\lambda} t\right) \\ &= \frac{\kappa |\underline{\mu}_D| |\underline{\mu}_A|}{4\pi\epsilon_0 |\underline{r}|^3} \cos\left(\frac{2\pi c}{n(\lambda)\lambda} t\right) \end{aligned} \quad (14.30)$$

Eqn. 14.30 shows that the orientation factor κ originates in the dipole interaction dependence on the orientation, with the bracketed term in the center expression substituted by κ on the right. The rate of energy absorption by the acceptor is proportional to the square of the donor electric field at the acceptor (Eqn. 2.11) averaged over time, using κ to select the electric field along the acceptor dipole and σ_A to describe the acceptor absorption ($\sigma_A = k_A(\lambda)/\rho_A$, where ρ_A is the density of A in number per cm³). This yields

$$\langle \frac{dU}{dt} \rangle_{DA} = \frac{3c\epsilon_0\sigma_A(\lambda)}{2n(\lambda)} |\kappa \underline{E}_D|^2 = \frac{3c\sigma_A(\lambda) |\underline{\mu}_D|^2}{32\pi^2\epsilon_0 |\underline{r}|^6 n(\lambda)} \quad (14.31)$$

This energy transfer rate may be compared to the total rate of energy loss by the excited donor in the absence of an acceptor,

$$\langle \frac{dU}{dt} \rangle_D = \left(\frac{4\pi^3 |\underline{\mu}_D|^2 c [n(\lambda)]^3}{3\epsilon_0 \lambda^4} \right) \frac{1}{\eta_{PL}(\lambda)} \quad (14.32)$$

Note that all parameters which are material-dependent in Eqn. 14.32 have the properties of the donor and material surrounding it, just as those in Eqn. 14.31 are for the acceptor. A non-unity η_{PL} implies there are other, non-radiative pathways available for decay and

Appendix G. Derivations and Discussion of Energy Transfer

scales the radiative decay rate (in parentheses in Eqn. 14.32) to account for these events.

Finally, the Förster radius R_0 may be derived as “the critical distance for which excitation transfer and spontaneous deactivation of the sensitizer [donor] are of equal probability,”²⁰³ by equating Eqn. 14.31 and Eqn. 14.32 and solving for $|\underline{r}|$. This yields the Förster radius for a material emitting at wavelength λ . Molecules emit and absorb light across a range of wavelengths, each of which contributes to this radius. This is accounted for by integrating over all wavelengths, namely the wavelength-dependent terms σ_A , $\eta_{PL} \lambda$, and n . A final substitution of the overall η_{PL} and F_D for $\eta_{PL}(\lambda)$ gives the familiar relation in Eqn. 2.11.

G.2. Quantum-Mechanical Derivation of Förster Energy Transfer

As expressed originally by Förster, energy transfer can also be viewed as an artifact of quantum mechanics, with slightly different interpretations.^{204,218,265} First, the molecules D^* (excited donor, denoted by an * on the subscript) and A (ground-state energy acceptor) are considered to have wavefunctions $\psi_i(u_i, \underline{x}_i)$ describing their electron density, where u_i and \underline{x}_i are the energy and position in space of molecule i , respectively. These two wavefunctions interact electronically according to the integral products of their complex conjugates (ψ_i^*) and an interaction operator, $\hat{\mathcal{H}}(\underline{x}_A, \underline{x}_D)$

$$U_{DA}(u_{D^*}, u_A, u_D, u_{A^*}) = \iint \psi_{D^*}^* \psi_A^* \hat{\mathcal{H}} \psi_D \psi_{A^*} d\underline{x}_A d\underline{x}_{D^*} \quad (14.33)$$

For conciseness, functional arguments have been omitted where already defined. Here, $\hat{\mathcal{H}}$ is the electronic interaction operator, defined as the Coulomb interaction of moving charge e , approximating the intermolecular separation as much larger than the intramolecular separation between constituent atoms:

Appendix G. Derivations and Discussion of Energy Transfer

$$\hat{\mathcal{H}} = -\frac{e^2}{4\pi n^2 |\underline{x}_D - \underline{x}_A|} = -\frac{e^2}{4\pi n^2 |\underline{r}_{DA}|} \quad (14.34)$$

Eqn. 14.33 thus far contains all electronic interactions, dipole-dipole, dipole-quadrupole, etc., making it analytically intractable. For molecules which are separated by a large amount relative to the molecule size (the “point dipole approximation”), this reduces to the interaction energy between two dipoles with transition moments $\underline{\mu}_i(u_i, u_{i^*})$, given by

$$U_{DA} = \frac{1}{4\pi n^2 |\underline{r}_{DA}|^3} \left\{ \underline{\mu}_D \cdot \underline{\mu}_A - 3 (\underline{\mu}_D \cdot \hat{\underline{r}}_{DA}) (\underline{\mu}_A \cdot \hat{\underline{r}}_{DA}) \right\} = \frac{|\underline{\mu}_D| |\underline{\mu}_A|}{4\pi n^2 |\underline{r}_{DA}|^3} \kappa \quad (14.35)$$

with

$$\underline{\mu}_i = -e \int \psi_i^* \underline{r}_i \psi_i^* d\underline{r}_i \quad (14.36)$$

and \underline{r}_i defined around the molecular center of mass for molecule i . These transition moments describe the change in the electric dipole moment (how charges are distributed in space and time) and its related probability as molecules transition from the excited to ground states.

The interaction energy described in Eqn. 14.35 can be used to describe the transition rate, k_F , according to Fermi’s (Dirac’s) Golden Rule:^{204,213,218,265}

$$k_F = \frac{2\pi}{\hbar} \int |U_{DA}|^2 \mathfrak{D} dU \quad (14.37)$$

where \mathfrak{D} is the functional determinant to convert between the energy units u_i used here and the quantum numbers conventionally used. Careful normalization of the wavefunctions equates \mathfrak{D} to unity and allows for the form of Eqns. 14.34-14.35, with an explicit definition of ΔU (total energy change) equal to zero to obey conservation of energy between the initial

Appendix G. Derivations and Discussion of Energy Transfer

and final systems states, $\Delta U = u_D + u_{A^*} - u_{D^*} - u_A \equiv 0$.

If these states are now allowed to assume a distribution of energies with probability density $g_i(u_i)$ during the transition, then Eqn. 14.37 becomes

$$k_F = \frac{2\pi}{\hbar} \iiint_0^\infty g_{D^*} g_A |U_{DA}|^2 du_{D^*} du_A dU \quad (14.38)$$

The fact that g_i and $\underline{\mu}_i$ depend only on u_i and U means that those components may be integrated separately and related to the emission (g_{D^*}) and absorption (g_A) spectra as a function of the total energy. Using this and Eqn. 14.35 transforms Eqn. 14.38 into

$$k_F = \frac{\kappa^2}{8\pi\hbar|\underline{r}_{DA}|^6} \int \left[\frac{\int g_{D^*} |\underline{\mu}_D|^2 du_{D^*} \int g_A |\underline{\mu}_A|^2 du_A}{n^4} \right] dU \quad (14.39)$$

The final steps are to convert energy distributions and dipole moments into measureable quantities. For the excited donor, the decay rate and thus lifetime can be related to $\underline{\mu}_D$:¹⁹⁶

$$\tau = \frac{3c^2}{4U^3 |\underline{\mu}_D|^2} \eta_{PL} \quad (14.40)$$

Next, the absorption spectrum is convoluted into the second integral according to²⁶⁵

$$\int g_A |\underline{\mu}_A|^2 du_A = \frac{3nc\hbar\sigma_A}{4\pi^2 U} \quad (14.41)$$

After substituting these relations and considerable unit and integral conversions, Eqn. 2.4 is recovered.

G.3. Derivation Consequences for Förster Theory

The underlying physics in Eqn. 2.7 elucidated by Eqns. 14.29-14.32 and Eqns. 14.33-14.41 define Förster energy transport, with several remarkable implications. First, resonant

Appendix G. Derivations and Discussion of Energy Transfer

states on the donor and acceptor molecules, represented by the overlap of the emission and absorption spectra, are required for energy exchange to be possible since the exciton must have a comparable energy state available on the energy acceptor in order to transfer while conserving energy. Second, molecular photoluminescence efficiency is highly influential in this mode of energy transfer because it describes the ratio of decay processes which are capable of establishing an electric field (radiative) relative to parasitic losses which are not (non-radiative). The stronger the transition dipole moment, the more efficiently and quickly a given material will radiatively emit and absorb, which translates to a greater probability of the exciton releasing energy in a useful, conserved mode rather than to the lattice as heat. It should be stressed that real photons do not mediate Förster transfer; rather, the rate and efficiency with which they are produced is directly correlated to the strength of the electric field which couples the donor and acceptor states. Finally, intermolecular spacing and alignment play a significant role modulating the strength of the donor electric field or wavefunction at the acceptor and the coupling of the acceptor to this field, respectively.

There are also limits of this mechanism that are often neglected.¹⁷⁰ Key approximations used to simplify the relations leading to Eqns. 14.29 and 14.35 describe the electronic interaction in terms of dipolar, specifically point dipolar, terms. In some situations, these approximations break down, such as when molecules have strong quadrupole (or higher, like SubPc²²²) interactions or are spatially close relative to the size of the molecules.^{170,202} Problems arise when these neglected higher-order corrections to the Coulombic interaction are of appreciable magnitude relative to purely dipolar coupling, which can lead to

Appendix G. Derivations and Discussion of Energy Transfer

anomalously high rates or non-physical values for extracted parameters.¹⁷⁰ Fortunately, these interactions relatively short-range and weak in most systems.²³⁶ The point dipole approximation breaks down when the energy-transferring groups are comparable to or larger than their separation, as in some nanoscale systems.^{170,201,802,803}

A more nuanced argument surrounds the coherence of the excited state: the use of Fermi's Golden Rule in Eqn. 14.37 implies short coherence times relative to the interaction time, which is not always true.²¹³ In strongly coupled systems, such as molecular aggregates or crystals,^{202,804,805} the exciton can remain coherent and exists as a delocalized superposition of states, moving as a wave collocating on several molecular sites.¹⁷⁰ In addition to altering the energy transfer rates and enabling “dark” states to contribute to energy transfer, this coherent limit can also lead to “memory effects”, where the surrounding medium retains some non-equilibrium state (as perturbed by the presence of the excitation) after transfer has occurred.¹⁷⁰ The successful applications of Förster theory to general exciton motion implies that these effects are uncommon, but cautionary.^{198,237,238,365,470,686,707,716,806,807}

G.4. Förster Energy Transfer in Anisotropic Media

As described above, the molecules in Förster's theory couple electromagnetically through a material, with the interaction strength modulated by the surrounding dielectric properties and the coupling of the molecules to the modified field. In anisotropic materials, these refraction and absorption coefficients may become anisotropic, and take on a tensor form n_{ij} and k_{ij} in index (Einstein) notation.^{629,777,808–812} With appropriate choice of optic

Appendix G. Derivations and Discussion of Energy Transfer

axes, these tensors may be diagonalized to n_{ii} and k_{ii} , and for crystals of orthorhombic or higher symmetry, these axes may be aligned mathematically.^{629,808}

The values of n experienced by a wave propagating in the crystal are given by the index ellipsoid (indicatrix) cut by a plane orthogonal to the wave propagation direction. To determine the values of n experienced by a transverse wave propagating along an arbitrary wave direction $\underline{\hat{s}}$, the following eigenvalue problem may be solved for the two index eigenvalues n and transverse oscillation electric flux eigenvectors \underline{D} within the material⁸⁰⁸

$$-\underline{\hat{s}} \times (\underline{\hat{s}} \times \underline{\underline{\eta D}}) = \frac{1}{n^2} \underline{D} \quad (14.42)$$

where $\underline{\underline{\eta}}$ is the inverse indicatrix

$$\underline{\underline{\eta}} = \epsilon_0 \underline{\underline{\epsilon}}_R^{-1} = \underline{\underline{\epsilon}}^{-1} = \begin{bmatrix} n_{xx}^{-2} & 0 & 0 \\ 0 & n_{yy}^{-2} & 0 \\ 0 & 0 & n_{zz}^{-2} \end{bmatrix} \quad (14.43)$$

The above equality converting the impermeability tensor $\epsilon_0 \underline{\underline{\epsilon}}_R^{-1}$ to index only holds for the diagonalized form along the principle optic axes. An equivalent form solving for the wavenumber k_{ab} is^{629,808}

$$\sum_{i=1}^3 \frac{\hat{s}_i^2 k_{ab}^2}{k_{ab}^2 - n_{ii}^2 k_o^2} = 1 \quad (14.44)$$

Summation over all axes and multiplication through by the denominators gives a quartic function of k_{ab} , which gives solutions $\pm k_a$ and $\pm k_b$. The orthogonal indices may be solved as the positive roots $n_a = k_a/k_o$ and $n_b = k_b/k_o$, with the polarized oscillation directions determined by solution of a modified form of Eqn. 14.42 using the wavevector \underline{k}'

Appendix G. Derivations and Discussion of Energy Transfer

$$\underline{\mathbf{k}}' \times (\underline{\mathbf{k}}' \times \underline{\mathbf{D}}) + \underline{\eta} \underline{\mathbf{D}} = \underline{\mathbf{0}} \quad (14.45)$$

written in matrix form as

$$\begin{bmatrix} n_{xx}^{-2} - k_y'^2 - k_z'^2 & k_x' k_y' & k_x' k_z' \\ k_y' k_x' & n_{yy}^{-2} - k_x'^2 - k_z'^2 & k_y' k_z' \\ k_z' k_x' & k_z' k_y' & n_{zz}^{-2} - k_x'^2 - k_y'^2 \end{bmatrix} \begin{bmatrix} D_x \\ D_y \\ D_z \end{bmatrix} = \begin{bmatrix} 0 \\ 0 \\ 0 \end{bmatrix} \quad (14.46)$$

This set of equations may be solved for the ratio of the E_i s. Once solved, the proportion of energy oscillating along the two directions is related to the polarization of radiation leaving the energy donor, meaning that the effective index for coupling between dipoles is the weighted average of the polarization projected onto the transverse wave directions (see, e.g., Appendix D.2.):

$$\bar{n} = n_1(\hat{\mathbf{P}} \cdot \hat{\mathbf{D}}_1) + n_2(\hat{\mathbf{P}} \cdot \hat{\mathbf{D}}_2) \quad (14.47)$$

This is the effective index for a wave travelling along $\hat{\mathbf{s}}$ in a non-absorbing medium.

Calculating the effective extinction coefficient along $\hat{\mathbf{s}}$ proceeds similarly, although now the (im)permeability tensor includes imaginary components which correspond to the conductivity tensor. For crystals of orthorhombic or higher symmetry, the principle optic axes for index n and extinction coefficient k may be manipulated to be aligned, and thus n_{jj} and k_{jj} diagonalized on the same axes. For monoclinic or triclinic symmetries, the following discussion must be modified. Inclusion of the imaginary components requires redefinition of the complex index and dielectric constants as $\tilde{n}_{jj} = n_{jj}(1 + ik''_{jj})$ and $\tilde{\epsilon}_{jj} = \epsilon_{jj} + \frac{4\pi i}{\omega} \sigma_{jj}$, with $k''_{jj} = k_{jj}/n_{jj}$. Eqns. 14.42-14.47 are all still valid, and may then be solved for \tilde{n}_{jj} and D_i . One notable difference in this solution is that the transverse oscillation vectors $\underline{\mathbf{D}}$ are not necessary perpendicular to $\hat{\mathbf{s}}$, but the math is still valid.⁶²⁹

Appendix G. Derivations and Discussion of Energy Transfer

Strict application of these equations to Förster energy transfer is less than clear, which may be why many groups performing such calculations use density functional theory to rigorously estimate the energetic coupling.^{93,188,202} Reasons for this may be obviated by examination of the rationale in the previous sections of this appendix. The use of the extinction coefficient in Förster theory approximates the available probabilities of molecular excitation between single molecules, whereas the optical anisotropy observed or measured in organic crystals is a chimera of molecular and crystal anisotropy.^{221,594,781} Optical measurements on crystals thus may not be transferrable because of the molecular nature of energy transfer which requires knowledge of the single-molecule anisotropy; indeed, the some of the more accurate energy transfer calculations use data from single-molecule spectroscopy or absorption.⁸⁰³ There is also the distinction between far-field, traveling wave phenomena like light propagation and such near-field decaying wave effects as energy transfer.⁸¹³ Such equations derived to describe propagating waves may not necessarily be valid for determining the effective dielectric constant in near-field circumstances. Fortunately, differences in n along different crystal directions are typically small (birefringence values $\Delta n < 0.2$) in many materials, though differences in k can be proportionally larger due to feature disappearance from transition dipole orthogonality with the impinging field oscillation.^{594,744,781}

G.5. Quantum-Mechanical Derivation of Dexter Energy Transfer

Dexter was able to invoke energy transfer between forbidden or non-radiative states by describing the wavefunctions of Eqn. 14.33 as $\psi_i(\underline{x}_i, \underline{\sigma}_i) = \phi_i(\underline{x}_i)\chi(\underline{\sigma}_i)$, where ϕ_i and χ_i

Appendix G. Derivations and Discussion of Energy Transfer

are the normalized position (\underline{x}_i) and spin ($\underline{\sigma}_i$)-dependent wavefunctions.²³⁶ Expression of these states as Slater determinants, followed by application of the Coulomb operator in Eqn. 14.34 results in the following interaction energy:

$$\begin{aligned} U_{DA} = & \iint [\phi_{D^*}^*(\underline{x}_D) \phi_A^*(\underline{x}_A) \hat{\mathcal{H}} \phi_D(\underline{x}_D) \phi_{A^*}(\underline{x}_A)] \\ & \cdot [\chi_{D^*}^*(\underline{\sigma}_D) \chi_A^*(\underline{\sigma}_A) \chi_D(\underline{\sigma}_D) \chi_{A^*}(\underline{\sigma}_A)] d\underline{x}_i d\underline{\sigma}_i \\ & + \iint [\phi_{D^*}^*(\underline{x}_D) \phi_A^*(\underline{x}_A) \hat{\mathcal{H}} \phi_{A^*}(\underline{x}_D) \phi_D(\underline{x}_A)] \\ & \cdot [\chi_{D^*}^*(\underline{\sigma}_D) \chi_A^*(\underline{\sigma}_A) \chi_{A^*}(\underline{\sigma}_D) \chi_D(\underline{\sigma}_A)] d\underline{x}_i d\underline{\sigma}_i \end{aligned} \quad (14.48)$$

The first integral is the Coulomb integral of Förster transfer in Eqn. 14.33, the second an electronic exchange integral (note the difference in subscripts of the wavefunctions and quantum numbers). Both have been rearranged to depict the fact the $\hat{\mathcal{H}}$ does not act on the spin-dependent components. Spin conservation yields spin-selection rules of the form $\int \chi_i^*(\underline{\sigma}_j) \chi_k(\underline{\sigma}_l) = \delta_{jl}$ IFF $\chi_i = \chi_k$,²³⁶ which requires $\chi_{i^*} = \chi_i$ for the Coulomb integral, *i.e.* all transitions must be spin-allowed to couple appreciably. The exchange integral is more lenient, requiring $\chi_{D^*} = \chi_{A^*}$ and $\chi_D = \chi_A$, permitting spin-disallowed transitions if both donor and acceptor flip spin in the process.

Closer inspection of Eqn. 14.48 shows the spatial components of the overlap integral to be extents of orbital overlap between donor and acceptor. These can be expressed in terms of the rate equation in Eqn. 14.38 (with unit conversions) as

$$k_D = \frac{2\pi}{\hbar} Z^2 \int F_D(E) A_A(E) dE \quad (14.49)$$

where A_A is the area-normalized acceptor absorption and Z^2 is defined as

Appendix G. Derivations and Discussion of Energy Transfer

$$Z^2 = \sum_i \sum_j \frac{e^4}{m_{D^*} m_A n^2} \left| \int \phi_{D^*}^*(\underline{x}_D) \phi_A^*(\underline{x}_A) \left(\frac{1}{|\underline{r}_{DA}|} \right) \phi_{A^*}(\underline{x}_D) \phi_D(\underline{x}_A) dt \right|_{ij}^2 \quad (14.50)$$

summed over all initial (i) and final (j) states, cancelling out double-counting degenerate transitions by accounting for the multiplicity of the donor (m_D) and acceptor (m_A) states, with the orbital overlap integrated over the transition time. Approximating the orbital overlap to decay exponentially with distance gives the familiar Dexter energy transfer rate:

$$k_D = KJ \exp\left(-\frac{2d}{L}\right) \quad (14.51)$$

where the quantum-mechanical terms have been lumped into K , and the emission- and absorption-normalized overlap integral is represented in J . The characteristic distance scale is the average van der Waals radius L of the two interacting species.

Appendix H. Additional Images from Chapter 10.

H.1. BP2T Template Optimization

The following images are a more extensive characterization of the morphologies

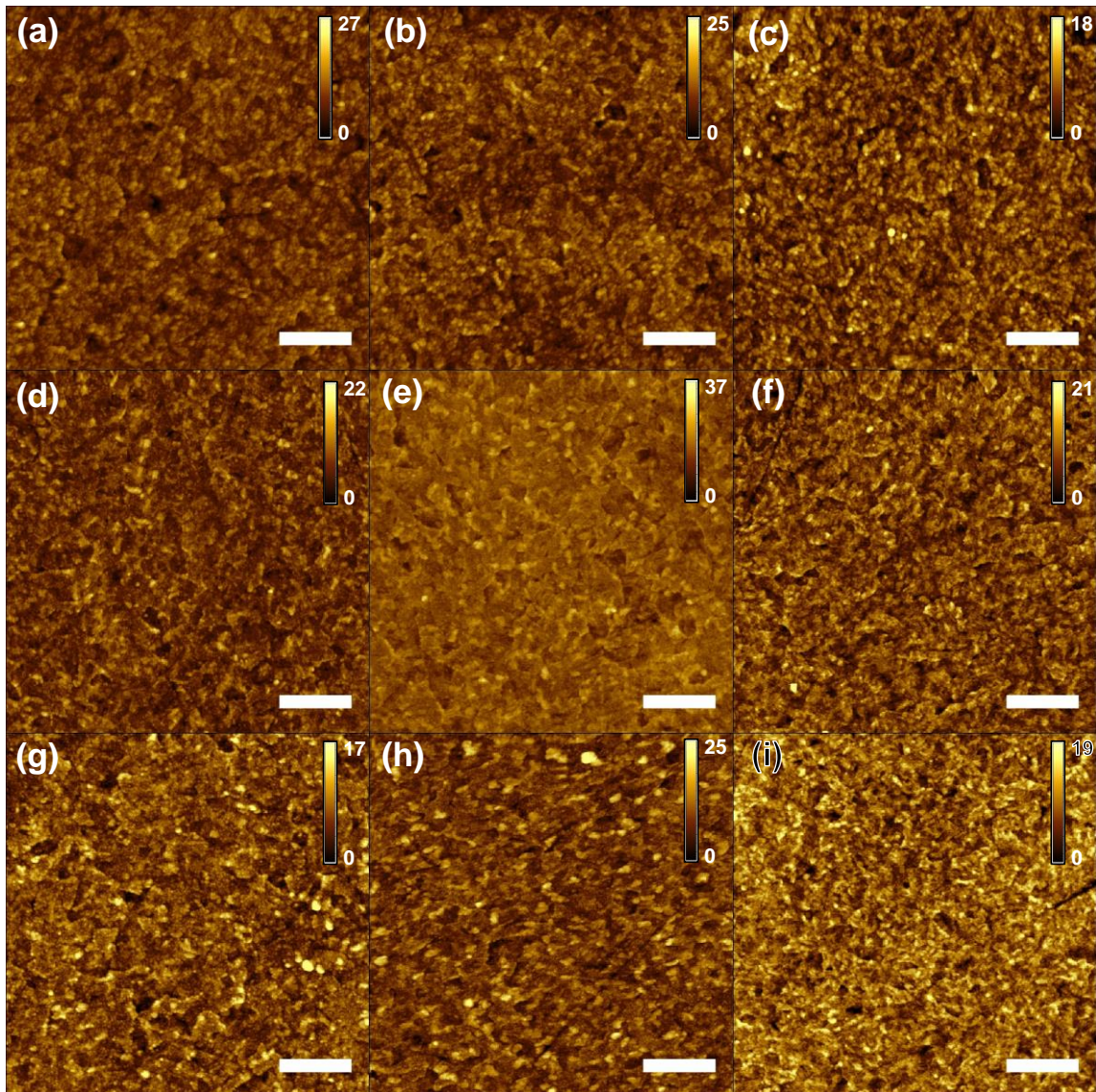


Figure 14.12. (a) Morphology of BP2T deposited onto bare ITO as a function of deposition rate and substrate temperature. Deposition rate increases across columns: (a), (d), (g) 0.1 Å/s, (b), (e), (h) 0.3 Å/s, and (c), (f), (i) 1 Å/s, while temperature increases down rows: (a)-(c) 75 °C, (d)-(f) 100 °C, and (g)-(i) 115 °C. All scale bars 1 μm, height scales in nm.

Appendix H. Additional Images from Chapter 10.

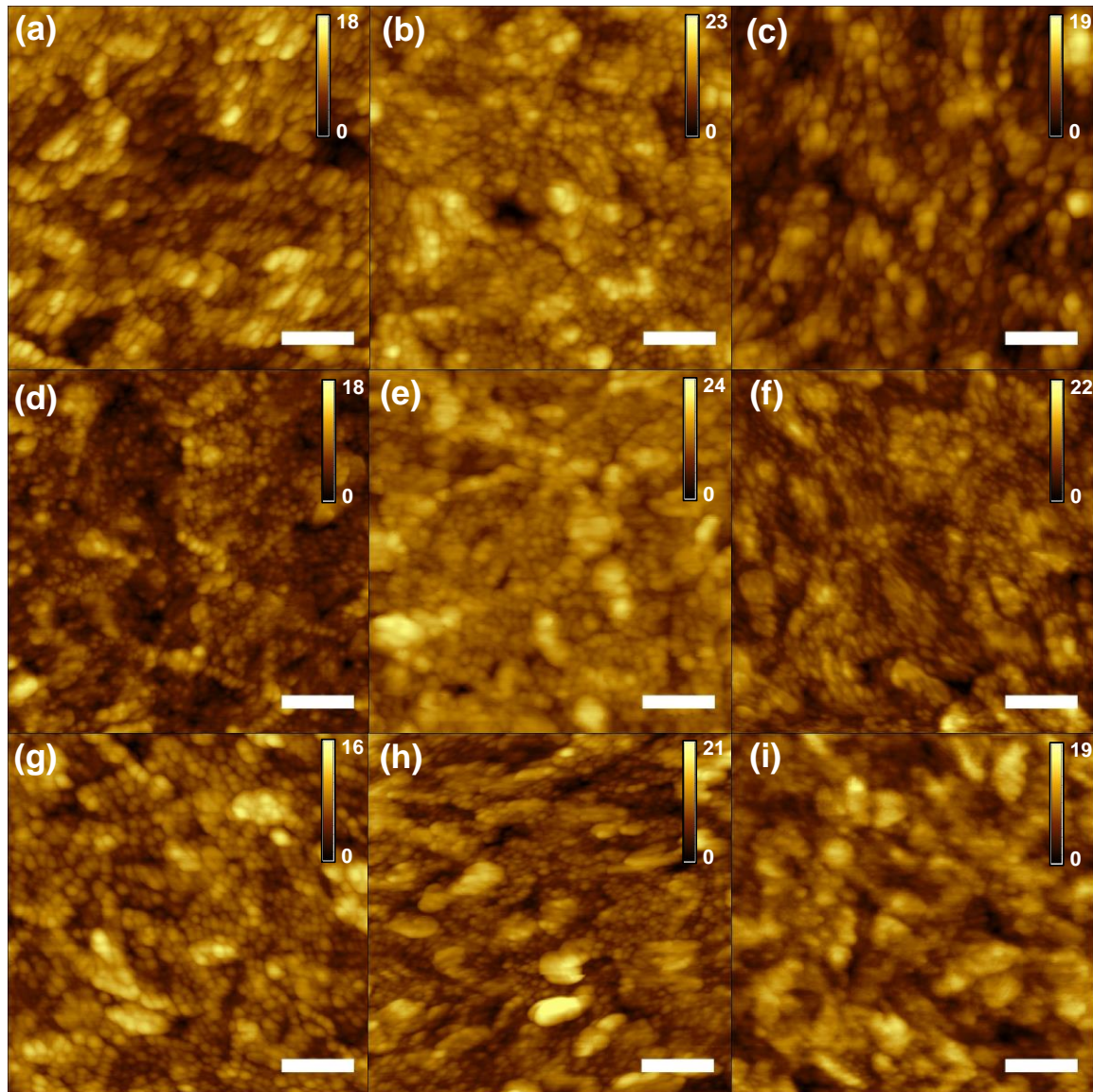


Figure 14.13. (a) Closer examination of the morphology of BP2T deposited onto bare ITO as a function of deposition rate and substrate temperature. Deposition rate increases across columns: (a), (d), (g) 0.1 \AA/s , (b), (e), (h) 0.3 \AA/s , and (c), (f), (i) 1 \AA/s , while temperature increases down rows: (a)-(c) 75°C , (d)-(f) 100°C , and (g)-(i) 115°C . All scale bars 200 nm , height scales in nm.

presented in Section 10.2. The morphologies presented in the $5 \times 5 \mu\text{m}$ images on ITO are largely indistinguishable from one another (Figure 14.12), with a possible coarsening of the BP2T layer observed at higher substrate temperatures. Closer inspection of these layers

Appendix H. Additional Images from Chapter 10.

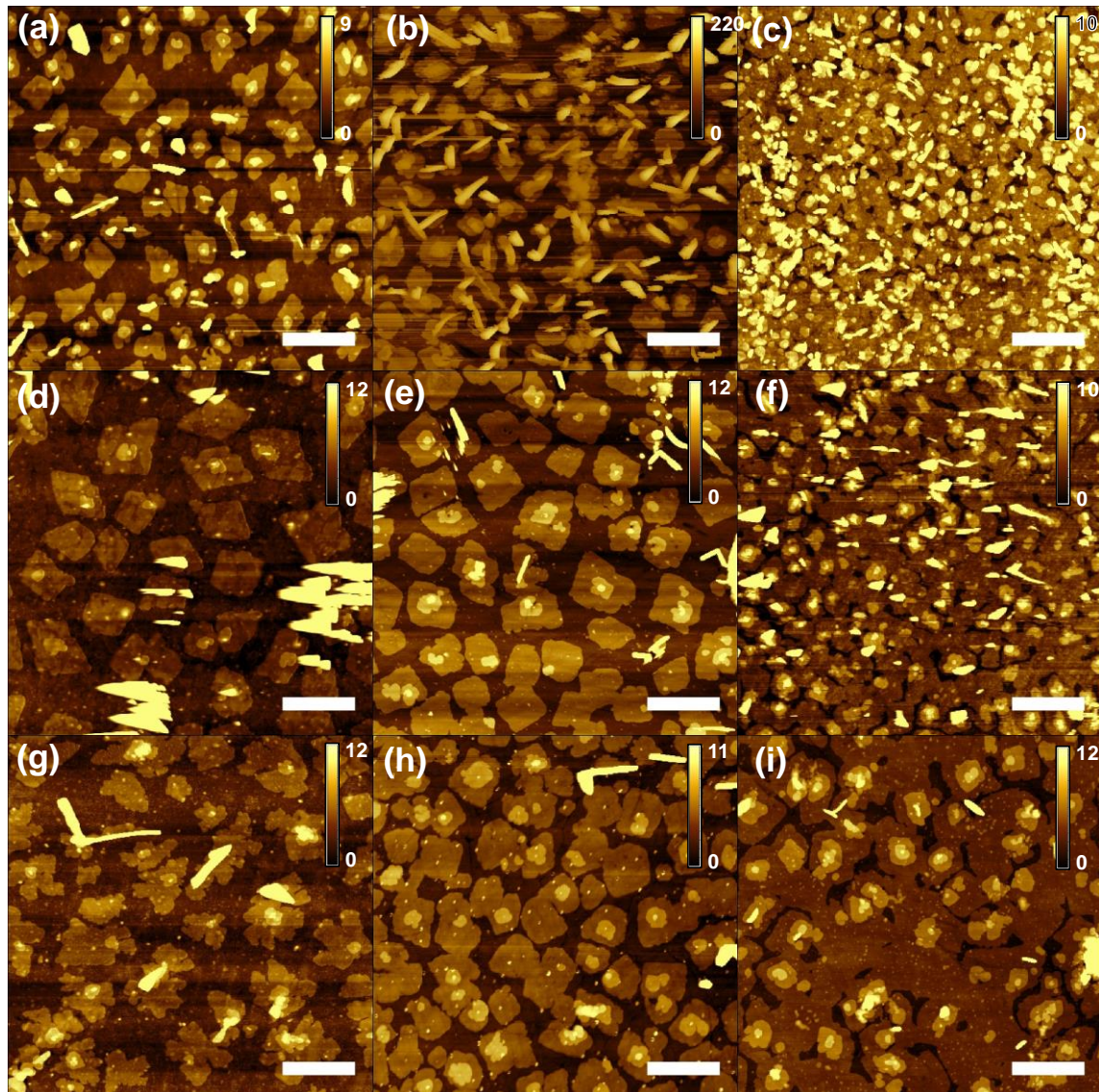


Figure 14.14. (a) Morphology of BP2T deposited onto bare quartz as a function of deposition rate and substrate temperature. Deposition rate increases across columns: (a), (d), (g) 0.1 Å/s, (b), (e), (h) 0.3 Å/s, and (c), (f), (i) 1 Å/s, while temperature increases down rows: (a)-(c) 75 °C, (d)-(f) 100 °C, and (g)-(i) 115 °C. All scale bars 1 μ m, height scales in nm.

shows this to be largely true (Figure 14.13), with slight larger domains observed at high substrate temperatures and a weak dependence (increasing size) on deposition rate. For BP2T deposited on quartz (Figure 14.14), the films grow in a layer-by-layer mode with

Appendix H. Additional Images from Chapter 10.

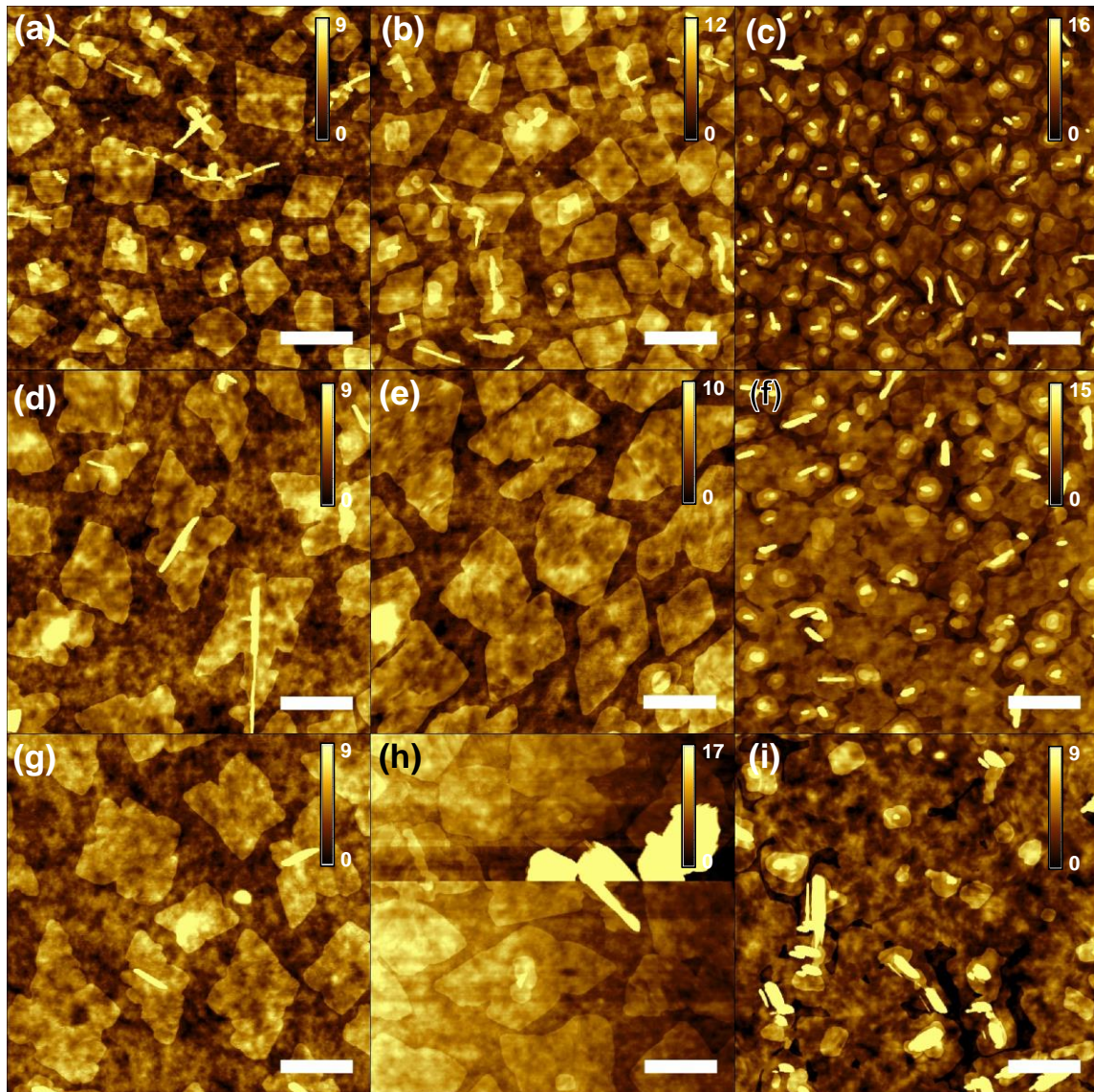


Figure 14.15. (a) Morphology of BP2T deposited onto ITO with 50 nm PEDOT:PSS as a function of deposition rate and substrate temperature. Deposition rate increases across columns: (a), (d), (g) 0.1 Å/s, (b), (e), (h) 0.3 Å/s, and (c), (f), (i) 1 Å/s, while temperature increases down rows: (a)-(c) 75 °C, (d)-(f) 100 °C, and (g)-(i) 115 °C. All scale bars 1 μ m, height scales in nm.

increasing coverage at higher temperatures and growth rates. This behavior can be mimicked on rough substrates by planarizing with a spin-coated polymer layer, which produces even larger grains on both ITO (Figure 14.15) and quartz (Figure 14.16). The

Appendix H. Additional Images from Chapter 10.

grain size increases with decreasing deposition rate, with disruptive vertical spikes of material produced under most conditions.

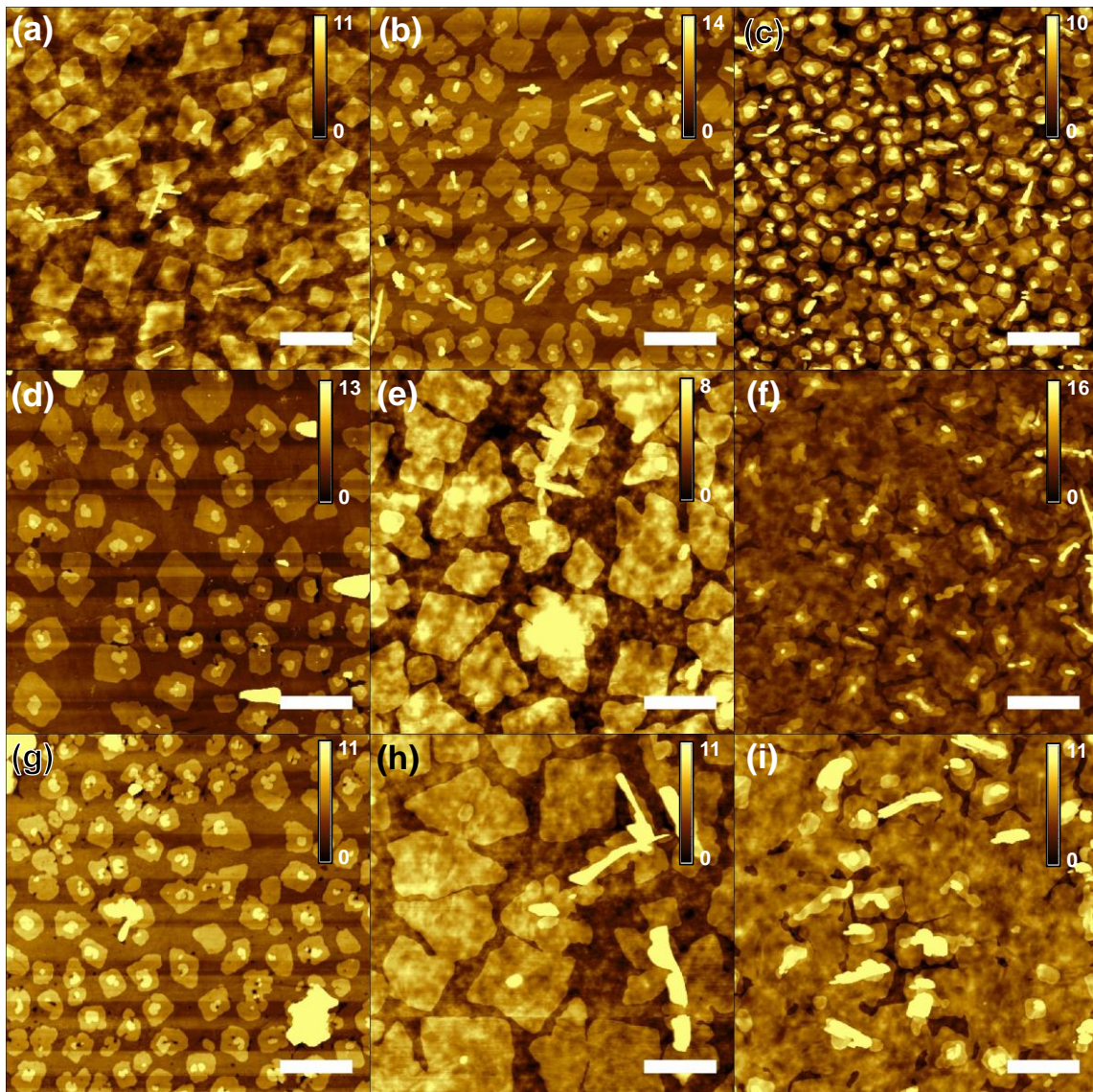


Figure 14.16. (a) Morphology of BP2T deposited onto quartz with 50 nm PEDOT:PSS as a function of deposition rate and substrate temperature. Deposition rate increases across columns: (a), (d), (g) 0.1 Å/s, (b), (e), (h) 0.3 Å/s, and (c), (f), (i) 1 Å/s, while temperature increases down rows: (a)-(c) 75 °C, (d)-(f) 100 °C, and (g)-(i) 115 °C. All scale bars 1 μm, height scales in nm.

H.2. SubPc, C₆₀, and C₇₀ Synchrotron Characterization

The images in this section are provided to show clean diffraction patterns obtained from a synchrotron lightsource, which may be compared to the much lower signal-to-noise data

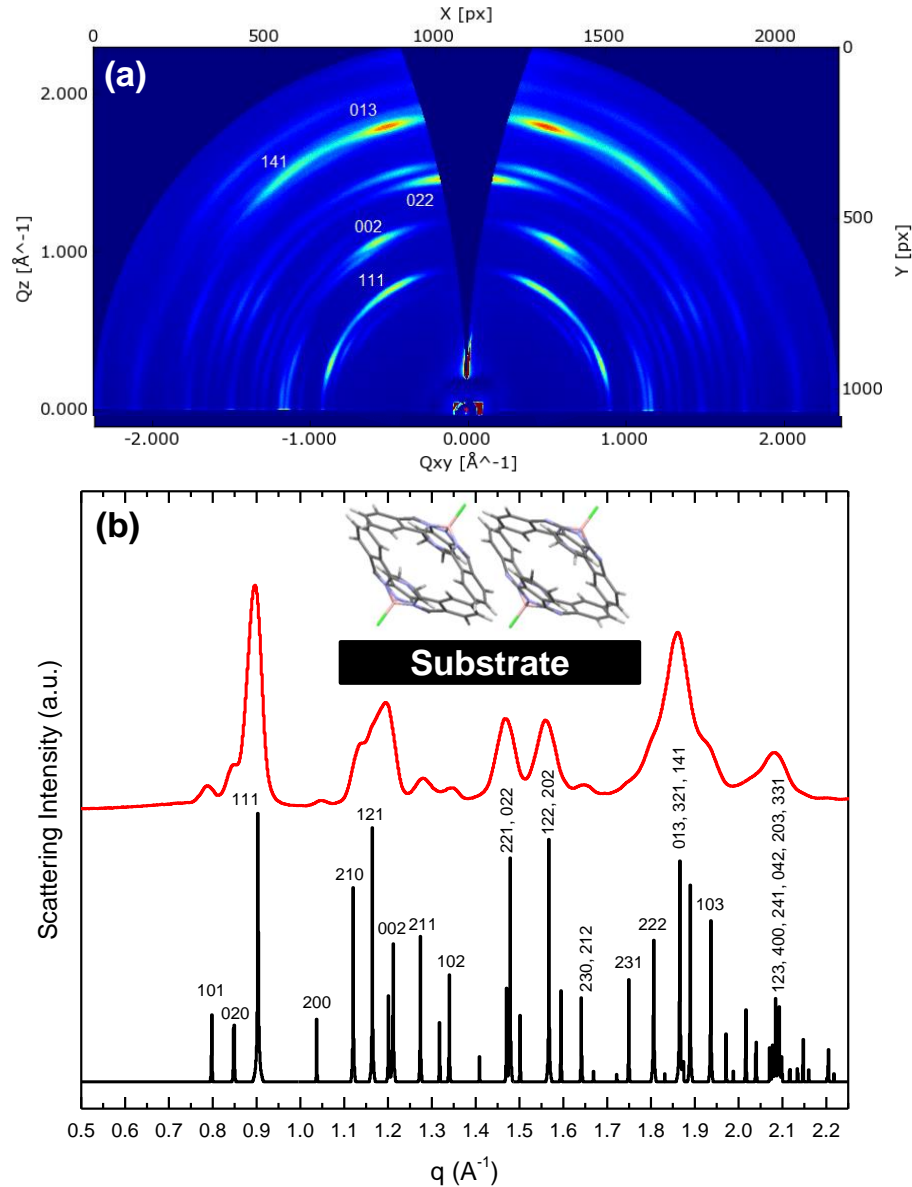


Figure 14.17. (a) 2D GIWAXS pattern of neat 13 nm SubPc film on silicon, with (b) the χ -integrated pattern. The inset in (b) shows the dominant orientation of the SubPc crystallites with the (022) plane parallel to the substrate. GIWAXS data collected at the Stanford Synchrotron Radiation Lightsource (SSRL) beamline 11-3.

Appendix H. Additional Images from Chapter 10.

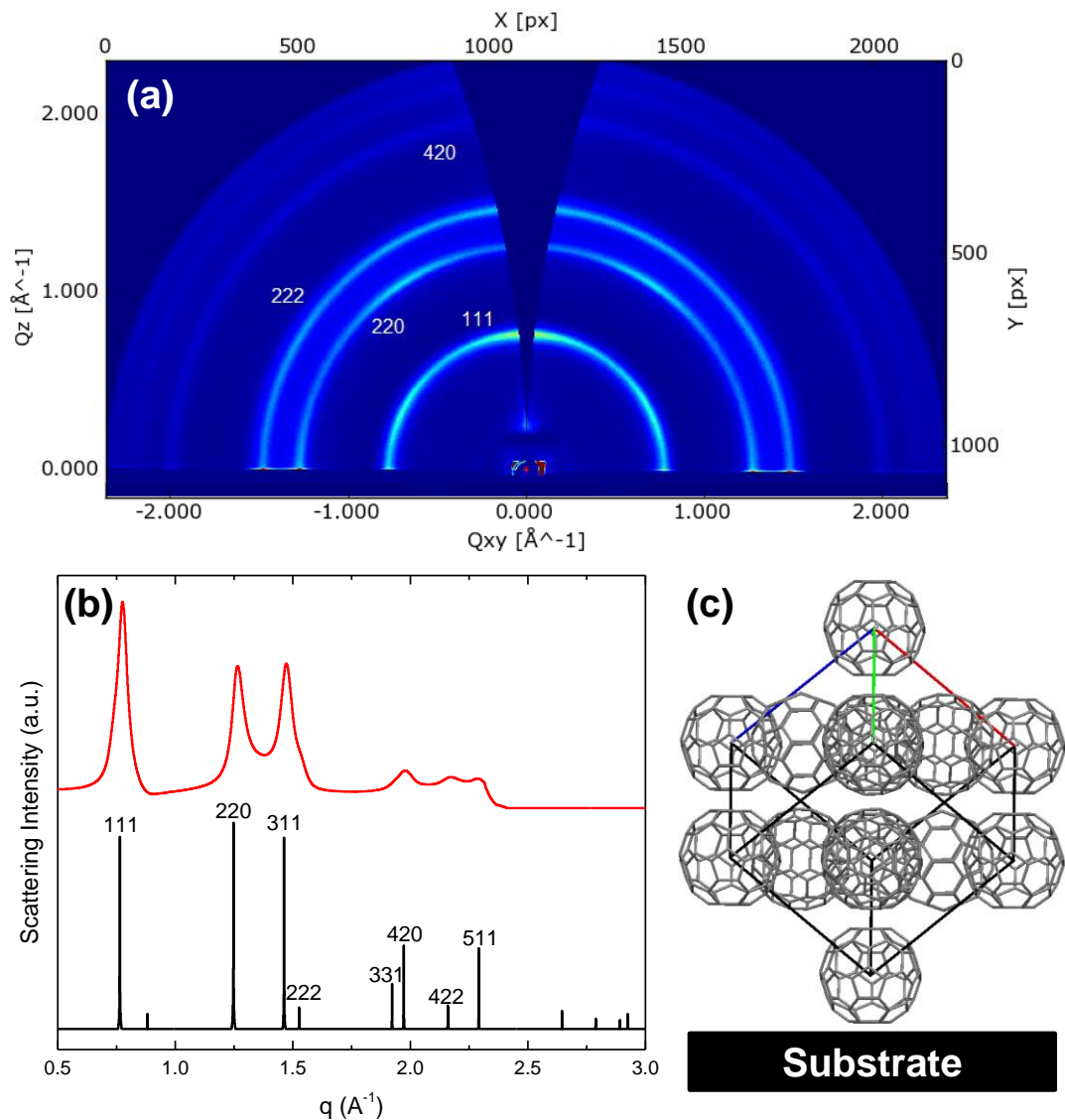


Figure 14.18. (a) 2D GIWAXS pattern of neat 13 nm C_{60} film on silicon, with (b) the χ -integrated pattern. (c) shows the textured orientation of the C_{60} crystallites with the (111) plane parallel to the substrate. GIWAXS data collected at the Stanford Synchrotron Radiation Lightsource (SSRL) beamline 11-3.

obtained at the university. SubPc crystallizes in an orthorhombic spacegroup and is weakly textured out-of-plane, giving rather spectacular diffraction patterns and multiple peaks (Figure 14.17). C_{60} has cubic symmetry, yielding a much simpler pattern (Figure 14.18).

Appendix H. Additional Images from Chapter 10.

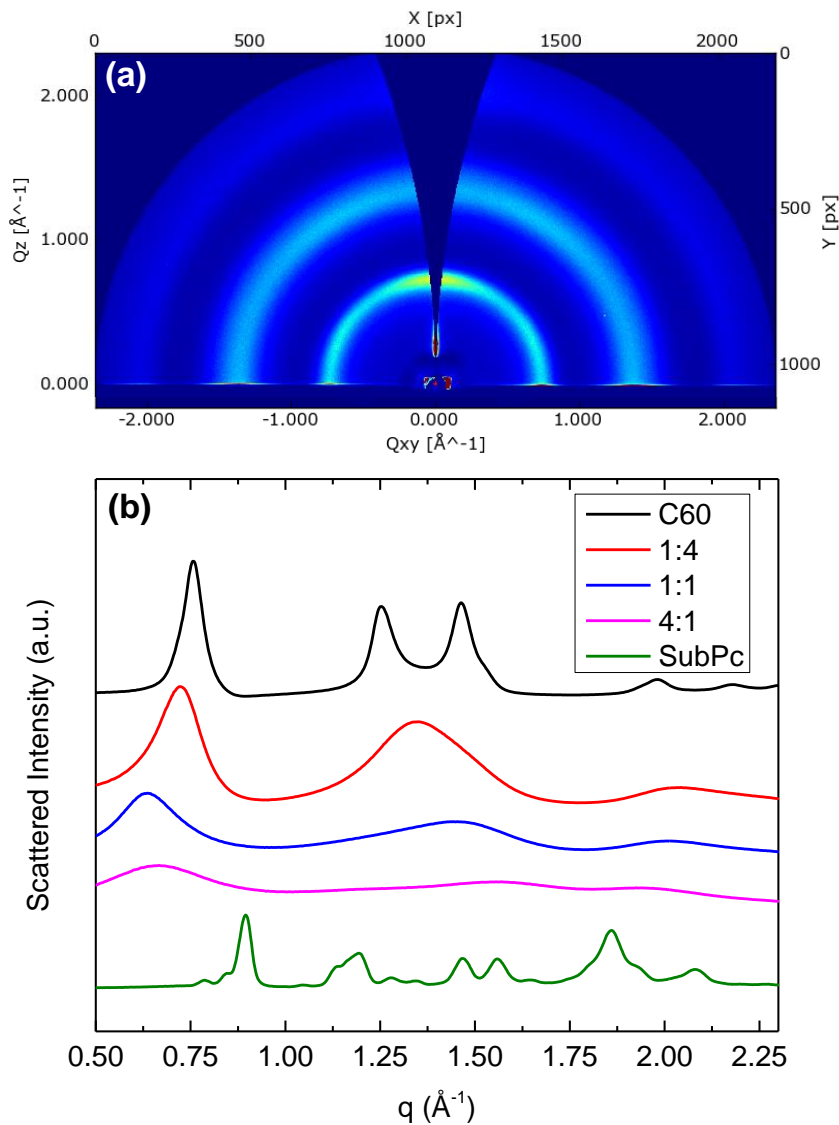


Figure 14.19. (a) 2D GIWAXS pattern of mixed SubPc:C₆₀ films with a volume ratio of 1:4, with (b) the χ -integrated pattern for films of various composition. The peak widths give crystallite sizes of 9.1 nm (C₆₀), 3.7 nm (1:4), 2.5 nm (1:1), 1.5 nm (4:1), and 15.6 nm (SubPc). GIWAXS data collected at the Stanford Synchrotron Radiation Lightsource (SSRL) beamline 11-3.

Surprisingly, neat films show a small degree of orientation of the densest (111) plane parallel to the substrate. When SubPc and C₆₀ are mixed, the pattern changes considerably and gives more diffuse rings which signify much smaller crystallites compared to the neat

Appendix H. Additional Images from Chapter 10.

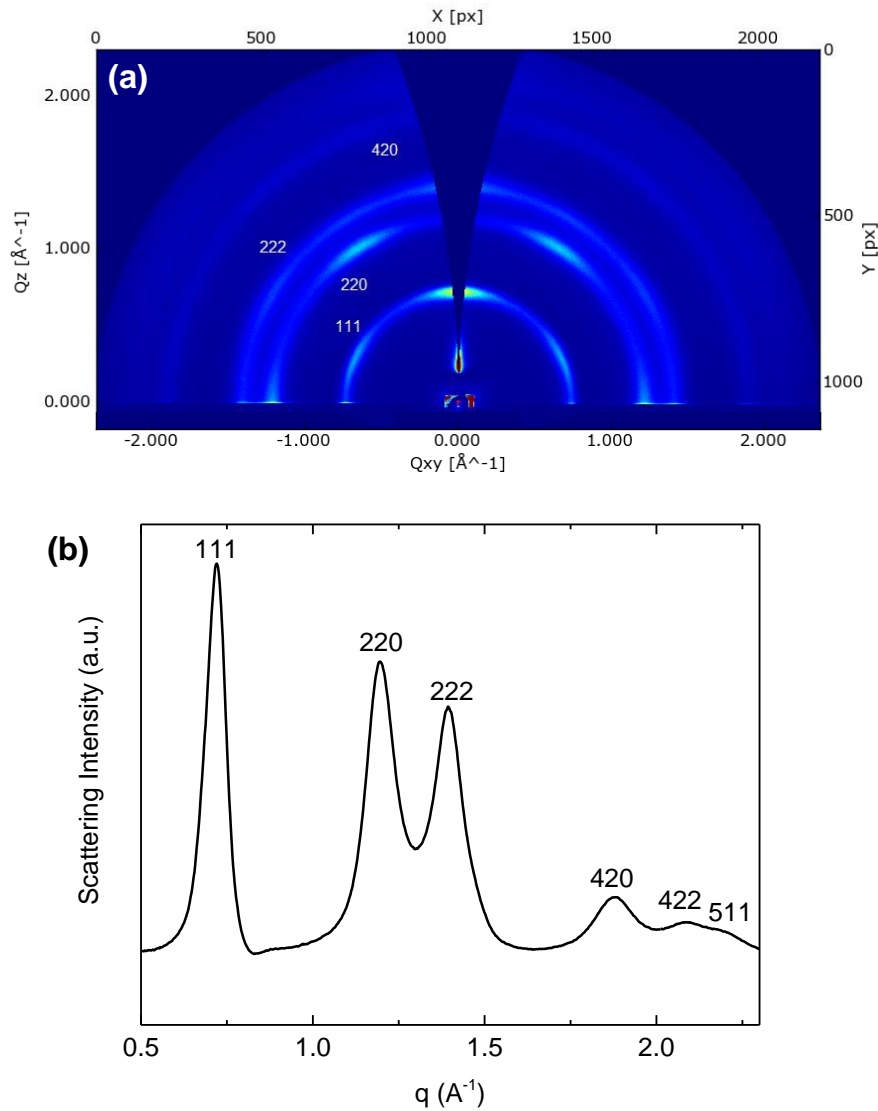


Figure 14.20. (a) 2D GIWAXS pattern of a neat C₇₀ film on silicon, showing stronger orientation of the (111) parallel to the substrate than C₆₀. (b) is the χ -integrated pattern, showing a very similar pattern to C₆₀ but with slightly larger d-spacing shifting the peak to smaller q. GIWAXS data collected at the Stanford Synchrotron Radiation Lightsource (SSRL) beamline 11-3.

C₆₀ (9.1 nm) and SubPc (15.6 nm) cases, as shown in Figure 14.19. C₇₀ films show even stronger orientation of the (111) plane, with slight larger d-spacing shifting the pattern features to smaller q (Figure 14.20).

Appendix H. Additional Images from Chapter 10.

H.3. BP2T, SubPc, and C₆₀ TEM Characterization

Determination of the zone axis and crystallographic orientation in the electron diffraction images of Chapter 10. was accomplished by overlaying simulated patterns

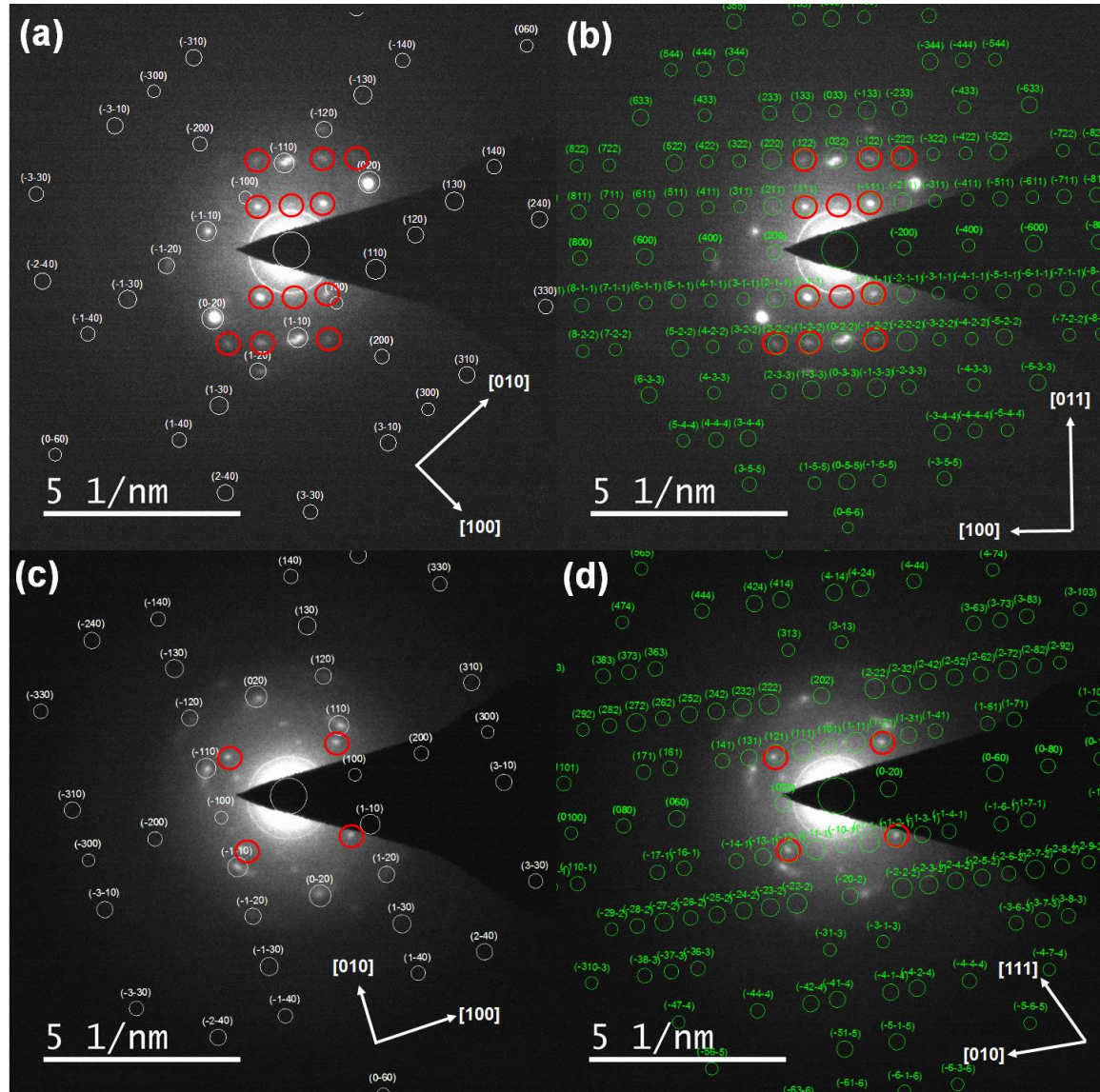


Figure 14.21. Selected area electron diffraction on a $\sim 1.6 \mu\text{m}$ diameter area of 25 nm SubPc (1 Å/s, 25 °C) on 8 nm BP2T (0.3 Å/s, 100 °C) on a Quantifoil grid. Simulated BP2T pattern along the [001] zone is overlaid for (a) and (c), with simulated SubPc patterns overlaid, with (b) [01 $\bar{1}$] and (d) [10 $\bar{1}$] zones. Red circles denote SubPc peaks. These orientations were used to deduce the epitaxial relationships shown in Figure 10.8. Patterns collected by Dan Cremons, analysis by the author.

Appendix H. Additional Images from Chapter 10.

(simulation code given in Appendix R.6.) onto the experimental. This is shown for the images from Figure 10.8 in Figure 14.21, with good agreement between simulation and experiment.

There were also some oddities observed in this study, such as BP2T crystals which appear to be strained compared to neighboring crystals, as shown in Figure 14.22a. This could be from edge nucleation of nearby grains or uneven thermal relaxation when the film cooled after deposition. BP2T grains were also clearly visible with dark field TEM imaging, as shown in Figure 14.22b. The large grains match those observed in AFM, but

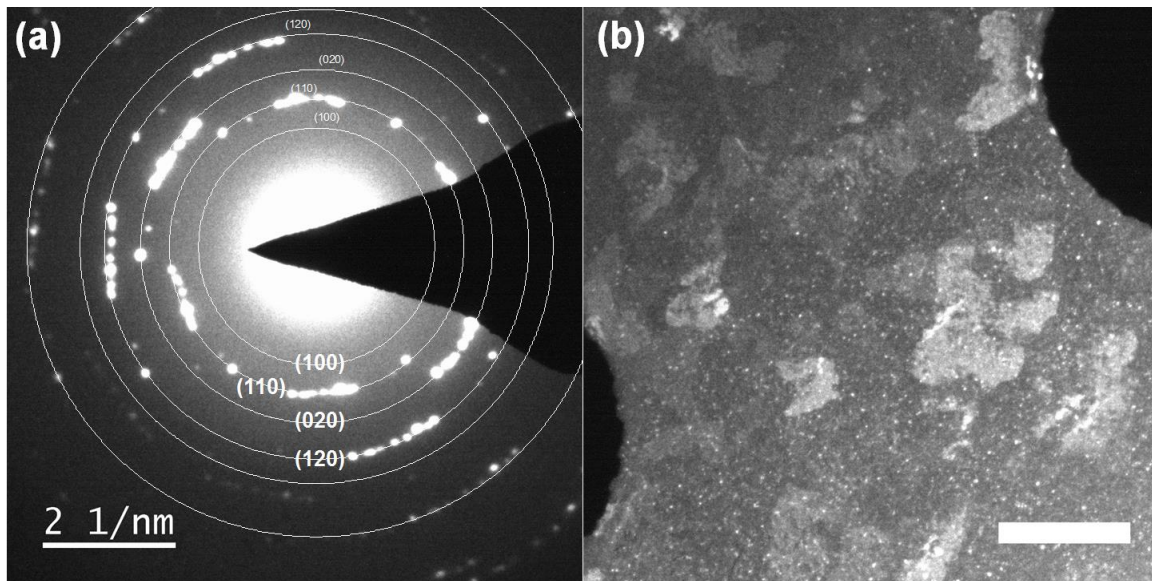


Figure 14.22. (a) Selected area electron diffraction on a ~1.6 μm diameter area of 25 nm SubPc (1 $\text{\AA}/\text{s}$, 25 $^{\circ}\text{C}$) on 8 nm BP2T (0.3 $\text{\AA}/\text{s}$, 100 $^{\circ}\text{C}$) on a Quantifoil grid. Simulated BP2T pattern along the [001] zone is overlaid on the image. (b) Dark-field TEM image of BP2T grains (8 nm, 0.3 $\text{\AA}/\text{s}$, 100 $^{\circ}\text{C}$) underneath SubPc (13 nm, 1 $\text{\AA}/\text{s}$, 25 $^{\circ}\text{C}$) and 35 nm C₆₀ (35 nm, 2 $\text{\AA}/\text{s}$, 25 $^{\circ}\text{C}$), showing a grain sizes 500-1000 nm. Scale bar 1 μm . Data collected by Dan Cremons, analysis by the author.

the small spots are unexpected and perhaps contribute to the differently oriented SubPc grains.

H.4. Kelvin Probe Force Microscopy Measurements

Although intrinsically linked to the HOMO or work function, surface potential measurements can also be sensitive to contact potential offsets and interface dipoles and should be interpreted cautiously when used to determine changes in HOMO levels. An

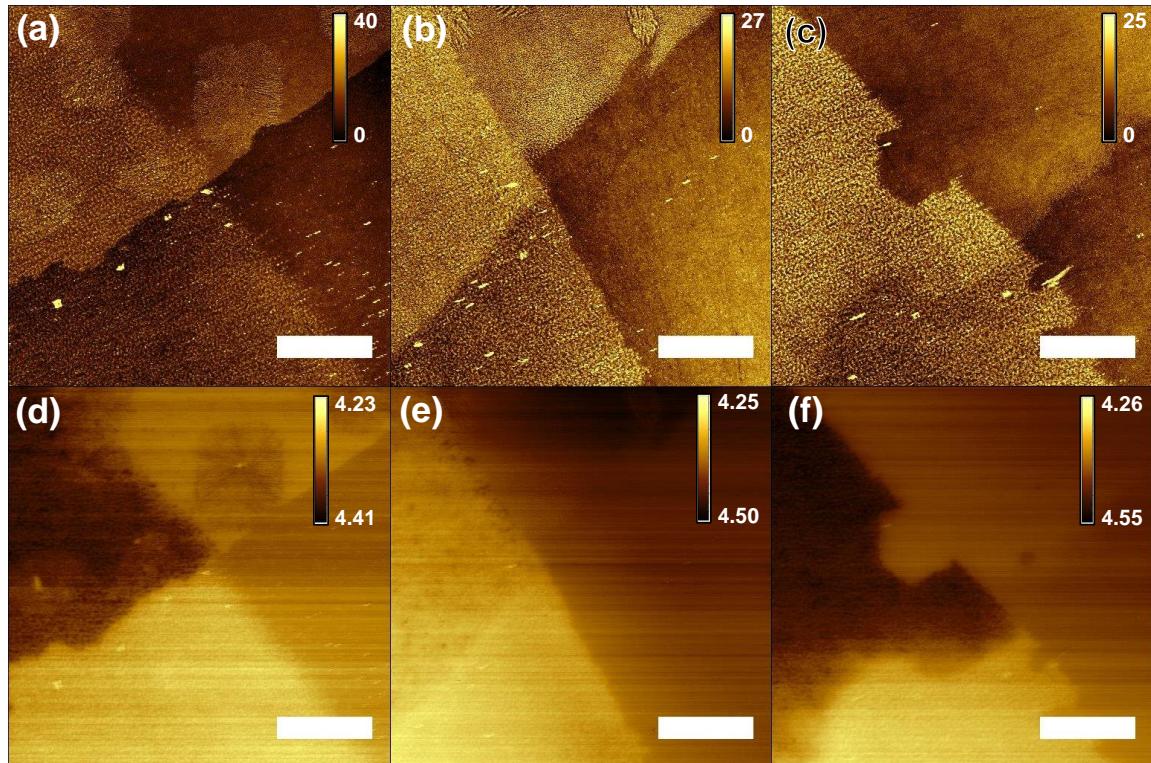


Figure 14.23. KPFM measurements on 25 nm SubPc on 8 nm BP2T (0.3 \AA/s , 100°C) on ITO, with (a)-(c) topography images and (d)-(f) surface potential images. SubPc deposited at 25°C and (a), (d) 0.1 \AA/s , (b), (e) 1 \AA/s , and (c), (f) 10 \AA/s . Regions in each image are (clockwise from top) SubPc, ITO, BP2T, BP2T/SubPc. Scale bars $10 \mu\text{m}$, height scales in (a)-(c) in nm, (d)-(f) in V below vacuum, calibrated to a clean gold film.

interface dipole is likely occurring between the layers presented in Figure 14.23, differing slightly across SubPc deposition rates. These samples were created by cross-masking an ITO piece with cleaved silicon, deposited without rotation for a well-defined edge. At higher rates, the SubPc layer takes on the potential of the underlying ITO, but differs in

Appendix H. Additional Images from Chapter 10.

response to the BP2T layer, which consistently has a surface potential of ~ 4.25 eV. SubPc on BP2T (of the most interest for this chapter) varies significantly and not monotonically with deposition rate, complicating conclusions.

Interestingly, spherulitic crystals of SubPc are observed in Figure 14.23a and Figure 14.23d and present a different (deeper) contact potential than amorphous SubPc. Additional work with films of different thickness, corroborated with UPS would be necessary to more precisely quantify these crystalline regions.

H.5. External Quantum Efficiency Fitting Plots

An extended set of plots for η_{EQE} fitting are given in Figure 14.24, corresponding to the additional values in Table 10.2. These fits are all reasonable matches to the measured

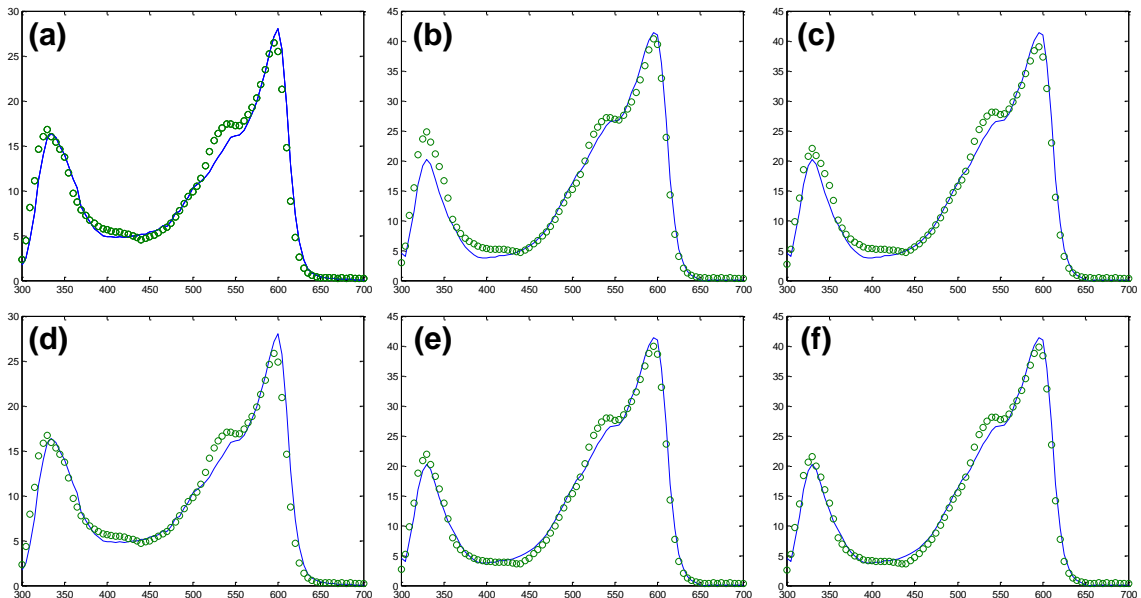


Figure 14.24. Plots showing the results of η_{EQE} fitting, with (a), (d) bare, (b), (e) BP2T not dissociating, and (c), (f) BP2T dissociating. (a)-(c) are for $\eta_{CC} = 0.99$, (d)-(f) η_{CC} optimized for goodness of fit. Device structures given in Figure 10.18, fit parameters in Table 10.2.

spectra, with agreement in the ultraviolet achieved by including glass absorption before the

Appendix H. Additional Images from Chapter 10.

device stack.

Extraction of reasonable parameters from η_{EQE} fitting requires an estimate of charge collection, which may be accomplished by examining the bias dependence of η_{EQE} , shown in Figure 14.25. High leakage currents which saturated the preamplifier and device shorting limited the voltage range which could be explored.

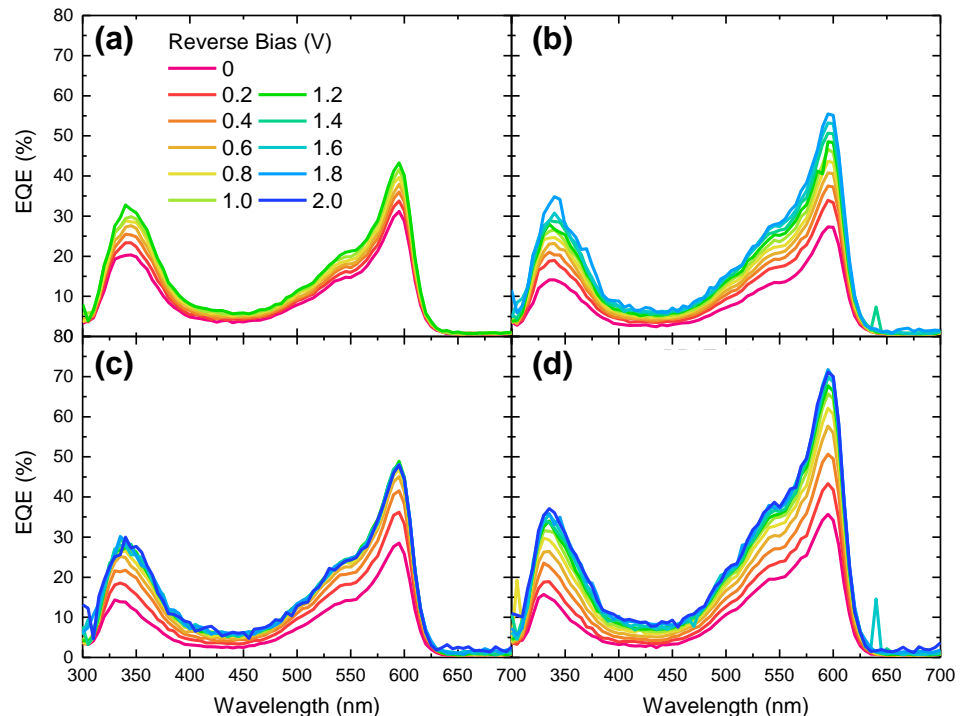


Figure 14.25. Reverse biased η_{EQE} plots for the devices described in Figure 10.19. (a) Bare, 13 nm SubPc, (b) Bare, 20 nm SubPc, (c) BP2T, 13 nm SubPc, (d) BP2T, 20 nm SubPc.

Appendix I. Secondary Film Evolution Mechanisms

Understanding the modes of motion in a material is critical in applications where film uniformity and stability matter, as in organic electronics. In these situations, creating films of good quality and coverage can be paramount, usurping other goals of crystallization in order to produce functional devices. This chapter discusses secondary film evolution mechanisms which often occur concurrent with crystallization.

I.1. Introduction

There are four primary methods for material to move and evolve on a substrate: surface diffusion, bulk diffusion, sublimation, and flow. These effects have been given excellent theoretical treatment by Mullins and lead to the following expression for a material surface or height $z(x, t)$ initially perturbed about $z = 0$ by a sinusoid $z = a \sin\left(\frac{2\pi}{\lambda}x\right)$, with $a/\lambda \ll 1$, and allowed to evolve in time:⁶¹⁹

$$\frac{\partial z}{\partial t} = -(F + E + B + S)z \quad (14.52)$$

where F is the contribution due to viscous flow

$$F = \frac{\gamma}{2\mu} \left(\frac{2\pi}{\lambda} \right) \quad (14.53)$$

E is the contribution from evaporation or sublimation followed by vapor diffusion

$$E = \frac{P_o^{sat}\gamma\Omega}{\sqrt{2\pi m(k_B T)^3}} \left(\frac{2\pi}{\lambda} \right)^2 + \frac{\rho_o D_V \gamma \Omega^2}{k_B T} \left(\frac{2\pi}{\lambda} \right)^3 \quad (14.54)$$

where P_o^{sat} is the vapor pressure over a flat surface, Ω is molecular volume, ρ_o is the vapor number density in equilibrium with the surface, and D_V is the vapor diffusivity. B is the contribution from bulk diffusion, with D_B the bulk self-diffusivity

Appendix I. Secondary Film Evolution Mechanisms

$$B = \frac{\mathcal{D}_B \gamma \Omega^2}{k_B T} \left(\frac{2\pi}{\lambda} \right)^3 \quad (14.55)$$

and S the contribution due to surface diffusion:

$$S = \frac{\mathcal{D}_S \gamma \Omega^2 \nu}{k_B T} \left(\frac{2\pi}{\lambda} \right)^4 \quad (14.56)$$

with \mathcal{D}_S the surface diffusivity and ν the number of molecules per area surface.

Each of these processes varies differently with the surface wavelength, making them separable in principle, *e.g.*, with a diffraction grating embossed into a material surface which is allowed to evolve.^{311,319,326,814} For these mechanisms, examining the dependence with feature size implies that viscous flow will occur over all length scales, with sublimation and diffusion largely contributing to shorter-range evolution. It is also important to recall the (approximately exponential) temperature dependence hidden in coefficients such as viscosity (decay), vapor pressure (increase), and diffusivity (increase). Finally, although these parameters should in principle act to smooth a surface, when the perturbation grows large enough, films can actually roughen, as discussed below.

I.2. Flow and Capillarity

For materials which can liquefy at the experimental temperatures and pressures under study, flow can act to cause long-distance transport of material. This is important for glasses especially, as the glass transition can occur well below appreciable sublimation temperatures.³¹⁹ Amorphous or crystalline materials which melt may also show viscous flow, but in those systems, sublimation tends to compete with melting because of the substantially higher vapor pressure at high temperature – see Appendix M.1.

Appendix I. Secondary Film Evolution Mechanisms

Most commonly in thin-film annealing, the effects of flow are visible (and disruptive) when the film dewets from the substrate. This is due to an instability driven by unfavorable interaction between the film and substrate, which can be written mathematically in terms of the intermolecular interaction energy per area, ΔG , and film thickness h as $\frac{\partial^2 \Delta G}{\partial h^2} < 0$, that is, the system exhibits negative (unstable) concavity with change in thickness. Then, any void introduces a new method to minimize film energy: parting away from the substrate. The associated time scale, t_r , of perturbation growth through the film can be estimated from the energy driving the repulsion and the viscous force restraining flow:³⁵⁶

$$t_r = 12\mu\gamma \left[h_o^3 \left(\frac{\partial^2 \Delta G}{\partial h^2} \right)^2 \right]^{-1} \ln \left(\frac{h_o}{\delta} \right) \quad (14.57)$$

Here, h_o is the initial film thickness and δ is the film thickness perturbation size. The parameters μ , γ , and h_o are all tangibles that may be measured, and ΔG may be calculated given some knowledge of the system;³⁵⁶ however, the high temperatures and molecular diversity in organic semiconductors means that few cases have been measured, especially in the small-molecule class. The implications of this equation are that for film stability under annealing conditions, highly viscous and high-energy materials on exceedingly smooth substrates are favored. In reality, many of the organic materials used in this thesis are likely to be relatively low-energy owing to their lack of polar functional groups, and heating to crystallization temperatures reduces the film viscosity to the point that molecular motion becomes appreciable. The key is to reduce the interfacial energy between film and substrate or the δ/h_o ratio by cleaner substrates.

Appendix I. Secondary Film Evolution Mechanisms

Although challenging to measure in a thin-film geometry, the parameters which influence perturbation growth also influence the dewetting rate of the film once a defect site has nucleated. This domain growth rate is rather complex due to substrate slip conditions and various time-varying parameters,^{354,355,681,682,815,816} but basic insight is possible by observing the dewetting front velocity, given by⁸¹⁵

$$v(t) = \frac{1}{12\sqrt{2}} \frac{\gamma \theta_{ls}^3}{\mu \ln[c_A w(t)]} \quad (14.58)$$

Here, θ_{ls} is the liquid-solid contact angle, c_A is a constant related to the dynamic contact angle, and $w(t)$ is the time-varying width of the rim of accumulated liquid at the edge of the parting film. Note the energetic and dissipative effects present as γ/μ , identical to Eqn. 14.53. The contact angle may be converted using the Young-Laplace equation²⁵⁴

$$\gamma \cos \theta_{ls} = \gamma_{sv} - \gamma_{sl} \quad (14.59)$$

but this introduces the additional variables of the solid-vapor and solid-liquid surface energy γ_{sv} and γ_{sl} .

I.3. Sublimation and Deposition

At higher temperatures, the exponential dependence of vapor pressure on temperature can lead to significant sublimation from solids and evaporation from melts. In vacuum, this is strictly a material loss term, but in atmospheres which are significantly dense, the small molecular mean-free path allows for deposition from the localized vapor phase given suitable surface temperatures.

The primary observation of sublimation for this thesis was as a loss mechanism for

Appendix I. Secondary Film Evolution Mechanisms

films annealed on the purged heated microscope stage. The rubrene vapor eventually escaped the kinetic boundary layer and would be carried by the purge stream, often forming thin needle-like crystals on the coverslip where the purge gas would exit the system.

I.4. Diffusion: Surface and Bulk

The simplest and most common process for motion in these films is diffusion,^{319,335,420,422,427,429,433,814,817–820} with motion on the surface being considerably faster than that in bulk (> 6 orders of magnitude in some organic systems).³¹¹ In systems evolving at temperatures below the point where sublimation becomes appreciable,

The effects of surface motion on film evolution can easily be seen in thin films which are capped with a material which is less impacted by temperature, such as a metal or a high-T_g material. In the case of rubrene, capping with TPBi effectively eliminates crystal growth by forcing bulk diffusion to act as the crystal growth mechanism.

I.5. Surface Reactions and Adsorbates

As discussed in Chapter 4, rubrene films are very sensitive to air. In general, thin organic semiconducting films are often hygroscopic and thus susceptible to water adsorption and absorption. There are further issues with oxidation or photooxidation when the films are exposed to air and light. This is perhaps most commonly observed when the triplet of oxygen quenches exciton emission in thin films.

In this thesis, the main issues with air exposure were observed during initial experiments on the heated microscope stage (before installation of a nitrogen purge) when rubrene films would oxidize, exacerbated by the combination of air, light, and heat. This

Appendix I. Secondary Film Evolution Mechanisms

produced thin, ragged crystals which would rarely cover the film surface.

Appendix J. Selected Organic Molecule Crystal Lattice Parameters

J.1. OLED Materials

Molecule	Crystal Type	Space Group	a (Å)	b (Å)	c (Å)	α (°)	β (°)	γ (°)	Reference(s)
α-Alq₃[†]	Triclinic	P-1	6.245	12.871	14.737	69.9	89.47	82.52	821
δ-Alq₃[†]	Triclinic	P-1	6.181	13.268	14.43	66.06	88.56	84.03	821
β-Alq₃[‡]	Triclinic	P-1	8.443	10.252	13.171	71.42	82.94	89.74	821
ϵ-Alq₃[‡]	Triclinic	P-1	13.519	15.855	18.711	95.494	109.774	114.627	821
BCP	Monoclinic	C2/c	16.275	10.692	11.467	90	109.198	90	138
BPhen	Orthorhombic	C2cb	7.253	10.810	21.14	90	90	90	138
NPD	Triclinic	P-1	10.3077	11.345	14.478	82.229	77.657	75.562	822
TPBi[§]	Monoclinic	P2 ₁ /c	11.253	18.692	17.763	90	101.58	90	290
TPD	Monoclinic	P2 ₁	14.447	11.0153	17.803	90	90.602	90	823
TPD	Orthorhombic	P2 ₁ 2 ₁ 2 ₁	11.068	14.472	17.82	90	90	90	824
mCP	Orthorhombic	P2 ₁ 2 ₁ 2 ₁	9.0744	12.5038	19.0417	90	90	90	5

[†]Facial isomer

[‡]Meridional Isomer

[§]Solvate with methanol

Appendix J. Selected Organic Molecule Crystal Lattice Parameters

J.2. Acenes and Acene Cores

Molecule	Crystal Type	Space Group	a (Å)	b (Å)	c (Å)	α (°)	β (°)	γ (°)	Reference(s)
Rubrene	Monoclinic	P2(1)/c	8.739	10.125	15.635	90	90.98	90	612
Rubrene	Orthorhombic	Cmca	26.86	7.193	14.433	90	90	90	482
Rubrene	Triclinic	P-1	7.02	8.543	11.948	93.04	105.58	96.28	612
Rubrene†	Triclinic	P-1	14.239	6.774	11.281	81.26	100.38	101.77	564
F-Rubrene	Orthorhombic	Pnma	7.116	31.179	14.208	90	90	90	825
Fm-Rubrene	Orthorhombic	Pbcm	7.144	14.051	7.144	90	90	90	825
Fdm-Rubrene	Orthorhombic	Pbcm	7.532	14.634	32.424	90	90	90	825
m-Rubrene	Orthorhombic	Pna2(1)	15.205	13.901	14.31	90	90	90	825
mm-Rubrene	Monoclinic	C2/c	41.257	10.146	24.038	90	96.739	90	825
mdm-Rubrene	Monoclinic	P2(1)	12.749	9.414	14.503	90	99.576	90	825
Pentacene	Triclinic	P-1	7.93	6.14	16.03	101.9	112.6	85.8	826
Perfluoropentacene‡	Monoclinic	P21/c	15.51	4.49	11.449	90	91.567	90	827
Perfluoropentacene§	Monoclinic	-	15.76	4.51	11.48	90	90.4	90	828
Tetracene	Triclinic	P-1	7.98	6.14	13.57	101.3	113.2	87.5	826
Tetracene	Triclinic	P-1	6.06	7.84	13.01	77.13	72.12	85.79	829
5-chlorotetracene	Monoclinic	P21/c	10.775	14.371	8.067	90	93.868	90	244
5,11-chlorotetracene	Triclinic	P-1	3.861	8.664	19.686	93.37	92.02	99.47	244
5-bromotetracene	Monoclinic	P21/c	10.853	14.396	8.177	90	93.091	90	244
Anthracene	Monoclinic	P2 ₁ /a	8.561	6.036	11.163	90	124.42	90	830

†High-pressure (7.39 GPa) phase

‡Bulk, single-crystal phase

§Thin-film phase

Appendix J. Selected Organic Molecule Crystal Lattice Parameters

J.3. Phthalocyanines and SubPhthalocyanines

Molecule	Crystal Type	Space Group	a (Å)	b (Å)	c (Å)	α (°)	β (°)	γ (°)	Reference(s)
α -CoPc	Monoclinic		25.88	3.75	24.08	90	90.2	90	831
β -CoPc	Monoclinic		19.352	4.773	14.542	90	120.82	90	831
α -CuPc	Triclinic	P-1	12.886	3.769	12.061	96.22	90.62	90.32	832
β -CuPc	Monoclinic	P2 ₁ /a	19.407	4.79	1.639	90	120	90	833
γ -CuPc	Monoclinic	C2/n	26.33	3.81	23.71	90	94.3	90	834
ε -CuPc	Monoclinic	P2 ₁ /c	5	23.071	10.571	90	96.02	90	834
α -H ₂ Pc	Monoclinic	C2/n	26.124	3.801	23.889	90	94.182	90	835
β -H ₂ Pc	Monoclinic	P2 ₁ /n	14.796	4.733	17.357	90	104.32	90	836
χ -H ₂ Pc	Orthorhombic	Pna2 ₁	21.01	4.915	23.11	90	90	90	836
NiPc	Monoclinic	P2 ₁ /a	19.9	4.71	14.9	90	121.9	90	837
PbPc	Monoclinic		25.48	25.48	3.73	90	~90	90	831
PbPc	Triclinic		13.123	16.131	12.889	94.22	96.20	114.19	831
PtPc	Monoclinic	P2 ₁ /a	23.9	3.81	16.9	90	129.6	90	837
β -ZnPc	Monoclinic								
Cl-SubPc	Orthorhombic	Pnma	12.123	14.824	10.378	90	90	90	697
F-SubPc	Orthorhombic	Pnma	12.111	14.321	10.3258	90	90	90	838
Br-SubPc	Orthorhombic	Pnma	12.016	15.061	10.406	90	90	90	838

Appendix J. Selected Organic Molecule Crystal Lattice Parameters

J.4. Fullerenes

Molecule	Crystal Type	Space Group	a (Å)	b (Å)	c (Å)	α (°)	β (°)	γ (°)	Reference(s)
C ₆₀ (>249K)	Cubic, Simple	Fm-3	14.052	14.052	14.052	90	90	90	839
C ₆₀ (<249K)	Cubic, Simple	Pa-3	14.04	14.04	14.04	90	90	90	840
C ₇₀ (~290K)†	Cubic, FCC		14.93	14.93	14.93	90	90	90	841
C ₇₀ (~290K)	Hexagonal	P6 ₃ /mmc	10.56	10.56	17.18	90	90	120	841
C ₇₀ (~290K)	Hexagonal	P6 ₃ /mmc	10.11	10.11	18.58	90	90	120	841
C ₇₀ (220K)	Hexagonal	P6 ₃ /mmc	20.04	20.04	18.53	90	90	120	841
C ₇₀ (100K)	Monoclinic		19.96	18.51	19.96	90	120	90	841

†Dominant phase in thin film

J.5. Perylenes and Related

Molecule	Crystal Type	Space Group	a (Å)	b (Å)	c (Å)	α (°)	β (°)	γ (°)	Reference(s)
Perylene†	Orthorhombic		20.7	19.3	3.4	90	90	90	842
Perylene	Monoclinic	P2 ₁ /c							
Pyrene	Monoclinic	P2 ₁ /a	13.64	9.25	8.47	90	100.28	90	843
PTCDA	Monoclinic		3.74	11.96	17.34	90	98.8	90	497
PTCDA	Monoclinic		3.87	19.3	10.77	90	83.6	90	497
PTCDI	Monoclinic	P2 ₁ /c	4.871	14.685	11.806	90	113.003	90	844
PTCDI	Monoclinic	P2 ₁ /n	4.879	14.678	10.874	90	91.117	90	844
PTCBI	Monoclinic		4.749	8.88	28.24	90	100.16	90	171
NTCDA	Monoclinic	P2/c	7.867	5.305	12.574	90	72.73	90	171

†Thin-film polymorph grown here on Cu (110)

Appendix J. Selected Organic Molecule Crystal Lattice Parameters

J.6. Miscellaneous Organics

Molecule	Crystal Type	Space Group	a (Å)	b (Å)	c (Å)	α (°)	β (°)	γ (°)	Reference(s)
DTDCTB	Monoclinic	P2 ₁ /c	7.679	16.934	18.359	90	92.984	90	845
DTDCPB	Monoclinic	P2 ₁ /c	8.996	13.099	20.889	90	93.997	90	845
BP2T	Monoclinic	P2 ₁ /c	5.708	7.604	52.869	90	97.14	90	846
Sexithiophene	Monoclinic	P2 ₁ /n	44.708	7.851	6.029	90	90.76	90	847

J.7. Common Substrate Materials

Material	Crystal Type	Space Group	a (Å)	b (Å)	c (Å)	α (°)	β (°)	γ (°)	Reference(s)
Silicon	Cubic	Fd-3m	5.43107	5.43107	5.43107	90	90	90	848,849
ITO	Cubic		10.22	10.22	10.22	90	90	90	850
ITO	Cubic	Ia ₃	10.118	10.118	10.118	90	90	90	851
In₂O₃	Cubic	I2 ₁ 3	10.12	10.12	10.12	90	90	90	852
Quartz	Hexagonal	P3 ₂ 1	4.9134	4.9134	5.4052	60	60	90	853,854

Appendix K. Selected Organic Semiconductor Properties

Material	HOMO (eV)	LUMO (eV)	T ₁ (eV)	E _{opt} (eV)	μ_h (cm ² /Vs)	μ_e (cm ² /Vs)	T _g (°C)	T _o (°C)	T _c (°C)	T _m (°C)	L _D (nm)	τ (ns)	η_{PL} (%)
3TPYMB	6.8 ⁸⁵⁵	3.3 ⁸⁵⁵	2.95										
4p-NPD													
AQ-1200 (Plexcore)	5.1-5.2	-	-	-									
α -6T	5.3 ¹⁵⁰	2.57 ¹⁵⁰		2.43 ¹⁵⁰	0.03 ³⁴⁹					290			
Ag	4.6	-	-							962			
Al	4.3	-	-							660			
Alq ₃	5.65 ¹⁵⁰	1.96 ¹⁵⁰	2 ⁸⁵⁶	2.75 ¹⁵⁰	2E-8 ³⁴⁹	5E-5 ³⁴⁹	175			>300			
Anthracene	5.70 ¹⁵⁰	1.7 ¹⁵⁰		3.25 ¹⁵⁰						240			
Au	5.1 ⁷³⁵	-	-	-			-			1064			
BCP	6.5 ¹⁵⁰	1.56 ¹⁵⁰	2.5 ⁸⁵⁶	3.43 ¹⁵⁰						279-283			
BPhen	6.4 ⁸⁵⁷	3.0 ⁸⁵⁷	2.5							130			
BP2T	5.3 ⁷⁵⁴	2.8 ⁷⁵⁴		0.66 ⁵²⁷									
C ₆₀	6.17 ¹⁵⁰	3.5 ¹⁵⁰ - 3.7 ¹⁹⁰		1.95 ¹⁵⁰	2.8E-7 ¹⁰⁰	3.3E-2 ¹⁰⁰							
C ₇₀	6.3 ⁶⁹¹	4.5											
CBP	6.1 ¹⁵⁰	1.9 ¹⁵⁰	2.6 ⁸⁵⁶	3.46 ¹⁵⁰			62			281-285	16.8 ³⁶⁵	0.7 ³⁶⁵	
CuPc	4.82 ¹⁵⁰	2.65 ¹⁵⁰		1.80 ¹⁵⁰	0.01-1 ³⁴⁹								
DPDCPB	5.50 ⁸⁴⁵	3.36 ⁸⁴⁵											
DPDCTB	5.35 ⁸⁴⁵	3.44 ⁸⁴⁵											
DTDCPB	5.43 ⁸⁴⁵	3.35 ⁸⁴⁵											
DTDCTB	5.30 ⁸⁴⁵	3.44 ⁸⁴⁵											
HATCN	7.5	4.4											

Appendix K. Selected Organic Semiconductor Properties

Material	HOMO (eV)	LUMO (eV)	T1 (eV)	E _{opt} (eV)	μ _h (cm ² /Vs)	μ _e (cm ² /Vs)	T _g (°C)	T _o (°C)	T _c (°C)	T _m (°C)	L _D (nm)	τ (ns)	η _{PL} (%)
Ir(ppy)₃	5.1 ⁸⁵⁸	2.6 ⁸⁵⁸	2.4 ⁸⁵⁶									800 ⁸⁵⁶	
ITO	4.5- 4.75 ⁸⁵⁹	-									1500+		
mCP	5.9	2.4					65 ⁸⁶⁰						
MoO_x	6.4	-									795		
NPD	5.30 ¹⁵⁰ - 5.48 ⁵⁷	1.52 ¹⁵⁰ - 2.3 ⁸⁵⁷		3.12 ¹⁵⁰	6.1E-5 ³⁴⁹		95			~220 ^{\$}	279-283	5.1 ³⁶⁵	3.5 ³⁶⁵
NTCDA	7.97 ¹⁵⁰	4.02 ¹⁵⁰		3.54 ¹⁵⁰									
Pentacene	4.85 ¹⁵⁰ - 5.2 ¹⁹⁰	2.8 ¹⁵⁰ - 3.0 ¹⁹⁰		2.06 ¹⁵⁰							>300		
Pentacene-X	5.0 ⁵⁴	3.2 ⁵⁴		0.75 ⁵²⁷									
PTCBI	6.2 ⁷²⁵	4.3 ⁷²⁵									>600		
PTCDA	6.95 ¹⁵⁰	4.10 ¹⁵⁰		2.20 ¹⁵⁰								10.4 ³⁶⁵	3.2 ³⁶⁵
PTCDI	6.2 ⁸⁶¹	4.4 ⁸⁶¹									>300		
Rubrene-A	5.3 ⁷¹³	2.7 ⁷³⁶					150?			110 ^{\$} - 130 ⁴⁵¹	330- 335 ^{\$}	6.4 ⁷¹⁶	9.1 ⁷¹⁶
Rubrene-X	4.85 ⁷¹³	3.15 ⁷³⁵		20 ⁵⁹⁵	-						330- 335 ^{\$}	5000 ¹⁹⁵	1000 ¹⁹⁵
SubPc-Cl	5.57 ⁷⁰⁵ - 5.6 ⁶⁹¹	3.2 ¹⁹⁰ - 3.6 ⁶⁹¹		4.5E-8 ¹⁰⁰	5.2E- 10 ¹⁰⁰						>375	10.7 ¹⁹⁸	0.5 ¹⁹⁸
SubNc-Cl	5.35 ⁷⁰⁵ - 5.5 ²³⁷	3.47 ⁷⁰⁵ - 3.5 ²³⁷											1.0 ¹⁹⁸
TCTA	5.7	2.4	2.85 ⁸⁶²	3.46 ⁸⁶²			151 ⁸⁶²			237 ⁸⁶²	268 ⁸⁶²		
Tetracene-X	5.1 ¹⁵⁰	1.8 ¹⁵⁰		2.51 ¹⁵⁰						357	5400 ¹⁴⁶	62500 ¹⁴⁶	

Appendix K. Selected Organic Semiconductor Properties

Material	HOMO (eV)	LUMO (eV)	T1 (eV)	E _{opt} (eV)	μ_h (cm ² /Vs)	μ_e (cm ² /Vs)	T _g (°C)	T _o (°C)	T _c (°C)	T _m (°C)	L _D (nm)	τ (ns)	η_{PL} (%)
TPBi	6.1	2.8				0.25- 1.7E-5 ³⁴⁹	122- 124 ¹²		~210	272-277			
TPD	5.5	2.3	2.3 ⁸⁵⁶		8.7E-5 ³⁴⁹		57 [†] - 60 ²²⁸	75 ^{†228}		175-177			
UGH1							26 ⁸⁶⁰						
UGH2	7.2 ¹⁹⁰	2.8 ¹⁹⁰	3.87 ⁸⁶³				< 50 ⁸⁶⁴						
ZnPc	5.28 ¹⁵⁰	3.3 ¹⁵⁰		1.82 ¹⁵⁰									

Values which are not cited are from a material vendor, such as Sigma Aldrich

† Thin-film measurements

§ Estimates or measurements from this work

Appendix L. Inventions

Completion of this thesis was made possible through considerable innovation on simple tools. All devices in this appendix were designed and built by the author, in some cases with inspiration from professional models. In the hope that these designs may help others, they are freely offered, but are to be used at your own risk with no liability of the author.

L.1. Heated Microscope Stage

A heated microscope stage is useful for characterizing properties which are temperature-sensitive and induce optically resolvable changes on the microscale. Typical professional designs cost \$10,000-20,000 USD depending on added features. For the purposes of this thesis, there were a few primary concerns, some of which are challenging to address even with skillfully engineered professional devices:

1. Rapid access to sample compartment
2. Inert sample atmosphere
3. Temperature range 25-300 °C
4. Compatibility with “normal” working distance objectives with or without coverslip correction
5. Simple mounting and removal on a standard microscope stage with 1” vertical travel below standard height
6. Inexpensive design for stage, temperature control, and power supply

All of these criteria were met in the final design.

The key component of this design is the heater element, which is an aluminum block with a serpentine channel milled or cut to hold insulated 31 AWG nichrome wire ($8 \Omega/\text{ft}$ purchased from Ultimachine), as shown in Figure 14.26. The wire is glued in place with

Appendix L. Inventions

Omega® CC High Temperature Cement, which is electrically insulating after drying.

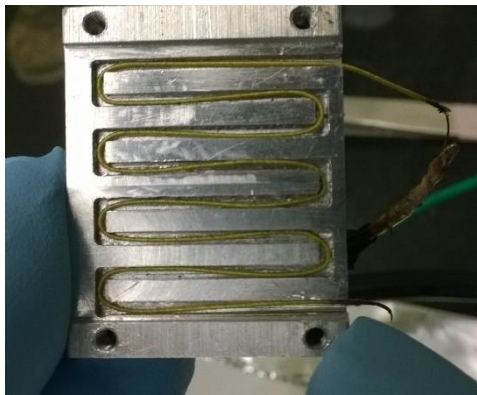


Figure 14.26. Heater element, with yellow mm standard glass slide with clips held on by nichrome wire inset into aluminum.

Nichrome wire solders well to copper wire with silver solder and flux, but melts if heated too much. This wire may be insulated with quartz wool or fiberglass sheathing to prevent shorting to the chassis. The heater itself is held onto a 3" x 1"x 1

screws in the tapped holes of Figure 14.26, and a thermocouple is inserted into a hole drilled into the side of the aluminum block. Mounting on a glass slide is inexpensive, standard (*i.e.* easy to replace if broken), and thermally insulating, increasing the achievable temperature per input power. For this design, a calculated diffusive heat load of 12 W for a heater at 400 °C was doubled, requiring 5-6 Ω of wire at 12 VDC, or about 7-8" of 31 AWG nichrome, achieved with 8 passes slightly under 1" wide. In reality, these calculations omitted flow of gas over the heater (an inert environment was not an original design criterion), so the heating element reaches ~300 °C with purge but heats fairly quickly (~50 °C/min without purge, ~25-35 °C/min with purge).

The heater is contained within a housing which holds the microscope slide firmly and also forms a purged sample compartment (Figure 14.27). There are a number of important features to this housing which address the points laid out at the beginning of the section. Fast access to the sample compartment is accomplished by a sliding lid, which slides along a u-shaped track milled into the stainless steel lid, visible from the back. This forms a

Appendix L. Inventions

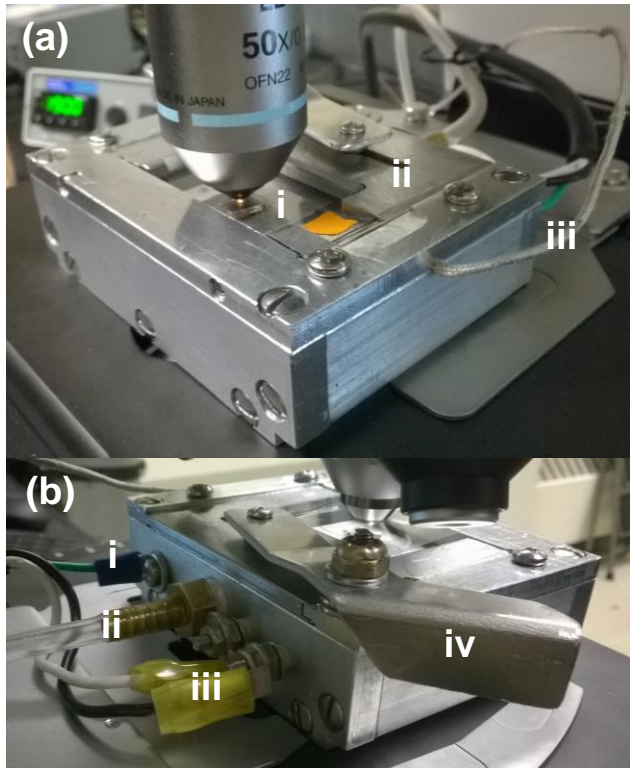


Figure 14.27. Completed heater from (a) the front, showing (i) sample compartment, (ii) sliding door, (iii) thermocouple wire, and (b) from the back, with (i) ground wire, (ii) nitrogen purge source, (iii) 12 VDC power input, and (iv) spring-loaded actuating lever for the sliding door.

reasonably air-tight seal which allows small amounts of the purge gas to escape. All other metal components are aluminum. Viewing the sample is accomplished with reflected light through a cover slip which fits into a recess sized for a standard 14 x 25 mm coverslip, protecting the objectives and allowing easy replacement when material inevitably sublimes onto it. A glass slide company provided samples of 20 and 30 μm glass which work well even for 500x magnification with

non-corrected objectives. The housing is sized to be 2" x 3" on the bottom surface, fitting into the space of two standard microscope slides that many microscopes are equipped for. Furthermore, the body height is less than 1", allowing for simple insertion of the heated stage directly onto the microscope stage. The chassis is grounded and has two bolts acting as feed-throughs to power the heater, insulated with ceramic tubular washers from the housing. Careful inspection of Figure 14.27a shows four screws located on the cover that seem to have no purpose. These screws fill holes that allow access to adjustment bolts which support the clamps on the microscope slide on which the heater sits, allowing the

Appendix L. Inventions

entire heater surface to be leveled with respect to the microscope stage so that the entire field is in focus and adjusted for sample thickness so that the sample surface is within the objective working distance of the coverslip (only critical for 500x, 0.75 mm).

The design was verified by measuring the temperature distribution across the surface with a purge flow (Figure 14.28). The temperature uniformity is better than 2 °C across the sample placement area, and better than 1 °C across a typical samples size of 0.25" x 0.25". Considering the purge gas originates from the top of the figure and the nichrome leads exit on the right, this uniformity is actually quite good and adequate for the work in this thesis.

The power supply was chosen as 12 VDC for safety and to ease heater design considerations (insulation, resistance, grounding, etc.). An ideal power supply at 12 VDC is a computer power supply unit (PSU), which are typically capable of supplying 100-500 W on 12 V, 5 V, and 3.3 V lines (color coded yellow, red, and orange respectively on most PSUs) with high reliability and low cost – the supply used in this thesis was scrapped out of an old desktop computer for free. Unfortunately, on most PSUs these voltages with respect to ground (black) are mutually exclusive and cannot be combined to produce *e.g.*, 9 and 7 V sources at any significant power output. In addition, PSUs have ground-fault and short-circuit protection which prevent personal shock and equipment damage. Modification of a PSU for a benchtop

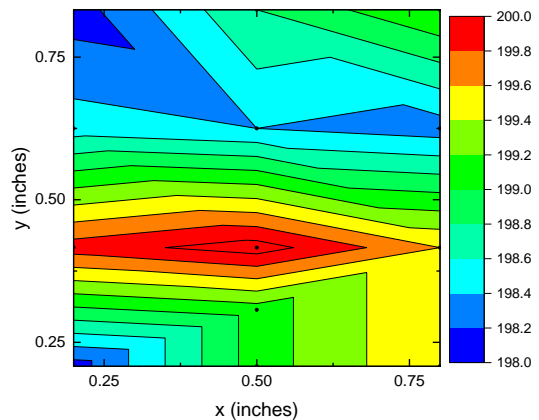


Figure 14.28. Temperature over the sample viewing area when set at 200 °C. Colorbar in °C.

Appendix L. Inventions

supply requires finding the on/off switch wire (green on most PSUs) and connecting it to ground to turn the supply on, recommended with a switch. Many supplies require a minimum electrical load in order to function smoothly, but this is not an issue when used with a resistive heater over a few watts. If desired, the output can be used in parallel to light an LED to observe the heater duty cycle. Note again: these details are provided for use at your own risk - only work inside of electronics if you are confident in what you are doing.

The temperature controller used in this work is an Omega Engineering CSi-32 benchtop controller purchased new for ~\$550. This model reads in K-type thermocouples and independently pulse-width modulates two 120 VAC outlets according to tunable PID control, one of which is used to power the PSU. With correct tuning, this controller is able to maintain the stage temperature to within ± 0.2 °C. Initial testing used a Variac with a thermocouple reader to manually control temperature, which was functional but time-consuming.

L.2. Gradient Heater

Considerable work has demonstrated the desirability of modulating substrate temperature during deposition in glasses and epitaxial growth.^{109,228,334,342,484} In exploring the available parameter space for single films and heterojunctions, high-throughput techniques are essential to quickly identify viable routes.

The Ediger group at the University of Wisconsin developed one such route, wherein a substrate is actively cooled at one end and heated at another, resulting in a continuous gradient of temperatures along the substrate during deposition.^{227,228} This approach uses

Appendix L. Inventions

liquid nitrogen offset with a resistive heater to cool, and a resistive heater to heat. While quite clever and effective, this technique requires liquid nitrogen and substrates which are capable of spanning the gap between the two heating ends. Adding liquid nitrogen to a deposition system is non-trivial, and many substrates of interest are considerably smaller than a couple inches long, requiring some modification of this concept.

The design used in this work features a heating element at the end of a steel platform which both conducts heat and supports the substrates, connected to a massive copper block which passively cools the other end of the steel platform (Figure 14.29). At a 200 °C

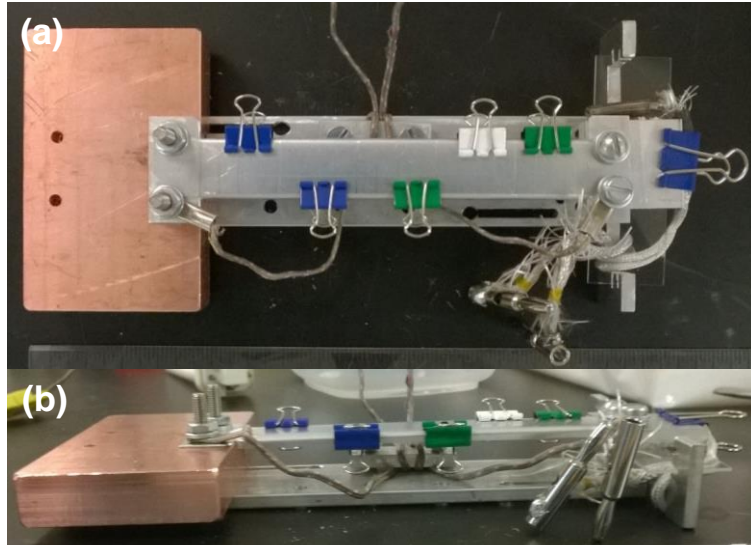


Figure 14.29. Gradient heater as viewed from the (a) top and (b) side.

Figure 14.29. Gradient heater as viewed from the (a) top and (b) side. differential, this block warms less than 5 °C over an entire 45 minute deposition process. Substrates are clipped to the gradient platform using binder clips, and the entire assembly mounts to the substrate chuck with bolts through holes drilled into the base. Power is supplied through banana clips insulated with fiberglass, and two K-type surface thermocouples enable monitoring of the heater and copper block surface temperature, the temperatures of interest. The same power supply and temperature controller from the microscope stage heater is used here, with the chamber chassis grounded to the power supply ground wire *via* alligator clip.

Appendix L. Inventions

This design (without the glass slide support) is fairly efficient and can reach 275 °C in

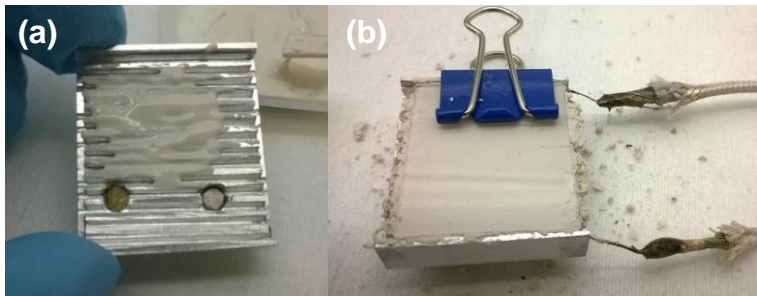


Figure 14.30. Gradient heating element (a) as cement is applied and (b) with a glass slide piece clipped on to protect the cement.

a vacuum environment with a 10 W heating element, made with ~20" of 31 AWG insulated nichrome inset into high-temperature cement, as

with the microscope stage heater (Figure 14.30). The heater design was simplified somewhat by simply cutting slits for the nichrome wire with a hack saw, followed by milling out the edges to recess the wire before cementing. Surprisingly, this cement is vacuum-safe at least to 10^{-7} torr and does not form virtual leaks, even with a slide clipped over it. Care was also taken to avoid virtual leaks in the framing by venting any blind screw taps.

This design could be modified to include clips or anchors on the copper block and heater to clip a substrate directly between them if temperature uniformity is a concern. The type and size of material used as a substrate would change the time required to reasonably approach equilibrium, which for this design with a 5" x ¾" x 1/16" bar is approximately 30-40 minutes for heating from 25 °C to 250 °C.

L.3. Heated Ellipsometry Stage

Ellipsometry provides an extremely accurate method to measure thickness and optical properties of thin films. These properties change with temperature and can be used to track morphological or chemical changes within the film as it is heated or cooled. Examples of

Appendix L. Inventions

such behaviors are reactions, polymorphic interconversion, melting/freezing, glass and associated transitions, diffusion, etc., all of which have implications in organic semiconducting materials. Professional designs are available, but cost >\$15,000 USD.

This design mimics the microscope stage heater in many ways: there is a heating element supported by a glass slide inside of a purged aluminum housing, but differs in some important ways (Figure 14.31). The ellipsometer used in this work has adjustments for angle and height alignment, so levelling screws are not necessary. The glass slide is simply mounted directly onto a shelf milled into the aluminum housing under straps of

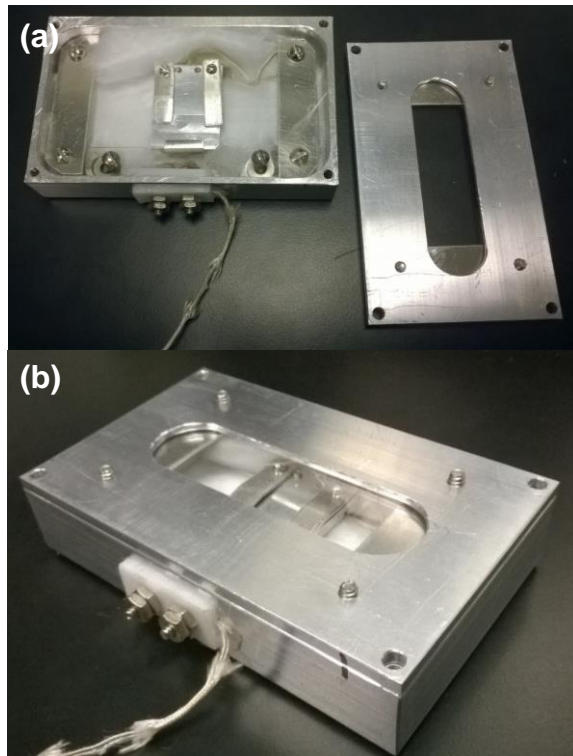


Figure 14.31. Heated ellipsometer stage (a) with cover off and (b) assembled.

sheet aluminum. The viewing window is similarly a standard glass slide held into a milled slot by two other aluminum straps. Instead of using tubular ceramic washers as electrical feed-throughs, two pieces of Teflon (melting point ~340 °C) were sandwiched around a slot milled in the housing side, then bolted together, with the bolts also acting as electrical conductors. The ellipsometer stage is vertical, necessitating bolting the heater on rather

than sitting under gravity, requiring two mounting holes in the housing and clips on the sample stage. Temperature changes (temperature ramp rates) are important for sample

Appendix L. Inventions

characterization, so the heater was milled very thin (~1/8" thick before slotting) to minimize the thermal inertia. This makes PID tuning considerably more sensitive, but with a $6\ \Omega$ heater, this design can controllably change at over $4\text{ }^{\circ}\text{C}/\text{min}$ at 5 VDC (the CSi-32 ramps up, but not down, in temperature). At 12 VDC, this heating rate can of course be much faster.

Examples of raw ellipsometric data collected with this stage are given in Figure 14.32. As the film is heated and cooled below its onset temperature, the transitions are reversible, but just before reaching the onset temperature there is a pronounced change in Ψ and Δ and the film properties are permanently altered.

Fitting this data can yield useful properties including thickness, index of refraction, and orientation. When fitting data collected with a cover, "window effects" due to the window strain birefringence must be accounted for (in WVASE32, right-click Model -> Options -> Window Effects). Examples of such data fitted from those in Figure 14.32 are shown in Figure 14.33. Note that the thickness and index of the film change reversibly below the onset temperature, as suggested by the raw data. Measurement of thickness also

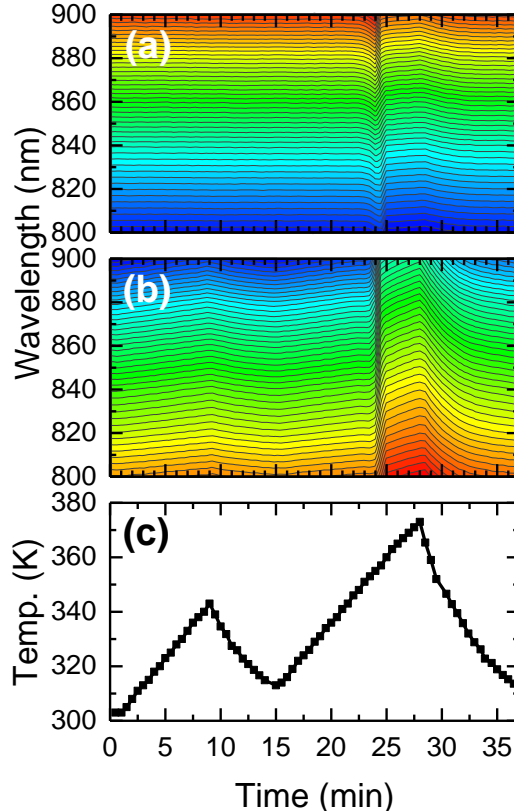


Figure 14.32. Raw ellipsometric data (a) Ψ and (b) Δ collected on a sample of TPD over time, with (c) temperature profile of $4\text{ }^{\circ}\text{C}/\text{min}$ heating rate and average convective cooling rate of $\sim 7\text{ }^{\circ}\text{C}/\text{min}$. Data collected without cover in ambient.

Appendix L. Inventions

allows for the determination of the thermal expansion coefficient of the film with

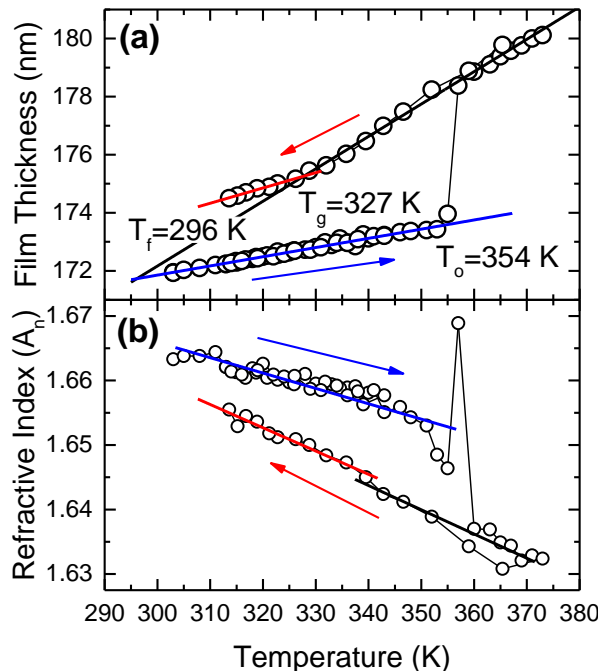


Figure 14.33. Fitted parameters for a TPD film on silicon: (a) thickness and (b) static index of refraction from the Cauchy model A_n parameter.

temperature, which changes depending on the phase (dense glass, supercooled liquid, ordinary glass). This allows for determination of the fictive, onset, and glass transition temperatures discussed in Section 3.1.3. For this film, T_g is 327 K, which compares favorably with the previously measured value of 330 K in thin film and 333 K in bulk.^{228,346} There is

some hysteresis upon cooling the melt, but this is anticipated to be due to

irregular cooling rates. Interestingly, the index changes significantly upon initial melting, with a lower index corresponding to but a lower density, but is essentially unaffected by vitrification. These measures may be used to correlate film density to device performance.

Appendix M. High School Mentor Projects

I was lucky enough to work with talented students from Breck School, Minneapolis MN for two summers. The Melt Crystallization project was with students Wolfgang Ofstedahl and Easton McChesney in summer 2014, co-lead with Nathan Morgan. The Organic Lasers project was with students Sung-Won Huh and Jiaheng (Julien) He in summer 2016, co-lead with Kyle Hershey and John Bangsund.

M.1. Melt Crystallization of Anthracene

Melt crystallization of organic semiconductors is challenging because organic liquids tend not to wet inorganic substrates well in the thin films necessary for electronic devices.^{535,549} Furthermore, in small molecules like anthracene, the appreciable vapor pressure of the melt causes substantial evaporation which competes with crystallization processes in reusable open ampules and flat substrates.

A solution to this is to use capillary action to pull the organic melt into a thin slot between solid materials, the velocity u of which depends on the liquid surface energy γ , dynamic viscosity μ , slot height h , and advancing contact angle θ_c according to

$$u \propto \frac{hy}{\mu L} \cos(\theta_c) \quad (14.60)$$

As demonstrated by Kena Cohen *et al.*,^{541,542} this technique works well for creating well-defined crystalline microcavities between highly planar substrates separated by a controlled thickness, but is relatively wasteful of material. In a field where typical materials cost \$100-1000 per gram, conservation is desirable. What is necessary then is a capillary device with a small reservoir for material.

Appendix M. High School Mentor Projects

The device used in this study achieves this using two glass or quartz slides held in contact, with the top slide having a hole bored into it (Figure 14.34a). This is accomplished with a metal rod of the desired hole diameter pressed against the substrate with lapping compound (abrasive) while being spun. This method has yields of ~75 % for glass and slightly lower for quartz from slide breakage during boring. These slides are held in contact within an aluminum block with bolt-on cover, with a thermocouple well drilled in through the side of the block (Figure 14.34b). In this design, it is important

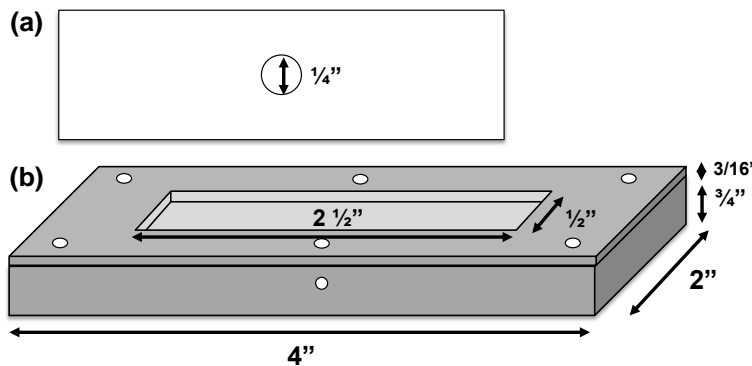


Figure 14.34. Diagrams of (a) glass slides and (b) melt crystallization apparatus used in this work.

to allow enough space in all dimensions for slide expansion, else the slides will crack upon heating from the dissimilar thermal expansion coefficients of aluminum and glass. In a typical experiment, the slides are gently bolted into the holder, then the block is placed onto a hotplate. The block may be insulated with quartz wool, etc. to achieve a desired cooling rate. The system is heated to above the melting point of anthracene (~240 °C) and a measured mass of anthracene powder is dropped into the glass slide hole, where it melts and wicks between the slides (~1-2 min). The system is then cooled to room temperature, where the slides are removed and excess anthracene is cleaned from the aluminum holder.

Crystals grown between glass slides often fall into one of three morphologies, as shown in Figure 14.35. Dendritic polycrystalline growth (Figure 14.35a) is often observed near

Appendix M. High School Mentor Projects

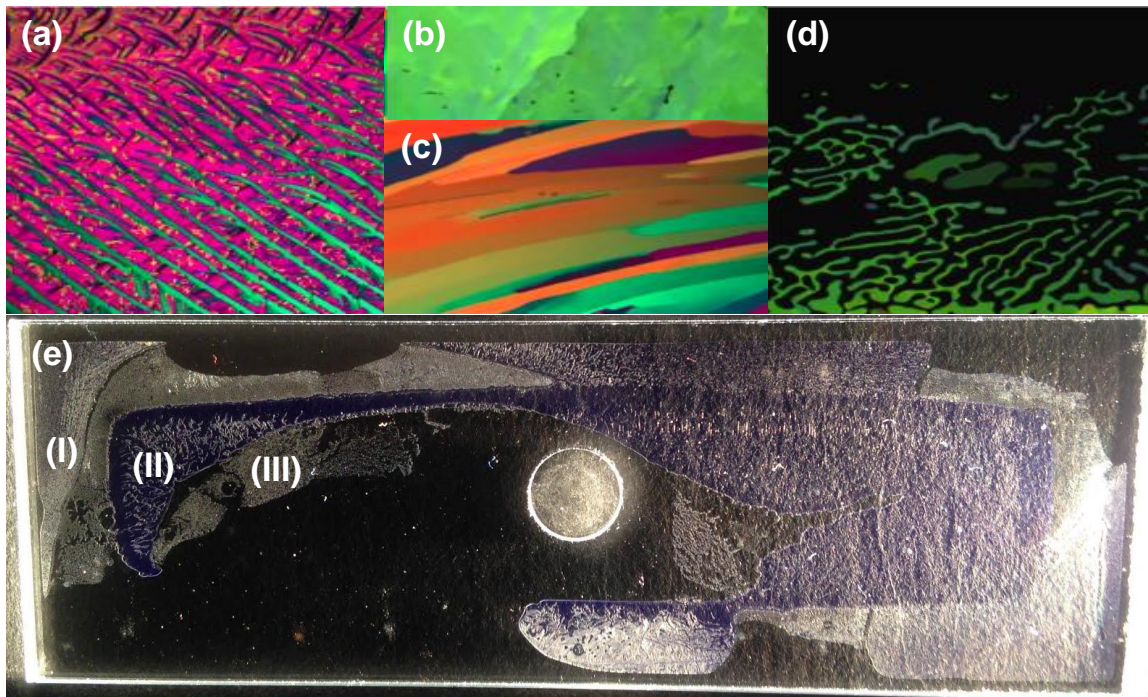


Figure 14.35. Different melt-grown anthracene crystal morphologies (a) dendritic polycrystal, (b)-(c) single crystal, (d) dewetted. All polarized optical micrographs are 2.94 mm wide. (e) photograph of slides post-growth, showing regions that correspond to (I) dendritic polycrystal, (II) single crystal, and (III) dewetted.

the slide edges, beneath the aluminum covering, with single-crystal growth (Figure 14.35b-c) just inside the aluminum edge and dewetted, depleted crystals (Figure 14.35d) around the central hole and near the outer edges. An explanation for this morphology relies on temperature, cooling rate, and thickness differences across the slide. The slide temperature where it is exposed beneath the aluminum top plate is likely cooler than that underneath, so when the anthracene powder melts in the center hole, it is well above the melting point at the edges. The Marangoni effect causes continual flow from colder to hotter regions (surface tension imbalance), resulting in flow towards the edges until the melt viscosity becomes high enough to slow flow. This depletes regions near the center hole, leaving behind immobilized, uneven tendrils of dewetted material which may further sublime.

Appendix M. High School Mentor Projects

Since the glass slides are macroscopically wavy on the μm length scale, there are substantial thickness variations which cause material to be depleted faster from thick areas or not wet at all through disruption of the film continuity across the slide gap. Variations between slides and clamping pressures give variation in material placement within the slides. Material which does occupy regions between the slides cools below the melt temperature soonest and slowest (early in the cooling process) in the exposed middle with a thermal gradient towards the edges. This gives favorable conditions for directional solidification, yielding large single-crystalline regions and parallel crystalline stripes parallel to the temperature gradient, perpendicular to the slide edges. Beneath the aluminum cover, it is possible the material is incubated while the inner slide regions crystallize, then cooled relatively quickly below the melting point. A faster cooling rate would give this diffusion-limited dendrite growth.

Perhaps not surprisingly, the herringbone-structured anthracene crystals (Figure 14.36a-b) stand with the long molecular axis away from the substrate as shown in Figure 14.36c-d, similar to what is observed in other acenes. The crystals formed are fairly high quality, as judged by the peak width of the pattern in Figure 14.36c.

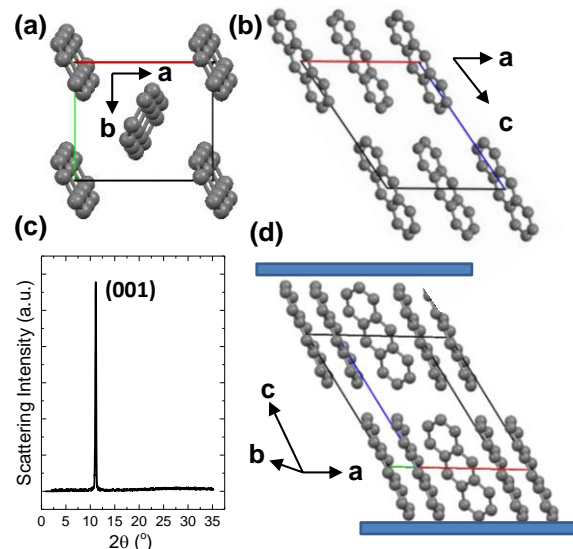
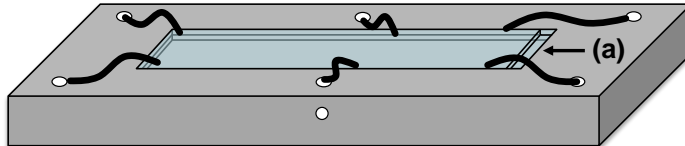


Figure 14.36. (a)-(b) Crystal structure of anthracene, with (c) x-ray scattering with a $\text{Cu } K_{\alpha}$ source and (d) inferred orientation of the unit cell between glass slides

Appendix M. High School Mentor Projects

There are a number of conclusions and recommendations from this work. First, capillary action remains a highly effective method of producing thin crystalline organic films. In all cases with small gaps between slides, anthracene successfully infiltrated the gap. Second, using a slide with a hole to feed material rather than around the edges resulted in significant material savings, proving a successful design concept. A similar effect could likely be achieved by having a trimmed slide offset on top of a full-length slide, placing the material on the long slide at the intersection of the two (Figure 14.37). The two primary recommendations from this work center around more precise temperature and gap control. As evidenced by Figure 14.35e, having slides beneath the aluminum top plate changes crystallization behavior, generally for the worse. Greater temperature uniformity would help control crystallization, and this could be achieved with either no metal top (only clips) or a solid metal top with milled



hole to allow placement of the

Figure 14.37. Suggested revised melt crystallization design, with raw powder. The crystallization clips and offset slides allowing for material placement at (a).

behavior suggests no top may be the most promising route to try, easily implemented using the existing apparatus (Figure 14.37). Improved coverage could be realized by more coplanar substrates; smoother faces (like quartz) and more precise gaps (from, *e.g.*, PVD metal films) in conjunction with more uniform pressure applied during crystal growth would each improve capillarity and coverage.

M.2. Growth and Characterization of Optically-Pumped Organic Lasers

Electrically-driven organic lasers are one of the “final frontiers” for organic electronics, even playing a role in the infamous Schön scandal.⁸⁶⁵ Optically-pumped lasers have been successfully demonstrated in several architectures,^{866–869} but there remain significant challenges in electrical generation and maintenance of a sufficient exciton population to lase due to various quenching and loss mechanisms.^{668,669,868} The goals of this project were to explore optically-pumped laser architectures and characterization as reported by Kozlov *et al.*^{866,868} in order to bring these capabilities to the lab.

The lasers manufactured were from the materials tris(8-hydroxyquinolinato) aluminum (Alq_3 , Figure 14.38a) and 4-(dicyanomethylene)-2-methyl-6-(4-dimethylaminostyryl)-4H-pyran (DCM, Figure 14.38b). Alq_3 and DCM form a complimentary pair due to the overlap of Alq_3 emission with DCM absorption, facilitating downconversion and energy transfer from the original nitrogen arc laser pulse (337 nm). Alq_3 serves as the host and DCM as the guest and emitter in this configuration. The object of these materials is to create an extremely high exciton density on DCM which can then undergo stimulated emission by light which is trapped in waveguided modes within the film. There were two laser architectures explored in this

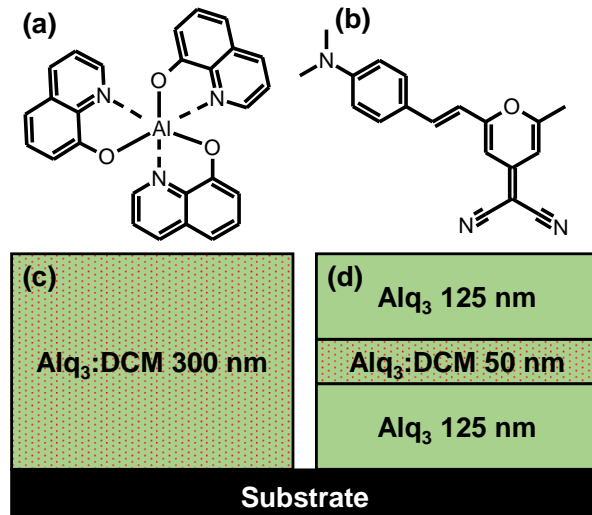


Figure 14.38. Molecular structures of (a) Alq_3 and (b) DCM, and architectures of (c) slab and (d) cladded lasers.

Appendix M. High School Mentor Projects

project, a basic slab laser (Figure 14.38c) and a cladded laser (Figure 14.38d). Each of these lasers works by confining light in the plane of the film by mismatches in index of refraction, with the cladded structure somewhat more efficient because of the additional confinement. The lasers were deposited onto silicon with thermal oxide ~200 nm thick, glass, polyethylene, and polypropylene, enabling fabrication of flexible lasers (Figure 14.39a). When optically pumped with a nitrogen arc laser, the organic lasers emitted a beam of focused orange light (Figure 14.39b).

One of the primary challenges associated with this project was laser characterization. This required arrangement of focusing, collection, and detection optics as shown in Figure 14.40. The organic lasers produced weak, short pulses which required substantial focusing to reach the noise floor of the spectrometer in particular. This in turn makes the collection sensitive to sample position, suggesting the use of a translation stage and goniometer to aid alignment and test angle resolution.

The organic lasers produced all lased, with the most efficient being the cladded structure on SiO₂/Si followed by those on Si, glass, and polymer. For the most efficient lasers, it was challenging to observe an onset in spectral narrowing or lasing threshold due

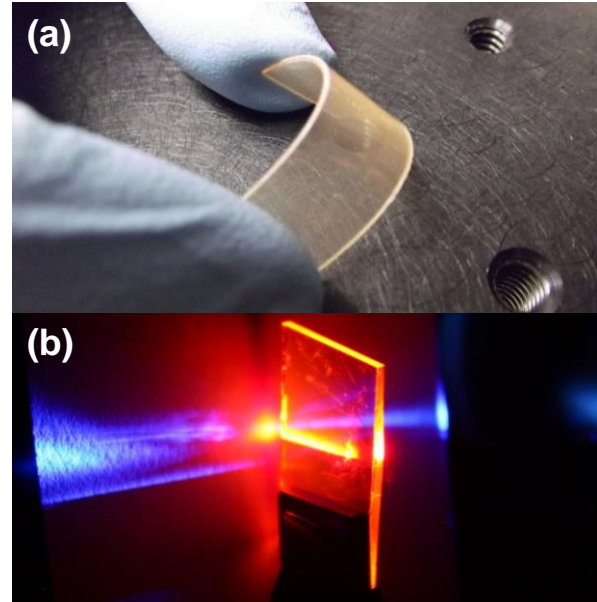


Figure 14.39. Photographs of (a) laser deposited onto a flexible plastic substrate and (b) lasing of the organic laser (orange) as pumped by a nitrogen arc laser (visible by blue paper fluorescence in background)

Appendix M. High School Mentor Projects

to the detection limits of the detector and spectrometer which were used, but glass and

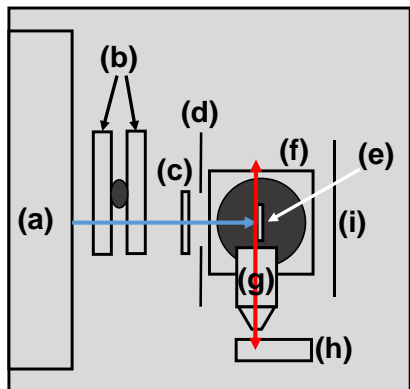


Figure 14.40. Schematic of the laser characterization setup, including the nitrogen laser (a) which produces 337 nm light (blue arrow) which goes through neutral density filter wheels (b), horizontal cylindrical lens (c), and beam stops (d) onto the organic laser (e) which is mounted on a goniometer translation stage (f). Extra laser light is blocked by a beamstop (i). The organic laser emits light in the substrate plane (red arrows), one side of which is focused using a microscope objective (g) into a detector or spectrometer (h).

polymer lasers yielded onsets and evidence of spectral narrowing. Low-intensity measurements required the use of a fluorimeter, rather than the nitrogen laser.

The project was largely successful, although some recommendations remain. To better elucidate the lasing threshold at detectable intensities, inefficient substrates (plastics) serve as simple methods to raise the threshold while still allowing for lasing to

occur at powers below the film ablation threshold. The lasing wavelength and efficiency should also change with DCM concentration, which was not broadly explored in this study.

With these avenues in mind, more careful calibration of the laser power and neutral density filters would allow for quantitative calculation of the laser intensity and comparison to literature values, with the scheme in Figure 14.40 also allowing for angle-resolved and polarization-dependent measurements.

Appendix N. Substrate Cleaning and Film Annealing Procedure

The methods used to prepare, clean, and anneal substrates have proven to be critical in some of the experiments presented in this thesis. For this reason, a detailed description of cleaning and annealing procedures are given below.

N.1. Substrate Cleaning

The cleaning procedure features sonication, bombardment with sound to induce cavitation in the extreme and simple agitation in less powerful cases.^{870,871} The first step degreases the substrates using Tergitol, a non-ionic surfactant with structure shown in Figure 14.41 which is capable of forming micelles with greasy residues on substrate surfaces. Next, deionized water (to prevent accumulation of solids after evaporation)

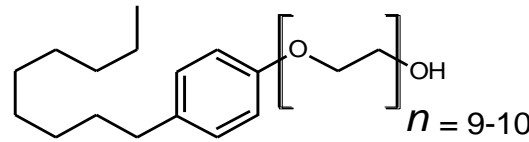


Figure 14.41. Chemical structure of Tergitol NP-40.

is added to rinse off any leftover Tergitol and other water-soluble compounds. Acetone baths follow to aid in dissolution of polymeric, resinous, and general ketone-soluble molecules while also reducing the remaining water content and thus surface tension to help solvent exchange between nearby substrates. Finally, boiling isopropanol is used to further agitate and loosen any leftover grease or oil and evaporate quickly when drying the substrates. Isopropanol has a higher boiling point than acetone (82.6 vs. 56.1 °C), allowing any leftover acetone to boil off. Substrates are optionally exposed to ultraviolet light, which radicalizes molecular oxygen to ozone, $\cdot O_3$, a powerful oxidizer, and further catalyzes its reaction with surfaces.⁸⁷² Ozone has two primary purposes: react with any leftover carbon

Appendix N. Substrate Cleaning and Film Annealing Procedure

in the reaction $\text{C} + \text{O}_3 \rightarrow \text{CO}_2 + 2\text{O}_2$ (although the effectiveness may be limited by deposit thickness and light intensity), and to oxidize the material surface to increase its surface energy. For example, the surface reaction of hydrogen-passivated silicon proceeds according to $\text{Si-H} + \text{O}_3 \rightarrow \text{Si-OH} + \text{O}_2$,⁸⁷² giving an extremely hydrophilic surface (see Figure 14.42). Incidentally, ozone also reacts with glass to produce a clear yellow-brown surface, similar to that observed on alumina which bleaches above 160 °C.⁸⁷² For hydrophilic molecules or molecules with high-energy functional groups, this treatment can improve wetting of the film on the surface. Thin films of the molecule TPBi are an example of this behavior. Oxidation also has the effect of increasing (deepening) the work function of ITO to increase the built-in field in electronic devices,^{873–875} beneficial for reducing charge carrier injection barriers and increasing the open-circuit voltage of solar cells. This thesis has not measured the time required for the oxidized surface to reduce, but it appears to be at least 30 minutes in ambient and 60 in vacuum.

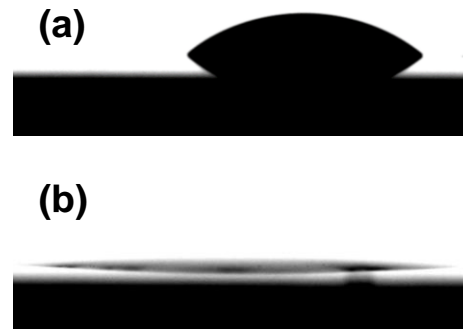


Figure 14.42. DI water on (a) solvent-cleaned silicon and (b) solvent-cleaned with 10 minutes UV-ozone.

The formal procedure for cleaning substrates is as follows:

1. Scribe or cut the substrates to the desired size, if necessary
2. Place substrates on Teflon holders (disks with slots to keep substrates vertical) and insert sequentially into the following for 5 minutes duration:
 - i. Deionized water with ~1 vol% Tergitol, sonicated
 - ii. Deionized water, sonicated
 - iii. Acetone bath 1 and bath 2, sonicated

Appendix N. Substrate Cleaning and Film Annealing Procedure

- iv. Boiling isopropanol bath 1 and bath 2
3. After removal from bath (vi), immediately blow dry with house nitrogen gas
4. Optionally, expose to a UV-Ozone ambient for 10 minutes immediately before transfer into the deposition system

N.2. Film Annealing

Much of the work in this thesis utilized *in situ* annealing and observation visualized with an optical microscope on the heated microscope stage described in Appendix L.1. . For sake of completeness, the annealing procedure is given here.

1. Films were typically grown on scribed substrates, which were broken along scores inside of the glovebox using a metal piece approximately shown in Figure 14.43.
2. Broken pieces were separated into compartments of a petri dish to allow random sampling from different substrates for a given annealing condition
3. The heated stage was purged with 20 SCFH of house N₂, with the temperature set > 10 minutes before use and capture software ready to run
4. Substrates were removed one at a time from the glovebox in a small, sealed petri dish (without evacuating antechamber during takeout). The substrates travelled directly to the microscope, were placed on the pre-heated surface, and captured annealing using the software in Appendix R.2. Typical time from glovebox to capture starting is 30 seconds or less, with direct exposure to air less than 5 seconds.
5. Once annealing was complete, substrates were removed and system reset before returning to lab to choose a sample from another compartment.
6. Temperatures were ultimately tested in randomized order, although preliminary work used a consecutive series.

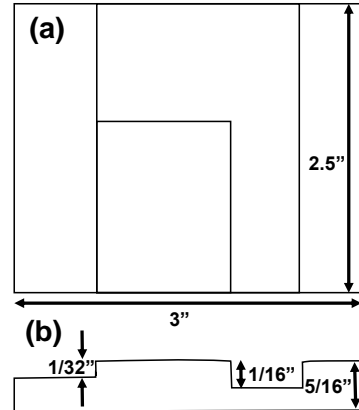


Figure 14.43. Schematic of stainless steel plate used to break scored substrates in the glovebox. Diagram not to scale.

Appendix O. Morphology of ITO, Glass, and Metals

Questions often arise about the smoothness and grain size of materials used in the creation of films and devices. Often, it is surprising the degree of roughness on surfaces which appear optically smooth. To answer these questions and for future reference, some common example materials and statistics are provided here.

O.1. Indium Tin Oxide Films on Glass

The ITO used for electronic devices is perhaps most variable in morphology because of the irregularities in deposition. Unfortunately, the smoothness, transparency, and conductivity of this layer are critical for applications. Figure 14.44 shows the ITO used in

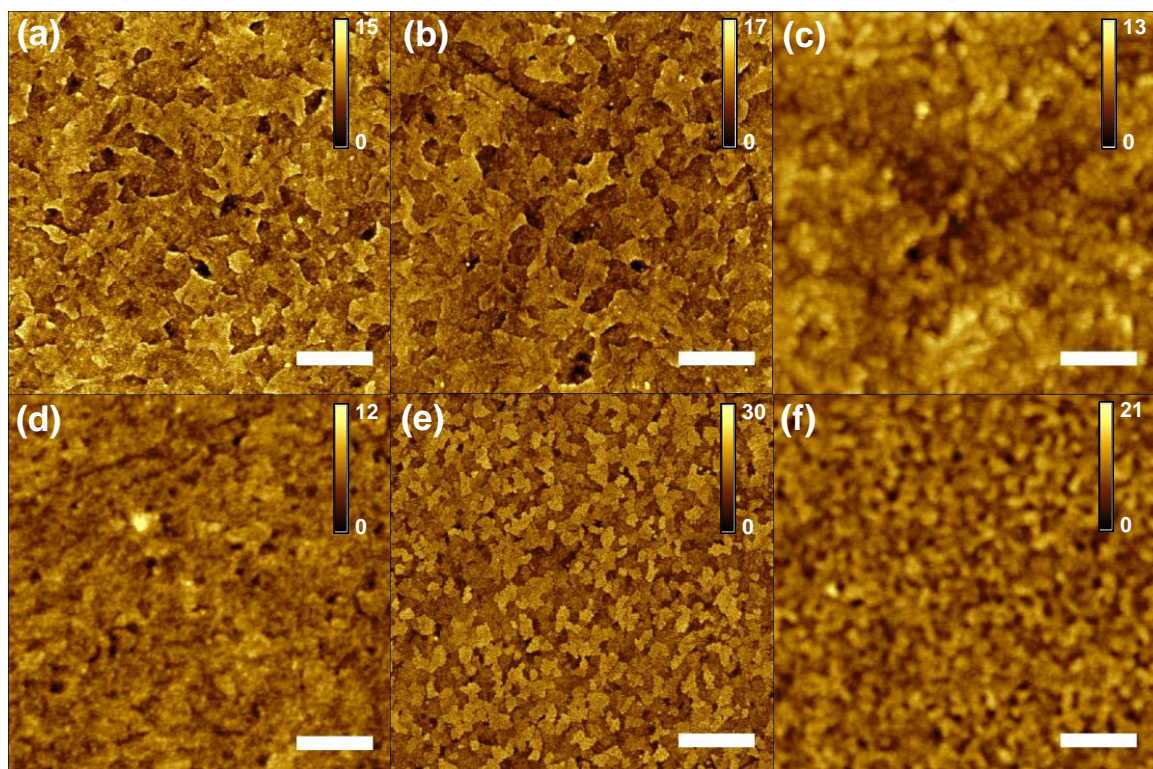


Figure 14.44. Images of ITO with and without film deposited on it. Bare Xin Yan ITO from 9/18/13 with RMS roughness (a) 2.31 and (b) 2.40 nm. (c) is Xin Yan ITO with 20 nm rubrene, RMS roughness 1.4 nm, and (d) is Xin Yan ITO with 50 nm PEDOT:PSS, RMS roughness 1.69 nm. ITO from Delta Technologies, with RMS roughness (e) 3.89, and (f) 2.2 nm with 20 nm rubrene. The film roughness in (c) and (f) give increased interface areas of 0.08 % and 0.22 %, respectively. All scale bars 1 μ m, height scales in nm.

Appendix N. Morphology of ITO, Glass, and Metals

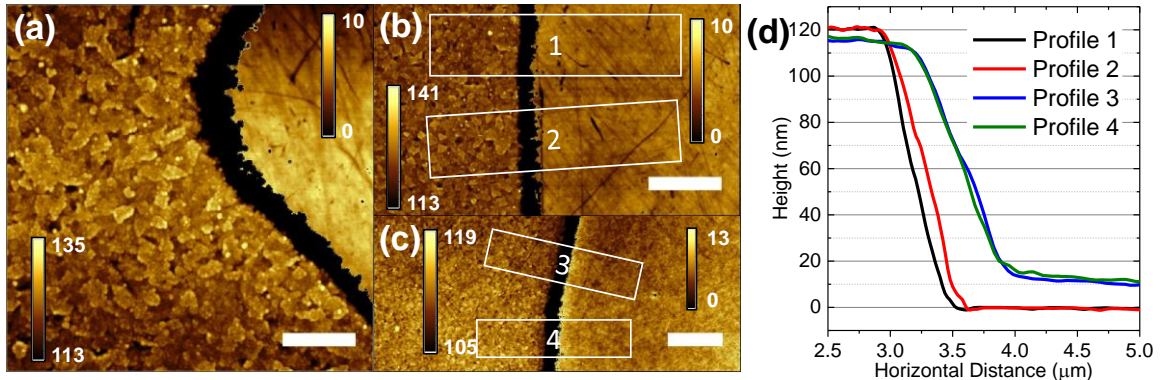


Figure 14.45. Morphology and step characterization of patterned Xin Yan ITO as of 9/20/14. (a) View of patterned corner region with two images stitched together (height scales for the ITO in lower left, glass substrate in upper right). Scale bar 2 μ m. (b) Edge characterization of bare ITO, with two images stitched together as in (a), scale bar 1 μ m. (c) Edge characterization of ITO planarized with 50 nm PEDOT:PSS, scale bar 3 μ m. (d) Height profiles of the regions shown in (b)-(c). All height scales in nm.

this thesis for unpatterned device manufacture and film annealing, specifically Xin Yan ITO. When devices were patterned, either for packaging in inert atmosphere or for greater electrical signal, the patterned ITO shown in Figure 14.45 was used. The patterned ITO has an extremely sharp edge of 120 nm vertical drop over 500 nm lateral distance, which can complicate device manufacture and requires the use of a planarizing layer like PEDOT:PSS for some architectures, smoothing the edge somewhat.

Closer inspection shows each ITO flake is comprised

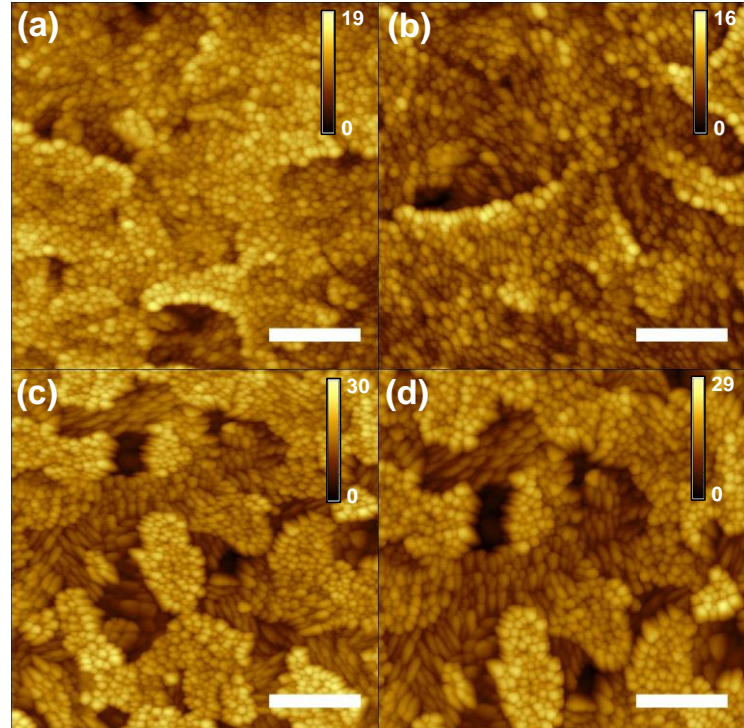


Figure 14.46. Morphology of (a), (b) Xin Yan ITO and (c), (d) Delta Technologies ITO. Scale bar 250 nm, height scales in nm.

Appendix N. Morphology of ITO, Glass, and Metals

of many small grains which are approximately 20 nm diameter but exhibit varying degrees of elongation and grouping between different ITO types (Figure 14.46).

O.2. Metals: Evaporated Aluminum, Silver, and Gold

Although they may appear optically smooth, metals typically deposit as small aggregates, if they wet at all (Figure 14.47). Aluminum and silver each deposit well on inorganic and organic substrates, but gold tends to dewet from silicon without a wetting layer (commonly chromium).

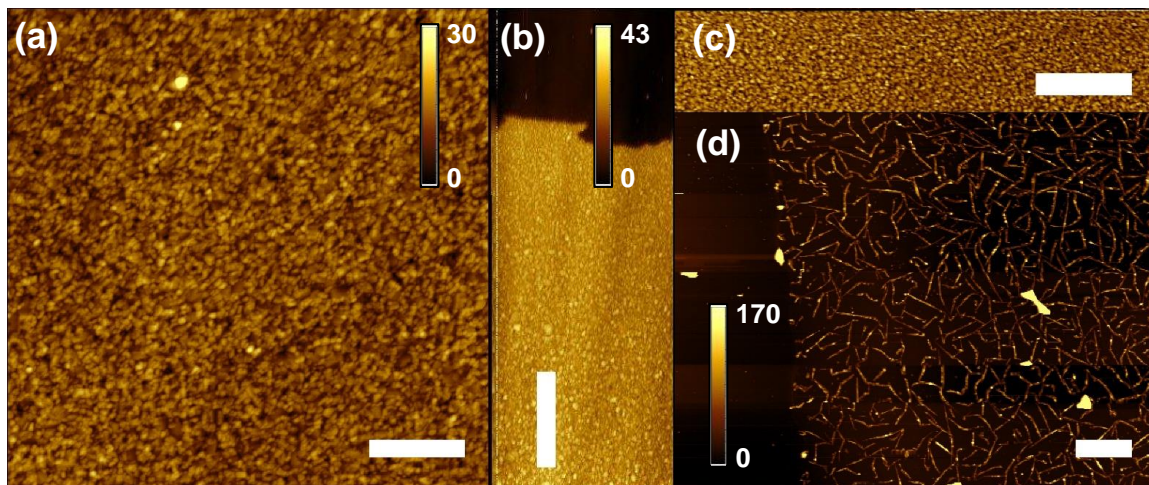


Figure 14.47. Morphology of vapor-deposited metals, including (a) 100 nm aluminum on C₆₀ (scale bar 1 μm), (b) silver on silicon (scale bar 2 μm), (c) 150 nm gold on 3 nm chromium wetting layer (scale bar 1 μm, height scale 7 nm), and (d) 50 nm gold on silicon (scale bar 10 μm). All height scales in nm.

Appendix P. Chamber Chuck Rotation and Heating

The Angstrom Engineering deposition system is equipped with a substrate holder (chuck) which is capable of rotation and heating during film deposition. The chuck rotational speed varies roughly linearly from 0 to 60 RPM, as shown in Figure 14.48.

At typical deposition conditions

(5), the chuck spins at 30 RPM. The lamp and chuck temperatures may be correlated to one another, but only at steady state. Owing to their differing thermal masses, the lamp

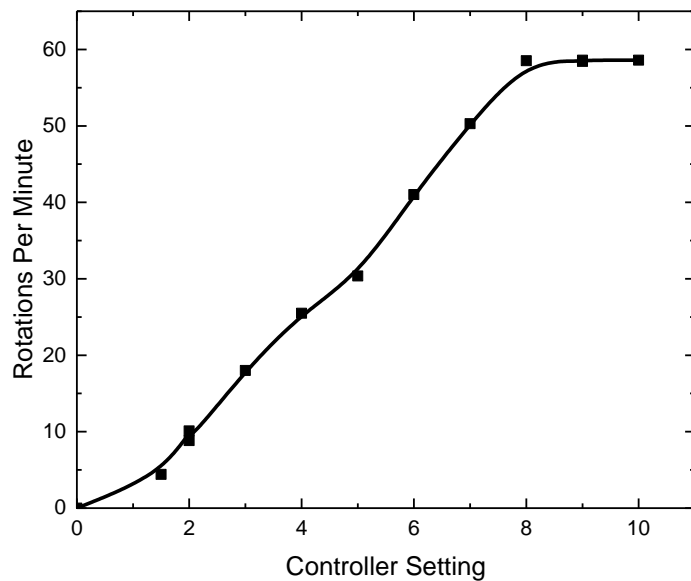


Figure 14.48. Chuck rotational speed in terms of the control dial setting on the control console.

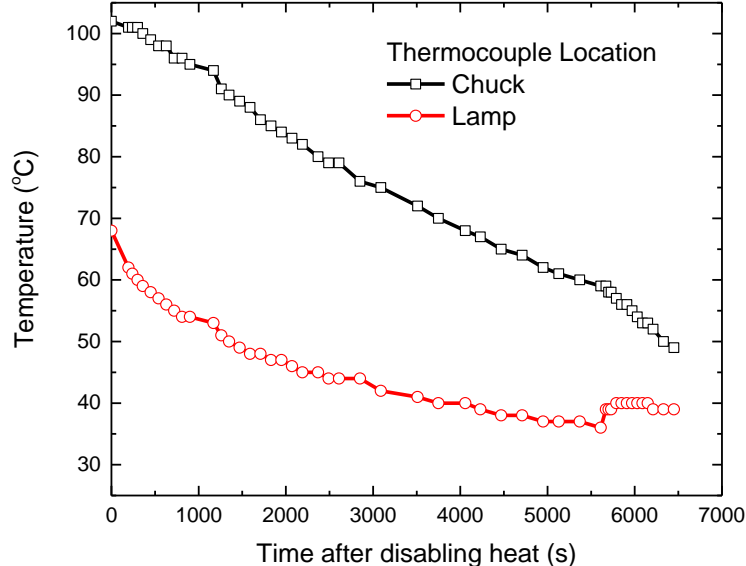


Figure 14.49. Cooling characteristics of the Angstrom chamber chuck and lamp, according to thermocouples mounted onto the 9" copper chuck ("Chuck") and in the chamber shroud next to the lamp ("Lamp").

thermocouple and chuck also cool at different rates. Being in a vacuum environment, the chuck cools extremely slowly; approximately 30 °C per hour as shown in Figure 14.49. The system was vented at approximately 5500 seconds.

Appendix Q. Finite Difference Methods

The numerical solution method in Chapter 8. uses finite differences, where derivatives are approximated using a Taylor series expansion and solved as a linear system. How the Taylor series is used depends on which type of approximation; we use the central difference approximation for spatial derivatives, which uses the values on either side of the point of interest to calculate the derivative:

$$\frac{\partial^2 n}{\partial x^2} \equiv \frac{n_{x-\Delta x}^t - 2n_x^t + n_{x+\Delta x}^t}{(\Delta x)^2} \quad (14.61)$$

Here, n_x^t is the exciton density at position x for time t , and Δx is the distance step size for discretization of the layer. For time derivatives, we use a forward difference approximation

$$\frac{\partial n}{\partial t} \equiv \frac{n_x^{t+1} - n_x^t}{\Delta t} \quad (14.62)$$

with Δt the time step for time domain discretization. The forms in Eqns. 14.61 and 14.62 may be proved to be numerically stable and convergent for $\Delta t/(\Delta x)^2 \leq 0.5$, setting limits on relative step sizes for stability. With these expressions, the error from the Taylor series approximation scales with $(\Delta x)^2$, but in the small-step limit, numerical round-off errors dominate. It is important to test simulations results across different step sizes (and relative to analytical solutions where possible) to ensure that the solution converges correctly and accurately.

Eqns. 14.61 and 14.62 allow for reformulation of the diffusion equation with Förster energy transfer in terms of discrete positions in space and time (for bulk energy transfer) as

Appendix Q. Finite Difference Methods

$$\frac{n_x^{t+1} - n_x^t}{\Delta t} = \mathcal{D} \frac{n_x^t - 2n_x^t + n_x^t}{(\Delta x)^2} + n_x^t \left(\frac{\pi}{2} \sum_{x_j \neq x_i} \left[\frac{1}{(x_j - x)^4} \left(\frac{\rho_i R_{0,ji}^6}{\tau_j} - \frac{\rho_j R_{0,ij}^6}{\tau_i} \right) \right] - \frac{1}{\tau_i} \right) + G(x) \quad (14.63)$$

In this equation, the current layer i is implicit relative to the surrounding layers j , which are determined by the spatial position x within the layer stack. This leads naturally to a matrix representation $\underline{\underline{A}} \cdot \underline{n} = \underline{b}$, where $\underline{\underline{A}}$ is the matrix of coefficients on any n_x^t and \underline{b} the remaining non-exciton-density-dependent terms, including generation and boundary conditions. Boundary conditions in this approach are specified at the domain edges, with a flux F boundary condition at the stack origin specified as

$$-\mathcal{D}_{i=1} \frac{\partial n}{\partial x} \Big|_{x=0,t} \equiv \mathcal{D}_{i=1} \frac{n_0^t - n_{\Delta x}^t}{\Delta x} = F \quad (14.64)$$

and a quenching condition at the stack thickness L as

$$n(L, t) \equiv n_L^t = 0 \quad (14.65)$$

Similarly, the initial condition is specified in the time domain as

$$n(x, 0) \equiv n_x^0 = 0 \quad (14.66)$$

Finally, there are the coupling equations between adjacent layers at the interface x_{ij} , where the flux must be conserved according to

$$\mathcal{D}_i \frac{\partial n_i}{\partial x} \Big|_{x_{ij}} \equiv \mathcal{D}_i \frac{n_{x_{ij}-\Delta x}^t - n_{x_{ij}-2\Delta x}^t}{\Delta x} = \mathcal{D}_j \frac{n_{x_{ij}+\Delta x}^t - n_{x_{ij}}^t}{\Delta x} \equiv \mathcal{D}_j \frac{\partial n_j}{\partial x} \Big|_{x_{ij}} \quad (14.67)$$

The convention of this work is to assign x_{ij} to layer j since the concentrations are discontinuous across the interface. This discontinuity invalidates the second derivative of two points: x_{ij} and $x_{ij-\Delta x}$. This requires two replacement equations of the type of Eqn.

Appendix Q. Finite Difference Methods

S10, for which we have chosen to extend from the interfacial flux balance to a second point, from x_{ij} to $x_{ij-2\Delta x}$. For small enough Δx , $n_{x_{ij}-\Delta x}$, $n_{x_{ij}-2\Delta x}$, and $n_{x_{ij}-3\Delta x}$ should be approximately collinear, and referencing the flux at two points of low exciton density with one of high density should improve numerical accuracy relative to the opposite case. These values are entered into the appropriate matrix positions to set these conditions on the solving of the linear equation $\underline{\underline{A}} \cdot \underline{n} = \underline{b}$.

Appendix R. Relevant Computer Software

There have been many programs written to capture, consolidate, analyze, visualize, and model data for this thesis. Of those programs, only a small fraction are suspected of potentially being useful to other people. Those programs are given below, with short examples of their capabilities and brief descriptions of their functionality. All software provided as-is; for use at own risk.

R.1. Transfer Matrix Model (Matlab)

The steady-state electric field within a collection of films much thinner than the wavelength of light can vary significantly from coherent reflection of light at film interfaces (see Figure 14.50). For this reason, it is important to accurately calculate these fields by mapping the transmission and

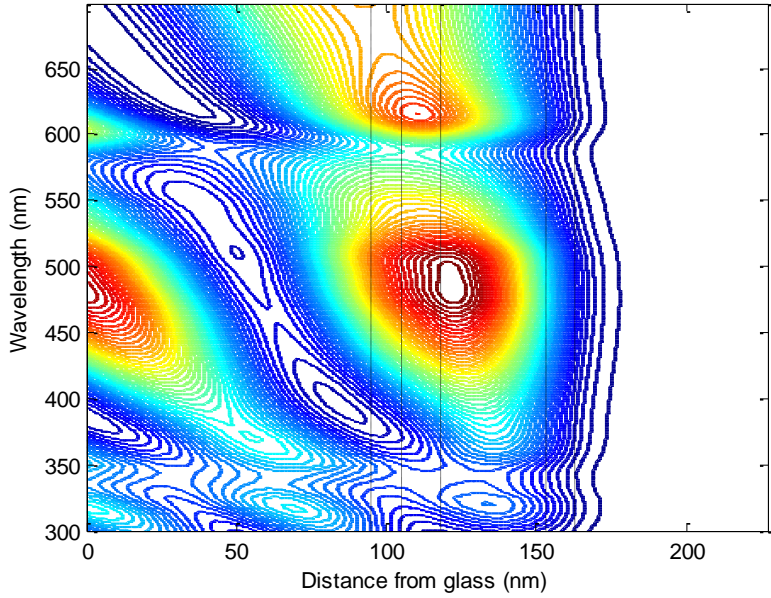


Figure 14.50. Simulated electric field in a SubPc planar OPV described in Zou & Holmes.⁷³⁷ Intensity scale ranges from 0-150% of the incident field.

reflection coefficients for each interface throughout a given film stack. A highly successful and elegant method to perform these calculations is with a transfer matrix formalism, as described by Pettersson *et al.*⁶⁹⁴ The following code implements this model for an arbitrary stack of materials and also calculates the photocurrent which results.

Appendix R. Relevant Computer Software

```

function Photocurrent1
% This function calculates the electric field within a multilayer
% device and exciton and photocurrent generation within said device.
%%
% The program assumptions are that
% 1. The data matrix for n and k is located on the desktop, in a file named
    "Index_of_Refraction_Library.xls"
%
% Model assumptions are:
% 1. Device layers are homogeneous and isotropic
% 2. Interfaces are parallel and flat relative to wavelength
% 3. Incident light can described by plane waves
% 4. Exciton diffusion described by diffusion equation
% 5. Excitons contributing to photocurrent dissociate into charge carriers at interfacial sites
% 6. Exciton diffusion range is independent of wavelength (energy)
% 7. All generated charges contribute to photocurrent (no charge traps)
%
% Based entirely on "Modeling Photocurrent Action Spectra of Photovoltaic Devices Based on Organic
% Thin Films" by L.A.A. Pettersson, L.S. Roman, and O. Inganäs. J. App. Phys. 86 (1), pp 487-496, 1999
%
% Thomas R. Fielitz, University of Minnesota, January 10, 2013
%%
% Input solar cell design, with ||'material' thickness(nm)|| for each row. Glass (SiO2) must be first and air
% last, with zero thickness
Substrate = {'Air' 0*10^6}; % Substrate for absorption, thickness nm
    % Calculations assume that substrate is first material in stack. If not desired, set thickness to zero.
CellDesign = {'Air' 0
%
    'ITO' 110
    'SubPc' 17.8
    'BP2T' 8
%
    'C60' 35
%
    'BCP' 10
%
    'Al' 100
%
    'SiO2' 0};

Absorber = [2]; % Set which layers contribute to photocurrent - format [2,4,...]
Interface = [3,2]; % Set boundary conditions for exciton density (left = closer to light source):
% 1 = both dissociate; 2 = left dissociates, right zero flux;
% 3 = left zero flux, right dissociates; 4 = both zero flux

%
% ***** Iteration Parameters *****
Angle = 65; % Angle of incidence (degrees from normal)
dx = 0.1; % x step size, in nm
LongWave = 525; % Longest wavelength in nm
ShortWave = 525; % Shortest wavelength in nm
dwave = 5; % Step size of wavelength iteration, nm

%
% ***** Output Options *****
PlotCurr = 0; % Plot photocurrent
Plot_EQE = 0; % Plot EQE

```

Appendix R. Relevant Computer Software

```

colorEQE = 'k';
PrintEQE = 0; % Print EQE array
PlotExcGen = 1; % Plot exciton generation profile
PlotWave = 1; % Wavelength to plot exciton profile; 1 for all
PrintExGen = 1; % Print exciton generation profile
CalcJsc = 0; % Calculate and display Jsc

% ***** Charge Generation Parameters *****
tau = 1^-9; % Mean exciton lifetime, seconds
theta1 = 1; % Quantum efficiency of exciton generation
coll = 1; % Collection efficiency
absorp = 1; % Absorption efficiency
theta2 = [1 1 1 1]; % Efficiency of exciton dissociation at each absorber interface
diffL = [9.8,5,5,5]; % Exciton diffusion length for each absorbing film, nm
% SubPc ~ 10.7, C60 ~ 22
E0 = 1000; % Incident intensity W/m^2

%===== End of User Input =====
%===== Constants =====
Diff = diffL.^2/tau; % Exciton diffusion constant
c = 2.998*10^8; % speed of light, m/s
h = 6.626*10^-34; % Planck's constant, J s
q1 = 1.602*10^-19; % charge of electron, C

%Import Spreadsheet, then find names and columns
cd('F:\UMN Data\Matlab Data Analysis');
[num,text,raw] = xlsread('Index_of_Refraction_Library.xls','Ellips');
[nr,nc] = size(raw); [Nlayers,z] = size(CellDesign); column = zeros(2*Nlayers,1); nonexistent = 0;
for i = 1:Nlayers % Find columns for the layer compounds n & k
    layer_n = sprintf('%s_n',CellDesign{i,1}); layer_k = sprintf('%s_k',CellDesign{i,1});
    Thickness(i,1) = CellDesign{i,2};
    for j = 1:nc
        lay = raw(1,j); N = strcmp(layer_n, lay); K = strcmp(layer_k, lay);
        if N == 1
            column(2*i-1,1) = j;
        end
        if K == 1
            column(2*i,1) = j;
        end
    end
end
nonexistent = find(column==0);
if nonexistent > 0
    CellDesign{ceil(nonexistent/2),1}
    error('Name error; check the above compound')
end
CheckMat = {'Name' 'Thick'};
for i = 1:Nlayers % Generate matrix to check correctness
    CheckMat{i+1,1} = raw{1,column(2*i)}; CheckMat{i+1,2} = Thickness(i);

```

Appendix R. Relevant Computer Software

```

end
CheckMat
LamMat = ShortWave:dwave:LongWave; spectrum = importdata('Normalized Solar Spectrum.txt');
Nwave = length(LamMat);
for k1 = 1:Nwave
    lambda = LamMat(k1);
    n0 = num(lambda-299, column(1));
    for j1 = 1:Nlayers % Generate n~, q, xi, L where j1 is the j1th device layer
        n = num(lambda-299, column(2*j1-1)); %index of refraction
        k = num(lambda-299, column(2*j1)); % loss coefficient
        nVec(j1) = n; kVec(j1) = k; n_cp(j1) = n + k*1i; % complex index of refraction
        q(j1) = (n_cp(j1)^2-n0^2*sin(Angle*pi/180)^2)^0.5; xi(j1) = 2*pi/lambda*q(j1);
        L{j1} = [exp(-1i*xi(j1)*Thickness(j1)),0,0,exp(1i*xi(j1)*Thickness(j1))];
    end
    for j2 = 1:(Nlayers-1) % Generate r, t, I where j2 is the j2th interface
        qj = q(j2); qk = q(j2+1); nj = n_cp(j2); nk = n_cp(j2+1);
        %TE (s-polarized) light waves
        r_TE(j2) = (qj-qk)/(qj+qk); t_TE(j2) = 2*qj/(qj+qk); I_TE{j2} = 1/t_TE(j2)*[1,r_TE(j2);r_TE(j2),1];
        %TM (p-polarized) light waves
        r_TM(j2) = (nj^2*qk-nk^2*qj)/(nk^2*qj+nj^2*qk); t_TM(j2) = 2*nj*nk*qj/(nk^2*qj+nj^2*qk);
        I_TM{j2} = 1/t_TM(j2)*[1,r_TM(j2);r_TM(j2),1];
    end
    I = I_TE;
    for sp = 1:2 % Loop to generate TE, TM values
        xtot = 0;
        m = 1;
        for j3 = 2:Nlayers-1 %S'(S1) and S"(S2)for j3th layer
            S1c = 1; S2c = 1; % Reset loop values
            for v1 = 2:j3-1 % S'(S1)
                S1c = S1c*I{v1-1}*L{v1};
            end
            for v2 = j3+1:Nlayers-1 % S"(S2)
                S2c = S2c*I{v2-1}*L{v2};
            end
            S1{j3} = S1c*I{j3-1}; S2{j3} = S2c*I{Nlayers-1}; r1(j3) = S1{j3}(2,1)/S1{j3}(1,1);
            r1n(j3) = -S1{j3}(1,2)/S1{j3}(1,1); t1(j3) = 1/S1{j3}(1,1); r2(j3) = S2{j3}(2,1)/S2{j3}(1,1);
            t2(j3) = 1/S2{j3}(1,1); tp(j3) = t1(j3)/(1-r1n(j3)*r2(j3)*exp(1i*2*xi(j3)*Thickness(j3)));
        end
        I = I_TM;
    end

    % Calculate exciton density and charge generation
    Nab = length(Absorber); % number of absorbing layers
    kSpec = find(spectrum(:,1)>lambda, 1 );
    interpSpec = spectrum(k1,2)*exp(-4*pi*kVec(1)*Substrate{1,2}/lambda);
    N = E0*interpSpec*lambda/10^9/(h*c); % Incident photon flux on device, photons/ sec m^2
    m1 = 0; % track thickness through total absorbing layer
    for j5 = 1:Nab
        layer = Absorber(j5); Boundaries = Interface(j5); d1 = Thickness(layer); k2 = kVec(layer);
        n1 = nVec(layer); alpha1 = 4*pi*k2/lambda; rho = abs(r2(layer)); delta = angle(r2(layer));
        T = n1/n0*abs(tp(layer))^2; beta = 1/(diffL(j5)); gamma = 4*pi*n1/lambda;
    end

```

Appendix R. Relevant Computer Software

```

C1 = rho^2*exp(-2*alpha1*d1);
C2 = (beta^2-alpha1^2)/(beta^2+(4*pi*n1/lambda)^2)*2*rho*exp(-alpha1*d1);
if Boundaries == 1 %Both dissociate
    A = (exp(beta*d1)-exp(-alpha1*d1)+C1*(exp(beta*d1)-
exp(alpha1*d1))+C2*(exp(beta*d1)*cos(gamma*d1+delta)-cos(delta)))/(exp(-beta*d1)-exp(beta*d1));
    B = -(exp(-beta*d1)-exp(-alpha1*d1)+C1*(exp(-beta*d1)-exp(alpha1*d1))+C2*(exp(-
beta*d1)*cos(gamma*d1+delta)-cos(delta)))/(exp(-beta*d1)-exp(beta*d1));
elseif Boundaries == 2 %Left diss, right no flux
    A = -(alpha1*exp(-alpha1*d1)+beta*exp(beta*d1)+C1*(beta*exp(beta*d1)-
alpha1*exp(alpha1*d1))+C2*(beta*exp(beta*d1)*cos(gamma*d1+delta)-
gamma*sin(delta))/(beta*(exp(-beta*d1)+exp(beta*d1)));
    B = (alpha1*exp(-alpha1*d1)-beta*exp(-beta*d1)-C1*(alpha1*exp(alpha1*d1)+beta*exp(-
beta*d1))-C2*(gamma*sin(delta)+beta*exp(-beta*d1)*cos(gamma*d1+delta))/(beta*(exp(-
beta*d1)+exp(beta*d1)));
elseif Boundaries == 3 %Left no flux, right diss
    A = (-alpha1*exp(beta*d1)-beta*exp(-alpha1*d1)+C1*(-
beta*exp(alpha1*d1)+alpha1*exp(beta*d1))+C2*(-
beta*cos(delta)+gamma*exp(beta*d1)*sin(gamma*d1+delta))/(beta*(exp(-beta*d1)+exp(beta*d1)));
    B = (alpha1*exp(-beta*d1)-beta*exp(-alpha1*d1)-C1*(beta*exp(alpha1*d1)+alpha1*exp(-
beta*d1))-C2*(beta*cos(delta)+exp(-beta*d1)*gamma*sin(gamma*d1+delta))/(beta*(exp(-
beta*d1)+exp(beta*d1)));
elseif Boundaries == 4 %Both zero flux
    A = (alpha1*(beta*exp(beta*d1)-exp(-beta*d1)+exp(beta*d1)-exp(-
alpha1*d1))+C1*alpha1*(exp(alpha1*d1)-beta*exp(beta*d1)+exp(-beta*d1)-
exp(beta*d1))+C2*gamma*(sin(delta)-(beta*exp(beta*d1)+exp(beta*d1)-exp(-
beta*d1))*sin(gamma*d1+delta))/(beta*(exp(-beta*d1)-exp(beta*d1)));
    B = (alpha1*(beta*exp(-beta*d1)-exp(-alpha1*d1))+C1*alpha1*(exp(alpha1*d1)-beta*exp(-
beta*d1))+C2*gamma*(sin(delta)-beta*exp(-beta*d1)*sin(gamma*d1+delta))/(beta*(exp(-beta*d1)-
exp(beta*d1)));
end
nxit = floor(d1/dx);
for xit = 1:nxit
    x = dx*xit;
    nExc(xit+m1,k1) = theta1*alpha1*T*N/(Diff(j5)*(beta^2-alpha1^2))*(A*exp(-
beta*x)+B*exp(beta*x)+exp(-alpha1*x)+C1*exp(alpha1*x)+C2*cos(gamma*(d1-x)+delta))/1000; %
Excitons/cm^3
    xVec(xit+m1,1) = x+m1*dx;
end
Jphoto(k1,2*j5-1) = 100*q1*theta1*theta2(j5)*alpha1*T*N/(beta^2-alpha1^2)*(-beta*A+beta*B-
alpha1+alpha1*C1+gamma*C2*sin(gamma*d1+delta)); % photocurrent produced at x = 0, uA/cm^2
Jphoto(k1,2*j5) = -100*q1*theta1*theta2(j5+1)*alpha1*T*N/(beta^2-alpha1^2)*(-beta*A*exp(-
beta*d1)+beta*B*exp(beta*d1)-alpha1*exp(-
alpha1*d1)+alpha1*C1*exp(alpha1*d1)+gamma*C2*sin(delta));% photocurrent produced at x = d,
uA/cm^2
m1 = m1+nxit;
PlotEQE(k1,2*j5-1) = Jphoto(k1,2*j5-1)*1240/(E0*spectrum(k1,2)*lambda);
PlotEQE(k1,2*j5) = Jphoto(k1,2*j5)*1240/(E0*spectrum(k1,2)*lambda);
end
end

if CalcJsc == 1

```

Appendix R. Relevant Computer Software

```

JphotoSum = coll*absorp*trapz(sum(Jphoto,2),-LamMat)/1000; % mA/cm^2
disp(sprintf('Calculated Jsc is %d mA/cm^2',JphotoSum))
end
nPlots = PlotCurr+Plot_EQE+PlotExcGen;
if nPlots > 1
    ncol = 2; nrow = 1;
    if nPlots > 2
        nrow = 2;
    end
else
    nrow = 1; ncol = 1;
end
gnum = 1; EQESum = coll*absorp*sum(PlotEQE,2);
if PlotCurr == 1
    subplot(nrow,ncol,gnum), plot(LamMat,Jphoto,LamMat, sum(Jphoto,2))
    title('Photocurrent'); ylabel('J, uA/cm^2'); xlabel('Wavelength (nm)'); xlim([ShortWave LongWave]);
    gnum = gnum + 1;
end
if Plot_EQE == 1
    subplot(nrow,ncol,gnum), plot(LamMat,EQESum,colorEQE)
    title('Total EQE'); ylabel('EQE (%)'); xlabel('Wavelength (nm)'); xlim([ShortWave LongWave]);
    gnum = gnum + 1;
end
if PlotExcGen == 1
    if PlotWave == 1
        ExcProfile = sum(nExc,2); % Excitons/cm^3
    else
        ExcProfile = nExc(:,(PlotWave-ShortWave)/dwave);
    end
    subplot(nrow,ncol,gnum), plot(xVec, ExcProfile); ylabel('Number of Excitons (#/cm^3)');
    xlabel('Distance from edge of first absorber (nm)'); title('Exciton Generation Profile');
end
if PrintEQE == 1
    EQE = [LamMat', EQESum]
end
if PrintExGen == 1
    ExcitonX = xVec
    if PlotWave == 1
        ExcProfile = sum(nExc,2) % Excitons/cm^3
    else
        ExcProfile = nExc(:,(PlotWave-ShortWave)/dwave)
    end
    ExcTot = trapz(xVec*10^-7, ExcProfile)
end
end % function

```

R.2. Microscope Image Capture (Fiji/ImageJ)

Although most microscope software comes with a time-series acquisition feature, this can be ponderously slow on less expensive versions (< 1 fps). The camera frame rate on the microscope used in this work varies between 5-8 fps depending on processor load, so a simple solution was to write a screen-capture program. The below code allows for multiple frame rates (for fast/slow/etc. processes) and records other user parameters which are saved in the file name. A time stamp is also placed in the upper-left part of the image.

This code is written in the ImageJ language for Fiji.

```
// Click on Log window and push Esc to stop
frameRate1 = 1; // first frame rate, FPS
frameRate2 = frameRate1/3; // second frame rate, FPS
frameRate3 = 0.1; // third frame rate, FPS
fSwitch = 100; // frame at which frame rate changes
fSwitch2 = 200; // frame at which frame rate changes
MaxFrames = 3600; // Maximum number of frames
SaveDir = "C:\\Users\\HolmesGroup\\Desktop\\User Data\\Tom\\2017\\"; // File save directory
Folder = ""; // Folder to save into, optional
file = "F1687 TCTA30"; // filename
Temp = 235; // Temperature, degrees celcius
Mag = 4; // Magnification
N2flow = 20; // Nitrogen flow rate, SCFM
Lamp = 5; // Lamp intensity
Exposure = 200; // Exposure time, ms
Gain = 3; // Software pixel gain
i = 1; // Starting loop index
*****+
setBatchMode(true);
file = file + " +d2s(Temp,1)+C "+d2s(Mag,0)+"x E"+d2s(Exposure,0)+" N"+d2s(N2flow,0)+"
L"+d2s(Lamp,1)+" G"+d2s(Gain,2)+"
+d2s(frameRate1,2)+_+d2s(frameRate2,2)+_+d2s(frameRate3,2)+"FPS
S"+d2s(fSwitch,0)+_+d2s(fSwitch2,0);
fShort = split(file, " "); setBatchMode(true); file = Folder+file; division = round(1000/frameRate1);
getDateTime(year, month, dayOfWeek, dayOfMonth, hour1, minute1, second1, msec1);
while (i<fSwitch){
    setBatchMode(true);
    getDateTime(year, month, dayOfWeek, dayOfMonth, hour2, minute2, second2, msec2);
    trig = ((hour2-hour1)*3600*1000+(minute2-minute1)*60*1000+(second2-second1)*1000+(msec2-
msec1))/division;
    if (round(trig)==trig) {
```

Appendix R. Relevant Computer Software

```

run("Capture Screen"); setFont("Courier New", 30, "bold antialiased"); setColor("white");
time = d2s((hour2-hour1)*3600+second2-second1+60*(minute2-minute1)+(msec2-msec1)/1000,3);
drawString(time+" sec", 20, 30, "black");
ZeroIter = 6-lengthOf(d2s(i,0)); // determine how many zeros to add after image name
ZeroHold = "";
for (q=0; q<ZeroIter; q++) // create zeros string to insert before image number
    ZeroHold = ZeroHold + "0";
SaveDir1 = SaveDir+file+"-"+ZeroHold+d2s(i,0)+".tif";
saveAs("tif", SaveDir1); // Save modified image
close(); print(fShort[0]+---+i+" "+time); i = i + 1;
}
}

division = round(1000/frameRate2);
while (i<fSwitch2){
    setBatchMode(true);
    getDateAndTime(year, month, dayOfWeek, dayOfMonth, hour3, minute3, second3, msec3);
    trig = ((hour3-hour2)*3600*1000+(minute3-minute2)*60*1000+(second3-second2)*1000+(msec3-msec2))/division;
    if (round(trig)==trig) {
        run("Capture Screen"); setFont("Courier New", 30, "bold antialiased"); setColor("white");
        time = d2s((hour3-hour1)*3600+second3-second1+60*(minute3-minute1)+(msec3-msec1)/1000,3);
        drawString(time+" sec", 20, 30, "black");
        ZeroIter = 6-lengthOf(d2s(i,0)); // determine how many zeros to add after image name
        ZeroHold = "";
        for (q=0; q<ZeroIter; q++) // create zeros string to insert before image number
            ZeroHold = ZeroHold + "0";
        SaveDir1 = SaveDir+file+"-"+ZeroHold+d2s(i,0)+".tif";
        saveAs("tif", SaveDir1); // Save modified image
        close(); print(fShort[0]+---+i+" "+time); i = i + 1;
    }
}

division = round(1000/frameRate3);
while (i<MaxFrames){
    setBatchMode(true);
    getDateAndTime(year, month, dayOfWeek, dayOfMonth, hour4, minute4, second4, msec4);
    trig = ((hour4-hour3)*3600*1000+(minute4-minute3)*60*1000+(second4-second3)*1000+(msec4-msec3))/division;
    if (round(trig)==trig) {
        run("Capture Screen"); setFont("Courier New", 30, "bold antialiased"); setColor("white");
        time = d2s((hour4-hour1)*3600+second4-second1+60*(minute4-minute1)+(msec4-msec1)/1000,3);
        drawString(time+" sec", 20, 30, "black");
        ZeroIter = 6-lengthOf(d2s(i,0)); // determine how many zeros to add after image name
        ZeroHold = "";
        for (q=0; q<ZeroIter; q++) // create zeros string to insert before image number
            ZeroHold = ZeroHold + "0";
        SaveDir1 = SaveDir+file+"-"+ZeroHold+d2s(i,0)+".tif";
        saveAs("tif", SaveDir1); // Save modified image
        close(); print(fShort[0]+---+i+" "+time); i = i + 1;
    }
}

setBatchMode(false);

```

R.3. Image Compilation and Sorting (Matlab)

The image capture software in Appendix R.2. saves a massive set of images into the specified folder. For future processing and to extract key information about the images (magnification, filename, stack size), these images are compiled into sets sorted by folder with key parameters stored in a spreadsheet called “Movie_List.csv”. The code which accomplishes this is written for Matlab and is given below.

```

function MakeAndMove_Movie_3_7
% This program follows a specified folder path, creates new folders corresponding to all .avi files, and
% generates a .csv file compatible with AVI_to_Images.ijm Fiji macro and Crystal_Growth_3.7-8.ijm
% Created by Tom Fielitz, December 11, 2014
%***** Specify file properties *****
filepath = 'C:\Users\HolmesGroup\Desktop\User Data\Tom';
FolderNames = {'2017-02-21 OM Nikon.tif'
    '2017-02-24 OM Nikon.tif'}; % Name of folder within the above directory
NumParts = 3; % Number of spaces folder names will be truncated after
SaveCSV = 1; % Save a .csv file compatible with Fiji macro AVI_to_Images.ijm
MakeFolders = 1; % Toggle whether to make folders
MoveFiles = 1; % Toggle whether to move files to created folders
extension = 'tif'; % File extension, e.g. 'avi' for AVI movies, 'tif' for tif files
%===== End of User Input =====
%
format compact
[nrCell, ncCell] = size(FolderNames);
for i1 = 1:nrCell
    files = [];
    if (nrCell == 1)
        FolderName = FolderNames{1};
    else
        FolderName = FolderNames{i1};
    end
    year = FolderName(1:4);
    cd(sprintf('%s/%s/%s',filepath,year, FolderName));
    sprintf('%s/%s/%s',filepath,year, FolderName)
    files = dir(sprintf('*.%s',extension));
    CSV_array = {0};
    if isempty(files)==1
        error('Check file extension type: no files found')
    end
    folderTitle = {''};
    for i = 1:length(files) % Trim the file names to NumParts length to create folders
        Name = files(i).name;
        parts = strread(Name,'%s','delimiter',' '); % split file name using space as a delimiter

```

Appendix R. Relevant Computer Software

```

folderTitle{i} = " ;
for j = 1:NumParts
    if j==1
        folderTitle{i} = parts{j};
    else
        folderTitle{i} = sprintf('%s %s', folderTitle{i}, parts{j});
    end
end
FileTitle{i} = Name(1:(length(Name)-length(extension)-8)); % File name without extension & #
end
[FTitleReduced, IA, IC] = unique(folderTitle); % Identify unique folder names
[~, col] = size(FTitleReduced);
for j = 1:col % Make new folders and move corresponding files
    disp(sprintf('%d/%d %s',j,col,FTitleReduced{1,j})) % Print folder name to see progress
    if MakeFolders == 1
        mkdir(sprintf('%s/%s/%s',filepath,year, FolderName), FTitleReduced{1,j});
    end
    NewFolder = FTitleReduced{1,j};
    FileDistinct = FileTitle{IA(j)};
    x = find(FileDistinct=='x');
    Magnification = str2double(FileDistinct(x-2:x-1));
    if MoveFiles == 1 && MakeFolders == 1
        movefile(sprintf('%s*.%s',NewFolder,extension),sprintf('%s/%s/%s/%s',filepath,year,
        FolderName,NewFolder));
    end
    if SaveCSV == 1
        CSV_array{j,1} = NewFolder; % Folder name
        CSV_array{j,2} = sprintf('%s%s',FileDistinct,'-{iiii}') % File Name
        CSV_array{j,3} = 1; % Beginning of crystallization
        CSV_array{j,5} = 15; % Options
        CSV_array{j,6} = 10; % Background subtraction frame
        CSV_array{j,7} = Magnification; % Magnification, times
        if j == col
            CSV_array{j,4} = length(IC)-IA(j)+1; % End of crystallization
        else
            CSV_array{j,4} = IA(j+1)-IA(j);
        end
    end
    if (strcmpi(extension, 'jpg') || strcmpi(extension, 'tif') == 1 || strcmpi(extension, 'avi') == 1)&&
    MakeFolders == 1
        mkdir(sprintf('%s/%s/%s',filepath,year, FolderName), '_Movies')
        mkdir(sprintf('%s/%s/%s',filepath,year, FolderName), 'z_Image_Params')
        mkdir(sprintf('%s/%s/%s',filepath,year, FolderName), '_Image_Stats')
    end
    table = cell2table(CSV_array,
    'VariableNames',{'Folder','Movie_Name','tZero','tEnd','Options','BackSub','Mag'})
    writetable(table, 'Movie_List.csv');
end % Loop over folders
end %function

```

R.4. Crystal Growth Image Analysis (Fiji/ImageJ)

The bulk of code written for crystals in this thesis is for the size extraction process because of the complexity and variability of crystal shape and color. Owing to the tediousness of data input, there are also simple GUIs incorporated to expedite data processing. The haphazard fashion with which different types of crystals were encountered lead to a less than cohesive code with some redundancy; a better-designed code would use compartmentalized subfunctions for image pre-processing, edge detection, and any number of other repetitive processes to save on code space and complexity.

Analyzing images using this function begins with inputting a folder path and name for the .csv file created in Appendix R.3. Then, processing information can be collected by setting TestMode = 2 and selecting which subfolder (image stack) number you would like to start with. Running the macro then steps through each image stack to collect data on what type of analysis is desired on which spots.

First, two images are presented: a raw, cropped image and processed image which has enhanced contrast. The program prompts “Compare the two images, then click OK”. This then brings up a set of options of how to proceed, shown in Figure 14.51. “Keep Default” will keep the settings (which can be changed ~line 37-40) which produced the images shown in the crystal analysis. Sometimes, images vary so that this is unacceptable, in which case thresholding (“Custom HSB”) or contrast and thresholding (“Custom BC&HSB”) can be

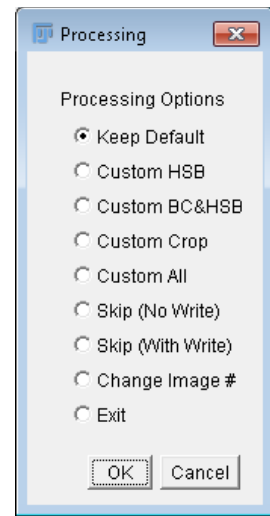


Figure 14.51. Processing options for images.

Appendix R. Relevant Computer Software

changed. If the image was centered differently than the default (line 38) or the previous image stack, “Custom Crop” may be necessary. This setting is saved as default for future stacks during this run of the program. If all parameters must be changed, “Custom All” will do so. Selection of any of these radio buttons walks the user through various mouse clicks and toggles to manipulate these parameters and enter them into dialogues. If collection of parameters is not necessary for this image (*e.g.*, if they have already been collected previously) “Skip (No Write)” will simply skip that stack. Note that all stacks in the range contained in lines 16-17 must have processing parameter files to run completely. “Skip (With Write)” writes a text file of all zeros, *e.g.*, if the image contains no useful points of analysis. If a different point in the image stack would provide greater clarity (*e.g.*, if all crystal had grown together at that point – default on line 35), “Change Image #” will allow a different point in the image stack to be chosen. If parameter collection is completed, “Exit” will close open images and stop the script.

Once this step has been completed, the user is prompted to click all nuclei of interest, which are then used to set up analysis for each site. There are a variety of analyses which are tailored for different types of crystals (Figure 14.52). “+45 deg”, “-45 deg”, and “+/-45 deg” each measure along lines radiating out from the nucleation site center along the defined angle(s), counterclockwise from the image horizontal. This is repeated for nAngles over a range of dAngle (lines 23-

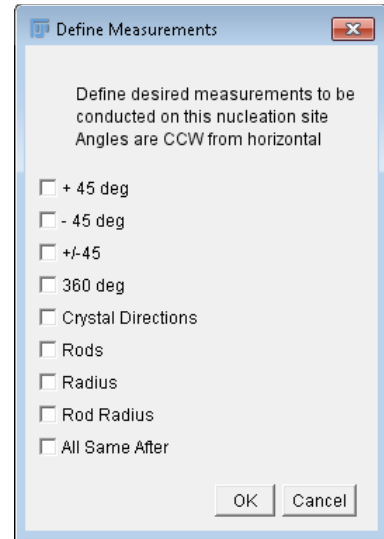


Figure 14.52. Nuclei measurement options.

Appendix R. Relevant Computer Software

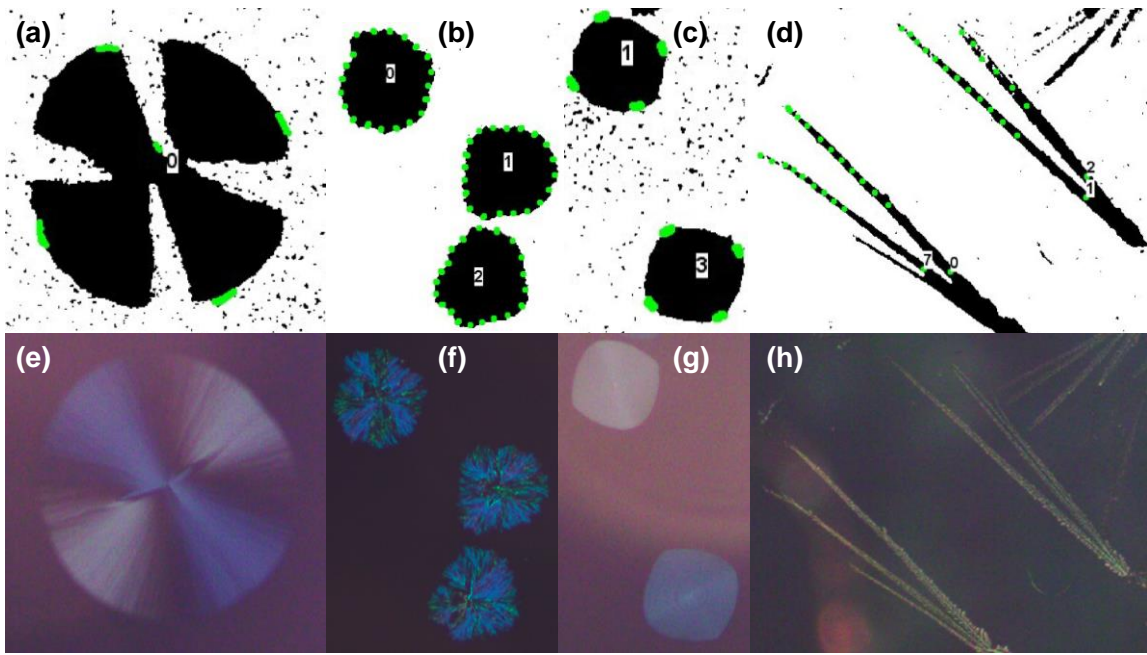


Figure 14.53. Examples of crystal analysis results and suitable crystals. (a),(e) ± 45 deg, (b),(f) 360 deg, (c),(g) crystal directions, and (d),(h) rod radius. Green dots in (a)-(d) denote areas that were tracked.

24) to get an average edge location. This type of analysis is best for smoothly spherulitic crystals which show a well-defined Maltese cross under crossed polarizers at 0° and 90° with respect to the camera axes (Figure 14.53a, e). Depending on the coloration of the intensity bands, one or both may be resolvable, leading to the three cases. “360 deg” measures nAngles distributed over an entire 360° around the nucleation site, and is best for thick or disordered phases showing constant brightness around the crystal (Figure 14.53b, f). “Crystal Directions” prompts the user to draw a line along a particular crystal axis, then to define that axis, other directions of interest, and the unit cell. In-plane angles are calculated from a metric tensor assuming the directions lie in the substrate plane. This method is best for single or twinned crystals with at least one clearly distinguishable axis (Figure 14.53c, g). The “Rods” algorithm was developed to deal with long, thin crystals

Appendix R. Relevant Computer Software

which may branch or change direction during growth. The user draws a line along the long axis of the rod, which the algorithm uses as a starting direction and then axially tracks the center of the rod width to the end (Figure 14.53d, h). “Radius” is similar to “Crystal Directions”, but is for only one direction from the nucleation site – a line must be drawn from the nucleation site in the direction of interest. “Rod Radius” uses the tracking algorithm of “Rods” with the directionality of “Radius”. Defaults for these analyses differ somewhat (lines 43-58) because the crystal types differ. In the event that all nucleation sites in an image stack require the same type (or combination) of analysis, “All Same After” will save many of the defaults for future sites, only requiring that lines be drawn to specify new directions when applicable. These parameters and settings for each image stack are saved into a .txt file in the “z_Image_Params” folder.

The processing parameters input during this stage may be tested by running the program with “TestMode = 1”, which runs analysis on one image within each stack. During analysis, the images will be cropped, brightness and contrast adjusted, an HSB threshold applied, a background image subtracted, noise removed, and finally converted to 8-bit gray scale. This allows the edge-finding algorithm to search along a given or inferred direction until the average pixel brightness drops below a certain threshold value, which trips a conditional statement. The algorithm then continues for a predetermined number of steps farther to search for more crystal (*e.g.*, if the crystal had holes or gaps in it). If it finds more crystal greater than a certain width within that number of steps, it will continue. If not, the analysis is stopped and the end measured as the last point where there was crystal (see lines

Appendix R. Relevant Computer Software

21, 22, 43, 51, and 53). This is repeated many times for each crystal and each image before writing the result to a tab-separated .txt file in the folder “_Image Stats”. The saved data file for each stack contains two sets of columns; one with lightly processed data according to crystal size and standard deviation values in microns, and the other all raw data in pixels. The end points are printed as green dots onto a test image with the site number, saved in the “z_Image_Params” folder for easy viewing to check the analysis before queuing up a complete analysis (“Rods” and “Rod Radius” print a series along the rod so that the path is shown). Individual images may be addressed by selection with lines 16-17 and using the “Skip (No Write)” function to skip over sets which do not need revisiting.

Once the analysis is satisfactory for each sample image, the program may be run with TestMode = 0 to automatically step through all images. While running, the program outputs the image number over the total number of images and the stack number out of the total number of stacks to the log window so that run progress is estimable. Data is saved with each column labelled according to the nucleation site number and type of analysis carried out on that site in the first row, with all user-input analysis parameters saved in the second row. The code runs best in Fiji with no other plugins necessary, and is given below.

```
//=====
//***** User Input Section *****
path="C:\\Users\\HolmesGroup\\Desktop\\User Data\\Tom\\2017\\2017-01-27 OM Nikon.tif"; // Directory to folder
fileName = "\\Movie_List_40.csv"; // Specify file name containing image information

imgIn = ".tif"; // Input image type
imgOut = ".jpg"; // Output (mask result) image type

TestMode = 0; // Test mode options.
// 2 collects processing info
// 1 runs one sample image from each (saving in z_Image_Params folder)
// 0 runs all images, saving in individual folders
```

Appendix R. Relevant Computer Software

```

FolderStart = 1; // Image folder to start analysis on, beginning with 1
FolderEnd = 200; // Image folder to end analysis on (if desired, else set to large number)

// ***** Data Processing *****
WhtSpace = 5; // Number of pixels of white to end particle sizing
BlkSpace = 15; // Width of region (pixels) to constitute a particle
nAngles = 20; // Number of angles to measure if using options > 10
dAngle = 20; // Range of angles scanned (20 = 20 degrees total)
dRAngle = 5; // Angle range for radius measurements (deg, total)
SizeThr = 2; // Exclude all measurements below this size (um)
StdDevThr = 50; // Exclude all measurements after the Std Dev exceeds this value (um)
StdDev360 = 20; // Std Deviation limit for 360 degree measurements
Outliers = 5; // Size of outlier pixels to remove
Append = ""; // Text to append to saved images and text files in testmode = 0

// ***** Default Values for TestMode == 2 *****
ImgFrac = 0.5; // Fraction of way through stack to assess, from 0 to 1
BC_Def = newArray(-2, 16); // Default brightness/contrast values
CropA = newArray(423, 31, 1310, 983); // Default crop
HSB_Def = newArray(0,255,0,255,95,255); // Default HSB values
BW_Def = newArray(0, 60); // Default black & white values
LW_Def = 10; // Default line width
LW_360Def = 20; // Default line width for 360 degree scans
Thr_Def = 150 // Default BW threshold for line profile
thetaMis = 20; // Maximum angle of misalignment for rod tracking (net +/-deg)
nLengths = 1.75; // Number of crystal widths rods will be measured along
minXtalWidth = 2; // Minimum rod-like crystal width to begin analysis (pix)
MinRodW = 5; // Minimum rod resize width (width lower bound)
rodWhtSpc = 2; // Number of white pixels allowed in length determination of rods
rodThresh = 35; // Intensity threshold for finding ends of rods (smaller = more sensitive)
rodLW = 10; // Linewidth for measurements perpendicular to rod length (pixels)
dRad = 20; // Total width of radius sweep (pixels)
nRad = 10; // Number of radius sweeps
checkDef = newArray(0,0,0,0,1,0,0,0); // Default nucleation checkboxes; (45, -45, +/-45, 360, Crystal
Axes, Rods, Radius, Rod Rad, Same Xtals)
Axis_Def = 100; Axis2_Def = 010; // Default crystal axes for custom orientations
color = "red"; // Default nucleation site color: "red", green, blue, cyan, black, white, yellow, orange,
magenta
setBatchMode(true); // True or false to display images while processing (display = false)

// ***** Given crystal systems *****
// List as (a, b, c, alpha, beta, gamma)
Rubrene_Orthorhombic = newArray(7.193, 14.433, 26.86, 90, 90, 90); // Orthorhombic rubrene lattice
params
TPBi = newArray(1,1,1,90,90,90); // TPBi lattice params (made up)
itemsX = newArray("Rubrene (Orth.)", "TPBi", "Other"); // Array of available crystal structures. Must
contain "Other".

// ***** END OF INPUT *****
//=====

```

Appendix R. Relevant Computer Software

```
/*
* README File:
This macro reads a set of images from a base folder and determines the size of particles which have grown
between frames.

Assumes:
1. All images are the same size and format
2. All images begin with index # 0
3. Only images are contained in the image folder
4. The .csv file contains columns which correspond to
    column 1 (data[0]) = image folder name, e.g. F381 20x
    column 2 (data[1]) = image name, e.g. F381 20x P90 E100 Ref-{iiiiii}
    column 3 (data[2]) = frame for t=0 or beginning of crystallization, e.g. 35
    column 4 (data[3]) = frame for end of crystallization, e.g. 50
    column 5 (data[4]) = options for processing of image i and i+1
        0 = i/i0 + i0/i, BW Thresh only (low-contrast, two-toned crystals)
        1 = " with Color, then BW threshold
        2 = i, no math (good for images with high contrast between crystal and background)
        3 = " with Color, then BW threshold
        4 = i-i0, BW Thresh only
        5 = " with Color, then BW threshold
        10+ the above number give analysis via line profile instead of particle analysis (e.g. 15)
    column 6 (data[5]) = frame for background subtraction
    column 7 (data[6]) = Magnification for radius conversion from pixels to um
```

Compatible with Matlab MakeAndMove_Movie2.csv file
Created by Tom Fielitz, University of Minnesota December 16th, 2014

Modifications:

1. 12/18/14 Added columns 8-13 for greater specificity, TestMode
2. 1/6/15 Added options 4,5
3. 1/9/15 Condensed and re-wrote from Crystal_Growth_2.0
4. 1/9/15 Added line profile size determination option
5. 1/13/15 Added feature to save nucleation site location and map of line profile lengths
6. 1/15/15 Added feature to skip white space in crystals, changed output precision, changed input to include default option for processing, changed to three types of nucl. sites (+/-45, 360)
7. 1/21/15 Changed processing to include data processing options (Std Dev threshold, size)
8. 1/30/15 Changed processing to include options to measure along specific axes
9. 2/3/15 Added ability to measure samples with 3,1FPS as single file, fixed bugs
10. 2/6/15 Added multiple frame rate options, 360 deg StdDev threshold, fixed several bugs
11. 2/23/15 Changed to automatic frame rate recognition, background subtraction =/= tZero
12. 3/30/15 Eliminated select threshold for line profile; added exit function
13. 4/22/15 Added "track rod length", and "+-45 Avg" functionality for doped rubrene, etc.; "same crystal type"
14. 4/23/15 Added "radius", fixed bugs
15. 9/9/16 Added "Change Image #" in modifications menu for test mode == 2
16. 1/19/17 Fixed bug in rod radius that caused the angle to be referenced to rod, not rod radius, angle column
17. 1/19/17 Changed rod, rod radius to have xtalWidth vary along length of crystal (inc. length measurement)

Appendix R. Relevant Computer Software

18. 2/6/17 Added option to save crystal direction associated with a radius measurement, fixed radius so it is measured (if statement index was incorrect) and changed to dRAngle

```
=====Beginning of
Code=====
=====
*/
Version = 3.8; // Program version number, e.g. 3.5
path1 = path + fileName;
DataString=File.openAsString(path1); // Open Movie_List.csv file as a string
lines=split(DataString, "\n"); // Split .csv into lines, delimiter = return
nIter1 = lengthOf(lines); // Number of folders to loop over
Results = 0; print(" "); print("Macro beginning! Hope this works..."); print(" ");
getDateAndTime(year1, month1, dayOfWeek1, dayOfMonth1, hour1, minute1, second1, msec1);
// Loop over folders
for (k=FolderStart; k<nIter1; k++) { // Iteration starts at k=1 to account for column titles in .csv file;
stupid = 0;
data=split(lines[k], ","); // Isolate data from line i, split into columns using comma delimiter
stupidArray = split(data[1], {"}); // in case image name has commas in it
while (stupidArray.length < 2){
stupid = stupid+1; data[1] = data[1]+","+data[stupid+1]; stupidArray = split(data[1],"{");
}
print("Folder # "+k+"/"+(nIter1-1)+" ----- "+data[1]); Img0 = parseInt(data[2+stupid]);
list = getFileList(path+'\\"+data[0]); // list of all files in image folder
Opt = parseInt(data[4+stupid]); // options
Bckgrnd = parseFloat(data[5+stupid]); // Frame for background
Mag = parseInt(data[6+stupid]); // Image Magnification
// Load image for t = 0 subtraction
File2 = split(data[1], {"}); // Figure out how many place holders and numbers to add after file name
File3 = split(File2[1], {"}); jString0 = d2s(Img0,0);
ZeroIter = lengthOf(File3[0])-lengthOf(jString0); // determine how many zeros to add after image name
ZeroHold = "";
for (q=0; q<ZeroIter; q++) // create zeros string to insert before image number
ZeroHold = ZeroHold + "0";
tZero = parseInt(File.lastModified(path+"\\" + data[0] + "\\" + File2[0]+ZeroHold+jString0 + imgIn));
jStringB = d2s(Bckgrnd,0);
ZeroIter = lengthOf(File3[0])-lengthOf(jStringB); // determine how many zeros to add after image name
ZeroHold = "";
for (q=0; q<ZeroIter; q++) // create zeros string to insert before image number
ZeroHold = ZeroHold + "0";
tZeroFile = File2[0]+ZeroHold+jStringB + imgIn;
open(path+"\\" + data[0] + "\\" + tZeroFile);
run("Set Scale...", "distance=1 known=1 pixel=1 unit=pixel global");

// **** TestMode == 2 ****
if (TestMode == 2) { // Acquire parameters on automated basis
ImgFrac1 = ImgFrac;
ChangeFrac = 1;
while (ChangeFrac == 1) {
// Run default, ask if it is good enough
File2 = split(data[1], {"}); // Figure out how many place holders and numbers to add after file name
```

Appendix R. Relevant Computer Software

```

File3 = split(File2[1], "}");
iString = d2s(round((parseInt(data[3+stupid])-  

    parseInt(data[2+stupid]))*ImgFrac1)+parseInt(data[2+stupid]),0);
ZeroIter = lengthOf(File3[0])-lengthOf(iString); // determine how many zeros to add after image name
ZeroHold = "";
for (q=0; q<ZeroIter; q++) { // create zeros string to insert before image number
ZeroHold = ZeroHold + "0";
}
NewFile = File2[0]+ZeroHold+iString; NewFileName = File2[0]+ZeroHold+iString + imgIn;
open(path+"\\" + data[0] + "\\" + NewFileName);
if (Opt==0||Opt==1||Opt==10||Opt==11){ // Options
run("Calculator Plus", "i1=[ "+NewFileName+" ] i2=[ "+tZeroFile+"] operation=[Divide: i2 = (i1/i2) x k1 +  

    k2] k1=75 k2=0");
}else if (Opt==4||Opt==5||Opt==14||Opt==15){
imageCalculator("Subtract", NewFileName, tZeroFile);
}
close(tZeroFile); selectWindow(NewFileName);
// ***** Brightness and Contrast *****
run("Brightness/Contrast..."); setMinAndMax(BC_Def[0],BC_Def[1]); selectWindow("B&C");
    run("Close");
// ***** Crop Image *****
makeRectangle(CropA[0],CropA[1],CropA[2],CropA[3]); run("Crop");
// ***** Mask Image *****
height = getHeight; width = getWidth; newImage("Mask1","8-bit white", width, height, 1);
makeRectangle(0,0,width,height); run("Create Mask"); run("Invert LUT"); run("RGB Color");
imageCalculator("Min", NewFileName,"Mask"); close("Mask"); close("Mask1");
selectWindow(NewFileName);
// Thresholding before analysis
if (Opt/2 == round(Opt/2)){ // Options is even
run("8-bit"); setAutoThreshold("Default"); setThreshold(BW_Def[0],BW_Def[1]);
} else { // Options is odd
// Color Thresholder 2.0.0-rc-15/1.49m
setOption("BlackBackground", false); min=newArray(3); max=newArray(3); filter=newArray(3);
    a=getTitle();
run("HSB Stack"); run("Convert Stack to Images"); selectWindow("Hue"); rename("0");
selectWindow("Saturation"); rename("1"); selectWindow("Brightness"); rename("2");
for (j1=0;j1<3;j1++){
min[j1]=HSB_Def[2*j1]; max[j1]=HSB_Def[2*j1+1];
}
filter[0]="pass"; filter[1]="pass"; filter[2]="pass";
for (j=0;j<3;j++){
selectWindow(""+j); setThreshold(min[j], max[j]); run("Convert to Mask");
if (filter[j]=="stop") run("Invert");
}
imageCalculator("AND create", "0","1"); imageCalculator("AND create", "Result of 0","2");
for (j=0;j<3;j++){
selectWindow(""+j); close();
}
selectWindow("Result of 0"); close(); selectWindow("Result of Result of 0"); rename(a);
// Colour Thresholding-----

```

Appendix R. Relevant Computer Software

```

run("8-bit"); setAutoThreshold("Default"); setThreshold(BW_Def[0],BW_Def[1]);
setAutoThreshold("Default");
}
if (Opt>=10){
run("Convert to Mask");
}
// Reduce noise
run("Remove Outliers...", "radius="+Outliers+" threshold=50 which=Bright"); run("Despeckle");
selectWindow(NewFileName); rename("Modified Image");
// Open original file for comparison
open(path+"\\" + data[0] + "\\\" + tZeroFile); open(path+"\\" + data[0] + "\\\" + NewFileName);
selectWindow(NewFileName); rename("Original Image");
if (Opt==0||Opt==1||Opt==10||Opt==11){ // Options
run("Calculator Plus", "i1=[Original Image] i2=[+tZeroFile+] operation=[Divide: i2 = (i1/i2) x k1 + k2]
k1=75 k2=0");
else if (Opt==4||Opt==5||Opt==14||Opt==15){
imageCalculator("Subtract", "Original Image", tZeroFile);
}
// ***** Crop Image *****
makeRectangle(CropA[0],CropA[1],CropA[2],CropA[3]); run("Crop");
// ***** Brightness and Contrast *****
run("Brightness/Contrast..."); setMinAndMax(BC_Def[0],BC_Def[1]);
selectWindow("B&C"); run("Close"); close(tZeroFile); setBatchMode("exit and display");
selectWindow("Original Image"); run("Out [-]"); run("Out [-]"); selectWindow("Modified Image");
run("Out [-]");
// Ask for user input good/bad
waitForUser("Is this image processing acceptable?", "Compare the two images, then click OK");
Dialog.create("Processing");
itemsD = newArray("Keep Default", "Custom HSB", "Custom BC&HSB", "Custom Crop", "Custom All",
"Skip (No Write)", "Skip (With Write)", "Change Image #", "Exit");
Dialog.addRadioButtonGroup("Processing Options", itemsD, 9, 1, "Keep Default"); Dialog.show();
DefaultChoice = Dialog.getRadioButton(); setBatchMode(false); PPTthresh = 0;
BC = newArray(BC_Def[0],BC_Def[1]);
HSB = newArray(HSB_Def[0],HSB_Def[1],HSB_Def[2],HSB_Def[3],HSB_Def[4],HSB_Def[5]);
BW = newArray(BW_Def[0],BW_Def[1]); radius = getWidth();
if (DefaultChoice == "Change Image #"){
Dialog.create("New % through stack")
Dialog.addMessage("Enter a new number 0<n<1 for new \nimage then click OK");
Dialog.addNumber("Fraction:", ImgFrac1); Dialog.show(); ImgFrac1=Dialog.getNumber();
setBatchMode(true); close("Original Image"); close("Modified Image");
open(path+"\\" + data[0] + "\\\" + tZeroFile);
run("Set Scale...", "distance=1 known=1 pixel=1 unit=pixel global");
else{
ChangeFrac = 0;
}
}
// Default Choice == Keep Default *****
if (DefaultChoice == "Keep Default"){
imageCalculator("Add", "Original Image", "Modified Image");
selectWindow("Original Image"); run("In [+]"); run("In [+]");
// Default Choice == Skip (No Write) *****

```

Appendix R. Relevant Computer Software

```

}else if (DefaultChoice == "Skip (No Write)") {
    print(" **** Skipped, not writing text file ****"); setBatchMode(true);
    close("Original Image"); close("Modified Image");
// Default Choice == Skip (With Write) ****
}else if (DefaultChoice == "Skip (With Write)") {
    print(" **** Skipped, writing text file of zeroes ****"); setBatchMode(true);
//***** Default Choice != Keep Default ****
} else if (DefaultChoice == "Exit") {
    close("Original Image");close("Modified Image"); setBatchMode(false);exit();
} else {
    setBatchMode(true);
    open(path+"\\" + data[0] + "\\\" + tZeroFile); open(path+"\\" + data[0] + "\\\" + NewFileName);
    close("Original Image"); close("Modified Image");
    if (Opt==0||Opt==1||Opt==10||Opt==11){ // Options
        run("Calculator Plus", "i1=[+NewFileName+] i2=[+tZeroFile+] operation=[Divide: i2 = (i1/i2) x k1 +
        k2] k1=75 k2=0");
    }else if (Opt==4||Opt==5||Opt==14||Opt==15){
        imageCalculator("Subtract", NewFileName, tZeroFile);
    }
    close(tZeroFile); selectWindow(NewFileName); rename("Modified Image");
// ***** Brightness and Contrast *****
if (DefaultChoice == "Custom All" || DefaultChoice == "Custom BC&HSB"){
    setBatchMode("Exit and Display"); run("Brightness/Contrast..."); //selectWindow("B&C");
    waitForUser("Macro paused", "Change B&C, then click OK");
    Dialog.create("Brightness and Contrast")
    Dialog.addMessage("Enter brightness and \ncontrast min & max values,\nthen click OK");
    Dialog.addNumber("Min", BC_Def[0]); Dialog.addNumber("Max", BC_Def[1]);
    Dialog.show();
    for (i=0; i<2; i++){
        BC[i]=Dialog.getNumber();
    }
    setBatchMode(true);
} else {
    run("Brightness/Contrast..."); setMinAndMax(BC_Def[0],BC_Def[1]);
}
selectWindow("B&C"); run("Close");
// ***** Define radius of largest point of interest *****
if (Opt<=10){
    setBatchMode("Exit and Display"); setTool("line");
    waitForUser("Macro paused", "Draw a line across the largest feature\nof interest, then click OK");
    run("Clear Results"); run("Measure"); radius = round(getResult("Length",0)/2);
    theta = getResult("Angle",0); selectWindow("Results"); run("Close"); setBatchMode(true);
} else if (Opt>10)
    radius = getWidth();
// ***** Crop Image *****
if (DefaultChoice == "Custom Crop"|| DefaultChoice == "Custom All"){
    if (DefaultChoice == "Custom All"){
        setBatchMode("Exit and Display"); Dialog.create("Crop Options");
        itemsC = newArray("New Crop Selection", "Use Previous");
        Dialog.addRadioButtonGroup("Crop Options", itemsC, 2, 1, "Use Previous");
        Dialog.show(); cropChoice = Dialog.getRadioButton();
    }
}

```

Appendix R. Relevant Computer Software

```

} else {
setBatchMode("Exit and Display"); cropChoice = "New Crop Selection";
}
if (cropChoice == "New Crop Selection"){
setTool("rectangle"); waitForUser("Macro paused", "Draw a box around area of image\ninto crop, then click OK");
getSelectionBounds(c0, c1, c2, c3); CropA = newArray(c0, c1, c2, c3);
}
makeRectangle(CropA[0],CropA[1],CropA[2],CropA[3]); run("Crop"); setBatchMode(true);
} else {
makeRectangle(CropA[0],CropA[1],CropA[2],CropA[3]); run("Crop"); cropChoice = "Not New";
}
// ***** Mask Image *****
height = getHeight; width = getWidth; newImage("Mask1", "8-bit white", width, height, 1);
makeRectangle(0,0,width,height); run("Create Mask"); run("Invert LUT"); run("RGB Color");
imageCalculator("Min", "Modified Image", "Mask"); close("Mask"); close("Mask1");
selectWindow("Modified Image");
// ***** Run color threshold *****
if (DefaultChoice == "Custom HSB" || DefaultChoice == "Custom All" || DefaultChoice == "Custom BC&HSB"){
if (Opt/2 != round(Opt/2)){ // Option is odd
setBatchMode("Exit and Display"); run("Color Threshold...");  

//selectWindow("Threshold Color");
waitForUser("Macro paused", "Change color threshold values,\nthen click OK");
Dialog.create("Color Threshold"); Dialog.addMessage("Enter threshold values, then click OK");
Dialog.addNumber("Hue Min", HSB_Def[0]); Dialog.addNumber("Hue Max", HSB_Def[1]);
Dialog.addNumber("Sat Min", HSB_Def[2]); Dialog.addNumber("Sat Max", HSB_Def[3]);
Dialog.addNumber("Br Min", HSB_Def[4]); Dialog.addNumber("Br Max", HSB_Def[5]);
Dialog.show(); selectWindow("Threshold Color"); run("Close");
for (i=0; i<6; i++){
HSB[i]=Dialog.getNumber();
}
setBatchMode(true); setOption("BlackBackground", false);
min=newArray(3); max=newArray(3); filter=newArray(3); a=getTitle();
run("HSB Stack"); run("Convert Stack to Images"); selectWindow("Hue"); rename("0");
selectWindow("Saturation"); rename("1"); selectWindow("Brightness"); rename("2");
for (j=0;j1<3;j1++){
min[j]=HSB[2*j]; max[j]=HSB[2*j+1];
}
filter[0]="pass"; filter[1]="pass"; filter[2]="pass";
for (j=0;j<3;j++){
selectWindow(""+j); setThreshold(min[j], max[j]); run("Convert to Mask");
if (filter[j]=="stop") run("Invert");
}
imageCalculator("AND create", "0", "1"); imageCalculator("AND create", "Result of 0", "2");
for (j=0;j<3;j++){
selectWindow(""+j); close();
}
selectWindow("Result of 0"); close(); selectWindow("Result of Result of 0"); rename(a);
}
} else { // Default color threshold

```

Appendix R. Relevant Computer Software

```

// Color Thresholder 2.0.0-rc-15/1.49m
setBatchMode(true); setOption("BlackBackground", false);
min=newArray(3); max=newArray(3); filter=newArray(3); a=getTitle();
run("HSB Stack"); run("Convert Stack to Images"); selectWindow("Hue"); rename("0");
selectWindow("Saturation"); rename("1"); selectWindow("Brightness"); rename("2");
for (j1=0;j1<3;j1++){
min[j1]=HSB_Def[2*j1]; max[j1]=HSB_Def[2*j1+1];
}
filter[0]="pass"; filter[1]="pass"; filter[2]="pass";
for (j=0;j<3;j++){
selectWindow(""+j); setThreshold(min[j], max[j]); run("Convert to Mask");
if (filter[j]=="stop") run("Invert");
}
imageCalculator("AND create", "0","1"); imageCalculator("AND create", "Result of 0","2");
for (j=0;j<3;j++){
selectWindow(""+j); close();
}
selectWindow("Result of 0"); close(); selectWindow("Result of Result of 0"); rename(a);
}
// ***** Run B & W Threshold *****
if (DefaultChoice == "Custom All"){
setBatchMode("Exit and Display"); run("8-bit"); setAutoThreshold("Default"); run("Threshold... ");
setAutoThreshold("Default");
waitForUser("Macro paused", "Change intensity threshold \nvalues, then click OK");
Dialog.create("B & W Threshold"); Dialog.addMessage("Enter threshold values, then click OK");
Dialog.addNumber("Min", BW_Def[0]); Dialog.addNumber("Max", BW_Def[1]); Dialog.show();
selectWindow("Threshold"); run("Close"); setBatchMode(true); BW = newArray(2);
for (i=0; i<2; i++){
BW[i]=Dialog.getNumber();
}
setThreshold(BW[0],BW[1]);
} else {
run("8-bit"); setAutoThreshold("Default"); setThreshold(BW_Def[0],BW_Def[1]);
setAutoThreshold("Default");
}
if (Opt>=10){
run("Convert to Mask");
}
// Reduce noise
run("Remove Outliers...", "radius="+Outliers+" threshold=50 which=Bright"); run("Despeckle");
// Open & process original file for nucleation site identification
open(path+"\\" + data[0] + "\\\" + tZeroFile); open(path+"\\" + data[0] + "\\\" + NewFileName);
selectWindow(NewFileName); rename("Original Image");
if (Opt==0||Opt==1||Opt==10||Opt==11){ // Options
run("Calculator Plus", "i1=[Original Image] i2=[\"+tZeroFile+] operation=[Divide: i2 = (i1/i2) x k1 + k2]
k1=75 k2=0");
} else if (Opt==4||Opt==5||Opt==14||Opt==15){
imageCalculator("Subtract", "Original Image", tZeroFile);
}
// ***** Crop Image *****
makeRectangle(CropA[0],CropA[1],CropA[2],CropA[3]); run("Crop");

```

Appendix R. Relevant Computer Software

```

// ***** Brightness and Contrast *****
run("Brightness/Contrast..."); setMinAndMax(BC[0],BC[1]); selectWindow("B&C"); run("Close");
close(tZeroFile); setBatchMode("exit and display"); selectWindow("Modified Image");
run("Invert LUT");
if ((DefaultChoice == "Custom Crop") && (cropChoice == "New Crop Selection"))||DefaultChoice ==
    "Custom BC&HSB"){
imageCalculator("Min", "Original Image", "Modified Image");
} else {
imageCalculator("Max", "Original Image", "Modified Image");
}
selectWindow("Original Image");
}// If Default choice != keep default
// ***** All Code - Analyze Particles *****
if (Opt < 10 && DefaultChoice != "Skip (No Write)" && DefaultChoice != "Skip (With Write)"){ //
    Analyze particles
setBatchMode(true); run("Analyze Particles...", "size=200-Infinity show=[Overlay Outlines] display clear
    include");
run("Labels...", "color=white font=18 show draw bold");
saveAs("Results", path+"\\\"+data[0]+"\\\"+data[0] + " " + d2s(Bckgrnd,0) + "-" + iString +".txt"); Results =
    1;
} else if (Opt>=10 && DefaultChoice != "Skip (No Write)") {
if (DefaultChoice == "Skip (With Write)") {
NR2 = 0; xA = newArray(1); yA = newArray(1);
} else {
// *** Define points of interest *****
makeLine(0,0,1,1); run("Clear Results"); setTool("point"); bgSpc = " ";
run("Point Tool...", "type=Hybrid color=Red size=[Large] label");
// Collect nucleation sites
waitForUser("Macro paused", "Click all nuclei to measure \n\n-Holding shift allows multiple selections\n-
    Push ALT and click to remove points\n-Click and drag to move points");
run("Clear Results"); run("Measure"); NR2 = nResults; xA = newArray(1); yA = newArray(1);
if (isNaN(getResult("X",0)) == 0){
for (i=0; i<nResults; i++){
xA = Array.concat(xA,getResult("X",i)); yA = Array.concat(yA,getResult("Y",i));
}
}
selectWindow("Results"); run("Close");
}
ABC = newArray(6*NR2); UVW = newArray(6*NR2); nCustom = 0; angle = newArray(8*NR2);
cBox = newArray(4); SameType = 0; RadDir = newArray(NR2);
if (xA.length > 1){
for (i=0; i<NR2; i++){ // Figure out orientation
if (SameType == 1){ // If crystals are all the same type, streamline the process
angle[i*8]=angle[iSame*8]; angle[1+i*8]=angle[iSame*8+1]; angle[2+i*8]=angle[iSame*8+2];
angle[3+i*8]=angle[iSame*8+3]; angle[4+i*8]=angle[iSame*8+4]; angle[5+i*8]=angle[iSame*8+5];
angle[6+i*8]=angle[iSame*8+6]; angle[7+i*8]=angle[iSame*8+7];
if (angle[3+i*8]==0){ // crystal directions
makeRectangle(xA[i+1]-200,yA[i+1]-200, 400, 400); run("To Selection"); makePoint(xA[i+1],yA[i+1]);
makeRectangle(xA[i+1]-5,yA[i+1]-5, 10, 10);
run("Rounded Rect Tool...", "stroke=10 corner=20 color="+color+" fill=none");
setTool("line"); run("Line Width...", "line=2");
}
}
}
}

```

Appendix R. Relevant Computer Software

```

waitForUser("XTAL DIRECTIONS", "Draw a line along the crystal axis of interest\nfor the nucleation site
shown, then click OK");
run("Original Scale"); run("Clear Results"); run("Measure"); angle[3+i*8] = getResult("Angle",0);
for (i1=0;i1<6;i1++){
    UVW[i1+i*6]=UVW[i1+iSame*6];
}
if (xtalSystem == "Rubrene (Orth.)"){
    for (i1=0;i1<6;i1++){
        ABC[i1+i*6] = Rubrene_Orthorhombic[i1];
    }
}else if(xtalSystem == "TPBi"){
    for (i1=0;i1<6;i1++){
        ABC[i1+i*6] = TPBi[i1];
    }
}else if(xtalSystem == "Other"){
    for (i1=0;i1<6;i1++){
        ABC[i1+i*6]=Dialog.getNumber();
    }
selectWindow("Results"); run("Close");
}else{ // fill arrays with zeroes
for (i1=0;i1<6;i1++){
    UVW[i1+i*6]=0;
}
for (i1=0;i1<6;i1++){
    ABC[i1+i*6] = 0;
}
}
if (angle[4+i*8]!=0){ // rods
makeRectangle(xA[i+1]-200,yA[i+1]-200,400,400); run("To Selection");makePoint(xA[i+1],yA[i+1]);
makeRectangle(xA[i+1]-5,yA[i+1]-5,10,10);
run("Rounded Rect Tool...", "stroke=10 corner=20 color="+color+" fill=none");
setTool("line"); run("Line Width...", "line=2");
waitForUser("RODS", "Draw a line along the rod axis of interest\nfor the nucleation site shown, then click
OK");
run("Original Scale"); run("Clear Results"); run("Measure"); angle[4+i*8] = getResult("Angle",0);
}
if (angle[6+i*8]!=0){ // radius
makeRectangle(xA[i+1]-200,yA[i+1]-200,400,400); run("To Selection");makePoint(xA[i+1],yA[i+1]);
makeRectangle(xA[i+1]-5,yA[i+1]-5,10,10);
run("Rounded Rect Tool...", "stroke=10 corner=20 color="+color+" fill=none");
setTool("line"); run("Line Width...", "line=2");
waitForUser("RADIUS", "Draw a line along the direction of interest\n (DIRECTION MATTERS)\nfor
the nucleation site shown, then click OK");
run("Original Scale"); run("Clear Results"); run("Measure"); angle[6+i*8] = getResult("Angle",0);
Dialog.create("Crystal Direction"); Dialog.addMessage("Define crystal axis line represents:");
Dialog.addNumber("Axis = ", 100); Dialog.show(); RadDir[i]=Dialog.getNumber();
}
if (angle[7+i*8]!=0){ // rod radius
makeRectangle(xA[i+1]-200,yA[i+1]-200,400,400); run("To Selection");makePoint(xA[i+1],yA[i+1]);
makeRectangle(xA[i+1]-5,yA[i+1]-5,10,10);
}

```

Appendix R. Relevant Computer Software

```

run("Rounded Rect Tool...", "stroke=10 corner=20 color="+color+" fill=None");
setTool("line"); run("Line Width...", "line=2");
waitForUser("ROD RADIUS", "Draw a line along the rod direction of interest\n (DIRECTION MATTERS)\nfor the nucleation site shown, then click OK");
run("Original Scale"); run("Clear Results"); run("Measure"); angle[7+i*8] = getResult("Angle",0);
}
}else{ // Individual crystal selection
makeRectangle(xA[i+1]-200,yA[i+1]-200, 400, 400); run("To Selection"); makePoint(xA[i+1],yA[i+1]);
makeRectangle(xA[i+1]-5,yA[i+1]-5, 10, 10); setForegroundColor(255,0,0);
run("Rounded Rect Tool...", "stroke=10 corner=20 color="+color+" fill=None");
Dialog.create("Define Measurements");
Dialog.addMessage("Define desired measurements to be\nconducted on this nucleation site\n\nAngles are CCW from horizontal");
labels = newArray(" +45 deg", "- 45 deg", "+/-45", "360 deg", "Crystal Directions", "Rod", "Radius", "Rod Radius", "All Same After");
Dialog.addCheckboxGroup(labels.length, 1, labels, checkDef); Dialog.show();
angle[i*8]=45*Dialog.getCheckbox(); // +45
angle[1+i*8]=-45*Dialog.getCheckbox(); // -45
angle[5+i*8]=Dialog.getCheckbox(); // +/- 45
angle[2+i*8]=360*Dialog.getCheckbox(); // 360
angle[3+i*8]=Dialog.getCheckbox(); // Custom
angle[4+i*8]=Dialog.getCheckbox(); // Rods Y/N
angle[6+i*8]=Dialog.getCheckbox(); // Radius
angle[7+i*8]=Dialog.getCheckbox(); // Rod Radius
SameType = Dialog.getCheckbox(); // Same type
if (SameType == 1){
iSame = i;
}
if (angle[3+i*8]==1){ // crystal directions
makeRectangle(xA[i+1]-200,yA[i+1]-200, 400, 400); run("To Selection"); makePoint(xA[i+1],yA[i+1]);
makeRectangle(xA[i+1]-5,yA[i+1]-5, 10, 10);
run("Rounded Rect Tool...", "stroke=10 corner=20 color="+color+" fill=None");
setTool("line"); run("Line Width...", "line=2");
waitForUser("CRYSTAL AXES", "Draw a line along the crystal axis of interest\nfor the nucleation site shown, then click OK");
run("Original Scale"); run("Clear Results"); run("Measure"); angle[3+i*8] = getResult("Angle",0);
Dialog.create("Select Axes"); Dialog.addMessage("Define crystal axis line represents:");
Dialog.addNumber("Axis = ", Axis_Def);
Dialog.addMessage("Define other crystal axes to measure \n Naming = 100 for [1,0,0]");
Dialog.addNumber("Axis 1: ", Axis2_Def); Dialog.addNumber("Axis 2: ", 0);
Dialog.addNumber("Axis 3: ", 0); Dialog.addNumber("Axis 4: ", 0); Dialog.addNumber("Axis 5: ", 0);
Dialog.addRadioButtonGroup("Select crystal system or enter one", itemsX, itemsX.length, 1, "Rubrene (Orth.)");
Dialog.addNumber("a = ", 1); Dialog.addNumber("b = ", 1); Dialog.addNumber("c = ", 1);
Dialog.addNumber("alpha = ", 90); Dialog.addNumber("beta = ", 90);
Dialog.addNumber("gamma = ", 90); Dialog.show();
for (i1=0;i1<6;i1++){
UVW[i1+i*6]=Dialog.getNumber();
}
xtalSystem = Dialog.getRadioButton();
if (xtalSystem == "Rubrene (Orth.)"){

```

Appendix R. Relevant Computer Software

```

for (i1=0;i1<6;i1++){
    ABC[i1+i*6] = Rubrene_Orthorhombic[i1];
}
else if(xtalSystem == "Other"){
for (i1=0;i1<6;i1++){
    ABC[i1+i*6]=Dialog.getNumber();
}
}
selectWindow("Results"); run("Close");
else{ // fill arrays with zeroes
for (i1=0;i1<6;i1++){
    UVW[i1+i*6]=0;
}
for (i1=0;i1<6;i1++){
    ABC[i1+i*6] = 0;
}
if (angle[4+i*8]==1){ // Rods
makeRectangle(xA[i+1]-200,yA[i+1]-200, 400, 400); run("To Selection");makePoint(xA[i+1],yA[i+1]);
makeRectangle(xA[i+1]-5,yA[i+1]-5, 10, 10);
run("Rounded Rect Tool...", "stroke=10 corner=20 color="+color+" fill=none");
setTool("line"); run("Line Width...", "line=2");
waitForUser("RODS", "Draw a line along the rod axis of interest\nfor the nucleation site shown, then click
OK");
run("Original Scale"); run("Clear Results"); run("Measure"); angle[4+i*8] = getResult("Angle",0);
selectWindow("Results"); run("Close");
}
if (angle[6+i*8]==1){ // Radius
makeRectangle(xA[i+1]-200,yA[i+1]-200, 400, 400); run("To Selection");makePoint(xA[i+1],yA[i+1]);
makeRectangle(xA[i+1]-5,yA[i+1]-5, 10, 10);
run("Rounded Rect Tool...", "stroke=10 corner=20 color="+color+" fill=none");
setTool("line"); run("Line Width...", "line=2");
waitForUser("RADIUS", "Draw a line along the radius of interest\n (DIRECTION MATTERS) \nfor
the nucleation site shown, then click OK");
run("Original Scale"); run("Clear Results"); run("Measure"); angle[6+i*8] = getResult("Angle",0);
selectWindow("Results"); run("Close"); Dialog.create("Crystal Direction");
Dialog.addMessage("Define crystal axis line represents:"); Dialog.addNumber("Axis = ", 100);
Dialog.show(); RadDir[i]=Dialog.getNumber();
}
if (angle[7+i*8]==1){ // Rod Radius
makeRectangle(xA[i+1]-200,yA[i+1]-200, 400, 400); run("To Selection");makePoint(xA[i+1],yA[i+1]);
makeRectangle(xA[i+1]-5,yA[i+1]-5, 10, 10);
run("Rounded Rect Tool...", "stroke=10 corner=20 color="+color+" fill=none");
setTool("line"); run("Line Width...", "line=2");
waitForUser("ROD RADIUS", "Draw a line in the direction of interest\n (DIRECTION MATTERS)
\nfor the nucleation site shown, then click OK");
run("Original Scale"); run("Clear Results"); run("Measure"); angle[7+i*8] = getResult("Angle",0);
selectWindow("Results"); run("Close");
}
} // Individual nucleation site selection
}// loop over custom nucleation sites

```

Appendix R. Relevant Computer Software

```

}// if xA.length > 1
// Set thresholding level
PPThresh = 60; LineWidth = 1; setBatchMode(true); close("Original Image"); close("Modified Image");
// ***** Save in text file *****
f = File.open(path+"\"+"z_Image_Params\""+data[0]+" Params.txt");
for (i=0; i< maxOf(6,lengthOf(xA)-1); i++){
if (i>=BC.length){
BCf = 0;
}else{
BCf = BC[i];
}
if (i>=xA.length-1){
xAf = 0; yAf = 0; theta = 0; ABCA = " "; UVWA = " "; thetaA = " "; thetaXA = " ";
for (i1=0;i1<6;i1++){
ABCA = ABCA + " \t"+d2s(0,6);
}
for (i1=0;i1<6;i1++){
UVWA = UVWA + " \t" +d2s(0,0);
}
for (i1=0;i1<4;i1++){
thetaA = thetaA + " \t" +d2s(0,6);
}
for (i1=0;i1<4;i1++){
thetaXA = thetaXA + " \t" +d2s(0,6);
}
}else{
xAf = xA[i+1]; yAf = yA[i+1]; theta = angle[i+1]; ABCA = " "; UVWA = " ";thetaA = " "; thetaXA = " ";
for (i1=0;i1<6;i1++){
ABCA = ABCA + " \t"+d2s(ABC[i1+i*6],6);
}
for (i1=0;i1<6;i1++){
UVWA = UVWA + " \t" +d2s(UVW[i1+i*6],0);
}
for (i1=0;i1<4;i1++){
thetaA = thetaA + " \t" +d2s(angle[i1+i*8],6);
}
for (i1=0;i1<4;i1++){
thetaXA = thetaXA + " \t" +d2s(angle[i1+4+i*8],6);
}
}
if (i>=HSB.length){
HSBf = 0;
}else{
HSBf = HSB[i];
}
if (i>=BW.length){
BWf = 0;
}else{
BWf = BW[i];
}
if (i>=CropA.length){

```

Appendix R. Relevant Computer Software

```

CropAf = 0;
}else{
CropAf = CropA[i];
}
if (i>=RadDir.length){
RadDirf = 0;
}else{
RadDirf = RadDir[i];
}
if (i==0){
print(f,B&C   +" \t"+ "CropA   +" \t"+ "Radius   +" \t"+ "LineWidth+" \t"+ "PPThresh+" \t"+ "Nucl.
xA +" \t"+ "Nucl. yA+" \t"+ "HSB Thresh+" \t"+ "BW Thresh+" \t"+ "+45"+ \t"+ -45"+ \t"+ "360"+ "
\t"+ "Custom"+ \t"+ "a"+ \t"+ "b"+ \t"+ "c"+ \t"+ "alpha"+ \t"+ "beta"+ \t"+ "gamma"+ \t"+ "Growth
Directions"+ \t"+ \t"+ \t"+ \t"+ \t"+ "Rod Angle"+ \t"+ "+45"+ \t"+ "Radius"+ \t"+ "Rod
Rad"+ \t"+ "Rad Dir");
}
print(f,d2s(BCf,0) + " \t" + d2s(CropAf,0) + " \t" + d2s(radius,6) + " \t" + d2s(LineWidth,0) + " \t"+
d2s(PPThresh,0)+ " \t" + d2s(xAf,0) + " \t" + d2s(yAf,0) + " \t" + d2s(HSBf,0) + " \t" + d2s(BWf,0) +
theta + ABCA + UVWA + thetaXA + " \t" + d2s(RadDirf,0));
}
File.close(f);
} // Options > 10
} // If TestMode == 2

//=====================================================================
//***** TestMode = 0, 1 *****
if (TestMode == 0 || TestMode == 1){
selectWindow(tZeroFile); rename("tZeroFile");
f = File.open(path+"\\\"_Image Stats\\\" + data[0]+ " Stats"+Append+.txt"); // Open file to save size
results to
if (File.exists(path+"\\z_Image_Params\\\"+data[0]+ " Params.txt")==0){
exit(data[0]+ " Params.txt not found: run macro with TestMode=2 first");
}
// Extract data from text file:
txtData = File.openAsString(path+"\\z_Image_Params\\\"+data[0]+ " Params.txt");
lines2 = split(txtData, "\n");BC = newArray(lines2.length); CropA = newArray(lines2.length);
xA = newArray(lines2.length); yA = newArray(lines2.length);
HSB = newArray(lines2.length); BW = newArray(lines2.length);
theta = newArray(lines2.length*6); thetaX = newArray(lines2.length*4);
ABC = newArray(lines2.length*6); UVW = newArray(lines2.length*6);
RadDir = newArray(lines2.length);
for (i=0; i<lengthOf(lines2)-1; i++){
Colms = split(lines2[i+1], " /t"); BC[i] = parseInt(Colms[0]); CropA[i] = parseInt(Colms[1]);
radius = parseInt(Colms[2]); LineWidth = parseInt(Colms[3]); threshold = parseInt(Colms[4]);
xA[i] = parseInt(Colms[5]); yA[i] = parseInt(Colms[6]);
HSB[i] = parseInt(Colms[7]); BW[i] = parseInt(Colms[8]);
if (Colms.length > 26){
for (i1=0;i1<4;i1++){
thetaX[4*i+i1] = parseFloat(Colms[25+i1]);
}
RadDir[i] = parseInt(Colms[29]);
}
}

```

Appendix R. Relevant Computer Software

```

} else{
for (i1=0;i1<4;i1++){
thetaX[4*i+i1] = 0;
}
RadDir[i] = parseInt(Colms[25]);
}
for (i1=0;i1<4;i1++){
theta[4*i+i1] = parseFloat(Colms[9+i1]);
}
for (i1=0;i1<6;i1++){
ABC[6*i+i1] = parseFloat(Colms[13+i1]); UVW[6*i+i1] = parseFloat(Colms[19+i1]);
}
}
xAL = 0;
for (j3=0;j3<xAL.length;j3++){ // determine how many nucleation sites there are
if (xA[j3]>0)
xAL = xAL + 1;
}
totCustom = 0;
for (j3=0;j3<xAL;j3++){ // Determine how many total angles there are per site & store them in array
for (j3a=0; j3a<3;j3a++){
if (theta[4*j3+j3a]!=0)
totCustom = totCustom + 1;
}
for (j3a=0; j3a<4;j3a++){
if (thetaX[4*j3+j3a]!=0)
totCustom = totCustom + 1;
}
for (j3a=0; j3a<6;j3a++){
if (UVW[6*j3+j3a]!=0)
totCustom = totCustom + 1;
}
}
sample = "Image #" + "\t" + "Time (sec)" + "\t"+ "Crys. Area (pix)" + "\t";
for (i2=0;i2<xAL; i2++){ // Loop over titles
if (thetaX[4*i2]!=0) // Add titles for text file for Rods if they exist
sample = sample + "Rod "+d2s(i2,0)+" (um)" + "\t" + "Rod StDev"+d2s(i2,0) + "\t";
if (thetaX[4*i2+1]!=0) // Add titles for text file for +/-45 deg if they exist
sample = sample + "+/-45 Rad"+d2s(i2,0)+" (um)" + "\t" + "+/-45 StDev"+d2s(i2,0) + "\t";
if (thetaX[4*i2+2]!=0) // Add titles for text file for Radius if they exist
if (RadDir[i2]>=100){
sample = sample + "Radius"+d2s(i2,0)+" [+d2s(RadDir[i2],0)+]" (um)" + "\t" + "Radius
StDev"+d2s(i2,0)+" [+d2s(RadDir[i2],0) + ] \t";
}else if (RadDir[i2]>=10){
sample = sample + "Radius"+d2s(i2,0)+" [0"+d2s(RadDir[i2],0)+"] (um)" + "\t" + "Radius
StDev"+d2s(i2,0)+" [0"+d2s(RadDir[i2],0) + "] \t";
}else {
sample = sample + "Radius"+d2s(i2,0)+" [00"+d2s(RadDir[i2],0)+"] (um)" + "\t" + "Radius
StDev"+d2s(i2,0)+" [00"+d2s(RadDir[i2],0) + "] \t";
}
if (thetaX[4*i2+1]!=0) // Add titles for text file for Rod Rad if they exist

```

Appendix R. Relevant Computer Software

```

sample = sample + "Rod Rad"+d2s(i2,0)+" (um)" + " \t" + "Rod StDev"+d2s(i2,0) + " \t";
for (j3=0;j3<3;j3++){ // Add titles for text file for +45, -45, 360 deg if they exist
if (theta[4*i2+j3]!=0)
sample = sample + "Rad"+d2s(i2,0)+" "+d2s(theta[4*i2+j3],0)+" (um)" + " \t" + "StDev"+d2s(i2,0)+" "
    "+d2s(theta[4*i2+j3],0) + " \t";
}
for (j3=0;j3<6;j3++){ // Add titles for text file for crystal directions if they exist
if (UVW[6*i2+j3]!=0){
if (UVW[6*i2+j3]>=100){
sample = sample + "Rad"+d2s(i2,0)+" ["+d2s(UVW[6*i2+j3],0)+"] (um)" + " \t" + "StDev"+d2s(i2,0)+" "
    "+d2s(UVW[6*i2+j3],0) + "] \t";
else if (UVW[6*i2+j3]>=10){
sample = sample + "Rad"+d2s(i2,0)+" [0"+d2s(UVW[6*i2+j3],0)+"] (um)" + " \t" + "StDev"+d2s(i2,0)+" "
    "[0"+d2s(UVW[6*i2+j3],0) + "] \t";
else {
sample = sample + "Rad"+d2s(i2,0)+" [00"+d2s(UVW[6*i2+j3],0)+"] (um)" + " \t" + "StDev"+d2s(i2,0)+" "
    "[00"+d2s(UVW[6*i2+j3],0) + "] \t";
}
}
}
}
// loop over titles
for (i2=0;i2<xAL; i2++){ // Same now for raw data
if (thetaX[4*i2]!=0) // Add titles for text file for Rods if they exist
sample = sample + "RRod"+d2s(i2,0)+" (um)" + " \t" + "RRod StDev"+d2s(i2,0) + " \t";
if (thetaX[4*i2+1]!=0) // Add titles for text file for +/-45 deg if they exist
sample = sample + "R+/-45 Rad"+d2s(i2,0)+" (um)" + " \t" + "R+/-45 StDev"+d2s(i2,0) + " \t";
if (thetaX[4*i2+2]!=0) // Add titles for text file for Radius if they exist
// sample = sample + "RRadius"+d2s(i2,0)+" (um)" + " \t" + "RRad StDev"+d2s(i2,0) + " \t";
if (RadDir[i2]>=100){
sample = sample + "RRadius"+d2s(i2,0)+" ["+d2s(RadDir[i2],0)+"] (um)" + " \t" + "RRad
    StDev"+d2s(i2,0)+" ["+d2s(RadDir[i2],0) + "] \t";
else if (RadDir[i2]>=10){
sample = sample + "RRadius"+d2s(i2,0)+" [0"+d2s(RadDir[i2],0)+"] (um)" + " \t" + "RRad
    StDev"+d2s(i2,0)+" [0"+d2s(RadDir[i2],0) + "] \t";
else {
sample = sample + "RRadius"+d2s(i2,0)+" [00"+d2s(RadDir[i2],0)+"] (um)" + " \t" + "RRad
    StDev"+d2s(i2,0)+" [00"+d2s(RadDir[i2],0) + "] \t";
}
}
if (thetaX[4*i2+3]!=0) // Add titles for text file for Rod Rad if they exist
sample = sample + "RRodRad"+d2s(i2,0)+" (um)" + " \t" + "RRodRad StDev"+d2s(i2,0) + " \t";
for (j3=0;j3<3;j3++){ // Add titles for text file for +45, -45, 360 deg if they exist
if (theta[4*i2+j3]>0)
sample = sample + "RawRad"+d2s(i2,0)+" "+d2s(theta[4*i2+j3],0)+" (um)" + " \t" +
    "RStDev"+d2s(i2,0)+" "+d2s(theta[4*i2+j3],0) + " \t";
}
for (j3=0;j3<6;j3++){ // Add titles for text file for crystal directions if they exist
if (UVW[6*i2+j3]>0{
if (UVW[6*i2+j3]>=100){
sample = sample + "RawRad"+d2s(i2,0)+" ["+d2s(UVW[6*i2+j3],0)+"] (pix)" + " \t" +
    "RStDev"+d2s(i2,0)+" ["+d2s(UVW[6*i2+j3],0) + "] \t";
else if (UVW[6*i2+j3]>=10){

```

Appendix R. Relevant Computer Software

```

sample = sample + "RawRad"+d2s(i2,0)+" [0"+d2s(UVW[6*i2+j3],0)+"] (pix)" + " \t" +
    "RStDev"+d2s(i2,0)+" [0"+d2s(UVW[6*i2+j3],0) + "] \t";
}else{
sample = sample + "RawRad"+d2s(i2,0)+" [00"+d2s(UVW[6*i2+j3],0)+"] (pix)" + " \t" +
    "RStDev"+d2s(i2,0)+" [00"+d2s(UVW[6*i2+j3],0) + "] \t";
}
}
}
}
} // raw data title loop
print(f, sample); // write titles to text file
print(f, "WhtSpace = "+d2s(WhtSpace,0)+ " \t"+ "BlkSpace = "+d2s(BlkSpace,0)+ " \t"+ "nAngles =
    "+d2s(nAngles,0)
+ " \t"+ "dAngle = "+d2s(dAngle,0)+ " \t"+ "SizeThr = "+d2s(SizeThr,0)+ " \t"+ "StdDevThr =
    "+d2s(StdDevThr,0)
+ " \t"+ "StdDev360 = "+d2s(StdDev360,0) + " \t"+ "LW_360Def = "+d2s(LW_360Def,0) + " \t"+ "thetaMis
    = "+thetaMis+ " \t"
+ "minXtalWidth = "+minXtalWidth+ " \t"+ "rodWhtSpc = "+rodWhtSpc+ " \t"+ "rodThresh =
    "+rodThresh+ " \t"+ "rodLW = "+ rodLW
+ " \t"+ "Outliers = "+Outliers+ " \t" + "Version = "+d2s(Version,0));
if (lengthOf(CropA)>1){
c0=CropA[0]; c1=CropA[1]; c2=CropA[2]; c3=CropA[3];
makeRectangle(c0, c1, c2, c3);
run("Crop");
}
if (Mag==4){ // Determine scaling for pixel to micron conversion
MagFact = 0.6965;
}else if (Mag==10){
MagFact = 1.7505;
}else if (Mag==20){
MagFact = 3.4743;
}else if (Mag==50){
MagFact = 8.7753;
}else { // if no magnification match, use pixels
MagFact = 1/getWidth();
}
Width1 = getWidth();
if (radius > 0 && Opt<=10){
height = getHeight; width = getWidth; newImage("Mask1","8-bit white", width, height, 1);
for (ROI=0; ROI<xAL; ROI++){
if (lengthOf(CropA)>1){
x = xA[ROI]-CropA[0]; y = yA[ROI]-CropA[1];
}else {
x = xA[ROI]; y = yA[ROI];
}
setKeyDown("shift"); makeOval(x-radius,y-radius,radius*2,radius*2);
}
run("Create Mask"); rename("Mask"); run("Invert LUT");
}else {
height = getHeight; width = getWidth; newImage("Mask1","8-bit white", width, height, 1);
makeRectangle(0,0,width,height); run("Create Mask"); run("Invert LUT"); run("RGB Color");
}
}

```

Appendix R. Relevant Computer Software

```

p = Img0+1; SkipThis = newArray(totCustom);
// Loop over all images
while (p<parseInt(data[3+stupid])) {
// Call up new image
if (TestMode==1)
p = round((parseInt(data[3+stupid])-parseInt(data[2+stupid]))*ImgFrac)+parseInt(data[2+stupid]);
File2 = split(data[1], " "); // Figure out how many place holders and numbers to add after file name
File3 = split(File2[1], " "); iString = d2s(p,0);
ZeroIter = lengthOf(File3[0])-lengthOf(iString); // determine how many zeros to add after image name
ZeroHold = "";
for (q=0; q<ZeroIter; q++) { // create zeros string to insert before image number
ZeroHold = ZeroHold + "0";
}
NewFile = File2[0]+ZeroHold+iString; NewFileName = File2[0]+ZeroHold+iString + imgIn;
open(path+"\\" + data[0] + "\\" + NewFileName);
if (lengthOf(CropA)>1){
c0=CropA[0]; c1=CropA[1]; c2=CropA[2]; c3=CropA[3]; makeRectangle(c0, c1, c2, c3); run("Crop");
}
print("Folder # "+k+"/"+(nIter1-1)+" "+p+"/"+d2s(data[3+stupid]-1,0)+" ----- "+NewFileName);
imageCalculator("Min create", NewFileName,"Mask"); close(NewFileName);
selectWindow("Result of "+NewFileName); rename(NewFileName);

if (Opt==0||Opt==1||Opt==10||Opt==11){ // Options
run("Calculator Plus", "i1=[ "+NewFileName+" ] i2=[tZeroFile] operation=[Divide: i2 = (i1/i2) x k1 + k2]
k1=75 k2=0");
}else if (Opt==4||Opt==5||Opt==14||Opt==15){
imageCalculator("Subtract", NewFileName, "tZeroFile");
}
run("Brightness/Contrast..."); setMinAndMax(BC[0],BC[1]); selectWindow("B&C"); run("Close");
// Thresholding before analysis
if (Opt/2 == round(Opt/2)){ // Options is even
run("8-bit"); setAutoThreshold("Default"); setThreshold(BW[0],BW[1]);setAutoThreshold("Default");
} else { // Options is odd
// Color Thresholder 2.0.0-rc-15/1.49m
setOption("BlackBackground", false); min=newArray(3); max=newArray(3); filter=newArray(3);
a=getTitle(); run("HSB Stack"); run("Convert Stack to Images"); selectWindow("Hue"); rename("0");
selectWindow("Saturation"); rename("1"); selectWindow("Brightness"); rename("2");
for (j=0;j<3;j++){
min[j]=HSB[2*j]; max[j]=HSB[2*j+1];
}
filter[0]="pass"; filter[1]="pass"; filter[2]="pass";
for (j=0;j<3;j++){
selectWindow(""+j); setThreshold(min[j], max[j]); run("Convert to Mask");
if (filter[j]=="stop") run("Invert");
}
imageCalculator("AND create", "0","1"); imageCalculator("AND create", "Result of 0","2");
for (j=0;j<3;j++){
selectWindow(""+j); close();
}
selectWindow("Result of 0"); close(); selectWindow("Result of Result of 0"); rename(a);
// Colour Thresholding-----

```

Appendix R. Relevant Computer Software

```

run("8-bit"); setAutoThreshold("Default"); setThreshold(BW[0],BW[1]); setAutoThreshold("Default");
}
// Try to reduce noise in image
run("Remove Outliers...", "radius=" + Outliers + " threshold=50 which=Bright"); run("Despeckle");
if (Opt < 10){ // Analyze particles
run("Analyze Particles...", "size=200-Infinity show=[Overlay Outlines] display clear include");
run("Labels...", "color=white font=18 show draw bold");
saveAs("Results", path + "\\" + data[0] + "\\" + data[0] + " " + d2s(Bckgrnd,0) + "-" + iString + ".txt");
Results = 1;
} else if (Opt < 20){ // Measure width using profile and threshold
PT = 0;
Size = newArray(totCustom); StDev = newArray(totCustom);
SizeR = newArray(totCustom); StDevR = newArray(totCustom);
PointX = newArray(2*nAngles*totCustom); PointY = newArray(2*nAngles*totCustom);
run("Analyze Particles...", "size=200-Infinity show=Nothing display clear include in_situ"); TotArea = 0;
for (j3=0;j3<nResults;j3++){
TotArea = TotArea + getResult("Area", j3)*getResult("% Area", j3);
}
Results = 1; selectWindow(NewFileName); run("Convert to Mask");
j3 = 0; j3a = 0; j3b = 1; sizeIndex = 0; pointIndex = 0;
while (j3 < xAL){ // loop over nucleation sites
// **** Measure Rods ****
if (thetaX[j3*4] != 0 && j3a == 0){
end1Reached = 0; end2Reached = 0; Theta1 = thetaX[j3*4]; Theta2 = thetaX[j3*4];
run("Line Width...", "line=20"); // Measure crystal width at nucleation site
dX = radius*cos((thetaX[j3*4]+90)*PI/180); dY = radius*sin((thetaX[j3*4]+90)*PI/180);
X1 = xA[j3]-dX; X2 = xA[j3]+dX; Y1 = yA[j3]+dY; Y2 = yA[j3]-dY;
makeLine(X1, Y1, X2, Y2); run("Plot Profile"); Plot.getValues(xProf, yProf);
run("Close"); E1a = round(radius/2); E1b = round(radius/2);
for (j2 = round(xProf.length/2); j2 < xProf.length; j2++) { // Loop to the right/down
if (yProf[j2]<rodThresh){
E1a = xProf[j2]; j2=xProf.length;
}
}
for (j2 = round(xProf.length/2); j2 > 0; j2--) { // Loop to the left/up
if (yProf[j2]<rodThresh){
E1b = xProf[j2]; j2=0;
}
}
XtalWidth1 = abs(E1b-E1a); XtalWidth = XtalWidth1;
if (XtalWidth > minXtalWidth) { // Run analysis if crystal exist; otherwise skip
run("Line Width...", "line=" + d2s(rodLW,0)); xA1 = xA[j3]; yA1 = yA[j3]; xA2 = xA[j3]; yA2 = yA[j3];
opp = XtalWidth*nLengths*tan(thetaMis*PI/180); nRodIter = 0; L1 = 0; L2 = 0;
while (end1Reached == 0) { // loop until end1 of rod reached
x0 = xA1 + XtalWidth*nLengths*cos(Theta1*PI/180); // Find new center
y0 = yA1 - XtalWidth*nLengths*sin(Theta1*PI/180);
X1 = x0 - opp*sin((Theta1)*PI/180); Y1 = y0 - opp*cos((Theta1)*PI/180); //Create new coordinates perp. to rod direction
X2 = x0 + opp*sin((Theta1)*PI/180); Y2 = y0 + opp*cos((Theta1)*PI/180);
makeLine(X1, Y1, X2, Y2); run("Plot Profile"); Plot.getValues(xProf, yProf); run("Close");
// Find end 1
}
}
}
}
}

```

Appendix R. Relevant Computer Software

```

if (yProf[round(yProf.length/2)] > rodThresh) { // Line centered on rod already; find edges
E1a = round(xProf.length/2); E1b = round(xProf.length/2); EndFound = 1;
for (j2 = round(xProf.length/2); j2 < xProf.length; j2++) {// Loop to the right/down
    if (yProf[j2]<rodThresh){
        E1a = xProf[j2]; j2=xProf.length;
    }
}
for (j2 = round(xProf.length/2); j2 > 0; j2--) {// Loop to the left/up
    if (yProf[j2]<rodThresh){
        E1b = xProf[j2]; j2=0;
    }
}
End = (E1a+E1b)/2;
} else{ // Need to find rod (nearest center)
E1a = xProf.length; E1b = xProf.length; E1c = 0; E1d = 0; EndFound = 0;
for (j2 = round(xProf.length/2); j2 < xProf.length; j2++) {// Loop to the right/down
    if (yProf[j2]>rodThresh && E1a == xProf.length){
        E1a = xProf[j2]; EndFound = 1;
    }
    if (yProf[j2]<rodThresh && E1a != xProf.length){
        E1b = xProf[j2]; j2=xProf.length;
    }
}
for (j2 = round(xProf.length/2); j2 > 0; j2--) {// Loop to the left/up
    if (yProf[j2]>rodThresh && E1c == 0){
        E1c = xProf[j2]; EndFound = 1;
    }
    if (yProf[j2]<rodThresh && E1c != 0){
        E1d = xProf[j2]; j2=0;
    }
}
}
EndR = abs((E1a+E1b)/2-xProf[round(xProf.length/2)]); EndL = abs(xProf[round(xProf.length/2)]-
(E1c+E1d)/2);
if (EndR < EndL){
    End = (E1a+E1b)/2;
} else {
    End = (E1c+E1d)/2;
}
}
PointX = Array.concat(PointX,xA1); PointY = Array.concat(PointY,yA1);
if (EndFound == 1){ // Still somewhere in the middle of the rod
if (End < opp){ // On top side
    Theta1 = Theta1 + 180/PI*atan((opp-End)/(XtalWidth*nLengths));
    xA1 = x0 - sin(Theta1*PI/180)*(opp-End); yA1 = y0 - cos(Theta1*PI/180)*(opp-End);
} else { // On bottom side
    Theta1 = Theta1 - 180/PI*atan((End-opp)/(XtalWidth*nLengths));
    xA1 = x0 + sin(Theta1*PI/180)*(End-opp); yA1 = y0 + cos(Theta1*PI/180)*(End-opp);
}
} else { // Must have reached end of rod: truncate and measure length
x0 = xA1 + 2*XtalWidth*nLengths*cos(Theta1*PI/180);
y0 = yA1 - 2*XtalWidth*nLengths*sin(Theta1*PI/180);

```

Appendix R. Relevant Computer Software

```

X1 = xA1; Y1 = yA1; X2 = x0; Y2 = y0; AT = 1; BT = 0; End = xProf[xProf.length-1];
run("Line Width...", "line="+d2s(floor(XtalWidth*2),0));
makeLine(X1, Y1, X2, Y2); run("Plot Profile"); Plot.getValues(xProf, yProf); run("Close");
for (j2 = 0; j2 < xProf.length; j2++) {// Loop to the left/up
    if (yProf[j2]<rodThresh){
        AT=1; BT = BT + 1;
    }
    if (yProf[j2]>rodThresh)
        AT=AT+1;
    if (AT>=2)
        BT = 0;
    if (BT>=rodWhtSpc){
        if(j2>=rodWhtSpc){
            End = xProf[j2-rodWhtSpc];
        }else {
            End = xProf[0];
        }
        j2=xProf.length;
    }
}
end1Reached = 1; PointX = Array.concat(PointX, xA1+End*cos(Theta1*PI/180));
PointY = Array.concat(PointY, yA1-End*sin(Theta1*PI/180));
RodLength1 = (L1 + End)*2048/(2*MagFact*Width1); RL1 = L1 + End;
}
nRodIter = nRodIter + 1; L1 = L1 + XtalWidth*nLengths;
if (abs(E1b-E1a) > MinRodW){
XtalWidth = abs(E1b-E1a);
}
} // While loop over End1
nRodIter = 0; run("Line Width...", "line="+d2s(rodLW,0)); XtalWidth = XtalWidth1;
while (end2Reached == 0) {// loop until end2 of rod reached
x0 = xA2 - XtalWidth*nLengths*cos(Theta2*PI/180);
y0 = yA2 + XtalWidth*nLengths*sin(Theta2*PI/180);
X1 = x0 - opp*sin(Theta2*PI/180); Y1 = y0 - opp*cos(Theta2*PI/180);
X2 = x0 + opp*sin(Theta2*PI/180); Y2 = y0 + opp*cos(Theta2*PI/180);
makeLine(X1, Y1, X2, Y2); run("Plot Profile"); Plot.getValues(xProf, yProf); run("Close");
// Find end 2
if (yProf[round(yProf.length/2)] > threshold) {// Line centered on rod already; find edges
E1a = round(xProf.length/2); E1b = round(xProf.length/2); EndFound = 1;
for (j2 = round(xProf.length/2); j2 < xProf.length; j2++) {// Loop to the right/down
    if (yProf[j2]<threshold){
        E1a = xProf[j2]; j2=xProf.length;
    }
}
for (j2 = round(xProf.length/2); j2 > 0; j2--) {// Loop to the left/up
    if (yProf[j2]<threshold){
        E1b = xProf[j2]; j2=0;
    }
}
End = (E1a+E1b)/2;
} else{// Need to find rod (nearest center)
}

```

Appendix R. Relevant Computer Software

```

E1a = xProf.length; E1b = xProf.length; E1c = 0; E1d = 0; EndFound = 0;
for (j2 = round(xProf.length/2); j2 < xProf.length; j2++) { // Loop to the right/down
    if (yProf[j2]>threshold && E1a == xProf.length){
        E1a = xProf[j2]; EndFound = 1;
    }
    if (yProf[j2]<threshold && E1a != xProf.length){
        E1b = xProf[j2]; j2=xProf.length;
    }
}
for (j2 = round(xProf.length/2); j2 > 0; j2--) { // Loop to the left/up
    if (yProf[j2]>threshold && E1c == 0){
        E1c = xProf[j2]; EndFound = 1;
    }
    if (yProf[j2]<threshold && E1c != 0){
        E1d = xProf[j2]; j2=0;
    }
}
EndR = (E1a+E1b)/2-xProf[round(xProf.length/2)]; EndL = xProf[round(xProf.length/2)]-(E1c+E1d)/2;
if (EndR < EndL){
    End = (E1a+E1b)/2;
} else {
    End = (E1c+E1d)/2;
}
}
PointX = Array.concat(PointX,xA2); PointY = Array.concat(PointY,yA2);
if (EndFound == 1){ // Still somewhere in the middle of the rod
if (End < opp){ // On top side
    Theta2 = Theta2 - 180/PI*atan((opp-End)/(XtalWidth*nLengths));
    xA2 = x0 - sin(Theta2*PI/180)*(opp-End); yA2 = y0 - cos(Theta2*PI/180)*(opp-End);
} else { // On bottom side
    Theta2 = Theta2 + 180/PI*atan((End-opp)/(XtalWidth*nLengths));
    xA2 = x0 + sin(Theta2*PI/180)*(End-opp); yA2 = y0 + cos(Theta2*PI/180)*(End-opp);
}
} else { // Must have reached end of rod: truncate and measure length
x0 = xA2 - 2*XtalWidth*nLengths*cos(Theta2*PI/180);
y0 = yA2 + 2*XtalWidth*nLengths*sin(Theta2*PI/180);
X1 = xA2; Y1 = yA2; X2 = x0; Y2 = y0; End = xProf[xProf.length-1]; AT = 1; BT = 0;
run("Line Width...", "line="+d2s(floor(XtalWidth*2),0));
makeLine(X1, Y1, X2, Y2); run("Plot Profile"); Plot.getValues(xProf, yProf); run("Close");
for (j2 = 0; j2 < xProf.length; j2++) { // Loop to the left/up
    if (yProf[j2]<rodThresh){
        AT=1; BT = BT + 1;
    }
    if (yProf[j2]>rodThresh)
        AT=AT+1;
    if (AT>=3)
        BT = 0;
    if (BT>=rodWhtSpc && j2>=rodWhtSpc){
        if(j2>=rodWhtSpc){
            End = xProf[j2-rodWhtSpc];
        }else {
    }
}

```

Appendix R. Relevant Computer Software

```

        End = xProf[0];
    }
    j2=xProf.length;
}
}
end2Reached = 1; PointX = Array.concat(PointX, xA2-End*cos(Theta2*PI/180));
PointY = Array.concat(PointY, yA2+End*sin(Theta2*PI/180));
RodLength2 = (L2 + End)*2048/(2*MagFact*Width1);//(nRodIter*XtalWidth*nLengths +
End)*2048/(2*MagFact*Width1);
}
nRodIter = nRodIter + 1; L2 = L2 + XtalWidth*nLengths;
if (abs(E1b-E1a) > MinRodW){
XtalWidth = abs(E1b-E1a);
}
} // While loop over End2
} else { //Output zeros for length - no crystal yet
RodLength1 = 0; RodLength2 = 0;
}
SizeR[sizeIndex] = (RodLength1+RodLength2)*(2*MagFact*Width1)/2048; StDevR[sizeIndex] = 0;
Size[sizeIndex] = RodLength1+RodLength2; StDev[sizeIndex] = 0; sizeIndex = sizeIndex + 1;
} // If Rods[j] == 1
// ***** +/-45 Averaged Together *****
if (thetaX[4*j3+1] != 0 && j3a == 0){
TFact = dAngle/nAngles; // +/- xx degrees
LW1 = LineWidth; thetaNuc = 45; radiusIndex = 0; PRadius = newArray(nAngles*2);
for (j4=0;j4<nAngles;j4++){ // loop over n angles
thet = thetaNuc + TFact*j4 - dAngle/2; run("Line Width...", "line="+LW1); dX = radius*cos(theta*PI/180);
dY = radius*sin(theta*PI/180); X1 = xA[j3]-dX; X2 = xA[j3]+dX; Y1 = yA[j3]+dY; Y2 = yA[j3]-dY;
makeLine(X1, Y1, X2, Y2); run("Plot Profile"); Plot.getValues(xProf, yProf); run("Close");
end2 = radius/2; end1 = radius/2; AT=1; BT=1;
for (j2 = round(xProf.length/2); j2 < xProf.length; j2++) {
if (yProf[j2]<threshold){
AT=1; BT = BT + 1;
}
if (yProf[j2]>threshold)
AT=AT+1;
if (AT>=BlkSpace)
BT = 1;
if (BT>=WhtSpace){
end2 = xProf[j2-BT-AT+2]; PointX[pointIndex] = xA[j3]+(end2-radius)*cos(theta*PI/180);
PointY[pointIndex] = yA[j3]-(end2-radius)*sin(theta*PI/180); pointIndex = pointIndex + 1;
BT=1; AT = 1; j2=xProf.length;
}
}
for (j2 = floor(xProf.length/2); j2 > 0; j2--) {
if (yProf[j2]<threshold){
AT=1; BT = BT + 1;
}
if (yProf[j2]>threshold)
AT=AT+1;
if (AT>=BlkSpace)

```

Appendix R. Relevant Computer Software

```

BT = 1;
if (BT>=WhtSpace){
    end1 = xProf[j2+BT+AT-2]; PointX[pointIndex] = xA[j3]-(radius-end1)*cos(theta*PI/180);
    PointY[pointIndex] = yA[j3]+(radius-end1)*sin(theta*PI/180); pointIndex = pointIndex + 1;
    j2=0;
}
}
PRadius[radiusIndex] = (end2-end1)*2048/(2*MagFact*Width1); radiusIndex = radiusIndex + 1;
} // loop over angles
thetaNuc = -45;
for (j4=0;j4<nAngles;j4++){ // loop over n angles
    theta = thetaNuc + TFact*j4 - dAngle/2; run("Line Width...", "line="+LW1);
    dX = radius*cos(theta*PI/180); dY = radius*sin(theta*PI/180);
    X1 = xA[j3]-dX; X2 = xA[j3]+dX; Y1 = yA[j3]+dY; Y2 = yA[j3]-dY;
    makeLine(X1, Y1, X2, Y2); run("Plot Profile"); Plot.getValues(xProf, yProf); run("Close");
    end2 = radius/2; end1 = radius/2; AT=1; BT=1;
    for (j2 = round(xProf.length/2); j2 < xProf.length; j2++) {
        if (yProf[j2]<threshold){
            AT=1; BT = BT + 1;
        }
        if (yProf[j2]>threshold)
            AT=AT+1;
        if (AT>=BlkSpace)
            BT = 1;
        if (BT>=WhtSpace){
            end2 = xProf[j2-BT-AT+2]; PointX = Array.concat(PointX, xA[j3]+(end2-radius)*cos(theta*PI/180));
            PointY = Array.concat(PointY, yA[j3]-(end2-radius)*sin(theta*PI/180)); BT=1; AT = 1; j2=xProf.length;
        }
    }
    for (j2 = floor(xProf.length/2); j2 > 0; j2--) {
        if (yProf[j2]<threshold){
            AT=1; BT = BT + 1;
        }
        if (yProf[j2]>threshold)
            AT=AT+1;
        if (AT>=BlkSpace)
            BT = 1;
        if (BT>=WhtSpace){
            end1 = xProf[j2+BT+AT-2]; PointX = Array.concat(PointX, xA[j3]-(radius-end1)*cos(theta*PI/180));
            PointY = Array.concat(PointY, yA[j3]+(radius-end1)*sin(theta*PI/180)); j2=0;
        }
    }
    PRadius[radiusIndex] = (end2-end1)*2048/(2*MagFact*Width1); radiusIndex = radiusIndex + 1;
} // loop over angles
Array.getStatistics(PRadius, minimum, maximum, mean, stdDev);
SizeR[sizeIndex] = mean*(2*MagFact*Width1)/2048; StDevR[sizeIndex] =
    stdDev*(2*MagFact*Width1)/2048;
Size[sizeIndex] = mean; StDev[sizeIndex] = stdDev;
// Do some preliminary data processing
if (mean < SizeThr){
    Size[sizeIndex] = 0; StDev[sizeIndex] = 0;
}

```

Appendix R. Relevant Computer Software

```

}else if ((StDev[sizeIndex] > StdDevThr|| SkipThis[sizeIndex] == 1) && thetaNuc!=360){
Size[sizeIndex] = 0; StDev[sizeIndex] = 0; SkipThis[sizeIndex] = 1;
}else if ((StDev[sizeIndex] > StdDev360|| SkipThis[sizeIndex] == 1) && thetaNuc==360){
Size[sizeIndex] = 0; StDev[sizeIndex] = 0; SkipThis[sizeIndex] = 1;
}
sizeIndex = sizeIndex + 1;
}
// **** Radius ****
if (thetaX[j3*4+2] != 0 && j3a == 0){
LW1 = LineWidth; run("Line Width...", "line="+LW1); radiusIndex = 0;
PRadius = newArray(nAngles); TFact = dRAngle/nAngles; thetaNuc = thetaX[j3*4+2];
for (j4=0;j4<nAngles;j4++){ // loop over n angles
thet = thetaNuc + dRAngle/2 - j4*TFact; dX = radius*cos(theta*PI/180); dY = radius*sin(theta*PI/180);
X1 = xA[j3]; X2 = xA[j3]+dX; Y1 = yA[j3]; Y2 = yA[j3]-dY; makeLine(X1, Y1, X2, Y2); run("Plot
Profile");
Plot.getValues(xProf, yProf); run("Close"); end2 = radius/2; AT=1; BT=1;
for (j2 = 1; j2 < xProf.length; j2++) {
if (yProf[j2]<threshold){
AT=1; BT = BT + 1;
}
if (yProf[j2]>threshold)
AT=AT+1;
if (AT>=BlkSpace)
BT = 1;
if (BT>=WhtSpace){
end2 = xProf[j2-BT-AT+2]; PointX[pointIndex] = xA[j3]+end2*cos(theta*PI/180);
PointY[pointIndex] = yA[j3]-end2*sin(theta*PI/180); pointIndex = pointIndex + 1; BT=1; AT = 1;
j2=xProf.length;
}
}
PRadius[radiusIndex] = end2*2048/(MagFact*Width1); radiusIndex = radiusIndex + 1;
} // loop over angles
Array.getStatistics(PRadius, minimum, maximum, mean, stdDev);
SizeR[sizeIndex] = mean*(MagFact*Width1)/2048;
StDevR[sizeIndex] = stdDev*(MagFact*Width1)/2048;
Size[sizeIndex] = mean; StDev[sizeIndex] = stdDev;
// Do some preliminary data processing
if (mean < SizeThr){
Size[sizeIndex] = 0; StDev[sizeIndex] = 0;
}else if ((StDev[sizeIndex] > StdDevThr|| SkipThis[sizeIndex] == 1)){
Size[sizeIndex] = 0; StDev[sizeIndex] = 0; SkipThis[sizeIndex] = 1;
}
sizeIndex = sizeIndex + 1;
} // Measure radius
// **** Rod Radius ****
if (thetaX[j3*4+3] != 0 && j3a == 0){
end1Reached = 0; end2Reached = 0; Theta1 = thetaX[j3*4+3]; Theta2 = thetaX[j3*4+3];
run("Line Width...", "line=20"); // Measure crystal width at nucleation site
dX = radius*cos((thetaX[j3*4]+90)*PI/180); dY = radius*sin((thetaX[j3*4]+90)*PI/180);
X1 = xA[j3]-dX; X2 = xA[j3]+dX; Y1 = yA[j3]+dY; Y2 = yA[j3]-dY;
makeLine(X1, Y1, X2, Y2); run("Plot Profile"); Plot.getValues(xProf, yProf);
}

```

Appendix R. Relevant Computer Software

```

run("Close"); E1a = round(radius/2); E1b = round(radius/2);
for (j2 = round(xProf.length/2); j2 < xProf.length; j2++) {// Loop to the right/down
if (yProf[j2]<rodThresh){
    E1a = xProf[j2]; j2=xProf.length;
}
}
for (j2 = round(xProf.length/2); j2 > 0; j2--) {// Loop to the left/up
if (yProf[j2]<rodThresh){
    E1b = xProf[j2]; j2=0;
}
}
XtalWidth = abs(E1b-E1a);
if (XtalWidth > minXtalWidth) { // Run analysis if crystal exist; otherwise skip
run("Line Width...", "line=" +d2s(rodLW,0)); xA1 = xA[j3]; yA1 = yA[j3]; xA2 = xA[j3]; yA2 = yA[j3];
opp = XtalWidth*nLengths*tan(thetaMis*PI/180); nRodIter = 0; L1 = 0;
while (end1Reached == 0) { // loop until end1 of rod reached
x0 = xA1 + XtalWidth*nLengths*cos(Theta1*PI/180); // Find new center
y0 = yA1 - XtalWidth*nLengths*sin(Theta1*PI/180);
X1 = x0 - opp*sin((Theta1)*PI/180); Y1 = y0 - opp*cos((Theta1)*PI/180); //Create new coordinates perp.
to axis
X2 = x0 + opp*sin((Theta1)*PI/180); Y2 = y0 + opp*cos((Theta1)*PI/180);
makeLine(X1, Y1, X2, Y2); run("Plot Profile"); Plot.getValues(xProf, yProf); run("Close");
// Find end 1
if (yProf[round(yProf.length/2)] > rodThresh) { // Line centered on rod already; find edges
E1a = round(xProf.length/2); E1b = round(xProf.length/2); EndFound = 1;
for (j2 = round(xProf.length/2); j2 < xProf.length; j2++) {// Loop to the right/down
if (yProf[j2]<rodThresh){
    E1a = xProf[j2]; j2=xProf.length;
}
}
for (j2 = round(xProf.length/2); j2 > 0; j2--) {// Loop to the left/up
if (yProf[j2]<rodThresh){
    E1b = xProf[j2]; j2=0;
}
}
End = (E1a+E1b)/2;
} else { // Need to find rod (nearest center)
E1a = xProf.length; E1b = xProf.length; E1c = 0; E1d = 0; EndFound = 0;
for (j2 = round(xProf.length/2); j2 < xProf.length; j2++) {// Loop to the right/down
if (yProf[j2]>rodThresh && E1a == xProf.length){
    E1a = xProf[j2]; EndFound = 1;
}
if (yProf[j2]<rodThresh && E1a != xProf.length){
    E1b = xProf[j2]; j2=xProf.length;
}
}
for (j2 = round(xProf.length/2); j2 > 0; j2--) {// Loop to the left/up
if (yProf[j2]>rodThresh && E1c == 0){
    E1c = xProf[j2]; EndFound = 1;
}
}
}

```

Appendix R. Relevant Computer Software

```

if (yProf[j2]<rodThresh && E1c != 0){
    E1d = xProf[j2]; j2=0;
}
}
EndR = abs((E1a+E1b)/2-xProf[round(xProf.length/2)]); EndL = abs(xProf[round(xProf.length/2)]-
(E1c+E1d)/2);
if (EndR < EndL){
    End = (E1a+E1b)/2;
} else {
    End = (E1c+E1d)/2;
}
}
PointX = Array.concat(PointX,xA1); PointY = Array.concat(PointY,yA1);
if (EndFound == 1){ // Still somewhere in the middle of the rod
if (End < opp){ // On top side
    Theta1 = Theta1 + 180/PI*atan((opp-End)/(XtalWidth*nLengths));
    xA1 = x0 - sin(Theta1*PI/180)*(opp-End); yA1 = y0 - cos(Theta1*PI/180)*(opp-End);
} else { // On bottom side
    Theta1 = Theta1 - 180/PI*atan((End-opp)/(XtalWidth*nLengths));
    xA1 = x0 + sin(Theta1*PI/180)*(End-opp); yA1 = y0 + cos(Theta1*PI/180)*(End-opp);
}
} else { // Must have reached end of rod: truncate and measure length
x0 = xA1 + 2*XtalWidth*nLengths*cos(Theta1*PI/180);
y0 = yA1 - 2*XtalWidth*nLengths*sin(Theta1*PI/180);
X1 = xA1; Y1 = yA1; X2 = x0; Y2 = y0; AT = 1; BT = 0; End = xProf[xProf.length-1];
run("Line Width...", "line=" + d2s(floor(XtalWidth*2),0));
makeLine(X1, Y1, X2, Y2); run("Plot Profile"); Plot.getValues(xProf, yProf); run("Close");
for (j2 = 0; j2 < xProf.length; j2++) { // Loop to the left/up
    if (yProf[j2]<rodThresh){
        AT=1; BT = BT + 1;
    }
    if (yProf[j2]>rodThresh)
        AT=AT+1;
    if (AT>=2)
        BT = 0;
    if (BT>=rodWhtSpc){
        if(j2>=rodWhtSpc){
            End = xProf[j2-rodWhtSpc];
        } else {
            End = xProf[0];
        }
        j2=xProf.length;
    }
}
end1Reached = 1; PointX = Array.concat(PointX, xA1+End*cos(Theta1*PI/180));
PointY = Array.concat(PointY, yA1-End*sin(Theta1*PI/180));
RodLength1 = (L1 + End)*2048/(2*MagFact*Width1);
}
nRodIter = nRodIter + 1; L1 = L1 + XtalWidth*nLengths;
if (abs(E1b-E1a) > MinRodW){
    XtalWidth = abs(E1b-E1a);
}

```

Appendix R. Relevant Computer Software

```

}
} // While loop over End1
} else { //Output zeros for length - no crystal yet
RodLength1 = 0;
}
SizeR[sizeIndex] = (RodLength1)*(2*MagFact*Width1)/2048; StDevR[sizeIndex] = 0;
Size[sizeIndex] = RodLength1; StDev[sizeIndex] = 0; sizeIndex = sizeIndex + 1;
} // Rod Radius
// ***** Crystal Directions, +45, -45, 360 *****
if (theta[j3*4]!=0 || theta[j3*4+1]!=0||theta[j3*4+2]!=0||theta[j3*4+3]!=0){
radiusIndex = 0; PRadius = newArray(nAngles);
a = ABC[6*j3]; b = ABC[6*j3+1]; c = ABC[6*j3+2];
alpha = ABC[6*j3+3]/180*PI; beta = ABC[6*j3+4]/180*PI; gamma = ABC[6*j3+5]/180*PI;
while (theta[j3*4+j3a]==0 && j3a<3){ // loop over crystal directions
j3a = j3a + 1;
}
if (j3b == 1)
thetaNuc = theta[j3*4+j3a];
if (thetaNuc==360){
TFact = 360/nAngles; // all 360 degrees in 18 degree intervals
LW1 = LW_360Def;
} else {
TFact = dAngle/nAngles; // +/- xx degrees
LW1 = LineWidth;
}
for (j4=0;j4<nAngles;j4++){ // loop over n angles
thet = thetaNuc + TFact*j4 - dAngle/2; run("Line Width...", "line="+LW1); dX = radius*cos(theta*PI/180);
dY = radius*sin(theta*PI/180); X1 = xA[j3]-dX; X2 = xA[j3]+dX; Y1 = yA[j3]+dY; Y2 = yA[j3]-dY;
makeLine(X1, Y1, X2, Y2); run("Plot Profile"); Plot.getValues(xProf, yProf); run("Close");
end2 = radius/2; end1 = radius/2; AT=1; BT=1;
for (j2 = round(xProf.length/2); j2 < xProf.length; j2++) {
if (yProf[j2]<threshold){
AT=1; BT = BT + 1;
}
if (yProf[j2]>threshold)
AT=AT+1;
if (AT>=BlkSpace)
BT = 1;
if (BT>=WhtSpace){
end2 = xProf[j2-BT-AT+2]; PointX[pointIndex] = xA[j3]+(end2-radius)*cos(theta*PI/180);
PointY[pointIndex] = yA[j3]-(end2-radius)*sin(theta*PI/180); pointIndex = pointIndex + 1; BT=1; AT = 1;
j2=xProf.length;
}
}
for (j2 = floor(xProf.length/2); j2 > 0; j2--) {
if (yProf[j2]<threshold){
AT=1; BT = BT + 1;
}
if (yProf[j2]>threshold)
AT=AT+1;
if (AT>=BlkSpace)

```

Appendix R. Relevant Computer Software

```

BT = 1;
if (BT>=WhtSpace){
    end1 = xProf[j2+BT+AT-2]; PointX[pointIndex] = xA[j3]-(radius-end1)*cos(theta*PI/180);
    PointY[pointIndex] = yA[j3]+(radius-end1)*sin(theta*PI/180); pointIndex = pointIndex + 1; j2=0;
}
}
PRadius[radiusIndex] = (end2-end1)*2048/(2*MagFact*Width1); radiusIndex = radiusIndex + 1;
} // loop over angles
Array.getStatistics(PRadius, minimum, maximum, mean, stdDev);
SizeR[sizeIndex] = mean*(2*MagFact*Width1)/2048;
StDevR[sizeIndex] = stdDev*(2*MagFact*Width1)/2048;
Size[sizeIndex] = mean; StDev[sizeIndex] = stdDev;
// Do some preliminary data processing
if (mean < SizeThr){
    Size[sizeIndex] = 0; StDev[sizeIndex] = 0;
} else if ((StDev[sizeIndex] > StdDevThr|| SkipThis[sizeIndex] == 1) && thetaNuc!=360){
    Size[sizeIndex] = 0; StDev[sizeIndex] = 0; SkipThis[sizeIndex] = 1;
} else if ((StDev[sizeIndex] > StdDev360|| SkipThis[sizeIndex] == 1) && thetaNuc==360){
    Size[sizeIndex] = 0; StDev[sizeIndex] = 0; SkipThis[sizeIndex] = 1;
}
sizeIndex = sizeIndex + 1;
if (j3a < 3)
    j3a = j3a + 1;

while (theta[j3*4+j3a]==0 && j3a<3){ // loop over crystal directions
    j3a = j3a + 1;
}
if (j3a == 3){ // determine next angle to measure
    if (theta[j3*4+j3a]==0){ // no directions specified
        j3 = j3 + 1; j3a = 0;
    } else if (UVW[6*j3+j3b]==0){ // no more directions to measure for this site
        j3 = j3 + 1; j3a = 0; j3b = 1;
    } else { // measure along direction
        if (UVW[6*j3]>=100){
            u0 = floor(UVW[6*j3]/100); v0 = floor((UVW[6*j3]-100*u0)/10);
            w0 = floor(UVW[6*j3]-100*u0-10*v0);
        } else if (UVW[6*j3]>=10){
            u0 = 0; v0 = floor(UVW[6*j3]/10); w0 = floor(UVW[6*j3]-10*v0);
        } else {
            u0 = 0; v0 = 0; w0 = floor(UVW[6*j3]);
        }
    // determine angle of original direction with respect to [100]
    uvwMag0 =
        sqrt(a*a*u0*u0+a*b*cos(gamma)*u0*v0+a*c*cos(beta)*u0*w0+b*b*cos(gamma)*u0*v0+b*c*v0*v0+
        b*c*cos(alpha)*v0*w0+a*c*cos(beta)*u0*w0+b*c*cos(alpha)*v0*w0+c*c*w0*w0); Mag100 = a;
    theta0 = 180/PI*acos((u0*a*a+v0*a*b*cos(gamma)+w0*a*c*cos(beta))/(uvwMag0*Mag100));
    if (UVW[6*j3+j3b]>=100){
        u = floor(UVW[6*j3+j3b]/100); v = floor((UVW[6*j3+j3b]-100*u)/10);
        w = floor(UVW[6*j3+j3b]-100*u-10*v);
    } else if (UVW[6*j3+j3b]>=10){
        u = 0; v = floor(UVW[6*j3+j3b]/10); w = floor(UVW[6*j3+j3b]-10*v);
    }
}

```

Appendix R. Relevant Computer Software

```

}else {
u = 0; v = 0; w = floor(UVW[6*j3+j3b]);
}
// direction of next plane to measure
uvwMag =
    sqrt(a*a*u*u+a*b*cos(gamma)*u*v+a*c*cos(beta)*u*v+a*b*cos(gamma)*u*v+b*b*v*v+b*c*cos(alpha)
        a)*v*w+a*c*cos(beta)*u*w+b*c*cos(alpha)*v*w+c*c*w*w);
theta1 = 180/PI*acos((u*a*a+v*a*b*cos(gamma)+w*a*c*cos(beta))/(uvwMag*Mag100));
dTheta = theta1 - theta0; thetaNuc = theta[4*j3+3]+dTheta; // new plane angle, degrees
j3b = j3b + 1;

} // Else measure along direction
} // Next angle to measure
}else{ // If crystal directions exist
j3 = j3 + 1;
}
} // while loop over nucleation sites
run("RGB Color"); setForegroundColor(0,255,0); run("Line Width...", "line=2");
for (j5=0;j5<PointX.length;j5++){
fillOval(PointX[j5]-3,PointY[j5]-3,6,6); setKeyDown("Shift");
}
setFont("Arial", 16, "bold antialiased"); setColor("black");

for (j7=0;j7<xA.length;j7++){
drawString(d2s(j7,0), xA[j7], yA[j7],"white");
}
// Now figure out how to save data
tImg = parseInt(File.lastModified(path+"\\" + data[0] + "\\" + NewFileName));
tStamp = d2s((tImg - tZero)/1000, 6); sample = ZeroHold + iString + '\t' + tStamp + '\t' +
    d2s(TotArea,0) + '\t';
for (i2=0;i2<Size.length; i2++){
if (Size[i2] == 0){ // eliminate zeros for ease of plotting
SizeF = "-"; StDevF = "-";
} else {
SizeF = d2s(Size[i2],6); StDevF = d2s(StDev[i2],6);
}
sample = sample + SizeF + '\t' + StDevF + '\t';
}
for (i2=0;i2<Size.length; i2++){ // write raw data
sample = sample + d2s(SizeR[i2],6) + '\t' + d2s(StDevR[i2],6) + '\t';
}
print(f,sample);// write data to text file
}
if (TestMode == 0){
selectWindow(NewFileName);
if (imgOut=="jpg") {
saveAs("Jpeg", path+"\\" + data[0] + "\\" + "Mask "+ data[0] + " " + d2s(Bckgrnd,0) + "-" + iString +
    Append+imgOut); // Save modified image
} else if (imgOut=="tif") {
saveAs("tif", path+"\\" + data[0] + "\\" + "Mask "+ data[0] + " " + d2s(Bckgrnd,0) + "-" + iString +
    Append+imgOut);
}
}

```

Appendix R. Relevant Computer Software

```

}
close("Mask " + data[0] + " " + d2s(Bckgrnd,0) + "-" + iString +Append+imgOut); // Close masked image
}
if (TestMode == 1){ // Save Test image into z_Image_Params folder
selectWindow(NewFileName);
if (imgOut=="jpg") {
saveAs("Jpeg", path+"\\"+"z_Image_Params\" + "Test " + data[0] + " " + d2s(Bckgrnd,0) + "-" + iString
+Append+imgOut); // Save modified image
} else if (imgOut=="tif") {
saveAs("tif", path+"\\"+"z_Image_Params\" + "Test " + data[0] + " " + d2s(Bckgrnd,0) + "-" + iString
+Append+imgOut);
}
close("Test " + data[0] + " " + d2s(Bckgrnd,0) + "-" + iString +Append+imgOut); // Close masked image
}
close(NewFileName); // Close original image
if (TestMode==1)
p = parseInt(data[3+stupid])+1; p = p + 1; // advance to next image otherwise
} // While loop over images
File.close(f); close("tZeroFile"); // Close tZero image
if (radius>0 && (TestMode==0||TestMode==1)){
run("Close All");
}
} // testMode == 0, 1
if (k==FolderEnd)
k = nIter1;
} // For loop over folders
if (Results == 1){
selectWindow("Results"); run("Close");
}
setBatchMode(false);
getDateAndTime(year2, month2, dayOfWeek2, dayOfMonth2, hour2, minute2, second2, msec2);
timeRequired = (dayOfMonth2-dayOfMonth1)*24*60+(hour2-hour1)*60+(minute2-minute1)+(second2-
second1)/60;
print(" ");print("Macro completed! Required "+d2s(timeRequired,2)+" minutes");print(" ");

```

R.5. Crystal Growth Fitting (Matlab)

When each image sequence can yield 5-50 individual crystal measurements, and each dataset has 5-30 sequences, automated parameter extraction is critical. The following code analyzes and condenses the output of the crystal growth image analysis in Appendix R.4.

In tracking crystal growth, there are many possible errors and artifacts that can be introduced. These include:

1. Random noise in crystal size
2. Crystals merging, causing a jump (discontinuity) in crystal size with time
3. Crystals stagnating, causing a plateau in size with time

To cut down on random noise, the fitting algorithm uses a linear regression over a specified number of data points to smooth the raw measurements. The program also waits until the crystal size grows above a specified threshold before beginning to fit that crystal.

In general, these two steps significantly reduce noise in the data.

Jump detection is somewhat more challenging. The program watches the time derivative of the incoming size data, flagging data with a slope above a specified threshold. Once this flag is thrown, the program tracks the next points until the regression quota is reached. At this point, the program fits data before and after the suspected jump, then compares the size calculated from each fit at the jump location. If the sizes differ by a more than a specified value, that particle is suspected of having merged with something and is truncated at the point of the jump before any final fitting.

When crystals stagnate, their slope of size with time approaches zero. Taking care of these “plateau” regions is as simple as monitoring the first linear regression and truncating

Appendix R. Relevant Computer Software

at the point where the slope drops below a specified threshold value.

From there, it is relatively simple to fit the growth data to extract a growth rate, then compile by temperature and crystal type. This data is output as a condensed .xls spreadsheet and as raw crystal sizes and data regressions in .txt files.

```
function CrystalFit_4
% This program fits crystal size data as a function of time to extract a growth rate and average temperature
% parameters depending % on the selected options.
% Modifications:
% 1. Many in versions before 1/16/17
% 2. 1/17/17 Added TAvg feature, AppendNew
%
% Created by Tom Fielitz, University of Minnesota March 17th, 2015

%***** Specify file location *****
filepath = 'F:/UMN Data/Optical Microscopy Data'; % Root directory of folder path, not including /year
FolderName = '2017-01-27 OM Nikon'; % Name of folder within the above directory containing movie csv
FileName = 'Movie_List_40.csv'; % Name of csv file
Append = ";" % Name of word appended in data file "[folder] Stats[Append].txt"
AppendNew = '_v4_R2 05'; % Phrase to append to end of data file summaries saved from Matlab

%***** Specify data processing and printing *****
GrRate = 1; % Growth rate fit
CutZeros = 4; % Eliminate zeros in dataset (only display data with nPoints > CutZeros)
RSqThresh = 0.7; % Eliminate data with R^2 less than this value
ActEng = 0; % Activation energy fit

GrRep = 1; % Print text file of growth rate data to plot externally
ActRep = 0; % Print text file of activation energy data to plot externally
TAvg = 1; % Find average of each type of crystal as function of temperature
Identify = {[100],[010]}; % Collection of crystal type/directions, e.g. {[100],[010]}
IncData = [1,0,1]; % Which data to include [Slope, Y-Int, #Points]

% ***** Specify conditions used in data processing
% Particle Size, Growth Rate
MinSize = 10; % Minimum particle radius (microns)
StdDevThr = 50; % Maximum particle size standard deviation (microns)
StdDev360 = 20; % Maximum particle std dev for 360 deg analysis (microns)
JFact = 4; % Minimum jump slope (multiple of previous slope)to trip jump detection
JSize = 50; % Minimum jump size (um) to prove jump
MinSlope = [0.25,8]; % [Minimum growth rate (microns/sec), number of points to evaluate slope]
RSqlB = 0.5; % R^2 lower bound for slope processing during jump evaluation

%***** End of input *****
%=====
%=====
```

Appendix R. Relevant Computer Software

```

year = FolderName(1:4);cd(sprintf('%s/%s/%s',filepath,year,FolderName))
[nData,~,FList] = xlsread(FILENAME); [nr1,~] = size(FList); % Open csv file
bSub = nData(:,4);Folders = FList(:,1); Files = FList(:,2);
GrSummary = {'Seq Name','Site','Rate (um/s)', 'y-Int', 'R^2', 'nPoints', 'dt'};
Index = 1; SIndex = 1; FIndex = 1; GrReport = (0); GrFitReport = (0); Titles = {" "}; FTitles = {" "};
Index1 = 1; Temp = 0; TempAvgData = zeros(1,length(Identify)+3);
for i = 2:nr1 % Loop over text files
    cd(sprintf('%s/%s/%s/%s',filepath,year, FolderName, '_Image Stats'))
    Data = {0}; Text = 0; nc2 = 1; Sites = 0; % Reset iterative variables
    DataFile = sprintf('%s Stats%s.txt',Folders{i}(:,1).Append); disp(DataFile); % Show current file
    fid = fopen(DataFile,'r'); Text = textscan(fid,'%s',10000,'delimiter','\n');
    fclose(fid); [nr, nc] = size(Text{1,1}); x = strfind(Files{i}(:,1),'C ');
    Temp(i) = str2double(Files{i}(x-5:x-1));
    for i1 = 1:nr % Extract data from text file
        col = 2; [token, remain] = strtok(Text{1}{i1,1},char(9)); Data{i1,1} = str2double(token);
        while isempty(remain{1}) == 0
            if i1 == 1
                nc2 = nc2 + 1;
            end
            [token, remain] = strtok(remain,char(9));
            if isnan(str2double(token{1})) == 1 && i1 < 3
                Data{i1,col} = token{1};
            elseif isnan(str2double(token{1})) == 1
                Data{i1,col} = NaN;
            else
                Data{i1,col} = str2double(token{1});
            end
            col = col + 1;
        end
    end
    if GrRate==1||ActEng==1||GrRep==1||ActRep==1 % % If needed for growth rate or activation energy
        [nr2,~] = size(Data); nSites = floor((nc2-3)/4); % Number of nucleation sites
        New = 1;
        for j = 1:nSites % loop over sites
            Points = [0,0,0]; PPoints = [0,0,0]; Skip = 0; SSkip = 0; kIndex = 1;
            PointsRaw = [0,0,0]; PPointsRaw = [0,0,0]; Subtract = 0; Jump = 0; JJ = 1; JumpFit = [0,0];
            SlopA(:,1) = linspace(10,0,MinSlope(2))+100; SlopA(:,2) = linspace(10000,0,MinSlope(2));

            if strfind(Data{1, 2*(j-1)+4}, '360') == 1
                Thresh = StdDev360;
            else
                Thresh = StdDevThr;
            end
            dataMax = 0;
            for k = bSub(i-1)+1:nr2 % loop over images, starting 1 after background subtraction image
                PPoints(k,1) = Data{k, 2};
                if isnan(Data{k, 2*(j-1)+4}) == 0
                    dataMax(k) = Data{k, 2*(j-1)+4};
                    if (Data{k, 2*(j-1)+4} > MinSize) && (Skip == 0)
% ====== COLLECT DATA TO FIT, PLOT ======
                    PointsRaw(kIndex,1) = Data{k, 2}; % Time

```

Appendix R. Relevant Computer Software

```

PointsRaw(kIndex,2) = Data{k, 2*(j-1)+4}; % Size data to fit
PointsRaw(kIndex,3) = Data{k, 2*(j-1)+5}; % Size error data
PPointsRaw(k,2) = Data{k, 2*(j-1)+4}; % Size data to plot
PPointsRaw(k,3) = Data{k, 2*(j-1)+5}; % Size error data plot
% ====== CALCULATE DATA SLOPE ======
SlopA(2:MinSlope(2),1) = SlopA(1:MinSlope(2)-1,1);
SlopA(2:MinSlope(2),2) = SlopA(1:MinSlope(2)-1,2);
SlopA(1,1)= Data{k, 2}; % x
SlopA(1,2)= Data{k, 2*(j-1)+4}; % y
[slope] = polyfit(SlopA(:,1),SlopA(:,2),1); % Fit line to determine min slope limit
% ===== CODE TO DEAL WTH JUMPS IN THE DATA =====
if Jump == 1 % If there may be a jump in the data
    JumpFit(JJ,1) = Data{k, 2}; JumpFit(JJ,2) = Data{k, 2*(j-1)+4}; JJ = JJ + 1;
end
if JJ == MinSlope(2) % Test to eliminate regions that have jumped
    [newSlope] = polyfit(JumpFit(:,1),JumpFit(:,2),1); yNew = polyval(newSlope,xQ);
    yOld = polyval(oldSlope,xQ); fitY = polyval(newSlope,JumpFit(:,1));
    yresid = JumpFit(:,2) - fitY;
    RSqS = 1-sum(yresid.^2)/(var(JumpFit(:,2))*(length(JumpFit(:,2))-1));

    if abs(yNew-yOld) > JSize || RSqS < RSqLB % Display why data eliminated
        Skip = 1; SSkip = 1;
        disp(sprintf(' Jump = %0.1f, R^2 = %0.2f, abs(yNew-yOld), RSqS)) )
        disp(sprintf('     Skipped, due to slope or R^2, # %f,k))
    end
    JJ = 1; Jump = 0;
end
if (kIndex > MinSlope(2)+3) && ((Data{k, 2}-Data{k-1, 2})/((Data{k, 2*(j-1)+4}-Data{k-1, 2*(j-1)+4})) > JFact*slopeOld(1)) && (Jump == 0)
    Jump = 1; oldSlope = slopeOld; xQ = Data{k, 2};
end
% ===== END OF JUMP CODE =====

% === CODE TO DEAL WITH PLATEAU REGIONS ====
if (Data{k, 2*(j-1)+5} > Thresh) || (slope(1) < MinSlope(1))
    Skip = 1;
disp(sprintf(' Trimmed @ # %0.0f StdD = %0.1f Slope = %0.1f, kIndex, Data{k, 2*(j-1)+5},slope(1)))
    if (slope(1) < MinSlope(1))
        SSkip = 1; % Denotes skipped because of slope
    end
end
% ===== END OF PLATEU CODE =====
kIndex = kIndex + 1; slopeOld = slope;
end
end
end % loop over images
% ===== CODE TO CLEAN UP DATA WITH SKIPS, JUMPS =====
if SSkip == 1
    Subtract = MinSlope(2)+1;
else
    Subtract = 0;

```

Appendix R. Relevant Computer Software

```

end
[nr3,~] = size(PPointsRaw);
for k = 1:(nr3 - Subtract) % Clean up array to eliminate plateau regions
    PPoints(k,2:3) = PPointsRaw(k,2:3);
end
for k = 1:(kIndex - 1 - Subtract) % Clean up array to eliminate plateau regions
    Points(k,1:3) = PointsRaw(k,1:3);
end
% ===== CALCULATE DATA FOR CRYSTALS =====
[nPoints,~] = size(Points);
if nPoints > 1 % Crystal detected, measured: calculate params
    rate = polyfit(Points(:,1),Points(:,2),1); yfit = polyval(rate,Points(:,1));
    yresid = Points(:,2) - yfit; RSq = 1-sum(yresid.^2)/((length(Points(:,2))-1)*var(Points(:,2)));
    dt = Points(nPoints,1)-Points(1,1); Sites = Sites + 1;
else % Crystal likely too small to be detected
    rate = [0,0]; RSq = 0; dt = Points(nPoints,1)-Points(1,1);
end

% ===== CODE TO SAVE DATA =====
if GrRate == 1 % Growth rate data summary
    if CutZeros > 0
        if nPoints > CutZeros && RSq > RSqThresh
            DataName = strsplit(Data{1, 2*(j-1)+4}, ',');
            GrSummary{Index1+1,1} = Folders{i};
            GrSummary{Index1+1,2} = sprintf('%s %s', DataName{2},DataName{1});
            GrSummary{Index1+1,3} = rate(1);
            GrSummary{Index1+1,4} = rate(2);
            GrSummary{Index1+1,5} = RSq;
            GrSummary{Index1+1,6} = nPoints;
            GrSummary{Index1+1,7} = dt;
            for k = 1:length(Identify)
                if length(strfind(Data{1, 2*(j-1)+4},Identify{k})) > 0
                    TempAvgData(Index1,k+1) = 11111;
                else
                    TempAvgData(Index1,k+1) = 0;
                end
            end
            TempAvgData(Index1,length(Identify)+2) = rate(1);
            TempAvgData(Index1,length(Identify)+3) = rate(2);
            TempAvgData(Index1,1) = Temp(i);
            Index1 = Index1 + 1;
        end
    elseif RSq > RSqThresh
        DataName = strsplit(Data{1, 2*(j-1)+4}, ',');
        GrSummary{Index1+1,1} = Folders{i};
        GrSummary{Index1+1,2} = sprintf('%s %s', DataName{2},DataName{1});
        GrSummary{Index1+1,3} = rate(1);
        GrSummary{Index1+1,4} = rate(2);
        GrSummary{Index1+1,5} = RSq;
        GrSummary{Index1+1,6} = nPoints;
        GrSummary{Index1+1,7} = dt;
    end
end

```

Appendix R. Relevant Computer Software

```

for k = 1:length(Identify)
    if length(strfind(Data{1, 2*(j-1)+4},Identify{k})) > 0
        TempAvgData(Index,k+1) = 11111;
    else
        TempAvgData(Index,k+1) = 0;
    end
end
TempAvgData(Index,length(Identify)+2) = rate(1);
TempAvgData(Index,length(Identify)+3) = rate(2);
TempAvgData(Index,1) = Temp(i);
end
end
if GrRep == 1 % Save fitted growth rate data
    if nPoints > 1
        fitPts = polyval(rate,Points(:,1));
        if New == 1
            for m = 1:nr2-2
                GrReport(m,SIndex) = PPoints(m+2,1); Titles{1,SIndex} = Folders{i};
            end
            SIndex = SIndex + 1;
        end
        for m = 1:nr2-2
            Titles{1,SIndex} = sprintf('%s %s',Data{1, 2*(j-1)+4},Folders{i});
            GrReport(m,SIndex) = PPoints(m+2,2);
            Titles{1,SIndex+1} = sprintf('%s %s',Data{1, 2*(j-1)+5},Folders{i});
            GrReport(m,SIndex+1) = PPoints(m+2,3);
        end
        [nrF,~] = size(fitPts);
        for m = 1:nrF
            GrFitReport(m,FIndex) = Points(m,1);
            FTitles{1,FIndex} = sprintf('%s_%d',Folders{i},j);
            GrFitReport(m,FIndex+1) = fitPts(m);
            FTitles{1,FIndex+1} = sprintf('%s %s',Data{1, 2*(j-1)+4},Folders{i});
        end
        SIndex = SIndex + 2; FIndex = FIndex + 2; New = New + 1;
    end
end
Index = Index + 1;
end % loop over sites
end % If statement for growth rate, activation energy
end % loop over text files
if TAvg == 1 % Average and sort data according to temperature
    Tarray = unique(Temp); % Find unique temperatures
    for i = 1:(length(Identify)+1)
        TempAvgData = sortrows(TempAvgData,length(Identify)+2-i);
    end
    TempAvgHeader = { 'Temperature (C)',Identify{:,1}, 'Rate', 'Y-Int' };
    for i = 1:length(Identify) % Loop over types of measurements
        for j = 1:length(Tarray) % Loop over temperatures
            AvgData = [0,0]; AIndex = 1; Index = 2; [nr, ~] = size(TempAvgData);
            for k = 1:nr % Loop over all sites

```

Appendix R. Relevant Computer Software

```

if TempAvgData(k,1)==Tarray(j)&& TempAvgData(k,i+1)==11111
    AvgData(AIndex,1:2) = TempAvgData(k,length(Identify)+2:length(Identify)+3);
    AIndex = AIndex + 1;
end
end
% Calculate averages and standard deviations
AvgArray(j,1) = Tarray(j); N = 2*(IncData(1)+IncData(2))+IncData(3);
if IncData(1) == 1 % Slope
    AvgArray(j,N*(i-1)+Index) = mean(AvgData(:,1));
    AvgHeader{1,N*(i-1)+Index} = sprintf('%s Slope Avg',Identify{i});
    Index = Index + 1; AvgArray(j,N*(i-1)+Index) = std(AvgData(:,1));
    AvgHeader{1,N*(i-1)+Index} = sprintf('%s Slope StDev',Identify{i});
    Index = Index + 1;
end
if IncData(2) == 1 % Y-intercept
    AvgArray(j,N*(i-1)+Index) = mean(AvgData(:,2));
    AvgHeader{1,N*(i-1)+Index} = sprintf('%s Y-int Avg',Identify{i});
    Index = Index + 1; AvgArray(j,N*(i-1)+Index) = std(AvgData(:,2));
    AvgHeader{1,N*(i-1)+Index} = sprintf('%s Y-int StDev',Identify{i});
    Index = Index + 1;
end
if IncData(3) == 1 % Number of points
    AvgArray(j,N*(i-1)+Index) = length(AvgData(:,1));
    AvgHeader{1,N*(i-1)+Index} = '# Points';
end
AvgHeader{1,1} = 'Temperature (C)';
end
warning off MATLAB:xlswrite:AddSheet
if TAvg == 1 % Save data sorted and averaged by temperature
    disp('Saving Temp Avg...')
    xlswrite(fullfile('F:\UMN Data\Summary Files'),year, sprintf('%s Condensed Data%s',
    FolderName,AppendNew)),AvgHeader,'T Avg','A1')
    xlswrite(fullfile('F:\UMN Data\Summary Files'),year, sprintf('%s Condensed Data%s',
    FolderName,AppendNew)),AvgArray,'T Avg','A2')
    xlswrite(fullfile('F:\UMN Data\Summary Files'),year, sprintf('%s Condensed Data%s',
    FolderName,AppendNew)),TempAvgHeader,'Sorted','A1')
    xlswrite(fullfile('F:\UMN Data\Summary Files'),year, sprintf('%s Condensed Data%s',
    FolderName,AppendNew)),TempAvgData,'Sorted','A2')
end
if GrRate == 1
    disp('Saving Growth Rate...')
    xlswrite(fullfile('F:\UMN Data\Summary Files'),year, sprintf('%s Condensed Data%s',
    FolderName,AppendNew)),GrSummary,'Growth Rate','A1')
end
% ====== SAVE GROWTH RATE DATA SUMMARY ======
if GrRep == 1
    [nr,nc] = size(Titles); [nr1,nc1] = size(FTitles); Title = matlab.lang.makeValidName(Titles{1,1});
    FTitle = matlab.lang.makeValidName(FTitles{1,1});

```

Appendix R. Relevant Computer Software

```
for m = 2:nc
    Title = sprintf('%s \t %s', Title, matlab.lang.makeValidName(Titles{m}));
end
for m = 2:nc1
    FTitle = sprintf('%s \t %s', FTitle, matlab.lang.makeValidName(FTitles{m}));
end
GrReportT = array2table(GrReport,'VariableNames',strsplit>Title,\t));
GrFitReportT = array2table(GrFitReport,'VariableNames',strsplit>FTitle,\t));
disp('Saving Growth Data and Fit...')
writetable(GrReportT,fullfile('F:\UMN Data\Summary Files',year, sprintf('%s Growth Data%s.txt',
FolderName,AppendNew)));
writetable(GrFitReportT,fullfile('F:\UMN Data\Summary Files',year, sprintf('%s Fit Data%s.txt',
FolderName,AppendNew)));
end
objExcel = actxserver('Excel.Application'); % Open Excel file.
objExcel.Workbooks.Open(fullfile('F:\UMN Data\Summary Files',year, sprintf('%s Condensed Data%s',
FolderName,AppendNew)));
try % Delete Sheets
    objExcel.ActiveWorkbook.Worksheets.Item('Sheet1').Delete;
    objExcel.ActiveWorkbook.Worksheets.Item('Sheet2').Delete;
    objExcel.ActiveWorkbook.Worksheets.Item('Sheet3').Delete;
catch % Throws an error if the sheets do not exist.
    ; % Do nothing.
end % Save, close and clean up.
objExcel.ActiveWorkbook.Save;
objExcel.ActiveWorkbook.Close;
objExcel.Quit;
objExcel.delete;
disp('Done.')
end % function
```

R.6. TEM Diffraction Pattern Simulation (Matlab)

This software uses the .hkl files which are output from the Cambridge Crystallographic Data Center (CCDC) program Mercury, coupled with the unit cell parameters, to calculate a two-dimensional representation of powder, CBED, and single crystal electron diffraction patterns. There are a number of options to change the circle size (SF), color (CColor), and text size (FontSize), color (TColor), offset (textOffset), and shift (shift) for powder patterns. To run this program, output a .hkl file from Mercury for the compound of interest, then input the unit cell parameters (a , b , c , α , β , γ), point Matlab to the .hkl file, and select which zone axis to simulate (zoneAxis) and whether to simulate single crystal (Powder = 0), oriented powder (Powder = 1), random powder (Powder = 2), or CBED (CBED = 1). Figure 14.54 shows single crystal, powder, and CBED patterns created with this program for the [001] axis of BP2T. A number of features are available, including pattern rotation, scaling,

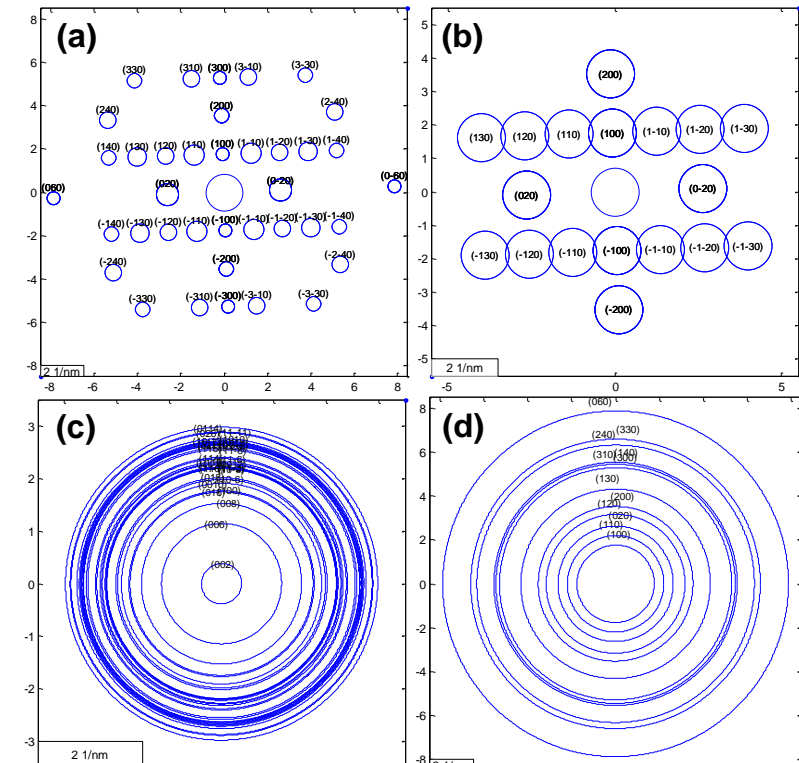


Figure 14.54. Simulated transmission electron diffraction pattern for the [001] zone of BP2T in (a) single crystal, (b) CBED, (c) randomly oriented powder, and (d) textured polycrystalline film.

Appendix R. Relevant Computer Software

background and text color change, scale bar, etc. The code is given below.

```

function ZoneAxisPattern
% This program calculates the diffraction pattern for a given crystal structure and zone axis. The program
% assumes that the .hkl file has already been generated using CCDC Mercury software with columns 'h k l
% d-spacing F^2 multiplicity'. Make sure Mercury generates a full set of hkls by customizing the powder
% XRD display limit options before saving.
% Created by Tom Fielitz, University of Minnesota, July 6th 2016

zoneAxis = [0,0,1]; % Zone axis, as [u,v,w]
Powder = 2; % Choose single crystal (0) or powder, textured(1)/random(2)
CBED = 1; % Create spots that are the same size if == 1
% ***** Image size and orientation *****
ImageRotate = 90; % degrees
PlaneAngle = [1,2,1,147.8]; % [h,k,l,theta(deg)] If desired, a plane and the angle it makes
% with the horizon (spot with smallest spacing) to align with an image. Otherwise, set to 0.
Lim = 3; % Extent of plot in 1/AngNM
IntLim = 1000; % Structure factor lower limit for displayed spots/rings
% ***** Coloration of Plot *****
TransBkgd = 0; % Make background transparent if ==1
CColor = 'b'; % Circle color
TColor = 'k'; % Text color
ScaleBar = 2; % Scale bar length in Ang/nm. Set to zero if not desired.
% ***** Formatting of spots and labels *****
PlotMirror = 1; % mirror points into other quadrants
AngNM = 0; % Plot axes in 1/angstroms (1) or 1/nm (0)
FontSize = 8; % point
textOffset = 0; % 1/angstroms/nm
shift = 5; % For powder pattern, +/- amount to shift labels (deg)
VaryWidth = 0; % Makes width of powder lines prop. to log(Int) if==1
SF = 2; % factor to multiply spot size/linewidth by
% ***** Enter information about unit cell parameters *****
a = 5.708; b = 7.6036; c = 52.869; % Lattice dimensions, angstroms
alpha = 90; beta = 97.147; gamma = 90; % Lattice angles, degrees
% Path to .hkl file with planes and spot intensity (F^2)
hklFile = 'F:\UMN Data\X-Ray Scattering Data\Calculated\BP2T.hkl';

% % =====
% %
fid = fopen(hklFile); IntLim = log(IntLim); Text = textscan(fid,'%s',100000,'delimiter','\n');
[nr, nc] = size(Text{1}); alpha = alpha*pi/180; beta = beta*pi/180; gamma = gamma*pi/180;
Permute = [-1,1,1;-1,-1,1;-1,1,-1;1,-1,-1;1,1,-1]; disp(' Calculating... ')
for i1 = 1:nr
    col = 2; [token, remain] = strtok(Text{1}(i1,1)); num(i1,1) = str2double(token);
    while isempty(remain{1}) == 0
        [token, remain] = strtok(remain); num(i1,col) = str2double(token{1}); col = col + 1;
    end
end
% Metric tensor
MT = [a^2, a*b*cos(gamma), a*c*cos(beta); b*a*cos(gamma), b^2, b*c*cos(alpha); c*a*cos(beta),
c*b*cos(alpha), c^2];

```

Appendix R. Relevant Computer Software

```

IMT = MT^-1;
if Powder == 1 % Textured powder rings
    theta = 0:0.001:2*pi; ImgRot = ImageRotate*pi/180; shift = shift*pi/180;
    for i = 2:nr
        hkl = num(i,1:3); Weiss = zoneAxis*hkl';
        if Weiss == 0
            if AngNM == 1
                d = 1/(hkl*IMT*hkl')^0.5;
            else
                d = (1/(hkl*IMT*hkl')^0.5)/10;
            end
            if log(num(i,5)*num(i,6)) > IntLim && 1/d < Lim
                if VaryWidth == 1
                    plot(1/d*cos(theta),1/d*sin(theta),'Color',CCColor,'LineWidth',log(num(i,5)*num(i,6))*SF/5);
                else
                    plot(1/d*cos(theta),1/d*sin(theta),'Color',CCColor);
                end
                hold on
                shift = shift*-1;
            text(1/d*cos(ImgRot+shift),1/d*sin(ImgRot+shift)+textOffset,sprintf('(%d%d%d)',hkl(1),hkl(2),hkl(3)),
                'FontSize',FontSize,'HorizontalAlignment','center','Color',TColor)
                end
            end
        end
    elseif Powder == 2 % Randomly oriented powder rings
        theta = 0:0.001:2*pi; ImgRot = ImageRotate*pi/180; shift = shift*pi/180;
        for i = 2:nr
            hkl = num(i,1:3);
            if AngNM == 1
                d = 1/(hkl*IMT*hkl')^0.5;
            else
                d = (1/(hkl*IMT*hkl')^0.5)/10;
            end
            if log(num(i,5)*num(i,6)) > IntLim && 1/d < Lim
                if VaryWidth == 1
                    plot(1/d*cos(theta),1/d*sin(theta),'Color',CCColor,'LineWidth',log(num(i,5)*num(i,6))*SF/5);
                else
                    plot(1/d*cos(theta),1/d*sin(theta),'Color',CCColor);
                end
                hold on
                shift = shift*-1;
            text(1/d*cos(ImgRot+shift),1/d*sin(ImgRot+shift)+textOffset,sprintf('(%d%d%d)',hkl(1),hkl(2),hkl(3)),
                'FontSize',FontSize,'HorizontalAlignment','center','Color',TColor)
                end
            end
        end
    else % Single crystal spots
        first = 0;
        for i = 2:nr
            hkl = num(i,1:3); Weiss = zoneAxis*hkl';
            if Weiss == 0
                if first == 0

```

Appendix R. Relevant Computer Software

```

plot(0,0,sprintf('o%s',CColor),'MarkerSize',20*SF); hold on; hklC1 = hkl;
if PlaneAngle == 0
    ImgRot = ImageRotate*pi/180;
else
    hkl1 = PlaneAngle(1:3);
    theta = real(acos((hkl1*IMT*hklC1')/((hkl1*IMT*hkl1')^0.5*(hklC1*IMT*hklC1')^0.5)));
    ImgRot = PlaneAngle(4)*pi/180 - theta;
end
if AngNM == 1
    d = 1/(hklC1*IMT*hklC1')^0.5;
else
    d = (1/(hklC1*IMT*hklC1')^0.5)/10;
end
if log(num(i,5)*num(i,6)) > IntLim
    if CBED == 0
        Int = log(num(i,5)*num(i,6));
    else
        Int = SF*10;
    end
    plot(1/d*cos(ImgRot),1/d*sin(ImgRot),sprintf('o%s',CColor),'MarkerSize',Int*SF);
text(1/d*cos(ImgRot),1/d*sin(ImgRot)+textOffset,sprintf('( %d%d%d)',hklC1(1),hklC1(2),hklC1(3)),
'FontSize',FontSize,'HorizontalAlignment','center','Color',TColor)
    if PlotMirror == 1
        for j = 1:length(Permute)
            hkl1 = hkl.*Permute(j,1:3);
            if hkl1*zoneAxis' == 0
                theta1 = real(acos((hkl1*IMT*hklC1')/((hkl1*IMT*hkl1')^0.5*(hklC1*IMT*hklC1')^0.5))+ImgRot);
                plot(1/d*cos(theta1),1/d*sin(theta1),sprintf('o%s',CColor),'MarkerSize',Int*SF);
text(1/d*cos(theta1),1/d*sin(theta1)+textOffset,sprintf('( %d%d%d)',hkl1(1),hkl1(2),hkl1(3)),
'FontSize',FontSize,'HorizontalAlignment','center','Color',TColor)
                    end
            end
        end
    end
    first = 1;
else
    if first == 1
        hklC2 = hkl;
    end
    theta3 = real(acos((hklC2*IMT*hklC1')/((hklC2*IMT*hklC2')^0.5*(hklC1*IMT*hklC1')^0.5)));
    first = 2;
end
theta = real(acos((hkl*IMT*hklC1')/((hkl*IMT*hkl')^0.5*(hklC1*IMT*hklC1')^0.5))+ImgRot);
if AngNM == 1
    d = 1/(hkl*IMT*hkl')^0.5;
else
    d = (1/(hkl*IMT*hkl')^0.5)/10;
end
if log(num(i,5)*num(i,6)) > IntLim
    if CBED == 0
        Int = log(num(i,5)*num(i,6));
    else

```

Appendix R. Relevant Computer Software

```

Int = SF*10;
end
if 1/d <= Lim
    plot(1/d*cos(theta),1/d*sin(theta),sprintf('o%s',CColor),'MarkerSize',Int*SF);
text(1/d*cos(theta),1/d*sin(theta)+textOffset,sprintf('(%d%d%d)',hkl(1),hkl(2),hkl(3)),FontSize,
'HorizontalAlignment','center','Color',TColor)
    if PlotMirror == 1
        for j = 1:length(Permute)
            hkl1 = hkl.*Permute(j,1:3);
            if hkl1*zoneAxis' == 0
theta1 = real(acos((hkl1*IMT*hklC1')/((hkl1*IMT*hkl1')^0.5*(hklC1*IMT*hklC1')^0.5)));
theta2 = real(acos((hkl1*IMT*hklC2')/((hkl1*IMT*hkl1')^0.5*(hklC2*IMT*hklC2')^0.5)));
                if (theta2 >= theta3 && theta2 >= theta1)|(theta2>= pi-theta3)
theta1 = real(-acos((hkl1*IMT*hklC1')/((hkl1*IMT*hkl1')^0.5*(hklC1*IMT*hklC1')^0.5))+ImgRot);
                    plot(1/d*cos(theta1),1/d*sin(theta1),sprintf('o%s',CColor),'MarkerSize',Int*SF);
text(1/d*cos(theta1),1/d*sin(theta1)+textOffset,sprintf('(%d%d%d)',hkl1(1),hkl1(2),hkl1(3)),FontSize,
tSize,'HorizontalAlignment','center','Color',TColor)
                else
                    theta1 = theta1 + ImgRot;
                    plot(1/d*cos(theta1),1/d*sin(theta1),sprintf('o%s',CColor),'MarkerSize',Int*SF);
text(1/d*cos(theta1),1/d*sin(theta1)+textOffset,sprintf('(%d%d%d)',hkl1(1),hkl1(2),hkl1(3)),FontSize',
FontSize,'HorizontalAlignment','center','Color',TColor)
                end
            end
        end
    end
end
end
xy = Lim+0.5;plot(-xy,-xy,'.');plot(xy,xy,'.');
if ScaleBar ~=0
rectangle('Position',[-xy -xy ScaleBar 0.5],'FaceColor',[1 1 1])
if AngNM == 1
    text(-xy+ScaleBar/2, -xy+0.25,sprintf('%d 1/angstroms',ScaleBar),'HorizontalAlignment','center')
else
    text(-xy+ScaleBar/2, -xy+0.25,sprintf('%d 1/nm',ScaleBar),'HorizontalAlignment','center')
end
end
hold off; fclose(fid); axis equal tight;
if TransBkgd == 1
    set(gcf,'color','none'); set(gca,'color','none');
end
disp(' Done.')
end %function

```

R.7. Simulating Energetic Disorder in Exciton Diffusion with KMC

(Matlab)

This code was written as a more accessible (Matlab) alternative to the Kinetic Monte Carlo (KMC) code previously written in C++ to describe exciton transport in energetically disordered media.²⁹⁷ Surprisingly, because of the implementation of parallel for loops in the key iteration step and matrix operations whenever possible, the code is not significantly slower than one written for C++, with the example looping over multiple values of the disorder parameter σ here requiring ~1 day to run on a quad-core i5-4440 CPU at 3.10 GHz running a 64-bit operating system and 64-bit Matlab 2014a.

The below code initializes and runs a KMC simulation according to the schematic shown in Figure 14.55. First, the desired experimental parameters (unit cell size, energy transfer physics, temperature, etc.) are initialized by the controlling code, the first section given below. This code then calls the actual KMC simulation, which extracts the necessary parameters and begins the simulation.

In this simulation, a new lattice is randomly generated for each exciton launched. This lattice contains points which have a Gaussian distribution of energies of standard deviation σ to approximate the energy distribution in the density of states “tail”. An exciton is then randomly placed in the lattice,

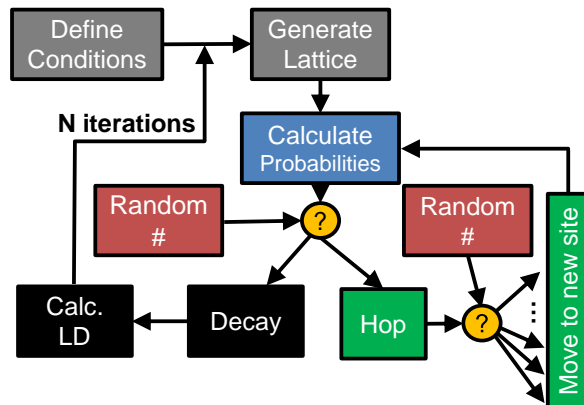


Figure 14.55. Schematic for exciton diffusion as simulated by Kinetic Monte Carlo.

Appendix R. Relevant Computer Software

and the rates of motion and decay are calculated for that site according to

$$k_F = \frac{R_{0,c}^6}{d^2\tau} \exp\left(-\frac{E_A}{k_B T}\right) \exp\left(\frac{E' - E}{k_B T}\right) \quad (14.68)$$

summing over all available sites nearby for motion and

$$k_{Decay} = \frac{1}{\tau} \quad (14.69)$$

for decay. The probabilities of these events are calculated from their magnitude normalized by the sum of all possible rates and accumulated into a summed probability vector. For example, if the rate of decay were 1 s^{-1} and there were rates of transfer of 2, 3, and 4 s^{-1} , the cumulative probability vector would be [0.1, 0.3, 0.6, 1]. One event is then chosen by drawing a random number and determining which interval it fits into to select exciton decay or motion. If the exciton decays, the total distance travelled is recorded and a new simulation is begun. A second random number is then chosen to determine which specific site the exciton will transfer to. The probabilities are then recalculated for the new site, total distance travelled updated, and the random number drawing repeated for N trials.

This code controls the KMC code, allowing simple implementation of multiple loops over variables of interest.

```
function run_trf_mm_kmc1
clear all
LatticeSize = 50; % Size of lattice (cube) on a side, #
d = 0.5; % Lattice constant, nm - 0.48 nm for SubPc
tau = 0.6; % Exciton total lifetime, ns
r0c = 1.4; % Forster radius/tauRad, nm^6/sec
sigma1 = 0.035; % Exciton density of states standard deviation, eV
sigma2 = 0.035; % End sigma
nSigma = 1; % Number of sigmas to use
Ea = 0.001; % PL activation energy, eV
T = 295; % Temperature, K
Layers = 10; % Number of molecular layers around exciton
Iterations = 10; % Number of iterations
```

Appendix R. Relevant Computer Software

```

Nruns = 5;      % Number of loops to see variance among trials
name = 'test1'; % File name, excluding .txt
path = 'F:\UMN Data\Simulations\' ;
sigmaA = linspace(sigma1,sigma2,nSigma);
for i = 1:length(sigmaA)
    sigma = sigmaA(i);
    % argOut = [LatticeSize,d,tau,r0c,sigma,Ea,T,Layers,Iterations,Nruns];
    argOut = [LatticeSize,d,tau,r0c,sigma,Ea,T,Layers,Iterations,Nruns];
    trf_mm_kmc1(argOut,name,path)
end
end

```

The following function performs the Kinetic Monte Carlo simulations, using input from the previous section. Data is saved directly from this function into the path specified. Nothing needs to be altered in this function, although parallel computing must be enabled in Matlab in order to run the `parfor` loop.

```

function trf_kmc_cpp_1(argIn,name,path)
% This function calculates the ensemble averaged exciton diffusion
% length accounting for local disorder according to Menke & Holmes,
% DOI 10.1039/c6tc00525j
tStart = tic;
LatticeSize = argIn(1); % Size of lattice (cube) on a side, #
d = argIn(2);           % Lattice constant, nm
tau = argIn(3);          % Exciton total lifetime, sec
r0c = argIn(4);          % Forster radius/tRad^1/6, nm/ns^1/6
sigma = argIn(5);         % Exciton density of states standard deviation, eV
Ea = argIn(6);           % PL activation energy, eV
T = argIn(7);            % Temperature, K
Layers = argIn(8);        % Number of molecular layers around exciton
Iterations = argIn(9);     % Number of iterations
Nruns = argIn(10);        % Number of loops to see variance among trials
% =====
% =====
kB = 8.6e-5; % actual 8.617e-5
e = 2.71; % natural log
Decay = 1/tau; EndSite = zeros(Iterations,1);
Move = zeros(Layers^3-1,3); m = 1; AvgLD = zeros(1,Nruns);
% Populate matrix to describe possible exciton moves
for i = -Layers:Layers
    for j = -Layers:Layers
        for k = -Layers:Layers
            Move(m,:) = [i,j,k];
            m = m + 1;
            if i == 0 && j == 0 && k == 0

```

Appendix R. Relevant Computer Software

```

m = m - 1;
end
end
end
Ensemble = zeros(Iterations,Nruns); Counter = zeros(2,Nruns);
kF0 = (r0c./(d*sqrt(sum(abs(Move).^2,2))).^6.*e^(-Ea/kB/T));
for i1 = 1:Nruns
    Hops = 0; Decays = 0;
    parfor i = 1:Iterations
        %Create array and starting point
        siteE = sigma*randn(LatticeSize,LatticeSize,LatticeSize); % Create distribution of lattice site energies
        Spot1 = [floor(LatticeSize/2),floor(LatticeSize/2),floor(LatticeSize/2)]; Spot = Spot1;
        ExcitonAlive = 1; l = 1;
        while ExcitonAlive == 1
            % Extract energy of sites around current spot
            [nr,~] = size(Move); k = floor((Spot-1)/LatticeSize);
            Spot_Latt = [ones(nr,1)*(Spot(1) - k(1)*LatticeSize),ones(nr,1)*(Spot(2) - k(2)*LatticeSize),
            ones(nr,1)*(Spot(3) - k(3)*LatticeSize)];
            New = Spot_Latt+Move; k1 = floor((New(:,1)-1)/LatticeSize); New1 = New(:,1)-k1*LatticeSize;
            k2 = floor((New(:,2)-1)/LatticeSize); New2 = New(:,2)-k2*LatticeSize;
            k3 = floor((New(:,3)-1)/LatticeSize); New3 = New(:,3)-k3*LatticeSize;
            ENeighbors = siteE(New1+(New2-1)*LatticeSize+(New3-1)*LatticeSize^2);
            ESite = ones(nr,1)*siteE(Spot_Latt(1,1)+(Spot_Latt(1,2)-1)*LatticeSize+(Spot_Latt(1,3)-
            1)*LatticeSize^2);
            Ecalc = ENeighbors - ESite; Neg = find(Ecalc < 0); Ecalc(~Neg) = 0;
            kF = kF0.*e.^(-Ecalc/kB/T); % Calc Forster transfer to each site
            Choice = cumsum([Decay;sum(kF)]); % compile all probabilities into array
            RandNum1 = rand(1)*Choice(2); % Pick a random number somewhere in Choice array
            j = 1;
            while(RandNum1 > Choice(j))
                j = j+1;
            end

            if j == 1 % Exciton decays
                EndSite(i,1) = norm(Spot - Spot1)*d;
                fprintf(' %0.2f %% LD = %0.1f nm', ((i1-1)/Nruns+i/Nruns/Iterations)*100, EndSite(i,1));
                disp(' ');
                ExcitonAlive = 0; Decays = Decays + 1;
            elseif j== 2 % Exciton hops to a new site
                kFChoice = cumsum(kF); RandNum2 = rand(1)*kFChoice(end); k = 1;
                while RandNum2 > kFChoice(k)
                    k = k + 1;
                end
                Spot = Spot + Move(k,:); Hops = Hops + 1;
            end
            l = l + 1;
        end
    end
    Counter(1,i1) = Decays; Counter(2,i1) = Hops;
    % Display progress so far and move to next set of iterations

```

Appendix R. Relevant Computer Software

```

fprintf('Pct Done: %0.2f  Avg LD = %0.3f nm',(i1/Nruns)*100, mean(EndSite)); disp(' ');
Ensemble(:,i1) = EndSite; AvgLD(1,i1) = mean(EndSite);
end
Counter(3,:) = Counter(2,:)./Counter(1,:);
Params = [LatticeSize;d;tau;r0c;Ea*1000;T;sigma*1000;toc(tStart)];
disp('Saving...')

fid = fopen(strjoin({path,'AvgLD ',name,'.txt'},{{",",""},'wt'});
fprintf(fid,'%0.3f\n',AvgLD); fclose(fid);

fid = fopen(strjoin({path,'Counter ',name,'.txt'},{{",",""},'wt'});
fprintf(fid,'%s\%s\%s\%s\%s\Decays\Hops\AvgHops');
fclose(fid);

fid = fopen(strjoin({path,'Ensemble ',name,'.txt'},{{",",""},'wt'});
fprintf(fid,'%0.3f\n',Ensemble);
fclose(fid);

fid = fopen(strjoin({path,'Params ',name,'.txt'},{{",",""},'wt'});
fprintf(fid,'%s\%s\%s\%s\%s\%s\%s\LatDim\%d(nm)\%tau(ns)\%r0(nm6)\%Ea(meV)\%T(K)\%sigma(me
    V)\%Time (sec)');
fprintf(fid,'%0.0f\%0.4f\%0.3f\%0.3f\%0.5f\%0.5f\%0.3f\%0.3f\%0.3f\%n',Params);
fclose(fid);

disp(' ');
fprintf('Done with Sigma = %0.3f, Time Required = %0.3f sec', sigma, toc(tStart));
disp(' ');

```

end % function

R.8. AFM Tip Motion Simulation (Matlab)

The following code runs and plots a simulation for an AFM tip which is initially static and then turned on. This code was used to generate figures for Appendix E.1. Equations and most values are taken from Garcia *et al.*⁷⁹⁹

```

function AFM_Tip_Transient1
%% This function calculates the transient behavior of an AFM tip
% using the theory explained in Garcia & San Paulo 2000
clc
Q = 10; % Quality factor
w0 = 250*10^3; % Tip resonant frequency, Hz (not angular yet)
kc = 40; % Tip stiffness, N/m
Fo = 1*10^-10; % Driving force, N
dw = 0; % Difference b/n tip resonant & driving freq (dw = w0-w), Hz
tspan = [0 6*10^-5];
%%%%= Simulation Below =====
w0 = w0*2*pi;
dw = dw*2*pi;
sol = ode45(@(t,z) TipODE(t,z,Q,w0,kc,Fo,dw),tspan,[0;0]);
fplot(@(t,z) deval(sol,t,1), tspan)
xlabel('Time (sec)'); ylabel('Tip Displacement (m)');
end %function

function dz = TipODE(t,z,Q,w0,kc,Fo,dw)
% Define tip-sample interaction - from Garcia, San Paulo 2000
R = 10*10^-9; % Tip radius, m
H = 6.4*10^-20; % Hamaker constant, J
E = 1.51*10^9; % Tip-sample elastic modulus, Pa
z0 = 10*10^-9; % Tip-sample equilibrium separation, m
a0 = 0.5*10^-9; % Intermolecular separation, m
% Equations to talk to solver
m = kc/w0^2;
w = w0 + dw;
if a0 <= z+z0
    Fts = -H*R/(6*(z(1)+z0)^2);
else
    Fts = -H*R/(6*a0^2)+E*R^0.5*(a0-z0-z(1))^3/2;
end

dz(1,1) = z(2);
dz(2,1) = -kc/m*z(1)-w0/Q*z(2)+Fts/m+Fo/m*cos(w*t);
end

```

R.9. Finite Element Exciton Gating Code (Matlab)

The following code runs, plots, and save simulations of exciton gating, and was used to generate the figures found in Chapter 8. Considerations for the finite element method as applied to this code may be found in Appendix Q.

```

function ExcitonGating10
% This function solves the exciton diffusion equation for a structure
with interfaces of arbitrary energy transfer rates and Forster energy
transfer between layers using a centered finite differences
approximation. These results are compared to an analytical solution for
simple diffusion and an analytical gating solution.
%
% Layer stack:
%
% -D*n'=F      K1        K2        K3        KN-1       n=0
% |           |         |         |           |           |
% | #1        | #2        | #3        |           | #N        |
% | G1        | G2        | G3        | . . .     | GN        |
% | R12->| R23->| R34->| RN-1N->|           |
% |           |<-R21   |<-R32   |<-R43     |<-RNN-1   |
% x=0        x1        x2        x3        xN-1      xN
%
% Steady-state exciton flux enters at left side of (1), fluxes
% match at internal boundaries, and concentration is zero at right side
% of (3), totally dissociating interface. Between layers, additional
% Forster transfer occurs between layers i and j with radius Rij.
%
% The steady-state exciton diffusion equation is
% 0 = D*n'' - n/tau + G
% Which yields a general solution of
% n = C1*exp(-x/LD) + C2*exp(x/LD) + G*tau
% The equations for each layer are solved simultaneously using the
% boundary
% conditions of known flux at x=0, known conentration ratio and equal
% fluxes at internal boundaries, and zero concentration at x(N) using
A*C = b
%
% This equation including interlayer Forster transport becomes
% 0 = D*n'' - n/tau + G + kF*n
% which must be solved numerically, here using finite differences.
%
% Created By Tom Fielitz, University of Minnesota, June 20, 2017
%
%% ===== Define Variables: =====
% Geometry
th = [5,5]; % Layer thicknesses, nm

```

Appendix R. Relevant Computer Software

```

dx1 = 0.005; % Thickness step size for gating
dx2 = 0.005; % dx for simple diffusion model

% Physics - all parameters have one value per layer (or interface:
R0ij)
R0ij = [1,1; 1,1];
    % Defined as [R011, R012, R013...; R021, R022, R033...]
tau = [0.5,0.5]; % Exciton lifetime, ns
d = [0.5,0.5]; % Molecular spacing, nm (lower bound for Forster d)
B0 = 5; % Buffer of material for calculating velocity at x = 0
BL = 5; % Buffer at x = L

% Boundary and source/sink terms
F = 0; % Exciton flux from the left interface, #/nm^2 s
G = 1; % Exciton generation rate in each layer, #/nm^3 s
Conc = 0; % Exciton concentration at x = L, #/nm^3

% ===== Information for saving file =====
filePath = 'F:\UMN Data\Simulations\Exciton Gating'; % Save directory
for profiles
fileName = '2017-07-16 Rate Study.xlsx'; % File name
sheetName = 'R0=1,B=5';
SS = 10; % Factor to reduce resolution by to reduce file size

%% ===== Start of code - DO NOT ALTER BELOW HERE =====
%% Set up basic variables for all simulations:
tic % Start timer for code execution
NL = length(th);
for i = 1:NL
    R0ii(i) = R0ij(i,i);
    if i < NL
        if R0ij(i+1,i) ~= 0
            K(i) = R0ij(i,i+1).^6./R0ij(i+1,i).^6;
        elseif R0ij(i+1,i) == 0 && R0ij(i,i+1) == 0
            K(i) = 1;
        else
            K(i) = R0ij(i,i+1)*10^9;
        end
    end
end
L = sum(th(1:NL)); % Total stack thickness
rhoA = 1./(pi*d.^2); % Energy acceptors per nm^2
LD = R0ii.^3./d.^2 % Exciton diffusion length by point-to-point Forster
x = cumsum(th); % Locations of boundaries x1, x2, ...

%% Analytical solution for simple diffusion with generation and decay
disp(' '); disp('----Analytical Simple Diffusion----');

A = zeros(NL*2); % Set up A matrix

```

Appendix R. Relevant Computer Software

```

A(1,1) = LD(1)/tau(1); A(1,2) = -LD(1)/tau(1); % Flux equals flux
A(NL*2,NL*2-1:NL*2) = [exp(-x(NL)/LD(NL)), exp(x(NL)/LD(NL))]; %
Concentration at x=L = 0

for i = 1:NL-1
    A(2*i,(2*i-1):(2*i+2)) = [exp(-x(i)/LD(i)), exp(x(i)/LD(i)), -exp(-
x(i)/LD(i+1)), -exp(x(i)/LD(i+1))];
    A(2*i+1,2*i-1:2*i+2) = [LD(i)/tau(i)*exp(-x(i)/LD(i)), -
LD(i)/tau(i)*exp(x(i)/LD(i)), -LD(i+1)/tau(i+1)*exp(-x(i)/LD(i+1)),
LD(i+1)/tau(i+1)*exp(x(i)/LD(i+1))];
end

b = zeros(NL*2,1);
b(1) = F;
for i = 1:NL-1
    b(2*i) = G*tau(i+1)-G*tau(i);
end
b(2*NL) = -G*tau(NL) + Conc;

C = A^-1*b;
xA = zeros(1000,1); yA = zeros(1000,1); stop = 0;
for i = 1:NL
    start = stop + 1; stop = stop + floor(1000*th(i)/L);
    if i == 1
        xA(start:stop,1) = linspace(0,x(i),floor(1000*th(i)/L))';
    elseif i == NL
        xA(start:1000,1) = linspace(x(i-1),x(i),1001-start)';
    else
        xA(start:stop,1) = linspace(x(i-1),x(i),floor(1000*th(i)/L))';
    end
    yA(start:stop,1) = C(2*i-1)*exp(-
xA(start:stop,1)/LD(i))'+C(2*i)*exp(xA(start:stop,1)/LD(i))+G*tau(i);
end
density(1) = trapz(xA,yA);
flux(1) = -LD(NL)/tau(NL)*(-C(2*NL-1)*exp(-
L/LD(NL))+C(2*NL)*exp(L/LD(NL)));
n0(1) = C(1)*exp(0)+C(2)*exp(0)+G*tau(1);
disp(sprintf('Flux = %0.4f, Density = %0.4f, n0 =
%0.5f',flux(1),density(1),n0(1)))

%% Finite Difference solution for simple diffusion with generation and
decay
disp(' '); disp('----FE Simple Diff----');
dx = dx2;
Nx = floor(L/dx); % number of points
x2 = linspace(0,L,Nx);
A = zeros(Nx); Diagonal = ones(Nx,1)*1/dx^2;
A = diag(Diagonal(1:Nx-1), -1) + diag(Diagonal(1:Nx-1), 1) -
diag(2*Diagonal,0);
b = ones(Nx,1).*(-G); stop = 0;

for i = 1:Nx
    A(i,i) = 1;
    A(i,i-1) = -1;
    A(i,i+1) = -1;
    b(i) = density(i);
end

```

Appendix R. Relevant Computer Software

```

dTh = floor(Nx*th(i)/L);
start = stop + 1; stop = stop + dTh;
Diag2 = ones(dTh,1)*1/LD(i)^2;
A(start:stop,start:stop) = A(start:stop,start:stop)-diag(Diag2,0);
b(start:stop,1) = b(start:stop,1)*(tau(i)/LD(i)^2);
if i < NL % Interfacial flux balance
    A(stop-2,(stop-3):stop+2) = [1*LD(i)^2/tau(i), -
1*LD(i)^2/tau(i), -1*LD(i+1)^2/tau(i+1), 1*LD(i+1)^2/tau(i+1), 0,
0]/dx;
    b(stop-2,1) = 0;
    A(stop-1,stop-4:stop+2) = [0,0,-1,1,0,0,0];
    b(stop-1,1) = 0;
end
end

% Boundary conditions
A(1,1:2) = [1/dx, -1/dx];
A(Nx,Nx-1:Nx) = [0,1];
b(Nx,1) = Conc; b(1,1) = F*tau(1)/LD(1)^2;
nx2 = A\b;
flux(2) = LD(end)^2/tau(end)*(nx2(end-1)-nx2(end))/dx;
density(2) = trapz(x2,nx2);
n0(2) = nx2(1);
disp(sprintf('Flux = %0.4f, Density = %0.4f, n0 =
%0.5f',flux(2),density(2),n0(2)))

%% Analytical Gating Scheme
disp(' '); disp('-----Analytical Gating-----');
A = zeros(NL*2); % Set up A matrix
A(1,1) = LD(1)/tau(1); A(1,2) = -LD(1)/tau(1); % Flux equals flux
A(NL*2,NL*2-1:NL*2) = [exp(-x(NL)/LD(NL)), exp(x(NL)/LD(NL))]; % Concentration at x=L = 0

for i = 1:NL-1
    A(2*i,(2*i-1):(2*i+2)) = [K(i)*exp(-x(i)/LD(i)),
    K(i)*exp(x(i)/LD(i)), -exp(-x(i)/LD(i+1)), -exp(x(i)/LD(i+1))];
    A(2*i+1,2*i-1:2*i+2) = [LD(i)/tau(i)*exp(-x(i)/LD(i)), -
    LD(i)/tau(i)*exp(x(i)/LD(i)), -LD(i+1)/tau(i+1)*exp(-x(i)/LD(i+1)),
    LD(i+1)/tau(i+1)*exp(x(i)/LD(i+1))];
end

b = zeros(NL*2,1);
b(1) = F;
for i = 1:NL-1
    b(2*i) = -K(i)*G*tau(i+1)+G*tau(i);
end
b(2*NL) = -G*tau(NL)+Conc;

C = A^-1*b;
xAg = zeros(1000,1); yAg = zeros(1000,1); stop = 0;
for i = 1:NL
    start = stop + 1; stop = stop + floor(1000*th(i)/L);

```

Appendix R. Relevant Computer Software

```

if i == 1
    xAg(start:stop,1) = linspace(0,x(i),floor(1000*th(i)/L))';
elseif i == NL
    xAg(start:1000,1) = linspace(x(i-1),x(i),1001-start)';
else
    xAg(start:stop,1) = linspace(x(i-1),x(i),floor(1000*th(i)/L))';
end
yAg(start:stop,1) = C(2*i-1)*exp(-
xAg(start:stop,1)/LD(i))'+C(2*i)*exp(xAg(start:stop,1)/LD(i))+G*tau(i)
;
end
density(3) = trapz(xAg,yAg);
flux(3) = -LD(NL)/tau(NL)*(-C(2*NL-1)*exp(-
L/LD(NL))+C(2*NL)*exp(L/LD(NL)));
n0(3) = C(1)*exp(0)+C(2)*exp(0)+G*tau(1);
disp(sprintf('Flux = %0.4f, Density = %0.4f, n0 =
%0.5f',flux(3),density(3),n0(3)))

%% Finite Difference Gating Scheme
dx = dx1;
disp(' '); disp('-----FE Gating-----');
Nx = floor(L/dx); % number of points
x1 = linspace(0,L,Nx);

A = zeros(Nx);
b = ones(Nx,1).*(-G); stop = 0;

R0ijV = zeros(NL,Nx); R0jiV = R0ijV; tauii = R0ijV; rhoii = R0ijV;
tauj = ones(1,Nx); rhoj = tauj; stop = 0;

for i = 1:Nx
    xv(1,i) = i; % Create distance vector without dx for now
end

for i = 1:NL
    dTh = floor(Nx*th(i)/L);
    start = stop + 1; stop = stop + dTh;
    xR(1,start:stop) = i; % array to determine which layer arbitrary x
is in
    for j = 1:NL
        R0ijV(j,start:stop) = R0ij(j,i);
        R0jiV(j,start:stop) = R0ij(i,j);
    end

    tauj(1,start:stop) = tau(i);
    tauii(i,1:Nx) = tau(i);
    rhoj(1,start:stop) = rhoA(i);
    rhoii(i,1:Nx) = rhoA(i);
    b(start:stop,1) = -G;
    dV(1,start:stop) = d(i);

```

Appendix R. Relevant Computer Software

```

end

stop = 0;
Diagonal = ones(Nx,1)*1/dx^2;
A = diag(Diagonal(1:Nx-1), -1) + diag(Diagonal(1:Nx-1), 1) -
(2)*diag(Diagonal,0);
for i = 1:NL
    dTh = floor(Nx*th(i)/L);
    start = stop + 1; stop = stop + dTh;
    Diag2 = ones(dTh,1)/tau(i);
    A(start:stop,:) = A(start:stop,:)*LD(i)^2/tau(i); % Diffusion
    A(start:stop,start:stop) = A(start:stop,start:stop)-diag(Diag2,0);
% Decay
end

for i = 2:Nx-1 % Add sink
    d4 = max(((xV-i)*dx).^4, ones(1,Nx)*d(xR(i))^4); % Distance^4
    vector with d as lower bound
    A(i,i) = A(i,i) +
dx*sum(1./dV.*pi.*rhoii(xR(i),:).*R0jiv(xR(i),:).^6./(2*tauj.*d4) -
1./dV.*pi.*rhoj.*R0ijV(xR(i),:).^6./(2*tauii(xR(i),:).*d4));
end

stop = 0;
for i = 1:NL-1
    dTh = floor(Nx*th(i)/L);
    stop = stop + dTh;
    % Interfacial flux balance
    A(stop-1,:) = 0;
    A(stop-1,stop-1:stop+2) = [1*LD(i)^2/tau(i), -1*LD(i)^2/tau(i), -
1*LD(i+1)^2/tau(i+1), 1*LD(i+1)^2/tau(i+1)]/dx;
    b(stop-1,1) = 0;

    % Second flux equality
    A(stop,:) = 0;
    A(stop,stop-2:stop+2) = [1*LD(i)^2/tau(i), -1*LD(i)^2/tau(i), 0, -
1*LD(i+1)^2/tau(i+1), 1*LD(i+1)^2/tau(i+1)]/dx;
    b(stop,1) = 0;
end

% Boundary conditions
A(1,1:2) = [1/dx, -1/dx]; % Flux at x = 0
A(Nx,Nx-1:Nx) = [0,1]; % Concentration at x = L
b(1,1) = F; b(Nx,1) = Conc;
nxg = A\b;
flux(4) = LD(end)^2/tau(end)*(nxg(end-1)-nxg(end))/dx;
density(4) = trapz(x1,nxg);
n0(4) = nxg(1);
disp(sprintf('Flux = %0.4f, Density = %0.4f, n0 = %0.5f', flux(4), density(4), n0(4)))

```

Appendix R. Relevant Computer Software

```

%% Convective Gating Finite Differences

dx = dx1;
disp(' '); disp('-----FE Convection-----');
Nx = floor(L/dx); % number of points
x1 = linspace(0,L,Nx);

A = zeros(Nx);
b = ones(Nx,1).*(-G);

R0ijV = zeros(NL,Nx); tauii = R0ijV; rhoii = R0ijV;
tauj = ones(1,Nx); rhoj = tauj; stop = 0;

for i = 1:NL
    dTh = floor(Nx*th(i)/L);
    start = stop + 1; stop = stop + dTh;
    xR(1,start:stop) = i; % array to determine which layer arbitrary x
is in
    for j = 1:NL
        R0ijV(j,start:stop) = R0ij(j,i);
    end
    tauj(1,start:stop) = tau(i);
    tauii(i,1:Nx) = tau(i);
    rhoj(1,start:stop) = rhoA(i);
    rhoii(i,1:Nx) = rhoA(i);
    dV(1,start:stop) = d(i);
    b(start:stop,1) = -G;
end

% Add on a buffer on either side of stack to eliminate velocity edge
effects
NBR = floor(BL/dx); NBL = floor(B0/dx);

for i = 1:Nx+NBR+NBL
    xv(1,i) = i-NBL; % Create distance vector without dx for now
end

R0R = ones(NL,NBR); R0L = ones(NL,NBL);
dR = ones(1,NBR)*d(1); dL = ones(1,NBL)*d(NL);
taur = ones(NL,NBR); tauL = ones(NL,NBL);
xRR = ones(1,NBR)*NL; xL = ones(1,NBL);
rhojR = ones(1,NBR)*rhoA(NL); rhojL = ones(1,NBL)*rhoA(1);
for i = 1:NL
    R0R(i,:) = R0R(i,:)*R0ij(i,NL);
    R0L(i,:) = R0L(i,:)*R0ij(i,1);
    tauR(i,:) = tauR(i,:)*tau(i);
    tauL(i,:) = tauL(i,:)*tau(i);
end

R0ijV = [R0L,R0ijV,R0R];
dV = [dL,dV,dR];
tauii = [tauL,tauii,taur];

```

Appendix R. Relevant Computer Software

```

xR2 = [xL,xR,xRR];
rhoj = [rhojL,rhoj,rhojR];

for j = 1:Nx % Calculate velocity term
    d4 = (xV-j)*dx; % Distance vector
    for i = 1:Nx+NBR+NBL % Add lower bound of distance: intermolecular
spacing
        if abs(d4(i)) < d(xR2(i)) && d4(i) > 0
            d4(i) = d(xR2(i));
        elseif abs(d4(i)) < d(xR2(i)) && d4(i) < 0
            d4(i) = -d(xR2(i));
        elseif abs(d4(i)) < d(xR2(i)) && d4(i) == 0
            d4(i) = 100; % No energy transfer to self if d4 == 0
        end
    end
    v(j) =
dx*sum(1./dV.*pi.*rhoj.*R0ijV(xR(j),:).^6./(2*tauui(xR(j),:).*d4.^3));
% velocity at each x
end

subplot(1,2,1); plot(x1, v); xlabel('Distance from starting interface
(nm)'); ylabel('Velocity (nm/ns)');
stop = 0;
Diagonal = ones(Nx,1)*1/dx^2;
A = diag(Diagonal(1:Nx-1), -1) + diag(Diagonal(1:Nx-1), 1) -
(2)*diag(Diagonal,0);
for i = 1:NL
    dTh = floor(Nx*th(i)/L);
    start = stop + 1; stop = stop + dTh;
    Diag2 = ones(dTh,1)/tau(i);
    A(start:stop,:) = A(start:stop,:)*LD(i)^2/tau(i); % Diffusion
    A(start:stop,start:stop) = A(start:stop,start:stop)-diag(Diag2,0);
% Decay
end

for i = 2:Nx-1 % Add convection
    A(i,i:i+1) = A(i,i:i+1) + [v(i)/dx, -v(i+1)/dx];
end

stop = 0;
for i = 1:NL-1
    dTh = floor(Nx*th(i)/L);
    stop = stop + dTh;
    % Interfacial flux balance - includes velocity now
    A(stop-1,:) = 0;
    A(stop-1,stop-1:stop+2) = [1*LD(i)^2/tau(i), -1*LD(i)^2/tau(i), -
1*LD(i+1)^2/tau(i+1), 1*LD(i+1)^2/tau(i+1)]/dx + [0,v(stop),-
v(stop+1),0];
    b(stop-1,1) = 0;

    % Second flux equality

```

Appendix R. Relevant Computer Software

```

A(stop,:) = 0;
A(stop,stop-2:stop+2) = [1*LD(i)^2/tau(i), -1*LD(i)^2/tau(i),0,-
1*LD(i+1)^2/tau(i+1), 1*LD(i+1)^2/tau(i+1)]/dx+ [0,v(stop-1),0,-
v(stop+1),0];
b(stop,1) = 0;
end

% Boundary conditions
A(1,1:2) = [1/dx, -1/dx]; % flux at x = 0 - no velocity included for
non-quenching
A(Nx,Nx-1:Nx) = [0,1]; % Concentration at x = L
b(Nx,1) = Conc; b(1,1) = F*tau(1)/LD(1)^2;
nx1 = A\b;
flux(5) = LD(end)^2/tau(end)*(nx1(end-1)-nx1(end))/dx;
density(5) = trapz(x1,nx1);
n0(5) = nx1(1);
disp(sprintf('Flux = %0.4f, Density = %0.4f, n0 = %0.5f',flux(5),density(5),n0(5)))

%% Plot solution

subplot(1,2,2); plot(x1, nxg, x1,nx1,'-',x2,nx2,:',xA,yA,xAg,yAg);
legend('FE Bulk', 'FE Convection','FE Simple Diffusion','Analytical
Diffusion','Analytical Gating');
ylabel('Exciton Density'); xlabel('Distance from starting interface
(nm)');

disp('Saving...')
dataArray = {0}; m = 2;
for i = 1:length(x1)
    if i/SS == round(i/SS)
        dataArray{m,1} = x1(i);
        dataArray{m,2} = nxg(i);
        dataArray{m,3} = nx1(i);
        dataArray{m,4} = v(i);
        m = m + 1;
    end
end
for i = 1:length(xA)
    dataArray{i+1,5} = xA(i);
    dataArray{i+1,6} = yA(i);
    dataArray{i+1,7} = yAg(i);
end

Header = {'Analytical Diffusion','FE Diffusion','Analytical Gating','FE
Bulk Sink','FE Convection'};
for i = 1:5
    dataArray{1,9+i} = Header{i};
    dataArray{2,9+i} = flux(i);
    dataArray{3,9+i} = density(i);
    dataArray{4,9+i} = n0(i);
end

```

Appendix R. Relevant Computer Software

```
DataArray{2,9}='Flux'; DataArray{3,9}='density'; DataArray{4,9} =
'n(0)';

Header = {'x1','FE Bulk Sink','FE
Convection','Velocity','xA','Analytical Diffusion','Analytical
Gating'};
for i = 1:7
DataArray{1,i} = Header{i};
end

H2 = {'B0','BL','dx1','dx2','F','G','Conc','d','tau','th','R0ij'};
data = {B0,BL,dx1,dx2,F,G,Conc,0,0,0,0};
for i = 1:11
DataArray{i+6,9} = H2{i};
DataArray{i+6,10} = data{i};
end

for i = 1:length(d)
    DataArray{14,9+i} = d(i);
    DataArray{15,9+i} = tau(i);
    DataArray{16,9+i} = th(i);
end
[nr,nc] = size(R0ij);
for i = 1:nr
    for j = 1:nc
        DataArray{16+i,9+j} = R0ij(i,j);
    end
end
warning off MATLAB:xlswrite:AddSheet
xlswrite(fullfile(filePath,fileName),DataArray,sheetName)

disp(' ');
disp(' ');
end % function
```

Notes

Notes

Notes